FUNDAMENTALS OF FOUNDATION ENGINEERING

and their applications

2nd Edition

G. Kouretzis

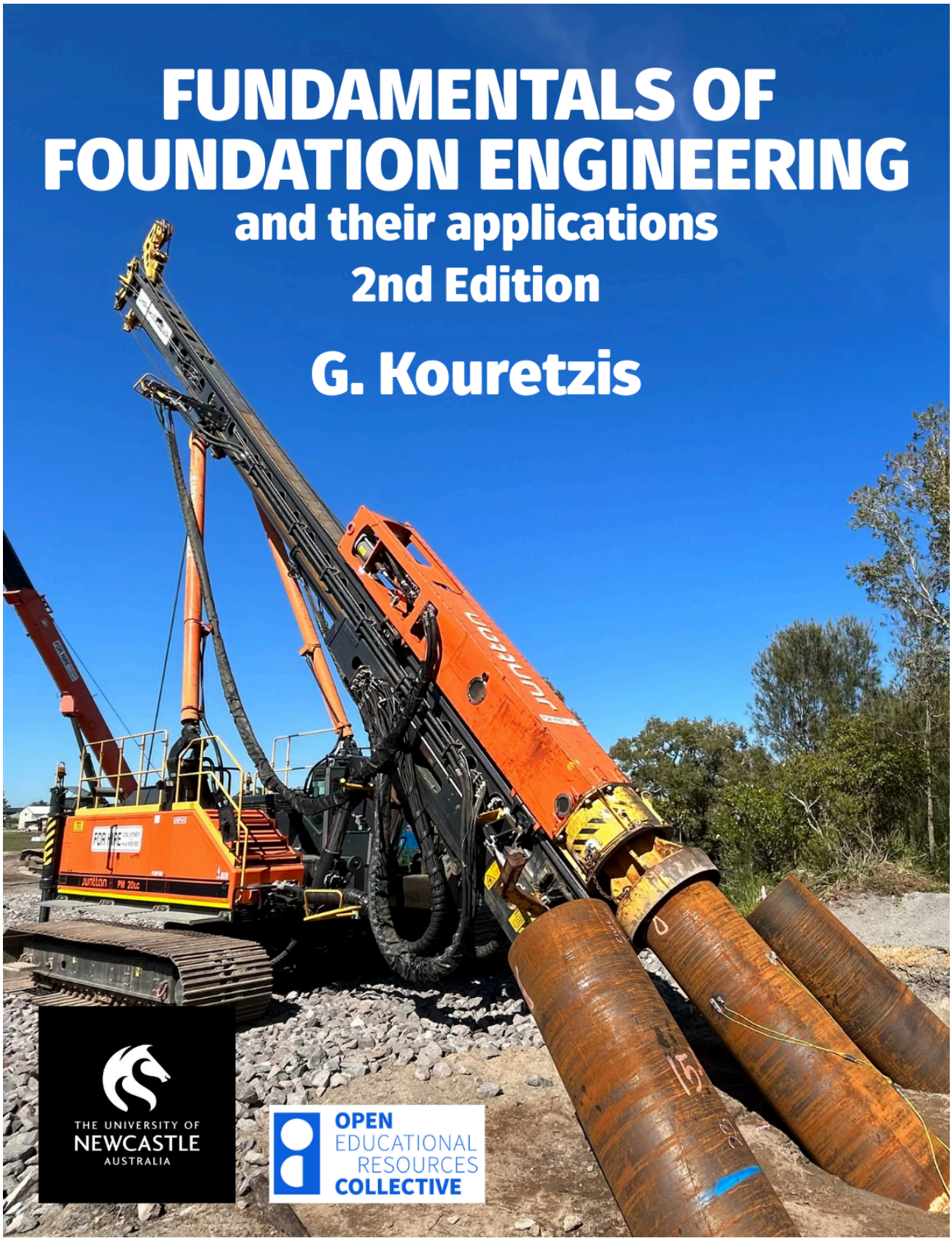

THE UNIVERSITY OF NEWCASTLE AUSTRALIA

OPEN EDUCATIONAL RESOURCES COLLECTIVE

Fundamentals of foundation engineering and their applications

FUNDAMENTALS OF FOUNDATION ENGINEERING AND THEIR APPLICATIONS

2nd edition

GEORGE KOURETZIS

University of Newcastle
Newcastle, Australia

Fundamentals of foundation engineering and their applications Copyright © 2025 by University of Newcastle & G. Kouretzis is licensed under a Creative Commons Attribution 4.0 International License, except where otherwise noted.

This book was published by University of Newcastle via the Council of Australasian University Librarians Open Educational Resources Collective. The online version is available at https://oercollective.caul.edu.au/fundamentals-of-foundation-engineering

Disclaimer

Note that corporate logos and branding are specifically excluded from the Creative Commons Attribution (CC BY) 4.0 Licence of this work, and may not be reproduced under any circumstances without the express written permission of the copyright holders.

Copyright

Unless otherwise noted, *Fundamentals of foundation engineering and their applications* by G. Kouretzis is licensed under a Creative Commons Attribution (CC BY) 4.0 Licence by University of Newcastle.

Recommended citation: Kouretzis, G. (2025). *Fundamentals of foundation engineering and their applications*. University of Newcastle. https://oercollective.caul.edu.au/fundamentals-of-foundation-engineering

Recommended attribution: *Fundamentals of foundation engineering and their applications* by G. Kouretzis is licensed under a Creative Commons Attribution (CC BY) 4.0 Licence by University of Newcastle.

Cover illustration attribution: Isaac Montford/Civil Sydney Pty Ltd., licensed under Creative Commons Attribution NonCommercial (CC BY) 4.0: https://creativecommons.org/licenses/by/4.0/

CONTENTS

Acknowledgement of Country xiii
About the Author xiv
Copyright xv
Accessibility Information xvii
Accessibility features of the web version of this resource xvii
Other file formats available xvii
Third-Party Content xvii
Known accessibility issues and areas for improvement xvii
Accessibility Improvements xviii
Acknowledgements xix
Introduction 1

1. GEOTECHNICAL SITE INVESTIGATION AND IN SITU TESTING

1.1 Introduction to Part 1 3
1.2 Preliminary site exploration 6
1.2.1 Desk study 6
1.2.2 Field reconnaissance visit 7
1.3 Site exploration plan 9
1.4 Boreholes and sampling methods 10
1.5 The Standard Penetration Test (SPT) 18
1.6 Establishing the Geotechnical Model of a site 26
Example 1.1 27
Establishing a geotechnical model for the geotechnical design of a bridge foundation
1.7 The Cone Penetration Test (CPT) 32

1.8 Interpretation of CPT measurements to derive soil parameters 40
1.8.1 Equivalent N-SPT values 41
1.8.2 Undrained shear strength, Su 43
1.8.3 Clay sensitivity, St 45
1.8.4 Overconsolidation ratio, OCR and lateral earth pressure coefficient at-rest, K0 46
1.8.5 Relative density Dr and friction angle φ' of sands 47
1.8.6 Soil unit weight, γ 49
1.8.7 Compressibility parameters E' and mv 49
1.9 The Vane Shear test 52
1.10 The Flat Dilatometer (DMT) Test 55
1.11 Geophysical methods for soil exploration 57
1.11.1. Seismic surveys 57
1.11.2. Electrical resistivity method 59
1.11.3. Ground penetration radar (GPR) 61
1.12 References 63
1.13 Additional problems 65

2. SOIL AND GROUNDWATER CONTAMINATION AND REMEDIATION TECHNIQUES – AN INTRODUCTION TO GEOENVIRONMETAL ENGINEERING

2.1 Introduction to Part 2 70
2.2 Characteristic cases studies of soil and groundwater contamination 73
2.3 Management framework for contaminated land in Australia 78
2.4 Sources of geoenvironment contamination 79
Natural processes 79
Human activities related to waste management 79
Other human activities/Accidents 79
2.5 Types of waste and pollutants and tolerable concentration levels 80
2.6 Geotechnical investigations in contaminated sites 84

2.7 Mechanisms of contaminants transport through soil 86
2.7.1 Advection or Hydraulic transportation 86
2.7.2 Diffusion or molecular diffusion 87
2.7.3 Dispersion or mechanical dispersion 88
2.8 Contamination control and remediation methods 91
2.8.1. Groundwater contamination control and remediation methods 91
2.8.2. Soil contamination control and remediation methods 97
Example 2.1 99
Selection of remediation method on the basis of comparative analysis
2.9 Design of a pump-and-treat installation 103
2.10 Design of a pollutant containment installation 107
2.11 References 110

3. STRESSES IN SOIL FROM EXTERNAL LOADINGS

3.1 Introduction to Part 3 112
3.2 Stresses in the soil due to a point load 115
3.3 Stresses in the soil due to a line load 116
3.4 Stresses in the soil due to a strip pressure 118
3.5 Stresses in the soil due to a circular pressure 120
3.6 Stresses in the soil due to a rectangular pressure 121
3.7 Discussion 123
Example 3.1 128
Stresses in soil due to a water tank founded on a ring-type foundation
Example 3.2 130
Numerical estimation of stresses below a ring-type foundation
3.8 References 134
3.9 Additional problems 135

4. SETTLEMENT OF SHALLOW FOUNDATIONS

4.1 Introduction to Part 4 140

4.2 Causes of settlement 142

4.3 Tolerable settlement 144

4.4 Components of settlement due to structural loading 146

4.5 Immediate settlement of shallow foundations 149

Example 4.1 157

Immediate settlement of a footing resting on saturated clay

Example 4.2 159

Numerical estimation of the load-settlement curve of a footing resting on a sand layer

4.6 Primary consolidation settlement of shallow foundations 165

Example 4.3 175

Estimation of 1-D primary consolidation settlement assuming linear elastic soil response

Example 4.4 177

Estimation of a 1-D primary consolidation settlement using the results of an oedometer test

Example 4.5 179

Estimation of 2-D primary consolidation settlement

4.7 Immediate and consolidation deformations underneath shallow foundations imposing 3-D loading conditions 181

A theory of elasticity approach

4.8 Evolution of primary consolidation settlement with time 188

4.9 Estimation of secondary compression settlement 193

Example 4.6 195

Numerical simulation of 1-D consolidation

Example 4.7 201

Numerical simulation of 2-D consolidation

Example 4.8 207

The importance of boundary conditions

4.10 References 211

4.11 Additional problems 212

5. BEARING CAPACITY OF SHALLOW FOUNDATIONS

5.1 Introduction to Part 5 217

5.2 Some fundamentals: Load and Resistance Factor Design (LRFD) & Shear strength of soils 218

Example 5.1 233

Design of a circular footing according to AS5100.3 with analytical methods

Example 5.2 235

Estimation of the short-term undrained collapse load with numerical methods

5.3 Some fundamentals of the bearing capacity of shallow foundations 240

5.4 Common bearing capacity equations and practical considerations 250

Example 5.3 258

Estimation of the long-term and short-term design capacity of a rectangular footing according to AS5100.3 with the bearing capacity equations

5.5 Bearing capacity of footings on layered soils 262

Example 5.4 269

Design capacity of a footing resting on a two-layer formation according to AS5100.3

Example 5.5 272

Design of shallow foundations at the Ultimate Limit State using numerical methods

5.6 Numerical modelling of footings resting on the surface of drained soil 279

5.7 Bearing capacity from Standard Penetration Test (SPT) results 281

Example 5.6 282

Design capacity from in situ tests: SPT

5.8 Bearing capacity from Cone Penetration Test (CPT) results 284

Example 5.7 285

Design capacity from in situ tests: CPT

5.9 References 287

5.10 Additional problems 288

6. PILE FOUNDATIONS

6.1 Introduction to Part 6 291

6.2 Common pile types 295

6.3 Installation of driven piles 299
6.4 Construction of drilled shafts 300
6.5 Load transfer mechanisms 302
6.6 Pile driving effects 304
6.7 Piles subjected to axial compressive loads - general concepts 308
6.8 Load and Resistance Factor Design of piles subjected to axial compressive loads according to AS2159 310
6.9 Ultimate geotechnical strength of piles subjected to axial compressive load under undrained conditions (α-Method) 314
6.10 Ultimate geotechnical strength of piles subjected to axial compressive load under drained conditions (β-Method) 318
6.11 Ultimate geotechnical strength of piles subjected to axial compressive load from SPT test results 323
6.12 Ultimate geotechnical strength of piles subjected to axial compressive load from CPT test results 325
6.13 Design of drilled shafts socketed in soft rock to resist axial compressive loads 339
6.14 Ultimate geotechnical strength of drilled shafts subjected to axial compressive loads 354
6.15 Ultimate geotechnical strength of piles subjected to axial tensile loads 357
Example 6.1 359
Estimation of the design bearing capacity of a pile according to AS2159 using the α-Method and the ICP method
Example 6.2 362
Estimation of the design bearing capacity of a single pile according to AS2159 using the α- and β-Methods - Multilayered soil profile case
Example 6.3 367
Numerical estimation of the ultimate geotechnical strength of a single pile in homogeneous soil, considering undrained behaviour
Example 6.4 374
Numerical estimation of the ultimate geotechnical strength of a single pile in multilayered soil
Example 6.5 379
Estimation of the ultimate geotechnical strength of a pile subjected to axial compressive load based on SPT test results

Example 6.6 381
Estimation of the ultimate geotechnical strength of a pile subjected to axial compressive load based on CPT test results
6.16 Static pile load tests 386
6.17 Pile driving formulas 395
6.18 Pile group effects on ultimate geotechnical strength 397
Example 6.7 401
Estimation of the design bearing capacity of a pile group
6.19 Immediate settlement of single piles 404
Example 6.8 415
Calculation of settlement of a friction pile in homogeneous soil
Example 6.9 418
Calculation of settlement of an end-bearing pile in layered soil
6.20 Immediate settlement of pile groups 422
Example 6.10 429
Calculation of settlement of a group of piles connected with rigid and flexible pile cap
6.21 Consolidation settlement of pile groups 432
6.22 Negative skin friction effects 435
Example 6.11 440
Numerical simulation of negative skin friction effects: estimation of the elevation of the neutral plane for different applied load levels
6.23 Lateral loading of piles – General considerations 446
6.24 Broms method – Piles in undrained soil 451
Example 6.12 460
Calculation of the ultimate geotechnical strength and of the pile head deflection of a laterally loaded pile driven in undrained soil
6.25 Broms method – Piles in drained soil 462
Example 6.13 470
Calculation of the ultimate geotechnical strength and of the pile head deflection of a laterally loaded pile driven in drained soil
6.26 Rigorous elasticity method for estimating pile deformations 472
Example 6.14 475
Calculation of pile head deflection and rotation with the Zheng et al. (2024) method

6.27 Numerical beam-on-nonlinear Winkler spring methods for the analysis of piles subjected to lateral loading 477
Example 6.15 491
Analysis of a concrete pile embedded in layered soil with the beam-on-nonlinear Winkler spring method for lateral loading
6.28 Pile group effects on the lateral load response of piles 494
Example 6.16 500
Estimation of the p-y curve reduction factor for a laterally loaded pile group
6.29 References 502
6.30 Additional problems 505

Appendix A: Phase relationships 509
Appendix B: List of main symbols 512
Version History 520

ACKNOWLEDGEMENT OF COUNTRY

The University of Newcastle Library acknowledges the traditional custodians of the lands within our footprint areas: the Awabakal, Darkinjung, Biripai, Worimi, Wonnarua, and Eora Nations. We also pay respect to the wisdom of our Elders past and present. We extend that respect to all Aboriginal, Torres Strait Islander, and other First Nations peoples who use this resource.

We acknowledge that sovereignty was never ceded. This always was, and always will be, Aboriginal land.

ABOUT THE AUTHOR

George Kouretzis obtained a Master in Civil Engineering from the Democritus University of Thrace, Greece, followed by a MSc and a PhD from the National Technical University of Athens (NTUA), Greece in 2005. In the following years, he continued his engagement with the School of Civil Engineering, NTUA first as a post-doctoral researcher and later as a (part-time) lecturer. After a 4-year period where he was primarily engaged with engineering consulting activities, George moved to Australia to join the University of Newcastle in 2012, where he currently holds an Associate Professor position in the School of Engineering.

His research interests lie in the fields of pipeline engineering, soil-foundation-structure interaction, computational geomechanics and geotechnical earthquake engineering. He has published over 100 refereed journal papers, peer-reviewed conference papers and book chapters on the analysis of buried pipelines affected by geohazards, the analysis of shallow and deep foundations under static and dynamics loads, the simulation of large deformation problems in geomechanics etc. In parallel he has served as associate editor of the Canadian Geotechnical Journal (2015-2021), currently sits on the editorial board of Computers and Geotechnics and of the Canadian Geotechnical Journal, and has served as a guest editor of special issues published in the Canadian Geotechnical Journal, Computers and Geotechnics etc.

Parallel to his academic activities, he has been involved since 2000 as an expert engineering consultant in a series of major energy and transportation infrastructure projects, including high- and medium-pressure natural gas and crude oil pipeline networks, bridges and motorway tunnels in areas of high seismicity, critical runway embankments etc.

Finally, George is the recipient of several awards for research and teaching excellence from the International Association for Computer Methods and Advances in Geomechanics IACMAG, the Institution of Civil Engineers ICE, UK, the Australian Association of Computational Mechanics ACCM etc.

More information: www.newcastle.edu.au/profile/georgios-kouretzis

Published works: www.researchgate.net/profile/George-Kouretzis

Email: georgios.kouretzis@newcastle.edu.au or gkouretz@gmail.com

COPYRIGHT

First published in 2025 by

University of Newcastle
University Drive Callaghan NSW 2308
AUSTRALIA

© 2025 University of Newcastle & George Kouretzis.

Unless otherwise indicated, this work is licensed under Creative Commons Attribution NonCommercial (CC BY) 4.0: https://creativecommons.org/licenses/by/4.0/

Note that corporate logos and branding are specifically excluded from the CC BY 4.0 Licence of this work, and may not be reproduced under any circumstances without the express written permission of the copyright holders.

Material directly reproduced from Australian Standards is © Standards Australia and used here with permission. Reuse outside of this work requires prior written permission from Standards Australia.

For other third-party materials, ownership and © is as indicated. Any reuse outside of this work will require reliance on the licensing already in place, use under an appropriate exception in your copyright legislation, or permission from the copyright owner/s, as applicable.

Every effort has been made to trace and acknowledge owners of copyright material. If notified of any errors or omissions the publisher will be pleased to rectify them at the earliest opportunity.

The moral rights of the creators have been asserted.

ISBN: 978-0-7259-0289-6 (digital)
ISBN: 978-0-7259-0335-0 (print)
DOI: https://doi.org/10.71862/55ad-r630

A catalogue record for this book is available from Libraries Australia.

Book design and layout: George Kouretzis, Ruth Cameron, and Anthony O'Brien.

Cover image courtesy of Isaac Montford/Civil Sydney Pty Ltd., licensed under Creative Commons Attribution NonCommercial (CC BY) 4.0: https://creativecommons.org/licenses/by/4.0/

ACCESSIBILITY INFORMATION

We believe that education must be available to everyone which means supporting the creation of free, open, and accessible educational resources. We are actively committed to increasing the accessibility and usability of the textbooks we produce.

Accessibility features of the web version of this resource

The web version of this resource has been designed with accessibility in mind by incorporating the following features:

- It has been optimized for people who use screen-reader technology.
  - all content can be navigated using a keyboard
  - links, headings, and tables are formatted to work with screen readers
  - images have alt tags
- Information is not conveyed by colour alone.

Other file formats available

In addition to the web version, this book is available in a number of file formats including PDF, EPUB (for eReaders), and various editable files. Choose from the selection of available file types from the 'Download this book' drop-down menu. This option appears below the book cover image on the eBook's landing page.

Third-Party Content

In some cases, our open text includes third-party content. In these cases, it is often not possible to ensure accessibility of this content.

Known accessibility issues and areas for improvement

While we strive to ensure that this resource is as accessible and usable as possible, we might not always get it right. Any issues we identify will be listed below. There are currently no known issues.

List of Known Accessibility Issues

Location of issue	Need for improvement	Timeline	Work around

Accessibility Improvements

While we strive to ensure that this resource is as accessible and usable as possible, we might not always get it right. We are always looking for ways to make our resources more accessible. If you have problems accessing this resource, please contact Ruth.Cameron@newcastle.edu.au to let us know so we can fix the issue.

Copyright Note: This accessibility disclaimer is adapted from BCampus's Accessibility Toolkit, licensed under a Creative Commons Attribution 4.0 International license and University of Southern Queensland's Enhancing Inclusion, Diversity, Equity and Accessibility (IDEA) in Open Educational Resources (OER) licensed under a Creative Commons Attribution-NonCommercial-ShareAlike 4.0 International License.

ACKNOWLEDGEMENTS

The author is grateful to Ruth Cameron for converting the material to a format compatible to the Pressbooks platform, and for providing continuous support during the typesetting and proofreading process. The author would also like to acknowledge Anthony O'Brien for his guidance on copyright and attribution issues.

INTRODUCTION

This resource is primarily based on teaching material developed by the author over several years for courses offered by the University of Newcastle, Australia. It builds upon fundamentals of Soil Mechanics and Foundation Engineering introduced elsewhere, and it assumes that the reader has some familiarity with basic soil mechanics concepts. The resource is focused on application of fundamental soil mechanics concepts to practical Geotechnical Engineering tasks, such as: interpretation of geotechnical investigation results, design of shallow foundations under serviceability and ultimate limit state conditions, and analysis and design of deep foundations. In addition to the above, the resource includes a brief introduction to Geoenvironmental Engineering, concentrating on the problem of soil and groundwater contamination, the description of relevant remediation techniques and the demonstration of simple methods for the design of remediation facilities.

The analytical and empirical state-of-practice and state-of-the-art methodologies covered in this resource conform (or have been adapted by the author) to the pertinent Australian Standards, which are extensively referenced in the text, whereas normative design concepts such as the Load and Resistance Factor Design are demonstrated, via their application in numerous worked examples.

In parallel, the use of numerical methods in Geotechnical and Foundation Engineering is introduced, by means of several example problems treated with the industry-standard finite element code PLAXIS. Emphasis is not put on linear and non-linear finite element theory or advanced numerical modelling techniques and soil constitutive models, but rather on the use of numerical methods to tackle fundamental Geotechnical (and Geoenvironmental) Engineering problems, and on key modeling issues encountered in everyday practice. The concept of using simpler, analytical methods to validate numerical analysis results and guide the development of more complex, real-world models is underlined.

Do you have feedback? Please let the author know, via the feedback form for *Fundamentals of Foundation Engineering and their Applications* at https://bit.ly/NewcastleOER.

Disclaimer:

Although every effort has been made to interpret the cited references correctly, there is no warranty expressed or implied that the interpretation is correct, complete or accurate. The interpretation reflects the views and experience of the author, and where applicable this is clearly stated in the text. If there is a question of whether the interpretation has been correctly made, the reader should consult the appropriate reference before applying it in practice. There is also no warranty that every equation in the text has been correctly typeset. It is the reader's responsibility to check the results of any equation that has been used. To catch equation errata the author, in addition to presenting the equation, has usually used the equation in an example. The author and the University of Newcastle, Australia are not liable for any loss of profit or any other commercial damages, including but not limited to special, incidental, consequential, or other damages. If professional advice or other expert assistance is required, the services of a competent professional should be sought. The contents do not necessarily reflect policy of the University of Newcastle, Australia.

1. GEOTECHNICAL SITE INVESTIGATION AND IN SITU TESTING

1.1 INTRODUCTION TO PART 1

Application of geotechnical engineering principles for the analysis and design of geostructures (shallow and deep foundations, earthworks etc.) is based on several soil parameters, which are used to quantify its behavior. Commonly, laboratory tests are performed to characterise and classify soils *(sieve analysis, hydrometer analysis, water content measurements*, *Atterberg limits tests)*, as well as to quantify their compressibility (*oedometer and constant-rate-of strain 1D compression tests*), shear strength *(triaxial tests, direct shear tests, etc.)* and permeability *(constant head and falling head tests)* parameters. All these tests are performed in soil samples, which are retrieved from the area of "geotechnical interest". The number of samples, the location from where these samples are retrieved, the depth, and the method of extraction *(sampling)* depend of course on the structure and its foundation properties, and are all part of the *Geotechnical Site Investigation.*

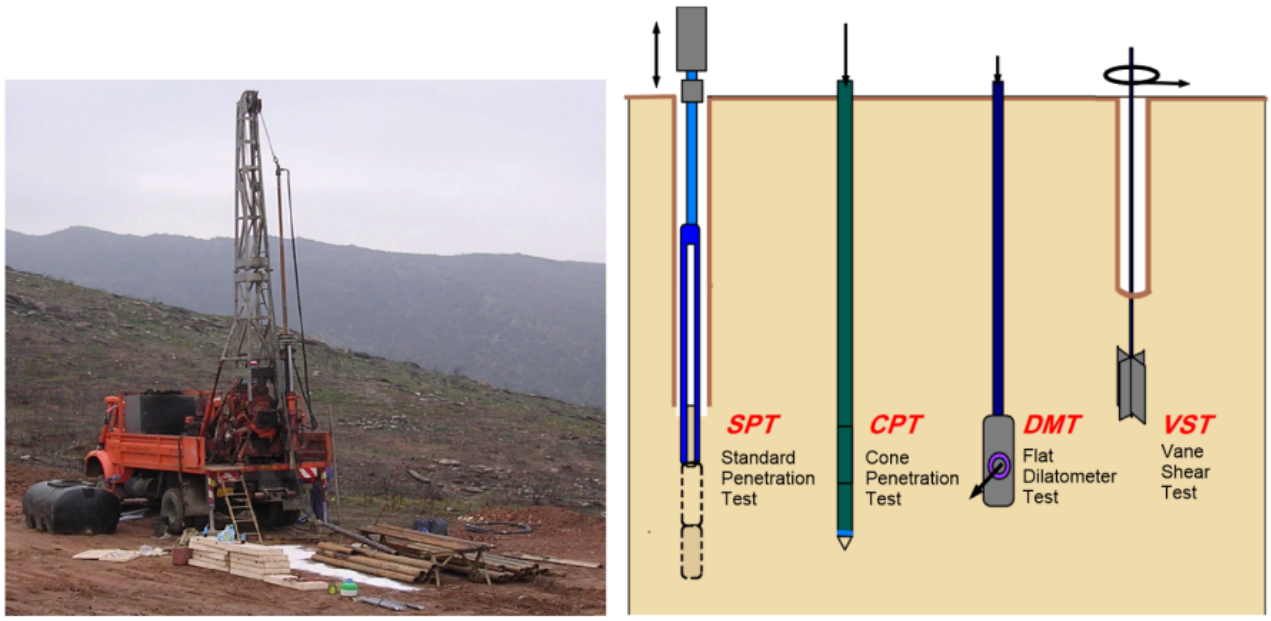

Figure 1.1. (a) Drilling of a sampling borehole (author's own photo); (b) In situ testing methods covered in Part 1 (FHWA 2006, no copyright restrictions).

Furthermore, retrieving soil samples from boreholes and testing them in the laboratory, is often complemented with (or even replaced with) *in situ* tests (Figure 1.1), which offer some advantages such as minimal soil disturbance due to sampling, fast and economical testing, as well as the retrieval of continuous information along the soil profile. Typically, measurements obtained during *in situ* tests are not directly correlated to soil properties, and proper interpretation of measurements is necessary to derive soil parameters by means of correlation formulas.

Australian Standard AS1726 formally defines Geotechnical Site Investigation as *"...the process of evaluating the geotechnical character of a site in the context of existing or proposed works or land usage"*. Evaluating the *geotechnical character* of a site may include one or more of the following:

- Evaluation of the geology and hydrogeology of the site.
- Examination of existing geotechnical information pertaining to the site.
- Excavating or boring in soil or rock.
- *In situ* assessment of geotechnical properties of subsoil materials.
- Recovery of samples of soil or rock for examination, identification, recording, testing or display.
- Testing of soil or rock samples to quantify properties relevant to the purpose of the investigation.

- Reporting of the results.

During planning and implementation of a geotechnical site investigation aimed at determining all the necessary geotechnical parameters for e.g., the design of a foundation system (i.e., determine the shallow footing's dimensions, the necessary number and length of piles etc.) the Geotechnical Engineer is called to answer certain key questions, such as:

- What is the necessary number of boreholes to obtain adequate information on the geotechnical character of the site?
- Where will these boreholes be drilled? What kind of equipment/drilling technique is appropriate for the particular site?
- What is the minimum required depth that the boreholes must reach to obtain sufficient information?
- Are any soil samples going to be retrieved for laboratory testing? How many samples are required for the proper assessment of the soil parameters? What sampling methods should be used?
- Should any *in situ* tests be performed to measure soil properties and, if so, what type of tests?
- Should any monitoring instruments be installed to measure groundwater table fluctuations, possible slope movements, etc.?

The results of a geotechnical investigation campaign are rarely straightforward, as subsoil itself is non-uniform: at the same site, layers of sand, clay, silt, gravels (and mixtures of them) or rock formations may co-exist. The role of the Geotechnical Engineer is to gather all this perhaps chaotic information resulting from the geotechnical investigation, including results from laboratory and *in situ* tests, and properly interpret them so as to:

- Explicitly define layers of different soil (or rock) formations, *that exhibit the same behavior in terms of engineering response, and thus can be described by a single set of compressibility, shear strength and permeability parameters.*
- Provide *characteristic* values of the shear strength, compressibility and permeability parameters of each one of the layers, suitable for the safe and economic design of the planned geotechnical works.
- Identify the groundwater table level and its possible variation within the lifetime of the project.

...in other words, built the "geotechnical model" of the site

Usually these results are reported in the form of geotechnical cross-sections (Figure 1.2), where the geometry and the extent of the different geotechnical layers is graphically depicted, together with groundwater table levels, key results from *in situ* tests, and any other critical information on the project. Description of geotechnical layers must be accompanied by lists/tables containing the interpreted characteristic values of the parameters required for the analysis of the behaviour and the design of geotechnical works.

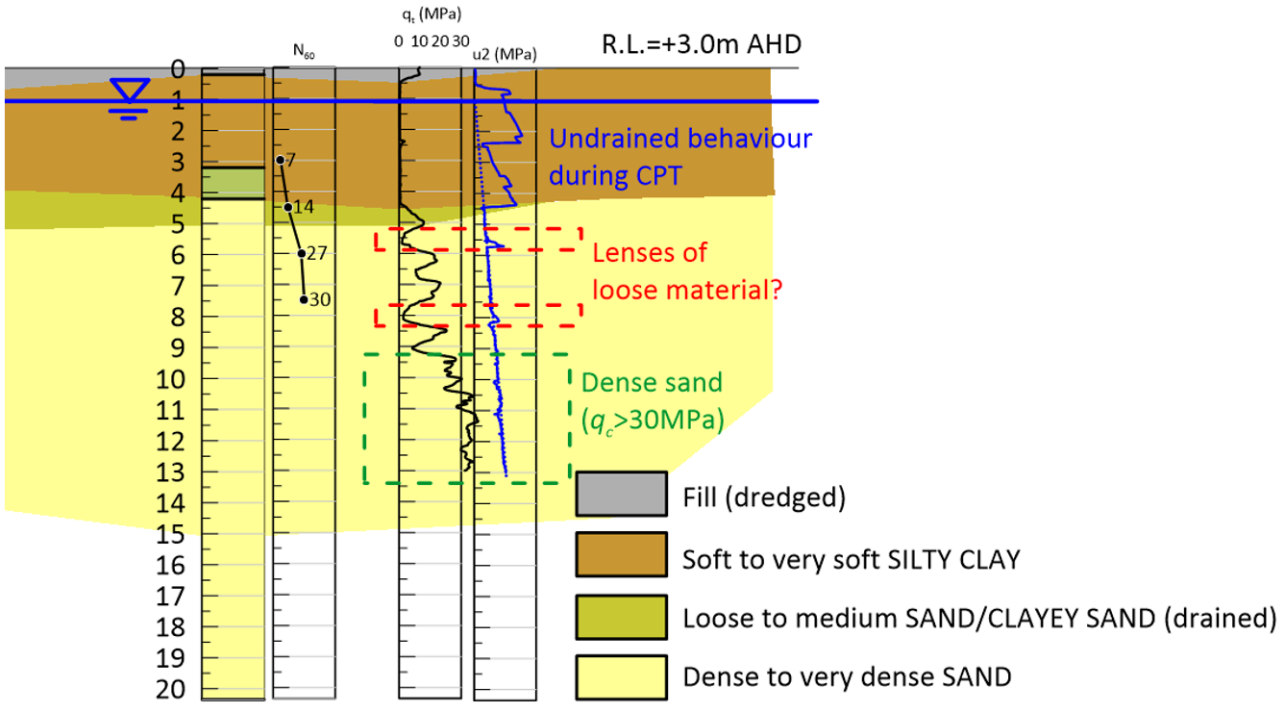

Figure 1.2. Typical geotechnical cross-section overlapped with in situ test data (CPT, SPT) and description of geotechnical layers.

Additionally, a geotechnical investigation and interpretation report should provide information regarding:

- Potential geological hazards e.g., earthquakes, landslides.
- Dewatering requirements during construction.
- Stability of temporary works during construction e.g., cuts.
- Potential effect of works on existing nearby structures, including cracks due to differential settlement, slope instability, effects of construction vibration due to possible pile driving etc.
- Construction access issues.

Certain key components of a geotechnical investigation campaign are described in the following chapters.

1.2 PRELIMINARY SITE EXPLORATION

1.2.1 Desk study

Any subsurface investigation program should primarily account for the type, size and importance of the structure, the existence of any other structures that could affect or be affected by construction works, and the location of underground utilities that may interact with the project or the investigation works e.g., gas pipelines.

Before moving the testing equipment on site, or deciding on the number and depth of boreholes (or *in situ* tests) to be performed, a desk study is necessary for collecting and analysing all existing relevant data (Table 1.1). A review of available information prior planning a new investigation program will help establishing what to look for in the site.

or, as Glossop (1968) stated in his Rankine Lecture (FHWA, 2006):

"If you don't know what you should be looking for in a site investigation, you are not likely to find much of value"

Table 1.1.Sources of historical data (with information from FHWA 2006).

Utility maps	• Identify buried utility locations • Prevent damage to utilities
Aerial photographs	• Track site changes over time • Identify possible landslide areas • Identify nearby structures or artificial fills
Topographic maps	• Identify possible access restrictions • Estimate site topography and physical features
Geological maps and reports	• Provide general information on soil/rock types encountered in the area, areas of possible instabilities, hydrogeological conditions, areas of potential acid sulfate soils
Seismic hazard maps	• Determine the design seismic acceleration and the expected earthquake magnitude during the lifetime of the project
Water well logs	• Assess current groundwater levels and fluctuation with time
Flood maps	• Identify floodplains • Provide information on scour potential • Determine the maximum groundwater level over the lifetime of the project
Geotechnical investigation reports from existing, nearby structures	... always a good point to start!

1.2.2 Field reconnaissance visit

After the desk study, a site inspection visit will always provide valuable information regarding access of drilling and *in situ* testing equipment, topography, areas of active or historical landslides, nearby structures etc. A field reconnaissance visit should include, according to FHWA (2006):

- Inspection of nearby structures to determine their performance with the particular foundation type

utilised. If settlement is suspected, the original structural plans should be reviewed, and the structure should be surveyed by using the original benchmark.
- For water crossings, inspection of existing foundations and of the stream banks for evidence of scour.
- Identification of the location, type and depth of any existing structures which may obstruct construction works.
- Relating site conditions with the proposed boring operations and record potential problems with utilities, site access, private property or obstructions.

A thorough site inspection is a must for planning a successful geotechnical investigation program, in order to avoid unnecessary delays and extra costs at later stages.

1.3 SITE EXPLORATION PLAN

Determining the extent and detail of the site investigation is a cost-benefit procedure. As illustrated in Figure 1.3, a properly planned geotechnical investigation, that will provide all the necessary information for rational and safe geotechnical design, will result in optimising project costs, but also prevent additional costs for repairs, or even possible failure of the structure.

The Geotechnical Engineer will often rely on their experience for preparing an appropriate exploration plan. There are however some guidelines, which can be used to estimate the minimum required number of sampling boreholes and their depth (Table 1.2) depending on the type and properties of the structure, when no other regulatory agency or project specific requirements prevail.

1.4 BOREHOLES AND SAMPLING METHODS

Sampling boreholes are a critical part of any geotechnical investigation campaign. They are performed to:

- Identify the distribution of geomaterials with distinctive properties into the subsoil, including the presence and thickness of layers.
- Retrieve samples for laboratory tests.
- Determine the depth of the groundwater table, through installation of piezometers.
- Provide access for the introduction of *in-situ* testing devices.

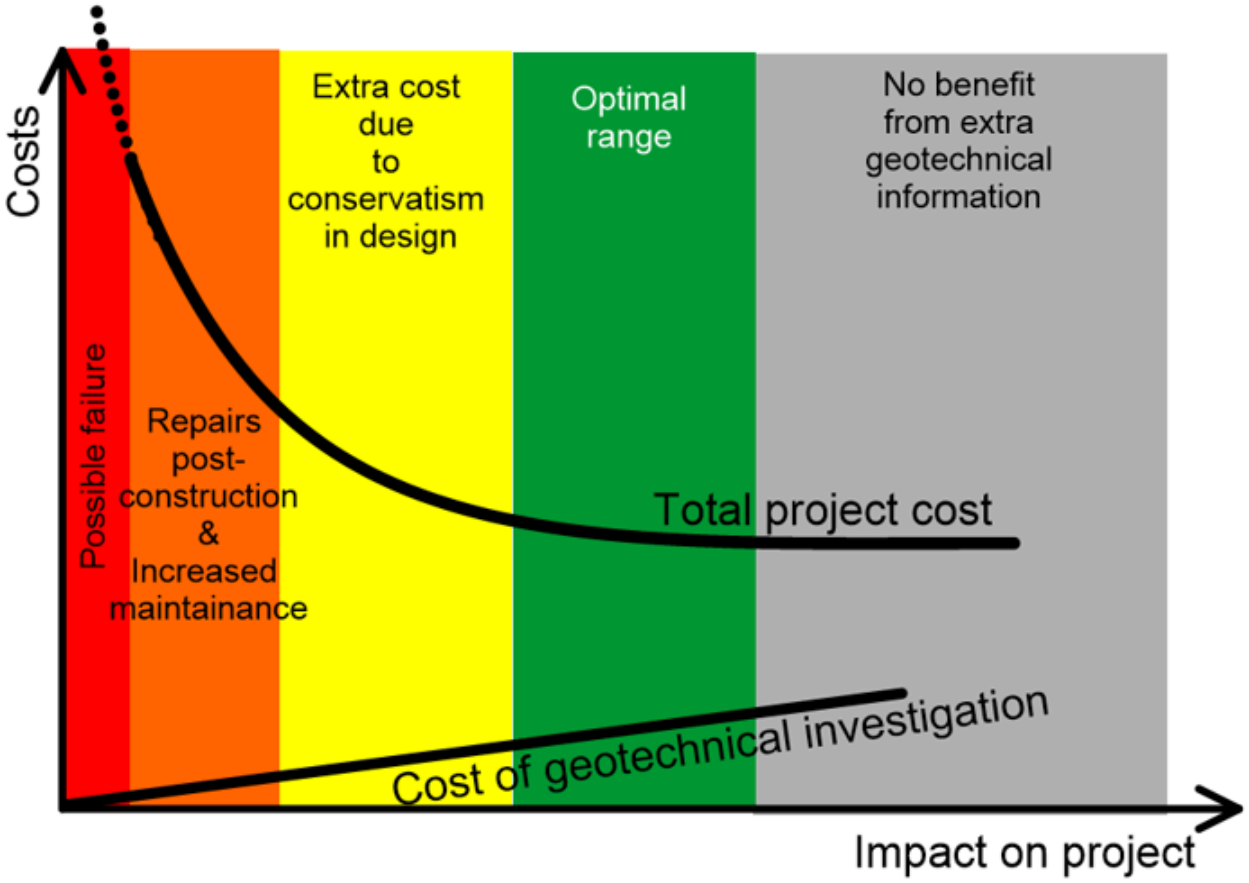

Figure 1.3. Effect of soil investigation on potential projects costs.

Table 1.2.Minimum number and depth of borings, for different (geo)structures (with information from Gunaratne 2006 and FHWA 2002).

(Geo)structure type	Minimum number of sampling boreholes	Minimum depth of sampling boreholes
Structural foundations	One per substructure unit for width ≤ 30 m	Advance boreholes: (1) Through unsuitable foundations soils e.g., peat, highly organic soils, soft fine-grained soils, uncontrolled fills into competent material of suitable bearing capacity (2) to a depth where stress increase due to external footing loading is less than 10% of existing effective vertical stress (see Part 3) or (3) a minimum of 3 m into bedrock, if bedrock is encountered at shallower depth
Retaining systems	Two per substructure unit for width > 30 m. Boreholes should be alternatively spaced every 30 m to 60 m in front of and behind wall	Advance boreholes to a depth of time times the retained height, or a minimum of 3 m into bedrock
Culverts	Two boreholes, depending on length	See structural foundations
Bridge approach embankments founded on soft soils	One borehole at each embankment location, to address issues associated with stability, settlement, negative skin friction, lateral pressure on bridge pile foundations.	See structural foundations. Additional shallow boreholes (trial pits) are an economical means to determine depth of unsuitable surface foundation soils
Earthworks (cuts and embankments)	One borehole every 60 m (erratic conditions) to 150 m (uniform conditions). For high cuts and fills (e.g. 10 m), two boreholes along a straight line perpendicular to centerline or planned slope face, to establish an appropriate cross-section for stability analysis	Cuts: (1) In stable materials, advance boreholes a minimum of 3 to 5 m below cut grade. (2) In soft/problematic soils, advance boreholes below cut grade to firm materials, or to the height of the cut below grade, whichever occurs first. Embankment: Advance boreholes to firm material, or to depth twice the embankment height, whichever occurs first

Many types of equipment and soil boring techniques are used in practice, and describing them in detail is beyond the scope of this Part. Only an overview of most common methods is provided in the following. Auger borings are commonly used for boring through soil formations (Day 1999, FHWA 2006). An auger is an apparatus with a helical shaft that is manually or, most commonly, mechanically advanced to drill a hole into soil by applying downwards pressure. The auger may be continuous, where the helix extends along the entire length of the shaft, or for shallow boreholes, discontinuous (single flight) where the auger helix is at the bottom of the drill stem (Figure 1.4).

There are two types of continuous flight augers: solid stem and hollow stem (Figure 1.5). The solid stem must be periodically removed from the borehole to allow retrieving soil samples. A hollow stem auger has a circular hollow core that allows for sampling through the center of the auger, which acts like casing to facilitate sampling in loose/soft soils under the groundwater table.

Figure 1.4. Large and small diameter continuous flight auger (FHWA 2006, no copyright restrictions).

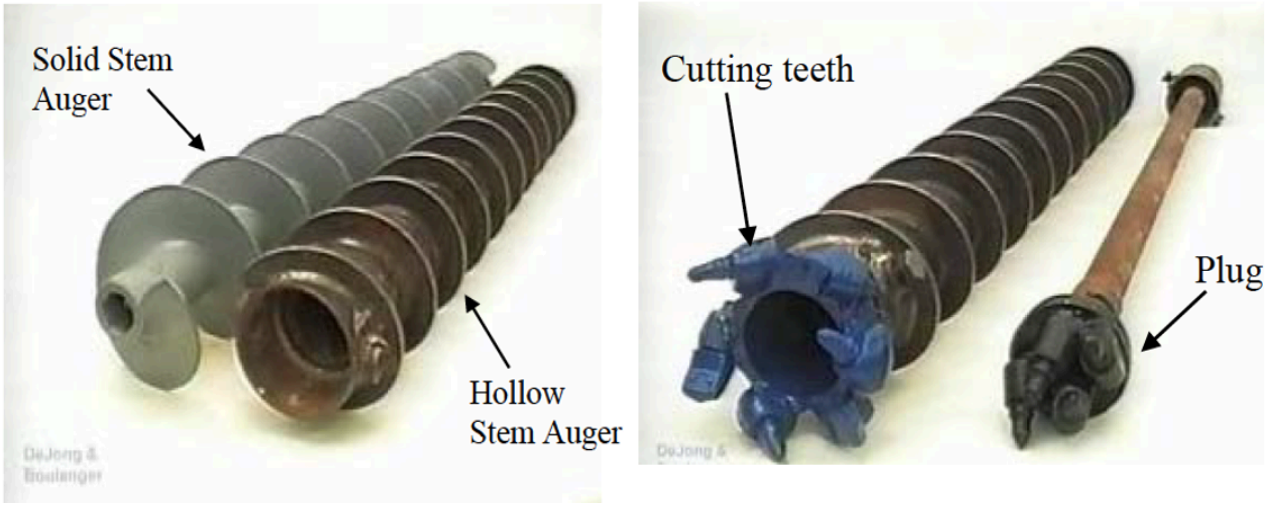

Figure 1.5. (Left) Hollow and solid stem auger, and (Right) Outer and inner assembly of a hollow stem auger (FHWA 2006, no copyright restrictions).

If relatively stiff/hard formations are encountered, a water-circulation system is used, that aids cutting and drawing the material to the surface *(wash boring-*Figure 1.6*)*. Casings are often used to prevent cave-in of the borehole. Casing of the borehole may require additional time and effort, but will result in a protected borehole, where monitoring instruments can be installed e.g., a piezometer to measure groundwater table level fluctuations, or an inclinometer for measure possible lateral soil movements.

When drilling through generally stiff formations, rotary coring is used (Figure 1.7) to retrieve intact core samples. Power rotation of the drilling bit is accompanied by the introduction of a circulating fluid to remove cuttings from the hole.

Besides the methods described above, which are the ones typically used in practice, a plethora of other methods are also used for boring through soils and rocks e.g. bucket auger boring, Becker hammer penetration, percussion drilling, sonic drilling etc.

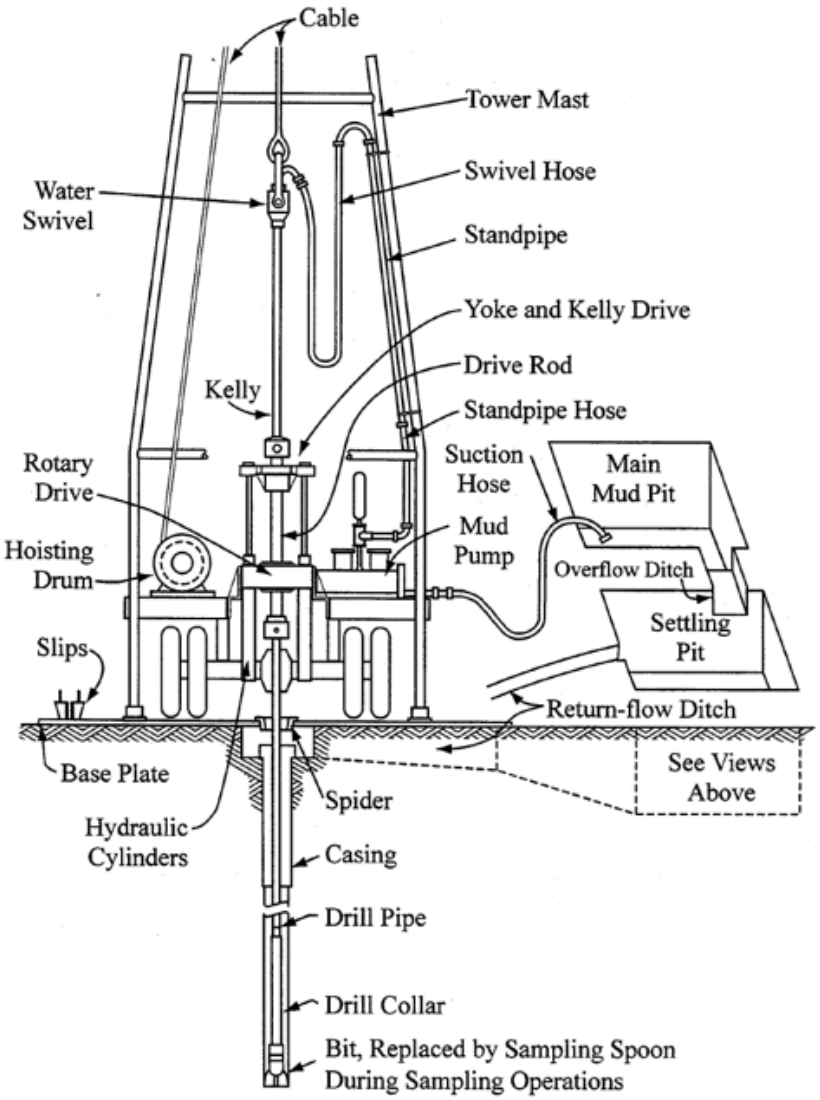

Figure 1.6. Schematic of a wash boring drill rig (FHWA 2006, no copyright restrictions).

(a) (b)

Figure 1.7. (a) Rotary drilling in action, and (b) Borehole core and undisturbed sample retrieved to surface (author's own photos).

When the borehole core is retrieved to surface (Figure 1.7b), a qualified person e.g., a geologist should observe the type, texture and color of the soil retrieved from different depths, and fill in a *borehole log* with all the information (Figure 1.8).

PROJECT NAME
LOCATION
ELEVATION

Depth (m)	sample	water level	GRAPHIC		DESCRIPTION
1	D			2.60m	Dark gray, fine to medium sand, medium dense with subangular gravels
2					
3	SPT				
4	D			5.10m	Brown clayey silt, firm, with a few gravels
5					
6	U			7.35m	Brown, firm sandy clay
7	SPT				
8	D			11.20m	Cobbles and gravels with a few dark brown sand. Between 10.20m and 10.60m a layer of brown, fine clayey sand
9					
10	SPT				
11	D				
12		11.95m		16.05m	Black grey, very soft to soft, sandy-clayey silt. Between 15.10m and 15.30m a layer of silty organic sand
13	U				
14	SPT				
15	D				
16					
17	SPT			20.00m	Black gray, locally blue gray dense fine silty sand
18	D				
19					
20	SPT				

END OF BOREHOLE AT 20.0m

Figure 1.8. Typical borehole log with information filled on site.

As far as the method used to retrieve soil samples to the surface is concerned, there are two main categories of soil sampling techniques: *disturbed sampling* and *undisturbed sampling*.

Disturbed sampling of soil provides the means to evaluate soil stratigraphy by visual examination, and soil specimens for laboratory index determination or testing of remolded samples. Disturbed samples are usually collected using split-barrel samplers (Figure 1.9). Shallow disturbed samples can be also obtained by using hand augers or from test pits.

Figure 1.9. Split barrel sampler for retrieving disturbed samples (FHWA 2006, no copyright restrictions).

Undisturbed, high-quality, soil samples on the other hand are required for performing laboratory shear strength and consolidation tests on soft to stiff fine-grained soils. In reality, it is impossible to collect truly undisturbed soil samples, as soil stress changes upon sampling and retrieving the sample to surface. The goal of undisturbed sampling is to minimise alteration of the soil structure, changes in the moisture content or the void ratio, and changes in the chemical composition of the soil. Various methods are used for undisturbed soil sampling, ranging from simple cost-effecting methods (which however induce significant disturbance during sampling), as the thin-walled Shelby tube (Figure 1.10a), up to extremely costly methods (e.g. soil freezing) used only in special projects.

As illustrated in Figure 1.11 thought, sampling even with the more advanced fixed-piston sampler (Figure 1.10b) with diameter 50 mm to 100 mm will result in some soil disturbance, particularly at the top and bottom parts of the sample. As the soil fabric is disturbed, laboratory test results may be compromised, and this must be properly considered when interpreting laboratory test results to retrieve soil parameters. More advanced sampling tools, such as mini-block sampler used in the University of Newcastle (Figure 1.12) will produce soil samples of optimum quality for laboratory testing.

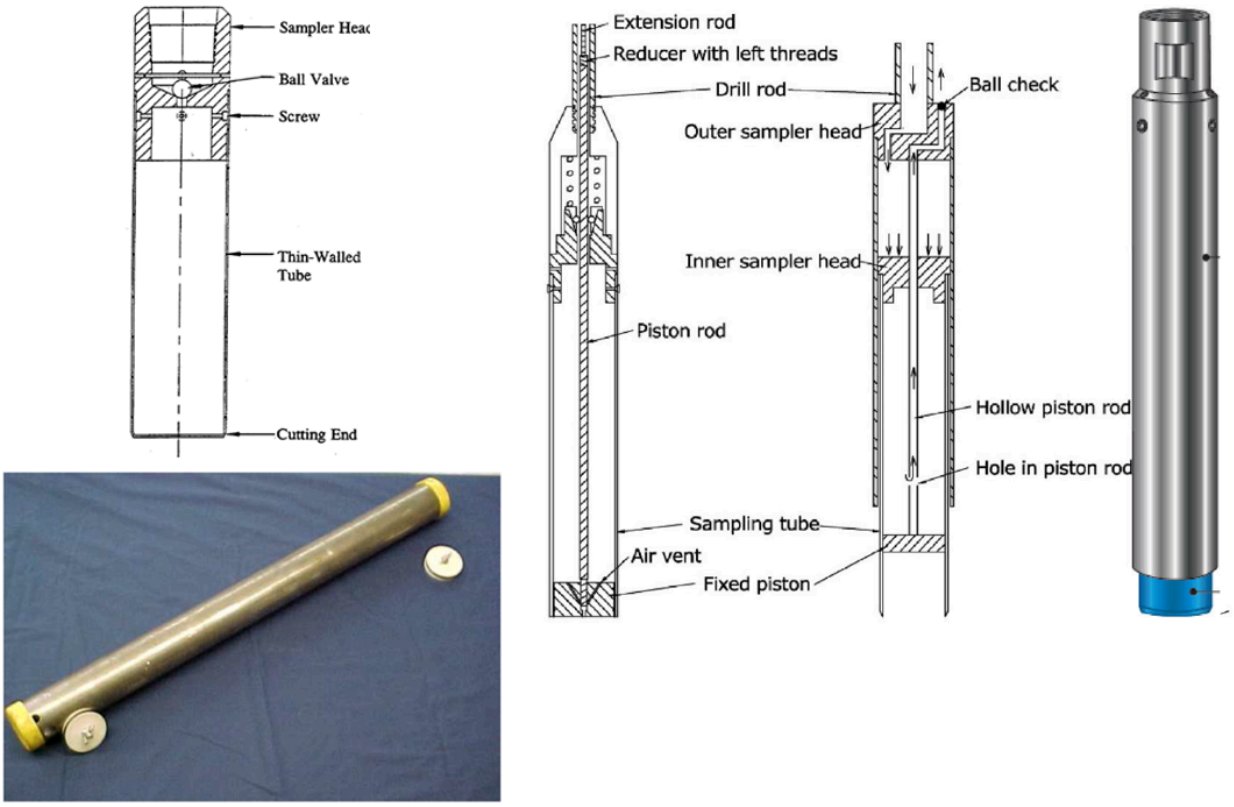

Figure 1.10. (a) Thin-walled Shelby tube sampler (FHWA 2006, no copyright restrictions) and (b) Osterberg composite hydraulic fixed-piston sampler for retrieving high-quality undisturbed samples (da Fonseca and Pineda 2017, reproduced with permission).

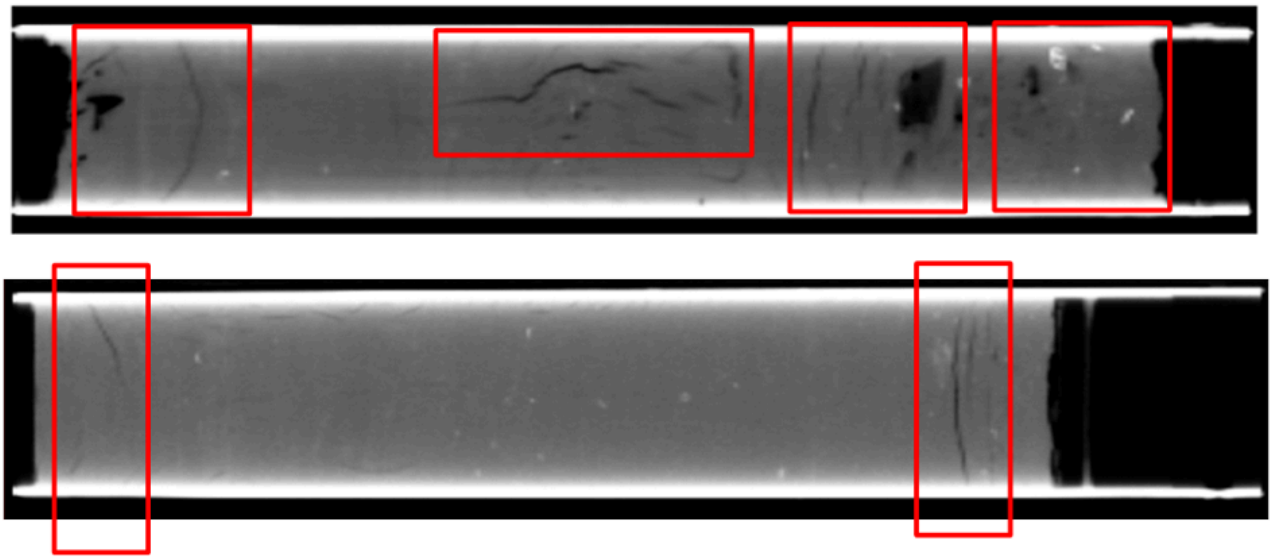

Figure 1.11. CT-scan of 75 mm-diameter Shelby tube (top) and 89 mm-diameter fixed-piston (bottom) samples (Pineda et al. 2016, reproduced with permission).

Figure 1.12. University of Newcastle mini-block sampler and block sample of soft silty clay (author's own photos).

1.5 THE STANDARD PENETRATION TEST (SPT)

The most common method of *in situ* soil testing is the Standard Penetration Test (SPT), used globally. It has its origins in Boston, USA of the early 20th century, and was first used by one Charles Gow. Gow was the first one to drill exploratory boreholes using 1-in diameter drive samplers (similar to the one shown in Figure 1.9). Up to that point, contractors used cuttings from wash borings to delineate the interface between soil and bedrock, as they used drilling methods similar to the ones used to drill water wells. Harry Mohr, one of Gow's engineers, standarised the procedure, and started recording the number of blow counts required to advance a 2-in sampler with a 140-lb hammer dropping 30 inches. Karl Terzaghi, arguably the father of Soil Mechanics, liked the idea and later developed correlations between the allowable bearing pressure and the number of blowcounts. The standard SPT procedure (Figure 1.13) presented herein is described in detail in AS1289.6.3, and hasn't changed much from Mohr's testing procedure.

In short, a 2-in (50 mm) split-barrel sampler is driven into the soil by dropping a 140-lb (63.5 kg) hammer from a height of 30 in (760 mm). The hammer is dropped repeatedly, until an ultimate penetration of 18 in (450 mm) is achieved. The number of blows of the hammer are recorded during 6 in (150 mm) penetration intervals. The necessary number of blows for advancing the sampler to the last 12 in (300 mm) is the SPT *N*- value (Figure 1.13). For example, during a SPT test, the following values were recorded:

- 5 blows/150 mm
- 6 blows/150 mm
- 10 blows/150 mm

Blows from the first 150 mm of penetration are disregarded, to account for soil disturbance due to boring, thus the *N*-value is equal to $N = 6+10 = 16$ (Figure 1.14).

The test is halted to prevent damage to equipment, and *refusal* (REF) is reported on the boring log if:

- More than 50 blows are required for any 150 mm increment.
- More than 100 blows are required for the last two increments.
- 10 successive blows produce no advance.

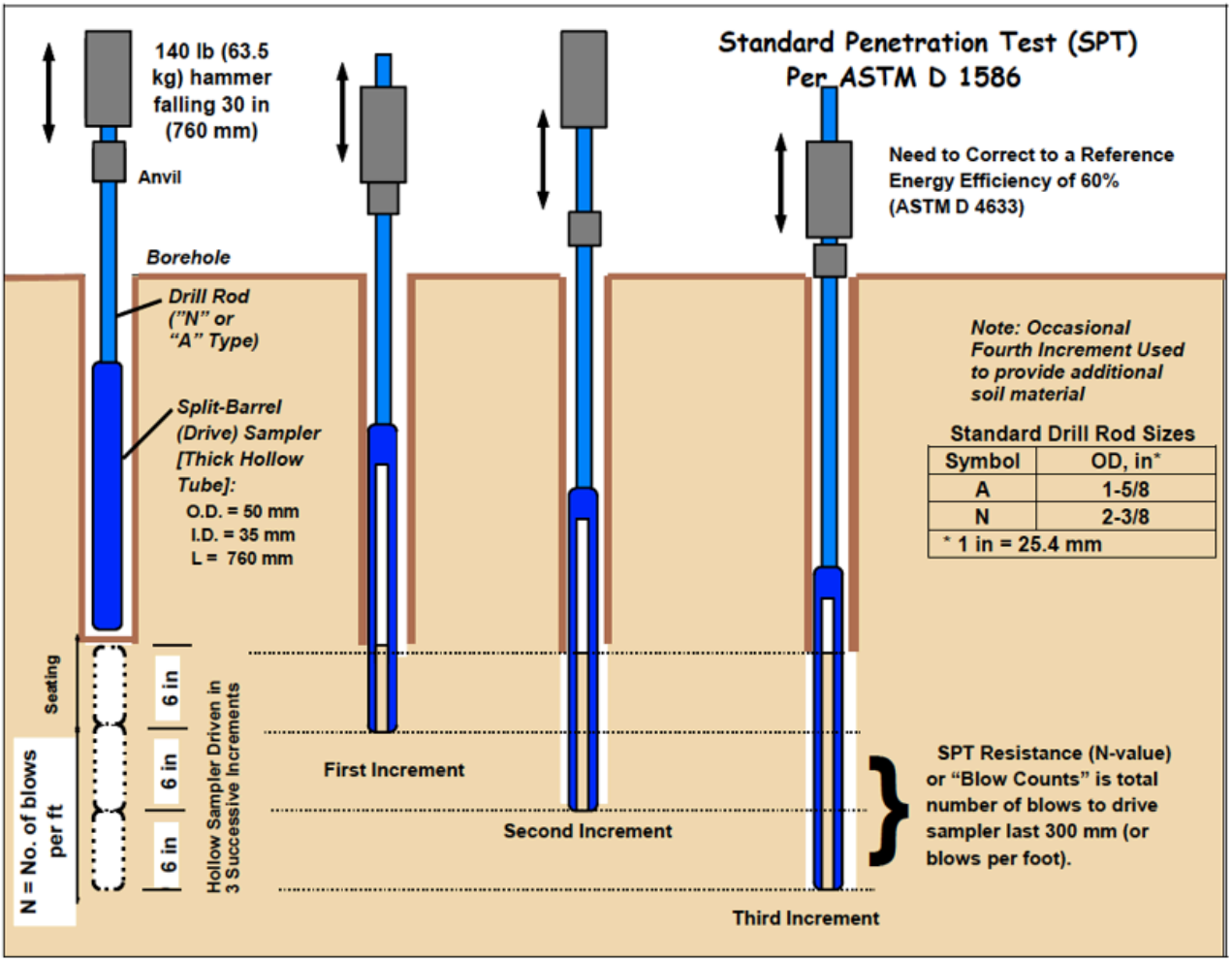

Figure 1.13. Sequence of driving the split-barrel sampler during the Standard Penetration Test (FHWA 2006, no copyright restrictions).

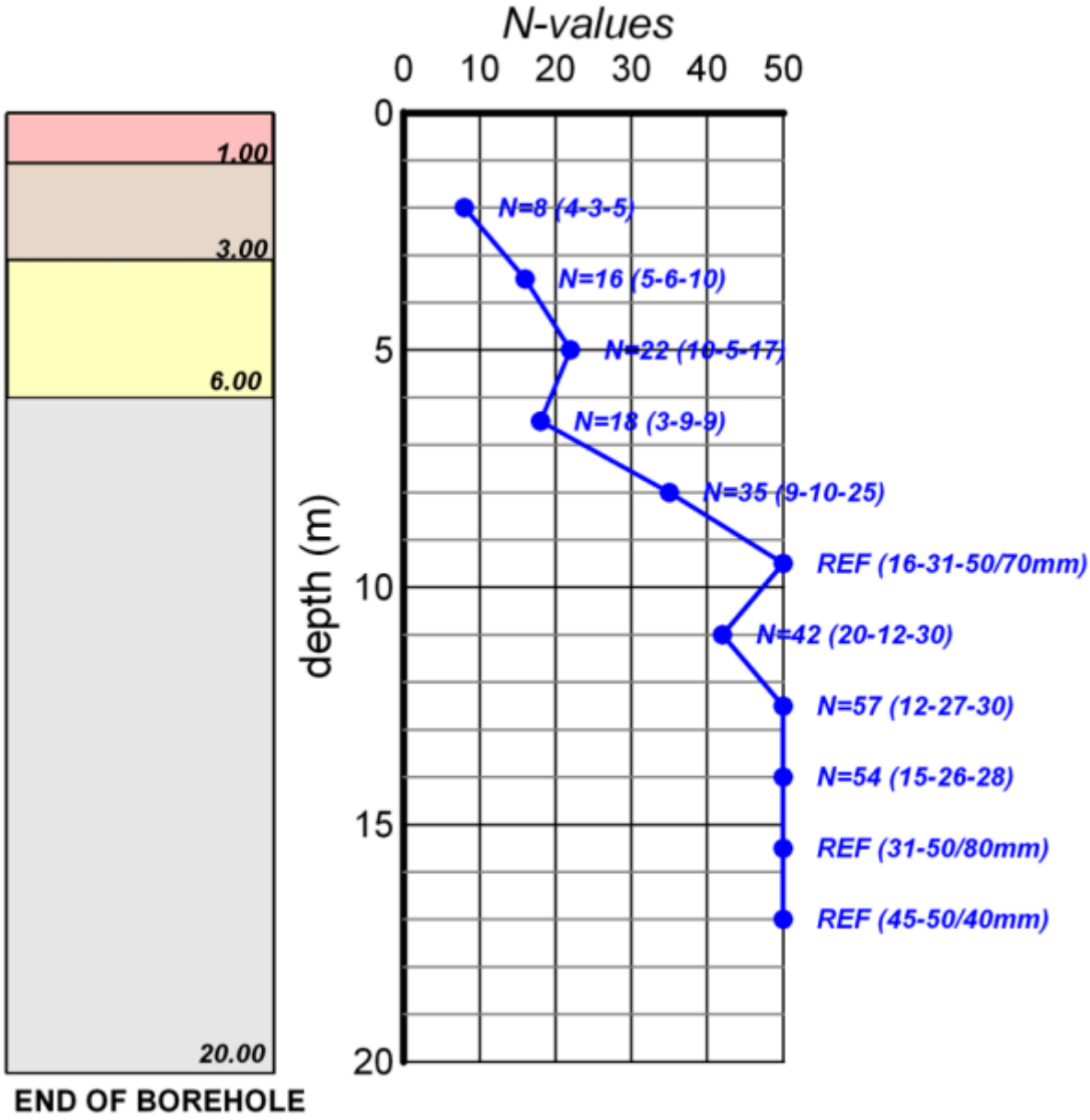

Figure 1.14. Typical SPT test results, as presented in a borehole log.

When the full test depth cannot be achieved, the boring log will report a ratio similar to 50/40 mm, indicating that the last 50 blows resulted in penetration of the sampler equal to 40 mm (Figure 1.14). After the test, the soil sample is retrieved, and is usually used for laboratory classification tests.

Several boring techniques can be used in combination with the SPT tests, such as continuous flight hollow stem augering, wash boring etc. provided that care will taken so that soil beneath the advancing borehole is not significantly disturbed during drilling. SPT tests are performed about every 1.5 m, unless otherwise dictated by soil conditions e.g., encountering very stiff to hard formations, or sampling needs (undisturbed sampling).

Based on the soil type, characterised by the retrieved sample through laboratory classification tests, and the number of blow counts, empirical correlations have been proposed that provide the *in situ* soil shear strength and compressibility properties. This implies that there is a unique correlation between the penetration resistance and the mechanical characteristics of the soil.

Many of these correlations, which are useful in everyday geotechnical engineering practice in lack of more advanced test results, require as input the corrected SPT blow count, N' (often referred to in the literature

as N_1), as the ones presented in Table 1.3. Corrected blow counts account for the *in situ* geostatic stress state of the soil, at the depth where it is tested. For example, sands of identical mineralogy, structure and density will appear stronger and exhibit higher blow counts at greater depths, than when tested at shallower depths, due to the effect of confining stresses. Thus, some soil properties that are derived from SPT test results, such as the unit weight or the friction angle, may be better estimated if we normalise blow counts to remove overburden effects. Note that some correlations, such as the ones provided in Table 1.4, require as input the uncorrected blow counts.

Table 1.3. Correlation of soil parameters with corrected SPT values for sands and clays.

Corrected SPT *N'*	**Description/ consistency**	**Soil parameters**		
Sand		**Relative density D_r (%)**	**Range of bulk unit weight γ (kN/m^3)**	**Range of friction angle φ' (deg)**
0	Very loose	0	11.0 to 15.7	25 to 30
4	Loose	15	14.1 to 18.1	27 to 32
10	Medium	35	17.3 to 20.4	30 to 35
30	Dense	65	18.8 to 22.0	35 to 40
50	Very dense	85	20.4 to 23.6	38 to 43
Clay			**Range of bulk unit weight γ (kN/m^3)**	**Undrained shear strength S_u (kPa)**
0	Very soft		15.7 to 18.8	0
2	Soft			12
4	Medium		17.3 to 20.4	25
8	Stiff			50
16	Very stiff		18.8 to 22.0	100
32	Hard			200

Eq. 1.1 is used to correct *N*-SPT blows to the effective vertical geostatic stress at the depth of the test σ'_{z0}:

(1.1) $N' = C_N N$

where the correction factor C_N is calculated as:

(1.2) $C_N = \sqrt{\frac{p_a}{\sigma'_{z0}}}$ (p_a is the atmospheric pressure approximately 100 kPa)

Table 1.4. Correlation of soil parameters with uncorrected SPT values for sands.

Uncorrected SPT N	Bulk unit weight γ (kN/m^3)	Friction angle φ' (deg)
0-2	15.7	26
3-4	15.7	28
4-10	16.5	29
10-20	17.3	30
20-30	18.1	32
30-40	18.9	33
>40	19.6	34

Figure 1.15. Different equipment used to perform Standard Penetration Tests (Geoengineering.org website, reproduced with permission).

The actual energy transmitted through each SPT blow, and thus of course the penetration achieved, depends also on the equipment used (Figure 1.15). Gunaratne (2006) identifies the following factors affecting the number of blow counts:

- Hammer efficiency
- Length of drill rod
- Type of sampler
- Borehole diameter

Values of N' can be further normalised over a *standard hammer efficiency* E, so that results from SPT tests performed with different equipment are comparable, and can be used in empirical correlations:

(1.3) $$N'_E = n_i N'$$

where different factors n_i (n_1 to n_4) account for the effect of the abovementioned parameters, if the test is not executed in a standard way, as per AS1289.6.3.1. Furthermore, as the standard hammer efficiency is E = 70%, it is:

(1.4) $$N'_{70} = N'$$

so the n_i value to convert blow count number to other common efficiencies e.g., 60% is directly proportional to the ratio of the corresponding efficiencies:

(1.5) $$N'_{60} = \left(\frac{60}{70}\right) N'_{70}$$

As SPT testing is simple, cheap and is performed while drilling most exploratory boreholes, numerous correlations have been proposed in the literature for estimating different soil parameters based on SPT blowcounts and soil type. Such correlations, as the few widely used ones shown below, are useful for estimating soil parameters when limited laboratory test data are available, or for cross-checking the reliability of laboratory tests. However, when using them one needs to appreciate their crude, empirical nature, the scatter of fitted data, and the lack of a robust theoretical interpretation model for converting "blow counts" to stiffness or soil strength parameters.

Table 1.5. Correlation of soil Young's modulus, E_s with N-SPT blow counts, for different soil types. Use the expressions of this table with $N = N_{55}$, converting it from standard hammer efficiency 70% via Eq. 1.5.

Soil	Drained E′ or Undrained E_u Young's modulus (kPa)
Sand	$E' = (2600 \text{ to } 2900)N$
Gravelly sand	$E' = 1200(N+6)$
Clayey sand	$E' = 320(N+15)$
Silt, sandy silt or clayey silt	$E_u = 300(N+6)$
Low plasticity clay (PI<15%)	$E_u = 1200+580N$
High plasticity clay (PI>15%)	$E_u = 400+1150N$

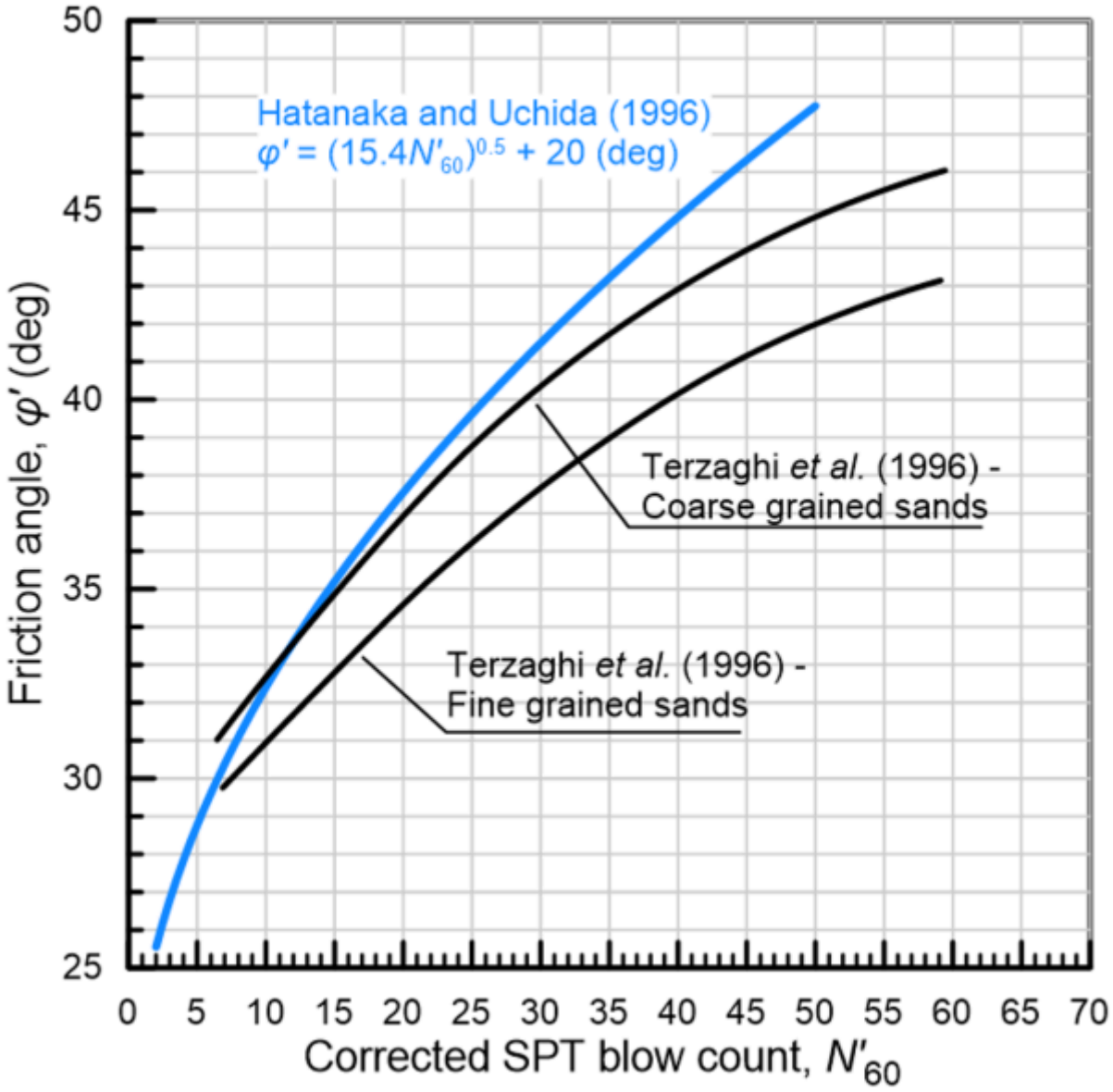

Figure 1.16. Estimation of the friction angle φ' of fine-grained and coarse-grained sands from the N'_{60} (N_{I60}) value, converted to standard hammer efficiency 60% and corrected for overburden stress according to Eq. 1.1

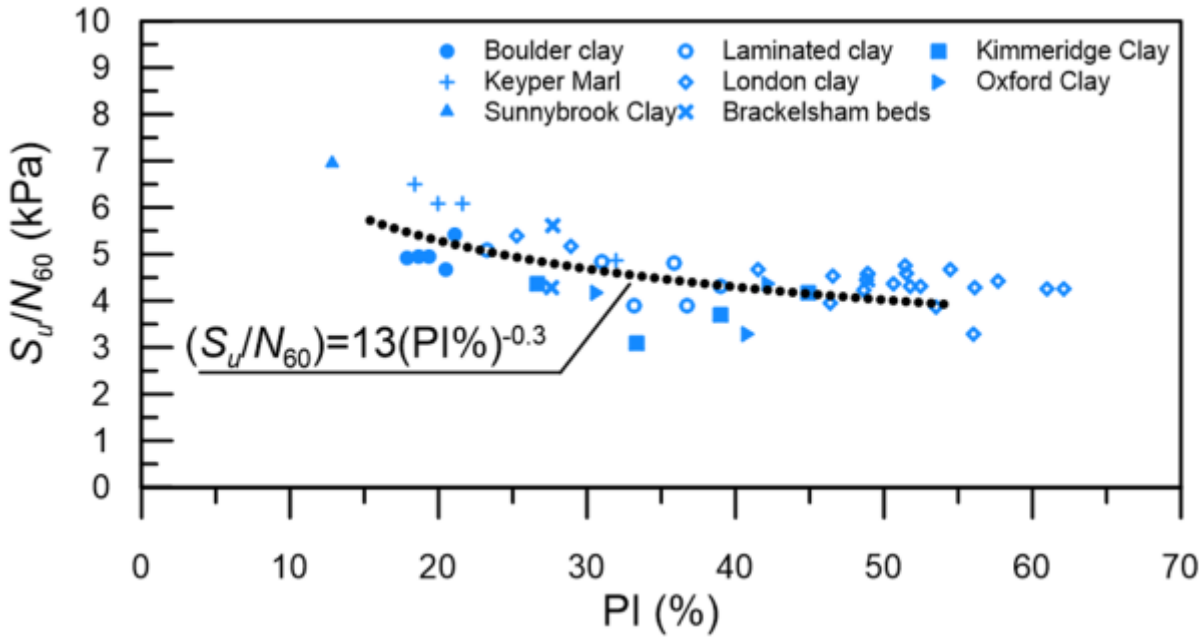

Figure 1.17. Estimation of the undrained shear strength S_u of clays from the uncorrected blow count N_{60} value and the clay plasticity index PI (%) (after Stroud 1974, with modifications).

1.6 ESTABLISHING THE GEOTECHNICAL MODEL OF A SITE

Establishing the geotechnical model of a site is a challenge for the Geotechnical Engineer. It requires profound knowledge of geomechanics theory, understanding of *in situ* and laboratory test procedures, experience and *Engineering Judgement.*

As engineering judgement plays perhaps the most important role in interpreting geotechnical site investigation results, every Geotechnical Engineer called to establish a geotechnical model of a specific area by interpreting the same test results, may end up with a different model. This is absolutely acceptable, provided that the model will lead to the *safe* and *economical* design of the structure under consideration.

Establishing a geotechnical model consists of identifying soil layers *(*called *"geotechnical layers" or "geotechnical units")* that, for engineering purposes, can be assumed to behave uniformly when subjected to different actions. Each borehole log (Figure 1.8) will perhaps include several, even dozens of different descriptions of soil layers, with thickness ranging from a few meters to a few centimetres. Using the USCS (Unified Soil Classification System) descriptions, examining the borehole cores (and/or their photos) and the *in situ*/laboratory test results, the Geotechnical Engineer will try to unify these layers, towards creating a simple yet realistic model. Keep in mind that, we do not want to end up neither with a model that includes too many geotechnical layers, for which we do not have enough data to quantify their geotechnical behaviour, nor with too few geotechnical layers, as too crude layers will not behave uniformly. Balancing between a too detailed and a too crude layer discretisation is simply a matter of experience, and good understanding of the behaviour of geomaterials.

The above concept is further explained in the following example, which presents the establishment of the geotechnical model in an area where a bridge is to be constructed.

EXAMPLE 1.1

Establishing a geotechnical model for the geotechnical design of a bridge foundation

For the geotechnical design of a new bridge, 3 boreholes (BH-1, BH-2 and BH-3) were drilled, spaced 15 m apart. SPT tests have been performed, while a piezometer was installed in BH-1, measuring the absolute groundwater table level at +7.10 m. Create a simplified geotechnical profile of the site, and determine the strength and compressibility parameters of each geotechnical layer; in other words, propose a geotechnical model of the area.

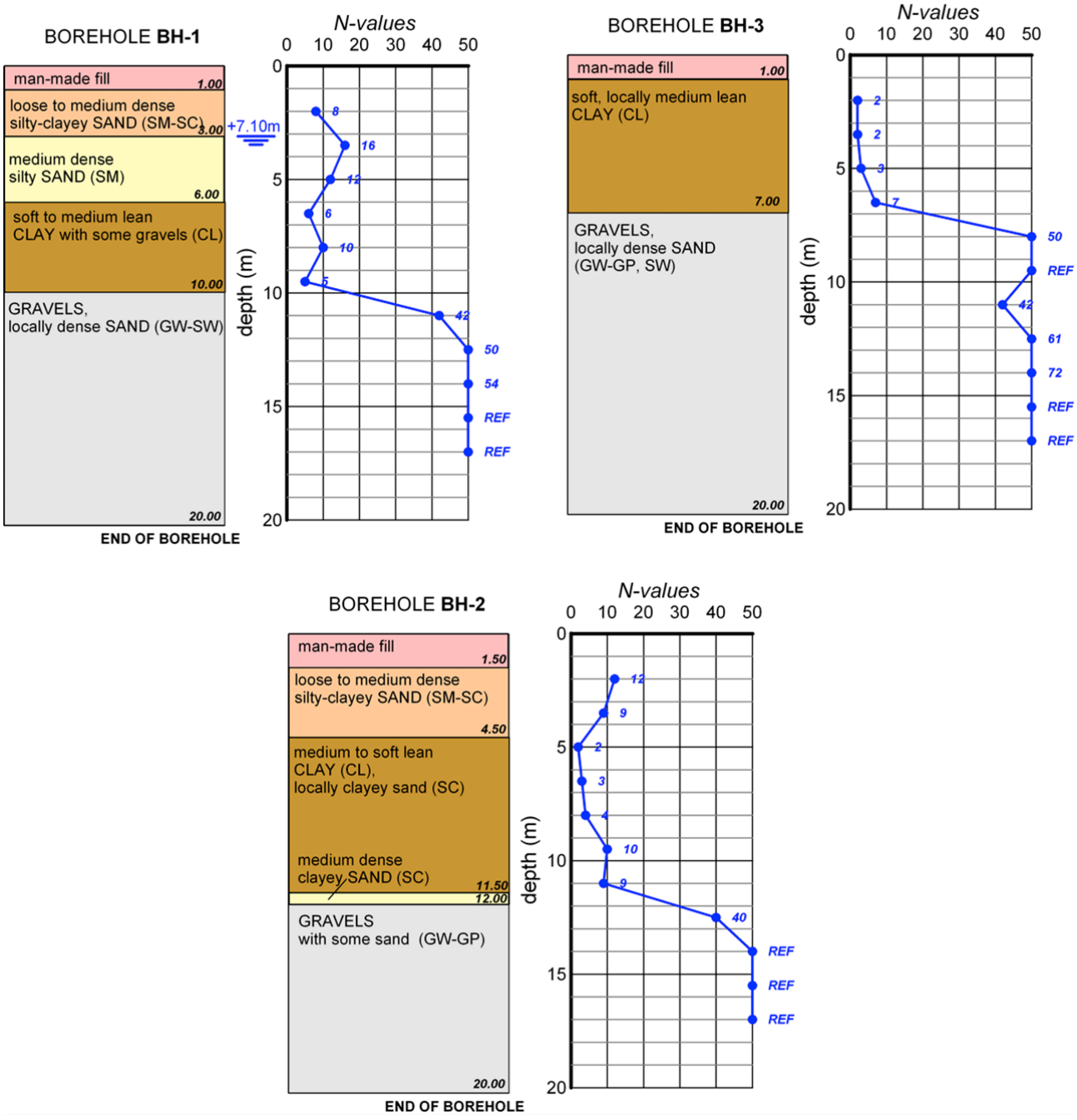

Example 1.1. Problem description and input parameters.

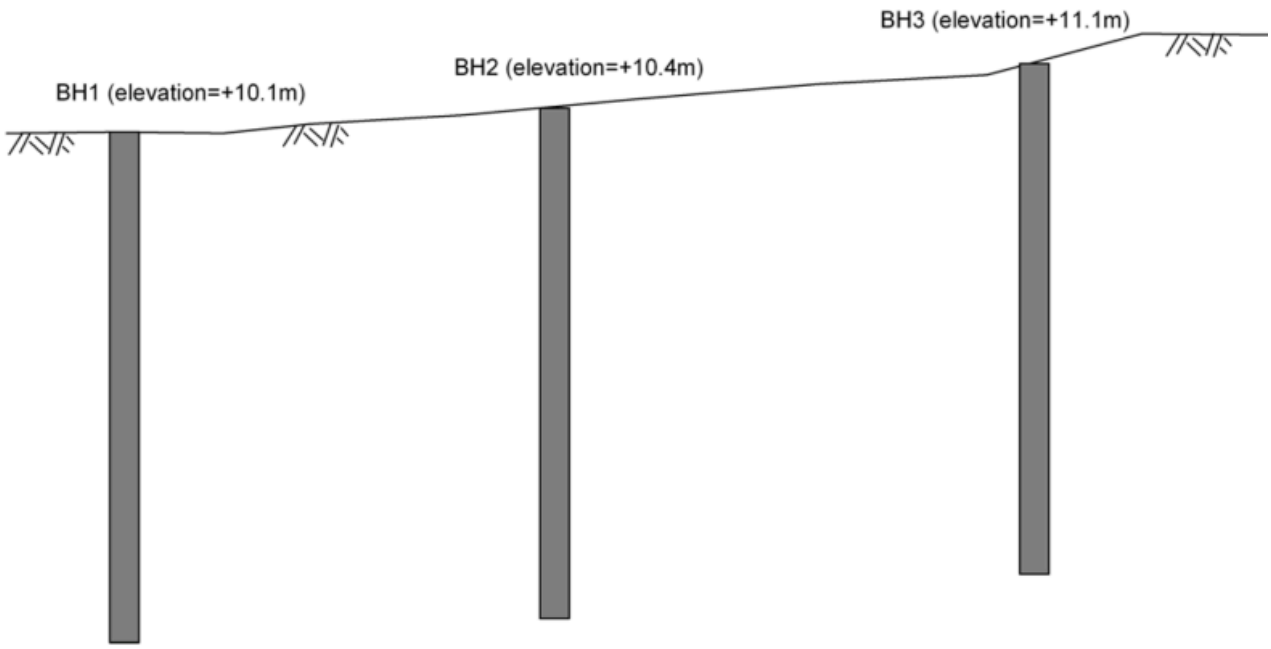

Example 1.1. Problem description and input parameters.

Answer:

Trying to unify findings from the borehole logs into layers that will exhibit similar geotechnical behavior includes identifying the number of layers required to sufficiently describe the subsoil conditions, their geotechnical description, and their extent both vertically and laterally.

In this particular case, one may define the geotechnical layers and their geometry, while considering the following:

- The top artificial fill layer, of thickness 1.0 m to 1.5 m, may have to be removed or treated before the construction of the foundation e.g., replaced with an improvement layer. Foundation of structures on uncontrolled (existing) fills is generally not recommended, due to their variable composition.
- Very thin layers, such as the medium dense clayey sand layer found in borehole BH-2 from 11.5 to 12.0 m can be effectively ignored, as they will not alter the overall geotechnical response of the foundation.
- Layers of similar classification according to USCS and similar degree of consistency, as the loose-to-medium dense silty-clayey sand found in boreholes BH-1 and BH-2 can be unified, while adopting a rather conservative approach to define their shear strength and compressibility parameters.
- When we are not sure about the geometry of a layer, use question marks (?)

Following the above guidelines, and considering the design groundwater level at least 2 m above the measured one to account for fluctuations during the lifetime of the project, we come up with the geotechnical layers and their possible geometry presented in the cross-section below (Figure 1.18).

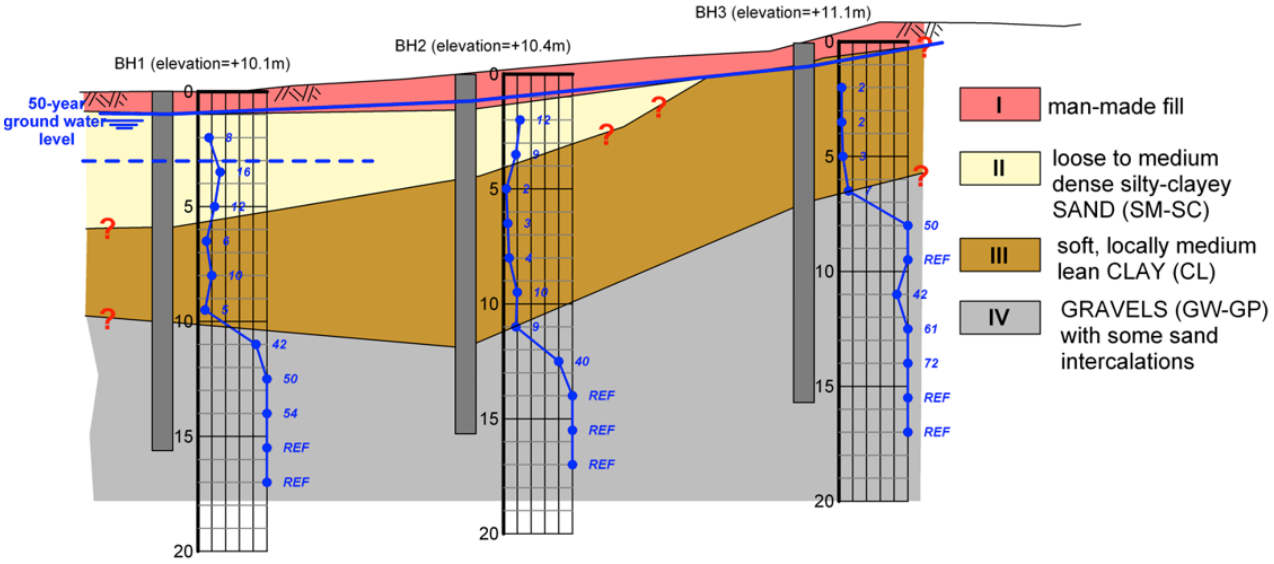

Figure 1.18. Geotechnical cross-section and layer description.

For the derivation of design geotechnical parameters, the SPT blow counts are used together with empirical correlations, and of course engineering judgement. Creating (corrected or uncorrected) SPT plots with depth, separately for each geotechnical layer, is very useful when it comes to defining an average and a *"characteristic"* SPT value for this layer, to be used with the empirical correlations. This approach is demonstrated in the following two figures, while more on the determination of characteristic values of soil parameters are provided in Part 5 and AS5100.3.

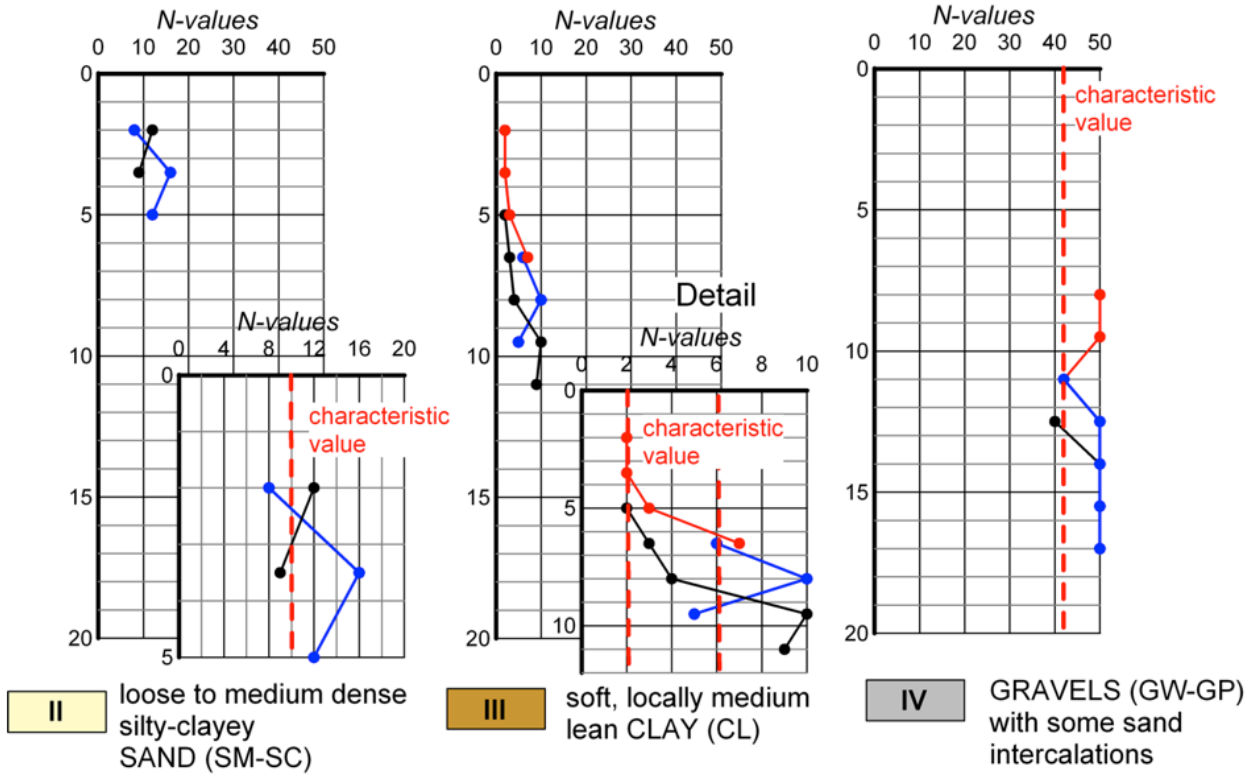

Figure 1.19. Uncorrected SPT values distribution with depth, separately for each geotechnical layer.

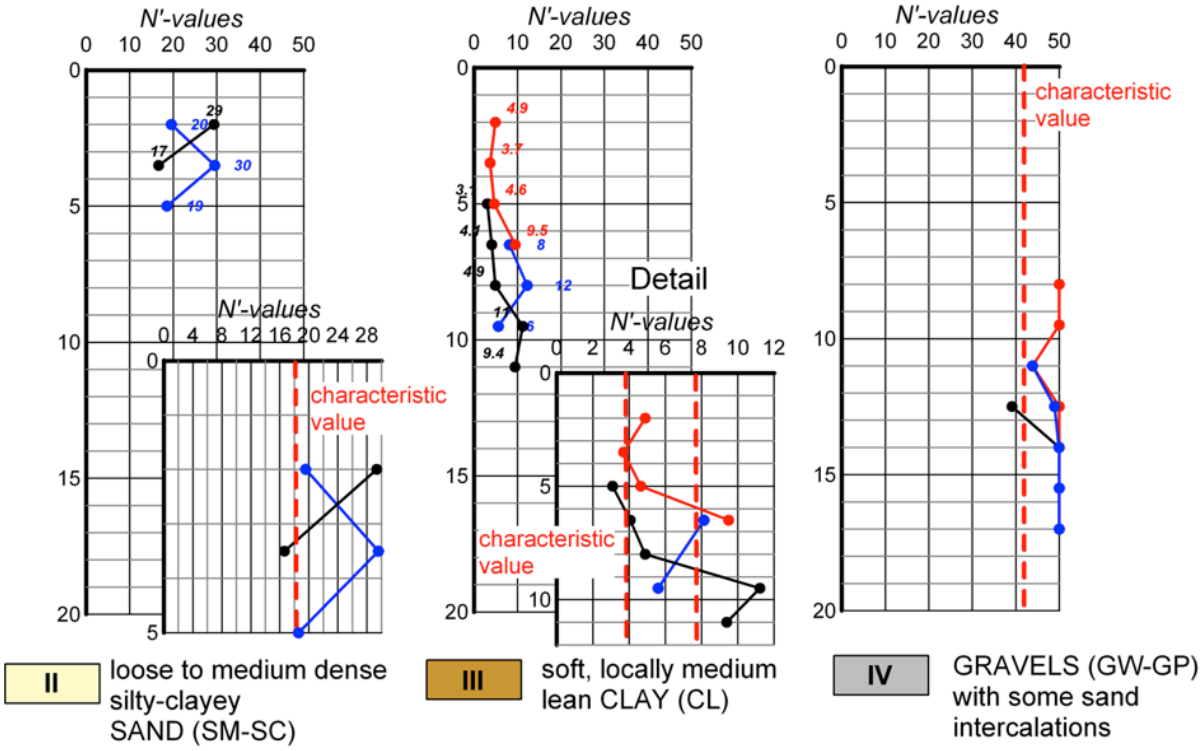

Figure 1.20. Corrected SPT values distribution with depth (Eq. 1.1), separately for each geotechnical layer.

For correcting SPT blow counts to overburden stress, it was assumed for simplicity that the unit weight of all soil layers is equal to γ = 18 kN/m^3 and, for the calculation of the distribution of geostatic vertical effective stress with depth σ'_{z0}, that the groundwater table at the time when boreholes were drilled was at the ground surface. Notice that, if SPT measurements suggest so, we may consider a different characteristic N value for the same layer, but for different depths, as for layer III.

Given the characteristic values from the above graphs, which correspond to a *reasonable lower bound* of SPT blow counts, we can estimate the friction angle φ' of the coarse-grained geotechnical layers II and IV from Figure 1.16. Selection of this characteristic value (or reasonable lower bound) depends on the amount of available information: If a large number of SPT measurements are available, it is reasonable to select a characteristic value close to the mean SPT value. On the other hand, if only a handful of measurements are available (refer to Unit II in Figures 1.19 and 1.20), it is prudent to select a characteristic value close to the lower bound of measurements.

The undrained shear strength S_u of the fine-grained geotechnical layer III can be estimated from Figure 1.17, while assuming that this low-plasticity clay has an *average* plasticity index PI = 20%, in the absence of laboratory test results. While doing so we need to keep in mind that the undrained shear strength is not a soil property, but function of both the water content and of the effective stress level (for normally consolidated clays it is $S_u/\sigma'_{z0} \approx 0.22$). It is therefore reasonable to consider that the undrained strength S_u will increase with depth.

Furthermore, the Young's modulus E_s of all three layers defined here is estimated from Table 1.5, from the expression for sand for layer II, the expression for gravelly sand for layer IV, and the expression for clay with PI > 15% for layer III. Note that blow counts must be converted from N_{70} to N_{55} for 55% hammer efficiency in order to be used with the expressions of Table 1.5, as:

$$N_{55} = \left(\frac{55}{70}\right) N_{70} = 0.785 N_{70}$$

Considering the dynamic nature of the SPT test, it is reasonable to consider that Young's moduli E_s interpreted from SPT tests in fine-grained soils are undrained moduli (E_u), while deformation moduli

interpreted from SPT tests in coarse-grained soil are drained moduli (E'). Results are presented in a summary table below, together with the characteristic N values considered, a table that is included in every geotechnical investigation report.

Example 1.1. Summary of geotechnical parameters.

Geotechnical Layer	Uncorrected characteristic SPT value, N	Corrected characteristic SPT value, N'	Effective cohesion, c' (kPa)	Friction angle, φ' (deg	Undrained shear strength,S_u (kPa)	Young's modulus,E_u *or* E' (MPa)	Behaviour under short term loads
II	10	18	–	31	–	21	Drained
III (above -8m)	2	4	*2**	*26**	12	2	Undrained
III (below -8m)	6	8	*2**	*26**	36	6	Undrained
IV	40	40	–	43	–	45	Drained

** Estimated from laboratory triaxial tests on undisturbed samples*

There are a number of empirical relations in the literature that we can base our soil parameter estimation on. Usually not just one, but rather two or more are considered for each parameter in everyday engineering practice. This provides us a range rather than a single value for each parameter, and accounts for uncertainties inherited in the use of such approximate expressions. Complementing laboratory test results with these findings will lead to more comprehensive evaluation of the response of the various geotechnical layers.

1.7 THE CONE PENETRATION TEST (CPT)

A very common method for *in situ* testing of soils is the Cone Penetration Test (CPT). A cone is hydraulically pushed into the soil at a constant rate, and the resistance to the penetration of the cone, as well as the frictional resistance of a surface sleeve, are continuously recorded. Today the piezocone test (CPTu) is more common, where pore pressure is also measured during penetration. Other variants allow for the measurement of S- and P- wave velocities (seismo-cone), moisture content, soil pH etc. A detailed description of the Cone Penetration Test procedure presented herein is included in AS1289.6.5.1.

Figure 1.21. University of Newcastle CPT testing equipment fitted on a truck truck (© TUNRA Geotechnic/University of Newcastle).

The Cone Penetration Test provides a continuous profile of soil stratigraphy, and allows also for continuous evaluation of soil properties; contrary to the SPT test where information about the soil penetration resistance is obtained at specific intervals. However, soil samples for visual inspection and laboratory index testing are not retrieved, as with the SPT test. CPT tests can be performed in very soft clays to dense sands alike, onshore and offshore (Figure 1.21). In addition, Cone Penetration Testing is often used in other geotechnical engineering applications, such as estimating the liquefaction potential of loose coarse-grained deposits.

However, CPT is unsuitable for gravelly soils, cemented soils and soft rocks, as the cone cannot penetrate through such formations. Some of the advantages and disadvantages of the CPT test are summarised in Table 1.6.

During a CPT sounding, the following quantities are measured:

- The *cone resistance* q_c (units: stress), which results from dividing the total force acting on the cone F_{cone} by the projected area of the cone, A_c (Figure 1.22).
- The *sleeve friction resistance* f_s (units: stress) which results from dividing the total friction force

acting on the sleeve F_{sleeve} by the area of the sleeve, A_s (Figure 1.22).

The diameter of standardised cones is 35.7 mm, and their projected area is A_c = 1000 mm^2.

Table 1.6. Advantages and disadvantages of the CPT test (with information from FHWA, 2006).

Advantages	Disadvantages
Continuous profiling	No soil samples are retrieved, estimates of soil type are indirect
Economical and productive. 100 m to 350 m/day, depending on equipment and soil conditions	High capital investment
Results are not operator-dependent	Requires skilled operator
Many interpretation methods based on rigorous theoretical background, and not just empiricism	Requires calibration, noise filtering as well as careful instrument preparation e.g., saturation of pore pressure sensor (tensiometer)
Particularly suitable for soft soils as well as applications such as assessment of seismic liquefaction potential	Unsuitable for fills, gravel/boulder deposits and cemented soils

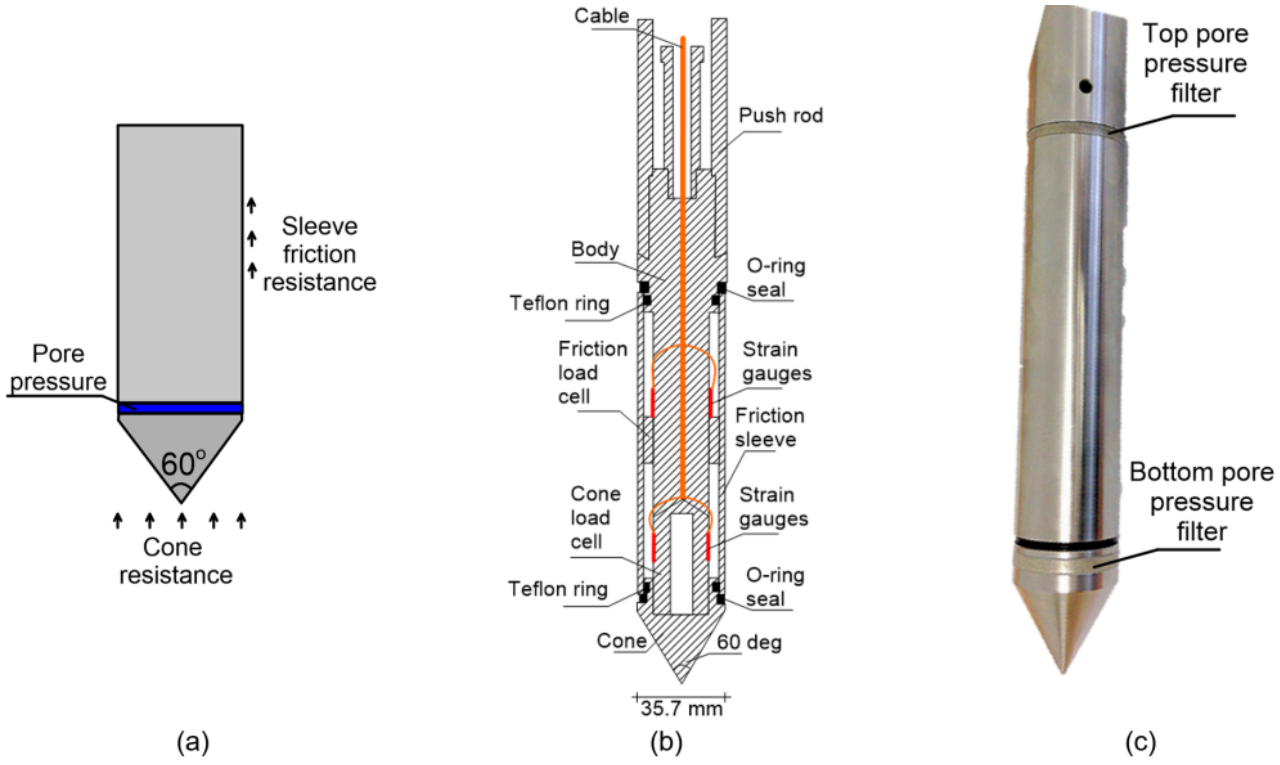

Figure 1.22. (a) Terminology for cone penetrometers, (b) Typical electrical friction-cone penetrometer, and (c) Typical cone featuring two transducers for pore pressure measurement.

CPT testing (Figure 1.23) must follow some standarised procedures (AS1289.6.5.1):

- To avoid damaging the cone when penetrating through artificial compacted fills or surficial hard soils, *pre-drilling* might be necessary.
- The cone thrust direction should be as near as possible to vertical. Its deviation, measured by means of an inclinometer installed on the rig, should not exceed 2 deg.
- Reference measurements must be obtained, and zero forces on the cone should be recorded at the

start and at the end of each CPT sounding.

- The rate of penetration of the cone should range between 10 to 20 mm/sec. This implies that a 20 m CPT sounding can be completed in about 30 min, and excess pore pressures will develop during CPT tests in low permeability soils (Figure 1.24).
- Measurements must be obtained at 25 mm to 35 mm intervals for soil under a pavement or for design of pavement depth, or every 150 mm to 200 mm for any other application. This is the minimum interval prescribed in the standard, more frequent measurements are obtained with modern equipment.
- During a pause in penetration, any excess pore pressure generated around the cone will start to dissipate. The rate of dissipation depends on the coefficient of consolidation, and thus the permeability of the soil. *Dissipation tests* can be performed in fine grained soils at any depth to get estimates of permeability, by measuring the decay of excess pore pressures with time.
- When CPTu tests are performed in saturated soft clays and silts, the cone resistance q_c must be corrected to account for the pore water pressure acting on the cone geometry as: $q_t = q_c + u_2(1-a)$ where u_2 is the measured pore water pressure and a is determined from calibration tests (Figure 1.25). Generally, the tip area ratio a ranges between a = 0.70 to 0.85, and should not be less than a = 0.75.

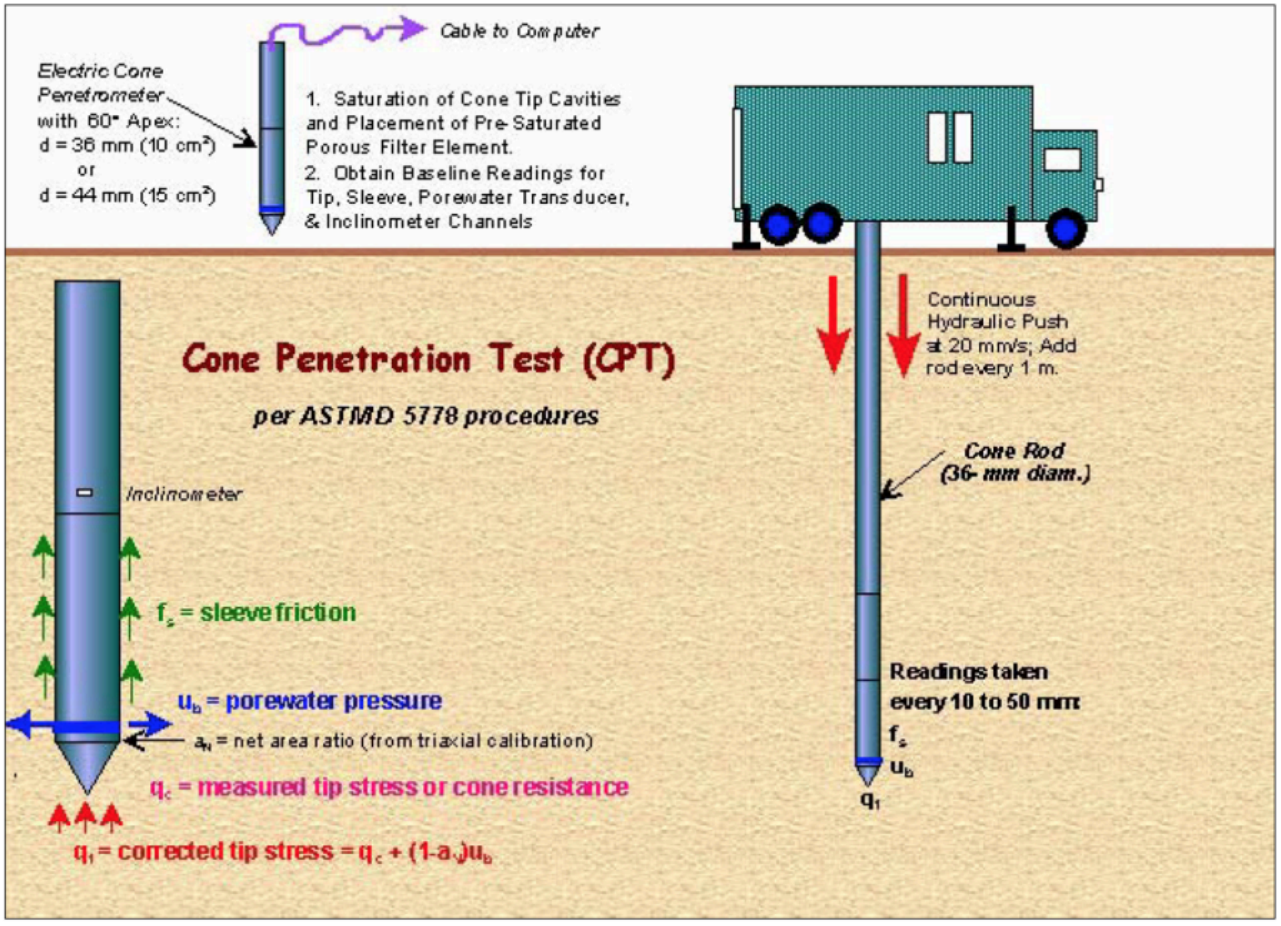

Figure 1.23. (Piezo)cone Penetration Test components and procedures (FHWA 2006, no copyright restrictions).

Interpretation of CPT tests is based on theoretical considerations regarding the properties of the failure surface that continuously develops near the cone tip (and around the sleeve) as the cone is being advanced into soil. While interpreting CPT tests one must consider that i) the soil near the cone tip reaches its peak shear strength, while ii) the soil's residual strength associated with large shear strains is mobilised around the sleeve.

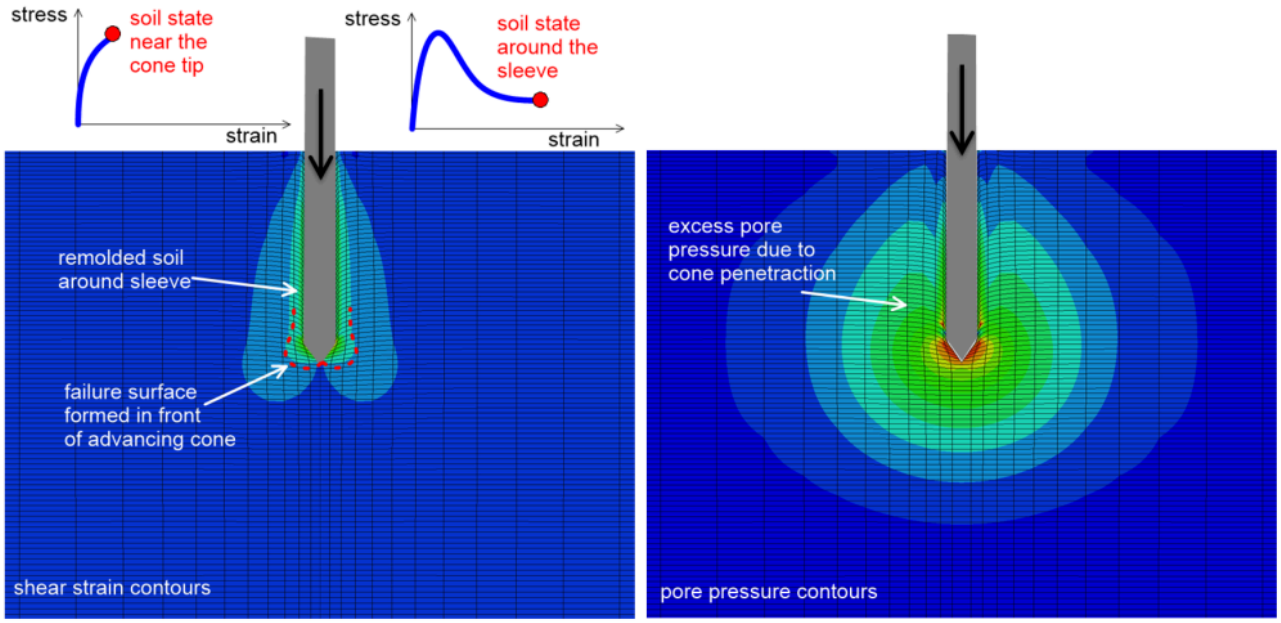

Figure 1.24. Cone Penetration Test mechanisms and background for interpretation.

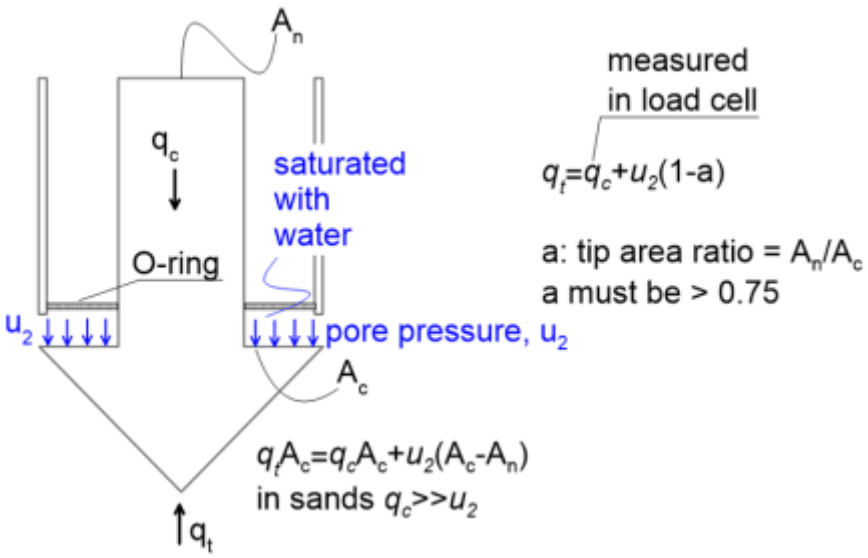

Figure 1.25. Correction of cone resistance for unequal end area effects.

Considering the above, the variation with depth of the following quantities is calculated (Figure 1.26), according to AS1289.6.5.1:

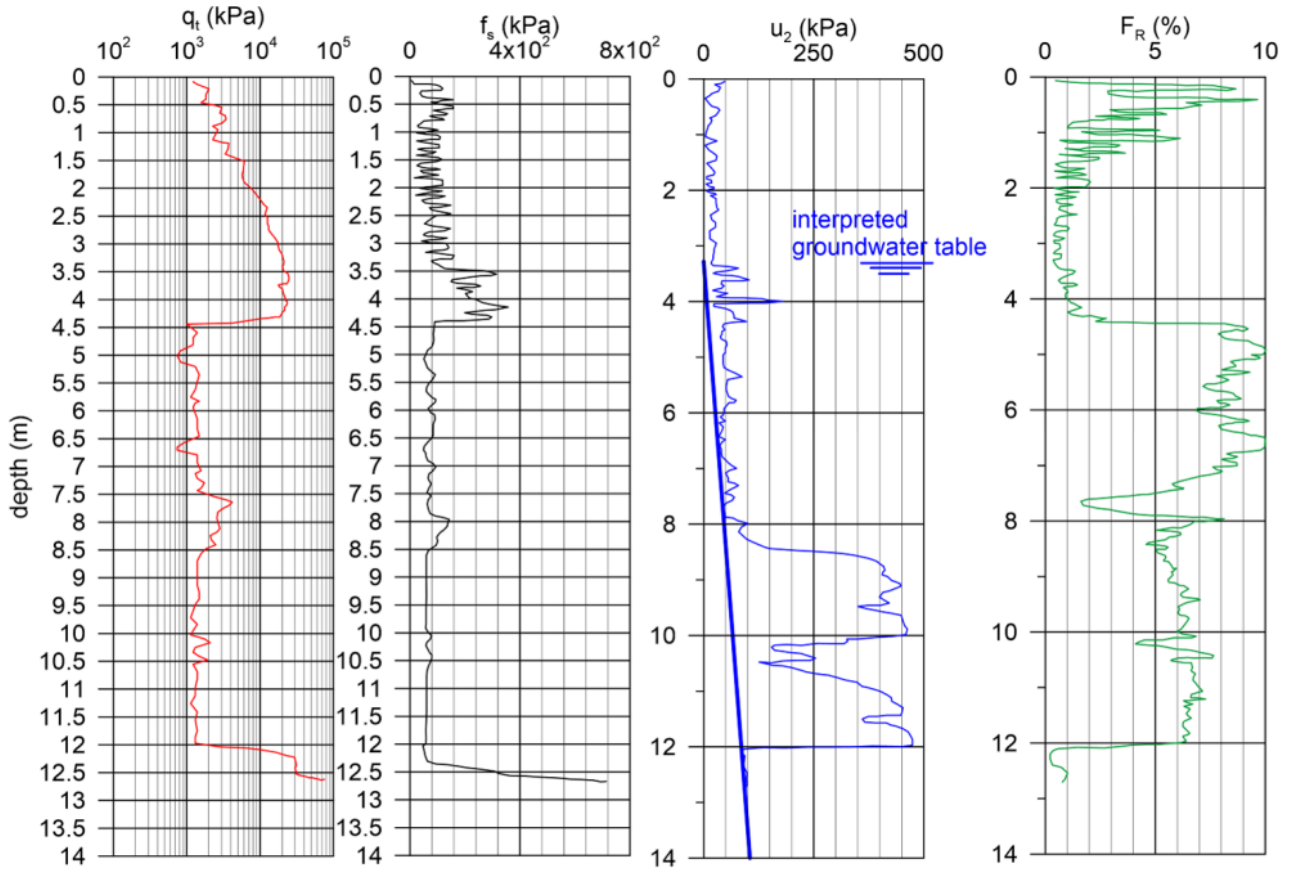

Figure 1.26. Typical CPTu test measurements.

The *cone resistance* q_c (kPa), determined as:

(1.6) $$q_c = 1000F_{cone} + 9.8m_g$$

where F_{cone} is the force acting on the cone tip (kN), measured by means of a load cell (cone strain gauge load cell, Figure 1.22b), and m_g is mass of the inner rods at the test depth (kg).

If necessary (i.e., in CPTu tests), cone resistance is corrected for pore pressure development, according to the mentioned above:

(1.7) $$q_t = q_c + u_2(1 - a)$$

Note that we may use the symbols q_c and q_t interchangeably: q_c refers to cone resistance from CPT tests, and q_t refers to cone resistance from CPTu tests, which has been correct for pore pressure effects.

The *sleeve friction resistance* f_s (kPa), determined as:

(1.8) $$f_s = \frac{F_{sleeve}}{A_s}10^6$$

where F_{sleeve} is the force on the sleeve, equal to the total force on the cone and sleeve (measured by means of the friction strain gauge load cell, Figure 1.22b) minus the force on the cone alone (kN), and A_s is the surface area of the friction sleeve (mm^2).

The *friction ratio* (%), which is equal to:

(1.9) $$F_R = \frac{f_s}{q_t}100 \text{ or } \frac{f_s}{q_c}100$$

and the *pore water pressure* u_2, measured via a pore pressure transducer installed above the tip of the cone in CPTu rigs.

One of the main applications of the CPT test is the indirect determination of subsoil stratigraphy i.e., the thickness of soil layers and the soil type. As a rule-of-thumb, the cone resistance q_c is high in sands and low in clays, and the friction ratio F_R is high in clays ($3\% < F_R < 10\%$) and low ($0.5\% < F_R < 1.5\%$) in sands. It was mentioned before that we cannot obtain soil samples from the CPT test for laboratory characterisation tests. Thus, the CPT test cannot provide direct characterisation of the soil based e.g. on its grain size distribution, but rather of the *Soil Behavior Type* (SBT), a quantity which can be correlated to its mechanical characteristics (Robertson and Kabal, 2022). The Soil Behavior Type is determined from the chart presented in Figure 1.27, based on the dimensionless cone resistance measured at a particular depth, divided against the atmospheric pressure q_c/p_a (or q_t/p_a, if applicable), and the corresponding friction ratio F_R at the same depth from Eq. 1.9.

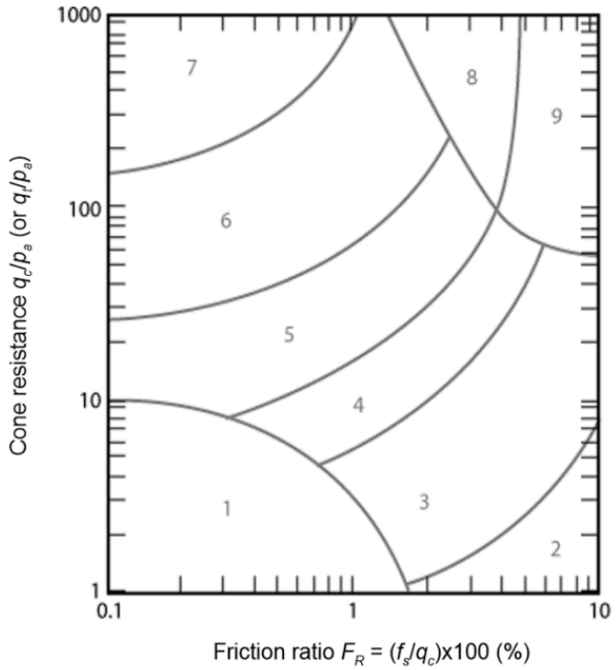

Soil Behavior Type/Zone	Description
1	Sensitive fine-grained soils
2	Organic soils – Clay
3	Clays: Clay to silty clay
4	Silt mixtures: Clayey silt and silty clay
5	Sand mixtures: Silty sand to sandy silty
6	Sands: Clean sands to silty sands
7	Dense sand to gravelly sand
8	Very stiff sand to clayey sand (probably cemented)
9	Very stiff fine grained (heavily overconsolidated or cemented)

p_a = Atmospheric pressure = 100 kPa

Figure 1.27. Non-normalised Soil Behaviour Type SBT chart (after Robertson and Kabal 2022).

A disadvantage of the soil stratigraphy interpretation method described above is that it does not account for the increase in cone resistance and sleeve friction resistance with overburden stress, as the cone is being pushed deeper into the soil. To alleviate this, interpretation methods based on normalised cone resistance and sleeve friction resistance have been proposed. Such a procedure is described in Robertson and Kabal (2022). First, the normalised cone resistance Q_{tn} is calculated as:

(1.10) $$Q_{tn} = \left(\frac{q_t - \sigma'_{z0}}{p_a}\right) C_c$$

where σ'_{z0} is the effective vertical geostatic stress at the depth where each cone resistance measurement q_t is obtained, p_a is the atmospheric pressure and C_c is a correction factor similar to that of Eq. 1.2, calculated as:

(1.11) $$C_c = \left(\frac{p_a}{\sigma'_{z0}}\right)^n$$

where $n \leq 1.0$ is an exponent provided by the following expression:

$$\textbf{(1.12)}\ n = 0.381 I_c + 0.05 \left(\frac{\sigma'_{z0}}{p_a} \right) - 0.15$$

The factor I_c is the so-called Soil Behaviour Type index, and is calculated as:

$$\textbf{(1.13)}\ I_c = \sqrt{(3.47 - \log Q_{tn})^2 + (1.22 + \log F_r)^2}$$

where F_r (%) is the normalised sleeve friction resistance:

$$\textbf{(1.14)}\ F_r = \left(\frac{f_s}{q_t - \sigma_{z0}} \right) 100$$

where σ_{z0} is the total vertical geostatic stress at the depth where each cone resistance and sleeve friction measurement is obtained. As it is clear from the above expressions, Q_{tn} must be calculated iteratively, by assuming an initial value of the exponent n e.g., $n = 1$ and iterating until the change in n between successive iterations becomes less than $\Delta n = 0.01$.

Accordingly, Figure 1.28 (Robertson and Kabal 2022) can be used to obtain the Soil Behaviour Type, as well as an estimate of the behaviour of non-cemented soils at large strains (dilative or contractive). CD in Figure 1.28 defines the boundary between contractive and dilative behaviour, while I_B is a modified Soil Behaviour Type index that defines the transition zone between sand-like and clay-like behaviour via an intermediate (transitional) soil zone.

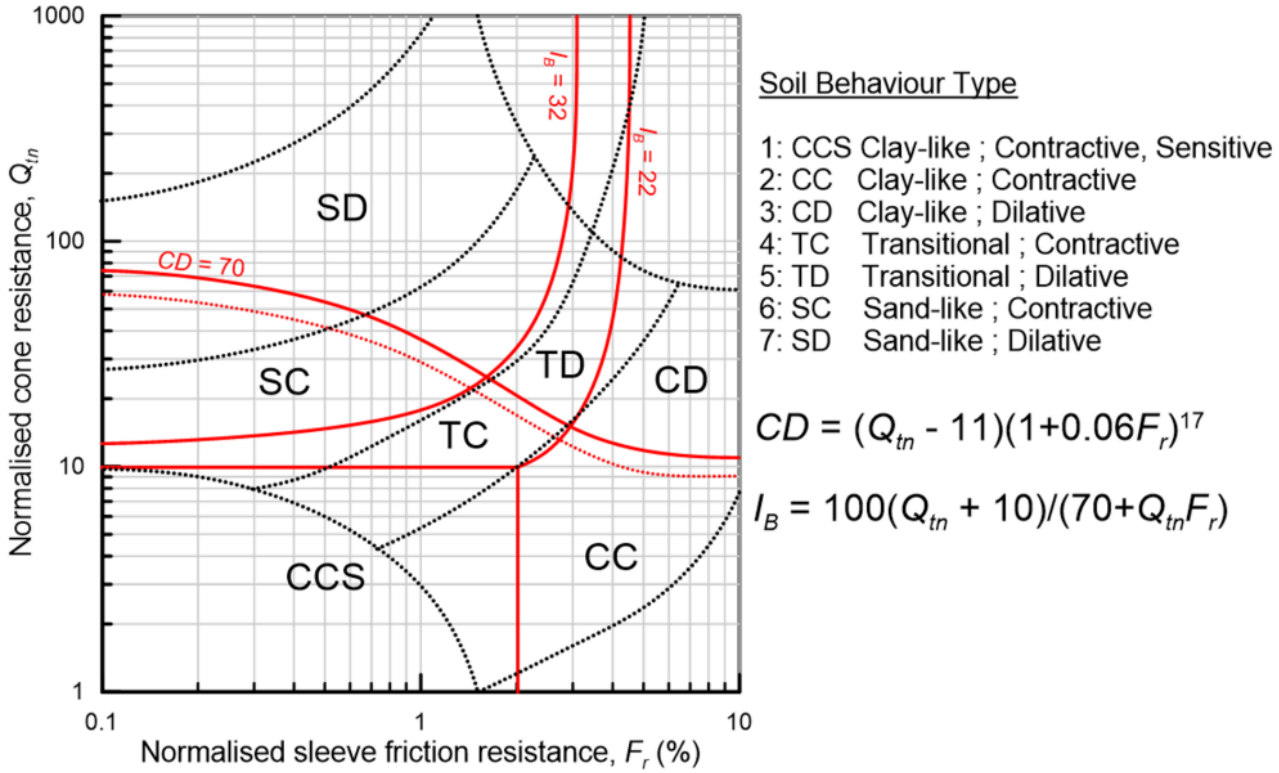

Figure 1.28. Normalised Soil Behaviour Type SBT chart (after Robertson and Kabal 2022).

An example soil behavior type profile determined with the method depicted in Figure 1.27 is presented in Figure 1.29. Different dots in the soil behavior type chart correspond to different cone resistance/friction ratio pairs, depicted from their distribution with depth on the left. Depending on the zone of the chart where each dot lies, a SBT is assigned to each pair, and a different color is used. Using the distribution of

SBT with depth, different layers can be identified along the soil profile, as presented on the right. Although it is clear that CPT provides a more "objective" evaluation of the soil profile, based on the SBT chart, engineering judgment is always necessary to interpret a rational soil stratigraphy.

1.8 INTERPRETATION OF CPT MEASUREMENTS TO DERIVE SOIL PARAMETERS

Except soil stratigraphy, CPT and CPTu sounding measurements can be used together with several empirical, semi-empirical as well as rigorous correlations, to determine the mechanical characteristics of soil. Soil parameters that can be derived with high-to-moderate accuracy from interpretation of CPT measurements are provided in Table 1.7. More details on the derivation of these parameters are provided in the following sections.

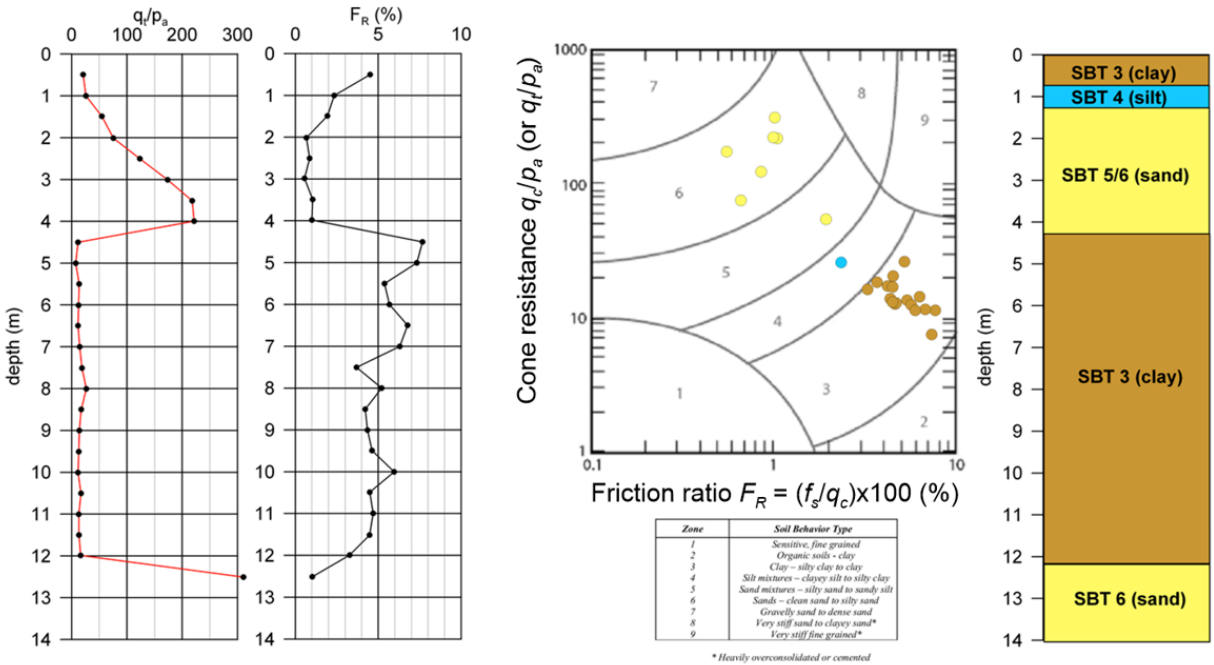

Figure 1.29. Example soil stratigraphy determined with a CPT test and the non-normalised Soil behavior type SBT chart.

Table 1.7. Soil parameters that can be reliably determined from CPT tests (with information from Robertson and Kabal 2022).

	Soil type	
	Coarse-grained (sand)	**Fine-grained (clay)**
Relative density, D_r	✓	N/A
Earth pressure coefficient at-rest, K_0	N/R	✓*
Overconsolidation ratio, OCR	N/R	✓
Sensitivity, S_t	N/A	✓**
Undrained shear strength, S_u	N/A	✓
Friction angle, φ'	✓	N/R
Permeability (via dissipation tests)	N/R	✓
Compressibility parameters (Young's modulus E', coefficient of volume compressibility m_v)	✓	✓
N/A: Not Applicable; N/R: Not Recommended		
** In the author's view, the DMT provide more reliable estimates of the earth pressure coefficient at-rest (see Chapter 1.10)*		
*** In the author's view, sensitivity values obtained by means of CPT tests must be treated with caution (see Section 1.8.3 and Part 6)*		

1.8.1 Equivalent *N*-SPT values

Determining equivalent *N*-SPT values from cone tip measurements means that we can combine CPT sounding results with the numerous empirical expressions and design methodologies that have been developed to be used together with SPT test results. Robertson and Kabal (2022) recommend using the chart presented in Figure 1.30 to estimate N_{60} values as a function of the cone resistance q_c/p_a or q_t/p_a, where p_a = 100 kPa is the atmospheric pressure, and of the mean grain (or particle) size D_{50}.

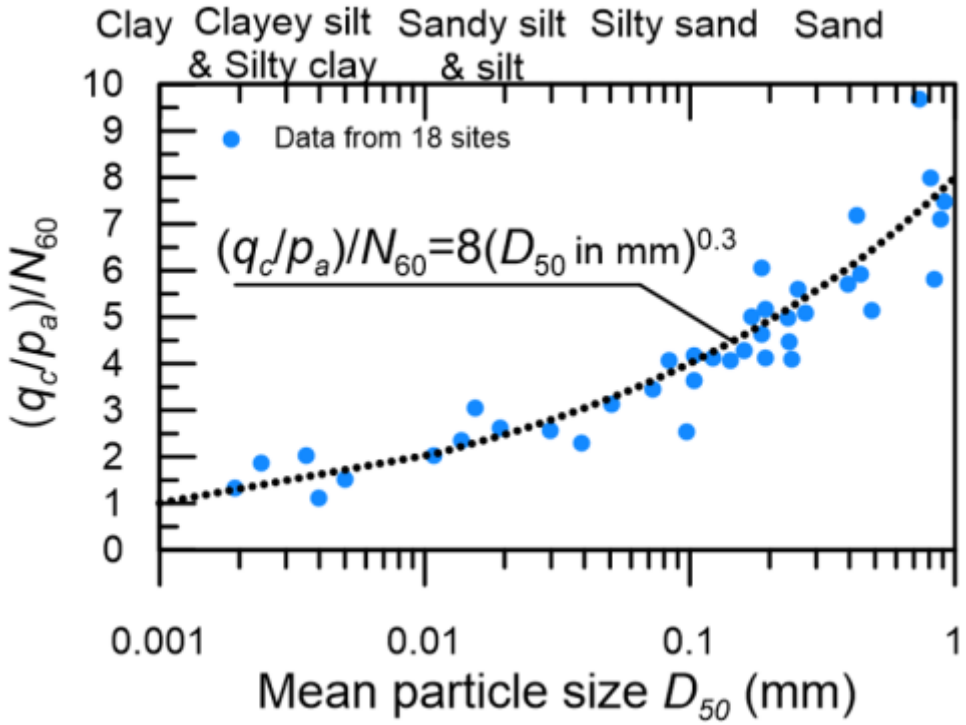

Figure 1.30. Cone resistance-N_{60} correlation with mean grain size D_{50} (after Robertson and Kabal 2022, with modifications).

Alternatively, N_{60} values can be correlated to the cone resistance q_c/p_a or q_t/p_a while considering the SBT instead of the mean grain size, as presented in Table 1.8.

Table 1.8. Normalized cone resistance-N_{60} correlation with SBT (Robertson 2010).

Soil Behavior Type/Zone	Description	$(q_c/p_a)/N_{60}$
1	Sensitive fine-grained soils	2.0
2	Organic soils – Clay	1.0
3	Clays: Clay to silty clay	1.5
4	Silt mixtures: Clayey silt and silty clay	2.0
5	Sand mixtures: Silty sand to sandy silt	3.0
6	Sands: Clean sands to silty sands	5.0
7	Dense sand to gravelly sand	6.0
8	Very stiff sand to clayey sand (probably cemented)	5.0
9	Very stiff fine grained (heavily overconsolidated or cemented)	1.0

For example, a clayey soil classified as SBT 3 and exhibiting cone resistance during penetration q_t = 2 MPa has an equivalent N_{60} value of:

(1.15) $$N_{60} = \frac{2000\ \text{kPa}/100\ \text{kPa}}{1.5} = 13.33$$

1.8.2 Undrained shear strength, S_u

The undrained shear strength of fine-grained soil is not a fundamental soil property, and depends on the stress level and the loading history i.e., the overconsolidation ratio OCR. The undrained shear strength can be correlated to the cone resistance by means of the following semi-empirical formula:

(1.16) $$S_u = \frac{q_t - \sigma_{z0}}{N_{kt}}$$

where σ_{z0} is the total vertical geostatic stress at the specific depth, and the cone factor N_{kt} ranges from 10 to 18. Equation 1.16 is analogue to the formula providing the bearing capacity of a foundation on undrained soil. Therefore, the cone factor accounts for the shape of the failure surface developing in the soil as the cone tip is being pushed downwards, and depends on the characteristics of the particular soil tested. An average value of N_{kt}= 14 to 16 provides acceptable, conservative results for usual cases. According to Lunne *et al.* (1976), N_{kt} can be correlated to the soil plasticity index PI (%) as:

(1.17) $$N_{kt} = 13 + 0.11\text{PI}(\pm 2)$$

A more recent expression for estimating the cone factor N_{kt} has been proposed by Mayne and Peuchen (2022), who statistically analysed data from 70 clay deposits to establish a correlation between N_{kt} and the normalised pore pressure parameter $B_q = \Delta u/q_n$:

(1.18) $$N_{kt} = 10.5 + 4.6\ln(B_q + 0.1)$$

where $\Delta u = u_2 - u_0$ (u_0 is the hydrostatic pore pressure) and $q_n = \sigma_t - \sigma_{z0}$.

The undrained shear strength ratio to the geostatic vertical effective stress (S_u/σ'_{z0}) is estimated as:

(1.19) $$\frac{S_u}{\sigma'_{z0}} = \frac{q_t - \sigma_{z0}}{\sigma'_{z0}} \frac{1}{N_{kt}} = \frac{Q_t}{N_{kt}}$$

where

$$Q_t = \left(\frac{q_t - \sigma_{z0}}{\sigma'_{z0}} \right)$$

is a dimensionless expression for the cone resistance. For normally consolidated clays with OCR = 1 it is Q_t = 3 to 4, thus the undrained shear strength ratio will attain a value of about $S_u/\sigma'_{z0} \approx 0.22$, as discussed in the Example 1.1.

An important drawback of the above expressions is that the cone factor N_{kt} must be assumed, determined from empirical expressions, or alternatively calibrated on the results of triaxial tests on undisturbed samples and/or *in situ* vane shear test data from the same site. Such data are not always available. While empirical equations such as Eq. 1.17 have some value in estimating the cone factor, they are not based on a rigorous theoretical background. An alternative method for interpreting CPTu measurements in soft clay to obtain undrained strength values, that does not require estimating a cone factor value and is based on a rigorous cavity expansion model has been proposed by Zhang *et al.* (2023). The undrained shear strength is calculated as:

(1.20) $$S_u = \frac{q_t - u_2}{N_u}$$

Where u_2 is the pore pressure measured during the piezocone test at a certain depth, and N_u is an alternative (because Eq. 1.20 uses pore pressure instead of total vertical stress used in Eq. 1.16) cone factor, defined as:

(1.21) $$N_u = \frac{2}{M_{cs}} + \frac{4}{3} + a_E \cot a$$

where M_{cs} is the inclination of the critical state line in p'–q space equal to $M_{cs} = 6\sin\varphi_{cs}/(3\text{-}\sin\varphi_{cs})$, that can be measured from standard triaxial compression tests. Typically, M_{cs} for Australian clays ranges between $M_{cs} = 1.2$ to 1.3; α_E is a factor that accounts for rate effects during cone penetration, and can be taken equal to $\alpha_E = 1.64$ if standard CPTu penetration rates have been applied during testing; a is the half of cone tip angle. For a standard cone $a = 30$ deg and $\cot a = 1.732$.

When using CPT sounding results to estimate the variation of undrained shear strength with depth, care must be taken so as to disregard any unrealistic, extreme values (Figure 1.31). Of course, undrained shear strength should not be estimated for layers expected to behave as drained, according to their Soil Behavior Type assessment.

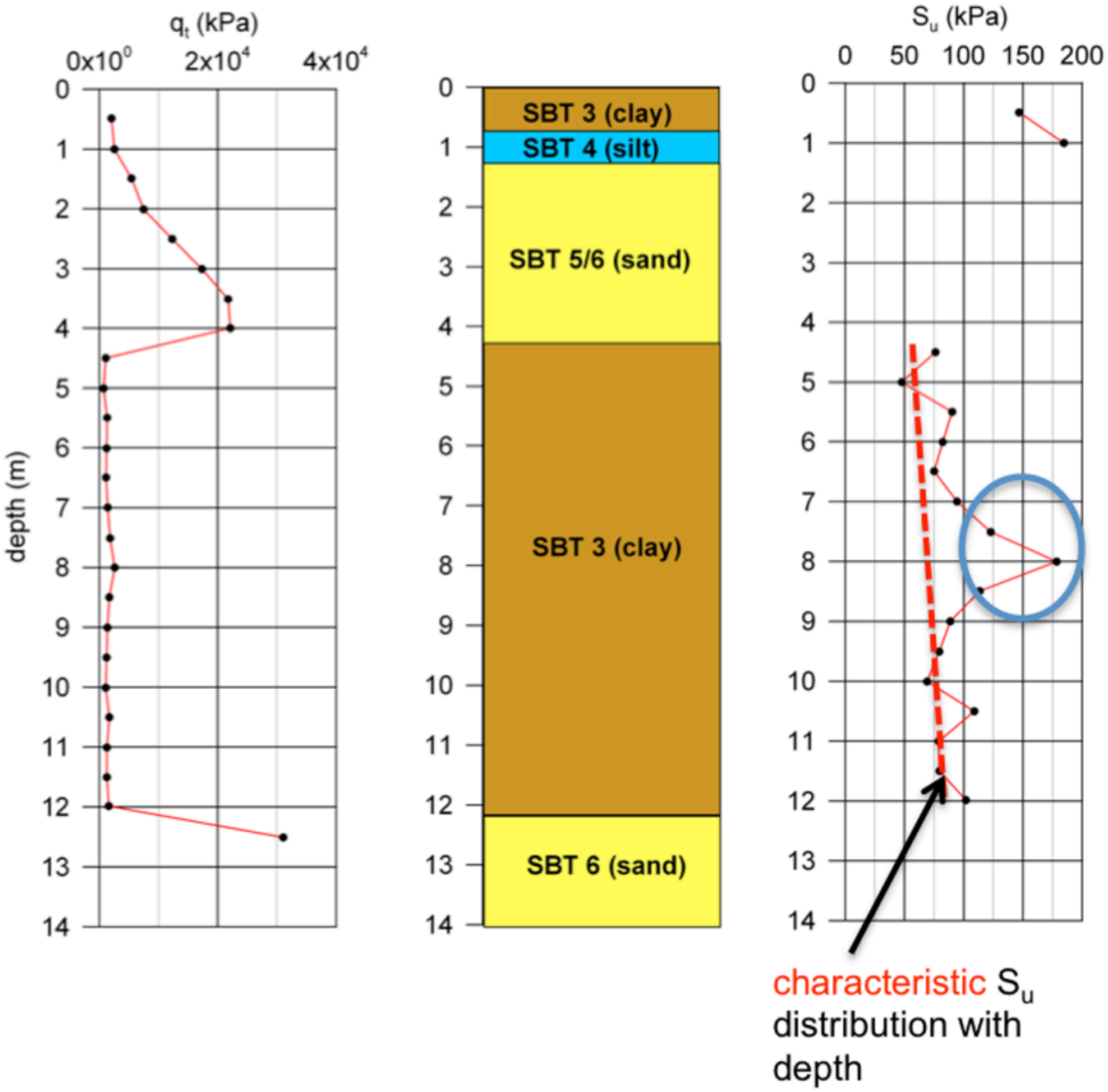

Figure 1.31. Estimation of the undrained shear strength distribution with depth from CPT results.

1.8.3 Clay sensitivity, S_t

Clay sensitivity is defined as the ratio of the undisturbed peak undrained shear strength to the remolded undrained shear strength, at the same moisture content (Table 1.9). If disturbed, the structure of very sensitive clays will be altered and they may undergo flow, a phenomenon that may result in catastrophic mudflows.

Sensitivity values can be estimated from CPT test results as:

(1.22) $$S_t = \frac{7}{F_r}$$

where F_r (%) is the normalised sleeve friction resistance, defined in Eq. 1.14.

Table 1.9. Classification of clay sensitivity values (after Mitchell 1976).

Clay classification	Clay sensitivity, S_t
Insensitive	~1.0
Slightly sensitive	1 to 2
Medium sensitive	2 to 4
Very sensitive	4 to 8
Slightly quick	8 to 16
Medium quick	16 to 32
Very quick	32 to 64
Extra quick	> 64

For very sensitive clays, the above estimate of sensitivity should be used as a guide only, due to difficulties in accurately measuring the sleeve friction is such clays (Robertson and Kabal 2022).

1.8.4 Overconsolidation ratio, OCR and lateral earth pressure coefficient at-rest, K_0

The overconsolidation ratio is commonly defined as the ratio of the maximum past vertical effective consolidation stress, σ'_p over the present vertical effective stress, σ'_{z0}. According to Robertson and Kabal (2022), OCR can be estimated from CPT test results as:

(1.23) $$\mathrm{OCR} = 0.25 Q_t^{1.25}$$

where

$$Q_t = \left(\frac{q_t - \sigma_{z0}}{\sigma'_{z0}} \right)$$

The above Eq. 1.23 has been derived while assuming that the undrained shear strength over geostatic vertical effective stress ratio of overconsolidated (OC) clays can be correlated to the corresponding ratio for normally consolidated (NC) clays as:

(1.24) $$\left(\frac{S_u}{\sigma'_{z0}} \right)_{\mathrm{OC}} = \left(\frac{S_u}{\sigma'_{z0}} \right)_{\mathrm{NC}} \mathrm{OCR}^m$$

where the exponent m is approximately equal to m = 0.8 to 0.85. This value of OCR can be also used to estimate the lateral earth pressure coefficient at-rest K_0 of low plasticity clays and silts (Kulhawy and Mayne, 1990):

(1.25) $$K_0 \approx (1 - \sin \varphi') \, \mathrm{OCR}^{0.5} = 0.5 \mathrm{OCR}^{0.5}$$

Alternatively, the method of Zhang *et al.* (2023) can be used to obtain a more rigorous estimate of the overconsolidation ratio of soft clays:

$$\textbf{(1.26)}\ \mathrm{OCR} = 2\left[\frac{6\left(q_t - u_2\right)}{N_u M_{cs}\left(1 + 2K_0\right)\sigma'_{z0}}\right]^{\frac{\lambda}{\lambda-\kappa}}$$

where K_0 can be calculated as K_0 = 1-sinφ' while λ = C_c/2.3 and κ = C_r/2.3 with C_c, C_r being the compression and recompression indexes, respectively, measured from oedometer tests. Note here that κ cannot be directly related to C_r, and some recommend considering κ = 2C_r/2.3 instead.

1.8.5 Relative density D_r and friction angle φ' of sands

The *relative density* of sands is defined as:

$$\textbf{(1.27)}\ D_r = \frac{e_{\max} - e}{e_{\max} - e_{\min}}$$

where e is the *in situ* void ratio, and e_{max}, e_{min} is the maximum and minimum void ratios corresponding to the loosest and densest state that specimens of this sand can be prepared using standarised procedures, respectively. According to Kulhawy and Mayne (1990), relative density D_r (%) of non-cemented sands can be estimated from the cone resistance as:

$$\textbf{(1.28)}\ D_r = 100\sqrt{\frac{Q_{tn}}{350}}(\%)$$

Where Q_{tn} is given by Eq. 1.10. Alternatively, the chart and expression presented in Figure 1.32 can be used.

For estimating the friction angle of non-cemented sands, Mayne (2006) recommends the following expression, based on *in situ* and laboratory test results (Figure 1.33):

$$\textbf{(1.29)}\ \varphi' = 17.6^o + 11\log\left(\frac{q_t - \sigma_{z0}}{\sqrt{\sigma'_{z0} p_a}}\right)$$

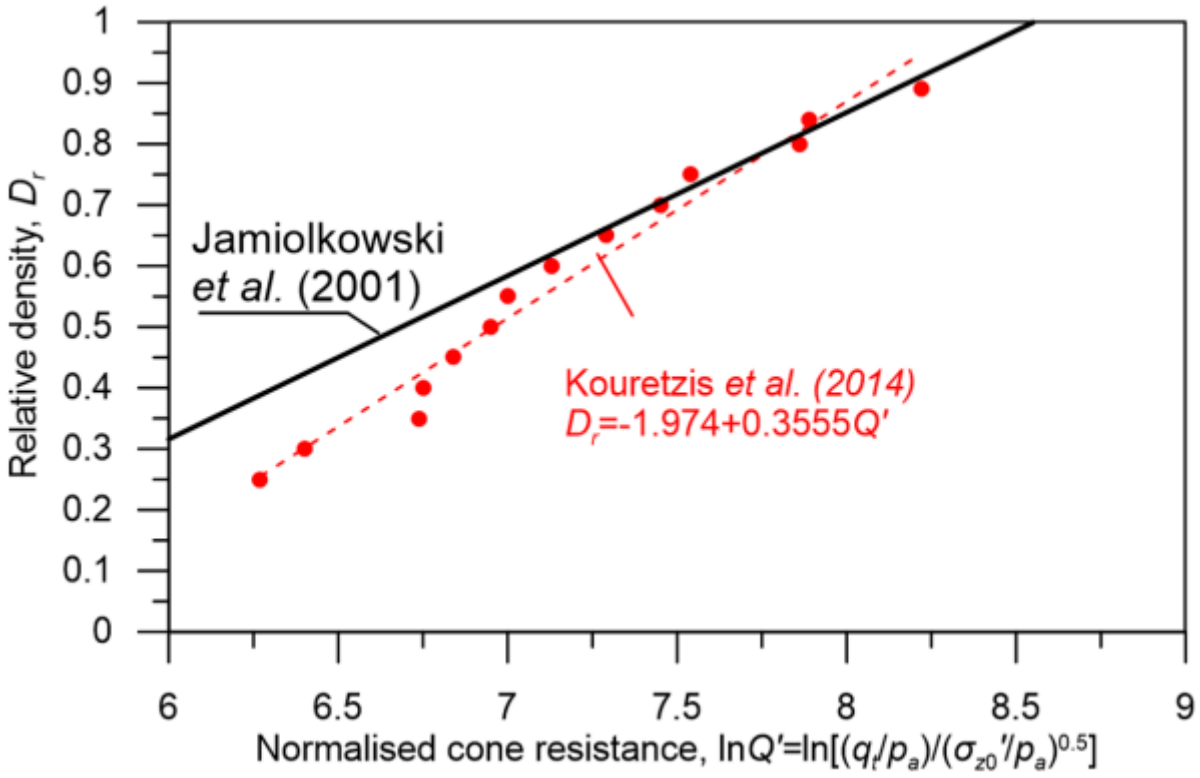

Figure 1.32. Correlation of cone resistance with the vertical effective stress and the relative density D_r (with information from Kouretzis et al. 2014, Jamiolkowski et al. 2001).

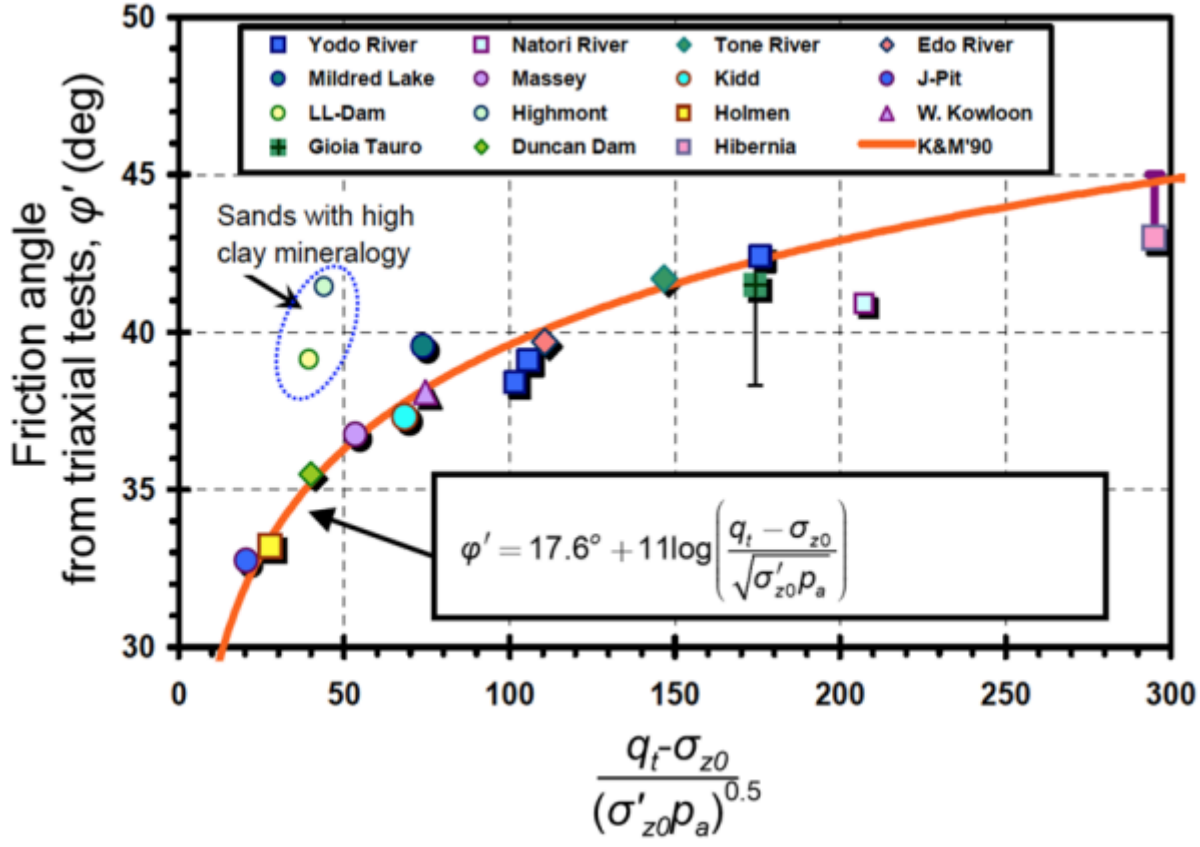

Figure 1.33. Friction angle φ' of non-cemented sands (Mayne 2006, reproduced with permission).

1.8.6 Soil unit weight, γ

When soil samples are not available, the bulk unit weight of soil can be estimated from CPT measurements as (Robertson and Kabal 2022):

(1.30) $$\frac{\gamma}{\gamma_w} = \left\{0.27\left(\log F_R\right) + 0.36\left[\log\left(\frac{q_t}{p_a}\right)\right] + 1.236\right\}\frac{G_s}{2.65}$$

where F_R is the friction ratio (%) from Eq. 1.9; γ_w is the unit weight of water (10 kN/m^3) and G_s is the specific gravity of soil, equal to about G_s = 2.65 for most silica-based soils.

1.8.7 Compressibility parameters E' and m_v

The drained Young's modulus E' of non-cemented silica sands to be used for settlement estimations (strain levels of the order of 0.1%) can be estimated from Eq. 1.31:

(1.31a) $$E' = \alpha_E\left(q_t - \sigma_{z0}\right)$$

where

(1.31b) $$\alpha_E = 0.015 \times 10^{(0.55I_c + 1.68)}$$

and I_c is the Soil Behaviour Type index, calculated according to Eq. 1.13. The parameter α_E can be estimated alternatively from Figure 1.34.

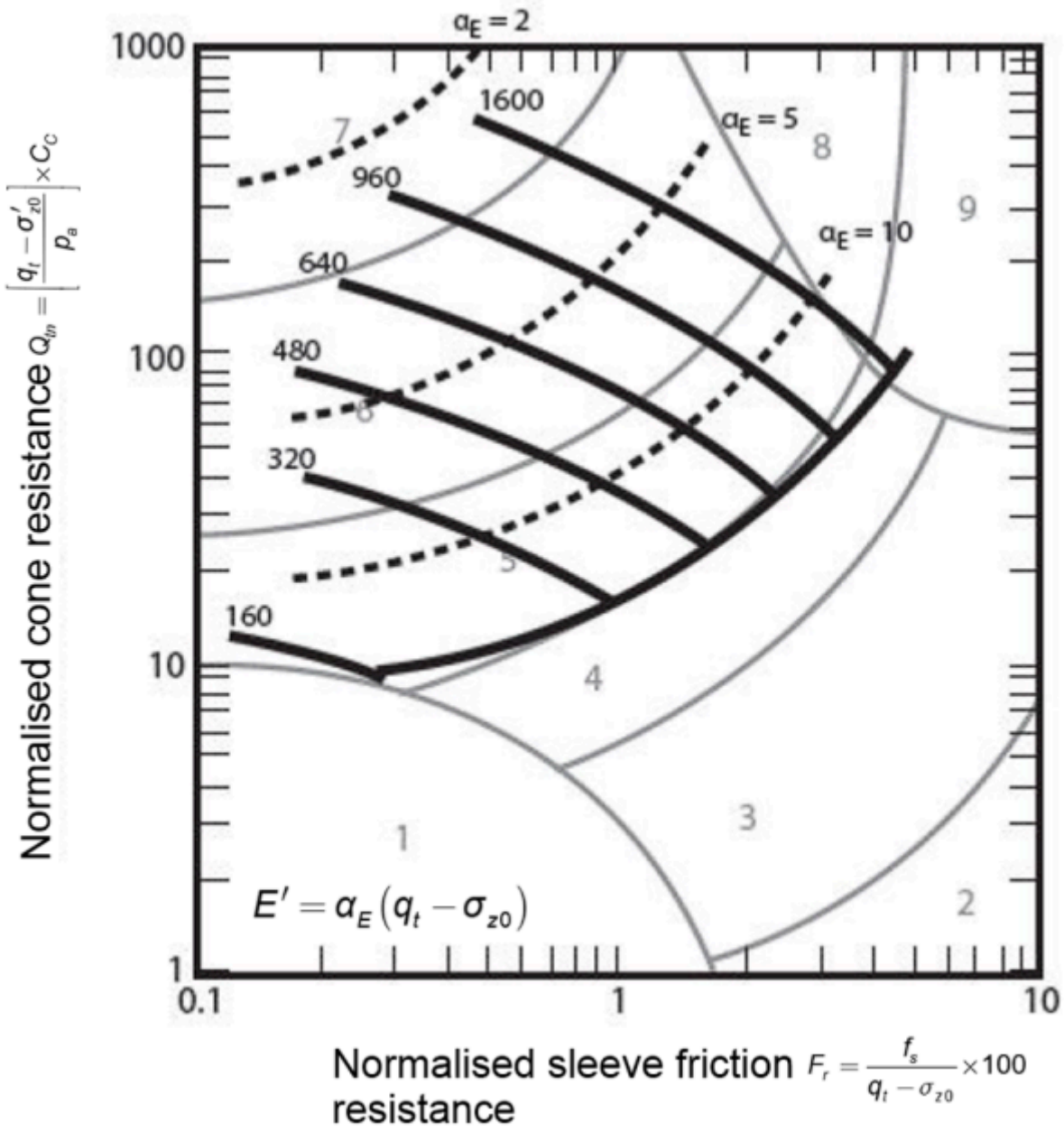

Figure 1.34. Evaluation of drained Young's modulus E' of non-cemented sands (after Robertson and Kabal 2022).

The coefficient of volume compressibility m_v of fine-grained soils, which is correlated to their Young's modulus and Poisson's ratio by means of theory of elasticity formulas (see Part 4), can be evaluated as:

(1.32) $$m_v = \frac{1}{\alpha_M (q_t - \sigma_{z0})}$$

where:

(1.33a) $$\alpha_M = Q_t = \left(\frac{q_t - \sigma_{z0}}{\sigma'_{z0}}\right) \text{ when } Q_t < 14$$

(1.33b) $$\alpha_M = 14 \text{ when } Q_t > 14$$

Note that the above expressions are valid when the Soil Behaviour Type index is $I_c > 2.2$, which corresponds to fine-grained soils.

1.9 THE VANE SHEAR TEST

The *vane shear* test is performed to measure *in situ* the undrained shear strength S_u of soft-to-medium clays with undrained shear strength less than 50 kPa.

The standard procedure for field vane shear tests is described in AS 1289.6.2.1 (Figure 1.35): A four-blade vane is pushed into the soil, at a depth no closer than four borehole diameters from the immediately above test location, and it is rotated until the soil shears to failure, while measuring the maximum torque T necessary to rotate the vane. The standard dimensions of the vane are 130 mm height (H) x 65 mm diameter (D) x 3 mm thickness (t). Both the peak shear strength and the remolded shear strength are measured: the former during the rotation of the vane for 1 minute at a constant rate of 6 deg/min, and the latter from the constant torque measured after 8-10 additional rapid revolutions. The sensitivity S_t of the clay is also estimated, as the ratio of the undisturbed peak undrained shear strength to the remolded undrained shear strength (see Section 1.8.3).

The undrained shear strength is estimated from the measurements obtained during the vane test as:

$$\textbf{(1.34)}\ S_u\,(\mathrm{kPa}) = \frac{272.83 \times 10^6 T\,(\mathrm{kNm})}{D^3\,(\mathrm{mm})}$$

The above Eq. 1.34 is valid for standard vanes, where $H = 2D$ (Figure 1.36). Note that the skin friction of the vane rod should be accounted for in the calculation of the maximum torque, T.

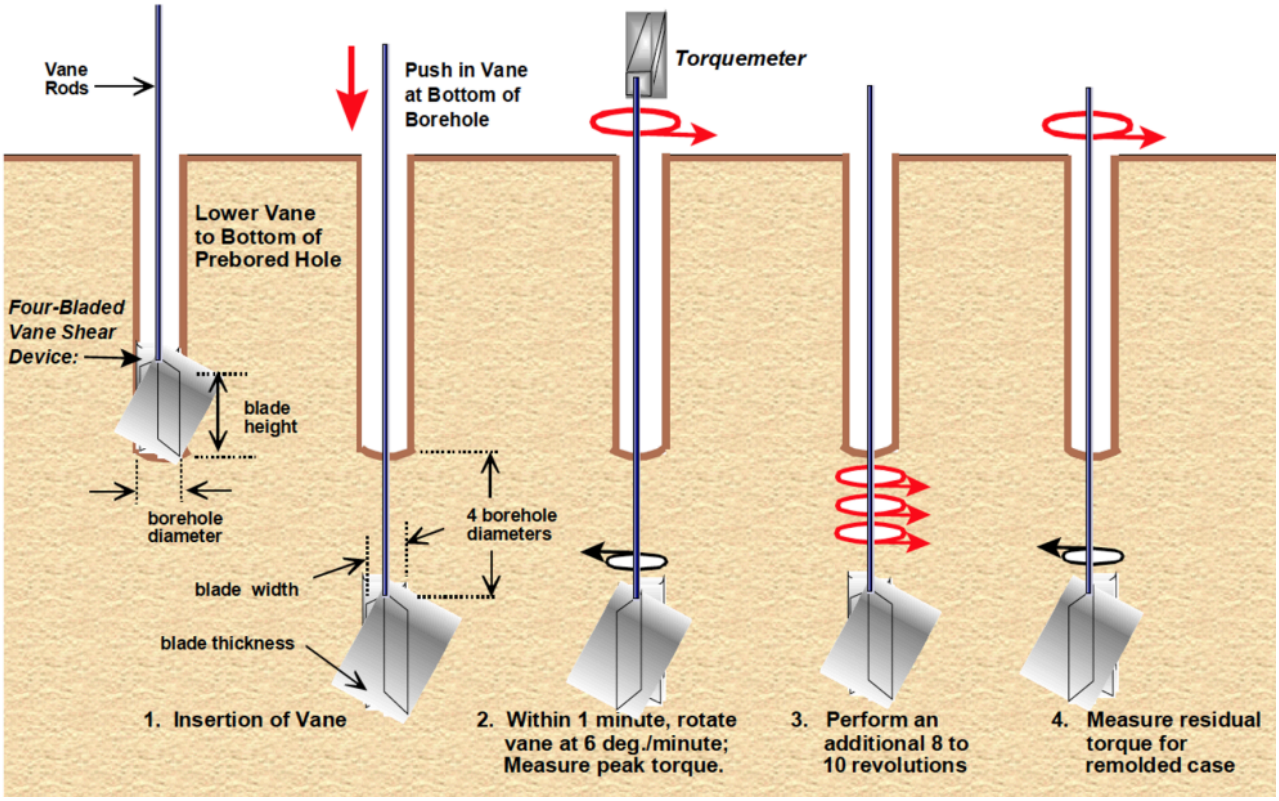

Figure 1.35. Vane shear test procedure (FHWA 2006, no copyright restrictions).

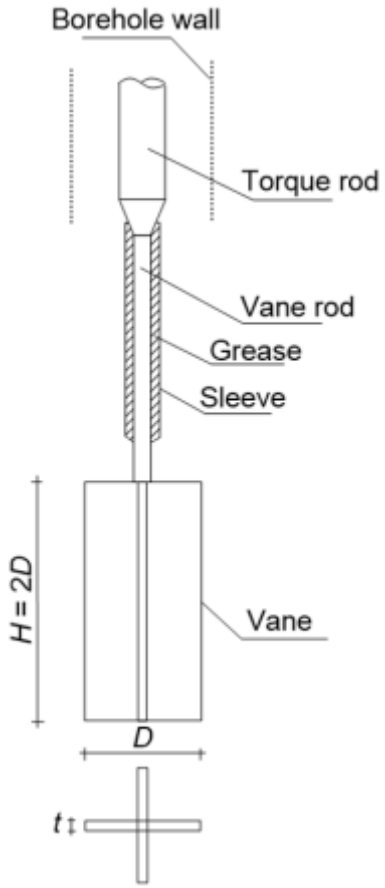

Figure 1.36. Vane and rod mounting

Based on experience from failures of embankments on soft clay immediately after construction, it is acknowledged that the shear vane test tends to overestimate the undrained shear strength. This is due to the fact that clays exhibit viscous behaviour, which suggests that their strength depends on the rate of shearing: the higher the rate, the higher the strength. Therefore a reduction factor λ_v needs to be considered when estimating the design undrained shear strength (corresponding to time to failure of the order of days/ weeks) from vane tests where failure takes place within 1-2 mins:

(1.35) $S_{u,design} = \lambda_v \times S_{u,vane}$

This reduction factor depends on the plasticity index PI of the clay (Figure 1.37), as the higher the plasticity index (increased clay content), the more prominent viscous effects are.

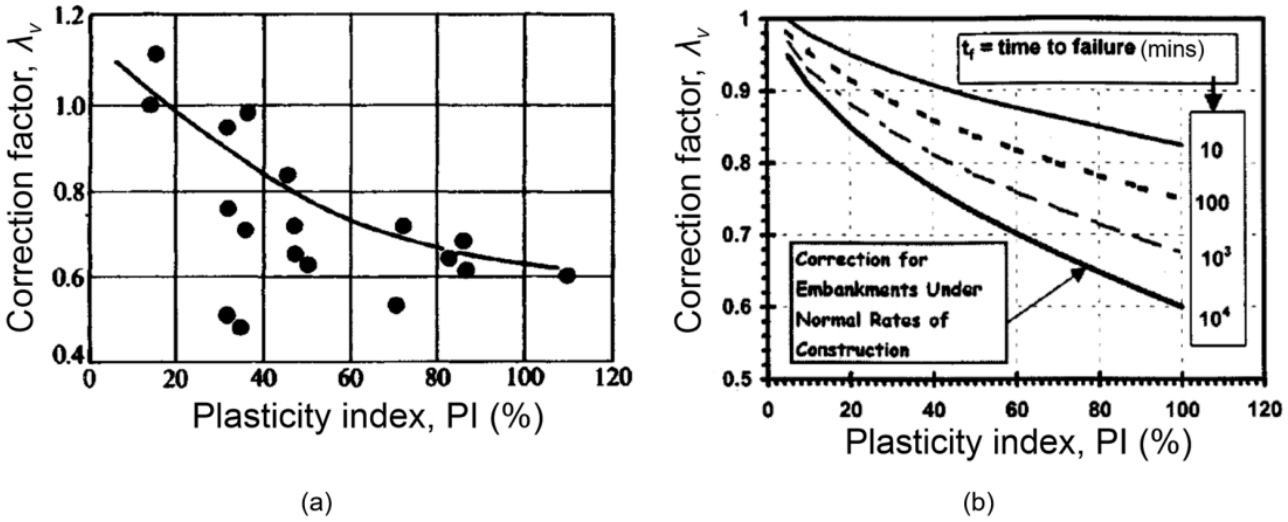

Figure 1.37. (a) Reduction factor of undrained shear strength obtained from vane shear tests for embankment stability analyses (after Bjerrum 1972); (b) Reduction factor curves as function of the time to failure and of the plasticity index (after Chandler 1988).

The advantage of the vane shear over other *in situ* testing methods for determining the undrained shear strength (CPTu, Eq. 1.16) is that the interpretation of the former is generally not sensitive to uncertainties regarding the shape of the failure surface (or value of the cone factor N_{kt}). It is widely accepted that rotation of a four-blade vane into soft soil will result in a cylindrical failure surface, and this is reflected in Eq. 1.34. Therefore, it is quite common to use vane shear tests to obtain site-specific cone factor values, in other words to calibrate the interpretation of cone test results on vane shear tests. Finally, it must be noted that the undrained shear strength measured by means of vane shear tests is the undrained strength under simple shear conditions (see Kouretzis *et al.* 2017), which in not equal to the undrained shear strength measured during common triaxial compression tests, as the stress path to failure is different. The implications of this when it comes to stability calculations are discussed in Part 5.

1.10 THE FLAT DILATOMETER (DMT) TEST

The flat dilatometer test is a soil testing method used to obtain a range of soil parameters, predominantly the *in situ* lateral soil stress and stiffness of sandy and clayey soils (Marchetti *et al.* 2001). The standard method of performing flat dilatometer tests is described in the ASTM D6635 standard. It consists of pushing a stainless-steel blade, on which a 60-mm steel membrane (Figure 1.38a) is mounted, into the soil and measuring the gas pressure required to begin moving the membrane relatively to its surrounding soil (lift-off or A-pressure) and the gas pressure required to move the centre of the membrane by 1.1 mm against the soil (B-pressure). Both measurements are taken within about 1 min. Following calibration to account for membrane stiffness, the pressure readings A and B are corrected to find the pressure values p_0 and p_1 acting on the membrane from the soil. During a DMT sounding pressure readings are obtained at various depths, spaced typically 200 mm apart.

One of the key parameters interpreted from DMT measurements is the horizontal stress index K_D, defined as:

$$\textbf{(1.36)} K_D = \frac{p_0 - u_0}{\sigma'_{z0}}$$

where p_0 is the calibrated lift-off pressure (see Figure 1.38b); u_0 is the hydrostatic pore pressure at the depth of testing; σ'_{z0} is the geostatic vertical effective stress at the same depth.

The horizontal stress index coefficient is rigorously correlated with soil stress history, therefore can be used to estimate the overconsolidation ratio OCR, and subsequently the earth pressure coefficient at-rest (K_0), which is particularly difficult to measure with other *in situ* testing methods. Of course, under ideal conditions where blade penetration would not introduce any soil disturbance, the horizontal stress index would be equal to the earth pressure coefficient at-rest.

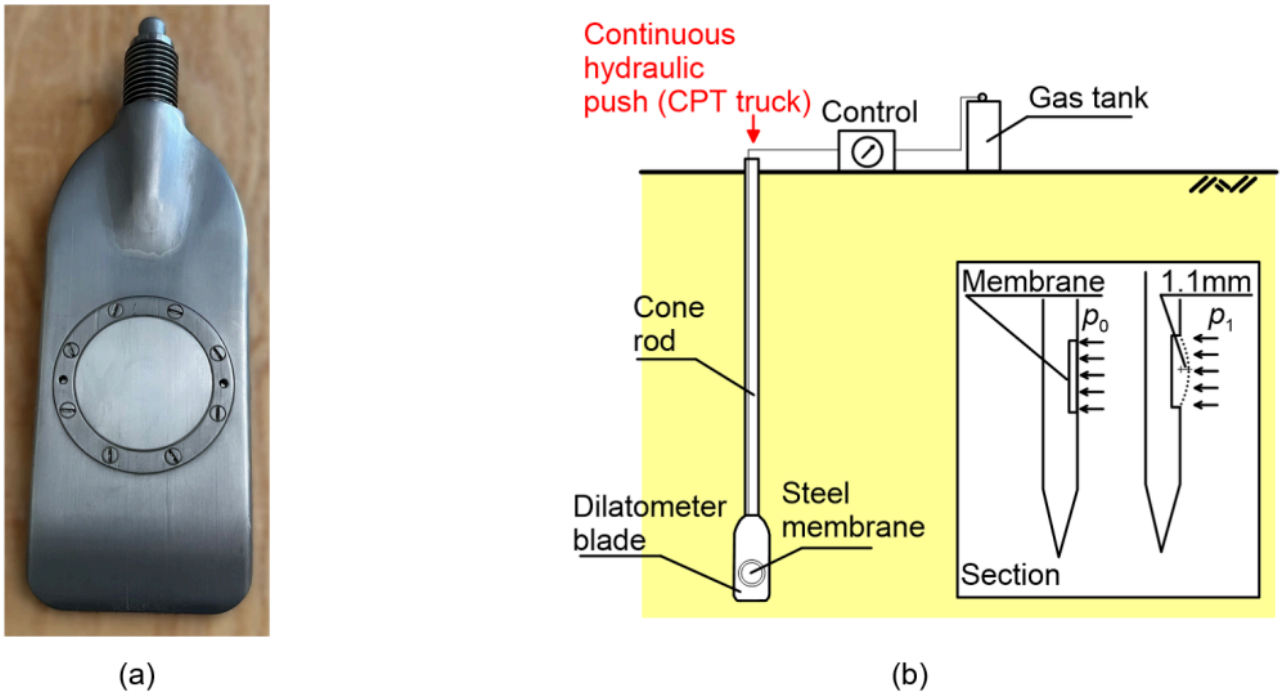

Figure 1.38. (a) Dilatometer blade (image courtesy of L. Bates), (b) Schematic of a DMT rig and test procedure.

However, this is never the case. Figure 1.39 presents certain popular expressions that link K_D measured in clay with OCR and K_0, together with field data from overseas (Powell and Uglow 1988) and Australia (Ballina clay, Kelly *et al.* 2015). Arguably OCR and K_0 values interpreted by means of DMT measurements are more reliable compared to those interpreted by means of CPT measurements (Chapter 1.8.4), due to the nature of the DMT.

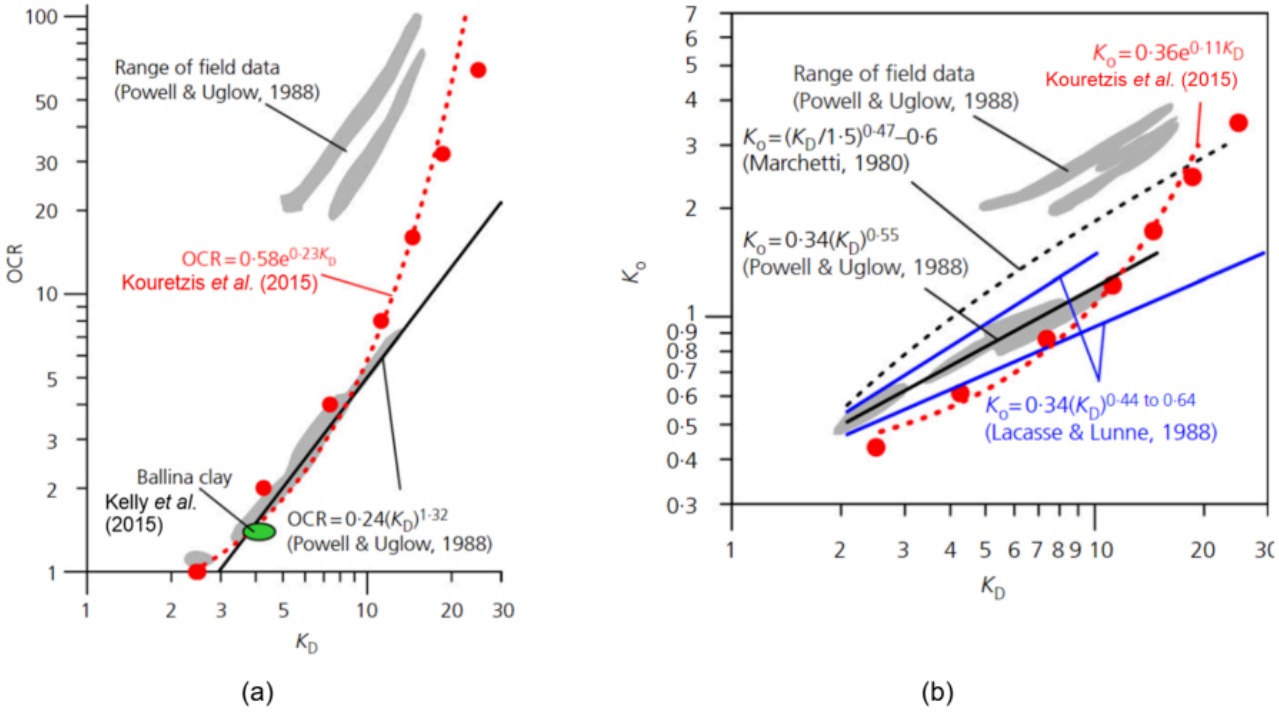

Figure 1.39. (a) Correlation of K_D with overconsolidation ratio OCR, (b) Correlation of K_D with earth pressure coefficient at-rest K_0 (Kouretzis et al. 2015).

1.11 GEOPHYSICAL METHODS FOR SOIL EXPLORATION

Non-destructive methods, where the term non-destructive suggests that no sampling, boring, or excavating of soil is involved, are also used to provide information on soil and rock properties, hydrogeological conditions, the subsoil profile etc. Information obtained through geophysical methods is generally two- (or three-) dimensional *(spatial),* compared to one-dimensional or point information provided by boreholes/ CPT soundings or soil samples, respectively (Figure 1.40).

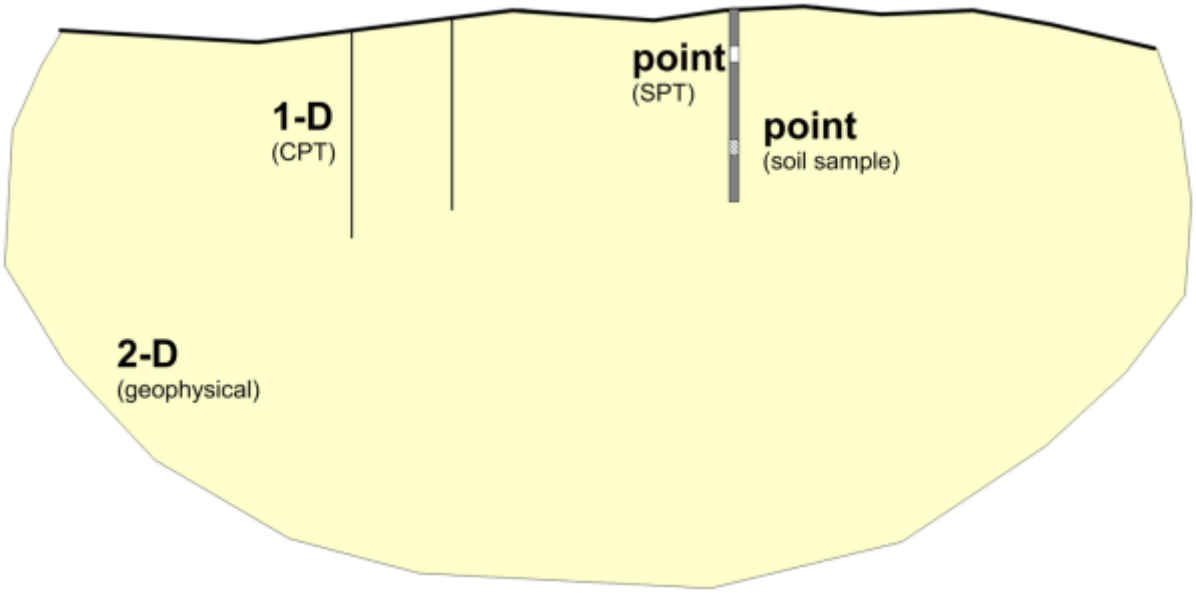

Figure 1.40. Different methods of soil exploration, compared in terms of area covered by each method.

The main advantage of geophysical methods is exactly their ability to provide spatial information on subsoil stratigraphy and groundwater levels, covering effectively a wide area. Geophysical methods are relatively quick and inexpensive, but their results are mainly qualitative, so they have limited applicability for deriving design geotechnical parameters. However, they can be implemented during early stages of a project, to better plan a detailed site investigation. Note that covering a wide area with geophysical methods requires real estate, to conduct tests properly**.**

The most common methods mentioned in AS1726 are described compendiously in the following paragraphs, as it is not within the scope of this Part to discuss the interpretation of geophysical tests.

1.11.1. Seismic surveys

Seismic surveying methods, such as Multichannel Analysis of Surface Waves (MASW) is based on the principle that waves travel within the earth crust at different velocities, which depend only on the geomaterial properties. For example, common *shear* waves propagate with a wave velocity V_S that is equal to:

(1.37) $V_S = \sqrt{\frac{G_0}{\rho}}$

where G_0 is the elastic small-strain shear modulus of the soil or rock layer, and ρ is its mass density. This implies that if we can measure the shear wave velocity, we can find the small-strain compressibility parameters of the specific material.

Measuring of the seismic velocity is possible by using *geophones*, which are motion-sensitive instruments that convert ground motion to electrical signals. This can be accomplished by generating a ground wave, simply by pounding a sledgehammer on the ground surface or by using a small amount of explosives. With geophones, we can measure the difference in the arrival time of the wave, t at two geophones spaced L meters apart. The propagation velocity of the wave is equal to $V = L/t$ (Figure 1.41).

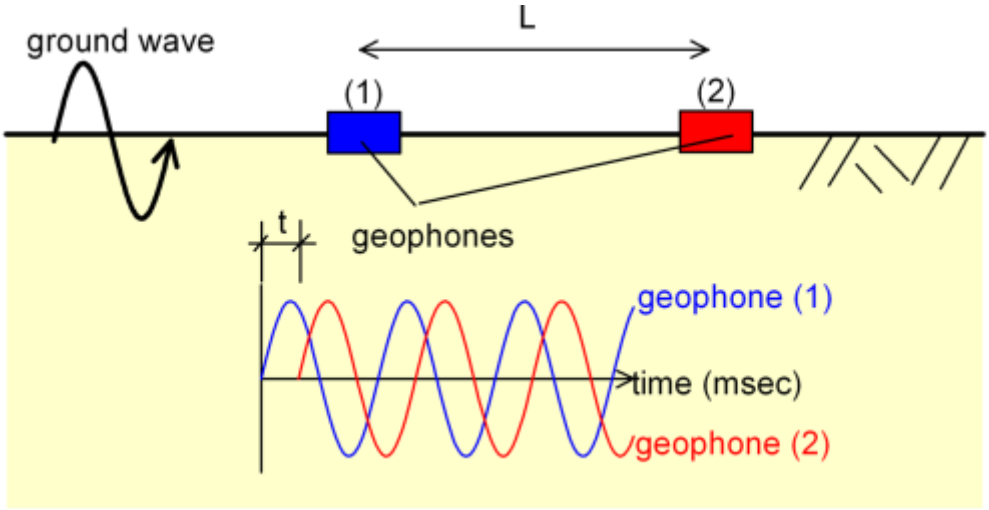

Figure 1.41. Principle of seismic surveys.

In real soils however, this procedure is more complicated, since when a wave encounters an interface between two soil/rock layers with different properties, and thus different wave propagation velocities, secondary waves are generated due to *reflection*, *refraction* and *diffraction* (Figure 1.42). However, we can take advantage of these secondary waves to determine not only the properties of the subsoil layers, but also the stratigraphy, with methods such as the *seismic refraction method* or the *Multi-Channel Analysis of Surface Waves* (MASW) method.

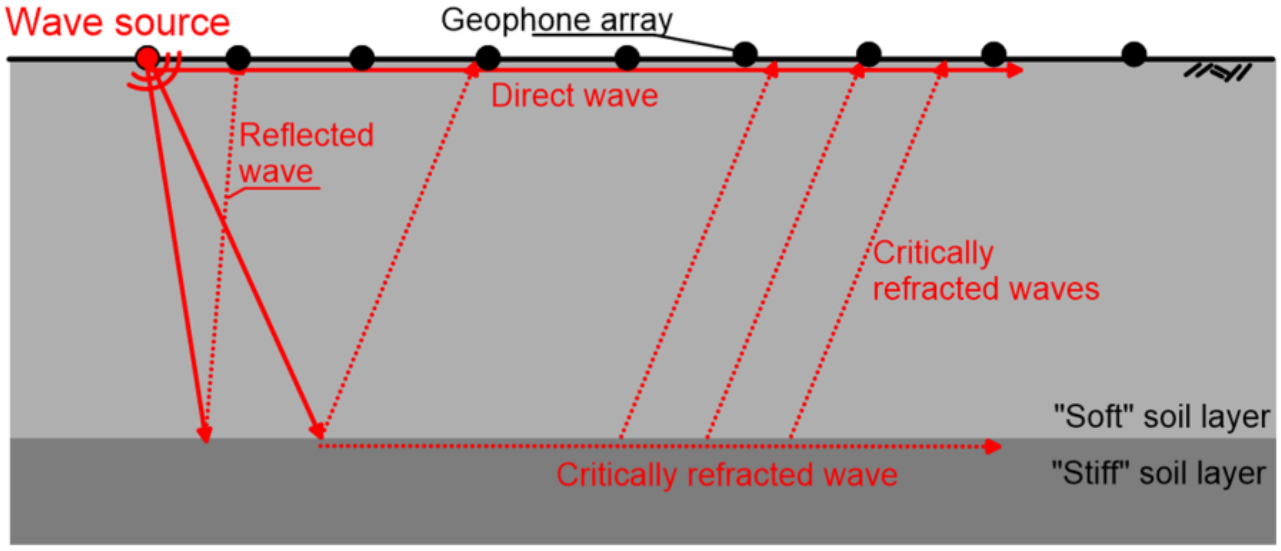

Figure 1.42. Direct, reflected and refracted wave paths generated by a wave source and recorded via geophones.

Employing the same principles, interpretation of multiple geophone recordings can provide information about subsoil stratigraphy (Figure 1.43). The seismic refraction method is mainly applied for determining the depth of a major refractor e.g., the bedrock, which has a wave propagation velocity significantly higher than the above softer formation. Other applications of the method include locating weathered fault zones, thickness of aquifer layers etc.

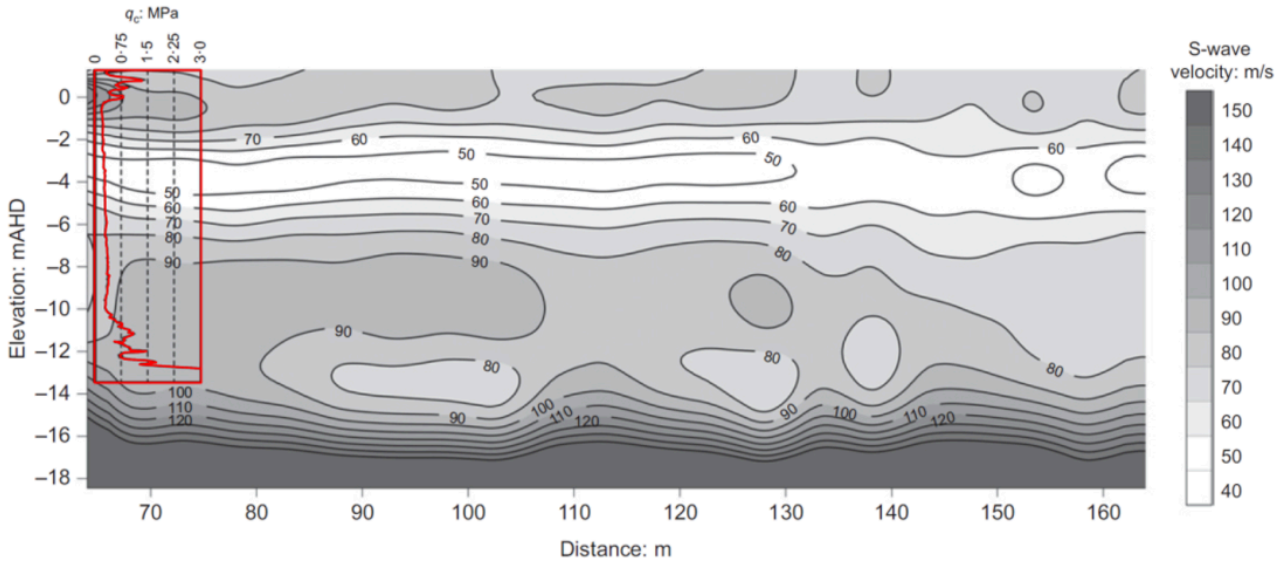

Figure 1.43. Typical MASW wave propagation velocity and cone resistance profiles of soft estuarine clay deposits, from the National Field Testing Facility for Soft Soils at Ballina, NSW (after Kelly et al. 2017).

1.11.2. Electrical resistivity method

The *electrical resistivity* method is used for determining the groundwater table level, the location of any possible subsoil cavities, the identification of the extent of fault zones etc. The concept on which the method is based consists of measuring the electrical potential difference (AC voltage) on the ground surface, created by an AC current. The potential difference reflects the "resistance" to the flow of the electric current through the soil, which is correlated to the soil's electrical resistivity. Soil resistivity varies with the water content: the pore fluid provides the only electrical path in sands, while both the pore fluid and the surface charged particles provide electrical paths in clays. So, differences in resistivity can be interpreted as differences in soil stratigraphy (Figure 1.44).

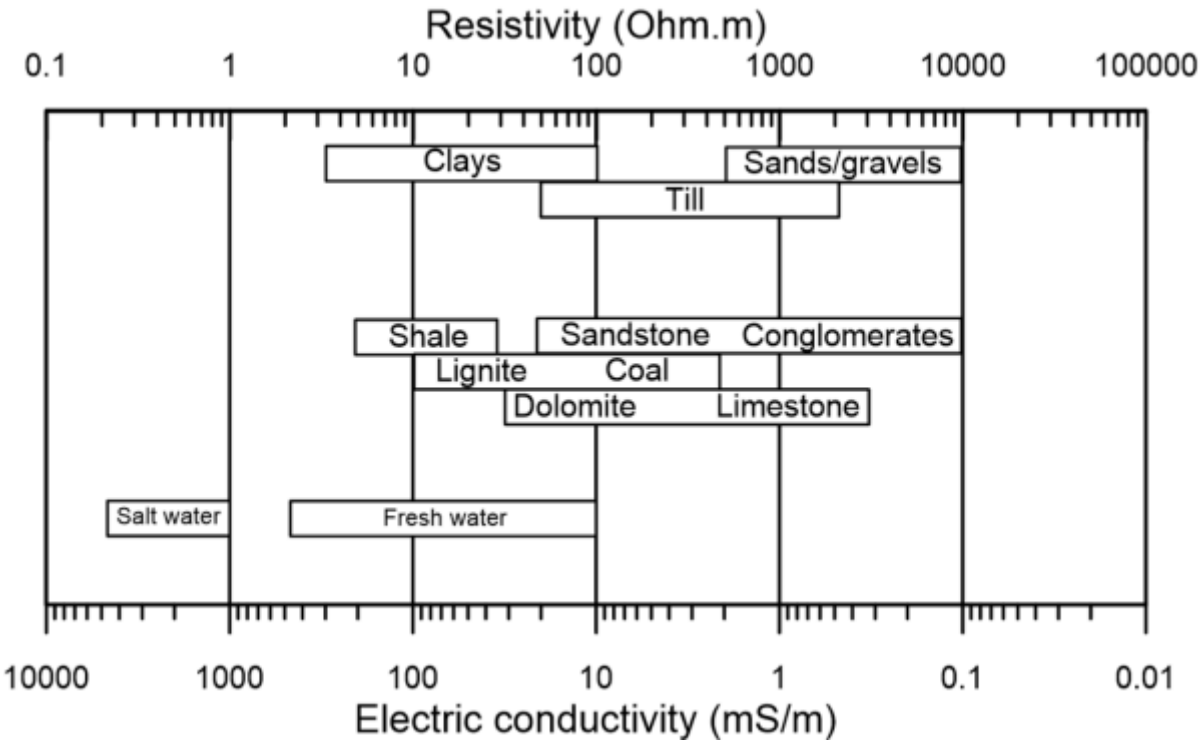

Figure 1.44. Typical soil and rock electric conductivity/resistivity values (after Samuelian et al. 2005).

Application of this method involves placing four electrodes on the ground surface, applying an AC current to the outer two electrodes, and measuring the AC voltage between the two inner electrodes (Figure 1.45). The spacing of the electrodes is related to the depth of the investigation: the greater the spacing, the larger the depth where we can get information from. A subsurface resistivity profile is created by performing successive measurements at different spacing (Figure 1.46).

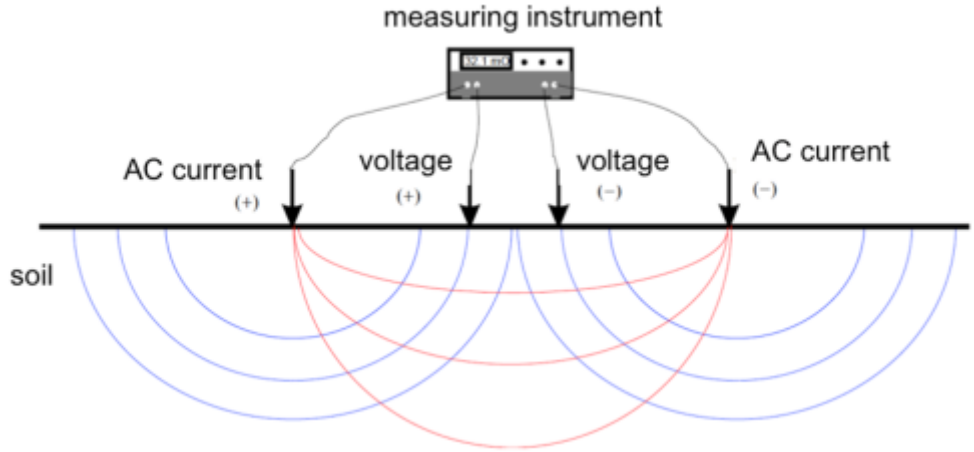

Figure 1.45. Layout of electrical resistivity surveys.

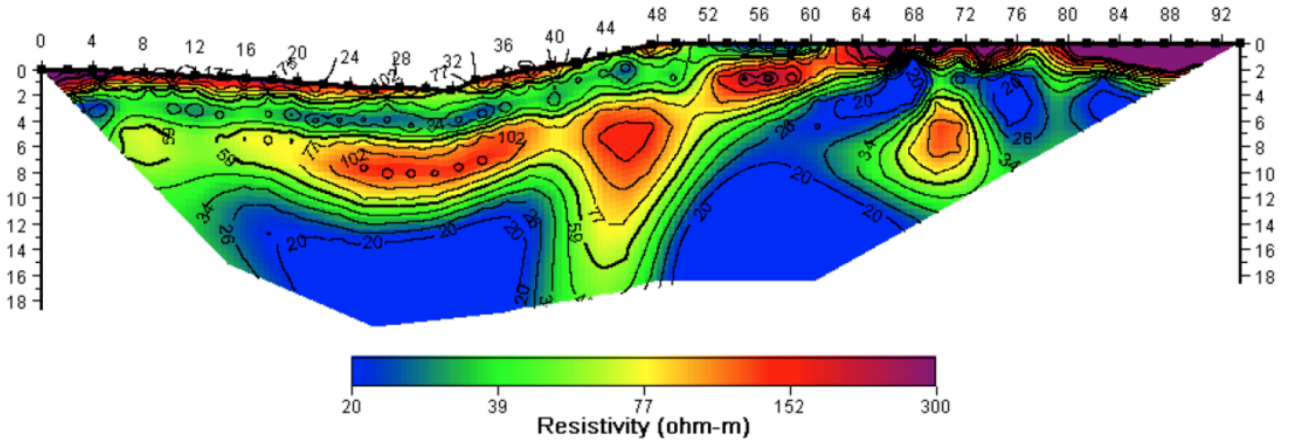

Figure 1.46. Typical electrical resistivity profile.

1.11.3. Ground penetration radar (GPR)

Ground penetration radar (or *georadar*) is based on the same principles as the radar used in aviation. An antenna is used to transmit and recover high frequency (10MHz to 1000 Mhz) electromagnetic pulses originating from a pulse generator. When the wave hits a buried object or a boundary with different dielectric constants, the reflected return signal is altered (Figure 1.47, Davis and Annan 1989). The method is practically based on the same concept as seismic surveys, only in this case electromagnetic waves are used.

GPR has many engineering applications in general. Its key applications in Geotechnical Engineering include identifying the location of buried objects (utility lines) or cavities, and soil profiling.

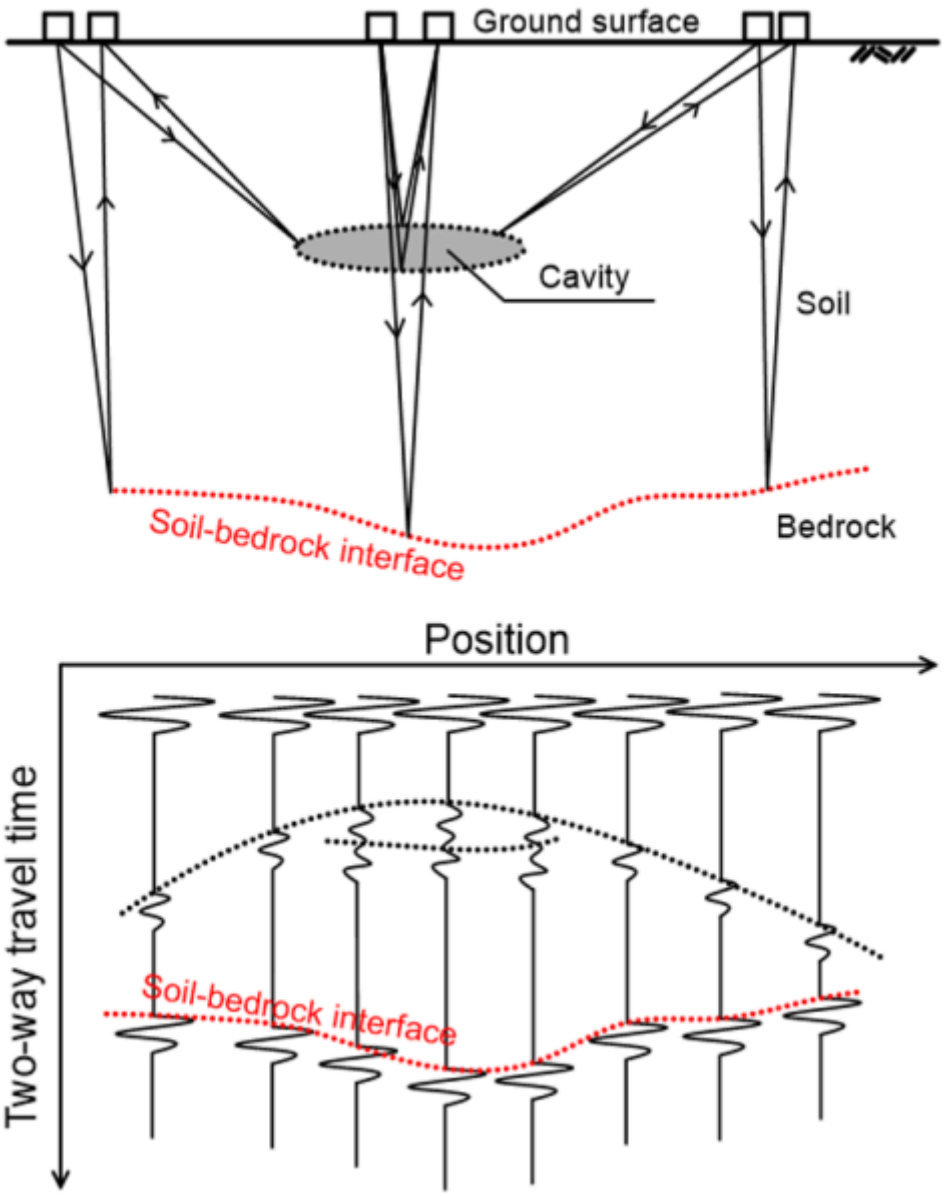

Figure 1.47. GPR used for soil profiling and identification of cavities.

1.12 REFERENCES

1. Australian Standard AS1289.6.2.1. Methods of testing soils for engineering purposes. Method 6.2.1: Soil strength and consolidation tests-Determination of the shear strength of a soil-Field test using a vane.
2. Australian Standard AS1289.6.3.1. Methods of testing soils for engineering purposes. Method 6.3.1: Soil strength and consolidation tests-Determination of the penetration resistance of a soil – Standard Penetration test (SPT).
3. Australian Standard AS1289.6.5.1. Methods of testing soils for engineering purposes. Method 6.5.1: Soil strength and consolidation tests-Determination of the static cone penetration resistance of a soil-Field test using a mechanical and electrical cone or friction-cone penetrometer.
4. Australian Standard AS1726. Geotechnical site investigations.
5. ASTM D6635. Standard test method for performing the Flat Plate Dilatometer. ASTM International.
6. Chandler, RJ (1988) The in-situ measurement of the undrained shear strength of clays using the field vane. Vane Shear Strength Testing in Soils: Field and Lab Studies. STP 1014, ASTM, West Conshohocken, PA, 13-44.
7. Day RW (1999). Geotechnical and foundation engineering: Design and construction. McGraw-Hill, NY.
8. Davis JL and Annan AP (1989). Ground-penetrating radar for high-resolution mapping of soil and rock stratigraphy. Geophys. Prosp., Vol. 37, pp 531-551.
9. da Fonseca AV and Pineda J (2017) Getting high-quality samples in “sensitive” soils for advanced laboratory tests. Innov. Infrastruct. Solut. 2:34
10. Federal Highway Administration FHWA (2002). Subsurface Investigations. Geotechnical Site Characterization, Publication No. FHWA NHI-01-031, US Department of Transportation, May 2002.
11. Federal Highway Administration FHWA (2006). Soils and Foundations. Reference Manual. Vols I & II, Publication No. FHWA NHI-06-088 and FHWA NHI-06-089, US Department of Transportation, December 2006.
12. Glossop R (1968). The rise of geotechnology and its influence on engineering practice. Géotechnique, Vol. 18(2), pp 107-150.
13. Gunaratne M (ed.) (2006). The foundation engineering handbook. Taylor and Francis Group.
14. Hatanaka M and Uchida A (1996) Empirical correlation between penetration resistance and effective friction of sandy soil. Soils and Foundations, Vol. 36(4), pp 1-9.
15. Jamiolkowski M, Lo Presti CDF and Manassero M (2001). Evaluation of relative density and shear strength of sands from CPT and DMT. Soil Behavior and Soft Ground Construction. ASCE Geotechnical Special Publication GSP 119;201-229
16. Kelly RB, Bates L and Pineda J (2012) Comparisons of DMT with in situ and laboratory tests in soft estuarine clay. Proc 3rd Int Conf on the Flat Dilatometer, Rome.
17. Kouretzis G, Sheng D and Wang D (2014). Numerical simulation of cone penetration testing using a new critical state constitutive model for sand. Computers and Geotechnics, Vol. 56, pp 50-60.
18. Kouretzis G, Ansari Y, Pineda J, Kelly R and Sheng D (2015) Numerical evaluation of clay disturbance during blade penetration in the flat dilatometer test. Géotechnique Letters 5(3), 91-95.
19. Kouretzis G, Pineda J, Krabbenhoft K and Wilson L (2017) Interpretation of vane shear tests for geotechnical stability calculations. Canadian Geotechnical Journal 54(12), 1775-1780.
20. Kulhawy FH and Mayne PH (1990). Manual on estimating soil properties for foundation design. Report EL-6800 Electric Power Research Institute, ERPI, August 1990.
21. Lacasse S and Lunne T (1998) Calibration of dilatometer correlations. Proc Int Symp on Penetration Testing ISOPT-1, Orlando FL 1, pp 359-548
22. Marchetti S (1980) Insitu tests by flat dilatometer. ASCE J Geotech Engng Div 106(3) 299-321.
23. Marchetti S, Monaco P, Totani G and Calabrese M (2001) The Flat Dilatometer Test (DMT) in soil investigations. A report by the ISSMGE Committee TC16 Proc. DMT 2006, Washington DC
24. Mayne PW (2006). Cone Penetration Testing. A synthesis of highway practice. National Cooperative Highway Research Program NCHRP 368, Transportation Research Board.
25. Mayne PW and Peuchen J (2022). Undrained shear strength of clays from piezocone tests: A

database approach. Conne Penetration Testing 2022, CRC Press.
26. Mitchell JK (1976). Fundamentals of soil behaviour. John Wiley & Sons, Inc.
27. Powell JJM and Uglow IM (1988) The interpretation of Marchetti dilatometer tests in UK clays. Proc ICE Penetration testing in the UK, Birmingham, pp 269-273
28. Reese LC, Isenhower WM, and Wang ST (2006). Analysis and design of shallow and deep foundations. John Wiley & Sons, Inc.
29. Reynolds MJ (2011). An introduction to applied and environmental geophysics. 2nd edition. John Wiley & Sons, Inc.
30. Robertson PK and Kabal K (2022). Guide to Cone Penetration Testing. 7th Edition. Gregg Drilling & Testing Inc.
31. Samouelian A, Cousin I, Tabbagh A, Bruand A and Richard G (2005) Electrical resistivity survey in soil science: a review. Soil and Tillage Research 83(2) 173-193
32. Stroud MA (1974). The standard penetration test in insensitive clays and soft rock. In: Proceedings, 1st European Symposium on Penetration Testing, Stockholm, Sweden, Vol. 2(2), pp 367-375.
33. Terzaghi K, Peck RB and Mesri G (1996). Soil mechanics in engineering practice. 3rd edition. John Wiley & Sons, Inc.
34. Zhang M, Wang C, Kouretzis G and Luan L (2023) Interpretation of piezocone tests in normally- and over-consolidated clay using a spherical cavity expansion solution. Computers and Geotechnics 160, 105521

1.13 ADDITIONAL PROBLEMS

1.13.1

For the design of a cut slope *(grey dashed line)*, 3 boreholes were drilled. The geological description of the encountered formations, their USCS classification and the SPT test results are provided below. Use the canvas to create a geotechnical model of the area to be introduced in the slope stability calculations, and propose the necessary parameters to be employed in the corresponding stability analyses.

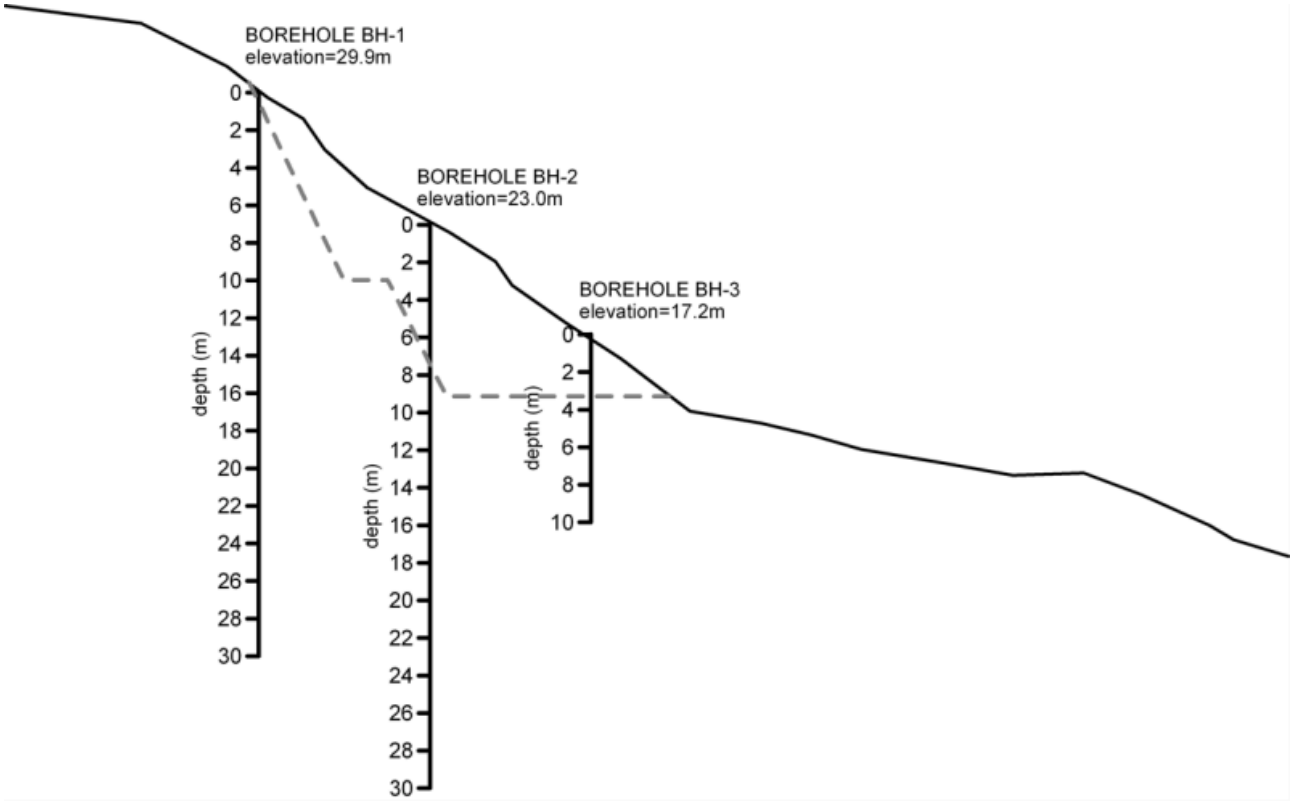

Additional Problem 1.13.1. Problem description and input parameters.

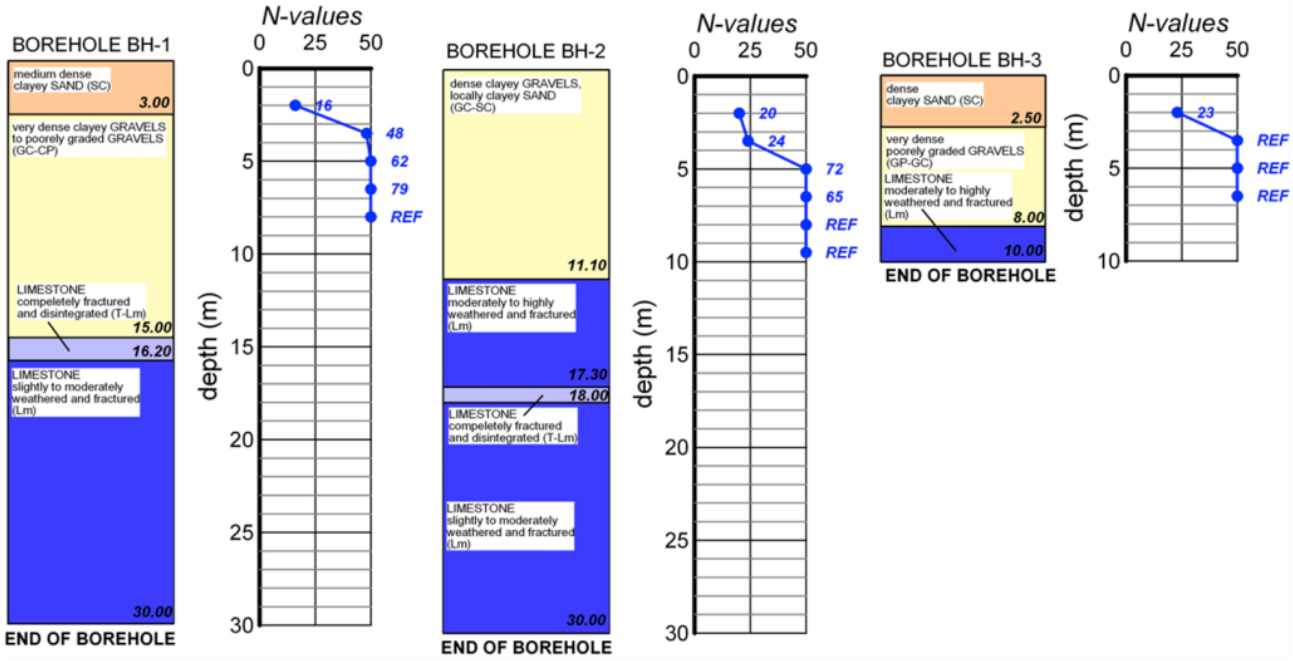

Additional Problem 1.13.1. Problem description and input parameters.

Answer:

Layer I: Dense clayey sand (SC) $\varphi' \approx 34°$, $\gamma = 18$ to 20 kN/m^3

Layer II: Very dense clayey gravels, poorely graded (GC-GP) $\varphi' \approx 40°$ to 43°, $\gamma = 18$ to 20 kN/m^3

Layer III: Fault zone: infinite strength for slope stability analyses

Layer IV: Slightly to moderately weathered limestone (Lm): infinite strength for slope stability analyses

---

1.13.2

For the design of the deep foundation of a tall building, two (2) sampling boreholes were drilled and two (2) CPT soundings were performed. Results of the geotechnical investigation revealed a (more-or-less) consistent geotechnical profile: a medium-to-stiff low plasticity (PI ≈ 20%) clay formation prevails, interrupted by a loose-to-medium silty-clayey sand layer. The bedrock, a sandstone formation is encountered at depths 12.0 to 16.0 m.

Use the *in situ* SPT and CPT test results, combined with the provided empirical relations/charts, to determine the characteristic undrained shear strength (S_u) of the clay layer and the effective friction angle of the sand layer (φ'). Assume the bulk unit weight of the clay/sand layers to be constant $\gamma = 17$ kN/m^3.

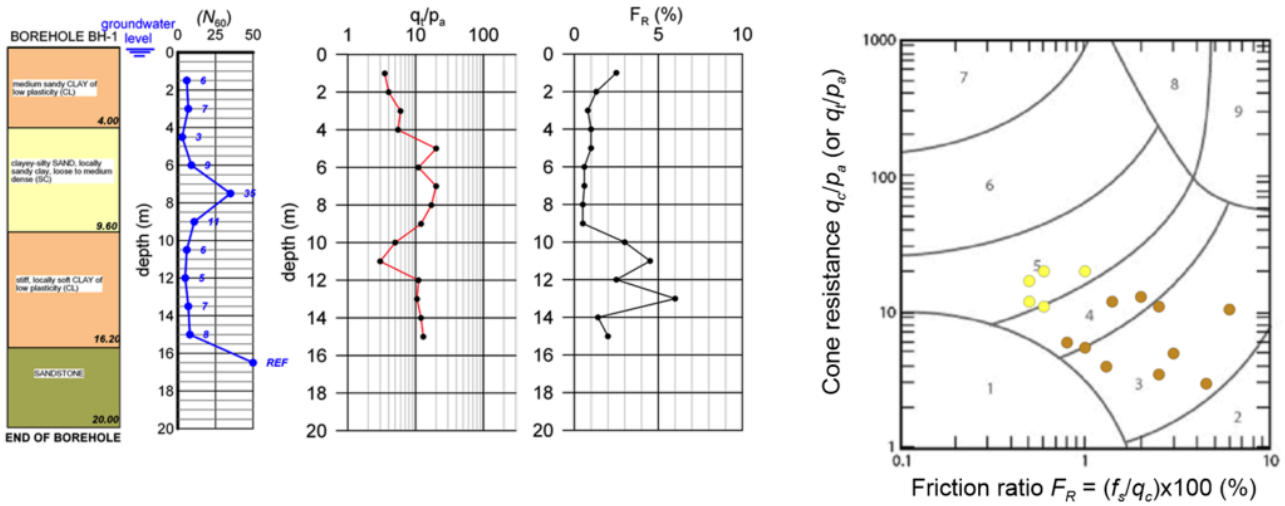

Additional Problem 1.13.2. Problem description and input parameters.

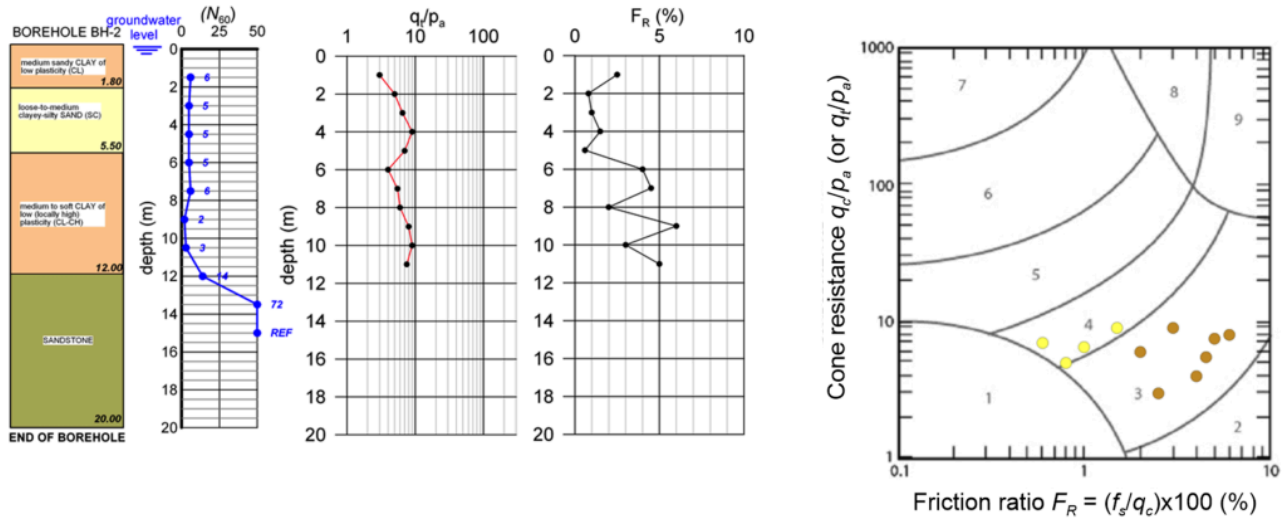

Additional Problem 1.13.2. Problem description and input parameters.

Example 1.13.2. CPT1 and CPT2 test results

CPT1			CPT2		
Depth (m)	q_t/p_a	F_R (%)	Depth (m)	q_t/p_a	F_R (%)
1	3.5	2.5	1	3	2.5
2	4	1.3	2	5	0.8
3	6	0.8	3	6.5	1
4	5.5	1	4	9	1.5
5	20	1	5	7	0.6
6	11	0.6	6	4	4
7	20	0.6	7	5.5	4.5
8	17	0.5	8	6	2
9	19	0.5	9	8	6
10	5	3	10	9	3
11	3	4.5	11	7.5	5
12	11	2.5			
13	10.5	6			
14	12	1.4			
15	13	2			

Answer:

Clay layer: $S_u = 20$ *kPa for depth* $z<4$*m and* $S_u = 20+2(z-6)$ *kPa for depth* $z>6$*m*

Sand layer: $\varphi' = 30^o$

2. SOIL AND GROUNDWATER CONTAMINATION AND REMEDIATION TECHNIQUES – AN INTRODUCTION TO GEOENVIRONMETAL ENGINEERING

2.1 INTRODUCTION TO PART 2

Geoenvironmental Engineering refers to the application of geotechnical engineering technologies for protecting the *geoenvironment* from contamination due to human activities or natural processes (Figure 2.1). The term *geoenvironment* includes the topsoil, subsoil and groundwater. Air and surface water pollution is a subject of other environmental sciences.

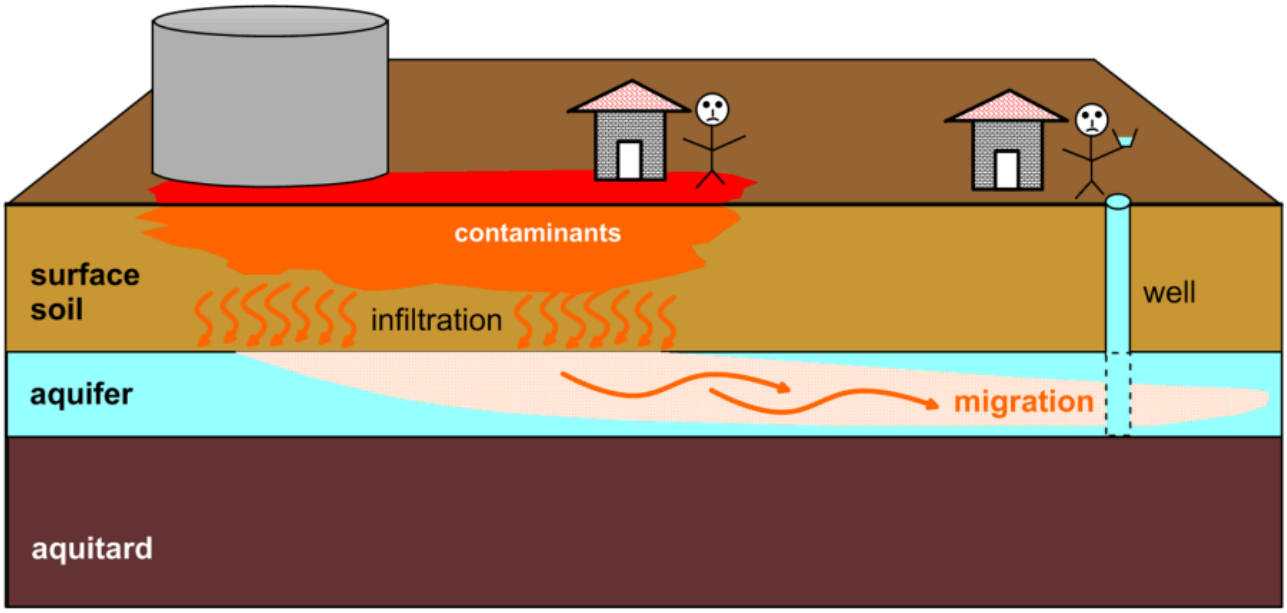

Figure 2.1. Outline of the soil and groundwater contamination problem.

Geoenvironmental Engineering deals not only with the protection of the geoenvironment from pollution, but also with the preservation of its quality e.g., protection of groundwater from overexploitation and salination (Figure 2.2).

Geoenvironmental Engineering is about offering solutions to complex problems encountered by the waste management and environment restoration industry, and involves experts spanning multiple disciplines such as Geotechnical Engineers, Environmental Engineers, Chemical Engineers, Geologists, Chemists, Microbiologists, Soil scientists etc.

Figure 2.2. Salt-affected soils (US Department of Agriculture, via Wikimedia Commons, marked as public domain).

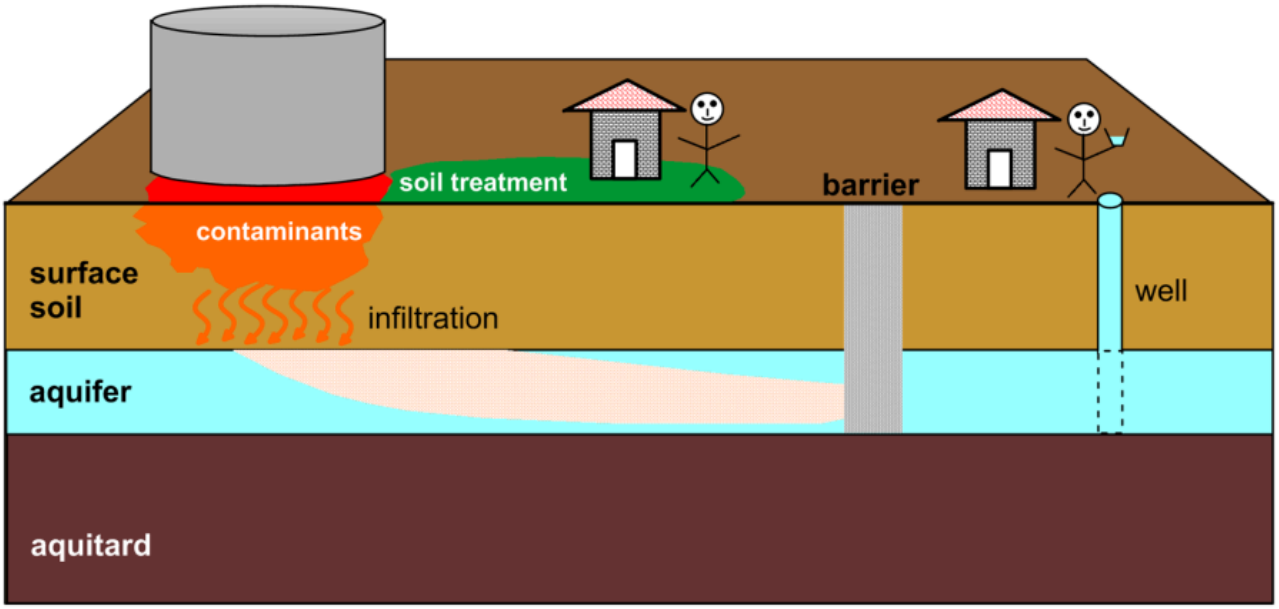

Figure 2.3. Remediation measures to mitigate soil and groundwater contamination.

Some of the specific tasks that fall under the scope of Geoenvironmental Engineering include:

- Measuring of contaminant concentration in soil.
- Implementing measures to constrain contaminant diffusion (see Figure 2.3).
- Techniques for extraction of polluting agents.
- Measuring quality deterioration in groundwater and implementation of mitigation measures.
- Minimising environmental impact of large engineering projects.

The above tasks are formulated as a *geoenvironmental study*, which consists of the following parts:

1. Identification of human activities or natural processes that may result in geoenvironment contamination. May refer to planned or existing engineering projects.
2. *In situ* and laboratory testing and interpretation of results, for determining the extent of contamination, and its evolution with time.

3. Design and construction of engineering solutions to mitigate contamination effects, which may include:

    - Design of hazardous waste repositories.
    - Implementation of monitoring systems to measure pollutant concentrations.
    - Extraction of pollutants from the subsoil or groundwater.
    - Design of containment measures e.g., slurry walls, grouting, sheet piling, electrokinetic barriers, ground freezing (Figure 2.3).

4. Risk assessment and risk management.

In this Part, emphasis is put on providing a brief overview of geotechnical aspects of geoenvironmental engineering, and more specifically on the use of geotechnical methods for containment of pollution, and extraction of polluting agents to mitigate contamination effects. Part 2 concludes with a demonstration of the use of simple numerical methods to support the design of containment facilities.

2.2 CHARACTERISTIC CASES STUDIES OF SOIL AND GROUNDWATER CONTAMINATION

Discussion on the impact of civil engineering works on the geoenvironment began in the USA during the 1970's, in the light of the development of nuclear power plants, and the need for deep underground storage of hazardous radioactive waste.

Perhaps the most characteristic case study of contamination of the subsoil, and its effects on the population of the area, is the Love Canal case in the USA, which lead to the development of geoenvironmental regulations for civil engineering works.

Love Canal was an attempt to create a navigation canal to connect Niagara River to Lake Ontario, near the area of the famous waterfalls (Figure 2.4). The project began in 1896, but it was abandoned for various reasons, leaving behind an incomplete 3000 m long canal. In 1942 a local chemical industry bought the canal to use it as a repository pit. Between 1947 to 1952, about 22,000 tons of solid and liquid toxic waste were deposited and buried in the canal (Figure 2.4). In 1953 the canal was backfilled and sold to the city of Niagara Falls for $1. The company included in the contract a term stating *"the grantee assumes all risk and liability incident to the use thereof"*. Nevertheless, until 1977 hundreds of houses and two schools were built in that area (Figure 2.5), despite the local population starting suffering from unexplained health issues.

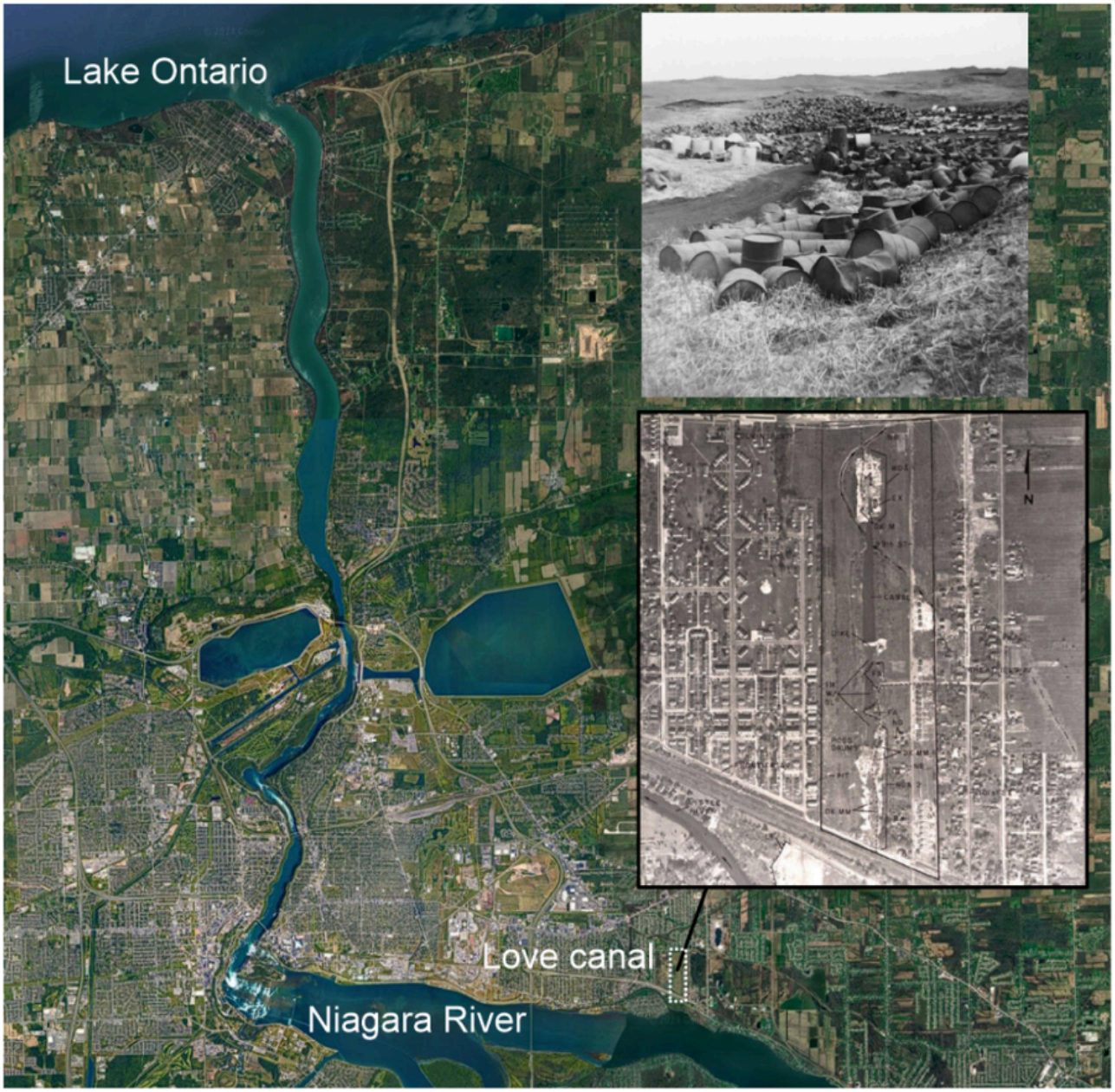

Figure 2.4. Location of the Love canal and 1951 conditions (Map data: Google, Airbus, NOAA, TerraMetrics. Images public domain).

A federal health emergency was declared in 1978, and the population was evacuated. The subsoil investigation that was conducted in the area revealed extremely high concentrations of toxic chemicals such as benzene and dioxin, and clinical studies results suggested that 33% of the local population had undergone chromosomal damage.

Restoration of the area (Figure 2.5) lasted about 20 years, and was completed only in 2004.

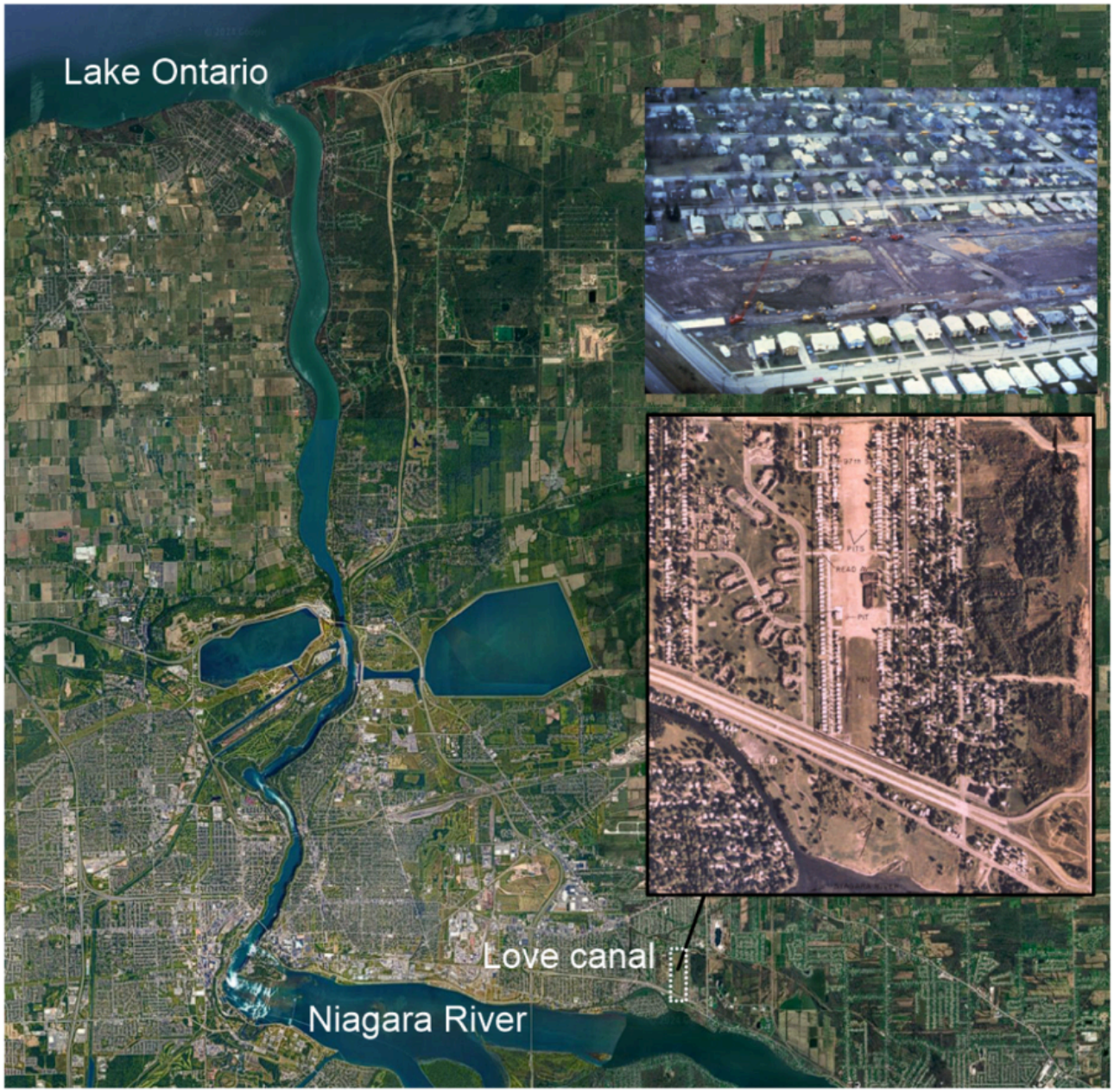

Figure 2.5. Love Canal clean up (Map data: Google, Airbus, NOAA, TerraMetrics. Images: US Environmental Protection Agency and US National Air and Space Museum, public domain).

Another case study that attracted public attention is the Hinkley, CA groundwater contamination with hexavalent chromium (Cr(VI)). Pacific Gas & Electric Corporation operates a natural gas pipeline compressor station in the town of Hinkley, in California. Between 1952 and 1966, the water used to cool the compressors was deposited in unlined ponds near the station (Figure 2.6a) This cooling water, rich in toxic hexavalent chromium, infiltrated and polluted the groundwater, which was used by the population of Hinkley.

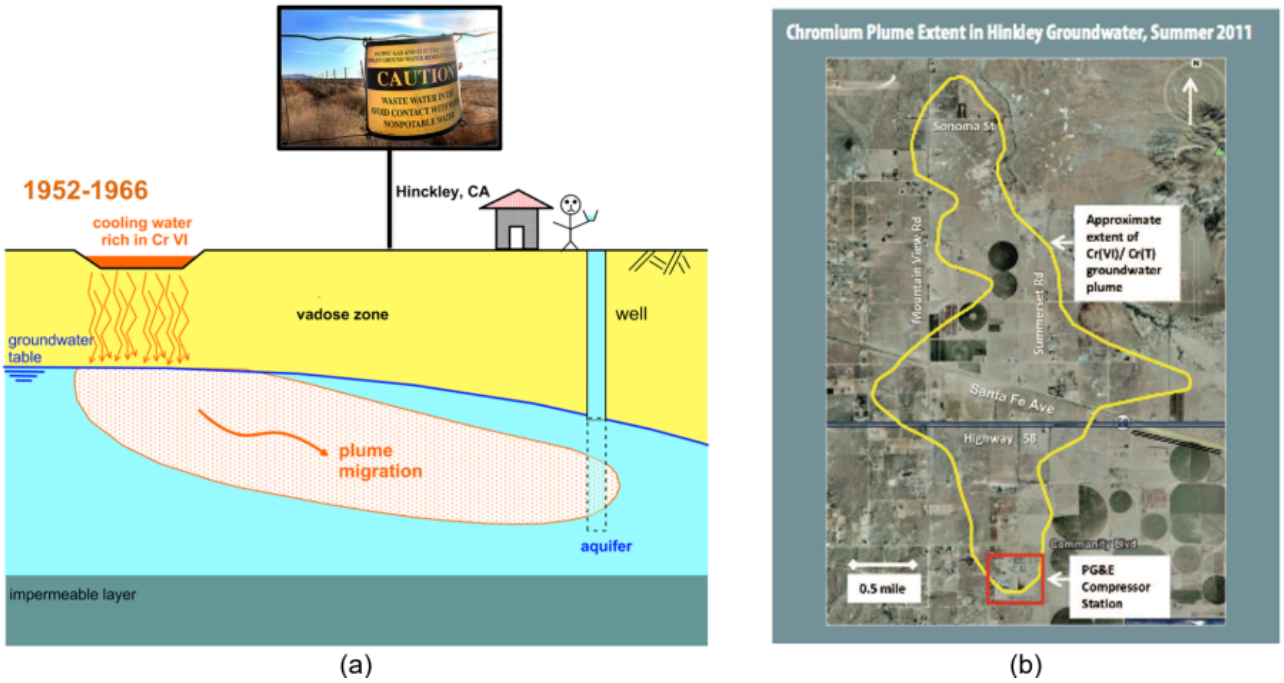

Figure 2.6. (a) Hinkley, CA groundwater contamination with hexavalent chromium and (b) Extent of the contaminated groundwater plume in 2011 (California State Water Resources Control Board [PDF], public domain).

Severe health problems, including about 200 cancer cases were attributed to pollution of the groundwater with Cr(VI). A multimillion-dollar legal settlement was achieved between the Pacific Gas & Electric Corporation and the citizens of Hinkley. Several years after, the plume of contaminated water has started migrating to the lower aquifer (Aug. 2010) at a rate of 1 ft per day, almost 1 mile per year (Figure 2.6b).

In 2012, approximately 300 significantly contaminated sites (Figure 2.7) had been reported in NSW, and are regulated under the Contaminated Land Management Act 1997 (NSW State of Environment 2012-Land).

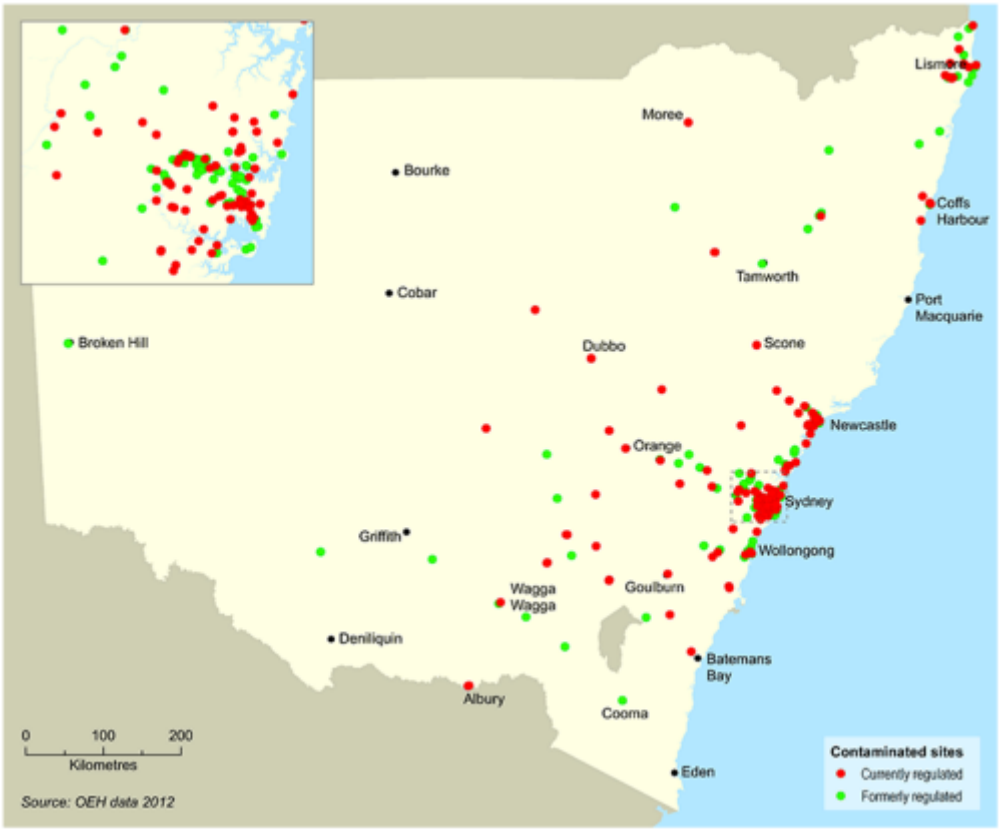

Figure 2.7. Contaminated sites regulated under the Contaminated Land Management Act 1997 in NSW (© State of New South Wales through the Environment Protection Authority).

Key contaminating activities include:

- Service stations and other petroleum industrial sites (37%)
- Chemical industry sites (10%)
- Metal industry sites (7%)
- Other industrial sites (16%)
- Former gasworks sites (12%)
- Landfill sites (9%)

Over the past years several large remediation projects have been completed in NSW, including the Rhodes Peninsula in Sydney and BHP Billiton's Hunter River remediation, the largest (to that date) sediment remediation project, which included cleaning up contaminated river sediments affected by operations of the former Newcastle steelworks.

2.3 MANAGEMENT FRAMEWORK FOR CONTAMINATED LAND IN AUSTRALIA

Depending on the perceived risk, management of contaminated land in Australia is regulated by:

- *Environment Protection Authority (EPA)*, which uses its powers under the Contaminated, *Land Management Act 1997 No 140.* Deals with site contamination that is significant enough to warrant regulation under the Act, given the site's current or approved use.
- *Local councils* which deal with other contamination sites under the planning and development framework, including the *State Environmental Planning Policy No. 55 – Remediation of Land and Managing Land Contamination – Planning Guides.* This applies to sites which, despite being contaminated, do not pose an unacceptable risk under their current or approved use.

2.4 SOURCES OF GEOENVIRONMENT CONTAMINATION

Sources of groundwater and subsoil contamination include:

Natural processes

- Dissolution of rock salt during the percolation of groundwater, which results in an increase in chlorides, sulphates, nitrates and iron ions concentration.
- Increase in salt concentration during evapotranspiration of shallow perched groundwater.
- Exposure of acid sulfate soils to oxygen through drainage or disturbance. Acid sulphate soils are widespread along the NSW coast.

Human activities related to waste management

- Industrial liquid waste stored in surface reservoirs, as in the case of Hinkley, CA mentioned earlier (Figure 2.6).
- Urban and industrial solid waste deposited in aboveground and underground repositories, as in the case of Love Canal mentioned earlier.
- Treated or untreated urban sewage deposited into the soil.
- Solid and liquid waste industrial byproducts e.g., tailings or flying ash deposited into the soil.
- Improperly disposed livestock waste.

Other human activities/Accidents

- Agriculture: use of pesticides, insecticides and fertilisers.
- Accidents during transportation or deposition e.g., derailing of a train transporting environmentally hazardous materials.
- Failure of engineering projects e.g., rupture of a sewage pipeline during an earthquake.
- Leakage of contaminants through their storage facilities/tanks.
- Uncontrolled waste disposal.

2.5 TYPES OF WASTE AND POLLUTANTS AND TOLERABLE CONCENTRATION LEVELS

Waste, mentioned above as the key source of geoenvironment contamination, can be classified into the following general categories:

- Mining waste.
- Radioactive waste.
- Non-point source discharge or diffused discharge waste, including pesticides, insecticides and fertilisers.
- Domestic sewage.
- *Solid waste,* including all solid, but also liquid waste not mentioned above.

Solid waste is a generic term, including all waste from municipal and industrial activities that can potentially contaminate the geoenvironment. Solid waste includes both hazardous (toxic) waste and non-hazardous waste. Toxic waste, which is mainly of interest here, include:

- Common industrial solvents.
- Wood treatment products.
- Chemical industry organic compounds and subproducts.
- Highly toxic compounds such as naphthalene, benzene, trichloroethylene (TCE), carbon tetrachloride (Freon, Halon), heavy metals (Hg, Pb) and various other compounds, such as arsenic, chromium, cyanides.

From a geoenvironmental engineering point of view, 4 major categories of soil waste are considered:

- *Inorganic waste,* suspended or dissolved in liquids, such as mercury, lead, chromium etc.
- *Water-soluble organic waste or Aqueous Phase Liquids (APLs).* Include solvents, pharmaceutical industry waste, pesticides, industrial waste etc.
- *Non-water-soluble organic waste or Non-Aqueous Phase Liquids (NAPLs).* Include oil paints, lubricants etc. Lighter than water NAPLs as petrol, kerosene, diesel are called *Light NAPLs,* while ones heavier than water are called *Dense NAPLs.* Trichloroethylene (TCE), one of the most common industrial solvents, is perhaps the most widespread organic waste traced in groundwater. Light NAPLs, which have a unit weight lower than water, are concentrated near the surface of the aquifer, while heavy NAPLs infiltrate and contaminate deeper aquifers.
- *Viscose fluid and solid waste.* Include oil refinery waste etc.

Various health organisations around the world have proposed different tolerable levels of contaminants concentration in the soil and groundwater, and different regulations apply in each country. Results of laboratory tests to measure pollutant concentration must be compared to reference, limit values (e.g., Table 2.1), which are related to the associated risk involved. In Australia, the following guidelines apply for soil contamination:

- Environmental Health Risk Assessment: *Guidelines for assessing human health risks from environmental hazard.* Department of Health and Ageing and EnHealth Council, Commonwealth of Australia, 2002.
- *National Environment Protection (Assessment of Site Contamination)* Measure 1999 – Schedule B (Guidelines).

Whereas the following guidelines refer to groundwater contamination:

- For drinking water: *Australian and New Zealand guidelines for fresh and marine water quality*.
- For aquatic ecosystems: NHMRC & NRMMC Australian *drinking water guidelines 6*.

Table 2.1. Proposed health-based soil guidelines for individual substances (EnHealth Council, 2001).

Substance	Health-based Investigation Levels (mg/kg)						Notes
	A	B	C	D	E	F	
Aldrin + Dieldrin	10			40	20	50	**A.** 'Standard' residential with garden/ accessible soil (home-grown produce contributing less than 10% of vegetable and fruit intake; no poultry): this category includes children's day-care centres, kindergartens, pre-schools and primary schools.
Arsenic (total)	100			400	200	500	
Benzo(a)pyrene	1			4	2	5	
Beryllium	20			80	40	100	
Boron	3000			12000	6000	15000	
Cadmium	20			80	40	100	**B.** Residential with substantial vegetable garden (contributing 10% or more of vegetable and fruit intake) and/or poultry providing any egg or poultry intake.
Chlordane	50			200	100	250	
Chromium (III)	12%			48%	24%	60%	
Chromium (IV)	100			400	200	500	
Cobalt	100			400	200	500	**C.** Residential with substantial vegetable garden (contributing 10% or more of vegetable and fruit intake); poultry excluded.
Copper	1000			4000	2000	5000	
Cyanides (complexed)	500			2000	1000	2500	
Cyanides (free)	250			1000	500	1250	**D.** Residential with minimal opportunities for soil access; includes dwellings with fully and permanently paved yard space such as high-rise apartments and flats.
DDT + DDD + DDE	200			800	400	1000	
Heptachlor	10			40	20	50	
Lead	300			1200	600	1500	
Manganese	1500			6000	3000	7500	**E.** Parks, recreational open space and playing fields; includes secondary schools.
Methyl mercury	10			40	20	50	
Mercury (inorganic)	15			60	30	750	
Nickel	600			2400	600	3000	**F.** Commercial/Industrial: includes premises such as shops and offices as well as factories and industrial sites. It is assumed that thirty years is the duration of exposure.
Polycyclic aromatic hydrocarbons (PAHs)	20			80	40	100	
PCBs (total)	10			40	20	50	
Phenol	8500			34000	17000	42500	
Total petroleum hydrocarbons							
>C_{16}-C_{35} aromatics	90			360	180	450	
>C_{16}-C_{35} aliphatics	5600			22400	11200	28000	
>C_{35} aliphatics	56000			224000	112000	280000	

Zinc	7000	28000	14000	35000	

2.6 GEOTECHNICAL INVESTIGATIONS IN CONTAMINATED SITES

Geotechnical investigations in potentially contaminated sites must follow certain procedures regarding personnel protection, avoiding contaminant migration through groundwater movement, and proper disposal of boring waste such as drilling water, soil samples etc. Some signs of possible contamination that should trigger further measures are (FHWA 2002):

- Prior land use (e.g., old fill, landfills, gas stations).
- Stained soil or rock.
- Apparent lack of vegetation or presence of dead vegetation and trees.
- Odors. Note that highly organic soils will have a rotten egg odour, which should not be mistaken as evidence of contamination. However, this odour may be indicative of highly toxic hydrogen sulphide.
- Presence of liquids other than groundwater.
- Signs of previous ground fires at landfill sites. Established landfill will emit methane gas, which is explosive.
- Presence of visible elemental metals (mercury).
- Low (<2.5) or High (>12.5) pH.

Easy-to-use methods such as air quality monitoring devices, pH measurement kits or photoionisation detectors can be used to perform preliminary tests to identify the presence of some contaminants.

Concentration of pollutants in soil and groundwater is determined via special chemical tests on soil and water samples, in the laboratory. These tests are often complemented with geophysical tests, such as electric resistivity tests or ground penetrating radar tests discussed in Part 1. The selection of the appropriate method depends on the type of pollutant.

Except of these common methods, a hydrogeological site investigation may be necessary, aiming to (CCME, 1994):

- Determine the direction and rate of groundwater movement.
- Determine the principal pathways and factors controlling the migration of contaminants in the subsurface.
- Quantify the physical parameters controlling groundwater flow and contaminant transport in the subsurface.

in other words, build the *hydrogeological model* of the site...

Drilling monitoring wells (Figure 2.8) may be necessary for determining groundwater levels, and water quality via samples retrieved for laboratory tests. Measuring the hydraulic conductivity (permeability) of the subsurface formations with the constant or falling head test in the laboratory or *in situ* (Figure 2.9) will provide the necessary input for developing a groundwater flow and contaminant transport numerical model, that can predict contamination evolution over time as described in the following chapter, and lead to the evaluation of the effectiveness of different mitigation measures.

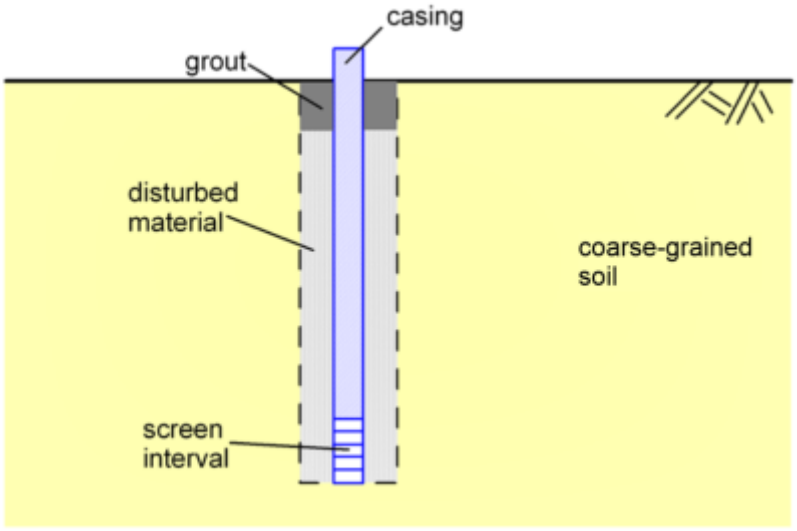

Figure 2.8. Outline of a monitoring well in coarse-grained soil.

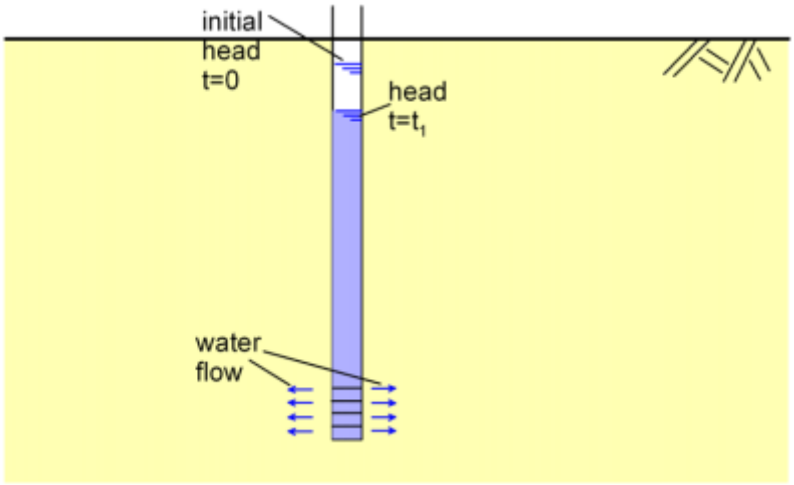

Figure 2.9. In situ test (Maag) to measure soil permeability.

2.7 MECHANISMS OF CONTAMINANTS TRANSPORT THROUGH SOIL

When a pollutant escapes from a repository, it moves through the *vadose zone,* which is the zone between the soil surface and the groundwater table (Figure 2.10). The soil grains retain part of the pollutant, either chemically or mechanically, while part of the pollutant reaches the aquifer. Water-soluble pollutants are then carried away downstream, following the groundwater flow, which is determined by the hydraulic gradient.

As pollutants are being carried away, contamination of the aquifer spreads and substance concentration decreases, as we move from the main zone to the neutral zone (Figure 2.10). Especially for saturated or partially saturated soils and pollutants that can be dissolved or suspended in water (light NAPLs that float are excluded), three basic mechanisms can be identified:

2.7.1 Advection or Hydraulic transportation

The contaminant is carried away by the groundwater though the soil voids, following the hydraulic gradient (Figure 2.10). Assuming saturated flow, the seepage velocity will be equal to:

(2.1) $$V = \frac{q}{n}$$

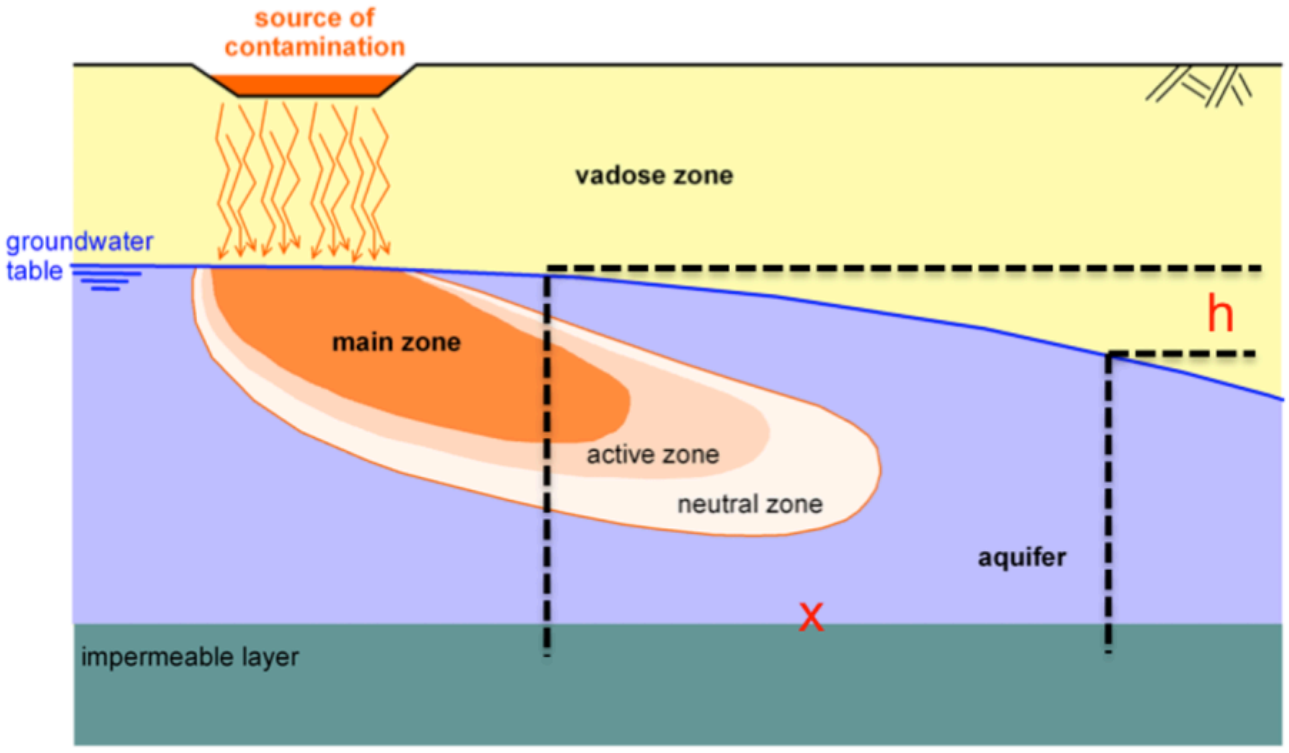

Figure 2.10. Pollutant movement through the subsoil.

where n is the soil porosity ($n=V_{voids}/V$) and q is Darcy's water flux, equal to the volume Q flowing though a unit cross-sectional area A:

(2.2) $$q = \frac{Q}{A} = -k\frac{\partial h}{\partial x} = ki$$

In Eq. 2.1 k is the permeability of the aquifer, h is the hydraulic head, i is the hydraulic gradient and x defines the flow direction (Figure 2.10). Based on the above the adjective mass flux of the contaminant, defined as the mass flowing through a unit cross-sectional area per time (units: mass/(time length^2)), is given as:

(2.3) $$J_{advection} = qc = nVc$$

where c is the concentration of the contaminant in the liquid phase. The concentration c in a specific location constantly varies with time, while concentration in a specific volume of water remains constant, as this volume of water flows following the hydraulic gradient.

2.7.2 Diffusion or molecular diffusion

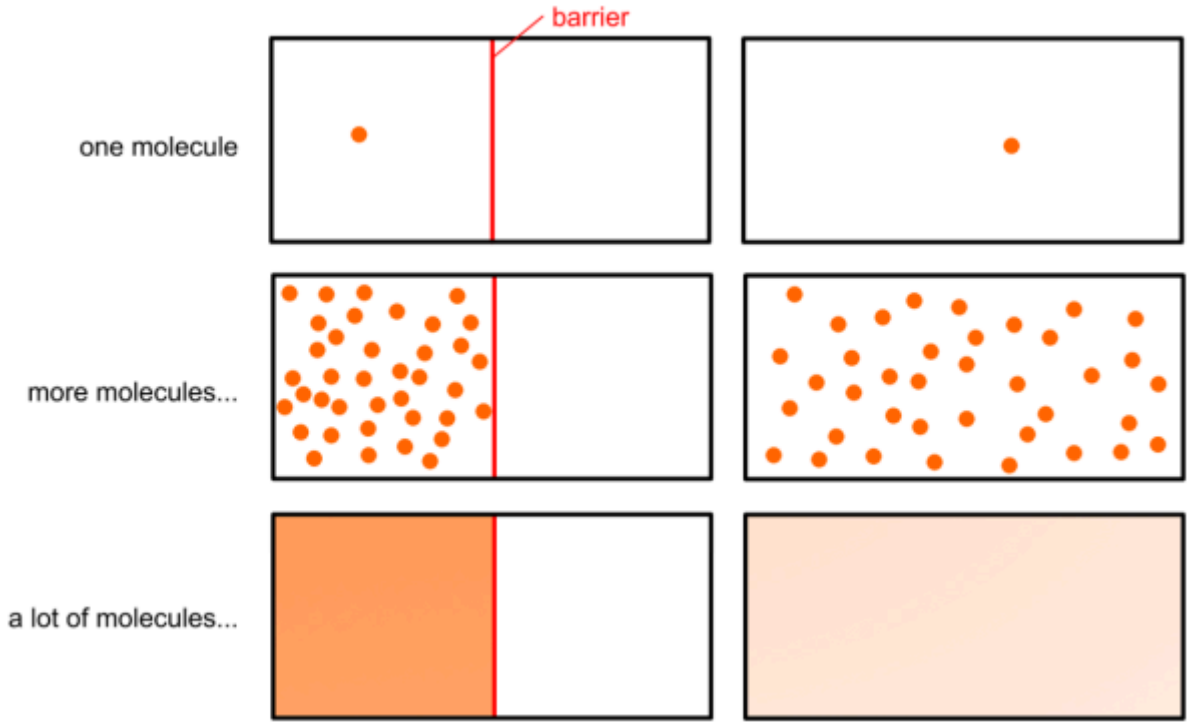

Figure 2.11. Diffusion transportation mechanism from a microscopic and macroscopic point of view.

Contrary to advection transport, which refers to macroscopic movement, diffusion is a molecular based phenomenon. The contaminant is diffused in the groundwater, due to variation in concentration, meaning that the substance moves from areas of high to areas of low concentration. Figure 2.11 illustrates this from a microscopic and macroscopic point of view. Initially there are solute molecules (or ions) of the contaminant only on the left side of a barrier. These molecules or ions move randomly. As a result of this motion, if we remove the barrier, the solute diffuses to fill the whole container, moving from the

high concentration area (left) to the low concentration area (right). Diffusion will continue until the concentration of the contaminant becomes equal everywhere. The rate at which these irregularities in concentration disappear can be quantified via Fick's first law of diffusion:

(2.4) $$J_{diffusion} = -D\frac{\partial c}{\partial x}$$

Eq. 2.4 suggests that the diffusive mass flux of the contaminant $J_{\text{diffusion}}$, which provides the mass of the contaminant flowing through a unit cross-sectional area per time (units: mass/(time length^2)), depends on the difference in concentration, the inverse of the distance, and a diffusion coefficient D. This is a function of the type of cation, temperature, soil porosity and soil tortuosity. In other words, diffusion of the contaminant does not depend on groundwater flow, and can take place in still water too.

2.7.3 Dispersion or mechanical dispersion

Movement of the contaminant is due to the presence of interconnected voids of the soil skeleton, of various shapes. Thus in microscopic scale, the velocity of water moving though the voids varies from place to place (Figure 2.12), and may diverge from the mean (macroscopic) groundwater flow i.e., the substance can be transported perpendicularly to the macroscopic groundwater flow too. Similar to the diffusion mechanism described above, the dispersive mass flux of the contaminant $J_{\text{dispersion}}$ provides the mass of the contaminant flowing through a unit cross-sectional area per time:

(2.5) $$J_{dispersion} = -D_d\frac{\partial c}{\partial x}$$

$J_{dispersion}$ (units: mass/(time length^2)) depends again on the difference in concentration, the inverse of the distance, and a dispersion coefficient D_{d}, which is a function of the seepage velocity and of the longitudinal dispersivity.

Often, these mechanisms may act antagonistically (Figure 2.13) or simultaneously (Figure 2.14). More specifically, the advection mechanism tends to transport the contaminant from right to left, from the area of high hydraulic potential to the area of lower hydraulic potential, following the hydraulic gradient. The diffusion mechanism on the other hand tends to transport the contaminant from the area of high concentration to the area of low concentration (Figures 2.13 and 2.14).

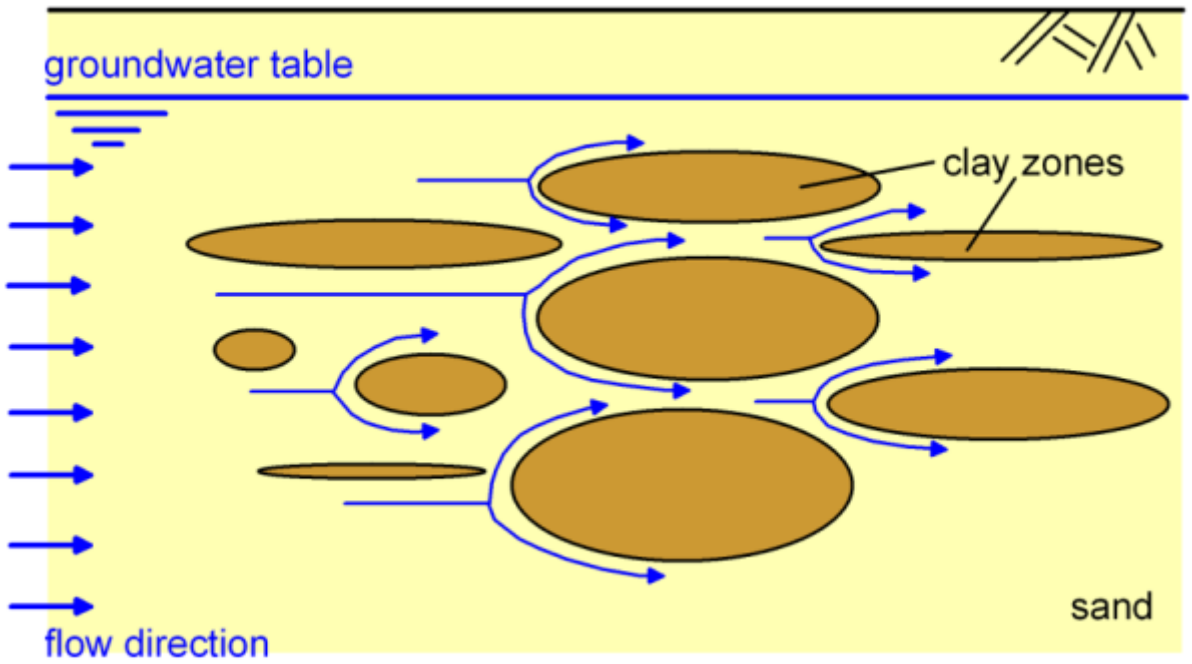

Figure 2.12. Mechanical dispersion of contaminant through soil.

Therefore to calculate the evolution of contaminant concentration with time we need to solve the continuity Eq. 2.6, which describes mathematically the transport of a conserved quantity (here the mass of the contaminant):

$$\textbf{(2.6)}\ \frac{\partial m}{\partial t} + \nabla J = S$$

where m is the mass density (mass of contaminant per unit volume), J is the mass flux vector considering the above mechanisms and S quantifies the increase ($S > 0$) or reduction ($S < 0$) of the contaminant mass. Positive S terms are referred to as "sources" and negative S terms are referred to as "sinks".

The gradient of the mass flux vector:

$$\textbf{(2.7)}\ \nabla J = \frac{\partial J}{\partial x} i + \frac{\partial J}{\partial y} j + \frac{\partial J}{\partial z} k, \text{ with } \hat{i} = \begin{bmatrix} 1 \\ 0 \\ 0 \end{bmatrix} \hat{j} = \begin{bmatrix} 0 \\ 1 \\ 0 \end{bmatrix} \hat{k} = \begin{bmatrix} 0 \\ 0 \\ 1 \end{bmatrix}$$

will provide the direction towards which the mass flux vector rises faster in the three-dimensional space, and its magnitude provides a measure of how fast the mass flux rises in this direction. For example, if the mass flux vector due to advection and diffusion is $J = -3x-4y$ where x is the horizontal axis and y is the vertical axis, then:

$$\textbf{(2.8)}\ \nabla J = -3i - 4j, \text{and } |J| = \sqrt{3^2 + 4^2} = 5 \left(\frac{\text{mass}}{\text{time} \times \text{length}^2} \right)$$

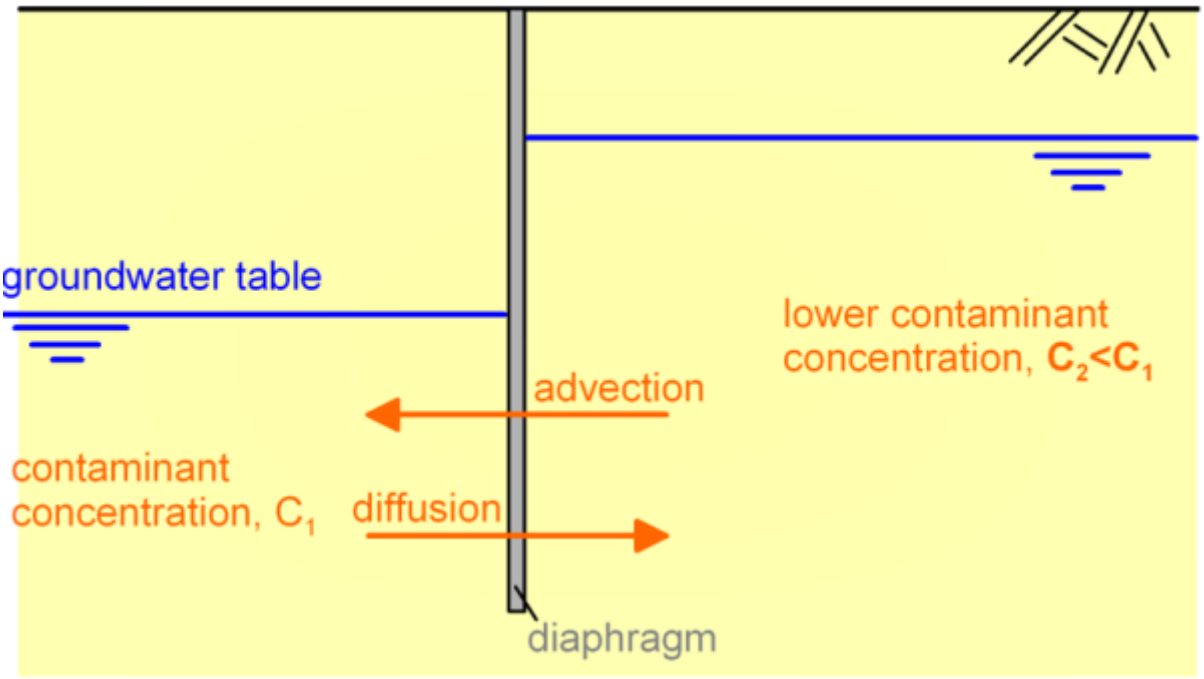

Figure 2.13. Antagonistic action of two mechanisms of contaminant transport.

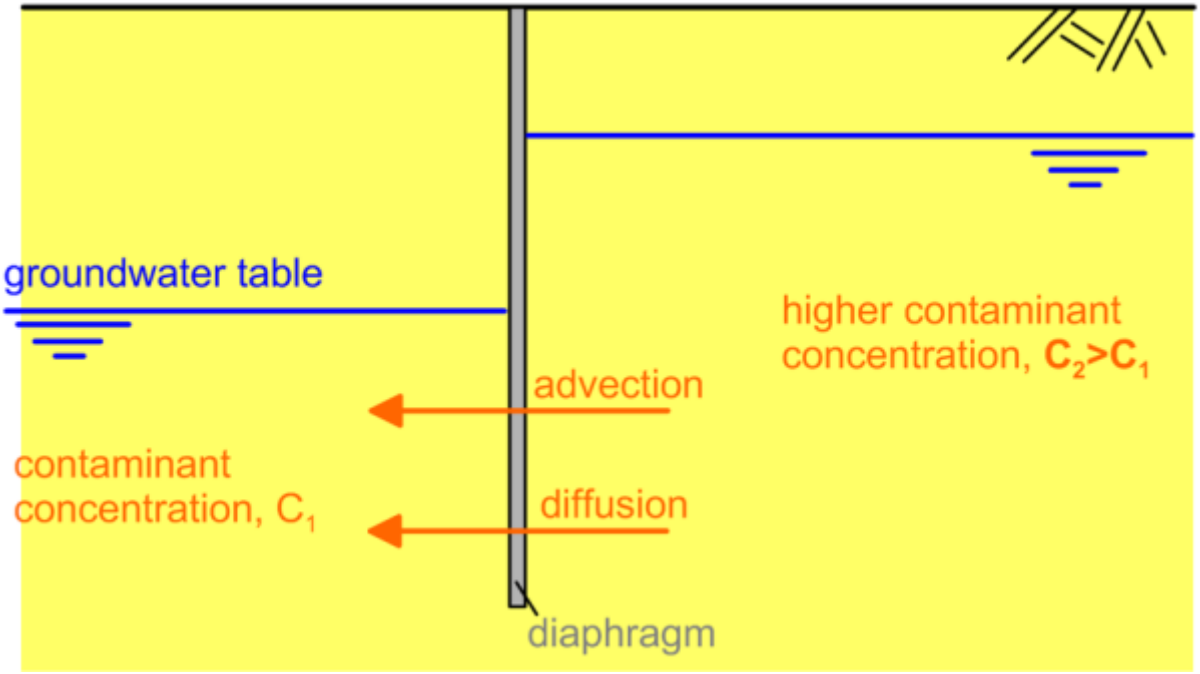

Figure 2.14. Combined action of two mechanisms of contaminant transport.

Other, non-mechanical mechanisms may also act to reduce and disperse the pollution load, and are introduced as "sinks" in Eq. 2.6:

- *Chemical interaction,* referring to the absorption of pollutants on the surface of clay particles or, ion exchange between pollutants and clay particles.
- *Biological and biochemical* reactions, such as the disintegration of organic pollutants by microorganisms.
- *Nuclear procedures,* such as particle decay.

2.8 CONTAMINATION CONTROL AND REMEDIATION METHODS

We use the terms *contamination control methods* and *contamination remediation methods* to describe methods for modifying an unacceptable set of environmental conditions, by:

- Removal of a pollutant after the source of pollution has been contained.
- Diversion of groundwater from flowing through a source of pollution, and from contacting a drinking water supply.
- Lowering the groundwater table below a source of pollution to prevent its contamination.

Different methods apply for groundwater and soil contamination. Groundwater control and remediation methods are based on the following general concepts:

- Extraction of groundwater from (or injection of fresh water into) wells or drains, to capture a pollutant or alter the direction of groundwater movement.
- Installation of gravity collection systems such as subsurface drains, designed to intercept groundwater.
- Construction of low hydraulic conductivity barriers, which consist of a vertical wall of low hydraulic conductivity materials build to divert groundwater flow.
- Biological or chemical *in situ* treatment methods.

Contaminated soil control and remediation methods on the other hand are based on:

- Disintegration of organic pollutants by microorganisms (*bio-remediation*). This method can, under some circumstances, be used for contaminated groundwater too.
- Chemical extraction of pollutants via soil washing.
- Thermal treatment of contaminated soil *in situ* or in a special furnace.
- Extraction of contaminants, with the vacuum method, or simply:
- Excavation and removal of contaminated soil, where the soil is moved to an appropriate repository. The cost of this method can be extremely high and the problem is not solved, just transferred elsewhere.

Some details on the most common methods used for contaminated groundwater and soil control and remediation are provided in the following sections.

2.8.1. Groundwater contamination control and remediation methods

One of the most widely used methods for groundwater treatment is the *groundwater pumping* or *"pump-and-treat"* method. When pumping from a well begins, the head in the well is lowered below the *free-field* level h_o in the surrounding aquifer (Figure 2.15). As a result, water will flow from the aquifer into the well, and the initial groundwater table is depressed, forming a *depression cone.* The surface of the cone

is called *draw-down curve*, and the outer limit corresponds to the *radius of influence R* (Figures 2.15 and 2.16). Assuming that Darcy's law is valid, axisymmetric conditions and a simplified soil stratigraphy, we can estimate the flow from the well Q as:

(2.9) $$Q = q \times \text{Area}$$

where the area depends on the thickness of the aquifer, and q is the Darcy's water flux (Figure 2.15):

(2.10) $$q = -k\frac{\partial h}{\partial r} = ki$$

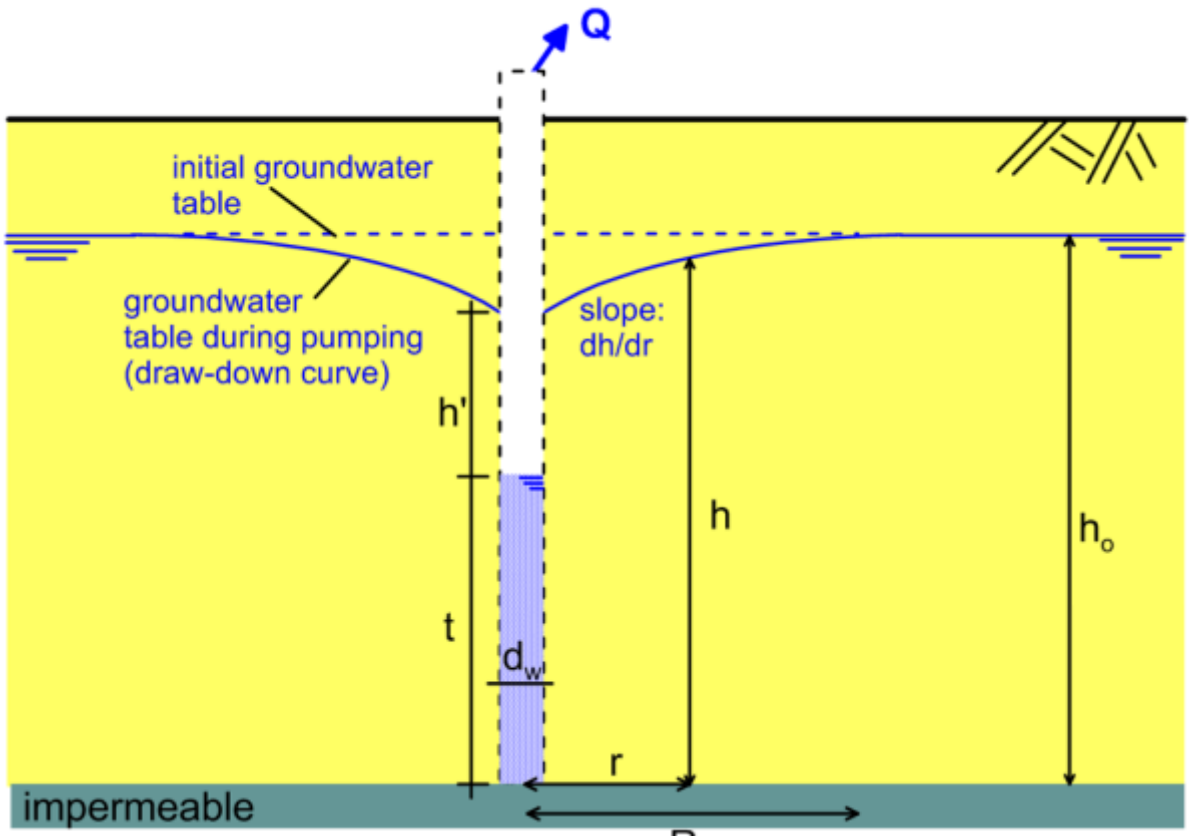

Figure 2.15. Flow to a fully penetrating well.

Adopting some further simplifying assumptions, such as a well penetrating down to the level of the aquitard (Figure 2.15) and an infinitely extending pervious stratum, we can estimate the draw-down curve geometry (and thus design the dewatering system) as:

(2.11) $$h_o^2 - h = \frac{Q}{\pi k}\ln\frac{R}{r}$$

where R is the radius of influence, that depends on the boundary conditions of the problem, h_o is the original elevation of the groundwater table, and Q is the pumping rate.

The above formulas are based on certain important simplifying assumptions, such as uniform soil and axisymmetric flow towards a single well. Numerical methods can be used for the design of a dewatering system in case where the conditions *in situ* do not match the mentioned assumptions, and this is demonstrated later in Part 2.

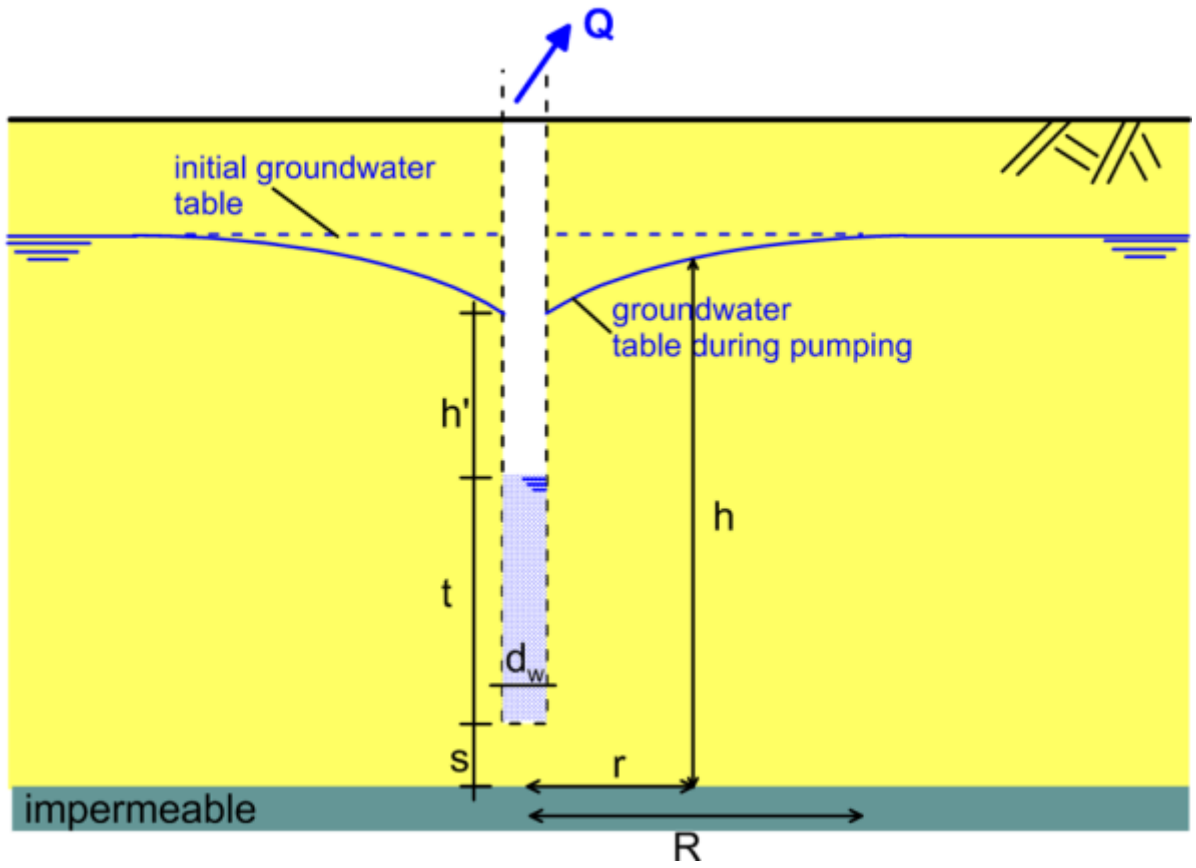

Figure 2.16. Flow to a partially penetrating well.

Groundwater pumping for contamination control can be used for:

- Lowering groundwater level in the vicinity of polluted sites.
- Increasing the separation between pollutants and groundwater.
- Supplementing a barrier system.
- Extract contaminated water for treatment.

Note that groundwater pumping and water table lowering can result in subsidence, due to the increase in soil effective stresses. Injection wells or recharge basins may need to be used in conjunction with the pumping wells to recharge the aquifer, and avoid affecting nearby structures.

Subsurface gravity drains can be used to:

- Reduce the flow from non-contaminated sources, such as a nearby stream or lake, thus reducing the amount of groundwater that must be collected through pumping for treatment (Figure 2.17).
- Lower the groundwater out of contact with a contaminated zone (Figure 2.18a).
- Used in conjunction with impermeable barriers, can completely isolate a contaminated zone (Figure 2.18b).

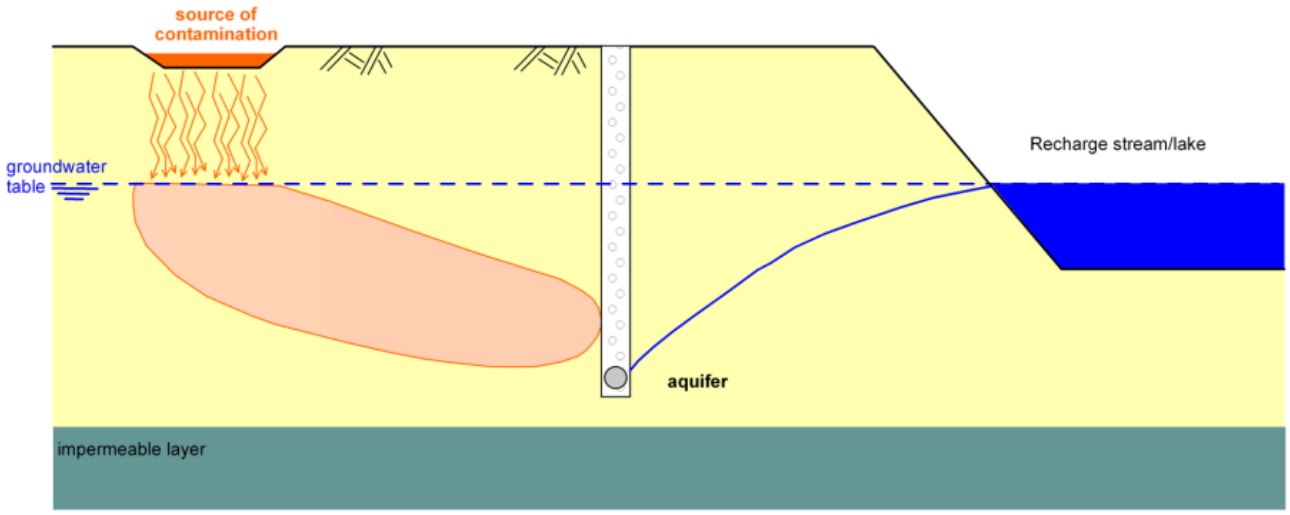

Figure 2.17. Use of gravity drains to reduce flow from non-contaminated recharge sources.

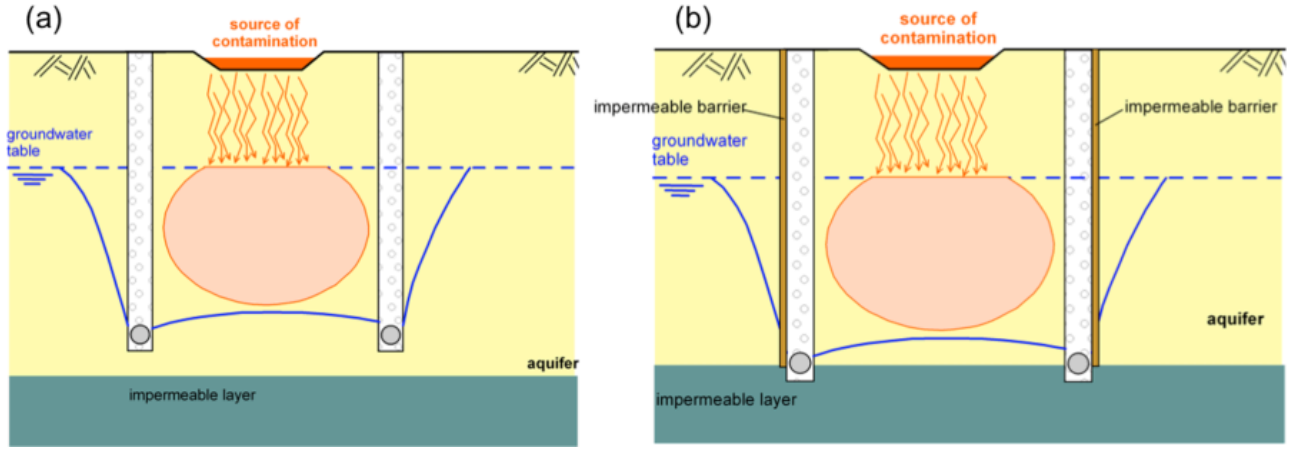

Figure 2.18. (a) Use of gravity drains to lower the groundwater level, and (b) Use of gravity drains to isolate a contaminated zone. Notice that drains must penetrate the impermeable layer.

Drains must be filled with filter coarse-grained material of proper gradation, and wrapped with geotextiles to avoid clogging (Figure 2.19). A pump can be used to remove groundwater from the pipes installed at the bottom of the drains.

Low hydraulic conductivity, practically impermeable, barriers are constructed to block the flow of groundwater, and thus prevent advection of the pollutant (Figure 2.20). For that, they should feature permeability of the order of 10^{-8} to 10^{-9} m/sec, or lower. Methods for constructing low hydraulic conductivity barriers include:

- Slurry walls, made of soil-bentonite of cement-bentonite mixes using special machinery (slurry wall hydraulic grab).
- Grouting curtains.
- Sheet piles.
- Ground freezing.
- Electrokinetic barriers.

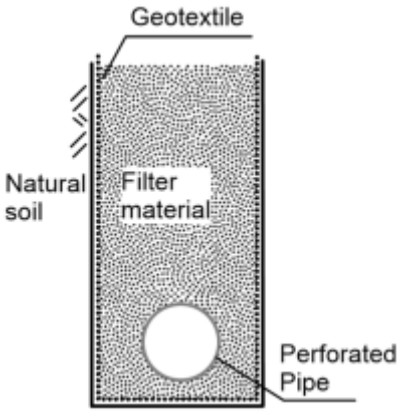

Figure 2.19. Filling of drains with coarse-grained filter material to avoid clogging.

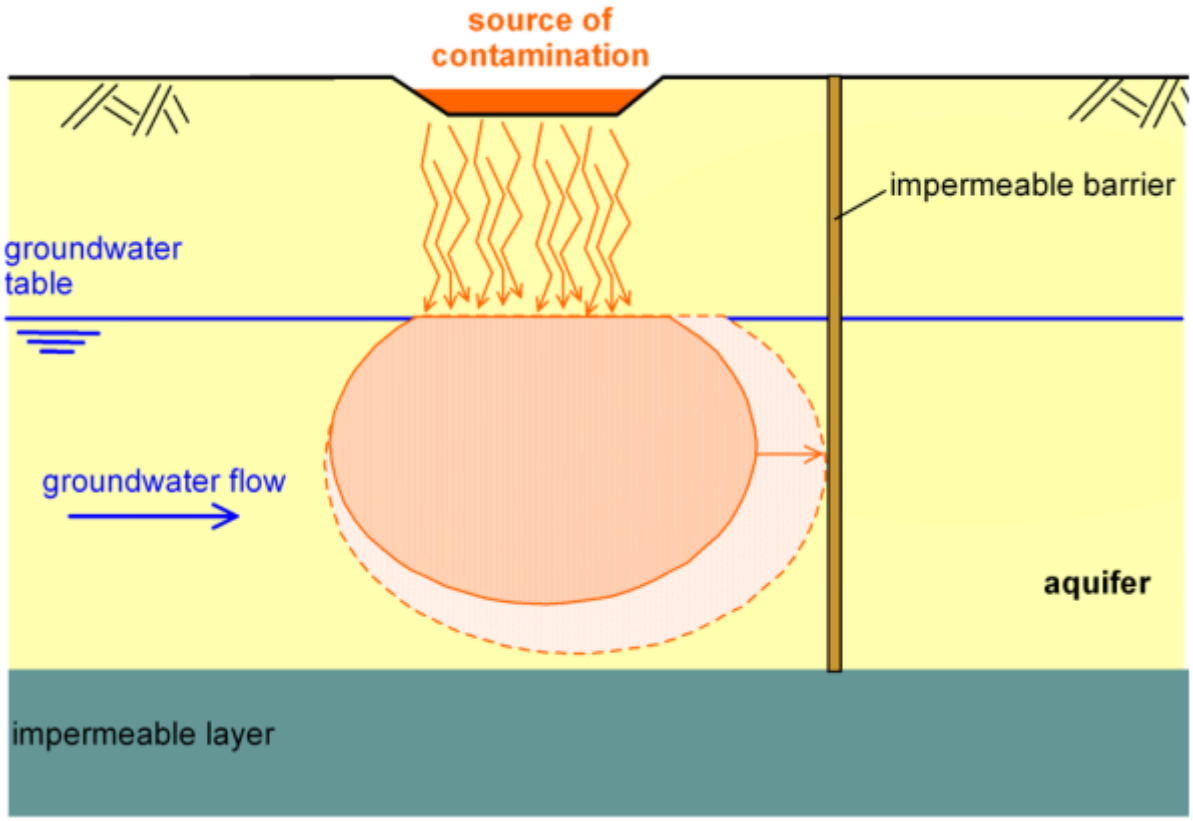

Figure 2.20. Use of impermeable barriers to prevent advection of the pollutant.

Barriers alone will not remove the pollutant of course, but they can be used in conjunction with pumping or drains as illustrated in Figure 2.18b. The design of such a system with the aid of numerical methods is discussed at the end of this Part. Note that long-term performance of barriers is rather questionable, and if the barrier begins to leak, further remedial measures must be implemented; an extremely expensive task if the area has been redeveloped.

Reactive barriers on the other hand can be used for the *in situ* treatment of polluted water, as it moves through an aquifer under natural hydraulic gradient (Figure 2.21). A portion of the aquifer is excavated, and subsequently backfilled with a porous reactive mixture. Reactive barriers are installed downstream of the contamination source, and the natural groundwater flow carries the polluted water through the barrier, thus costs related to pumping the contaminated water on the surface are minimised.

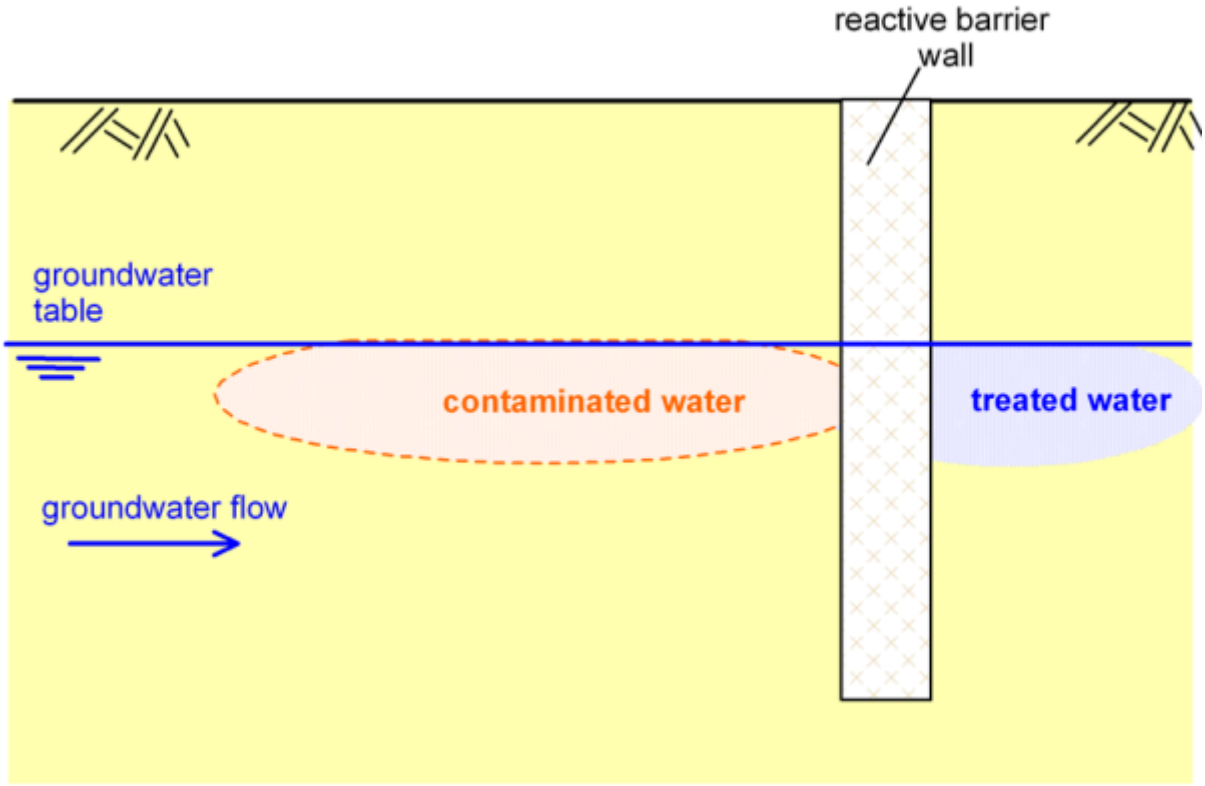

Figure 2.21. The concept of using a reactive barrier wall to treat contaminated groundwater.

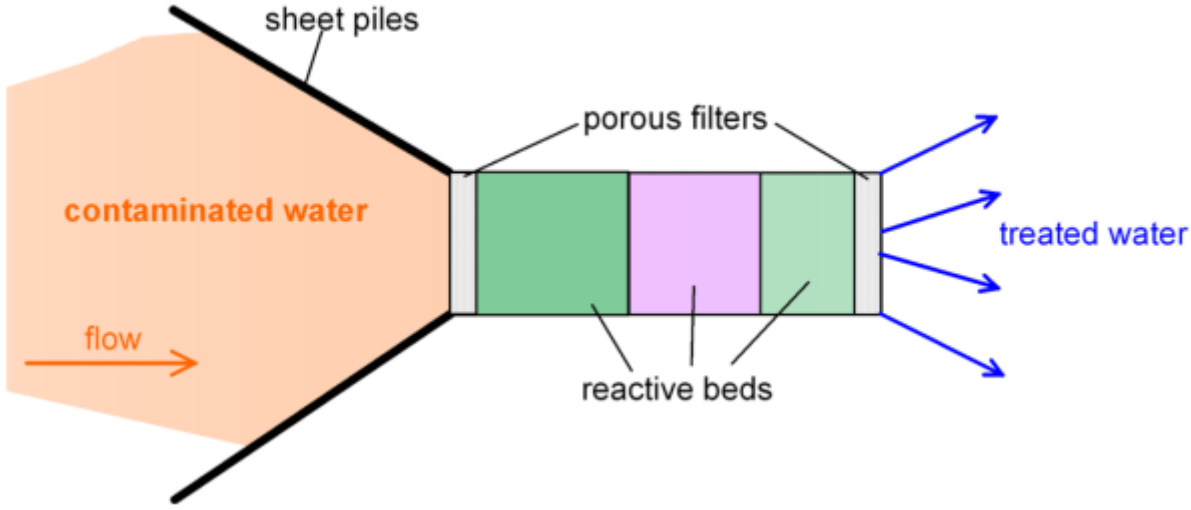

Figure 2.22. Plan view of a funnel-and-gate system.

Depending on the type of pollutants, different materials are used to backfill the reactive barrier. For example, mixtures of zero-valence metals, such as zero-valence iron mixed with clean sand can be used for the degradation of chlorinated organic compounds or hexavalent chromium. In practice, a *funnel-and-gate* system (Figure 2.22) is used to "drive" the contaminated water through the reactive beds with the aid of sheet piles, which also serve as temporary retaining measures for the excavation of the aquifer material.

2.8.2. Soil contamination control and remediation methods

Bio-remediation, one of the most common methods for treating contaminated soils but also groundwater, is based on the concept of biodegrading organic pollutants via introducing microorganisms that can metabolise the pollutants into non-toxic products.

The method has been used for decades in urban sewage treatment facilities. In recent times it is being also used to treat soils contaminated by polycyclic aromatic hydrocarbons (PAH), volatile organic compounds (such as BTEX, a mixture of benzene, toluene and xylene) and phenolic or nitroaromatic compounds. Microorganisms such as bacteria or fungi can metabolise these organic compounds, and grow using the carbon and/or energy produced. The final products of this process are inorganic compounds such as carbon dioxide and water, or other less harmful organic compounds, such as methane or sulphide. For the successful implementation of bio-remediation, certain conditions must be met:

- Appropriate microorganisms that can metabolise the specific pollutants must be introduced.
- Nutrients such as nitrogen, potassium and phosphorus are necessary for growth of the microorganisms, and must be available in the subsoil.
- Soil conditions i.e., temperature, humidity and pH must favour the development of microorganisms.

Given the above, a pilot application is highly recommended, to ensure effectiveness and optimise the procedure. Bio-remediation is a slow process that can take up to 20-30 years in some cases. It is more effective in coarse-grained, non-saturated soils, where oxygen is available and the metabolism is aerobic. Certain techniques such as soil venting via stirring can enhance the process.

The *vacuum extraction* method is used to remove volatile hydrocarbons from the vadose zone. A well is bored, and suction is applied to collect the hydrocarbons. The method is applicable to high-permeability soils, where the effective radius of each well is larger. The vadose zone must not be in contact with the air, thus it is necessary to cover the ground surface with an airtight material, to increase the effectiveness of the method (Figure 2.23).

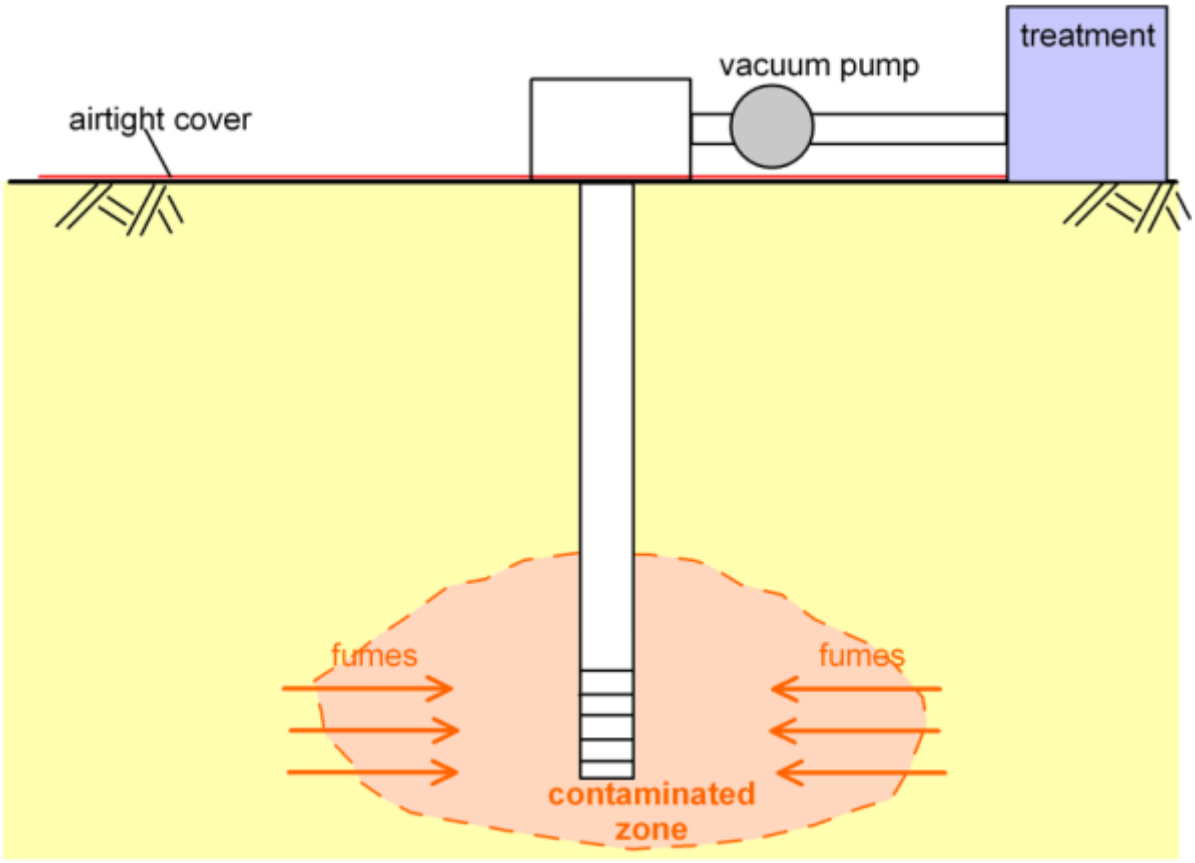

Figure 2.23. Outline of the vacuum extraction method.

Soil washing involves injecting a mixture of water and acids or detergents into the soil under high pressure, while stirring the soil to remove the pollutants. The main drawback of soil washing is that it requires significant amounts of water, which after the application of the method will contain a significant amount of pollutants. Thus the water used for washing must be treated too, before being recycled. Care must be taken so that the washing water does not infiltrate to contaminate lower aquifers.

Finally, *thermal treatment* is used to remove volatile pollutants such as oil products, cyanides, polycyclic aromatic compounds, asbestos etc. by heating them beyond the boiling point of the hazardous compound. Special control procedures must be implemented while applying this method, as toxic gases produced during heating under high temperatures may be released in the environment.

EXAMPLE 2.1

Selection of remediation method on the basis of comparative analysis

Establishment of various industries on the banks of a hypothetical river resulted in contamination of its waters and sediments. Analysis of sediments revealed that the concentration of heavy metals (lead, zinc, cooper) has exceeded by far the threshold concentrations indicating harmful effects. Samples retrieved from the riverbank indicate that the average thickness of the contamination sediment is 250 mm, and the total contaminated sediment volume is about 150,000 m^3.

Select the most effective remediation method, considering (permanent and temporary) environmental, technical and economic criteria.

Answer:

Five (5) remediation alternatives are tentatively selected for the comparative analysis (Mohamed and Antia 1998). These consist of (in order of increasing cost):

1. **Storage of sediments on land**

   Dredge sediments, reduce their volume (via dehydration), transport them and store them in a waste depository.

   Estimated Cost: $5 mil

2. On-site storage of sediments on the riverbed

Cover the sediments with a permeable geotextile, and compact them by overlaying a bed of crushed stones.

Estimated Cost: $6 mil

3. Encapsulation of sediments within the river area

Dredge sediments by means of suction flow-reversing, transport them via pipelines, and store them in watertight basins constructed within the river. This option will reduce the width of the river, but to acceptable levels.

Estimated Cost: $10 mil

4. Off-site stabilization of sediments

Dredge sediments and treat them with chemical agents to form a cement-like product. Use the material in landfills or for general embankment construction.

Estimated Cost: $6 mil to $12 mil

5. On-site stabilization of sediments

Mix the sediments directly with chemical agents and cement to create a highly resistant material of low permeability. Treated material can be left in place.

Estimated Cost: $12 mil to $24 mil

Each family of criteria (*permanent environmental, temporary environmental and technical/economical*) is divided into specific criteria/aims, and each remediation option is rated according to that criterion (1st, 2nd, 3rd etc.), in the order of most desirable to least desirable solution.

At the same time, each one of the criteria is assigned to an importance class IC, according to the project specifications, stakeholders feedback, risks etc. Three (3) importance classes are used in this example. In this way, ratings are weighted according to Table 2.2 in a five-level mark scale. Higher marks correspond to the most desirable option: A is the highest mark and E is the lowest. Tables 2.3 to 2.5 present the criteria, divided into three families, their ratings, and the importance class they are assigned to.

Table 2.2. Weighting of criteria according to the importance class.

Importance Class, IC	Weight of criterion		
	Rated 1st	Rated 2nd	Rated 3rd
1	A	B	C
2	B	C	D
3	C	D	E

Table 2.3. Permanent environmental family of criteria

Criterion	Options	Rating	IC
Eliminate the contamination of the river sediment	Complete treatment and elimination of pollutants	1st	**2**
	Confinement of pollutants	2nd	
Sediment management in the affected area	Sediments remain in the affected area	1st	**1**
	Part or all sediments transported outside affected area	2nd	
Preserve site conditions	No changes in the river layout	1st	**3**
	Changes in the river layout	2nd	
Minimise risk of polluting groundwater and surface water after treatment	No risk; contaminants transported outside affected area	1st	**2**
	Low risk; contaminants fully confined in the affected area	2nd	
	Moderate risk; contaminants partially confined in the affected area	3rd	
Riverbed characteristics following the completion of work	Riverbed similar to natural state	1st	**3**
	Riverbed composed of small stones (added material)	2nd	
	Cemented material covering the riverbed	3rd	

Twelve (12) criteria in total are considered in this example. Other, project-specific criteria may apply e.g. impact of works on industrial activity or local economy, potential for area redevelopment, timetable issues etc.

The ratings of the criteria are also project-dependent. For example in this case emphasis is put on criteria related to inconvenience of the local residents during works (IC1), compared to temporary environmental impact (IC3, Table 2.4), to minimise community reaction to the project.

Results are summarised in Table 2.6, where the marks scored by each remediation solution are reported, according to its technical details in the light of the offered options. The solution that scores more A- marks (encapsulation is this case) is the preferred one. If two or more alternatives have the same number of A- marks, we count the B- marks etc. Therefore the second most preferable option in this case is storage of sediments on land, followed by on-site stabilisation.

Table 2.4. Temporary environmental family of criteria.

Criterion	Options	Rating	IC
Inconvenience caused by construction site	Majority of works taking place outside affected area; minimal installations; works completed within 12 months	1st	**1**
	Majority of works taking place in affected area; installations and storage on site; works completed within 12 months	2nd	
	Majority of works taking place in affected area; installations and storage on site; works completed in more than 12 months	3rd	
Inconvenience due to trucking activity	Minimal trucking activity	1st	**1**
	Heavy trucking activity	2nd	
	Very heavy trucking activity	3rd	
Environmental impact of works	Little or no drop in river water; minimal dredging	1st	**3**
	Little or no drop in river water; dredging	2nd	
	Major drop in river water	3rd	

Table 2.5. Technical/Economical family of criteria.

Criterion	Options	Rating	IC
Effect of works on river functions	River section similar to original state	1st	**2**
	River section similar to original state, alteration of banks outline	2nd	
	Characteristics of river section altered	3rd	
Past experience and feasibility	Proven technology for similar treatment	1st	**1**
	Proven technology, but for a different treatment	2nd	
	Technology not proven in practice (pilot or pre-industrial stage)	3rd	
Necessity for monitoring	No follow up required; pollutants removed from the area	1st	**2**
	Small-scale monitoring required	2nd	
	Large-scale monitoring required	3rd	
Total cost	$10mil or less	1st	**1**
	$10 to 30mil	2nd	
	over $30mil	3rd	

Table 2.6. Ranking of alternative remediation solutions.

Mark	Storage on land	On-site storage	Encapsulation	Off-site stabilization	On-site stabilization
A	2	2	**3**	2	2
B	5	2	1	3	4
C	4	4	6	3	5
D	1	3	1	3	1
E	0	1	1	1	0
Ranking	2nd	5th	**1st**	4th	3rd

2.9 DESIGN OF A PUMP-AND-TREAT INSTALLATION

This chapter presents the use of the Finite Element method (computer code PLAXIS) to determine the capacity of water pumps required to dewater a 2 m wide by 30 m long shaft (Figure 2.24) used for the extraction of contaminated groundwater. The presented method is applicable to the design of any dewatering system when two-dimensional plane strain conditions apply i.e., when the width of the dewatered area is much longer than its length (see Part 3).

This problem involves modelling of steady state flow, and can be solved analytically using flow net-based methods under certain conditions i.e., uniform homogeneous and isotropic soil, with equal permeability k along both the horizontal and vertical directions. However, while for most soils the permeability along the vertical direction is not much lower than the permeability along the horizontal direction, the assumption of uniform soil conditions is rarely met *in situ*. Such assumptions are not required when using numerical methods to solve steady state flow problems.

Consider the soil conditions illustrated in Figure 2.24 where the shaft is excavated in a 10 m-thick silty sand layer of permeability k = 1 m/day (vertical permeability equal to horizontal permeability). The sand layer is underlain by a silty clay layer that can be considered as impermeable. Whilst the stability of the retaining system is not studied in this example, the length of the (assumed impermeable) sheet pile walls will affect flow of groundwater into the shaft (thus the hydraulic gradient i) and must be considered in the analysis. For the problem at hand, we assume that the minimum length of the sheet pile walls required to retain the excavation is equal to 6 m. Finally, the groundwater table is found at 2 m from the ground surface, and the target pump capacity should be such that the bottom of the excavation remains dry.

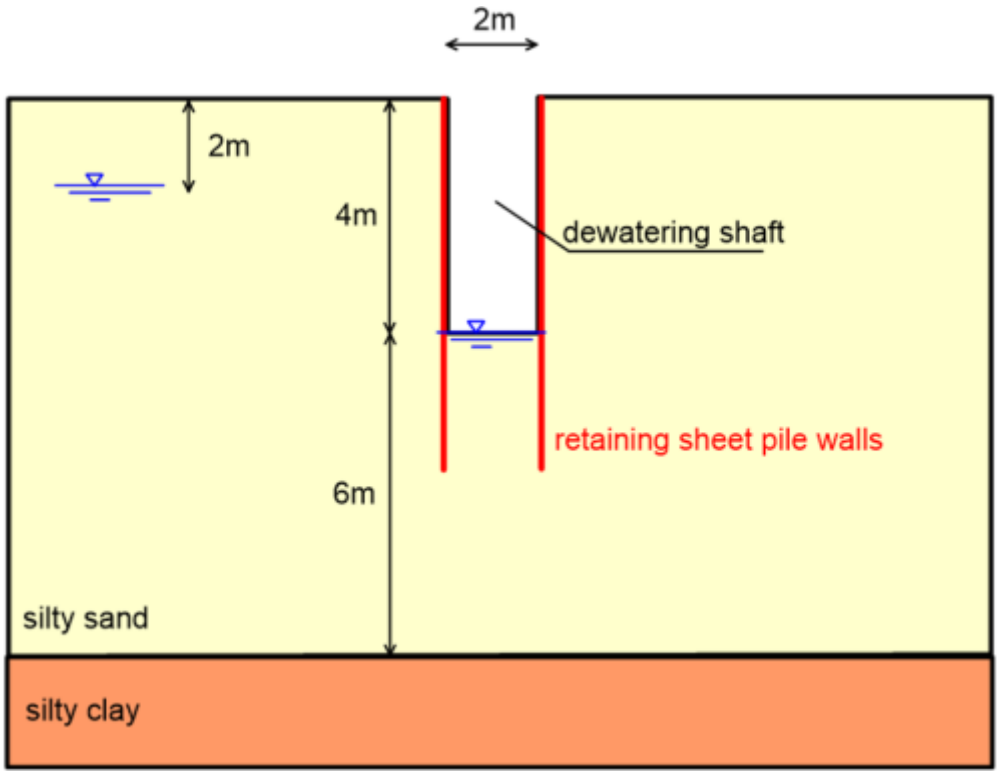

Figure 2.24. Schematic of the pump-and-treat problem.

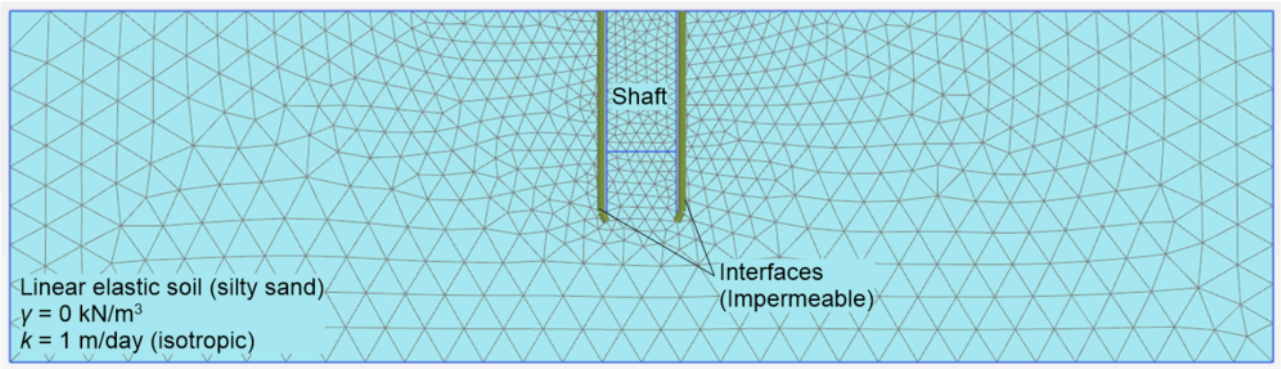

Figure 2.25. Finite Element mesh.

An outline of the numerical model and of the finite element mesh is presented in Figure 2.25. Only the 10m-thick silty sand layer is modelled, and the existence of the impermeable silty clay layer is considered by setting the bottom horizontal boundary of the model to be impermeable. The lateral boundaries of the model are placed at sufficient distance from the area of interest (shaft) so that boundary conditions will not affect the calculated flow into the shaft. Good practice suggests performing a sensitivity analysis with respect to the distance of the lateral boundaries from the area of interest, to confirm that results are not compromised by boundary effects. Sand is modelled as linear elastic material, however the unit weight of the material and its elastic properties (Young's modulus, Poisson's ratio) will not affect the results of the particular analysis, as displacements are not considered-only a steady state groundwater flow analysis is performed. Finally, the sheet pile walls are not explicitly modelled, as the structural properties of the retaining system are not of interest here. Instead, we model the retaining system by modelling two "interfaces" along the edges of the shaft, of length equal to the length of the sheet pile walls (6 m). These interfaces are assigned zero cross permeability (impermeable), although it is possible to model some flow through the retaining system.

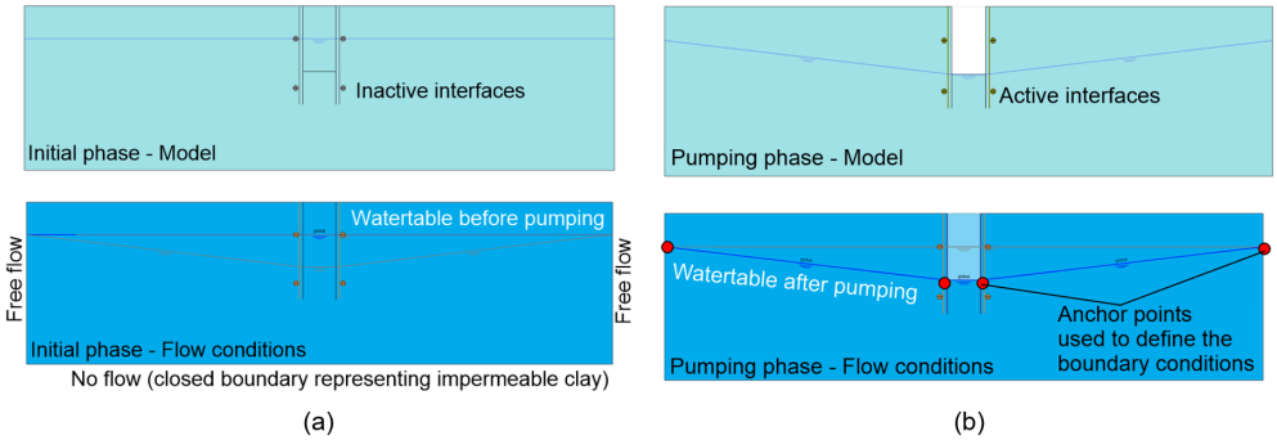

Figure 2.26. (a) Initial phase model and flow conditions; (b) Pumping phase model and flow conditions.

The analysis phases are presented in Figure 2.26. During both stages we model only flow (Calculation type: "Flow only") and calculation of pore pressures is based on "Steady state groundwater flow". The initial stage (Figure 2.26a) is used to calculate pore pressures before excavation and dewatering of the shaft. As such, the global water table is set to be horizontal, at 2 m from the ground surface. Free flow is allowed from the lateral boundaries, while no flow is allowed from the bottom boundary representing the impermeable clay layer. The interfaces are not active at this stage. It must be noted here that positive pore pressure values will be calculated above the water table with this model, representing suction in the unsaturated soil zone. While this does not affect the calculations described here, it is important to obtain a realistic suction profile if stability of the excavation is to be modelled too, as suction will affect soil strength and compressibility. This can be achieved by selecting a proper water retention model for soil, such as the Van Genuchten model, and allocating appropriate parameters to it.

The second analysis stage (Figure 2.26b) models lowering of the water table due to pumping inside the shaft, and will provide the total flow inside the shaft when the groundwater table is lowered at its bottom by means of pumping. As such, the geometry cluster representing soil inside the shaft must be de-activated, to model excavation of soil. At the same time the interfaces are activated, to account for zero horizontal flow from the sheet pile walls. The target phreatic line is input, as shown in Figure 2.26, by setting the water table level to be at 2 m from the surface at the lateral boundaries, and at 4 m from the surface inside the shaft. Note that this is not the actual phreatic line, the geometry of the phreatic line during steady state pumping will result from the analysis. Flow conditions at the boundaries remain unchanged, and are inherited from the initial stage.

Some key results from the analysis are shown in Figures 2.27 and 2.28. Figure 2.27a presents the phreatic line during steady state pumping and the active pore pressure contours. Notice that while the pore pressure at the elevation of the silty clay layer is equal to the hydrostatic pressure near the lateral boundaries (80 kPa), notable suction values are calculated above the phreatic line, as explained earlier. The required pumping capacity can be determined by plotting groundwater flow vectors (Figure 2.28) and finding the total discharge into the shaft along the cross section A-A, at the bottom of the shaft. Since the total discharge through the bottom of the shaft is 0.794 m^3/day/m, the required capacity of pumps to be installed in the 30 m-long shaft is 30×0.794 = 23.8 m^3/day.

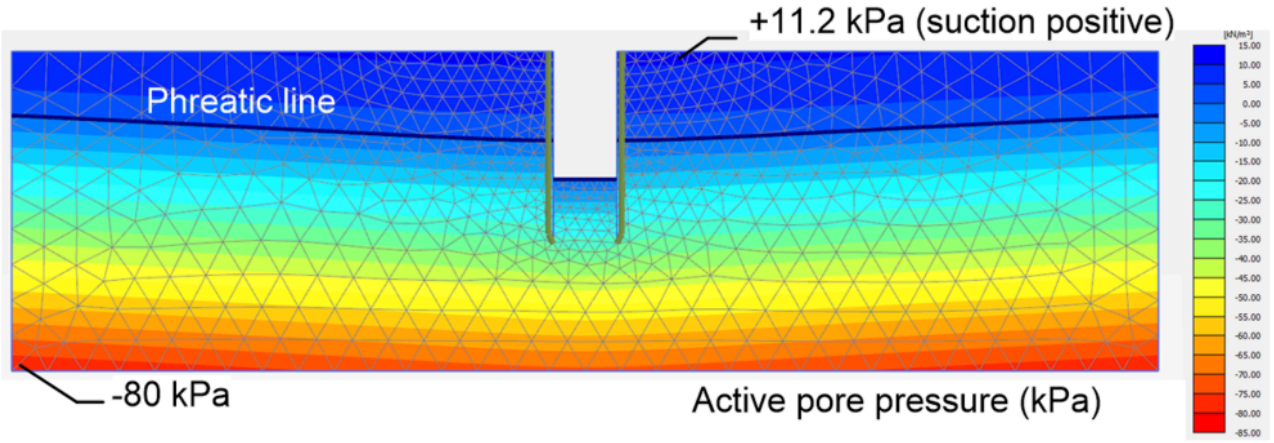

Figure 2.27a. Analysis results: Pore pressure contours and computed phreatic line.

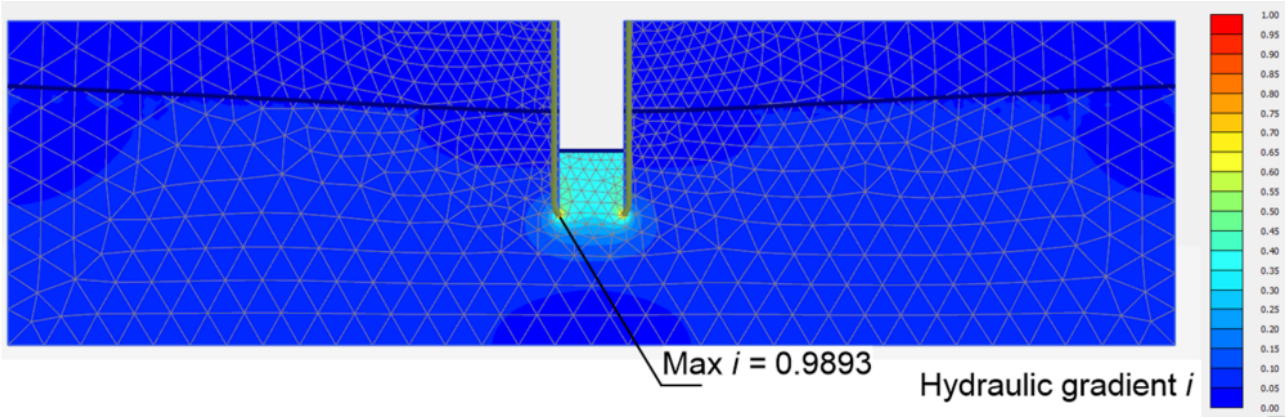

Figure 2.27b. Analysis results: Hydraulic gradient contours.

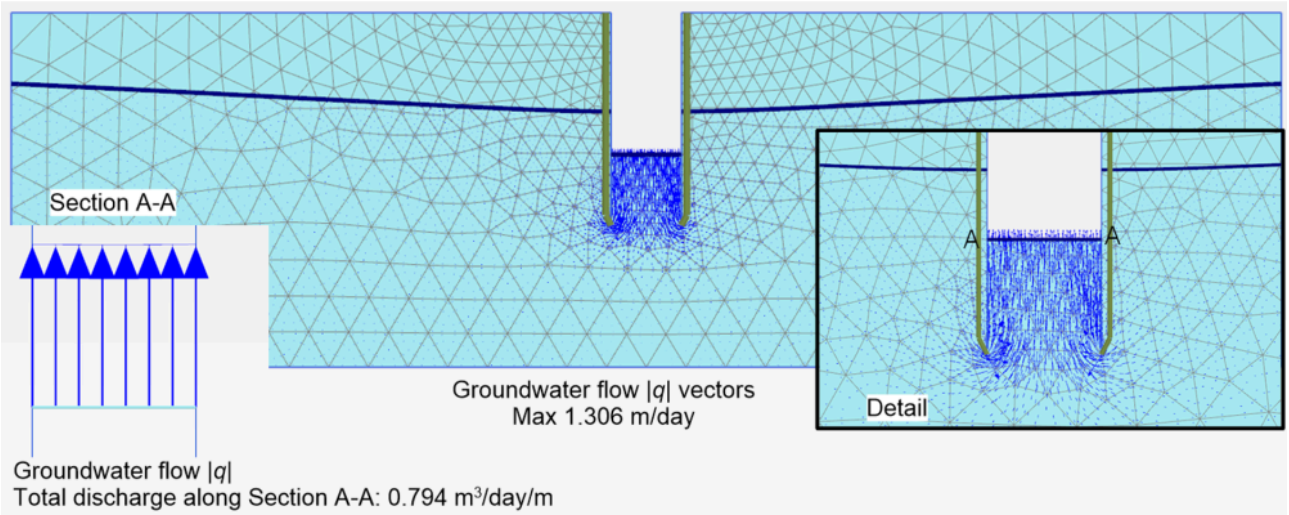

Figure 2.28. Analysis results: Groundwater flow vectors and cross-section along the bottom of the shaft.

However, notice in Figure 2.27b, which presents hydraulic gradient contours, that the maximum hydraulic gradient in soil underneath the excavation is near unity. It is reminded that the critical hydraulic gradient i_{cr}, required for sand "boiling" i.e., seepage failure to occur is:

$$\textbf{(2.12)}\ i_{cr} = \frac{\gamma'}{\gamma_w} = \frac{G_s - 1}{1 + e}$$

where γ' is the submerged unit weight of soil, γ_w is the unit weight of water, G_s is the specific gravity of soil (G_s = 2.65 for most silica-based soils) and e is the void ratio. The critical hydraulic gradient is of the order of i_{cr} = 1 for most soils, which suggests that failure of the excavation due to seepage is very possible in this case, if the specific retaining system is adopted.

This issue can be alleviated by increasing the length of the sheet pile walls, thus the energy consumed during flow of water underneath the sheet pile walls. Indicatively, an increase in the length of the sheet pile walls by 3 m (9 m long sheet pile walls in total) results in decrease of the maximum hydraulic gradient from i = 0.989 to i = 0.637. Increasing the length of the retaining system will of course result in reducing the required capacity of the pumps, from 23.8 m^3/day to 13.9 m^3/day. These calculations demonstrate the importance of considering flow effects in the design of retaining systems in high permeability materials, when high groundwater table conditions are present.

2.10 DESIGN OF A POLLUTANT CONTAINMENT INSTALLATION

As explained in Section 2.8.1, impermeable barriers can be used in conjunction with a dewatering system to lower the phreatic line underneath a pollutant source, and thus prevent contamination of the groundwater. Design of such a system requires, among others, to verify whether the capacity of the dewatering system to be installed is sufficient for lowering the water table to the desired level. Given the complexity of this problem, it is not possible to use analytical methods. This example demonstrates the use of the Finite Element method for the design of a pollutant containment installation.

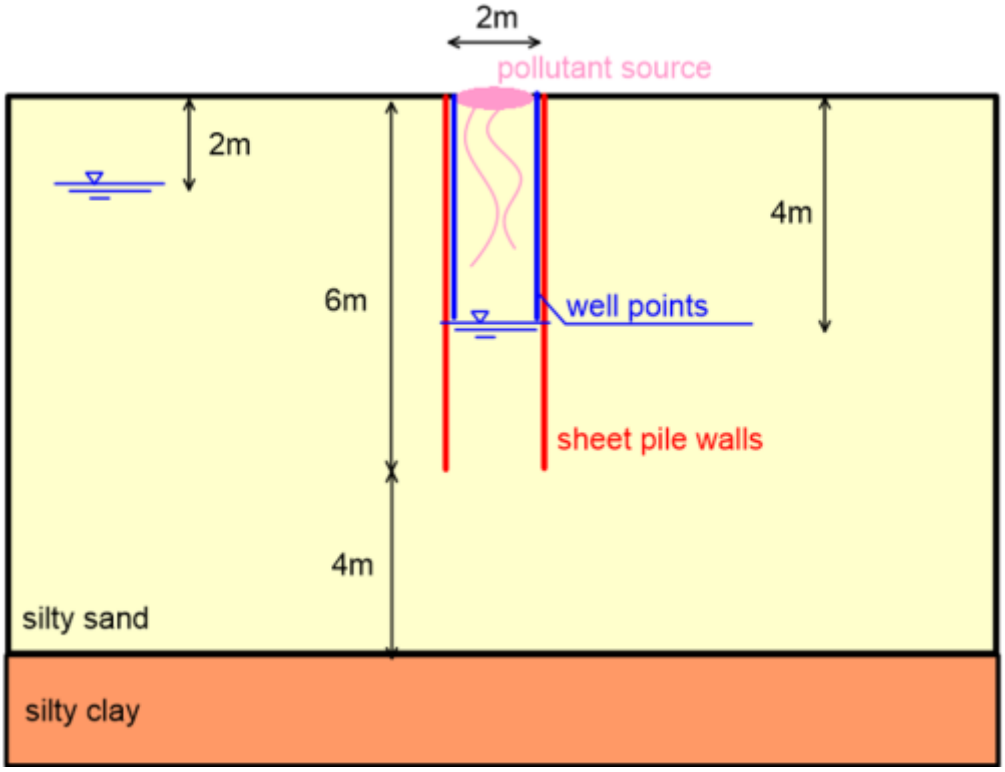

Figure 2.29. Schematic of the pollutant containment problem.

A schematic of the considered problem is shown in Figure 2.29. The width of the pollutant source is 2 m, and its length is assumed to be sufficiently larger than its width, so that the problem can be treated as two-dimensional plane strain (Part 3). Two parallel rows of sheet piles spaced at 2 m apart are driven into soil up to a depth of 6 m, and will act as impermeable barriers containing the pollutant source. The subsoil profile is the same as Chapter 2.9, and consists of a 10 m-thick homogeneous and isotropic silty sand layer of permeability 1 m/day, underlaid by an impermeable silty clay layer.

The *in situ* groundwater table is found at 2 m depth, and a dewatering system will be installed, to lower the groundwater table by 2 m underneath the pollutant source. The proposed dewatering system consists of a series of dewatering well points (spears) along the length of the pollutant source. The capacity of the pumping system is 0.4 m^3/day/m.

An outline of the numerical model used to simulate this problem is shown in Figure 2.30. As in Chapter 2.9, the silty sand is modelled as weightless linear elastic material. The compressibility parameters of the material are irrelevant, as only a steady state flow analysis is performed. The silty clay layer is not modelled explicitly, instead flow is not permitted from the bottom of the model, to simulate the existence of that

impermeable layer. The sheet pile walls are not explicitly modelled either, instead interfaces with zero cross permeability along their 6 m length are introduced to simulate containment of the pollutant zone by means of driving of sheet piles walls.

The dewatering spears are simulated by vertical one-dimensional "well" elements, extending from the elevation of the *in situ* groundwater table (-2 m) to the target phreatic line beneath the pollutant source (-4 m). The well elements require two input parameters. The first is their capacity, in m^3/day per unit length of the pollutant source along which the line of spears is to be installed. In this example we set the capacity to be 0.4 m^3/day/m, and we will explore whether this capacity is sufficient to lower the groundwater table to the target phreatic line elevation. The second parameter is the elevation h_{min}, which is the minimum depth where the pumps extract water from. This is set to be equal to the target phreatic line elevation, which means that water will be pumped from the spears if the water level is at 4 m or above. The lateral boundaries of the model are placed at sufficient distance from the area of interest, so that the existence of the free flow boundary conditions there will not affect the results of the simulation (see Chapter 2.9).

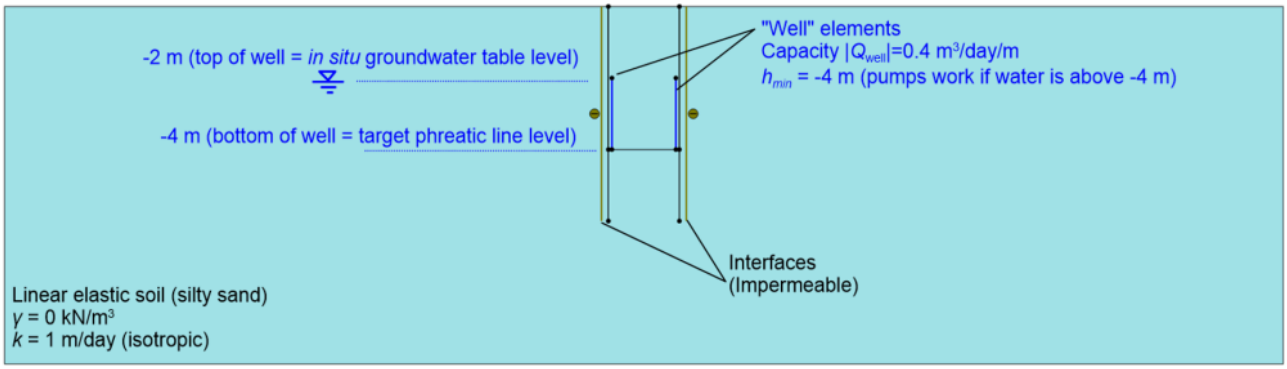

Figure 2.30. Outline of the Finite Element model.

As in Chapter 2.9, the analysis consists of two steady-state groundwater flow-only phases: During the initial phase we define the *in situ* groundwater table level and the flow conditions at the boundary (Figure 2.31a), and the software calculates the initial pore pressure profile. During the pumping phase we activate the wells and the interfaces (Figure 2.31b) while leaving the flow boundary conditions and the global water table level unchanged. Again, the phreatic line shown in Figure 2.31b is not the final but rather the target one. The final one will result from the calculation. Note that the model cluster between the interfaces is not deactivated here, as no soil is excavated.

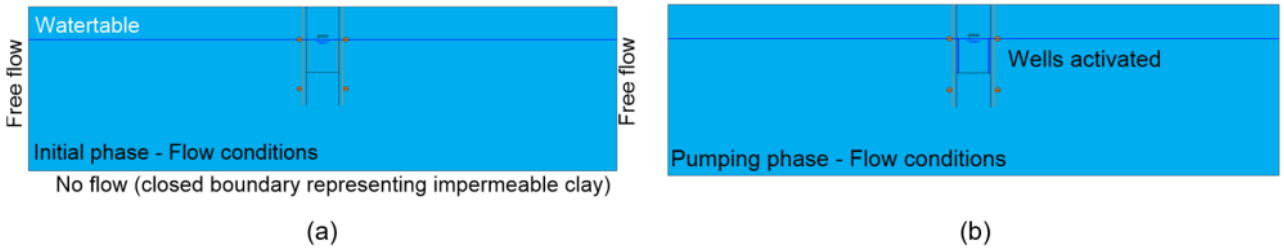

Figure 2.31. (a) Initial flow conditions, (b) Pumping phase flow conditions.

Key outcomes of this analysis are presented in Figure 2.33. Pore pressure contours are plotted together with the phreatic line resulting from steady-state pumping through the spears in Figure 2.32a. Inspection of the phreatic line underneath the contaminant source suggests that the capacity of the pumps is sufficient to achieve the desired lowering of the groundwater table. The predicted phreatic line level is of course sensitive to the distance between the sheet piles walls (or the wells). As in Chapter 2.9, positive pore pressures indicating suction are calculated above the phreatic line.

Finally, groundwater flow vectors are presented together with the finite element mesh in Figure 2.32b. Unlike Chapter 2.9, the maximum groundwater flow vectors are not observed at the toe of the sheet pile

walls (Figure 2.28), but rather at the bottom of the wells, where potential seepage failure will develop in this case. The magnitude of the groundwater flow depends again on the length of the impermeable sheet piles, and will be reduced if the sheet piles are embedded in larger depth.

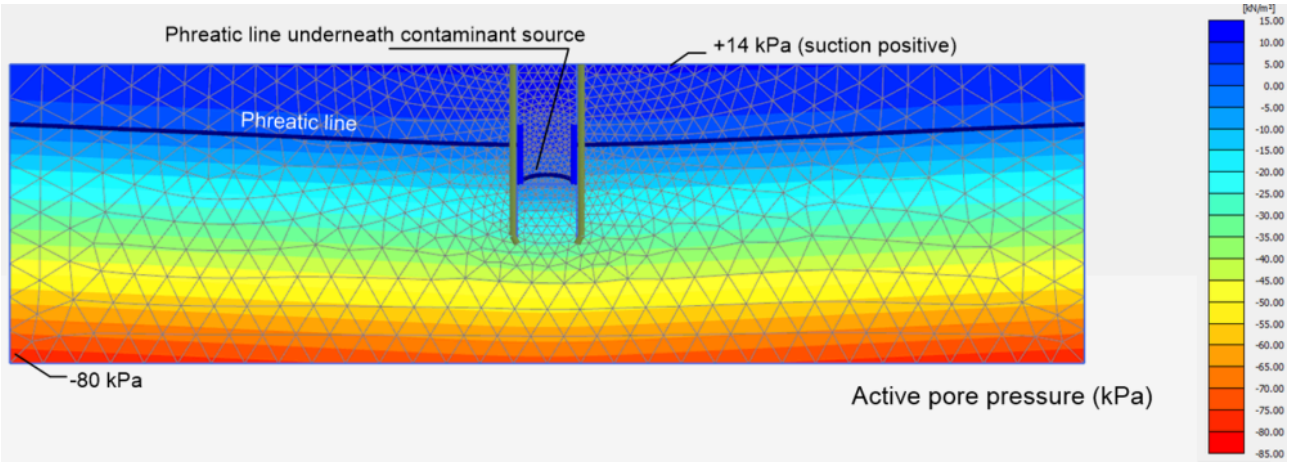

Figure 2.32a. Analysis results: Pore pressure contours and computed phreatic line.

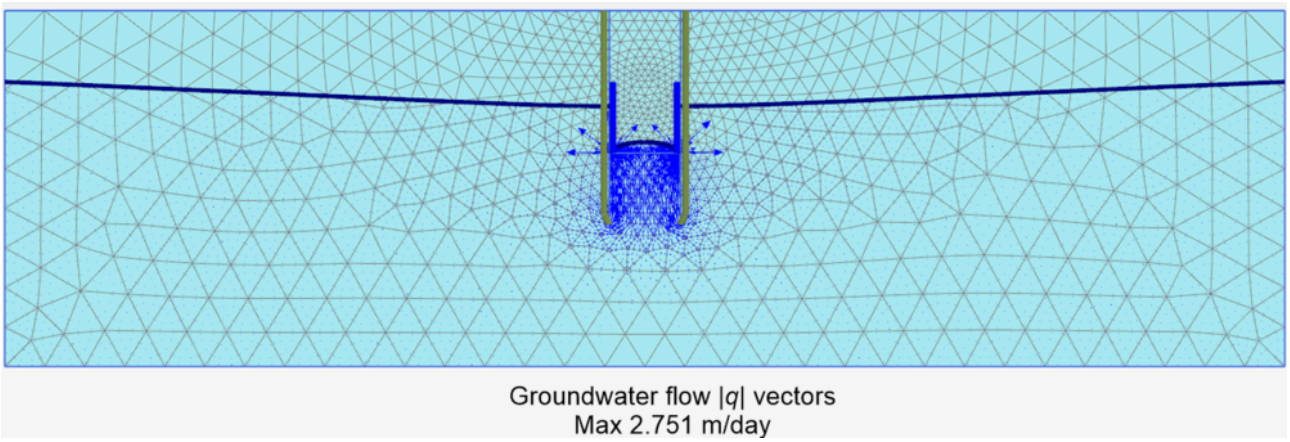

Figure 2.32b. Analysis results: Groundwater flow vectors.

2.11 REFERENCES

1. Canadian Council of Ministers of the Environment CCME (1994). Subsurface assessment handbook for contaminated sites. Report CCME EPC-NCSRP-48E, March 1994.
2. EnHealth Council (2001). Health-based soil investigation levels. Canberra, A.C.T.
3. Federal Highway Administration FHWA (2002). Subsurface Investigations. Geotechnical Site Characterization, Publication No. FHWA NHI-01-031, US Department of Transportation, May 2002.
4. Mohamed AMO and Antia HE (1998) Geoenvironmental Engineering. Elsevier Science BV.

3. STRESSES IN SOIL FROM EXTERNAL LOADINGS

3.1 INTRODUCTION TO PART 3

Consider the following practical problem: Two storage tanks are going to be founded on a layer of stiff saturated clay. Due to restrictions related to the cost of land, the Geotechnical Engineer is called to find the minimum distance that the silos can be placed apart. Keep in mind that when two foundations are placed too close to each other, stresses imposed to the soil will overlap, with (sometimes) detrimental consequences (Figure 3.1a). In order to provide an answer to the above practical question, we must find a way to calculate the magnitude of stresses that a foundation imposes in soil, and its area of influence i.e., the area where these additional stresses are significant.

Stress distribution in soil due to external loadings can be determined analytically, while considering a simplified geometry of the foundation (Figure 3.1b), and the soil to be a homogeneous, isotropic and *linear elastic* material.

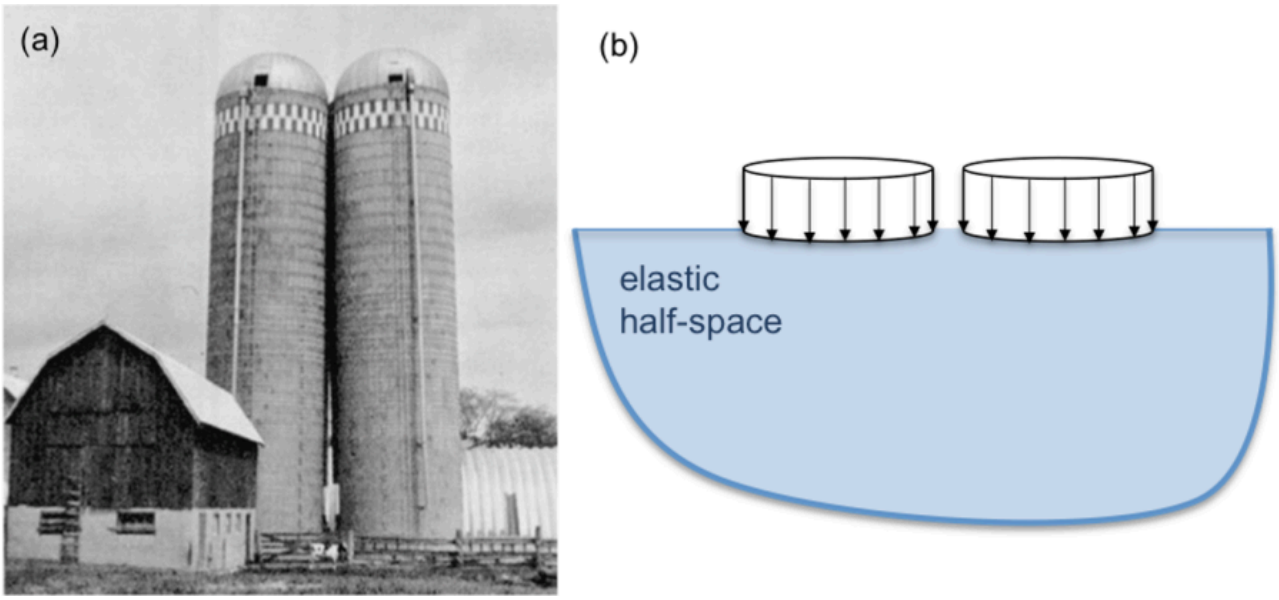

Figure 3.1. (a) The "kissing" silos (Bozozuk 1976, Canadian Government copyright – reproduced with permission), and (b) Equivalent idealised problem.

But unquestionably soil is not an elastic material. So why do we use linear elasticity theory to calculate stresses? There are three main reasons for that:

1. There are practical cases where soil actually behaves "elastically". For example, settlement of a foundation is estimated while considering the working load *(serviceability conditions),* which should be a fraction of the collapse load. For settlement to remain within the tolerable limits, soil should remain effectively in the elastic region (Figure 3.2).

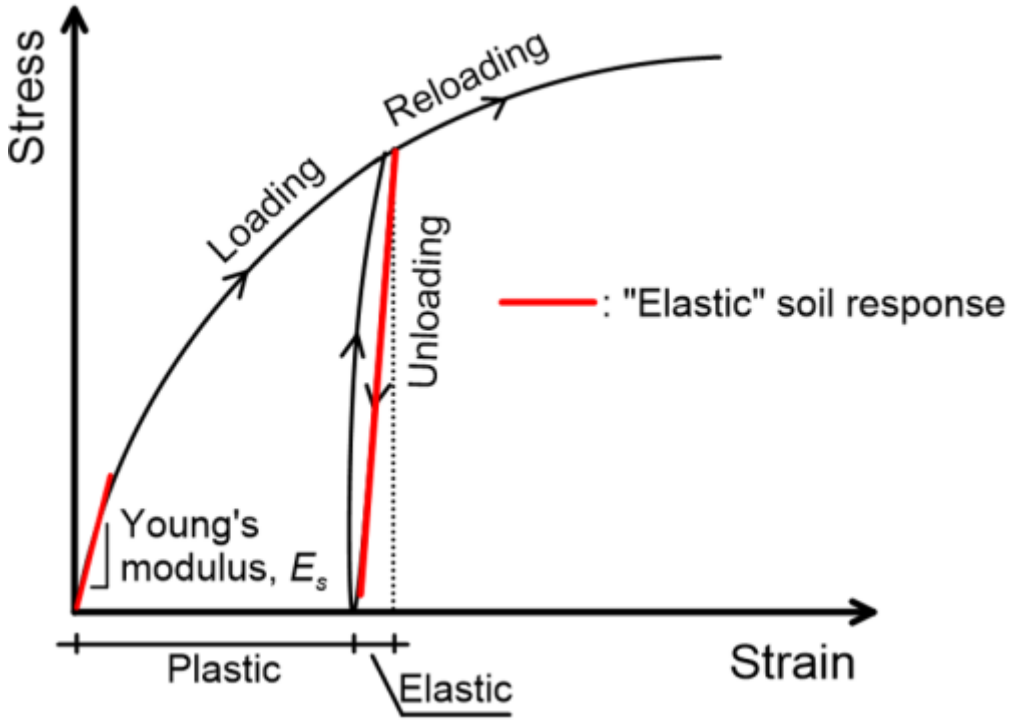

Figure 3.2. Elastic response of soils during loading and unloading.

2. Calculation of stresses *(but not strains)* is not particularly sensitive to material properties. For example, consider the uniaxially loaded sample made of any material (not necessarily soil) depicted in Figure 3.3. The axial stress σ_z will depend on the magnitude of the load Q and the area of the sample A, and is independent of the material properties. However, the axial and lateral strains ε_z and ε_x respectively, will depend on the material properties, namely the Young's modulus E_s and the Poisson's ratio, v_s.

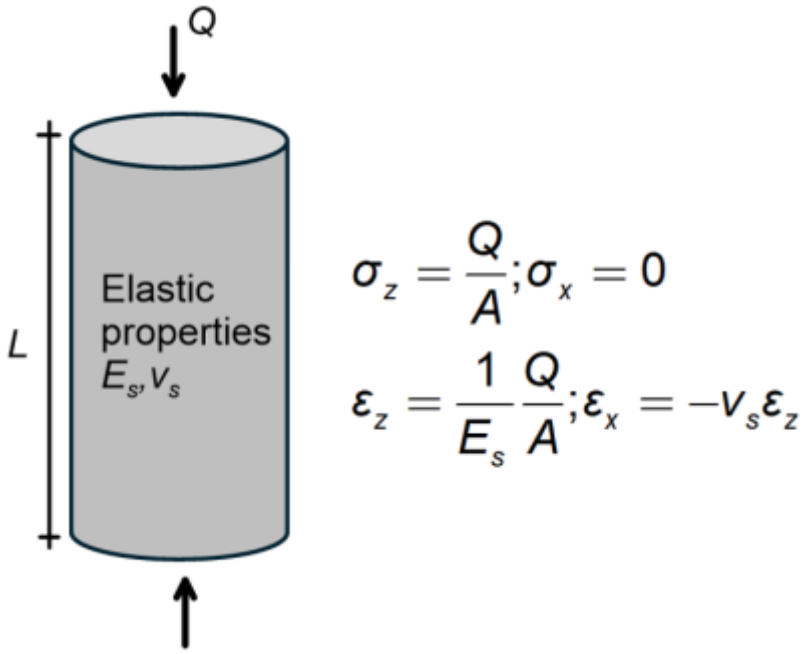

Figure 3.3. Calculation of stresses and strains in an uniaxially loaded material sample.

3. Simplicity. Considering soil to be a linear elastic material implies that only two (independent) soil

parameters, determined via soil testing, will be involved in the calculations: the soil's Young's modulus E_s and its Poisson ratio ν_s. On top of that, Poisson's ratio is not particularly sensitive to the type of soil, and ranges between ν_s = 0.2 to 0.5.

Based on the above, we can use analytical, closed-form solutions and charts to determine the distribution of stresses in soil, which are much easier and straightforward to apply compared to e.g., numerical analyses. Formulas for simple, characteristic load and pressure distributions are presented in the following chapters, considering idealised two-dimensional *axisymmetric* and *plane-strain* symmetry conditions.

It is reminded here that *plane-strain* symmetry corresponds to loading and geometry conditions where the out-of-plane dimension of the structure under consideration is large compared to the dimensions of its cross-section (Figure 3.4a), thus we can assume that the out-of-plane displacement and strain are both equal to zero.

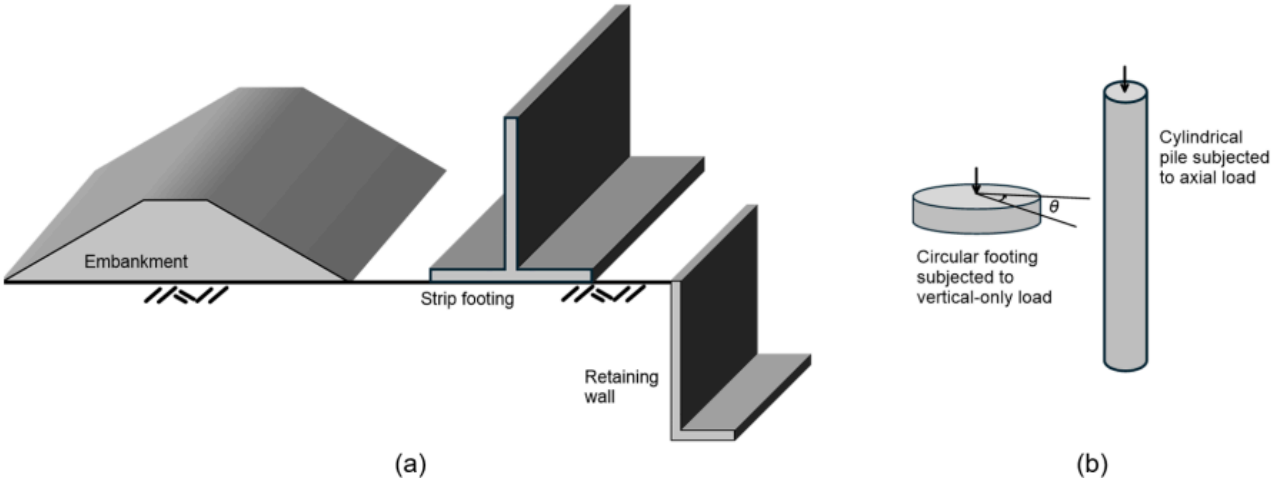

Figure 3.4. (a) Plane-strain, and (b) Axisymmetric loadings and geometries.

A two-dimensional plane-strain model may be used to simulate a continuous strip footing, a pipeline, a retaining wall or an embankment.

Axisymmetric conditions on the other hand correspond to cases of rotational symmetry about the vertical axis of the problem, where the radial displacement in cylindrical coordinates is zero $u_\theta = 0$ (Figure 3.4b). A two-dimensional axisymmetric model may be used to simulate a circular footing subjected to uniform vertical force, a pile subjected to a compressive or tensile vertical force, or a triaxially loaded soil sample. Keep in mind that both geometry and loading symmetry must co-exist e.g., the case of a laterally loaded pile or a horizontal force applied on a circular footing are rather three-dimensional problems, as contrary to the geometry, the loading is not symmetric.

In the following Chapters, we will use the term *load* to describe external forces (Q_{ext}) acting on soil, and the term *pressure* to describe external pressures (q_{ext}) acting on soil. *Loading(s)* is a general term, referring to both forces and pressures.

3.2 STRESSES IN THE SOIL DUE TO A POINT LOAD

Load transferred to the soil from e.g., the foundation of an electric power pole can be simulated as a point load Q_{ext} acting on the surface of a homogeneous elastic half-space (Figure 3.5). As both load and geometry are axisymmetric, additional soil stresses due to the application of the load can be calculated as:

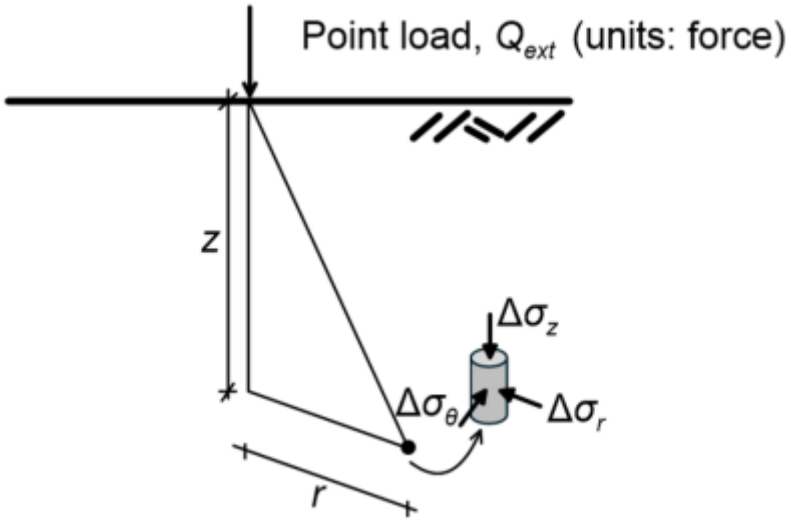

Figure 3.5. Stresses due to point load acting on the surface of a homogeneous elastic half-space.

(3.1) $$\Delta\sigma_z = \frac{3Q_{ext}}{2\pi z^2\left[1+\left(\frac{r}{z}\right)^2\right]^{\frac{5}{2}}}$$

(3.2) $$\Delta\sigma_r = \frac{Q_{ext}}{2\pi}\left(\frac{3r^2z}{(r^2+z^2)^{\frac{5}{2}}} - \frac{(1-2\nu_s)}{r^2+z^2+z(r^2+z^2)^{\frac{1}{2}}}\right)$$

(3.3) $$\Delta\sigma_\theta = \frac{Q_{ext}}{2\pi}(1-2\nu_s)\left(\frac{z}{(r^2+z^2)^{\frac{3}{2}}} - \frac{1}{r^2+z^2+z(r^2+z^2)^{\frac{1}{2}}}\right)$$

(3.4) $$\Delta\tau_{rz} = \frac{3Q_{ext}}{2\pi}\left(\frac{rz^2}{(r^2+z^2)^{\frac{5}{2}}}\right)$$

The above expressions provide the *stress increments* $\Delta\sigma$ due to the application of the point load, which should be added to existing geostatic stresses to find the total stress in the soil. In Eqs. 3.1 to 3.4 v_s is the Poisson ratio of the soil, while the corresponding stress components $\Delta\sigma_z$, $\Delta\sigma_r$, $\Delta\sigma_\theta$ and $\Delta\tau_{rz}$ and the vertical z and radial r distance from the point load are defined in Figure 3.5.

3.3 STRESSES IN THE SOIL DUE TO A LINE LOAD

Loading transferred to the soil from e.g., a rail track of limited width (Figure 3.6) can be modelled as an "infinitely long" line load acting on the surface of a homogeneous elastic half-space. As plane-strain symmetry conditions apply, additional soil stresses due to the application of a line load can be calculated as:

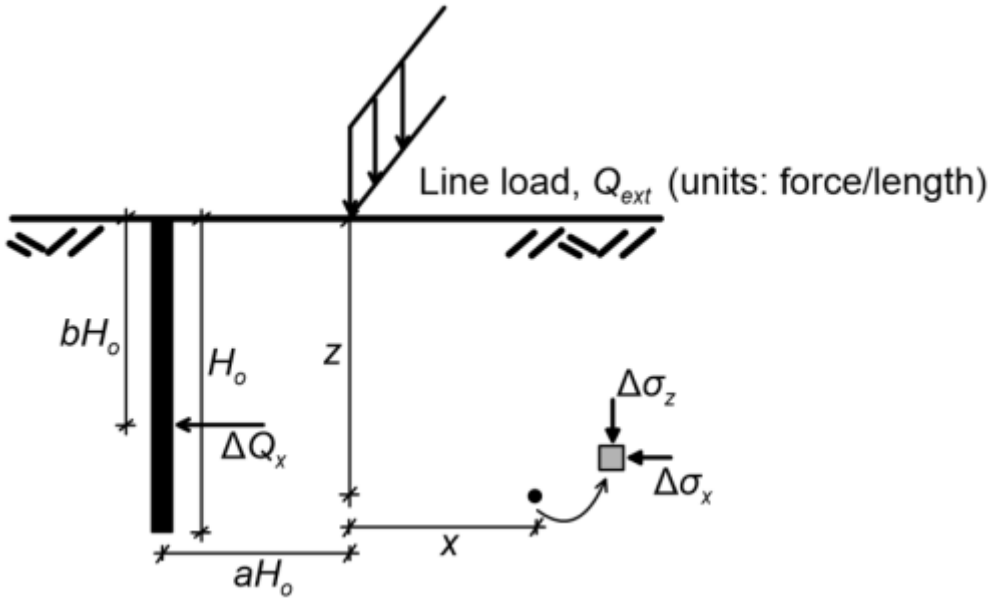

Figure 3.6. Stresses due to line load acting on the surface of a homogeneous elastic half-space (right), and in the vicinity of a retaining wall (left). Line loads carry units of force per running meter.

$$\textbf{(3.5)}\ \Delta\sigma_z = \frac{2Q_{ext}z^3}{\pi(x^2+z^2)^2}$$

$$\textbf{(3.6)}\ \Delta\sigma_x = \frac{2Q_{ext}x^2z}{\pi(x^2+z^2)^2}$$

$$\textbf{(3.7)}\ \Delta\tau_{zx} = \frac{2Q_{ext}xz^2}{\pi(x^2+z^2)^2}$$

The stress increment components and the vertical z and horizontal x distance from the line load considered in Eqs. 3.5 to 3.7 are defined in Figure 3.6.

In the special case where the line load is acting near the crest of a retaining wall, the horizontal stress distribution along the wall height can be determined as function of the height of the wall H_o (Figure 3.6):

$$\textbf{(3.8)}\ \Delta\sigma_x = \frac{4Q_{ext}a^2b}{\pi H_o(a^2+b^2)^2}$$

and the resultant horizontal force per running meter of the wall is equal to (Figure 3.6):

$$\textbf{(3.9)}\ \Delta Q_x = \frac{2Q_{ext}}{\pi\left(a^2+1\right)}$$

Note that Eq. 3.8 yields identical results to Eq. 3.5, the only difference between these expressions is that in Eq. 3.8 the coordinates x and z as expressed as function of H_o.

3.4 STRESSES IN THE SOIL DUE TO A STRIP PRESSURE

Stresses applied on the soil surface e.g., from a footing of "infinite" length can be modelled as an infinitely long (strip) pressure acting on the surface of a homogeneous elastic half-space (Figure 3.7a). As plane-strain symmetry conditions apply, additional stresses due to the application of the pressure q_{ext} can be calculated as:

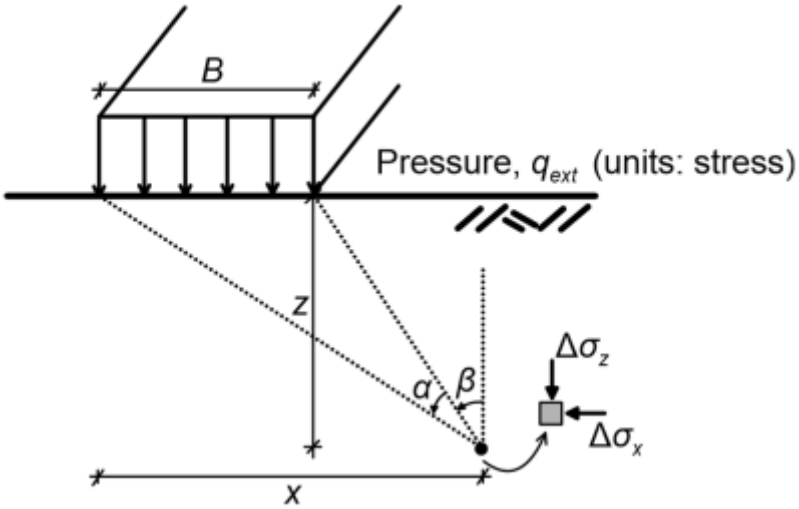

Figure 3.7a. Stresses due to strip pressure acting on the surface of a homogeneous elastic half-space.

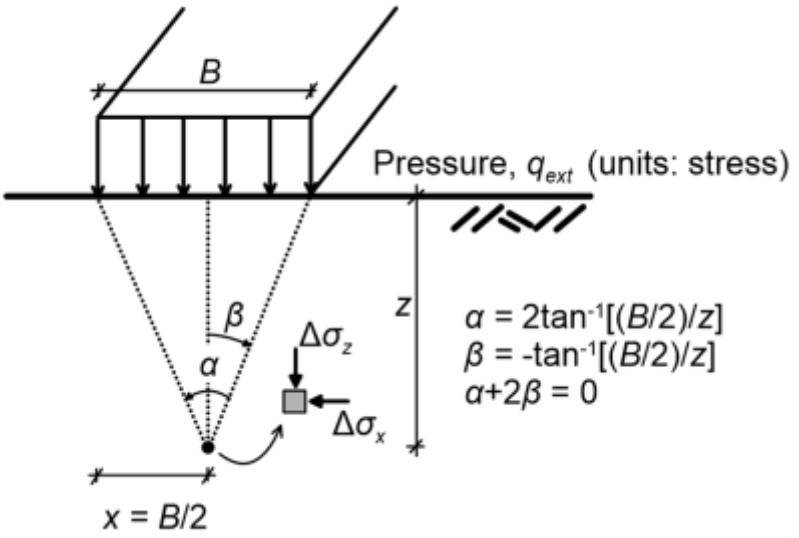

Figure 3.7b. Values of angles α and β in the special case where stresses are estimated below the axis of the strip pressure.

(3.10) $$\Delta\sigma_z = \frac{q_{ext}}{\pi}\left[\alpha + \sin\alpha\cos\left(\alpha + 2\beta\right)\right]$$

(3.11) $$\Delta\sigma_x = \frac{q_{ext}}{\pi}\left[\alpha - \sin\alpha\cos\left(\alpha + 2\beta\right)\right]$$

(3.12) $$\Delta\tau_{zx} = \frac{q_{ext}}{\pi}\left[\sin\alpha\sin\left(\alpha + 2\beta\right)\right]$$

The stress increment components and angles α and β are defined in Figure 3.6a. Angles α and β must be input in Eqs. 3.10 to 3.12 in radians, not in degrees, and may attain negative values too, as shown in Figure 3.7b.

3.5 STRESSES IN THE SOIL DUE TO A CIRCULAR PRESSURE

Stresses transferred to the soil from a circular footing such as e.g., the foundation of a tank or a silo, can be modelled as a circular pressure acting on the surface of a homogeneous elastic half-space (Figure 3.8). Considering a uniform vertical pressure, where both loading and geometry are axisymmetric, stress increments due to the application of the pressure q_{ext} *below the axis of the applied pressure* can be calculated as:

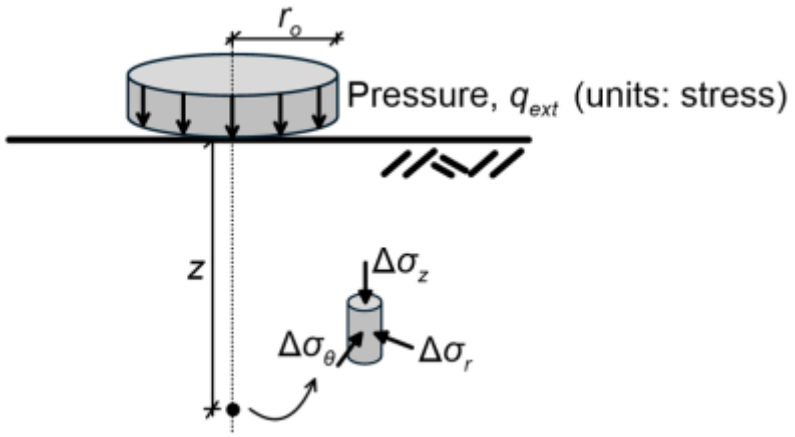

Figure 3.8. Stresses under the centre of circular pressure acting on the surface of a homogeneous elastic half-space.

$$\textbf{(3.13)}\ \Delta\sigma_z = q_{ext}\left[1-\left(\frac{1}{1+\left(\frac{r_o}{z}\right)^2}\right)^{\frac{3}{2}}\right]$$

$$\textbf{(3.14)}\ \Delta\sigma_r = \Delta\sigma_\theta = \frac{q_{ext}}{2}\left[(1+2\nu_s)-\frac{4\,(1+\nu)}{\left[1+\left(\frac{r_o}{z}\right)^2\right]^{\frac{1}{2}}}+\frac{1}{\left[1+\left(\frac{r_o}{z}\right)^2\right]^{\frac{3}{2}}}\right]$$

In Eqs. 3.13 and 3.14 v_s is the soil's Poisson ratio, r_o is the radius of the area where pressure is applied, while the corresponding stress increment components $\Delta\sigma_z$, $\Delta\sigma_r$ and $\Delta\sigma_\theta$ are defined in Figure 3.8.

3.6 STRESSES IN THE SOIL DUE TO A RECTANGULAR PRESSURE

The common case of a rectangular footing transferring vertical loads from the structure to the soil is neither a plane-strain nor an axisymmetric problem, as the ones discussed above (Figure 3.9). Therefore, finding the exact distribution of additional stresses with depth resulting from a rectangular pressure acting on the surface of a homogeneous elastic half-space requires some perhaps cumbersome mathematical manipulations.

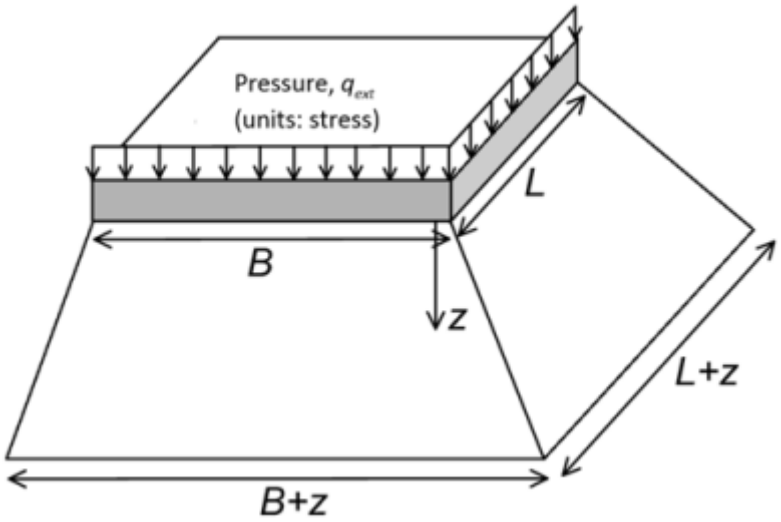

Figure 3.9. Rectangular pressure acting on the surface of a homogeneous elastic half-space.

If we assume 2:1 distribution of stresses in the half-space (Figure 3.9) we can obtain an approximation of the additional vertical stress $\Delta\sigma_z$ at any depth z, as:

$$\textbf{(3.15)}\quad \Delta\sigma_z = \frac{q_{ext} B L}{(B+z)(L+z)}$$

The above Eq. 3.15, albeit approximate, will provide reasonably accurate results for depths $z > B$.

Vertical stress increments under the corner of a rectangular pressure can be calculated using the so-called Fadum charts. Such a chart providing the factor $I_{qr} = \Delta\sigma_z/q_{ext}$ is presented in Figure 3.10. The use of this chart for calculating vertical stresses for geometries other than that illustrated in Figure 3.10 is discussed later in Chapter 3.7.

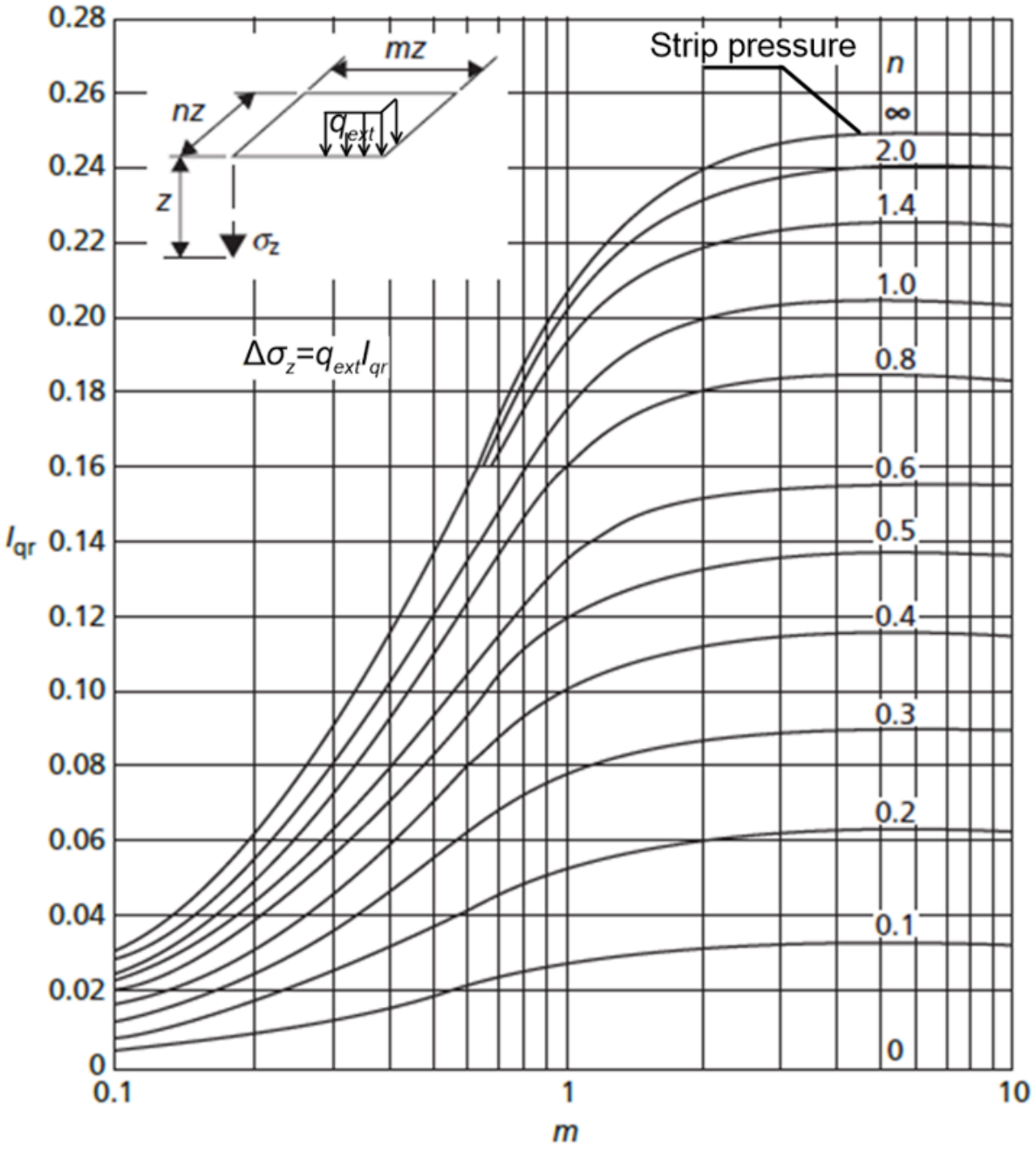

Figure 3.10. Values of influence factor I_{qr} to calculate vertical stress increments underneath the edge of a rectangular area of dimensions *nz* x *mz* on which a vertical pressure q_{ext} is applied (after Fadum 1948).

3.7 DISCUSSION

While applying the expressions presented in the above paragraphs, one should keep in mind that stress increments due to external loadings are *total* stresses, and initially will be resisted by both the pore water pressure and the soil skeleton. As discussed in Part 4, settlement in soils is due to *effective* stress changes only.

Application of these solutions can be extended to treat more complex loadings, under specific conditions: The Saint-Venant principle (1855) suggests that *"the difference between the effects of two dissimilar but statically equivalent loadings becomes very small at sufficiently large distances from the loading"*. Consider for example the different stress distributions presented in Figure 3.11, and assume we are interested in estimating soil stresses at a depth equal to about the diameter of the loaded area $2r_0$ (Figure 3.11). From that depth and below, stresses in soil depend on the magnitude of the resultant of the loading, and not on its distribution. In other words, in certain cases we can use elasticity theory expressions even if the actual distribution of the loading is not the same as the idealised uniform distribution, provided that the resultant is the same.

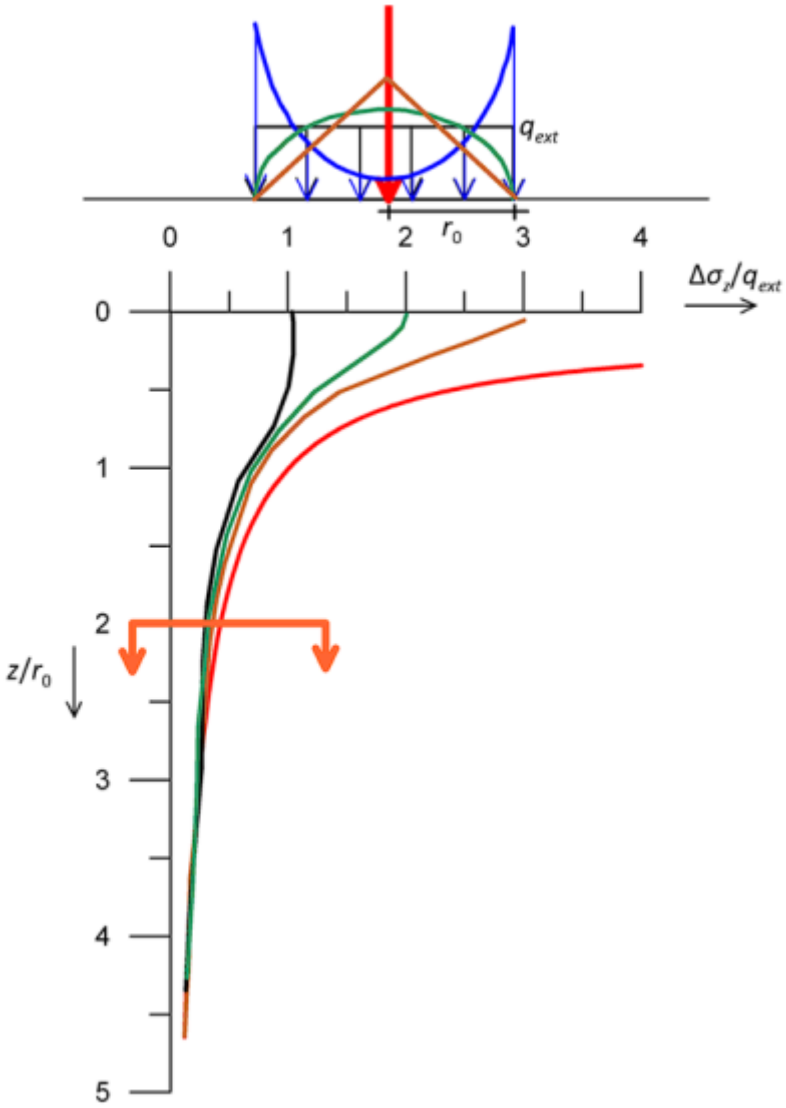

Figure 3.11. Vertical increment stress distribution below the axis of a circular area where different pressure distributions of equal resultant are applied.

The expressions provided in the previous paragraphs for the calculation of vertical stress increments with depth due to various loading types can be applied for the determination of the *influence depth* of the loading, defined as the depth where additional vertical stress $\Delta\sigma_z$ is reduced to 10% of the mean stress applied on the soil surface ($\Delta\sigma_z/q_{ext} = 0.1$).

Plotting the distribution of the additional normalised (against the pressure applied on the surface q_{ext}) stress with depth below the axis of symmetry of a circular area, and of a strip pressure with equivalent width (Figure 3.12a), we determine the influence depth to be:

(3.16) $$\left(\frac{z}{r_0}\right)_{\frac{\Delta\sigma_z}{q_{ext}}=0.1} = 4$$ for uniform pressure on a circular area of radius r_0

(3.17) $$\left(\frac{z}{r_0}\right)_{\frac{\Delta\sigma_z}{q_{ext}}=0.1} = 13$$ for strip pressure of width $B = 2r_0$

Similarly, plotting in Figure 3.12b the distribution of the additional normalised vertical stress with depth below the axis ($r = 0$, Figure 3.5) of a point load, provided from the expression:

(3.18) $$\Delta\sigma_z\,(r=0)=\frac{3}{2}\frac{Q_{ext}}{\pi}\frac{1}{z^2}$$

and below the axis (x = 0, Figure 3.6) of a line load, provided from the expression:

(3.19) $$\Delta\sigma_z\,(x=0)=\frac{2Q_{ext}}{\pi}\frac{1}{z}$$

we determine the influence depth to be 2 m for the point load, and 6.5 m for the line load.

The above findings may prove to be very useful for the preparation of a finite element model, for determining the extent of the geometry that must be simulated to accurately consider the effects of an external loading.

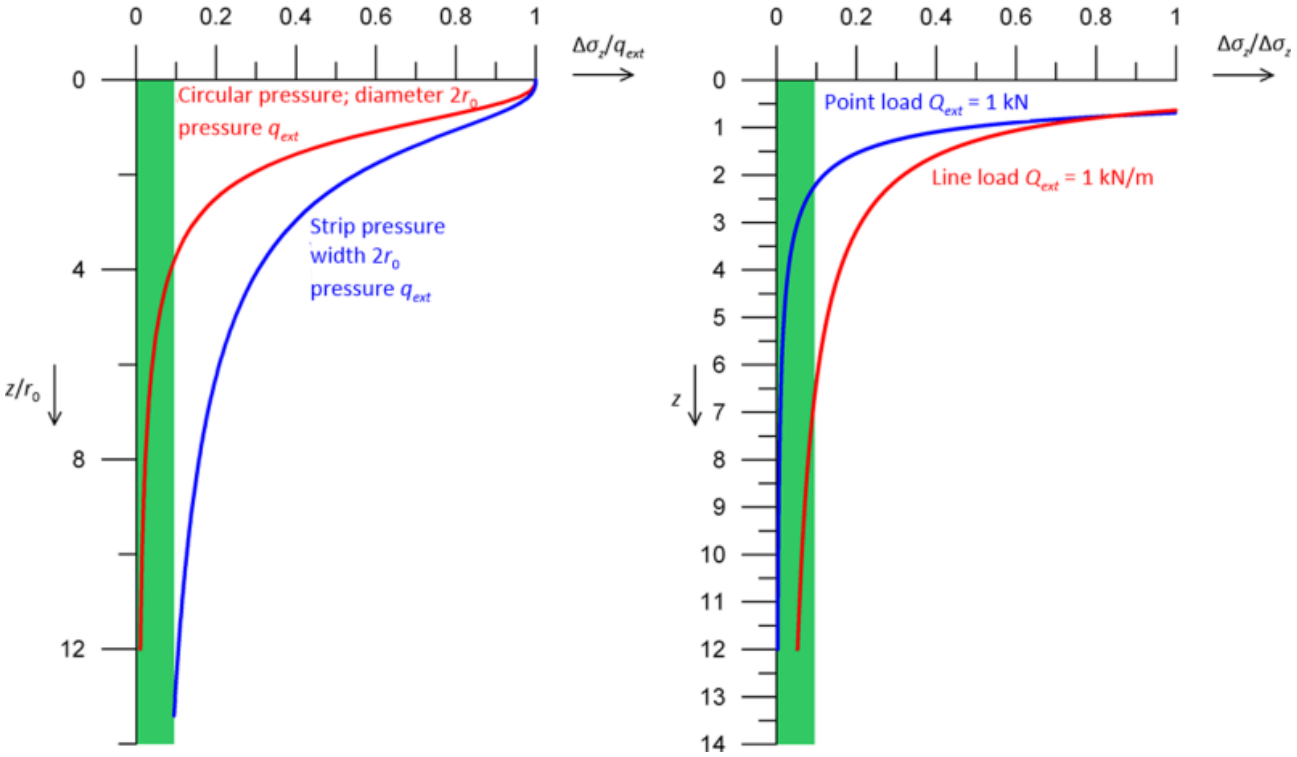

Figure 3.12. Vertical stress increment distribution below the axis of (left) a circular and a strip pressure of equal width, and (right) a point load and a line load of equivalent magnitude.

Another advantage arising from the consideration of the soil as a linear elastic material is that the *principle of superposition* applies. This suggests that stress increments due to multiple loadings acting simultaneously can be calculated as the sum of stress increments due to each one of the loads or pressures considered separately as (Figure 3.13):

(3.20) $$\Delta\sigma_z\,(Q_{ext}+q_{ext,1}+q_{ext,2})=\Delta\sigma_z\,(Q_{ext})+\Delta\sigma_z\,(q_{ext,1})+\Delta\sigma_z\,(q_{ext,2})$$

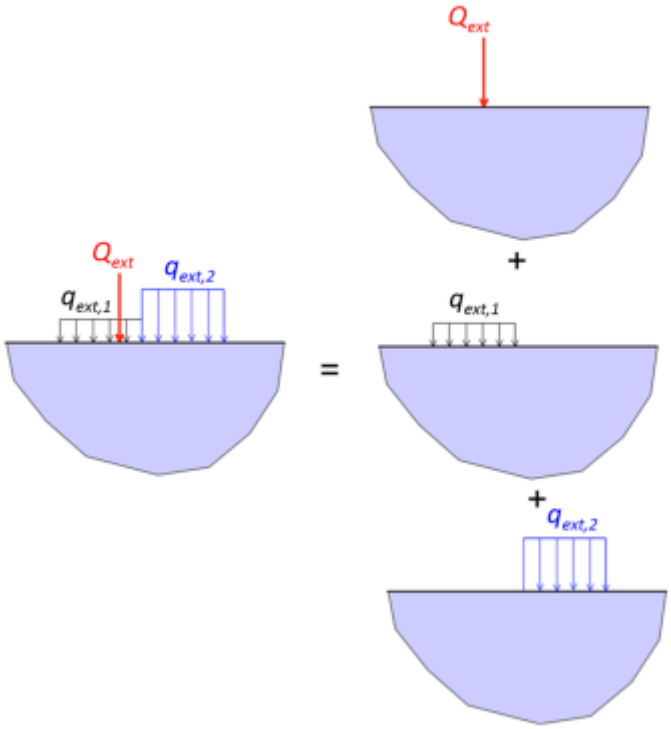

Figure 3.13. Estimation of total stress increments due to multiple loads and pressures acting simultaneously, by applying the principle of superposition.

Stresses resulting from other, more complex loading distributions can be also calculated, if "negative", tensile loadings are considered together with compressive loadings (Figure 3.14). This concept is demonstrated in Example 3.1.

(3.21) $\Delta\sigma_z\left(q_{ext}\right) = \Delta\sigma_z\left(q_{ext,1}\right) - \Delta\sigma_z\left(q_{ext,2}\right)$

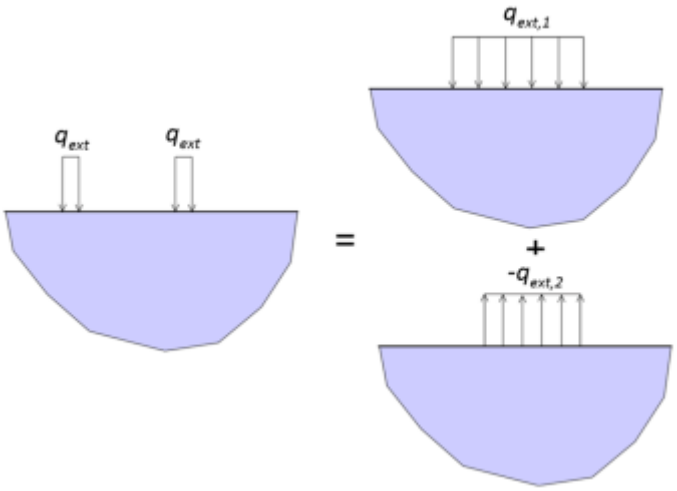

Figure 3.14. Estimation of stress increments due to complex pressure distributions, by taking advantage of the principle of superposition.

Figure 3.10 also can be used in tandem with the principle of superposition to obtain vertical stress increments underneath complex pressure distributions. For example, Figure 3.15a demonstrates how we can calculate vertical stress increments underneath point A, located midway from two rectangular areas

of dimensions $H \times B$ separated by distance Y on which pressure q_{ext} is applied e.g., underneath the tracks of a piling rig. The vertical stress increment at any depth at point A due to the two rectangular pressures shown in Figure 3.15a is equal to four (4) times the vertical stress increment at the edge of a rectangular pressure q_{ext} of dimensions $(Y/2+H) \times B/2$ *minus* four (4) times the vertical stress increment at the edge of a rectangular pressure q_{ext} of dimensions $(Y/2+H/2) \times B/2$. Vertical stress increments at the edge of rectangular pressures are calculated directly from Figure 3.10.

Similarly, Figure 3.15b demonstrates how we can calculate vertical stress increments underneath point B, located at the centre of a rectangular area of dimensions $H \times B$ on which pressure q_{ext} is applied e.g., underneath the centre of a rectangular footing. The vertical stress increment at any depth at the centre B of a rectangular pressure q_{ext} of dimensions $H \times B$ is equal to four (4) times the vertical stress increment at the edge of a rectangular pressure q_{ext} of dimensions $Y/2 \times B/2$, calculated according to Figure 3.10.

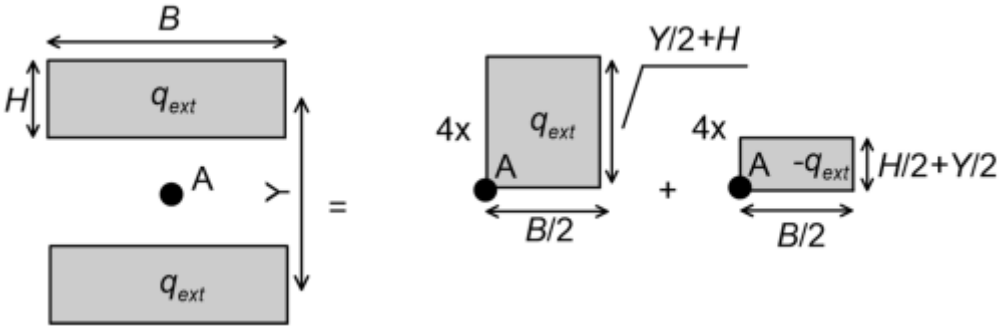

Figure 3.15a. Estimation of stress increments due to complex pressure distributions, by taking advantage of the principle of superposition and using Fadum's chart (Figure 3.10).

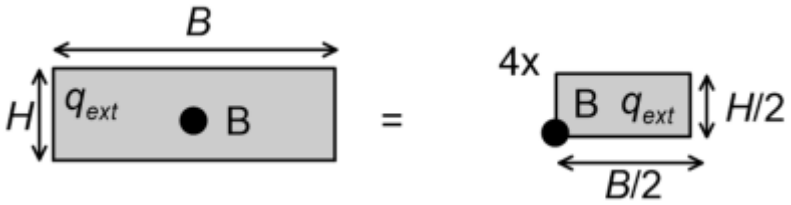

Figure 3.15b. Estimation of stress increments due to complex pressure distributions, by taking advantage of the principle of superposition and using Fadum's chart (Figure 3.10).

To end with, it should be noted that all the solutions presented above were derived for "flexible" loads and pressures, and do not account for the rigidity of the foundation. If the foundation is rigid, stress increments for the same loading on the surface would be generally lower by 15% to 30%. However, usually we do not correct stress distribution for the rigidity of the footing since, as soil non-linearity is not taken into account, we prefer the "error" to be on the conservative side.

EXAMPLE 3.1

Stresses in soil due to a water tank founded on a ring-type foundation

An H = 4 m tall water tank with radius $r_{external}$ = 5 m is going to be founded on a ring foundation, with the dimensions depicted in the following plan view. Assuming the tank is filled with water, determine the vertical stress due to the weight of the tank below the centre of the foundation, at a depth z = 5 m.

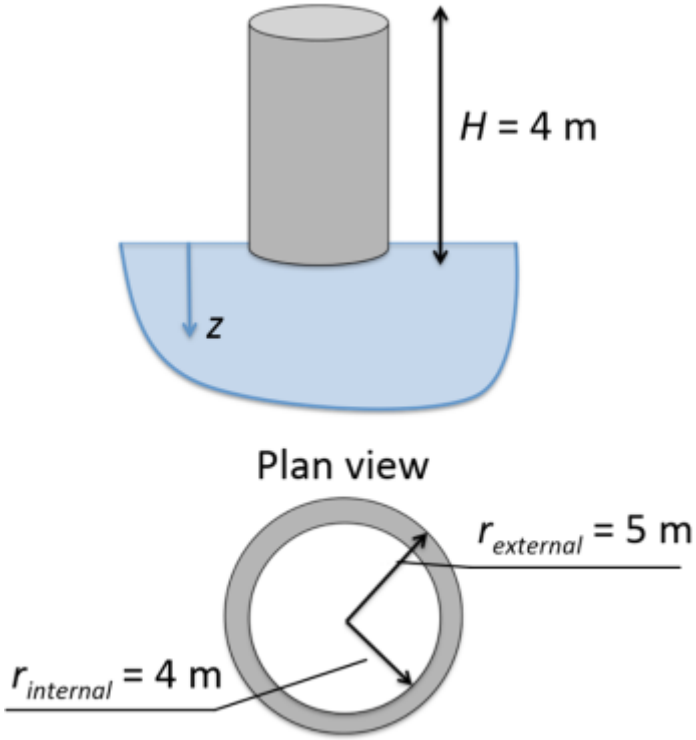

Example 3.1. Problem description and input parameters.

Answer:

First we have to determine the maximum load, Q_{ext} on the foundation, assuming that the tank is filled with water:

$A_{tank} = \pi r_{external}^2 = 78.54\ m^2$

$Q_{ext} = A \times H \times \gamma_w = 78.54\ m^2$ x 4 m x 10 kN/m^3 = 3141 kN where 10 kN/m^3 is the unit weight of water.

The area of the ring footing on which the load is applied is:

$A_{footing} = \pi r_{external}^2 - \pi r_{internal}2 = 78.54\ m^2 - 50.26\ m^2 = 28.28\ m^2$

thus the pressure applied on the ring foundation of the tank will be:

$q_{ext} = Q_{ext}/A_{footing} = 111$ kPa

Employing the principle of superposition discussed in Chapter 3.5, this ring pressure is equivalent, in terms of stresses applied to the soil, to a circular pressure $q_{\text{ext},1}$ = 111 kPa on a radius r_{external} = 5 m, plus a circular pressure $q_{\text{ext},2}$ = -111 kPa on a radius r_{internal} = 4 m (see also Figure 3.14). Negative pressure values correspond to tension. The additional vertical stress in the soil below the axis of symmetry of a circular pressure is provided by Eq. 3.13. At depth z = 5 m, the positive pressure of radius r_{external} = 5 m will result in a compressive stress:

$$\Delta\sigma_{z,ext} = q_{ext,1}\left[1-\left(\frac{1}{1+\left(\frac{r_{external}}{z}\right)^2}\right)^{\frac{3}{2}}\right] = 111\left[1-\left(\frac{1}{1+\left(\frac{5}{5}\right)^2}\right)^{\frac{3}{2}}\right] = 71.75\ \text{kPa}$$

while the negative pressure of radius r_{internal} = 4 m in a tensile stress:

$$\Delta\sigma_{z,\text{int}} = q_{ext,2}\left[1-\left(\frac{1}{1+\left(\frac{r_{\text{internal}}}{z}\right)^2}\right)^{\frac{3}{2}}\right] = -111\left[1-\left(\frac{1}{1+\left(\frac{4}{5}\right)^2}\right)^{\frac{3}{2}}\right] = -58.15\ \text{kPa}$$

The total stress increment due to the loading applied on the ring foundation is found from Eq. 3.21 as:

$$\Delta\sigma_z = \Delta\sigma_{z,ext} + \Delta\sigma_{z,\text{int}} = 13.6\ \text{kPa}$$

EXAMPLE 3.2

Numerical estimation of stresses below a ring-type foundation

Solve Example 3.1 numerically with PLAXIS, and compare the results to the analytical solution.

Answer:

The problem is simulated in PLAXIS as axisymmetric, considering soil to be a linear elastic material. To obtain a first approximation of the necessary thickness of the soil mass that must be simulated to get accurate results, one may consider Eq. 3.16 suggesting that the influence depth of a circularly loaded area is equal to four times the radius of the footing. In this case where $r_{external}$ = 5 m, we can assume that additional stresses due to the external loading will have attenuated to 10% of the stress applied on the foundation surface at a depth of 20 m, and start our simulation by modelling an area of dimensions 20 m x 20 m (Figure 3.16).

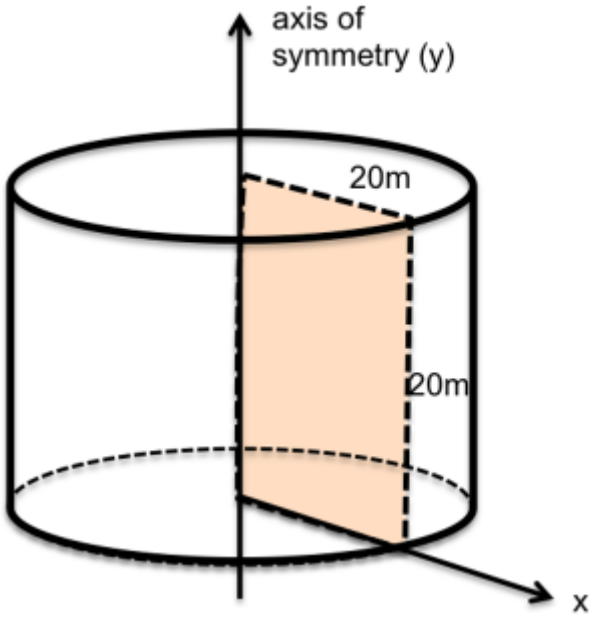

Figure 3.16. Idealised representation of the simulated axisymmetric soil geometry.

Since the problem is axisymmetric, we are simulating a "slice" of the soil, of thickness equal to 1 rad, as shown in Figure 3.17 below. The axis of symmetry of the numerical model will be the axis of symmetry of the ring foundation, passing through its centre.

The linear elastic material model is used to model soil response to the external loading. Since we are interested only in stress increments due to the external loading, the unit weight of the soil should be set equal to zero, so that geostatic stresses will not be calculated. As expected from theory (Chapter 3.5 and Eq. 3.13), the compressibility parameters that will be used as input for the linear elastic material model i.e., the Young's modulus and the Poisson's ratio should not affect the predicted magnitude and distribution of stresses. However, considering for example an unrealistically low value for the Young's modulus will result in extreme soil settlements, and perhaps affect the results due to numerical issues.

Footing pressure is applied as a vertical distributed pressure along the area of the ring footing (Figure 3.17). The footing itself is not simulated, and stress is applied directly on the soil surface, so as to be in line with the "flexible" foundation assumption inherited in the analytical formulas, as mentioned in Chapter 3.7.

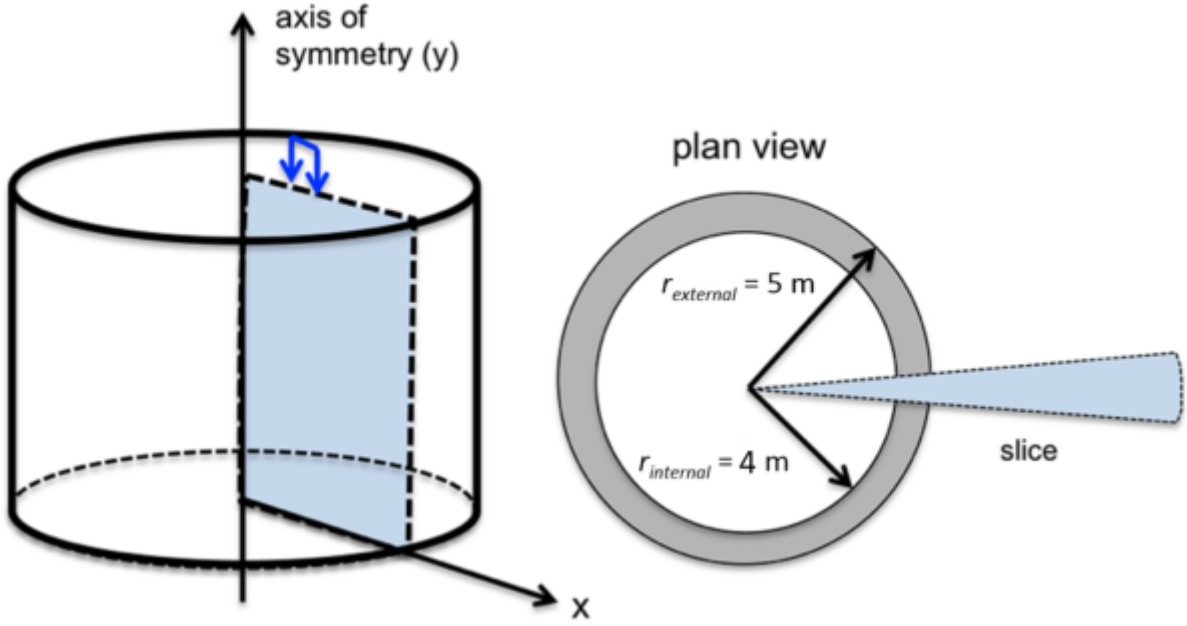

Figure 3.17. Idealised representation of the loaded area corresponding to the ring foundation.

A "coarse" mesh is defined after the application of the pressure (Figure 3.18), which should be adequate for the simulation of the elastic problem at hand, and standard fixities are applied at the boundaries of the grid. When an axisymmetric model is built in PLAXIS, standard fixities will apply the necessary zero in-plane displacement and zero in-plane rotation along the axis of symmetry defined by the center of the footing.

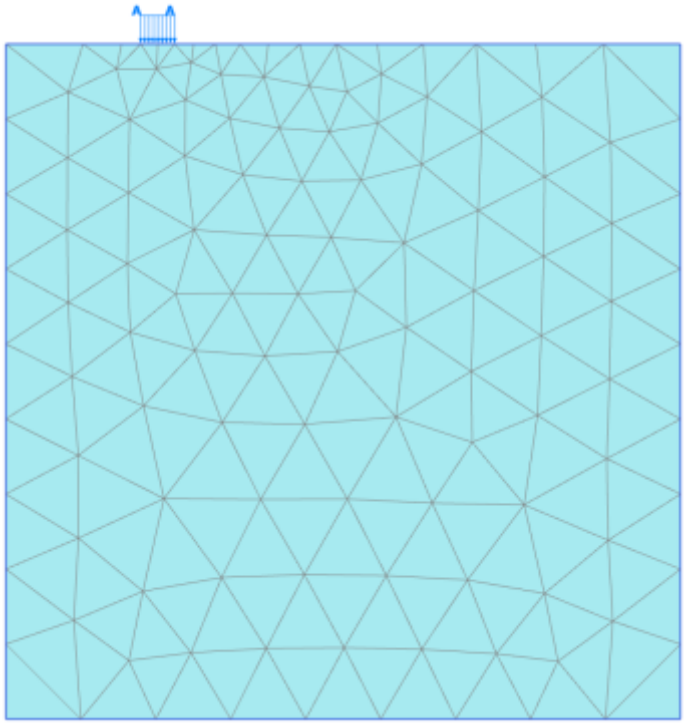

Figure 3.18. Finite element mesh and applied pressure.

The analysis is run in a single "plastic" step, whereas the initial "K_0-procedure" step should result in zero

geostatic stresses for this model, as the unit weight of the soil was assumed equal to zero. A plot of the resulting deformed mesh is presented in Figure 3.19a, and a plot of the vertical stress contours in Figure 3.19b.

Results are compared to the analytical solution in Figure 3.20, by plotting the additional vertical stress distribution with depth along the axis of the footing. Notice that the basic PLAXIS analysis (red line) compares well with analytical results (blue line), in the area of interest, where the maximum stress develops. However, the two solutions diverge at larger depths. This is expected, as the analytical solution has been derived while considering an elastic *half-space*. This assumption is not satisfied near the bottom boundary of the finite element mesh, where displacements are fixed along both the horizontal and vertical directions. An additional analysis performed for a 40-m deep model (black line) results in much better agreement with the analytical solution along the top 20 m of the axis of symmetry.

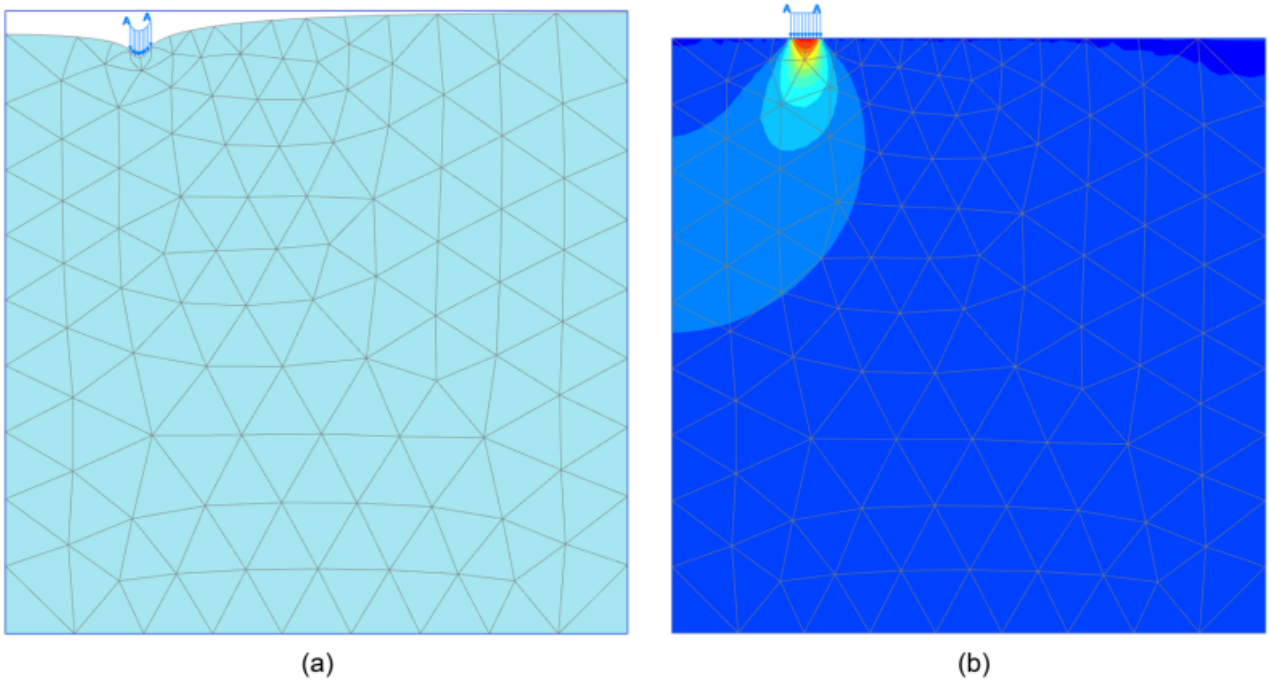

Figure 3.19. (a) Deformed mesh, and (b) vertical stress contours, $\Delta\sigma_z$.

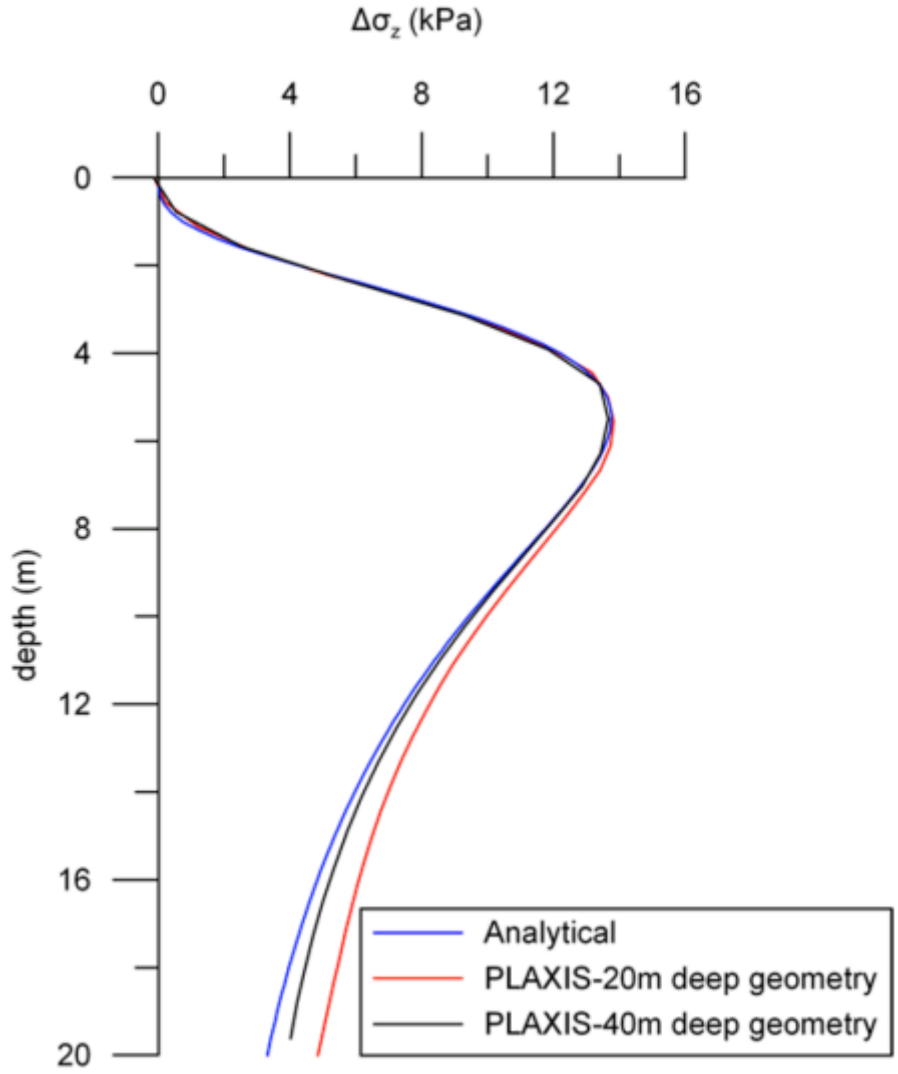

Figure 3.20. Comparison of analytical and numerical vertical stress distribution with depth, along the axis of the circular footing.

3.8 REFERENCES

1. Bozozuk M (1976). Tower silo foundations. CBD-177, Canadian Building Digest, National Research Council Canada. https://doi.org/10.4224/40000803
2. Fadum RE (1948) Influence values for estimating stresses in elastic foundations, In: Proceedings of the 2nd International Conference of SMFE, Rotterdam, Vol. 3, pp 77-84

3.9 ADDITIONAL PROBLEMS

3.9.1

You are called to verify Saint-Venant's principle on the difference between the effects of two dissimilar yet statically equivalent loadings becoming negligible at sufficiently large distances from the loading. For that, you should calculate the vertical stress increment $\Delta\sigma_z$ below the axis of an infinite strip pressure of magnitude q_{ext} = 100 kPa and width B = 2 m, and compare it with the corresponding value of $\Delta\sigma_z$ due to a *statically equivalent* line load, Q_{ext}. Try the comparison at depths z = 1 m, z = 3 m and z= 9 m from the ground surface.

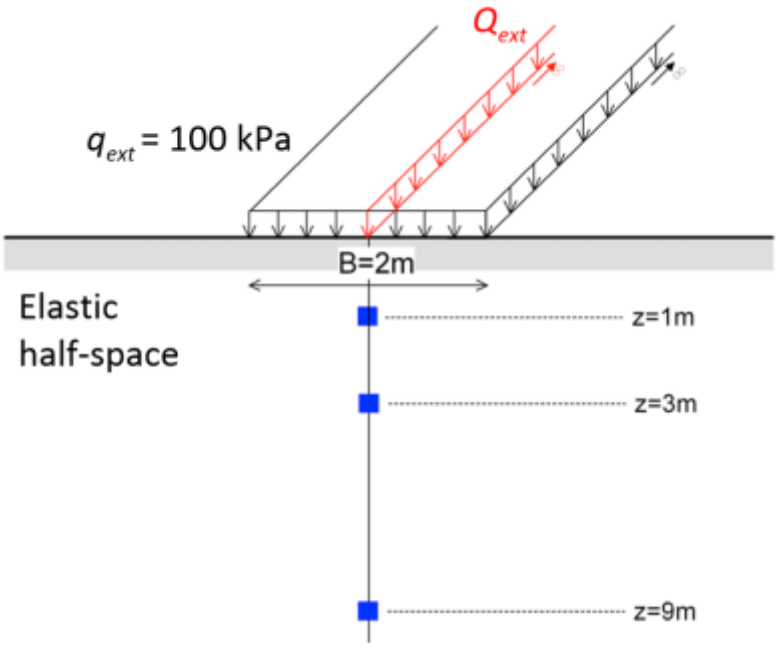

Additional problem 3.9.1. Problem description and input parameters.

Answer:

Additional problem 3.9.1 Answers

z (m)	*$\Delta\sigma_z$ (strip pressure, kPa)*	*$\Delta\sigma_z$ (line load, kPa)*	*Difference $(\Delta\sigma_{z,line}-\Delta\sigma_{z,strip})/\Delta\sigma_{z,line}$ (%)*
1.00	*81.83*	*127.32*	*55.59*
3.00	*39.58*	*42.44*	*7.22*
9.00	*14.03*	*14.15*	*0.82*

3.9.2

A line load of magnitude Q_{ext} = 100 kN/m is applied at 2 m from the crest of a 4 m-deep excavation, which is supported by a *flexible* retaining wall e.g., a sheet pile wall. Calculate the horizontal stress $\Delta\sigma_x$ due to the external load acting on the wall at z = 1 m and z = 3 m from the top of the wall. Calculate the stresses again, considering this time a *rigid* retaining wall e.g., a basement reinforced concrete wall.

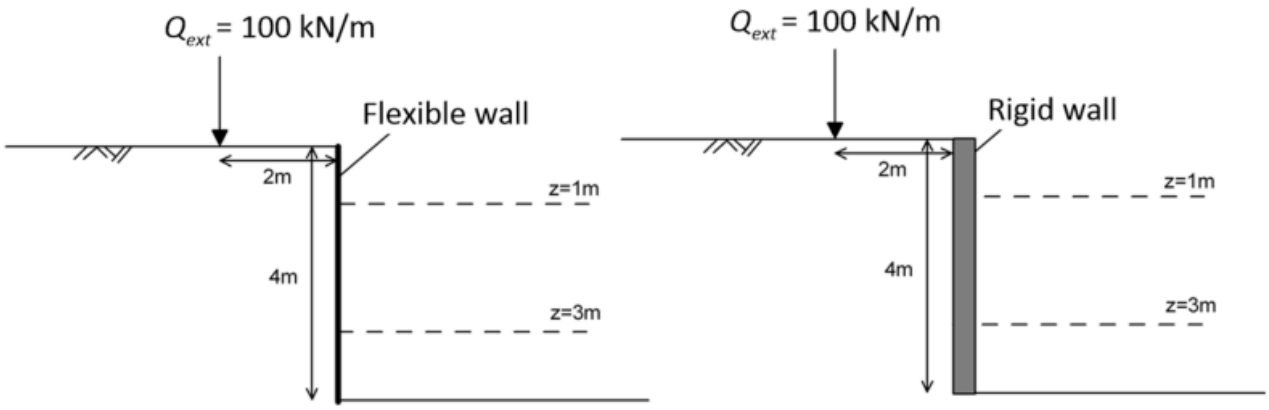

Additional problem 3.9.2. Problem description and input parameters.

Answer:

Additional problem 3.9.2 Answers

z(m)	*$\Delta\sigma_x$ (flexible wall, kPa)*	*$\Delta\sigma_x$ (rigid wall, kPa)*
1.00	*10.19*	*20.38*
3.00	*4.52*	*9.04*

3.9.3

Two alternative routes are examined for a sewage pipeline, passing below locations A and B. You are the designers of the pipeline. Which one would you prefer, and why? Justify your answer.

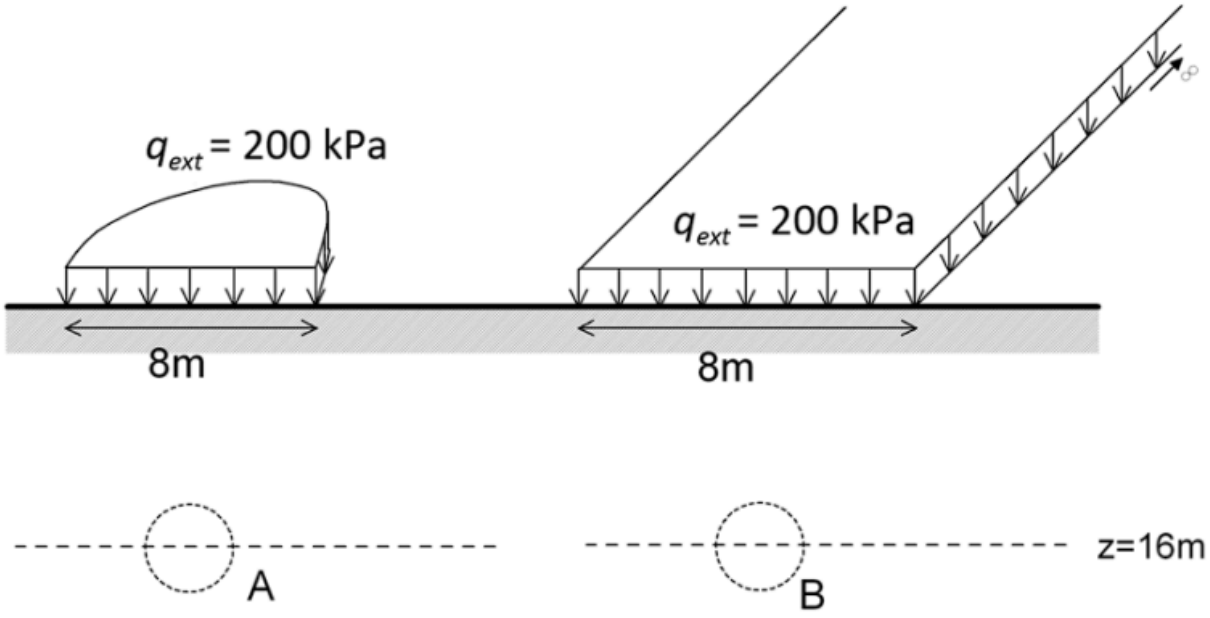

Additional problem 3.9.3. Problem description and input parameters.

Answer:

Location A.

3.9.4

Calculate the vertical stress below the axis of the embankment shown below, at a depth z = 10 m.

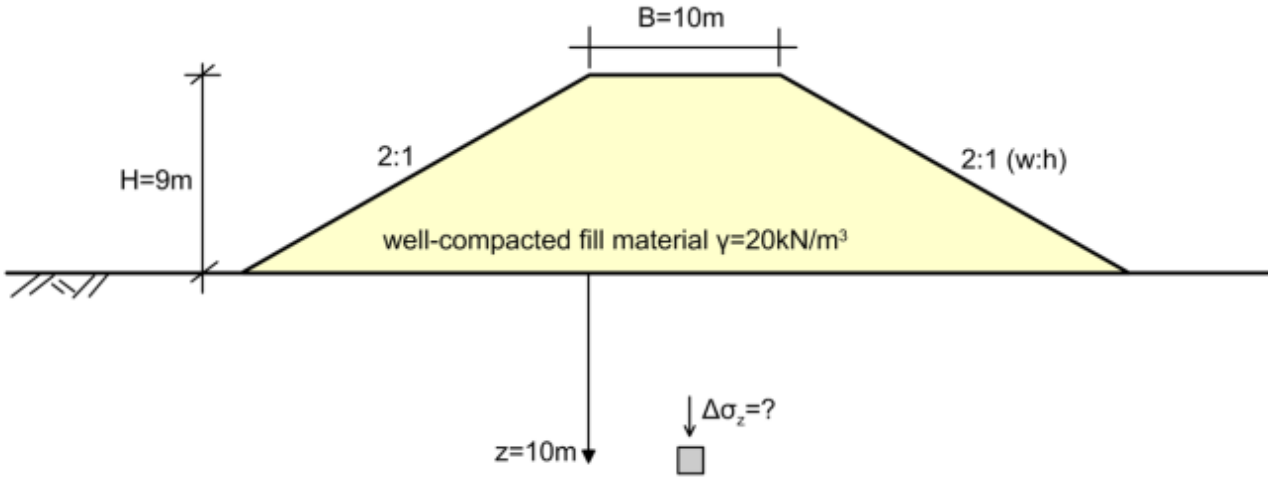

Additional problem 3.9.4. Problem description and input parameters.

Answer:

$\Delta\sigma_z = 136\ \text{kPa}$

4. SETTLEMENT OF SHALLOW FOUNDATIONS

4.1 INTRODUCTION TO PART 4

As soil is compressible, every shallow foundation will settle, at least for a few millimeters. The Geotechnical Engineer is called to design the foundation so that the settlement that will inevitably occur will not affect the integrity of the structure, and will not interrupt the function(s) for which the structure was designed for, thus satisfy *Serviceability Limit State* requirements.

Foundation settlement can be classified into three basic types: *uniform settlement, tilt and non-uniform settlement* (Figure 4.1) Uniform settlement may disrupt utilities function such as pipe connections, and therefore affect the serviceability of the structure, or interfere with nearby structures. On the other hand, distortion caused by non-uniform settlement induces bending in structural elements, which can result in cracking, and affect the integrity of the structure (Figures 4.1 and 4.2).

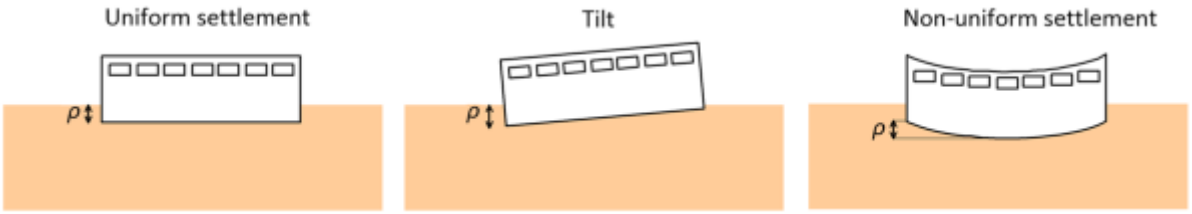

Figure 4.1. Types of settlement.

Figure 4.2. Non-uniform settlement in Mexico City (Mexico is sinking by Avi Dolgin, via Flickr, is licensed under CC BY-NC-SA 2.0).

4.2 CAUSES OF SETTLEMENT

The main reason for development of (intolerable) settlement is the application of (excessive) structural loading on the foundation. However, settlement may develop due to direct or indirect environmental loadings and actions too such as:

- Consolidation due to water table lowering, resulting in an increase in effective stress (Figure 4.3).
- Changes in soil density due to dynamic loadings e.g., seismic loading of dry coarse-grained soils resulting in *dynamic compaction* and saturated coarse-grained soils resulting in *liquefaction* (Figure 4.4).
- When a structure is founded on *expansive* soil deposits, heave i.e., upwards soil movement may develop due to soil moisture increase, or settlement due to soil shrinkage caused by decrease of its moisture content (Figure 4.5). Expansive soils, mainly high plasticity clays, tend to expand while absorbing water, and contract while expelling it.
- Collapse of the structure of *sensitive* soils.
- Poor compaction of fill materials.

The focus of this Part is on settlements due to application of structural loadings.

Figure 4.3. Differential settlement of a bridge due to over-pumping for irrigation purposes (author's own photos).

Figure 4.4. Settlement due to seismic liquefaction (Soil liquefaction 2, Katori-city, Japan by katorisi, via Wikimedia Commons, is licensed under CC BY-SA 3.0).

Figure 4.5. Masonry damage due to subsidence (US Geological Survey USGS website, marked as public domain).

4.3 TOLERABLE SETTLEMENT

As discussed above, limits on *uniform settlement* are usually associated to the function of the building e.g., access, connection to services etc. Limits on *differential settlement* (or *differential deflection*) and *angular distortion,* which are defined in Figure 4.6, depend on the type of the structure, and on the properties of the load-bearing frame. Building codes and standards, such as AS2870, impose limits on the maximum differential settlement to prevent e.g., cracks in masonry walls. Such limits for residential slabs and footings are presented in Table 4.1. Poulos *et al.* (2001) summarise typical limit values of uniform settlement, angular distortion, tilt and deflection for various types of structures. These limits are presented in Table 4.2. Of course other, perhaps stricter, project-specific limits may apply.

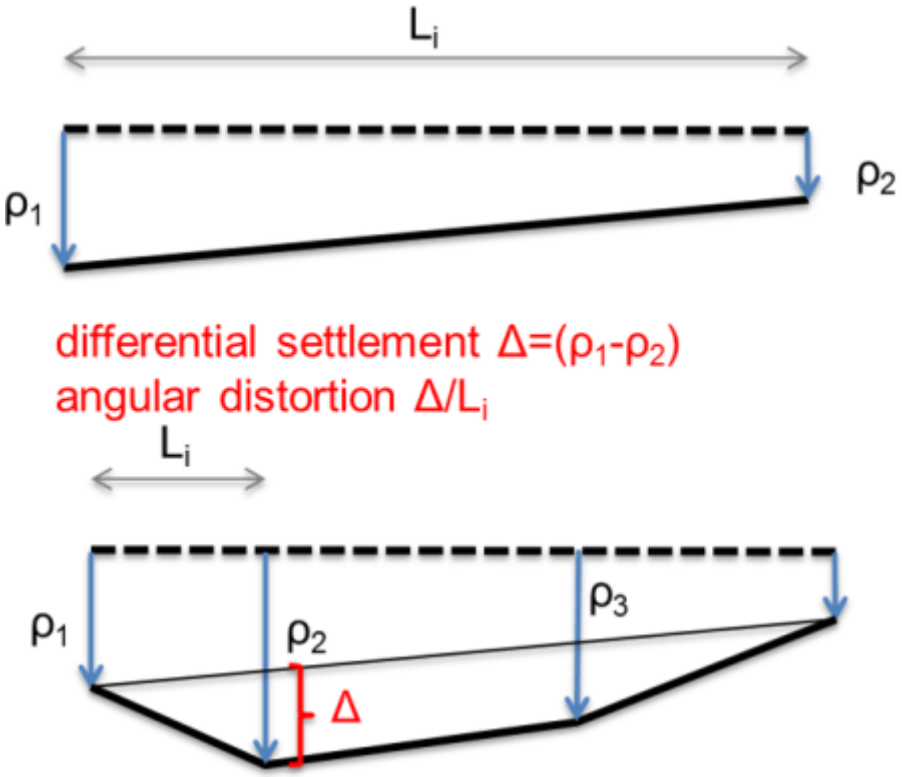

Figure 4.6. Definition of differential settlement and of angular distortion.

Table 4.1. Maximum allowable differential settlement (deflection) of footings and rafts (AS2870).

Structure type	Maximum allowable differential settlement (differential deflection), as function of span length, *L*	Maximum allowable differential settlement (differential deflection), (units: mm)
Clad frame	*L*/300	40
Articulated masonry veneer	*L*/400	30
Masonry veneer	*L*/600	20
Articulated full masonry	*L*/800	15
Full masonry	*L*/2000	10

Table 4.2. Recommended settlement, angular distortion, tilt and deflection criteria, for various types of structures (Poulos *et al.* 2001).

Structure type	Criterion	Limitation	Recommended value
Common framed buildings and reinforced load-bearing walls	Structural damage	Angular distortion	1/150 to 1/250
	Cracking in walls and partitions	Angular distortion	1/500; 1/1000 to 1/1400 for end bays
	Visual appearance	Tilt	1/300
	Connection to services	Total settlement	50 to 75 mm for coarse-grained foundation soil; 50 to 135 mm for fine-grained foundation soil
Tall buildings	Operation of lifts	Tilt	1/1200 to 1/2000
Unreinforced load-bearing structural elements (e.g., masonry)	Cracking by relative sag	Deflection ratio (maximum relative deflection in a panel/panel length)	1/2500 for wall length/height ratio = 1; 1/1250 for wall length/height ratio = 5
	Cracking by relative hog	Deflection ratio (maximum relative deflection in a panel/panel length)	1/5000 for wall length/height ratio = 1; 1/2500 for wall length/height ratio = 5
Bridges	Ride quality	Total settlement	100 mm
	Function	Horizontal movement	38 mm
	Structural damage	Angular distortion	1/250 for multispan bridges; 1/200 for single span bridges

4.4 COMPONENTS OF SETTLEMENT DUE TO STRUCTURAL LOADING

When estimating settlement, one should always keep in mind that application of external loadings to soil results in *total stress* increments, whereas settlement due to external loading are due to changes in *effective stress* only. The total settlement that will develop following the application of a load or pressure on the soil can be broken down into three components, with respect to their evolution with time (Figure 4.7):

- *Immediate settlement*, ρ_e
- *Primary consolidation settlement*, ρ_{pc}
- *Secondary compression settlement or creep*, ρ_{sc}

Immediate settlement (often referred to as elastic settlement) develops instantaneously, while primary consolidation and secondary compression settlement are time-dependent (Figure 4.7). The total settlement will be equal to the sum of the three settlement components as:

(4.1) $$\rho = \rho_e + \rho_{pc} + \rho_{sc}$$

To understand the mechanism of settlement development, consider an external pressure applied on the ground surface, and a soil particle below the groundwater table (Figure 4.8). Initially, only geostatic stresses are applied on the soil particle, and the pore pressure u_0 is the hydrostatic pore water pressure. After the pressure is applied, total stresses increase. We can calculate these total stresses according to the methods described in Part 3.

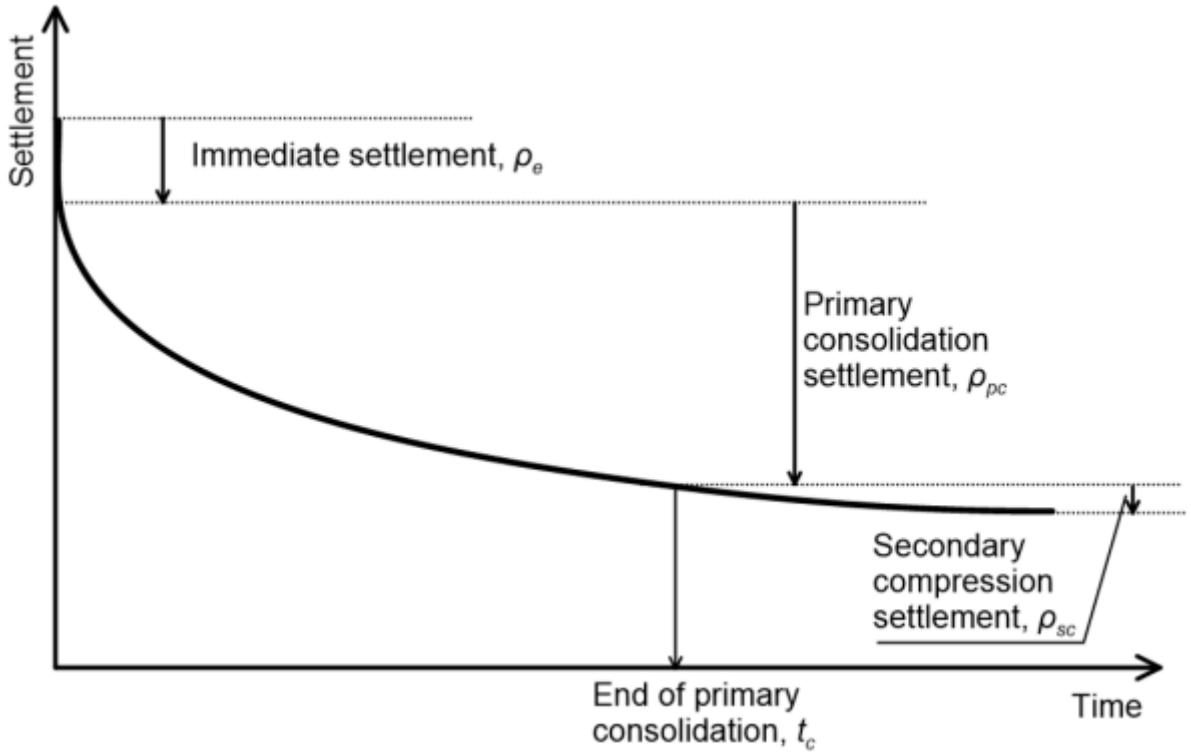

Figure 4.7. Settlement components and evolution of settlement with time.

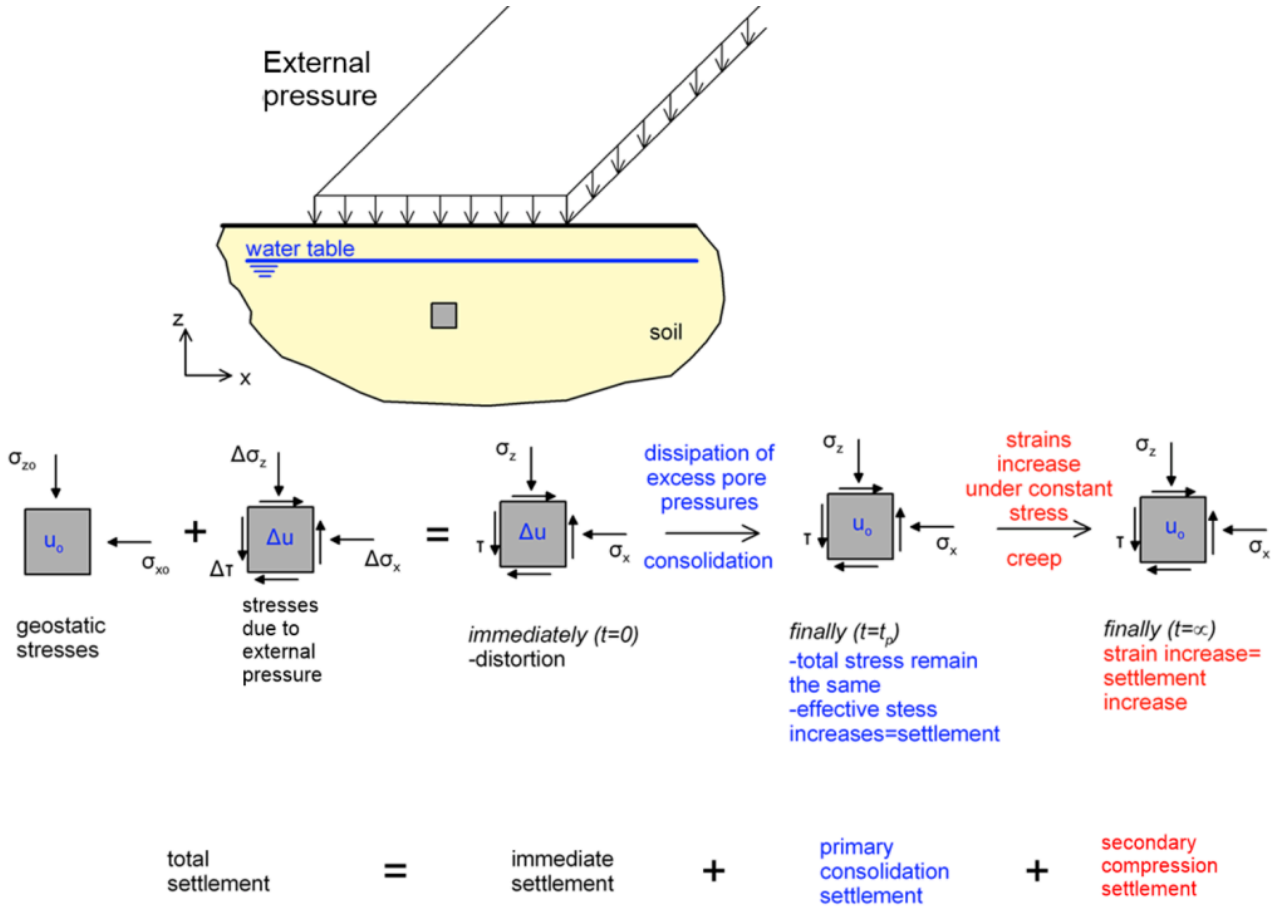

Figure 4.8. Outline of immediate, primary consolidation and secondary compression settlement mechanisms.

If the soil features high permeability (coarse grained, sand or gravel), then the external pressure will be transferred immediately to the soil skeleton. The effective stress after the application of the pressure will be:

(4.2) $\sigma'_z = \sigma'_{z0} + \Delta\sigma_z$

where σ'_{z0} is the initial, geostatic effective stress, and $\Delta\sigma_z$ is the additional stress due to the application of the pressure. Pore water pressure does not change, and it remains equal to the hydrostatic pore water pressure. This type of behavior is called *drained*. Immediate settlement that will develop instantaneously after the application of the pressure will be equal to the total settlement in this case.

However, if the soil features low permeability (fine grained, clay) and is saturated, initially the additional stresses due to the external pressure will be resisted by the development of excess pore water pressure Δu, and effective stresses will remain unchanged. If we assume 1-D loading conditions i.e., lateral soil strain is equal to zero, then:

(4.3) $\sigma'_z = \sigma'_{z0}$

(4.4) $\Delta u = \Delta\sigma_z$

When soil permeability is low, the generated pore water pressure cannot dissipate fast enough as the soil tends to deform, so excess pore water pressure Δu develops. This type of behaviour is called *undrained*. Some insight on the origin of the terms drained and undrained, which the reader may erroneously associate with drainage/pumping of water, is provided in Section 5.2.5. Shear distortion due to the application of the pressure e.g., from a shallow footing takes place without volume change $\Delta V = 0$ under *undrained* conditions (Figure 4.9). Zero volume change however does not necessarily mean zero deformation, as in the case of 1-D consolidation. Rather, in 3-D conditions below a shallow footing lateral strains are not

restricted, and immediate settlement will indeed develop, but will be combined with heave of soil around the footing (Figure 4.9). In that case Eq. 4.4 is not valid, and the developing excess pore pressure will be lower, exactly due to the development of lateral strains.

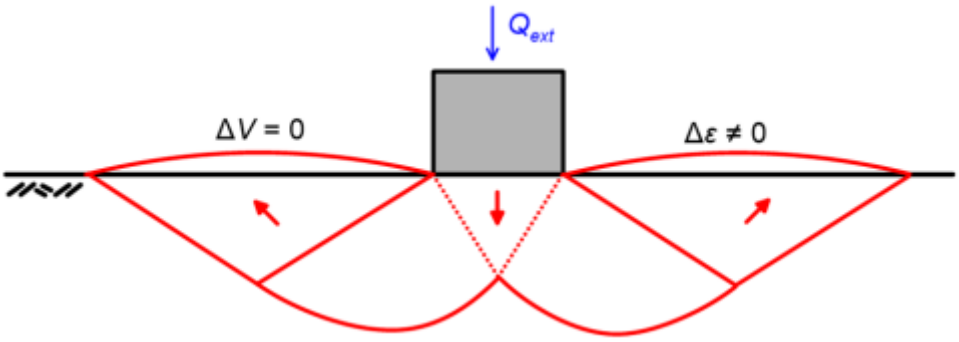

Figure 4.9. Shear distortion around a footing under undrained conditions.

As time passes, the excess pore water pressure that developed due to the application of the pressure dissipates gradually, at a rate which depends on the permeability of soil. As excess pore pressure Δu dissipates, effective stresses increase, and the loading is gradually transferred to the soil skeleton. Remember that total stresses remain constant, and equal to the geostatic total stresses plus the additional stresses due to the external loading:

(4.5) $\sigma_z = \sigma_{z0} + \Delta\sigma_z$

(4.6) $\sigma_z = \sigma'_z + (u_0 + \Delta u)$

Increase of effective stress results to soil deformation, and to the development of primary consolidation settlement (Figure 4.7).

After "enough" time $t = t_c$, excess pore water pressure will become zero $\Delta u = 0$, and the additional stress from the external loading will be transferred to the soil skeleton. At this point the primary consolidation has been completed, and the primary consolidation settlement has reached its final value (Figure 4.7).

Secondary compression settlement concerns mainly organic soils and soft clays. One mechanism (referred to as Hypothesis A) proposed in the literature to describe and quantify secondary compression is that, after the end of primary consolidation, strains (and thus settlement) continue to increase under constant effective stress, due to changes in soil structure associated with creep. It must be stated here that other researchers (of which the author is one) argue that the mechanisms of creep and consolidation are concurrent (Hypothesis B). Exploring this further is beyond the scope of this Part. Secondary compression settlement is usually neglected in sands yet, in some organic soils like fibrous peat, a large proportion of total settlement is due to secondary compression.

Summarising, depending on the nature of the soil, some of the components of total settlement can be zero:

- For sands primary consolidation and secondary compression settlement is usually neglected $\rho_{pc} \approx \rho_{sc} \approx 0$, so total settlement is equal to immediate settlement $\rho = \rho_e$.
- For most stiff clays, secondary compression settlement is neglected too $\rho_{sc} \approx 0$.

4.5 IMMEDIATE SETTLEMENT OF SHALLOW FOUNDATIONS

Elastic settlement of soil subjected to uniform, flexible loadings can be simply calculated as the sum of the volumetric strains ε_{vol} along the thickness of the compressible layer, H:

(4.7) $$\rho = \int_0^H \varepsilon_{vol} dz$$

The same basic concept applies for the estimation of settlement of shallow foundations. Nevertheless, we need to introduce some corrections in the above equation to account for the effect of the rigidity of the foundation, the embedment depth, and the shape of the footing, while appropriately considering drained or undrained conditions. These are discussed in the following paragraphs.

4.5.1 Effect of footing rigidity: Immediate settlement and contact stresses

Distortion of soil due to the application of an external load or pressure depends on the rigidity of the loaded area, and the type of soil (fine-grained or coarse-grained) i.e., whether immediately after application of a loading the soil will behave as drained or undrained. In case of *rigid* footings (Figure 4.10), settlement is of course uniform. The distribution of contact stresses below the footing is, nevertheless, highly non-uniform. Assuming that soil behaves as elastic material, contact stresses at the outer edge of the footing ($x = B/2$, Figure 4.10) would become infinite:

(4.8) $$\Delta\sigma_z = \frac{2q_{ext}}{\pi} \frac{1}{\sqrt{1 - \left(\frac{2x}{B}\right)^2}}$$

In a real *fine-grained* soil however, they are limited by its shear strength. The drained Young's modulus E' of *coarse-grained* soils depends on the degree of confinement, and this affects the distribution of stress underneath a loaded area. The fact that the drained Young's modulus E' depends on the confining stress is mathematically expressed as:

(4.9) $$E' = E'_{ref} \left(\frac{p'}{p_{ref}}\right)^m$$

where p' is the mean effective stress $p' = (\sigma'_1+\sigma'_2+\sigma'_3)/3$, E'_{ref} is the reference modulus value at a reference mean stress p_{ref}, while the exponent m is considered usually $m = 0.5$ for sands and $m = 1.0$ for clays. In other words, the Young's modulus is non-linear function of mean stress in sands. Near the outer edges, where confinement (i.e., the mean stress) is less compared to the centre of the footing, the stresses are lower (Figure 4.10b).

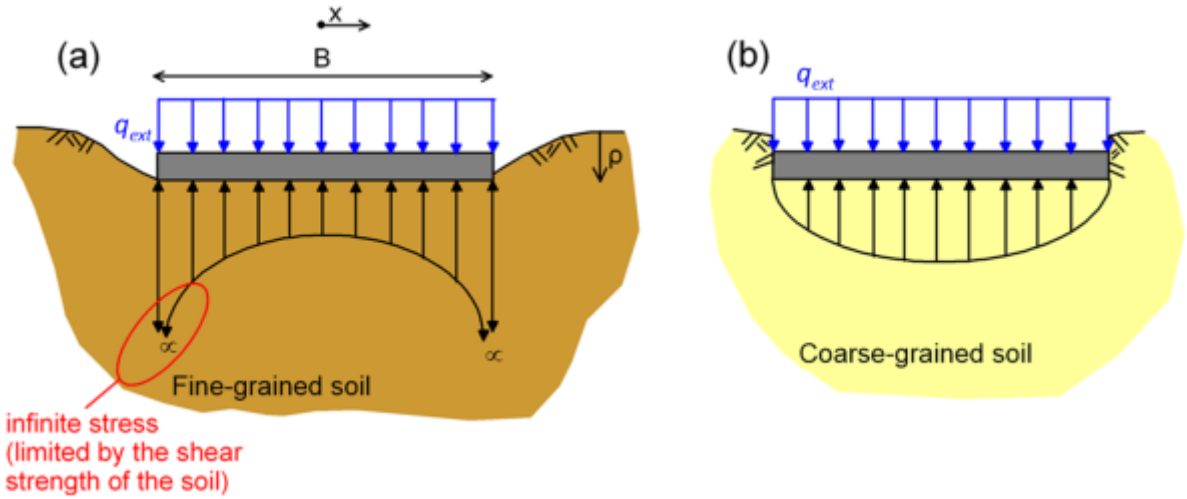

Figure 4.10. Distribution of contact stresses below a rigid footing transferring uniform vertical pressure to (a) fine-grained and (b) coarse-grained soil.

Contact stress distribution under a *flexible* loaded area is uniform, but the settlement profile varies as soil surface is free to deform, depending again on whether soil is fine-grained or coarse-grained (Figure 4.11). The shape of the deformed surface in the case of saturated clay *(undrained loading)* will be concave upward (Figure 4.11a), as it is reasonable to assume a uniform value of E_u across the thickness of the compressible clay layer, as in Figure 4.10a. On the other hand, the shape of the deformed surface in the case of a coarse-grained material (*drained loading*) will be concave downward (Figure 4.11b). That is because the Young's modulus of sands E' varies non-linearly with confining stress. As the latter are lower near the edge of the footing, compared to the stresses at its centre, the settlement developing near the edges will be higher than near the centre of the footing.

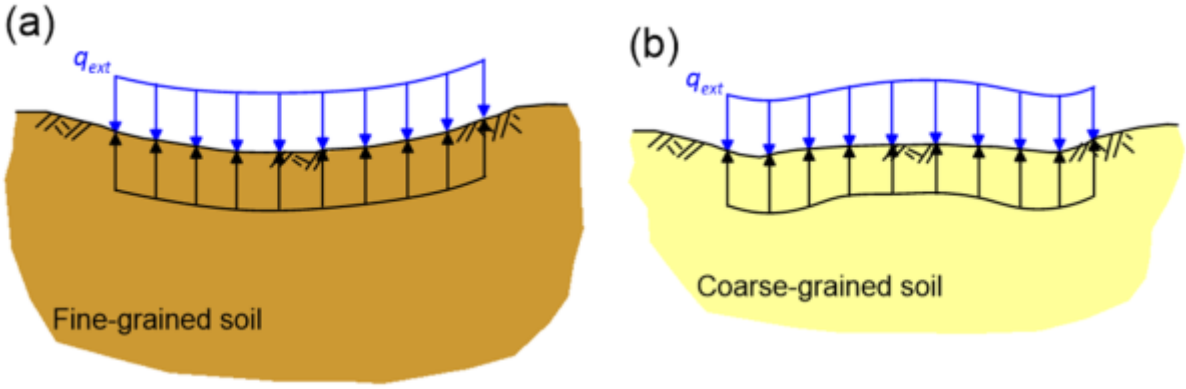

Figure 4.11. Distribution of contact stresses below a flexible footing transferring uniform vertical pressure to (a) fine-grained and (b) coarse-grained soil.

4.5.2 Effect of embedment depth

The pressure acting on the soil that will result in ground settlement is the *additional* pressure Δq_{ext} imposed at the level of the foundation, on top of the pre-existing geostatic vertical effective stress at this level, σ'_{z0}. Settlement due to the stress σ'_{z0} has already taken place during soil deposition, before application of the loading.

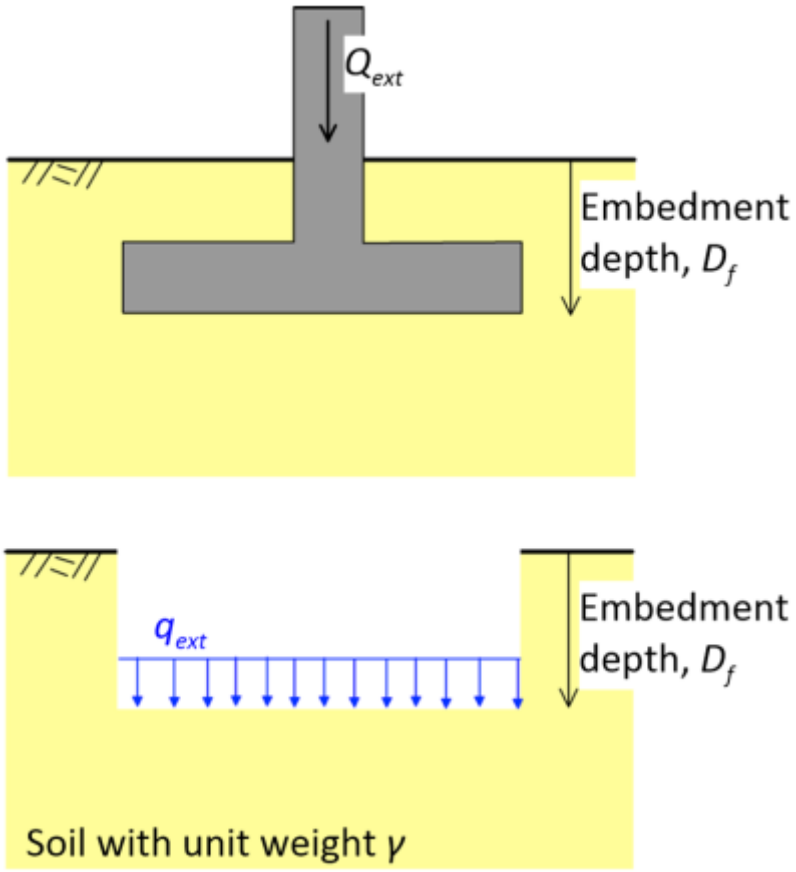

Figure 4.12. Effect of embedment depth.

If the foundation level is at the ground surface, and no other loads exist (e.g., preloading) then $\sigma'_{z0} = 0$ and the additional pressure Δq_{ext} is equal to the pressure from the footing q_{ext} i.e., the applied force divided by the area of the footing Q_{ext}/(Area). But in the common case where the topsoil is excavated for the construction of the foundation level at depth D_f (Figure 4.12) and soil is unloaded, the pre-existing vertical effective stress σ'_{z0} is equal to the geostatic stress at this level $\sigma'_{z0} = \gamma D_f$, where γ is the unit weight of the soil. In that case:

(4.10) $$\Delta q_{ext} = q_{ext} - \gamma D_f$$

Besides, embedment of a foundation will further reduce the expected settlement as:

- Soil stiffness generally increases with depth. Foundation on a stiffer soil layer will of course result in less settlement.
- Normal stresses from the soil above the foundation level increase confinement.
- Part of the loading may be transferred through the side walls, as shear resistance can be mobilised at the soil-walls interface. Accommodation of part of the loading by side resistance reduces settlement (Figure 4.13).

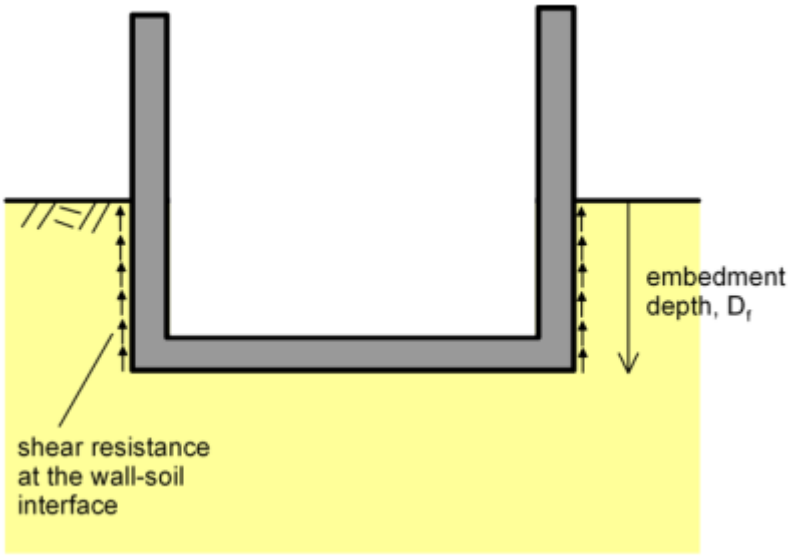

Figure 4.13. Development of shear resistance at the soil-wall interface.

4.5.3 Drained or undrained soil response for calculating immediate settlements

Methods for estimating settlement which are based on the theory of elasticity are often applied to predict settlement of structures founded on coarse-grained (sand, gravel) soils. We use such methods while considering the *drained* elastic parameters of soil i.e., the drained Young's modulus E' (also referred to as *compressibility modulus*, or *deformation modulus*) and the drained Poisson's ratio v'. As soil behaviour is actually non-linear, the appropriate value of the Young's modulus to be used with a method assuming linear elastic soil behaviour should take into account the stress levels that are expected to be applied in soil (Figure 4.14). Of course it is prudent to design the foundation so that strains in the foundation soil under serviceability conditions remain low, therefore elasticity formulas should provide a relatively good approximation of soil behaviour *in situ*. Furthermore, one should keep in mind that the Young's modulus generally increases with depth, as it is a function of the mean stress level (see Section 4.5.1).

For fine grained soils, if the applied stress is sufficiently less than the yield stress of soil, immediate (short term) settlement should indeed be approximately linear elastic. In fact, the author could argue that good design practice requires designing any foundation or earthwork (embankment) so that the yield stress of soil (i.e., its preconsolidation stress, see Section 4.6.2) is not exceeded immediately after loading the foundation soil. In that case, we can apply methods for estimating settlements that are based on the theory of elasticity, while considering the *undrained* elastic parameters of the soil i.e., the undrained Young's modulus E_u, which can be estimated from triaxial undrained tests in soil samples (Figure 4.15) and the undrained Poisson's ratio $v_u \approx 0.5$, that satisfies the requirement for zero volume change during undrained loading. Remember that according to the theory of elasticity, the undrained Young's modulus, for deformation under constant volume, is related to the drained Young's modulus as:

$$\textbf{(4.11)}\quad E_u = \frac{3}{2\,(1+v')}E'$$

The theory behind the above Eq. 4.11 is discussed in Chapter 4.7.

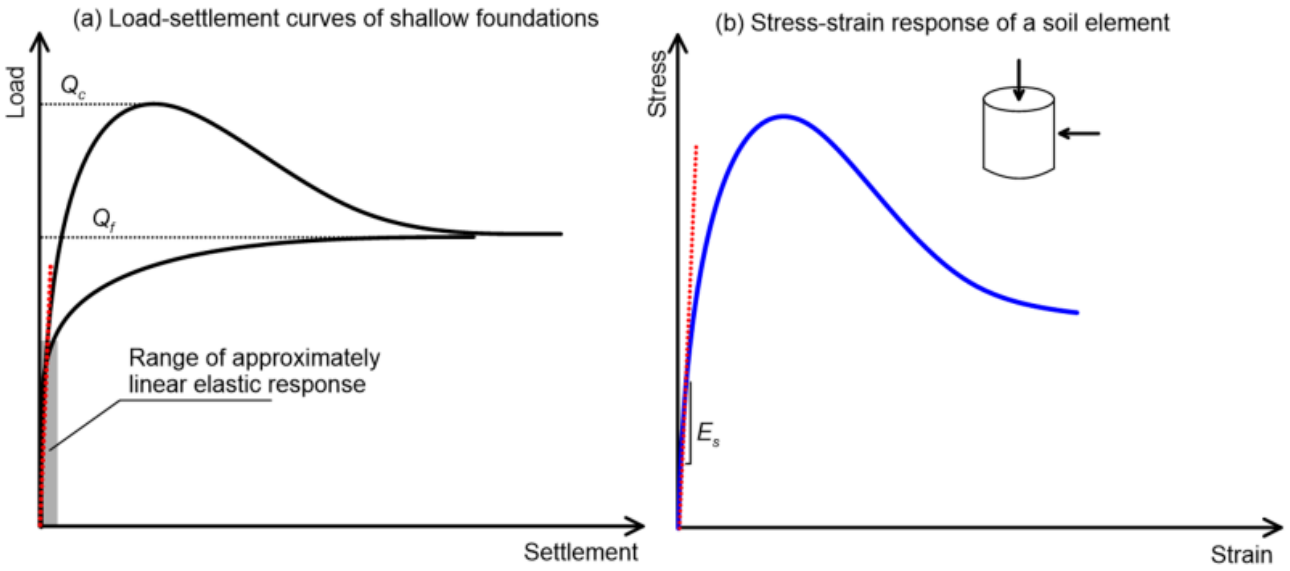

Figure 4.14. (a) Load-settlement curves of shallow foundations, and (b) Stress-strain soil response.

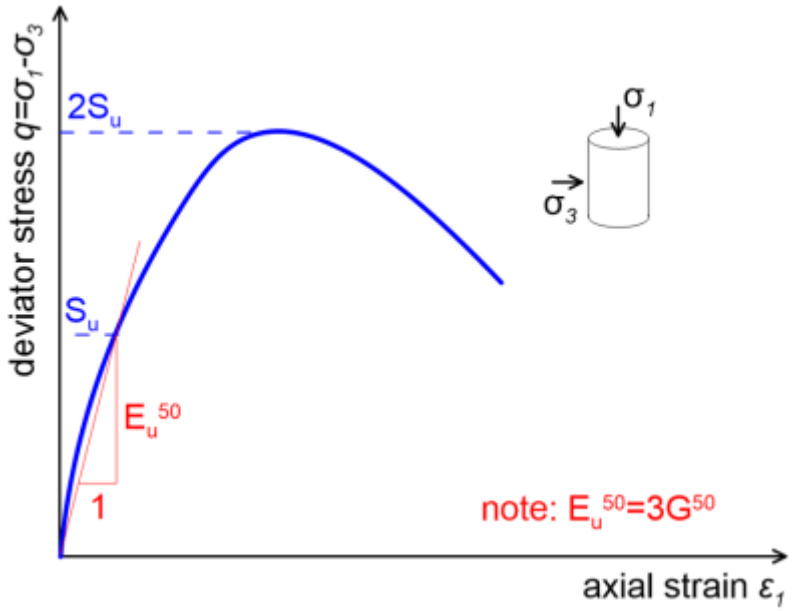

Figure 4.15. Estimation of the undrained Young's modulus E_u (at a stress level equal to half the failure stress) from triaxial compression tests.

Keep also in mind that undrained loading under constant volume does not necessarily mean zero deformation, as it is the case of one-dimensional consolidation in the oedometer test. In two-dimensional problems, as the problem of predicting the immediate settlement of shallow footings, lateral soil heave is allowed to develop, and immediate settlement can occur under constant volume (see also Figure 4.9). This is also depicted in Figure 4.15, where undrained triaxial loading of a soil sample results in axial, but also lateral strains.

4.5.4 Immediate settlement of arbitrarily-shaped rigid

footings on homogeneous half-space

The immediate (elastic) settlement of rigid shallow footings of arbitrary shape can be estimated using the following expression by Gazetas *et al.* (1985), which is based on the assumption of linear elastic soil resting on a homogeneous half-space (Figure 4.16):

(4.12) $$\rho_e = \frac{Q_{ext}}{E_s L}\left(1-\nu_s^2\right)\mu_s\mu_{emb}\mu_{wall}$$

where: Q_{ext} is the vertical load (units: force) acting on the footing under serviceability conditions; $E_s = E_u$ if the foundation soil is fine-grained (undrained conditions), or $E_s = E'$ if the foundation soil is coarse-grained (drained conditions). In that case Eq. 4.12 provides the total settlement; $\upsilon_s = \upsilon_u \approx 0.5$ if the foundation soil is fine-grained (undrained conditions), or $\upsilon_s = \upsilon'$ if the foundation soil is coarse-grained (drained conditions); L is the half-length of the circumscribed rectangle.

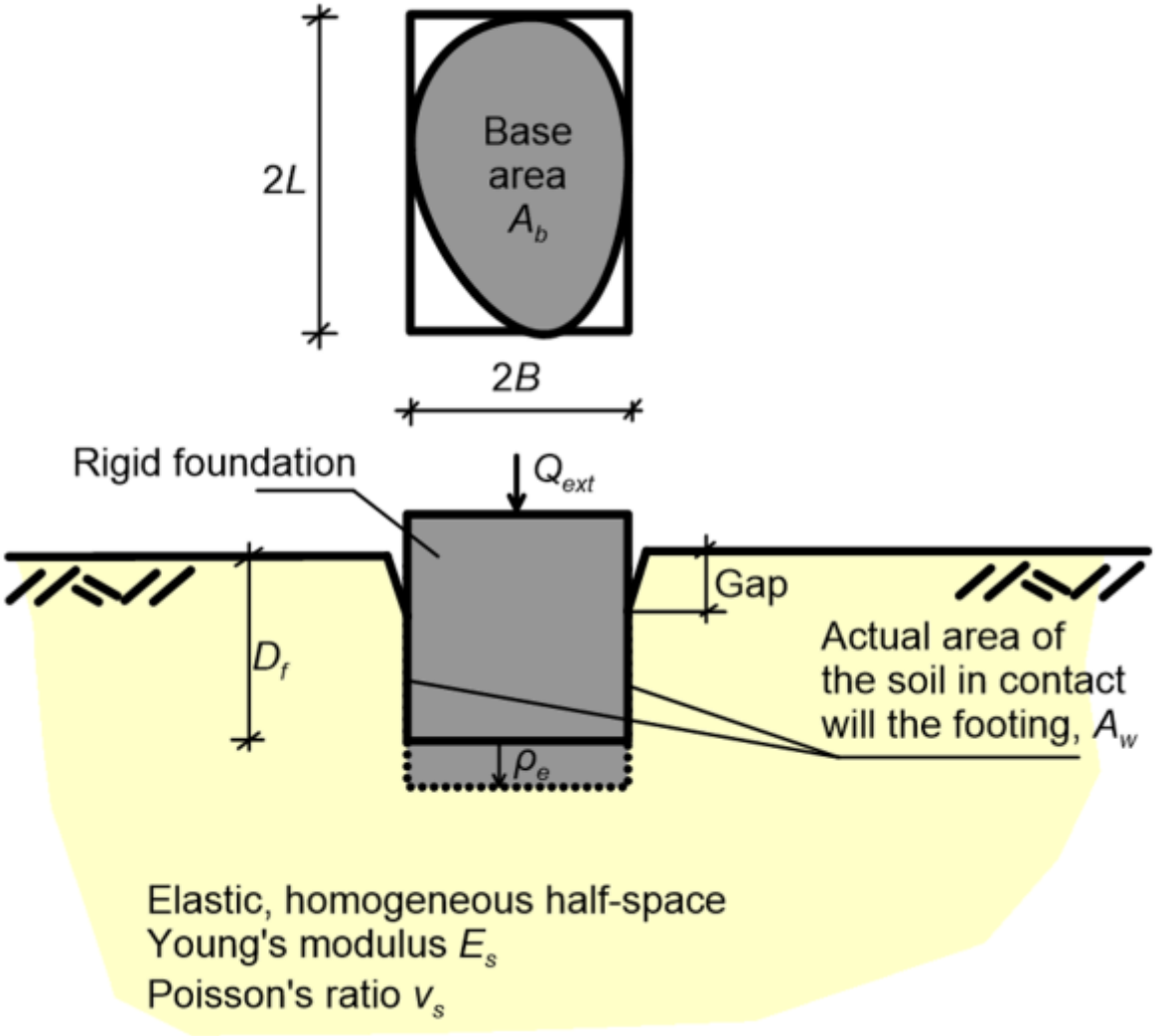

Figure 4.16. Geometry to calculate settlement of rigid shallow footings (after Gazetas et al. 1986).

Moreover, μ_s is a factor accounting for the shape of footing, equal to:

(4.13) $$\mu_s = 0.45\left(\frac{A_b}{4L^2}\right)^{-0.38}$$

μ_{emb} is a factor accounting for the effect of embedment:

(4.14) $$\mu_{emb} = 1 - 0.04\frac{D_f}{B}\left[1 + \frac{4}{3}\left(\frac{A_b}{4L^2}\right)\right]$$

μ_{wall} is a factor accounting for the effect of wall friction:

(4.15) $$\mu_{wall} = 1 - 0.16\left(\frac{A_w}{A_b}\right)^{0.54}$$

The parameters that appear in the above expressions are defined in Figure 4.16, while values of the ratio $A_b/4L^2$ for common footing shapes are presented in Table 4.3.

Table 4.3. Values of $A_b/4L^2$ for common footing shapes.

Footing shape	$A_b/4L^2$
Square	1
Rectangle	B/L
Circular	0.785
Strip	0

This method is valid for "deep" homogeneous soil. In practice this means that the thickness of the surficial compressive layer should be larger than the influence depth of the load. If that is not the case, the method will result in (over)conservative settlement predictions, as discussed in Example 4.8. In addition, it is the author's view that the factor accounting for the wall friction must be used with caution, as it is not at all certain that the interface's shear strength will be mobilised at the wall-soil interface under the serviceability load. It is therefore reasonable to assume that $\mu_{wall} = 1$ i.e., no load is transferred through friction.

Note that the method described above does not apply to strip footings, as it predicts infinite settlement. This is a consequence of assuming that the thickness of the compressible layer is infinite.

4.5.5 Immediate settlement of footings on fine-grained soil layer of limited thickness

When the thickness of the compressible soil layer relatively to the dimensions of the foundation is relatively small, and the compressible soil is underlain by a practically incompressible layer, the method described in Section 4.5.4 will provide over-conservative settlement predictions. If the foundation soil is fine-grained, the immediate settlement of a flexible footing transferring pressure q_{ext} to a soil layer of finite thickness can be calculated according to Christian and Carrier (1978) as:

(4.16) $$\rho_e = \frac{q_{ext}B}{E_u}\mu_0\mu_1$$

where μ_0 accounts for the effect of embedment and μ_1 accounts for the thickness of the compressible layer relatively to the dimensions of the footing (Figure 4.17). In addition B is the width of the footing and E_u is the undrained Young's modulus of the fine-grained soil. Note that Figure 4.17 depicts values of μ_0 and μ_1 that correspond to Poisson's ratio $\nu_u = 0.5$, hence the above are valid only for undrained loading conditions.

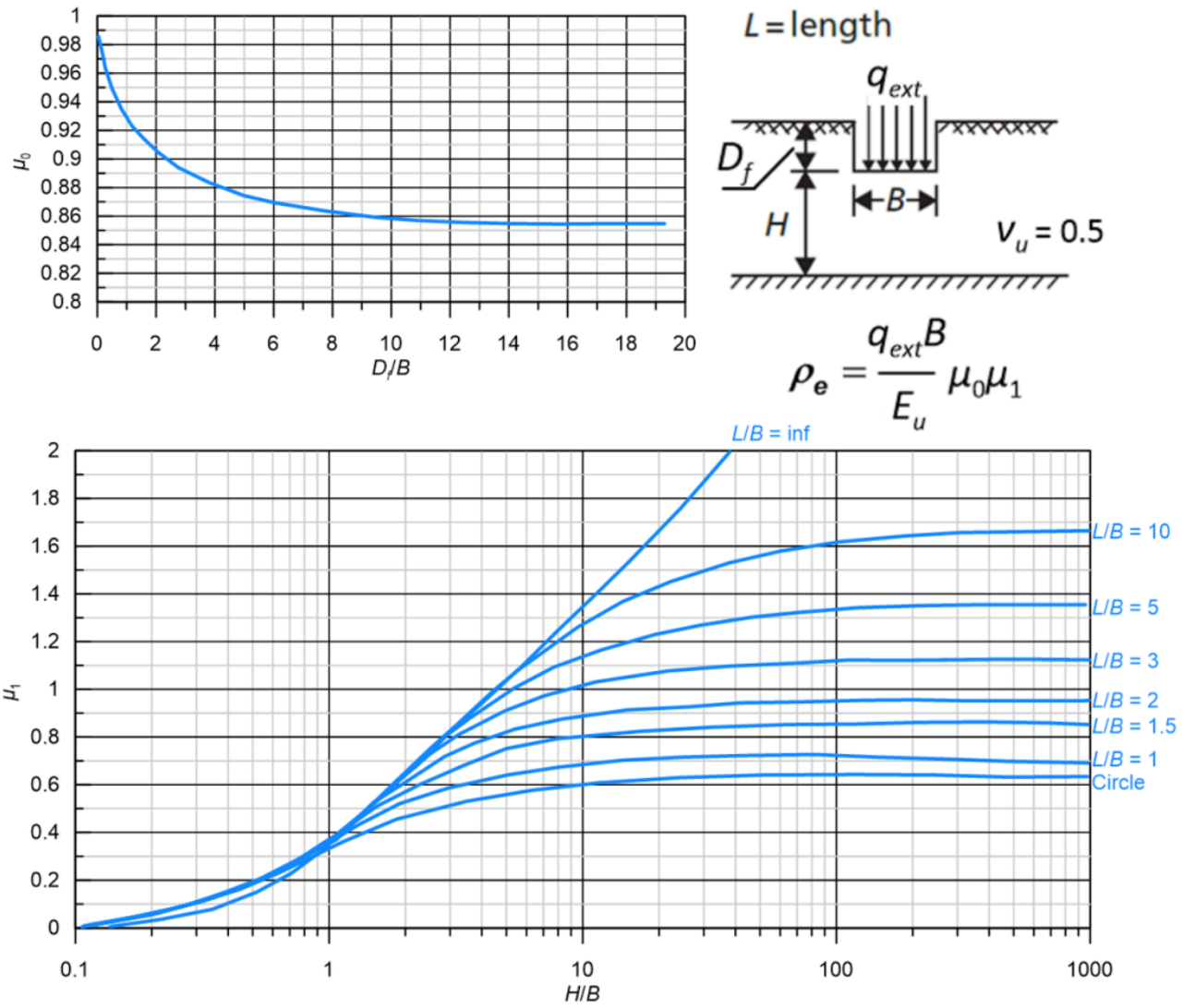

Figure 4.17. Coefficients μ_0 and μ_1 for Poisson's ratio v_u=0.5 (after Christian and Carrier 1978).

EXAMPLE 4.1

Immediate settlement of a footing resting on saturated clay

Estimate the immediate settlement of a square 4 m x 4 m footing resting on the surface of a deep homogeneous saturated clay layer, using the methodology described in Section 4.5.4. The working load under serviceability conditions is Q_{ext} = 3 MN, the embedment depth is D_f = 2 m, and the undrained clay compressibility parameters are E_u = 10 MPa and ν_u = 0.50.

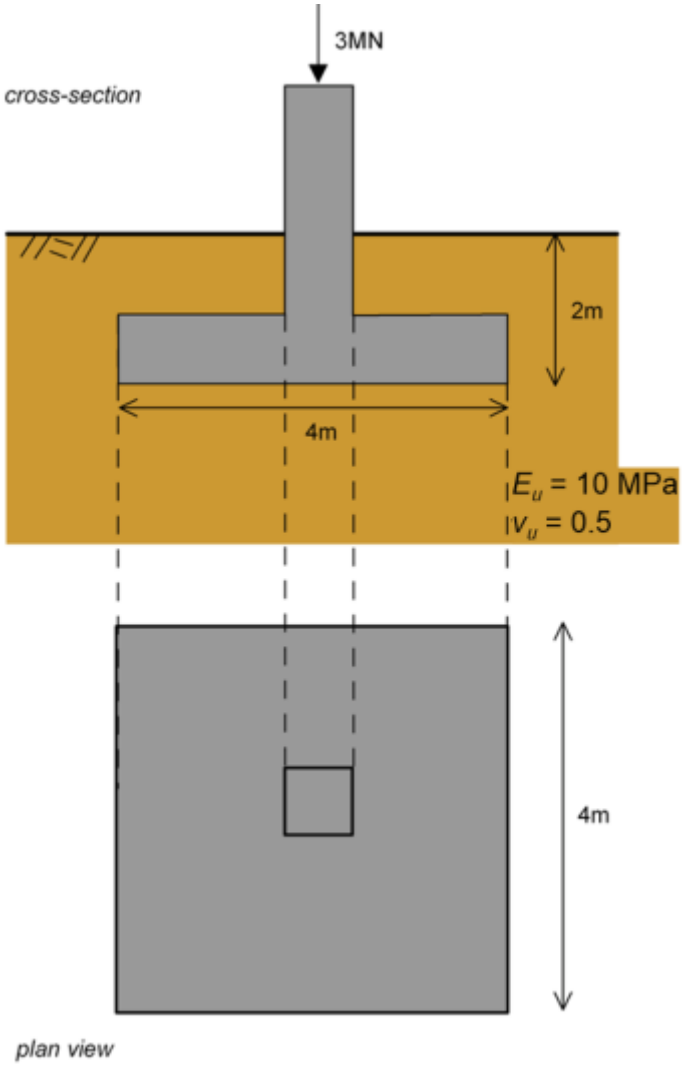

Example 4.1. Problem description and input parameters.

Answer:

The area of the rectangular footing is equal to:

A_b=4m x 4m =16 m^2

As the half-length of the rectangle side is L = 4 m/2 = 2 m, the factor $A_b/4L^2$ is equal to:

$A_b/4L^2 = 16/(4\times2^2) = 1$

Influence factors μ_s and μ_{emb} accounting for the effect of shape and of footing embedment, respectively, are provided from Eqs. 4.13 and 4.14. As the thickness of the footing is small, the shear resistance that may be mobilised is negligible, thus the influence factor accounting for the effect of wall friction μ_{wall} is taken conservatively equal $\mu_{wall} = 1.0$.

$$\mu_s = 0.45\left(\frac{A_b}{4L^2}\right)^{-0.38} = 0.45$$

$$\mu_{emb} = 1 - 0.04\frac{D_f}{B}\left[1 + \frac{4}{3}\left(\frac{A_b}{4L^2}\right)\right] = 1 - 0.04\frac{2}{2}\left[1 + \frac{4}{3}\times 1\right] = 0.906$$

The immediate settlement is therefore estimated from Eq. 4.12 as:

$$\rho_e = \frac{Q_{ext}}{E_u L}\left(1-\nu_u^2\right)\mu_s\mu_{emb}\mu_{wall} = \frac{3\text{MN}}{10\dfrac{\text{MN}}{\text{m}^2}\times 2\text{m}}\left(1-0.5^2\right)\times 1\times 0.906\times$$

$$0.45 = 0.046\text{m}$$

EXAMPLE 4.2

Numerical estimation of the load-settlement curve of a footing resting on a sand layer

Estimate the load-settlement curve of the circular footing illustrated below, for settlement up to 30 mm. Consider sand to behave as elastic-perfectly plastic, obeying the Mohr-Coulomb failure criterion. Assume the footing is: a) rigid and rough and b) flexible, made of reinforced concrete with thickness h = 0.2 m.

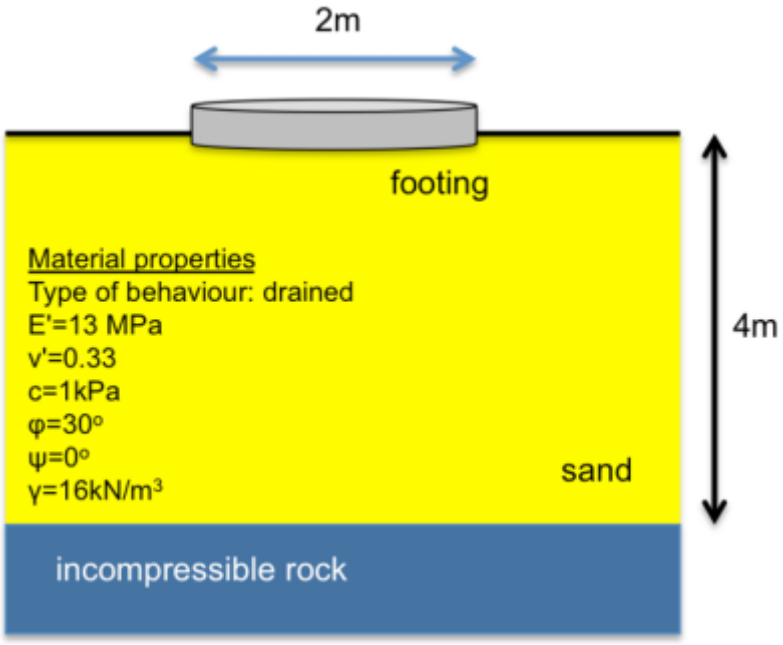

Example 4.2. Problem description and input parameters.

Answer:

As sand behavior is drained, total settlement will develop immediately after the application of the loading (Section 4.4), thus we do not need to consider the time factor in this analysis. Contrary to the method for determining immediate settlement described in Section 4.5.4, in this analysis the compressible sand layer has a limited thickness of 4 m, while it is assumed to behave non-linearly when loaded. While it is not common to assume non-linear soil response in serviceability analysis, we do so here to introduce the reader to non-linear finite element analyses, and their intricacies. A short description of the Mohr-Coulomb material model implemented in PLAXIS can be found in Section 5.2.5, and the reader can refer to it if not familiar with the elastic-perfectly plastic material model obeying the Mohr-Coulomb failure criterion.

The problem is axisymmetric, with the axis of symmetry passing through the center of the footing, as depicted in Figure 4.18. Only half of the footing is hence simulated.

The underlying rock layer will not be simulated. Instead, we will fix the displacements of the bottom boundary of the sand layer in both directions, which is essentially the same as considering an incompressible layer at that elevation. Thus, a 5 m x 4 m rectangular geometry would suffice for the simulation of this problem. Setting the lateral boundary to be at a distance of 5 times the footing radius from the axis of symmetry is a rational first-order approach. However, it is imperative to check the sensitivity of the model results to the distance of the area of interest from the lateral boundaries.

Standard fixities are applied, to account for symmetry along the left lateral boundary, and also fix the displacement along both directions at the bottom boundary, as discussed above.

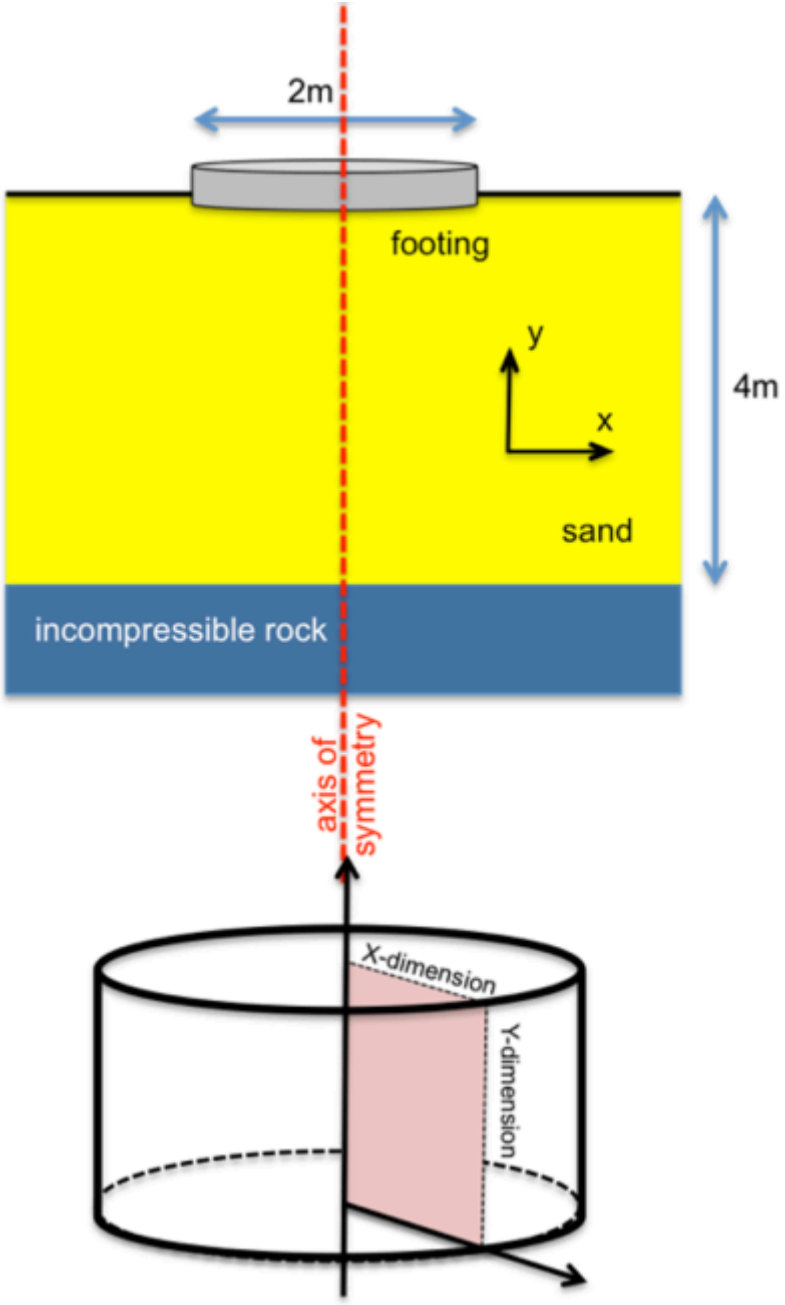

Figure 4.18. Simulated geometry taking advantage of symmetry along the footing axis. The coordinate system follows PLAXIS nomenclature, where *y* is the vertical axis.

Sand response is simulated with the Mohr/Coulomb-Drained material, using effective stress shear strength and compressibility parameters (Figure 4.19). High-permeability coarse-grained materials behave as drained under both short-term and long-term load conditions. Note that clean sands generally do not exhibit cohesion ($c' = 0$). However we use a small value $c' \leq 1$ kPa to avoid simulating a material of zero strength at the surface of the model ($y = 0$), for numerical stability reasons. Such a small cohesion value does not affect the results we are interested in. This is further discussed in Part 5.

Notice also that we consider the dilation angle ψ, which controls the amount of volumetric sand deformation that takes places as shear strains increase to failure, to be equal to $\psi = 0$. This implies that at failure shearing takes places under constant volume, whereas some contraction (compression) will take

place under elastic conditions (Figure 4.19). The simulated response is compatible with experimental tests in loose sands (and normally consolidated clays). On the other hand, the friction angle $\varphi' = 30$ deg controls the maximum (failure) shear stress that the soil can carry under the current normal stress.

When the dilation angle is considered equal to the friction angle $\psi = \varphi'$ then the flow rule of the Mohr-Coulomb model (which controls the amount of volumetric deformation at failure) is called "Associated" whereas when the dilation angle attains any other value $\psi \neq \varphi'$ is called "Non-associated" (Figure 4.19). Note that (unlike metals) the assumption of associated flow for soils is in contradiction with experimental data, as it will overestimate the amount of volumetric deformation that takes place during shearing. Hence the use of non-associated flow rule (i.e., a realistic dilation angle) will result in perhaps better approximation of the deformation behaviour. However, this also causes a number of numerical issues (localisation phenomena, non-uniqueness of the collapse load, poor convergence), even when techniques such as the "Arc-length" method are used to solve the system of non-linear equations (instead of Newton-Raphson methods), which is a good choice when the stiffness matrix is not a positive definite i.e., when softening is expected. A more detailed discussion on this is, however, beyond the scope of this Chapter. A technique to avoid such issues is again described in Part 5. Since we simulate serviceability conditions here, such issues should not affect the analysis, as yielding (failure) of soil elements will be limited.

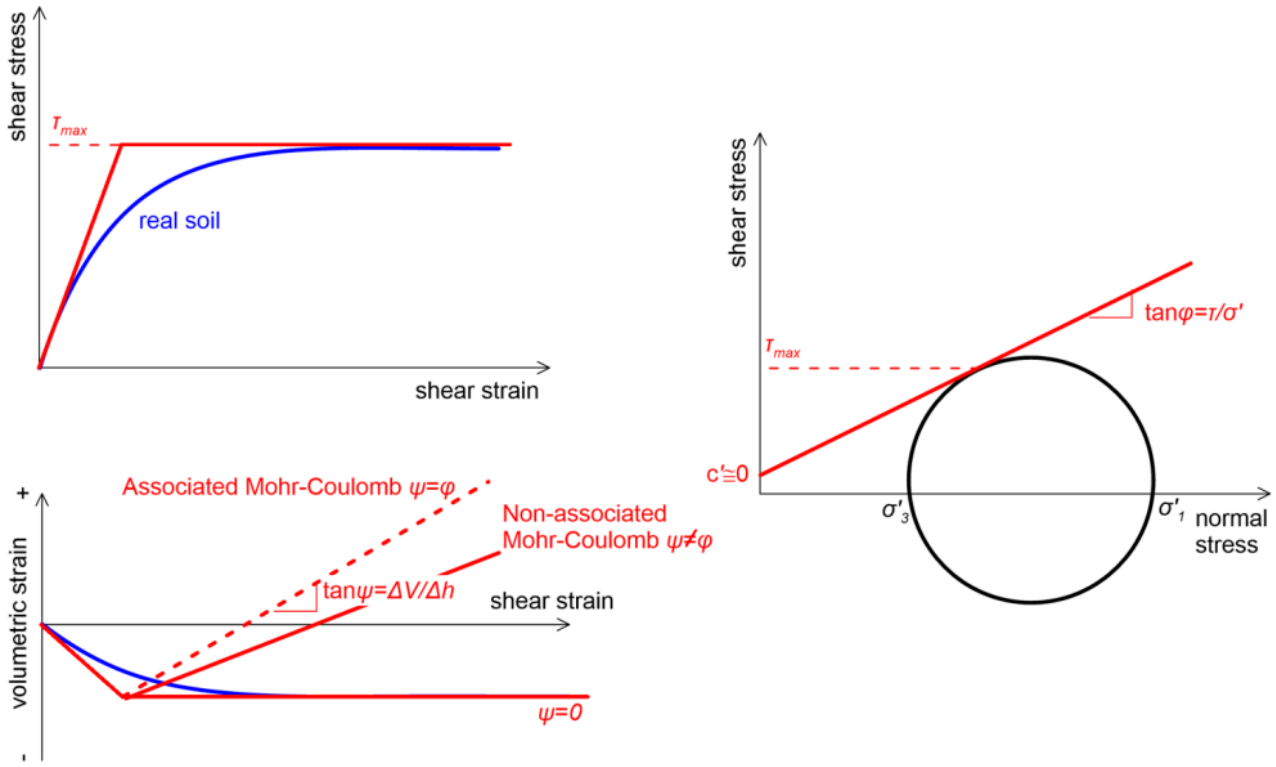

Figure 4.19. Simulated loose sand behaviour with an elastic-perfectly plastic material model obeying the Mohr-Coulomb failure criterion.

The *"rigid"* footing will settle uniformly (Figure 4.10), implying that the vertical displacement U_y be constant along the radius of the footing. Moreover, since the rigid footing is also assumed to be *"rough"*, no slippage will occur at the soil-footing interface, and the horizontal displacement U_x will be zero along the radius of the footing. In other words, we do not need to simulate the actual footing using structural elements, but we can replace it by a set of prescribed displacements acting along its radius:

- $U_x = 0$ to prohibit slippage at the soil-footing interface (*"rough"* footing)
- $U_y = -0.03$m to calculate the load-settlement curve up to a settlement of 30 mm (*"rigid"* footing)

Notice that the desired outcome from this analysis is the complete load-settlement curve, not settlement for a specific load. In fact, from the load-settlement curve we can estimate settlement under any load, up to the maximum reaction on the footing that will develop for $U_y = -0.03$m.

Simulating a *"flexible"* footing by introducing in the model its actual rigidity, which depends on its geometry and material properties, is more realistic. Moreover, this analysis will also provide the internal forces developing on the footing that can be used for the structural design of the footing. This is realised in PLAXIS by adding a *"plate"* in the model along the radius of the footing. The properties assigned to the plate elements include:

Flexural rigidity of the footing: $EI = \dfrac{E_f h^3}{12\left(1-\nu_f^2\right)}$

Axial rigidity of the footing: $EA = \dfrac{E_f h}{\left(1-\nu_f^2\right)}$

where h is the thickness of the footing, E_f is the Young's modulus of the footing's material, and v_f is the Poisson's ratio of the footing's material. The term $(1-\nu_f^2)$ in the above equations accounts for the fact that the plate elements used by PLAXIS are actually 2-D Kirchoff-Love plates and not 3-D Euler-Bernoulli beams, since we model axisymmetric or plane-strain problems. For the case at hand h = 0.2 m, E_f = 20 GPa and v_f = 0.2, considering a cracked concrete section so:

EI = 13,888 kNm^2

EA = 4,166,666 kN

A uniformly distributed pressure is applied on the footing which, for comparison purposes, will be determined as the pressure required to achieve footing settlement equal to 30 mm with the rigid footing model. The "fine" option is used to create the finite element mesh (Figure 4.20).

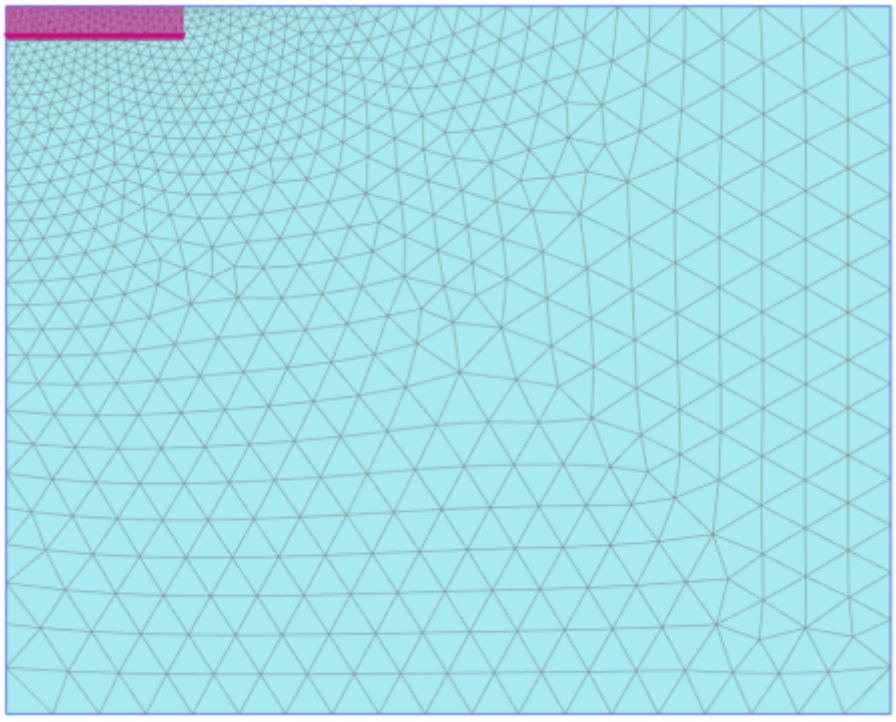

Figure 4.20. Finite element mesh for the rigid footing case.

Note that in the flexible footing model, use of standard fixities will also restrict in-plane rotation of the plate node lying on the axis of symmetry, and rotation of the footing at its center shall be zero. A coarse grid is used for the analysis with the flexible footing, to identify any possible mesh sizing effects on the solution.

Analysis is run in two stages. Before the application of the imposed displacement/pressure on the footing,

geostatic stresses must be calculated. When the soil surface, the boundaries between soil layers, and the phreatic level (groundwater table) are all horizontal, we can invoke the so-called *"K_0 procedure"* in PLAXIS to calculate initial geostatic stresses due to gravity. For the case at hand, with reference to the coordinate system of Figure 4.18 that follows PLAXIS nomenclature:

Vertical geostatic total stress $\sigma_{y0} = \gamma y$

where γ is the unit weight of the soil and y the vertical distance from the surface, and

Horizontal geostatic total stress $\sigma_{x0} = K_0 \sigma_y$

where K_0 is the lateral earth pressure coefficient at-rest. Effective stresses will be equal to the total stresses, as no groundwater is present. K_0 can be entered manually, or calculated automatically by PLAXIS as:

- $K_0 = 1\text{-}\sin\varphi'$ when the Mohr-Coulomb non-linear material model is used
- $K_0 = \nu'/(1\text{-}\nu')$ when the linear elastic material model is used

where φ' is the friction angle of soil, and ν' is its drained Poisson's ratio. Subsequently a "plastic" analysis step is executed, during which the loading is activated. The deformed mesh at the end of the analysis with the rigid footing is presented in Figure 4.21a, when displacement has reached its ultimate value of 30 mm.

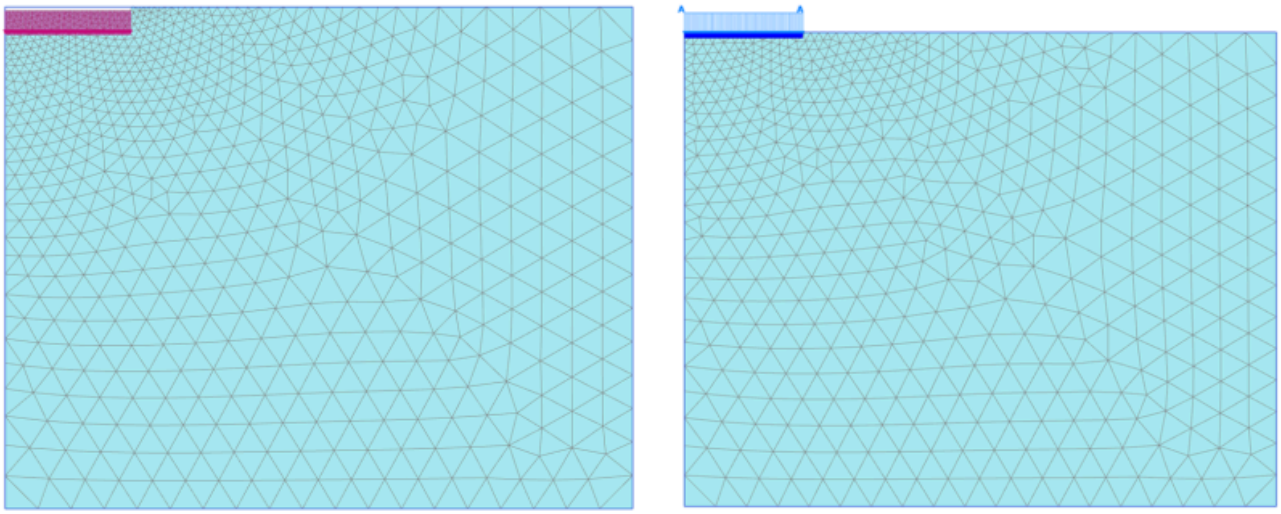

Figure 4.21. Deformed mesh of (a) rigid footing and (b) flexible footing models.

The corresponding pressure at the footing is 137.5 kPa. Note that PLAXIS provides the reaction force in axisymmetric problems in kN/rad, since we are simulating a 1-rad slice of the three-dimensional geometry (see Figure 3.17). To calculate the total reaction force, the reaction force from PLAXIS must be multiplied by 2π. The deformed mesh at the end of the analysis with the flexible footing is presented in Figure 4.21b. The deformed mesh shape is, as expected, very similar, while the ultimate settlement of the flexible footing is equal to 29 mm. Notice also that the normal stress distribution below the rigid footing, depicted in Figure 4.22, is compatible with the theoretical distribution presented in Figure 4.10b.

Figure 4.22. Contact (normal) stress distribution below the rigid footing.

The load-settlement curves, and the comparison between the solution for the rigid footing and the flexible footing are presented in Figure 4.23. Again, as expected, both curves are very similar, implying that the effect of the rigidity of the footing on the load-settlement response is minimal in this particular problem. However, this is not the case for the effect of flow rule (dilatancy). Notice that when associated flow is considered ($\psi = \varphi'$), settlements for given loading are underestimated considerably. A detailed discussion on the causes of that are again beyond the scope of this Part. However, the reader must bear in mind that when we are simulating a material with a non-associated flow rule we introduce localisations in the solution (observable in Figure 4.23 with the form of some "oscillations" in the force-displacement curve), that result in local yielding of finite elements and reduction of the overall stiffness of the soil below the footing. Secondly, the flow rule is related with constraints in the kinematics of the shear bands formed in sand, which are minimum in the case of associated flow. As consequence, settlement under the same loading is lower.

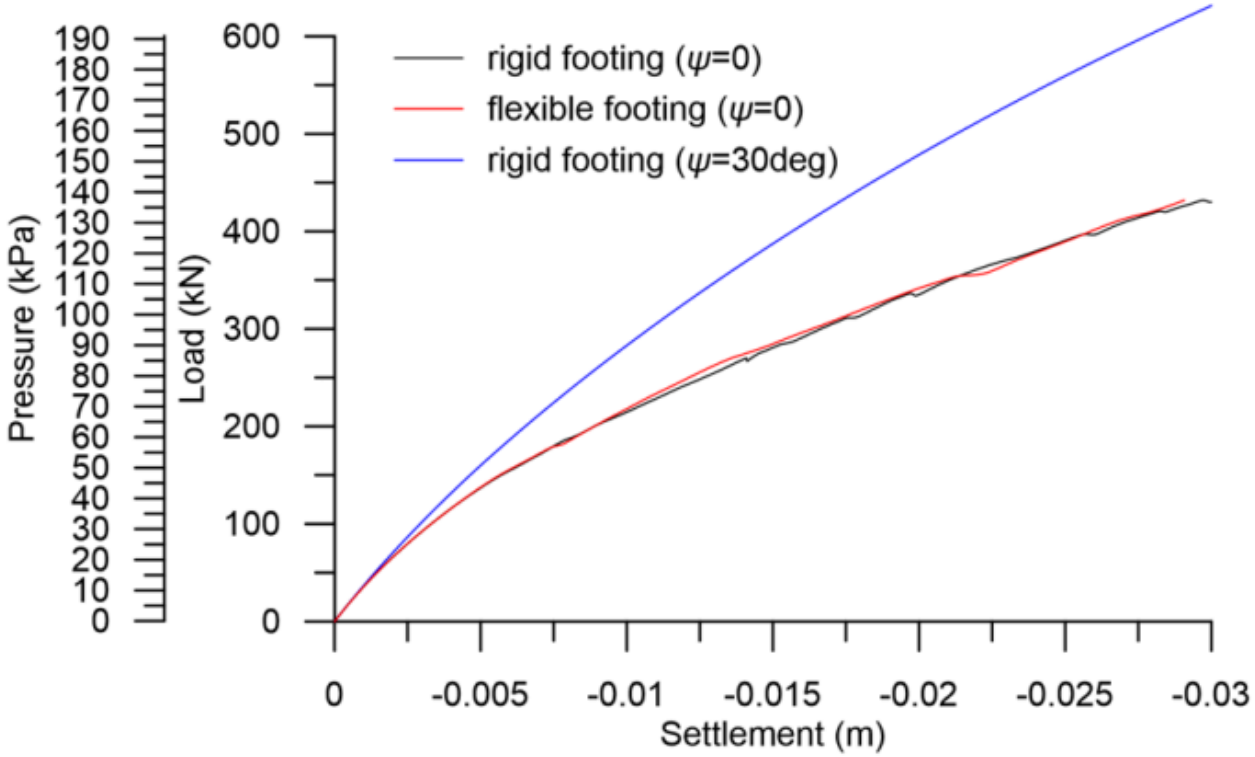

Figure 4.23. Load-displacement curves derived from the analyses for rigid (for $\psi = 0$ and for $\psi = \varphi'$) and flexible footing (for $\psi = 0$).

4.6 PRIMARY CONSOLIDATION SETTLEMENT OF SHALLOW FOUNDATIONS

4.6.1 General considerations

Primary consolidation settlement is usually the larger portion of the total settlement developing in structures founded in fine-grained soft soils, at least when the applied loading is a small fraction of the collapse loading. When the applied working loading is near the collapse loading, immediate settlement is also very important, but generally good engineering practice suggests that the working loading should be considerably less than the collapse loading. Generally, we are interested not only in the magnitude of the primary consolidation settlement, but also in the evolution of settlement with time. Depending on the properties of the soil, and especially on its permeability, consolidation settlement may continue evolving for years, as in the case of the famous Leaning Tower of Pisa (Figure 4.24), although the author would argue that time-dependent tilt of the Tower of Pisa involves more complex mechanisms than the ones described in this section.

The methodology that should be followed for the estimation of the consolidation settlement of shallow foundations depends on the geometry of the problem, and more specifically on the width of the foundation, B compared to the thickness of the compressible layer of saturated clay, H (Figure 4.25). Two cases are identified:

Figure 4.24. Leaning Tower of Pisa by Softeis, via Wikimedia Commons, is licensed under CC BY-SA 3.0.

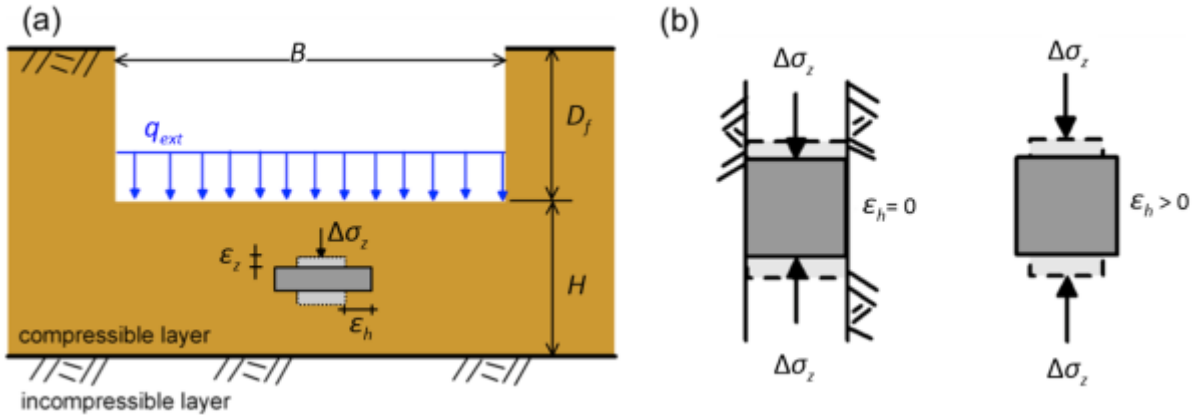

Figure 4.25. (a) Definition of the dimensions involved in the determination of consolidation settlement of shallow foundations, and (a) Lateral strain development under 1-D and 3-D consolidation conditions.

If the width of the loaded area is significantly larger than the thickness of the compressible layer $B >$ (3 to 4)H, we can assume 1-D loading conditions i.e., the lateral strain can be taken equal to zero $\varepsilon_x = \varepsilon_h = 0$. Furthermore, the additional total stress due to the applied loading $\Delta\sigma_z$ can be assumed practically constant with depth (see Figure 3.11 and Example 4.3), and will be equal to the applied pressure on the foundation level $\Delta\sigma_z = q_{ext}$. At the end of consolidation, when the excess pore pressures have dissipated it will be $\Delta\sigma'_z = q_{ext}$. In the light of these assumptions, the primary consolidation settlement ρ_{pc} is estimated from 1-D consolidation theory:

(4.17) $$\rho_{pc} = \rho_{1-D}$$

On the other hand, if the width of the loaded area is comparable to the thickness of the compressible layer $B <$ (3 to 4)H, significant lateral strain will inevitably develop $\varepsilon_x = \varepsilon_h \neq 0$ (Figure 4.25b and Figure 4.9), and loading conditions are no longer one-dimensional. As lateral strains develop, the excess pore pressure Δu immediately after the application of the external loading is lower than the 1-D case, where $\Delta u = \Delta\sigma_z$. On top of that, the variation of the additional stress $\Delta\sigma_z$ with depth must be considered (according to Part 3) so $\Delta\sigma_z < q_{ext}$.

In view of the above, the primary consolidation settlement ρ_{pc} will be less that the settlement that would be estimated from 1-D consolidation theory:

(4.18) $$\rho_{pc} = \mu\rho_{1-D}$$

where $\mu < 1.0$ is a factor depending on the geometry of the footing, the thickness of the compressible layer, and the properties of the soil.

Methodologies for estimating the magnitude of the primary consolidation settlement of shallow foundations for both cases mentioned above are presented in the following paragraphs, while the evolution of settlement with time is discussed in Chapter 4.8.

4.6.2 Estimation of primary consolidation settlement of shallow foundations and embankments under 1-D loading conditions

Primary consolidation settlement under 1-D conditions can be estimated either on the basis of linear consolidation theory, or using the oedometer laboratory test results. Focusing first on the former, consider a soil particle below the surface loaded with a compressive pressure q_{ext} (Figure 4.26). At $t = t_c$, (see Chapter 4.8) when excess pore pressures will have dissipatedand the full primary consolidation settlement will have developed, the total external pressure will have been transferred to the soil skeleton, as effective stress (Figure 4.26). The volume of a soil column with unit width will have decreased from:

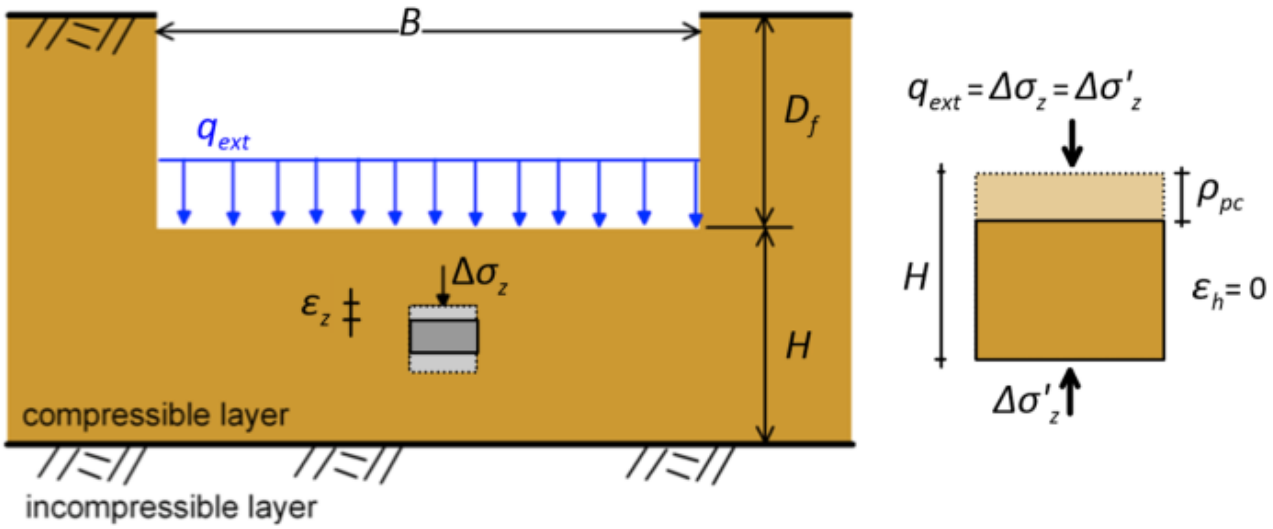

Figure 4.26. 1-D consolidation conditions.

(4.19) $V_{original} = H \times 1 \times 1$

to

(4.20) $V_{final} = (H - \rho_{pc}) \times 1 \times 1$

so the volumetric strain $\varepsilon_{vol} = \varepsilon_x + \varepsilon_y + \varepsilon_z = \varepsilon_z$ for 1-D conditions will be equal to:

(4.21) $$\varepsilon_{vol} = \frac{\Delta V}{V} = \frac{H - H + \rho_{pc}}{H} = \frac{\rho_{pc}}{H}$$

where ρ_{pc} is the primary consolidation settlement, and H is the thickness of the compressive layer. The volumetric strain is related to the soil properties via the *coefficient of volume compressibility* (or *coefficient of volume decrease*) m_v as:

(4.22) $\varepsilon_{vol} = m_v \Delta\sigma'_z$

where $\Delta\sigma'_z$ is the additional effective stress due to the application of the external loading. The coefficient of volume compressibility is associated to the drained Young's modulus and Poisson's ratio of the soil E', v' as:

(4.23) $$m_v = \frac{(1 + v')(1 - 2v')}{(1 - v')E'}$$

For the common case of $v' = 0.333$ it is $m_v = 2/(3E')$. Substituting now Eq. 4.22 into Eq. 4.21 yields the expression for estimating consolidation settlement assuming linear elastic response of the soil, as:

(4.24) $$\rho_{pc} = \varepsilon_{vol} H = m_v \Delta\sigma'_z H$$

The main drawback of this approach is that, in reality, the coefficient of volume compressibility m_v is not constant, but depends on the stress level (as E' does). This suggests that we must select an m_v value compatible with the expected stress level.

It is worth noting here that Eq. 4.24 can be used together with Eq. 4.23 to calculate total settlement of coarse-grained soils too, when subjected to 1-D loading conditions. It is based on the theory of elasticity, hence it is applicable to any material that can be assumed to behave as elastic. At the end of consolidation, when excess pore pressures have completely dissipated, both fine grained and coarse grained soils will behave as drained, therefore the same linear elastic formulas can be used to estimate their deformations.

Methods for calculating consolidation settlement of fine-grained soils provide reasonably accurate results, if the stress applied in soil does not result in soil yielding i.e., the final vertical effective stress of soil does not exceed its preconsolidation stress σ'_c which, for vertical loading, is the maximum vertical stress that the soil has undergone in the past σ'_{zc}. If this is not the case, then selecting an appropriate m_v value is cumbersome, because m_v increases rapidly as the applied stress in soil exceeds σ'_c.

Alternatively, 1-D consolidation settlement can be estimated on the basis of laboratory test results, considering explicitly non-linear soil response. In that case we do not have to select an appropriate stress level to "calibrate" soil stiffness. The phenomenon of consolidation can be replicated in the laboratory with the *oedometer* device: an undisturbed soil specimen is placed in a cylindrical mold, with porous stones positioned on the top and at the bottom of the sample, to allow drainage (Figure 4.27). The mold is rigid, and no lateral strains are allowed to develop, therefore ensuring 1-D conditions. A load is applied on the top of the specimen, and the variation of the void ratio of the soil with applied pressure and time is measured.

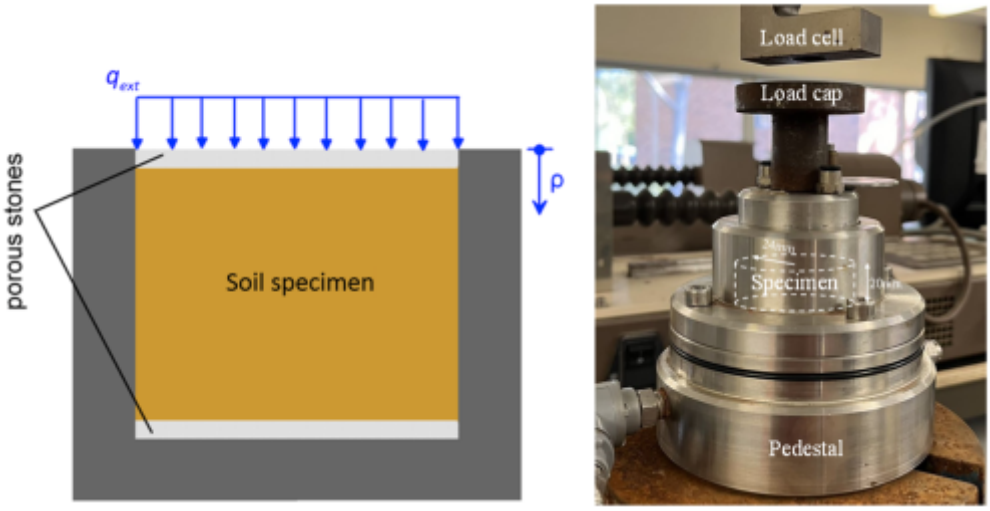

Figure 4.27. 1-D simulation of primary consolidation in the laboratory, with the oedometer test device. Schematic (left) and Constant-Rate-of-Strain oedometer rig at the University of Newcastle laboratory (right).

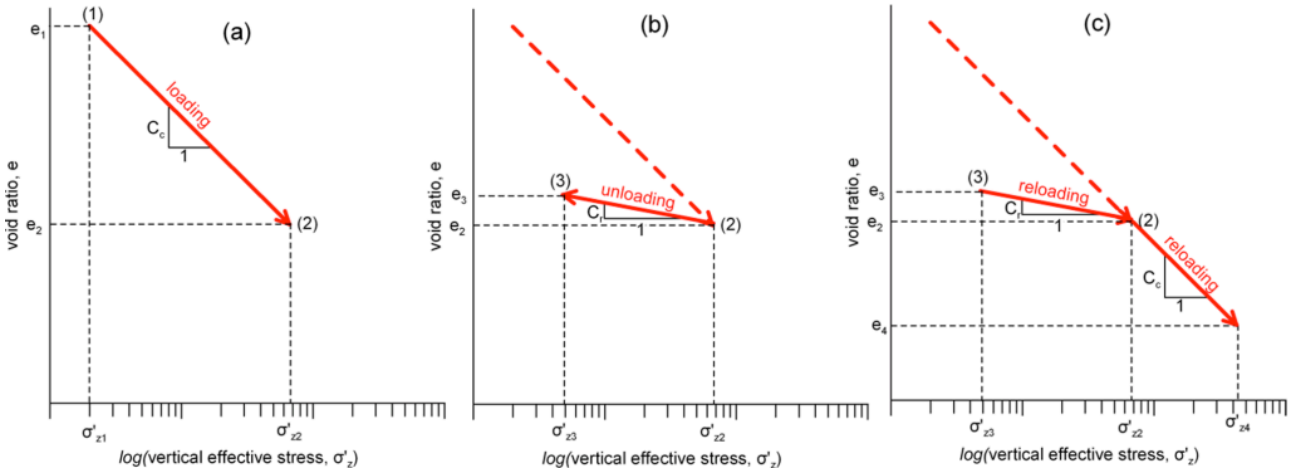

Figure 4.28. Stages of the oedometer test: (a) virgin loading, (b) unloading, and (c) reloading.

It is reminded that the *void ratio*, *e* is equal to the volume of the voids over the volume of solids of the soil specimen:

$$\textbf{(4.25)}\ e = \frac{V_v}{V_s}$$

and the initial *specific volume* of the soil sample is $v = 1+e_0$, with e_0 being the initial void ratio. Keeping in mind that changes in the soil volume are due to changes in the volume of voids only, the volumetric strain is written as:

$$\textbf{(4.26)}\ \varepsilon_{vol} = \frac{\Delta V}{V} = -\frac{\Delta e}{1+e_0}$$

The minus sign in Eq. 4.26 suggests that positive volumetric strains are compressive. Results of the oedometer test are usually plotted in *e*-logσ'_z graphs, as shown in Figure 4.28. From the initial loading stage, where the effective stress increases from σ'_{z1} to σ'_{z2} (Figure 4.28a), we can define the slope of the *normal consolidation line NCL* [path (1)-(2), Figure 4.29]:

$$\textbf{(4.27)}\ C_c = -\frac{e_2 - e_1}{\log\frac{\sigma'_{z2}}{\sigma'_{z1}}}$$

The slope of the normal consolidation line C_c in the *e*-logσ'_z space is called *compression index*. If we unload the sample from effective stress σ'_{z2} to a lower effective stress σ'_{z3}, the soil will not follow the initial loading line, but rather the *unloading-reloading line URL* [path (2)-(3), Figure 4.29] in Figure 4.28b. The slope of this line C_r called *recompression index*

$$\textbf{(4.28)}\ C_r = -\frac{e_3 - e_2}{\log\frac{\sigma'_{z3}}{\sigma'_{z2}}}$$

will be lower than the slope of the normal consolidation line, due to the fact that soil is actually a non-linear material, and application of the stress σ'_{z2} resulted in irreversible changes in the soil fabric. In the hypothetical case where the soil behaved elastically, the recompression index would be equal to the compression index $C_c = C_r$. If we reload the soil from stress σ'_{z3}, it will follow the unloading-reloading line [path (3)-(2)] until it reaches the maximum vertical effective stress applied previously, σ'_{z2}. The void ratio variation along the path (3)-(2), and thus the increase in vertical deformation (settlement), will be relatively small, because the soil fabric has been permanently changed in the past.

However, if the soil is further subjected to stresses higher than the past maximum vertical effective stress σ'_{z2}, along the path (3)-(2)-(4) in Figure 4.29, the settlement for the stress increase along the path (2)-(4) will be higher for the same stress increase, compared to the path (3)-(2), as the soil will now undergo further fabric change. The slope of the path (2)-(4) is equal to the slope of the path (1)-(2) i.e., equal to the compression index.

If the maximum vertical stress that the soil has undergone in the past is σ'_{zc} (referred to as yield stress or preconsolidation stress, as explained earlier) and its geostatic (current) vertical effective stress is σ'_{z0} we can define the *overconsolidation ratio* OCR as:

(4.29) $$\mathrm{OCR} = \frac{\sigma'_{zc}}{\sigma'_{z0}}$$

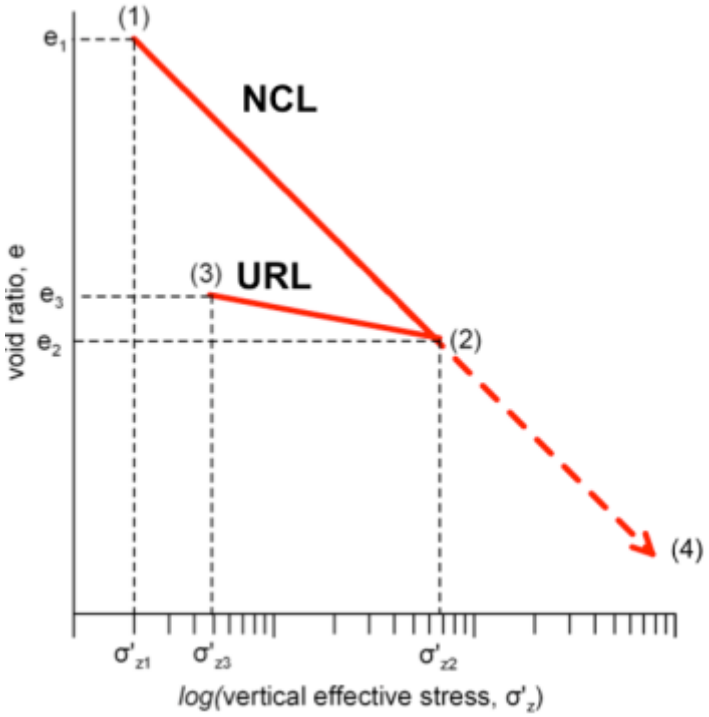

Figure 4.29. Reloading of a soil sample at a stress higher than the past maximum vertical effective stress in the oedometer test.

Soils with OCR > 1 are called *"overconsolidated"*, and will follow a path similar to (3)-(2)-(4) when loaded. Soils with OCR = 1 are called *"normally consolidated"*, and will follow a path similar to (1)-(2)-(4) upon loading. It must be noted here that natural soils on which onshore structures are founded rarely, if ever, feature OCR = 1. That is because fluctuation of water table levels over the geological history of a soil deposit will result in variation of effective soil stress, thus introduce some overconsolidation. Therefore even soft clays will generally have OCR > 1.1-1.2. This does not apply to soil samples that are reconstituted in the laboratory, for with OCR will be equal to OCR = 1. On a similar note, OCR cannot be less than 1 in the field, unless during soil deposition, when excess pore pressures may exist. However, this is mainly of theoretical interest.

Using the results obtained from oedometer tests in undisturbed soil specimens i.e., the values of the compression and the recompression index, the initial void ratio and the preconsolidation stress (or OCR), we can estimate the primary consolidation settlement of both normally consolidated and overconsolidated soils. Assume that the initial e.g., geostatic vertical effective stress is equal to σ'_{z0}, and an external loading is applied, increasing the effective stress after dissipation of excess pore water pressure by $\Delta\sigma_z$ to:

(4.30) $$\sigma'_{fin} = \sigma'_{z0} + \Delta\sigma_z$$

Consolidation settlement will be again equal to the product of the volumetric strain time the thickness of the compressible layer:

(4.31) $\rho_{pc} = \varepsilon_{vol} H$

In the case of a *normally consolidated* soil (Figure 4.30) the volumetric strain will be:

(4.32) $$\varepsilon_{vol} = -\frac{\Delta e}{1+e_0} = -\frac{e_{fin}-e_0}{1+e_0}$$

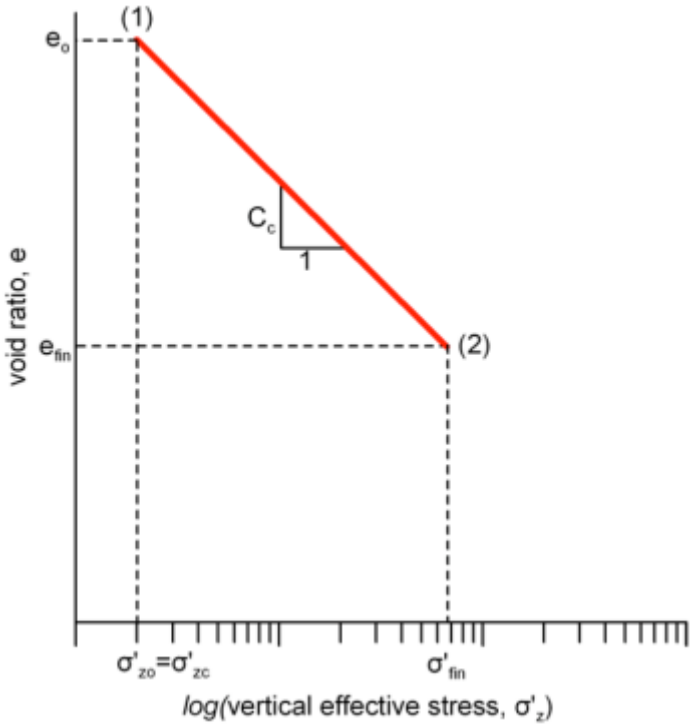

Figure 4.30. Estimation of the primary consolidation settlement of a normally consolidated soil from the oedometer test.

And, from Figure 4.30, the compression index will be:

(4.33) $$C_c = -\frac{e_{fin}-e_0}{\log\dfrac{\sigma'_{fin}}{\sigma'_{z0}}}$$

Combining Eqs. 4.31 to 4.33 provides the primary consolidation settlement as:

(4.34) $$\rho_{pc} = \frac{H}{1+e_0} C_c \log\frac{\sigma'_{fin}}{\sigma'_{z0}}$$

Observe in Figure 4.30 that the compression index C_c, unlike the coefficient of volume compressibility m_v, does not depend on the stress level (at least for soils without a natural structure). As mentioned above, when using linear theory to estimate consolidation settlement, the coefficient of compressibility m_v should be estimated while considering an average value of E' corresponding to stress levels between σ'_{z0} and σ'_{fin} (see also Figure 4.14b).

In the case of an *overconsolidated* soil, pre-consolidated at vertical stress σ'_{zc} (Figure 4.31), we have to distinguish two different subcases:

If the final stress is lower than preconsolidation stress $\sigma'_{fin} < \sigma'_{zc}$, then the soil will follow the URL in Figure 4.31, and the settlement will be:

(4.35) $$\rho_{pc} = \frac{H}{1+e_0} C_r \log \frac{\sigma'_{fin}}{\sigma'_{z0}}$$

In the case however where the final vertical stress is higher than the preconsolidation stress $\sigma'_{fin} > \sigma'_{zc}$, then the soil will follow initially the URL, until the applied stress reaches σ'_{zc}, and accordingly the NCL, along the path (2)-(4) (Figure 4.31). The settlement in that case will be:

(4.36) $$\rho_{pc} = \frac{H}{1+e_0} \left[C_r \log \frac{\sigma'_{zc}}{\sigma'_{z0}} + C_c \log \frac{\sigma'_{fin}}{\sigma'_{zc}} \right]$$

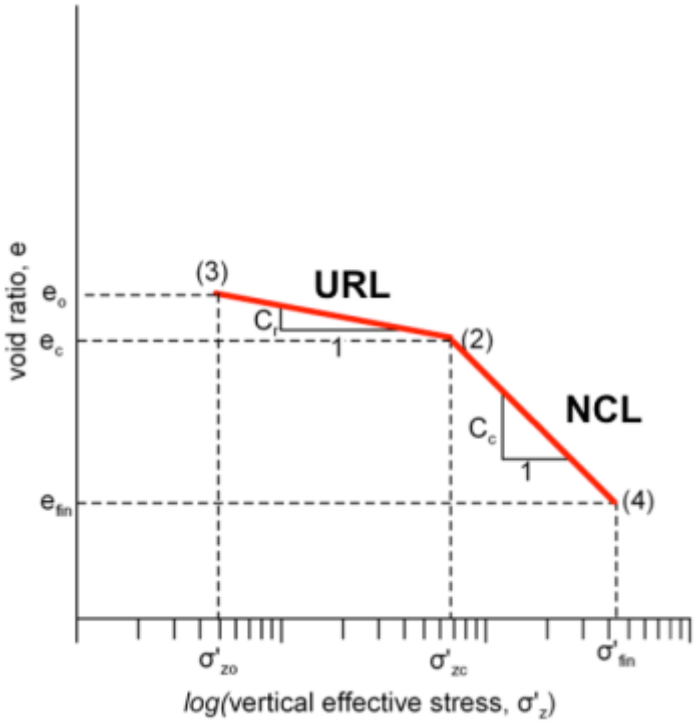

Figure 4.31. Estimation of the primary consolidation settlement of an overconsolidated soil from the oedometer test.

4.6.3 Primary consolidation settlement of shallow foundations under 3-D loading conditions.

Skempton and Bjerrum (1957) proposed a method to modify the one-dimensional consolidation Eq. 4.24 by introducing the factor μ_{SB}, to account for the development of lateral strains below footings of finite dimensions:

(4.37) $$\rho_{pc} = \mu_{SB} m_v \Delta\sigma'_z H$$

or, if we divide the compressible layer into n sublayers with thickness H_i :

(4.38) $$\rho_{pc} = \mu_{SB} \sum_{i=1}^{n} m_v \Delta\sigma'_z H_i$$

Values of μ_{SB} can be estimated from Figure 4.32, depending on the geometry of the footing, the thickness of the compressive layer H, and Skempton's pore water coefficient A at failure, calculated as $\Delta u = B[\Delta\sigma_3 + A(\Delta\sigma_1 - \Delta\sigma_3)]$ during triaxial undrained stress. As $B = 1$ for fully saturated samples, essentially A provides the excess pore pressure Δu that develops during the shearing stage of a triaxial test while applying a deviatoric stress $(\Delta\sigma_1 - \Delta\sigma_3)$. A is not constant during the test, and at failure it ranges from $A = 0.5$ to $A = 1.0$ for normally consolidated clays, and from $A = 0$ to $A = 0.5$ for stiff-to-hard overconsolidated clays. For linear elastic soil material it is $A = 1/3$. Thus while Eq. 4.37 resembles Eq. 4.24 used above to estimate consolidation settlement of linear elastic soil, the factor μ_{SB} actually accounts for non-linear soil behaviour via the coefficient A. For intermediate values of the thickness-to-width ratio H/B, linear interpolation can be used. Figure 4.32 is also applicable to square or rectangle footings, by considering an equivalent circular footing of diameter:

(4.39) $$B = 2\sqrt{\frac{A_f}{\pi}}$$

where A_f is the area of the square or the rectangle.

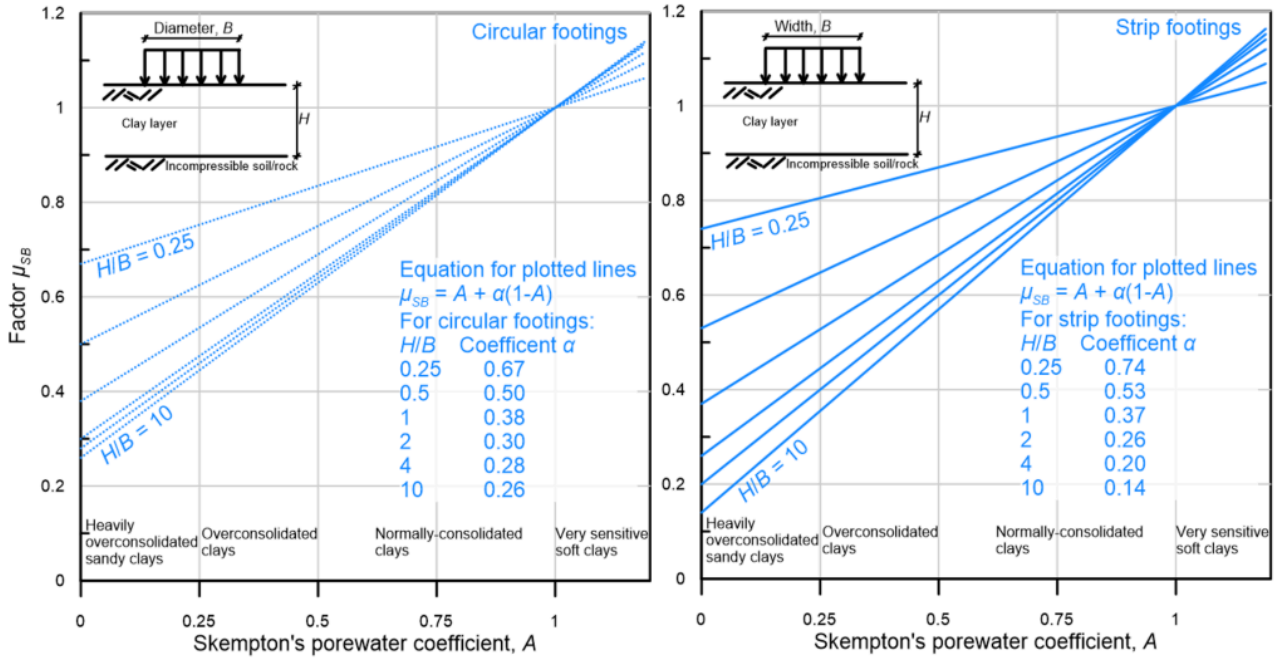

Figure 4.32. Values of the settlement factor μ_{SB} for circular and strip footings.

The above method provides only the settlement below the center of a footing. Finally, it is worth stressing out that this method provides settlement at the end of consolidation i.e., immediate settlement calculated according to Section 4.5.5 should be added to consolidation settlement calculated by means of Eq. 4.38.

EXAMPLE 4.3

Estimation of 1-D primary consolidation settlement assuming linear elastic soil response

Calculate the primary consolidation settlement due to the strip pressure of the figure, assuming linear elastic soil response.

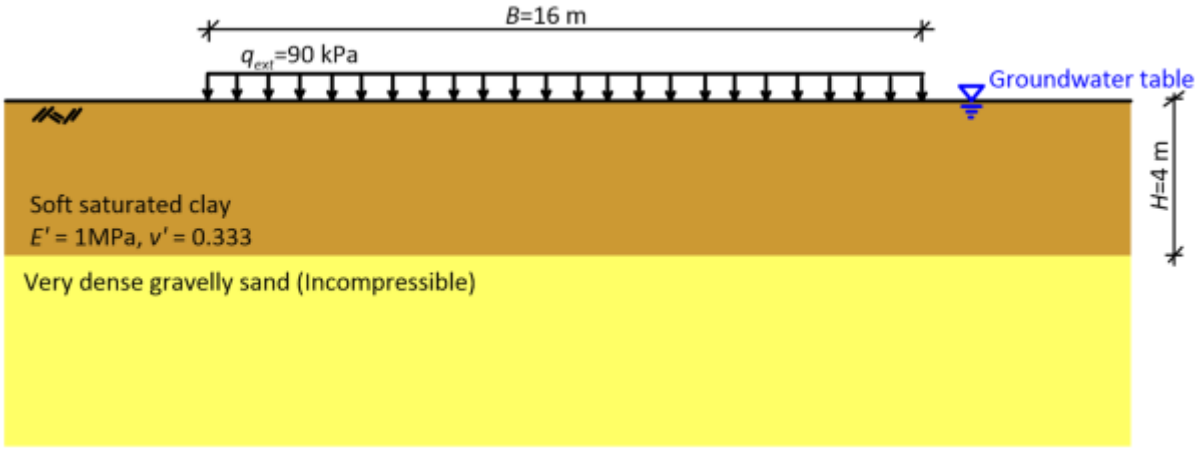

Example 4.3. Problem description and input parameters.

Answer:

The width of the loaded area B = 16 m is large, compared to the thickness of the compressible layer H = 4 m, B > (3 to 4)H so we can effectively assume 1-D consolidation conditions. After excess water pore pressure has dissipated, the additional effective stress $\Delta\sigma'_z$ due to the application of the external pressure will be equal to the applied pressure i.e., $\Delta\sigma'_z = q_{ext}$ = 90 kPa. In order to apply Eq. 4.24 to find the final value of consolidation settlement, we have to estimate first the coefficient of volume compressibility from Eq. 4.23 as:

$$m_v = \frac{(1+v')(1-2v')}{(1-v')E'} = \frac{2}{3E'} = 6.666 \times 10^{-4}\frac{\text{m}^2}{\text{kN}}$$

Substituting in Eq. 4.24 yields:

$$\rho_{pc} = m_v \Delta\sigma'_z H = 6.666 \times 10^{-4}\frac{\text{m}^2}{\text{kN}} \times 90\frac{\text{kN}}{\text{m}^2} \times 4\,\text{m} = 0.24\,\text{m}$$

Note that the effective stress in Eq. 4.24 is the additional effective stress due to application of the pressure, not including the geostatic effective stress: settlement is due to changes in effective stress, and is not related to its absolute value when linear elastic response is assumed.

The actual distribution of vertical stresses beneath the axis of the strip pressure is shown below, calculated according to the mentioned in Chapter 3.4. It is clear that assuming the additional stress in the compressible layer to be constant and equal to the applied pressure on the surface $\Delta\sigma'_z = q_{ext}$ = 90 kPa is a quite reasonable assumption, when the thickness of the compressible layer is small compared to the width of the pressure B > (3 to 4)H.

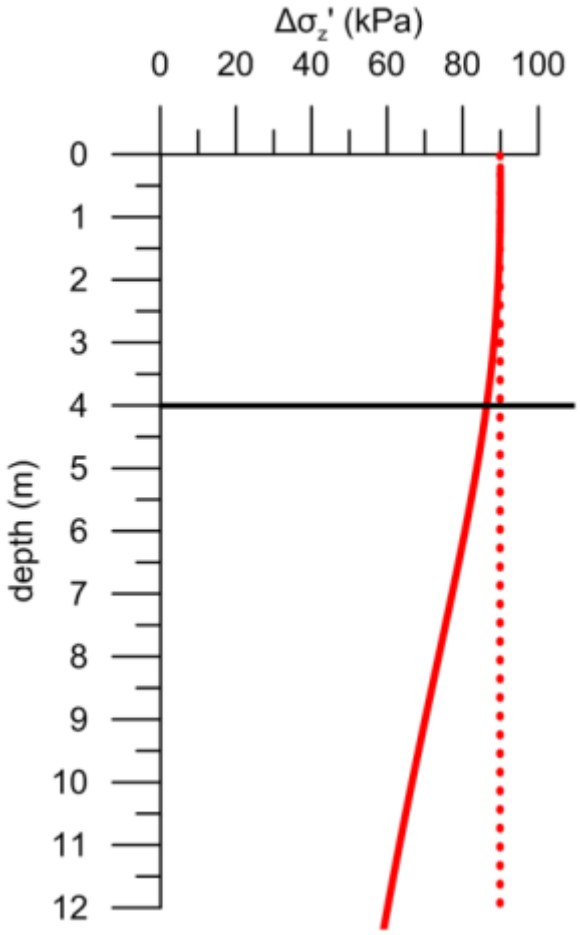

Example 4.3. Variation of additional vertical effective stresses with depth.

EXAMPLE 4.4

Estimation of a 1-D primary consolidation settlement using the results of an oedometer test

Calculate again the primary consolidation settlement due to the strip pressure, using this time the oedometer test results depicted in the figure.

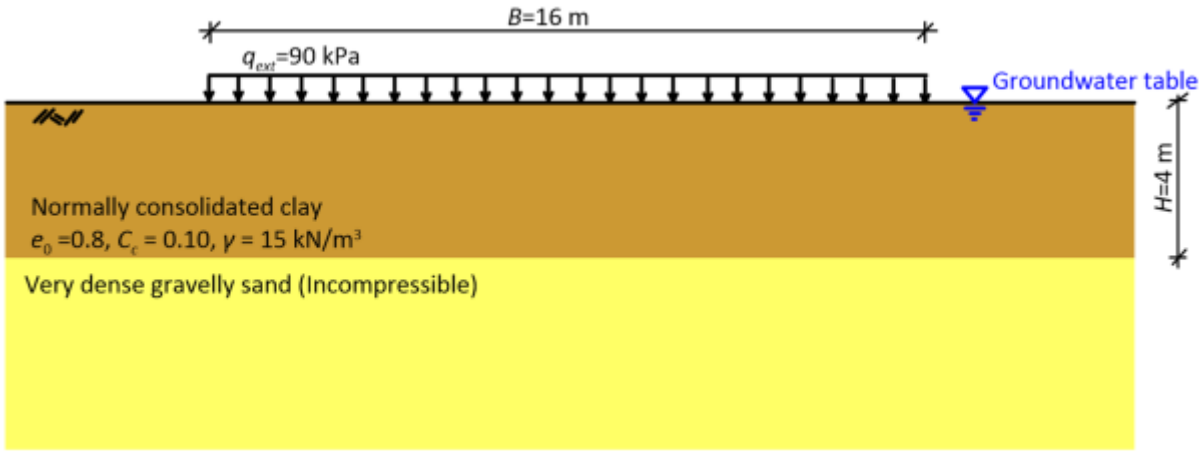

Example 4.4. Problem description and input parameters.

Answer:

As discussed in Example 4.3, the width of the loaded area is large, compared to the thickness of the compressible layer so we can well assume 1-D consolidation conditions. The additional effective stress $\Delta\sigma'_z$ due to the application of the pressure will be equal to the applied pressure $\Delta\sigma'_z = q_{ext} = 90$ kPa.

To improve accuracy when the problem involves rather thick compressible layers ($H > 2$ m) and we are using *non-linear consolidation theory*, we can divide the layer into sublayers, and find the settlement of each sublayer (Figure 4.33) separately.

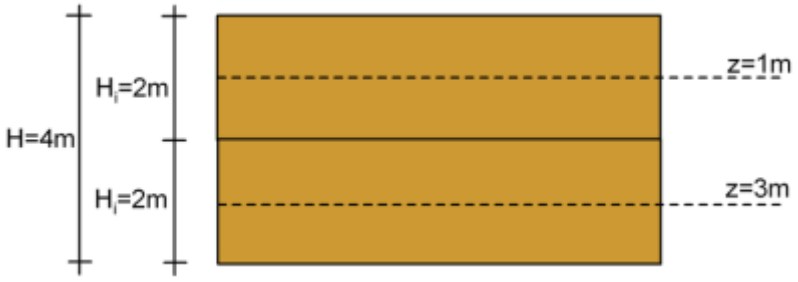

Figure 4.33. Dividing the compressible layer into two sublayers.

Accordingly, we sum individual settlements to find the settlement of the entire compressible layer. In the corresponding equations, H will be the thickness of each sublayer (H_i), and the effective stresses will be calculated at the middle of each sublayer.

As the clay is normally consolidated, we will apply Eq. 4.34 for the estimation of the settlement of each sublayer. The necessary calculations are presented in the table below:

Example 4.4. Settlement calculation.

	Geostatic total stress $\sigma_{z0} = \gamma z$	**Hydrostatic pore pressure $u_0 = \gamma_w z$**	**Geostatic effective stress $\sigma'_{z0} = \sigma_{z0} - u_0$**	**Final effective stress $\sigma'_{fin} = \sigma'_{z0} + q_{ext}$**	**$\log(\sigma'_{fin}/\sigma'_{z0})$**	**Settlement of each sublayer, ρ_{pc}**
Sublayer 1 (H_i = 2m)	15 kPa	10 kPa	5 kPa	95 kPa	1.278	0.14 m
Sublayer 2 (H_i = 2m)	45 kPa	30 kPa	15 kPa	105 kPa	0.845	0.09 m
				Total settlement:		**0.23 m**

As expected, settlement of sublayers 1 and 2 is not equal, as the preconsolidation stress (equal in this case to the initial, geostatic effective stress as the clay is normally consolidated) increases with depth, while the applied pressure on both is 90 kPa. This is illustrated in the figure below, where the path followed by a soil element at the middle of each sublayer is presented, and is a consequence of introducing soil non-linear response in consolidation calculations.

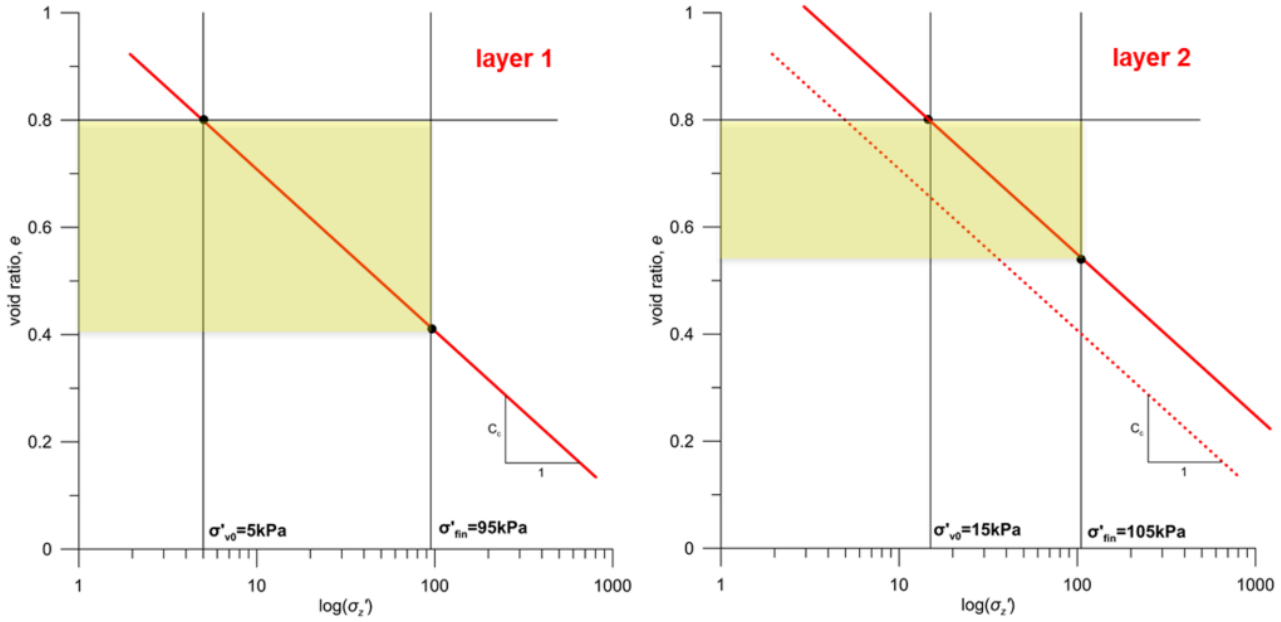

Example 4.4. Stress paths followed by soil elements at the middle of layer 1 and layer 2.

EXAMPLE 4.5

Estimation of 2-D primary consolidation settlement

Calculate the primary consolidation settlement below the axis of symmetry of the circular footing shown below.

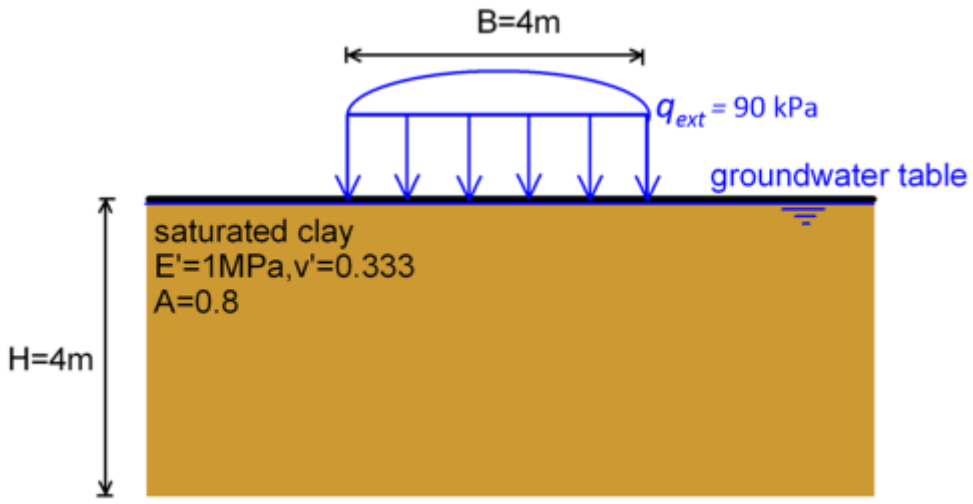

Example 4.5. Problem description and input parameters.

The diameter of the footing B = 4 m is comparable to the thickness of the compressible layer H = 4 m, B < (3 to 4)H so we have to take into account the development of lateral strains during the estimation of primary consolidation settlement.

For simplicity: a) we will consider the compressible layer as an elastic half-space for the calculation of stresses, as the additional effective stress due to the pressure from the footing $\Delta\sigma'_z$ cannot be assumed to remain constant with depth, and b) we will not divide the compressible clay layer into sublayers. The effect of the former assumption on settlement estimates is discussed in the next Chapter.

The expression for estimating vertical stresses below the axis of symmetry of a circular pressure is provided in Chapter 3.5:

$$\Delta\sigma_z = q_{ext}\left[1-\left(\frac{1}{1+\left(\frac{B}{2z}\right)^2}\right)^{\frac{3}{2}}\right]$$

where $B/2$ is the footing radius. At the middle of the compressible layer z = 2 m:

$$\Delta\sigma_z = 90\left[1-\left(\frac{1}{1+\left(\frac{2}{2}\right)^2}\right)^{\frac{3}{2}}\right] = 58.18\ \text{kPa}$$

At the end of consolidation $\Delta\sigma'_z = \Delta\sigma_z$. For $H/B = 1$, $A = 0.8$ and circular footing geometry, Figure 4.32 provides a settlement correction factor $\mu_{SB} \approx 0.87$. Furthermore, the coefficient of volume compressibility is calculated from Eq. 4.23 as:

$$m_v = \frac{(1+v')(1-2v')}{(1-v')E'} = \frac{2}{3E'} = 6.666 \times 10^{-4} \frac{\mathrm{m}^2}{\mathrm{kN}}$$

Substituting in Eq. 4.37 results in a primary consolidation settlement due to the pressure applied on the footing equal to:

$$\rho_{pc} = \mu_{SB} m_v \Delta\sigma'_z H = 0.87 \times 6.666 \times 10^{-4} \times 58.18 \times 4 = 0.13\ \mathrm{m}$$

4.7 IMMEDIATE AND CONSOLIDATION DEFORMATIONS UNDERNEATH SHALLOW FOUNDATIONS IMPOSING 3-D LOADING CONDITIONS

A theory of elasticity approach

There are many practical situations where we do not merely seek to predict settlement at the centre of a footing (or a loaded area in general), but instead we wish to predict how a footing or an embankment will deform immediately after construction, and at the end of consolidation e.g., when differential settlement, tilt or even horizontal ground movements are important. This task can be performed analytically by means of theory of elasticity formulas. However, these come with some pitfalls. These pitfalls are explored with the aid of the following example, where predictions of analytical formulas are compared against results of numerical simulations.

Consider the flexible strip footing applying uniform pressure studied in Example 4.3. The footing is transferring pressure q_{ext} = 90 kPa to a soft saturated clay layer, which is underlaid by practically incompressible dense gravelly sand deposits (Figure 4.34). Unlike Example 4.3, here the width of the loaded area B is less than (3 to 4)H, where H is the thickness of the compressible layer. As such we cannot treat this problem as 1-D. Settlement under the centre of the footing will not be equal to settlement near its edges, and the shape of the deformed soil surface will be concave upward, as shown in Figure 4.11. Here we will compute the profile of vertical soil deformations with depth immediately after application of the pressure, and at the end of consolidation at: i) The middle of the footing (Point A, Figure 4.34), and ii) its edge (Point B, Figure 4.34). We will use analytical formulas to compute soil stress and deformations on the basis of theory of elasticity, and we will compare our results to those of PLAXIS simulations. We will not consider geostatic stresses and hydrostatic pore pressures in the calculations, as settlement of elastic materials depends only on the additional stresses applied in soil from the external loading. Finally, the calculations shown below are for uniform soil, however the method is applicable to layered soil too.

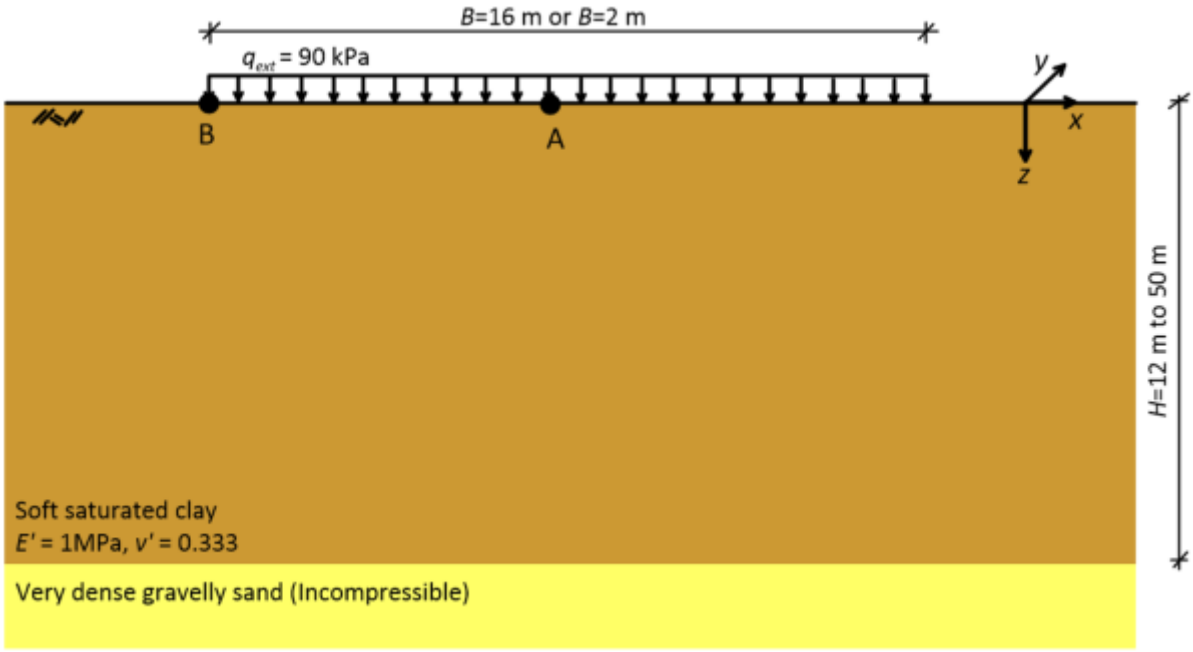

Figure 4.34. Outline of the 3-D settlement problem considered in this Chapter.

To obtain the profile of deformations at the two selected locations, we must first calculate stress increments with depth due to the strip pressure applied on the surface. Since this problem is plane-strain, out-of-plane-strains and deformations are zero, thus considering the coordinate system of Figure 4.34:

(4.40) $u_y = \varepsilon_y = \Delta\tau_{yz} = \Delta\tau_{yx} = 0$

The remaining expressions for increments of total stress due to a strip pressure acting on the surface of an infinite half-space are provided in Chapter 3.4 and are repeated here for completeness:

(4.41) $\Delta\sigma_z = \frac{q_{ext}}{\pi}\left[\alpha + \sin\alpha\cos\left(\alpha + 2\beta\right)\right]$

(4.42) $\Delta\sigma_x = \frac{q_{ext}}{\pi}\left[\alpha - \sin\alpha\cos\left(\alpha + 2\beta\right)\right]$

(4.43) $\Delta\sigma_y = v'\left(\Delta\sigma_x + \Delta\sigma_z\right)$

(4.44) $\Delta\tau_{zx} = \frac{q_{ext}}{\pi}\left[\sin\alpha\sin\left(\alpha + 2\beta\right)\right]$

where, referring to Figure 3.7, α = 2atan[$(B/2)/z$] and β = -atan[$(B/2)/z$] at Point A, while α = atan[$(B/2)/z$] and β = 0 at point B; $v'$is the drained Poisson's ratio of soil. Notice that we have three normal stress components here, which generally are all non-zero. Hence the problem is described as three-dimensional. Although these are not used as input in the calculation of soil vertical deformations, the expressions that provide principal stress increments under plane-strain conditions are shown below, for completeness.

(4.45) $\Delta\sigma_1 = \frac{q_{ext}}{\pi}\left[\alpha + \sin\alpha\right]$

(4.46) $\Delta\sigma_2 = \Delta\sigma_y$

(4.47) $\Delta\sigma_3 = \frac{q_{ext}}{\pi}\left[\alpha - \sin\alpha\right]$

The well-known constitutive expressions of an isotropic linear elastic material in three dimensions are:

(4.48) $$\varepsilon_x = \frac{1}{E'}\left[\Delta\sigma'_x - v'\left(\Delta\sigma'_y + \Delta\sigma'_z\right)\right]$$

(4.49) $$\varepsilon_y = \frac{1}{E'}\left[\Delta\sigma'_y - v'\left(\Delta\sigma'_z + \Delta\sigma'_x\right)\right]$$

(4.50) $$\varepsilon_z = \frac{1}{E'}\left[\Delta\sigma'_z - v'\left(\Delta\sigma'_x + \Delta\sigma'_y\right)\right]$$

(4.51) $$\gamma_{xy} = \frac{1}{G}\Delta\tau_{xy}; \gamma_{yz} = \frac{1}{G}\Delta\tau_{yz}; \gamma_{zx} = \frac{1}{G}\Delta\tau_{zx}$$

where E', v' are the drained Young's modulus and Poisson's ratio of soil, respectively, while G is the shear modulus. Notice that normal soil strains ε_x, ε_y, ε_z are function of effective soil stress increments, while Eqs. 4.41-4.43 provide total stress increments. At the end of consolidation it is:

(4.52) $$\Delta\sigma' = \Delta\sigma$$

Therefore we can substitute directly stress increments from Eqs. 4.41-4.43 into Eqs. 4.48-4.50 and compute soil strains and deformations.

This is not the case immediately after application of the pressure q_{ext}: Since the soft clay will behave as undrained in the short term, excess pore pressures Δu will develop in soil due to the application of the strip pressure and effective soil stresses increments will be:

(4.53) $$\Delta\sigma' = \Delta\sigma - \Delta u$$

In addition, the volumetric strain in soil $\varepsilon_{vol} = \varepsilon_x + \varepsilon_y + \varepsilon_z$ will be zero immediately after application of the strip pressure. Summation of Eqs. 4.48 – 4.50 yields:

(4.54) $$\varepsilon_{vol} = \frac{1}{K}\left(\frac{\Delta\sigma'_x + \Delta\sigma'_y + \Delta\sigma'_z}{3}\right) = 0$$

where $K = E'/3(1\text{-}2v')$ is the bulk modulus of linear elastic soil. As consequence, the mean effective stress p' under undrained conditions must be zero. Substituting Eq. 4.53 into Eq. 4.54 yields the excess pore pressure that develops at any point in soil, as function of the total stress increments provided by Eqs. 4.41-4.44:

(4.55) $$\Delta u = \left(\frac{\Delta\sigma_x + \Delta\sigma_y + \Delta\sigma_z}{3}\right)$$

It must be stated here that the above expression 4.55 holds only for linear elastic soil. In reality, excess pore pressure is function also of the deviatoric stress increment Δq, and can be calculated more accurately as:

(4.56) $$\Delta u = \Delta p + \left(A - \frac{1}{3}\right)\Delta q$$

where A is Skempton's pore pressure coefficient defined earlier in Section 4.6.3 and Figure 4.32. As mentioned earlier for linear elastic materials it is $A = 1/3$, while for soft clays a value of $A = 0.5$ is probably more representative. It is reminded here that the mean total stress increment Δp is calculated as:

(4.57) $$\Delta p = \frac{1}{3}\left(\Delta\sigma_1 + \Delta\sigma_2 + \Delta\sigma_3\right) = \frac{1}{3}\left(\Delta\sigma_x + \Delta\sigma_y + \Delta\sigma_z\right)$$

and the deviatoric stress increment Δq is calculated as:

$$\textbf{(4.58)}\ \Delta q = \frac{1}{\sqrt{2}}\sqrt{\left(\Delta\sigma_1 - \Delta\sigma_2\right)^2 + \left(\Delta\sigma_2 - \Delta\sigma_3\right)^2 + \left(\Delta\sigma_3 - \Delta\sigma_1\right)^2}$$

Let's now substitute Eq. 4.53 into Eqs. 4.50 that provides vertical strains, which are of interest here. We obtain the following expression for vertical strains as function of total stress increments and of the excess pore pressure:

$$\textbf{(4.59)}\ \varepsilon_z = \frac{1}{E'}\left[\Delta\sigma_z - v'\left(\Delta\sigma_x + \Delta\sigma_y\right) - \left(1 - 2v'\right)\Delta u\right]$$

If we combine Eq. 4.59 with Eq. 4.55 that provides Δu for linear elastic soil we obtain:

$$\textbf{(4.60)}\ \varepsilon_z = \frac{2\left(1+v'\right)}{3E'}\left[\Delta\sigma_z - \frac{1}{2}\left(\Delta\sigma_x + \Delta\sigma_y\right)\right]$$

or, in another form:

$$\textbf{(4.61)}\ \varepsilon_z = \frac{1}{E_u}\left[\Delta\sigma_z - v_u\left(\Delta\sigma_x + \Delta\sigma_y\right)\right]$$

where $E_u = 3E'/2(1+v')$ is the undrained Young's modulus of soil (Eq. 4.11) and $v_u = 0.5$ is the undrained Poisson's ratio that satisfies the requirement for zero volume change under undrained conditions. Similar expressions can be obtained for the remaining strain components, as:

$$\textbf{(4.62)}\ \varepsilon_x = \frac{1}{E_u}\left[\Delta\sigma_x - v_u\left(\Delta\sigma_y + \Delta\sigma_z\right)\right]$$

$$\textbf{(4.63)}\ \varepsilon_y = \frac{1}{E_u}\left[\Delta\sigma_y - v_u\left(\Delta\sigma_z + \Delta\sigma_x\right)\right]$$

Notice that Eqs. 4.61-4.53 are cast in terms on *total*, *not effective* stress increments, which are provided directly from Eqs. 4.41-4.43, and are independent of excess pore pressures Δu. Of course this would not be the case if we had employed Eq. 4.56, instead of Eq. 4.55, to estimate excess pore pressures.

We now have all the formulas required to calculate normal soil strains at the end of consolidation (Eqs. 4.48-4.50 together with Eq. 4.52) and immediately after application of the strip pressure (Eqs. 4.61-4.63) as function of the total stress increments. Since stress increments are function of depth z, we have to divide the soil profile into sublayers, of thickness ΔH each. As explained earlier, these sublayers may feature different compressibility properties (Young's modulus and Poisson's ratio) i.e., the method works for layered soils too. For coarse-grained layers all settlement will develop immediately after application of the pressure, and only Eqs. 4.48-4.50 are used.

After computing vertical strains at the middle of each sublayer immediately after application of the pressure with Eq. 4.61 and at the end of consolidation with Eq. 4.50, we can calculate settlement of each sublayer ρ_i as similarly to Eq. 4.24:

$$\textbf{(4.64)}\ \rho_i = \varepsilon_z \Delta H$$

Notice that in Eq. 4.64 we consider vertical strains, unlike Eq. 4.24 where we considered volumetric stains. Volumetric strains are not equal to vertical strains here, since the problem is three-dimensional. Settlement at the surface will be equal to the sum of the settlement of all sublayers.

Let's now see some typical results for the problem at hand (the relevant calculations are omitted for brevity). Figure 4.35 presents profiles of effective Cartesian stress increments and excess pore pressures with depth at the middle of the footing (Point A) and at its edge (Point B) immediately after application of the pressure, as well as profiles of total stress component increments with depth at the same locations. Results of the analytical expressions provided above are compared with the corresponding results of a PLAXIS model, developed to obtain the distribution of stresses in soil underneath the strip pressure shown in Figure

4.34 for the case of B = 16 m and H = 50 m. Good agreement is observed between stress computed with the two methods, particularly close to the surface (z = 0). There is a caveat though. The expressions provided above are for a soil profile of infinite depth, which cannot be simulated with a PLAXIS model. To obtain the results presented in the following, a 50m-thick soil layer was modelled in PLAXIS, and the bottom of the layer was fixed along both the horizontal and vertical direction. This fixity condition will affect the distribution of stresses, and consequently the predicted deformation profiles.

Profiles of vertical soil displacements at Points A and B immediately after application of the pressure and at the end of consolidation are presented in Figure 4.36. Analytical results are compared against results of a linear elastic PLAXIS simulation, considering this time B = 16 m and H = 12 m. Notice that, while the results of the analytical calculations and of the PLAXIS simulation are generally in agreement, they certainly do not match. The reason for that is the differences in the distribution of stresses that stem from the boundary conditions at the bottom of the soil layer: In PLAXIS we consider that an incompressible sandy layer is found at depth 12 m (Figure 4.34). While in the analytical calculations, even though we have considered only 12 m of soil, we are assuming that this soil layer is underlain by compressible material of infinite thickness. It is important to appreciate this limitation of hand calculations, *that is not associated with modelling soil as linear elastic material.* This suggests that the comparison between analytical results and PLAXIS will improve, as the dimensionless thickness of the layer H/B increases. Indeed, the gap between the predictions closes in Figure 4.37, which presents results for the same problem, but for H/B = 12 (case of B = 2 m wide footing on H = 24 m thick layer).

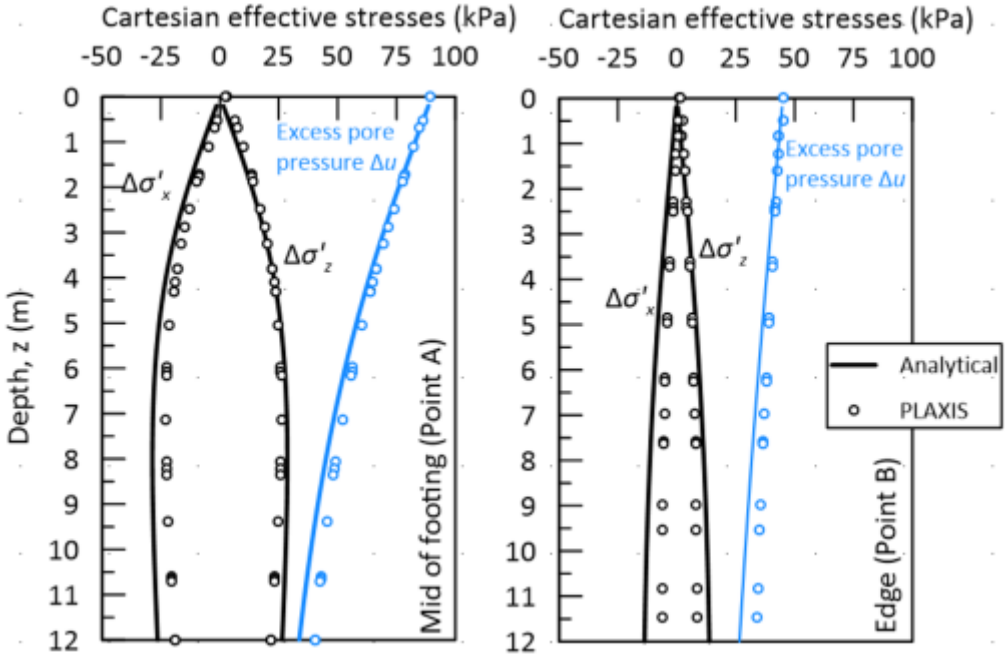

Figure 4.35a. Variation with depth of vertical and horizontal effective stress increments and of excess pore pressures immediately after application of the strip pressure, at Points A and B. Negative values correspond to tension. Results for 16m-wide footing on 50m-thick soil layer (H/B = 3.125).

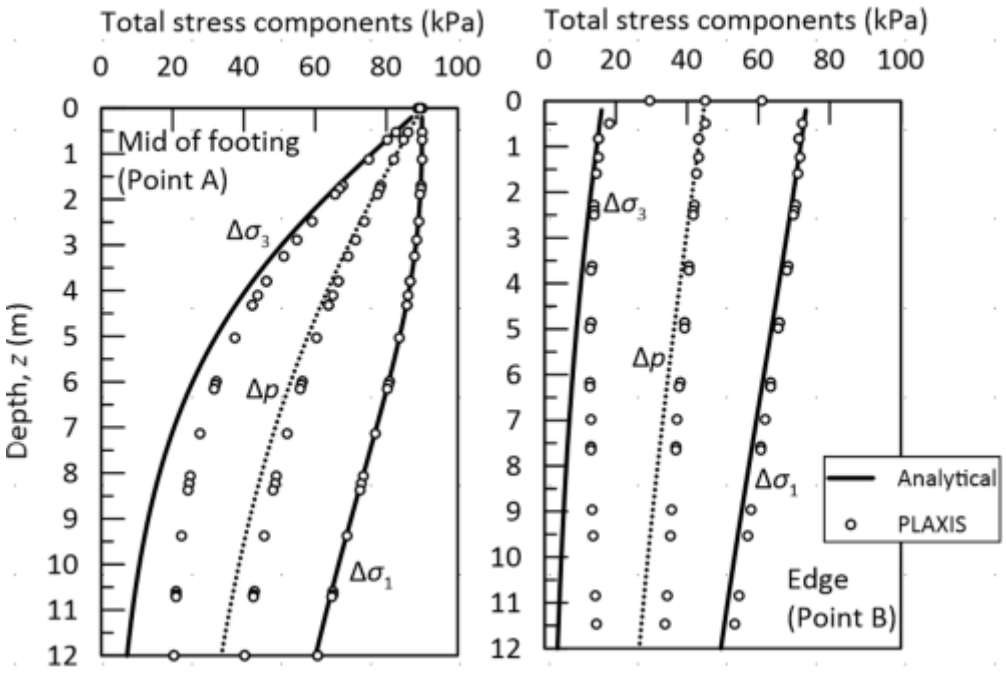

Figure 4.35b. Variation with depth of major total principal, minor total principal and mean total stress increments at Points A and B.

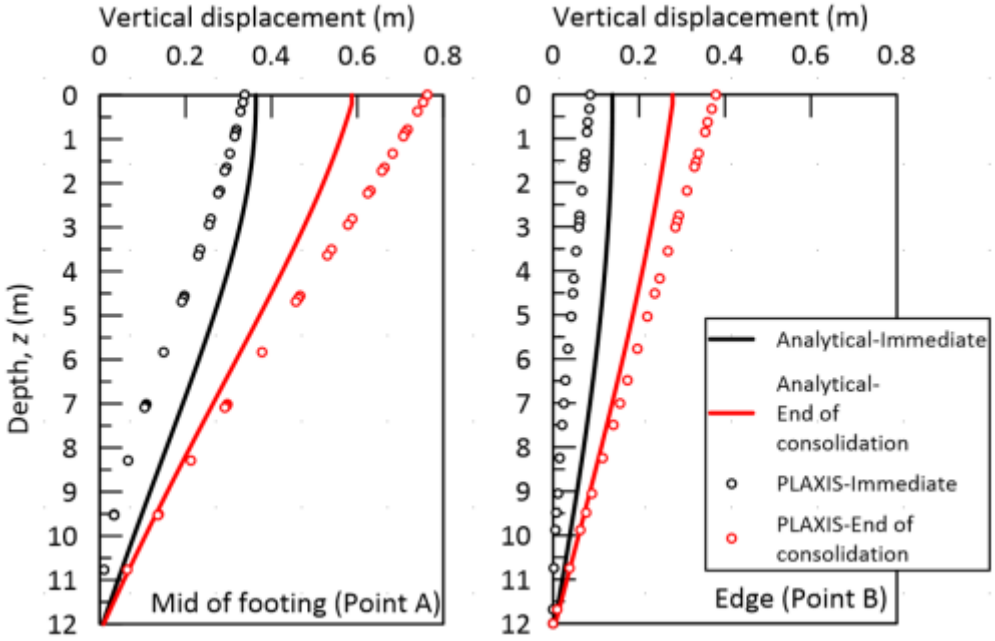

Figure 4.36. Variation of vertical soil displacement with depth at Points A and B. Results for 16m-wide footing on 12m-thick soil layer (*H/B* = 0.75).

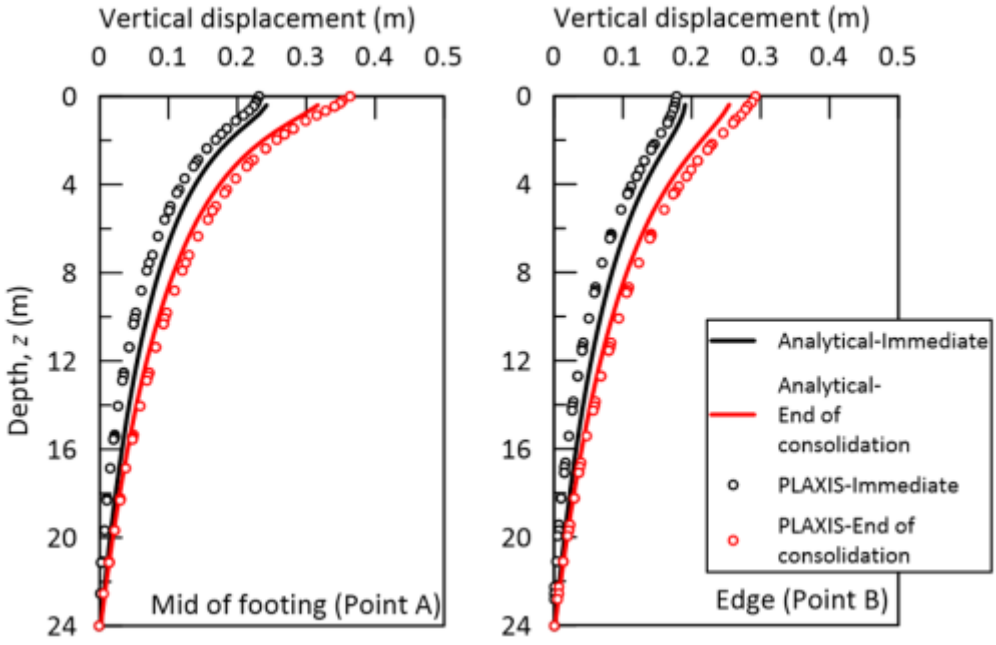

Figure 4.37. Variation of vertical soil displacement with depth at Points A and B. Results for 2m-wide footing on 24m-thick soil layer (*H/B* = 12).

4.8 EVOLUTION OF PRIMARY CONSOLIDATION SETTLEMENT WITH TIME

The rate of dissipation of excess pore water pressure, and thus the necessary time for the applied loading on the ground surface to be transferred to the soil skeleton resulting in increase of the effective stress, depends on the permeability, k of the soil. We can obtain a closed-form analytical expression that provides the rate of dissipation of excess pore pressure, and thus the evolution of settlement with time (Figure 4.7), under some simple assumptions:

- 1-D conditions prevail, with water flowing only vertically, as in the oedometer test (Figure 4.27).
- The soil is fully saturated, homogeneous and isotropic.
- Darcy's law is valid, thus flow q is equal to the permeability times the hydraulic gradient i i.e., $q=ki$
- Small strains.

Under the above assumptions, Terzaghi formulated the one-dimensional consolidation equation, describing the variation of excess pore pressure u with time t and depth z as:

$$\frac{\partial u}{\partial t} = c_v \frac{\partial^2 u}{\partial z^2} \quad \textbf{(4.65)}$$

The constant c_v in the differential equation 4.65 is called *coefficient of consolidation*, and depends on the coefficient of volume compressibility m_v and the soil permeability in the vertical direction k_z as:

$$c_v = \frac{k_z}{m_v \gamma_w} \quad \textbf{(4.66)}$$

where $\gamma_w \approx 10$ kN/m^3 is the unit weight of the water. The coefficient of consolidation carries units of length^2/time.

Solution of the differential equation 4.65 requires knowing the initial distribution of excess pore pressure with depth (Figure 4.38), and the permeability boundary conditions. For example, assuming uniform excess pore pressure distribution with depth, corresponding to a relatively thin clay layer (Figure 4.38) and double drainage, both from the top and the bottom of the layer (Figure 4.39a):

- at $t = 0$, the excess pore pressure will be uniform along the thickness, and equal to the applied pressure at the surface $\Delta u_0 = q_{ext}$
- at the top boundary $z=0$ where drainage is allowed, $\Delta u = 0$
- at the bottom boundary $z=H$ where drainage is allowed too, $\Delta u = 0$

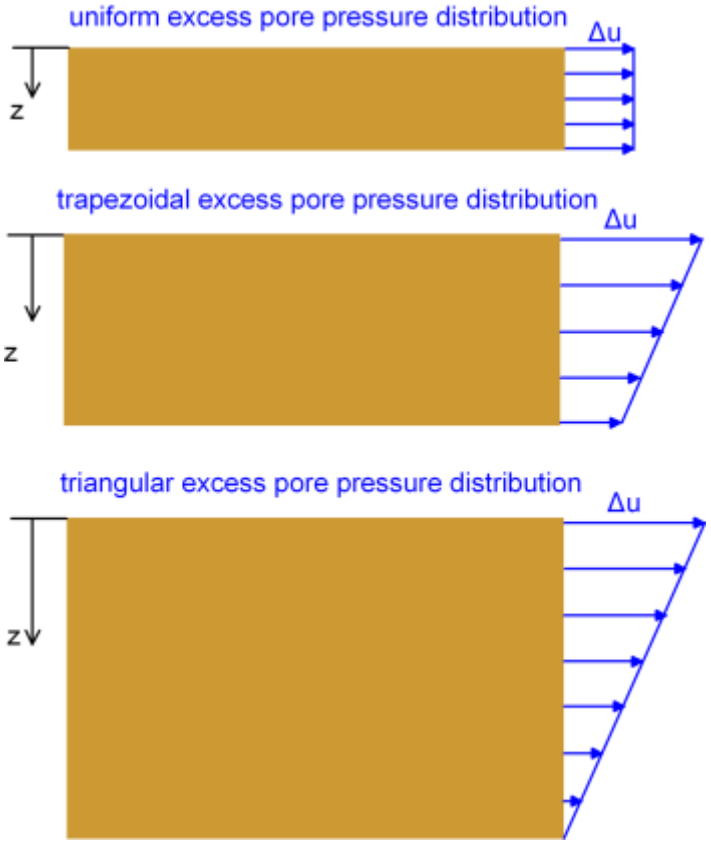

Figure 4.38. Initial excess pore pressure distribution with depth, for increasing thickness of the compressible layer.

The drainage boundary conditions suggest that excess pore pressure will immediately fall to zero at the permeable boundaries.

A closed-form solution of Eq. 4.65 exists for the above conditions and provides the variation of the excess pore pressure with depth at different time instances (Figure 4.40):

(4.67) $$\Delta u\left(z,t\right)=\sum_{m=0}^{\infty}\frac{2\Delta u_0}{M}\sin\left(\frac{Mz}{H_{dr}}\right)e^{-M^2T_v}$$

where $M=\dfrac{\pi\left(2m+1\right)}{2}$, and T_v is the *time factor*, equal to:

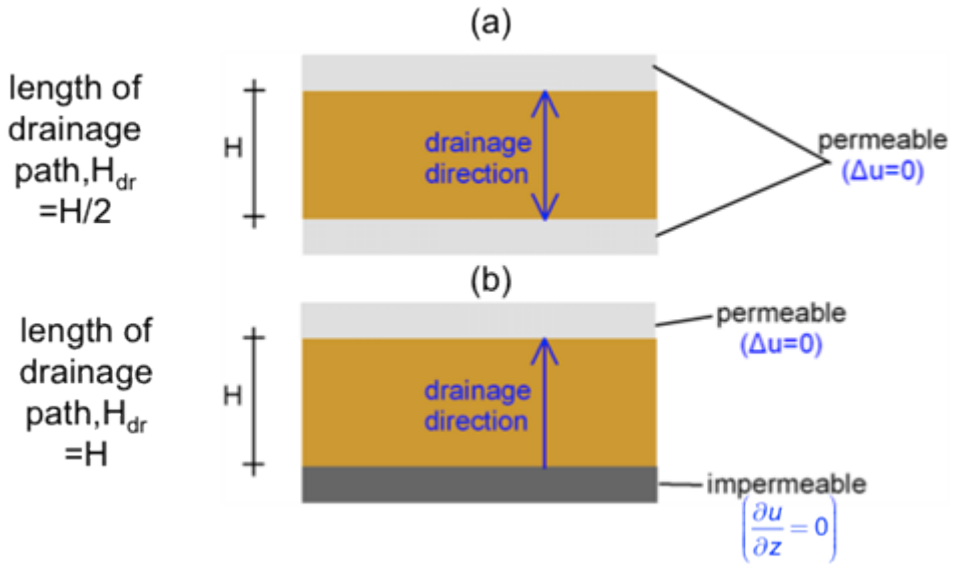

Figure 4.39. Boundary conditions and length of drainage path for (a) double drainage, and (b) drainage only from the top of the soil layer.

(4.68) $$T_v = \frac{c_v t}{H_{dr}^2}$$

The length of the drainage path, H_{dr} depends on the drainage boundary conditions, and is depicted in Figure 4.40.

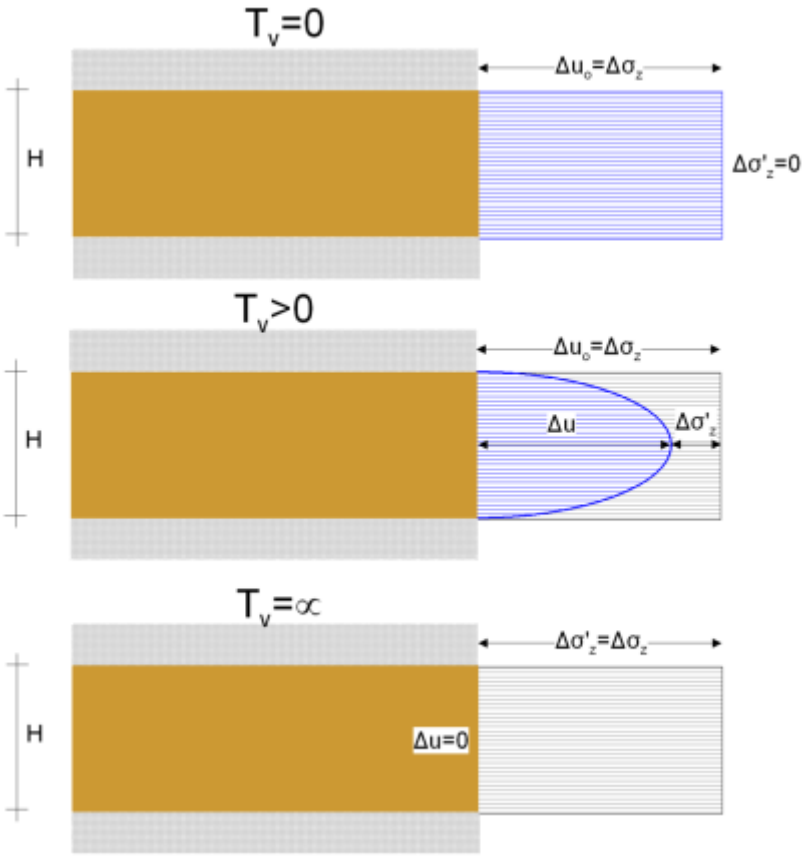

Figure 4.40. Graphical representation of excess pore pressure distribution with depth at different time instances, calculated from Eq. 4.67.

Instead of using the absolute value the of excess pore water pressure, consolidation progress can be described via the *degree of consolidation* (or *consolidation ratio*), $U(z)$ which defines the amount of consolidation completed at a particular time instance, at a specific depth, z:

(4.69) $$U\left(z\right) = 1 - \frac{\Delta u_z}{\Delta u_0}$$

The degree of consolidation is visualised as the grey shaded area in Figure 4.40. From an engineering point of view, we are rather interested in the *average* degree of consolidation, U of the whole compressible layer. For the special case where the initial excess pore pressure distribution is assumed constant with depth (Figure 4.38) the average degree of consolidation is calculated as:

(4.70) $$U = 1 - \sum_{m=0}^{\infty} \frac{2}{M^2} e^{-M^2 T_v}$$

The variation of the average degree of consolidation with the time factor Tv is illustrated in Figure 4.41.

Eq. 4.70 and Figure 4.41 are also valid when drainage is not allowed at the bottom of the clay layer. The length of the drainage path in that case will be $H_{dr} = H$ (Figure 4.39). Note that at an impermeable boundary, the gradient of pore pressure will be zero $\partial u / \partial z = 0$.

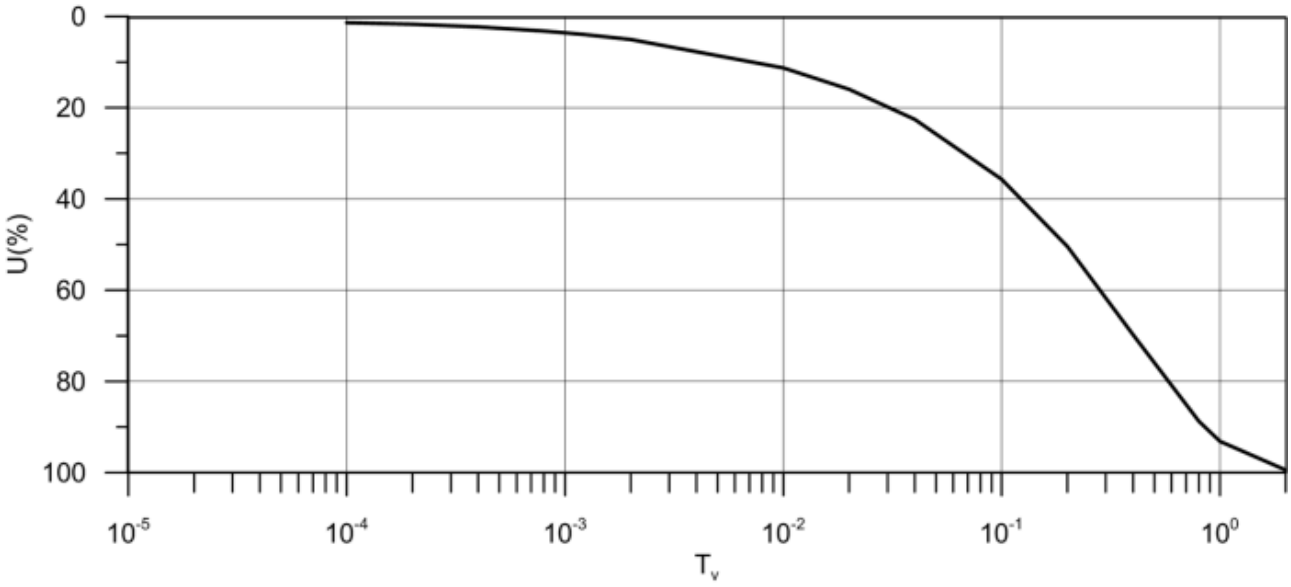

Figure 4.41. Variation of the average degree of consolidation U with the time factor T_v for uniform initial excess pore water pressure distribution.

Note that Figure 4.41 can be used to estimate settlement of a 1-D soil column at any given time t_1. By substituting t_1 into the expression for the time factor T_v (Eq. 4.68) we can find the average degree of consolidation U_1 at t_1 directly from Figure 4.41. Therefore, settlement at t_1 will be:

(4.71) $$\rho_1 = \frac{U_1\,(\%)}{100}\rho_{pc}$$

where the primary consolidation settlement ρ_{pc} is calculated according to Section 4.6.2, assuming linear elastic or non-linear soil behaviour.

4.9 ESTIMATION OF SECONDARY COMPRESSION SETTLEMENT

While delving into the mechanisms of soil creep is not within the scope of this Part, it is worth presenting the expression for estimating secondary compression or creep settlement ρ_{sc} at any time that stems from Hypothesis A i.e., that soil creep commences after soil excess pore pressures have dissipated (Figure 4.42):

(4.72) $$\rho_{sc} = \frac{C_\alpha}{1+e_c} H_c \log\left(\frac{t_{sc}}{t_c}\right)$$

where t_{sc} is the time when secondary compression is sought, t_c is the time required for 90% consolidation to be completed, or the time required to reach U = 90% estimated from Figure 4.41, according to the mentioned above. e_c and H_c in Eq. 4.72 are the void ratio and thickness of the soil layer at U = 90%, respectively, and these can be computed if we consider that:

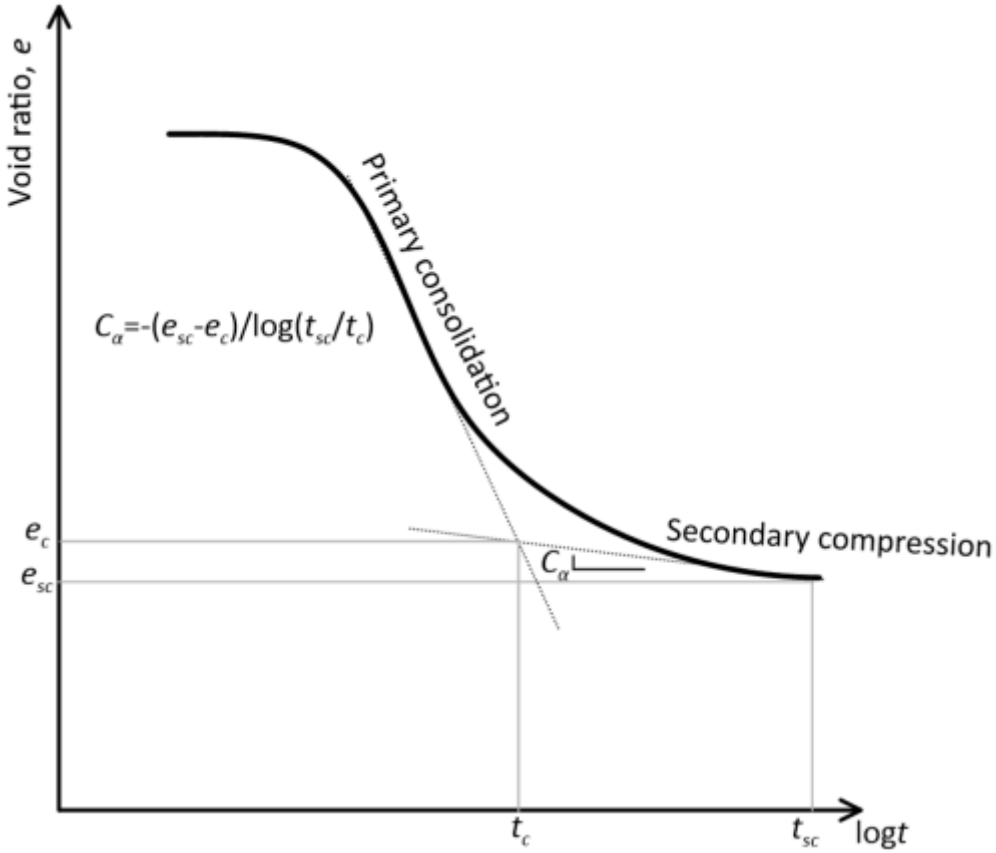

Figure 4.42. Calculation of creep coefficient C_α from oedometer tests.

(4.73) $$\frac{\rho}{H} = \frac{\Delta e}{1+e_0}$$

where e_0 is the initial void ratio of soil and Δe is the change in the soil void ratio that takes place during consolidation. In addition C_α is the creep coefficient, and is determined from oedometer tests (Figure 4.42).

The creep coefficient is related to the compression index C_c. In lack of soil-specific tests, one can consider that C_α/C_c = 0.03 to 0.08 for clays and silts, and C_α/C_c = 0.05 to 0.10 for organic soils (Mitchel and Soga, 2005).

EXAMPLE 4.6

Numerical simulation of 1-D consolidation

Calculate the degree of consolidation of the compressible clay layer depicted in the figure below a) 100 days, and b) 5 years after the application of an infinite strip pressure. Consider the bottom layer of dense sand with gravels to be incompressible and permeable. Compare the settlement below the center of the pressure at t = 5 years with the settlement estimated analytically in Example 4.3.

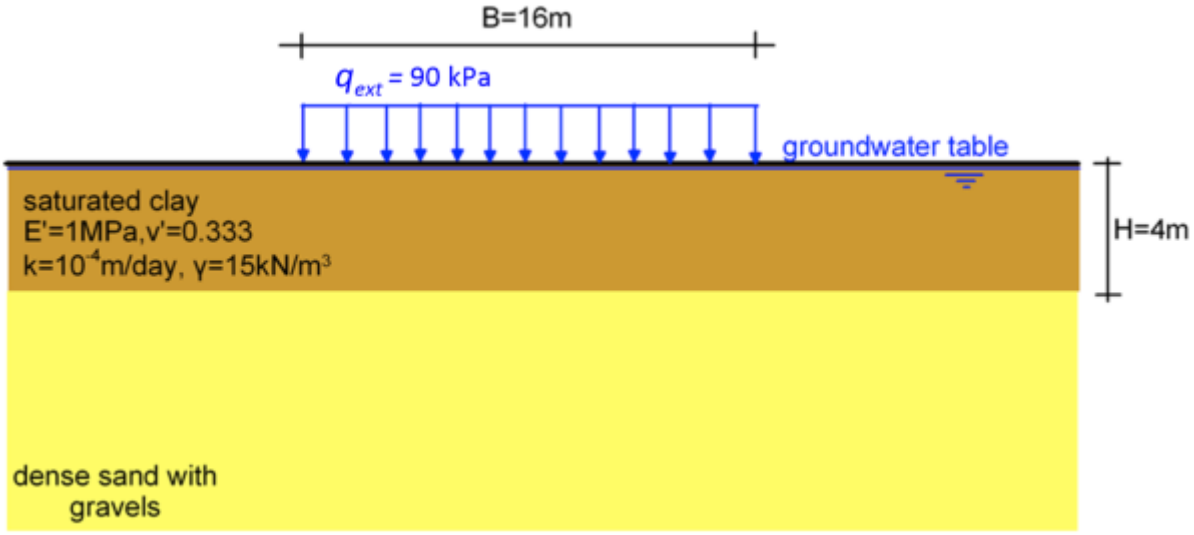

Example 4.6. Problem description and input parameters.

Answer:

As discussed in Example 4.3, we can assume 1-D consolidation conditions, given that the width of the loaded area is large, compared to the thickness of the compressible clay layer. This suggests that we do not need to simulate the full two-dimensional problem: a 1m-wide soil column (unit cell) would suffice, provided that the correct boundary conditions are applied (Figure 4.43). Note that the width 1 m is arbitrary, results are independent of the selected width of the unit cell, provided that pressure is applied across the entire width of the unit cell. As the strip pressure extents "infinitely" along the out-of-plane dimension, the problem will be simulated as plane-strain (Figure 3.4a).

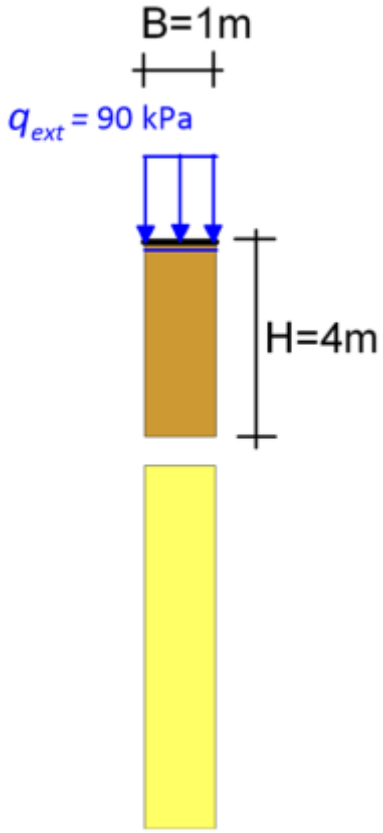

Figure 4.43. Equivalent 1-D problem.

As also discussed in Chapter 4.8, for the simulation of consolidation we also have to account for permeability boundary conditions, on top of displacement boundary conditions (Figure 4.44). *"Standard fixities"* in PLAXIS will apply the necessary displacement boundary conditions for the plane-strain problem. As the bottom layer of dense sand with gravels is incompressible, we can choose not to explicitly introduce it in the model, and fix the displacement at the bottom of the clay layer in both directions (Figure 4.44). Thus the dimensions of the model will be 1 m x 4 m.

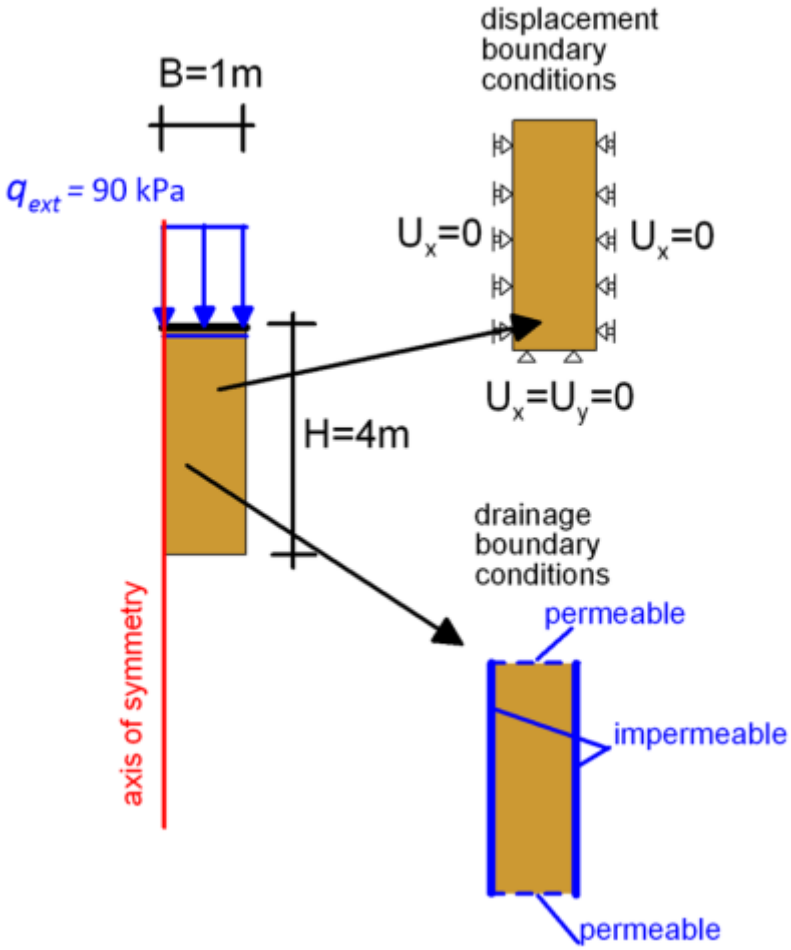

Figure 4.44. Displacement and drainage boundary conditions of the equivalent 1-D problem.

"Permeable" boundary conditions are applied at the top and bottom of the clay layer to specify that water is free to flow from these directions. *"Impermeable"* boundary conditions at the lateral boundaries account for symmetry and for vertical-only water flow. Note that the axis of symmetry always corresponds to impermeable boundary conditions. The considered boundary conditions ensure that lateral strains will be zero $\varepsilon_x = \varepsilon_h = 0$ and that excess pore water pressure dissipates only vertically.

The undrained (A) linear elastic model is used to simulate clay behaviour under the applied loading, which allows for the calculation of (excess) pore water pressures in plastic stages. Compressibility is defined in terms of effective parameters i.e., the drained Young's modulus E' and Poisson's ratio ν'. Note however that the undrained behavior stiffness parameters (E_u, $\nu_u = 0.495$) are calculated internally by PLAXIS, and the coefficient of earth pressure at-rest K_0 is automatically set equal to $K_0 = 1$. Note that in PLAXIS we do not input $\nu_u = 0.50$, but a value very close to 0.5. That it because the (undrained) bulk modulus of soil $K_u = E_u/3(1\text{-}2\nu_u)$ becomes infinite if $\nu_u = 0.50$ (soil is incompressible), resulting in a division-by-zero. The permeability of the clay, k is also entered as a material parameter.

The analysis consists of three stages:

- *Step 1: Initial phase.* The geostatic stresses and hydrostatic pore water pressures before the application of the external pressure are initialised with the "K_0-procedure". Drainage boundary conditions and groundwater table level are defined, as in Figure 4.44.
- *Step 2: Sudden application of the loading.* A "Plastic" step is introduced, where the external pressure is instantaneously applied on the ground surface i.e., the duration of this step (time interval) is 0.0 days.

- *Step 3: Consolidation.* A "Consolidation" step follows the previous plastic step, where the external pressure will remain on the ground surface for a prescribed time interval, and excess pore pressures developed during Step 2 will be allowed to dissipate through the free-draining boundaries. *"Reset displacements to zero"* should not be active, so that any immediate settlement will be co-estimated.

Results at the end of Step 2 are presented in Figure 4.45 in the form of contours of total vertical stress along the thickness of the clay layer, excess pore pressure distribution, and settlement. Notice that excess pore water pressures are not equal to the external applied pressure as you might expect, but somewhat lower, and some immediate settlement develops. This is because PLAXIS considers a large, yet realistic bulk modulus for water, unlike the analytical solution where we assumed that water is incompressible.

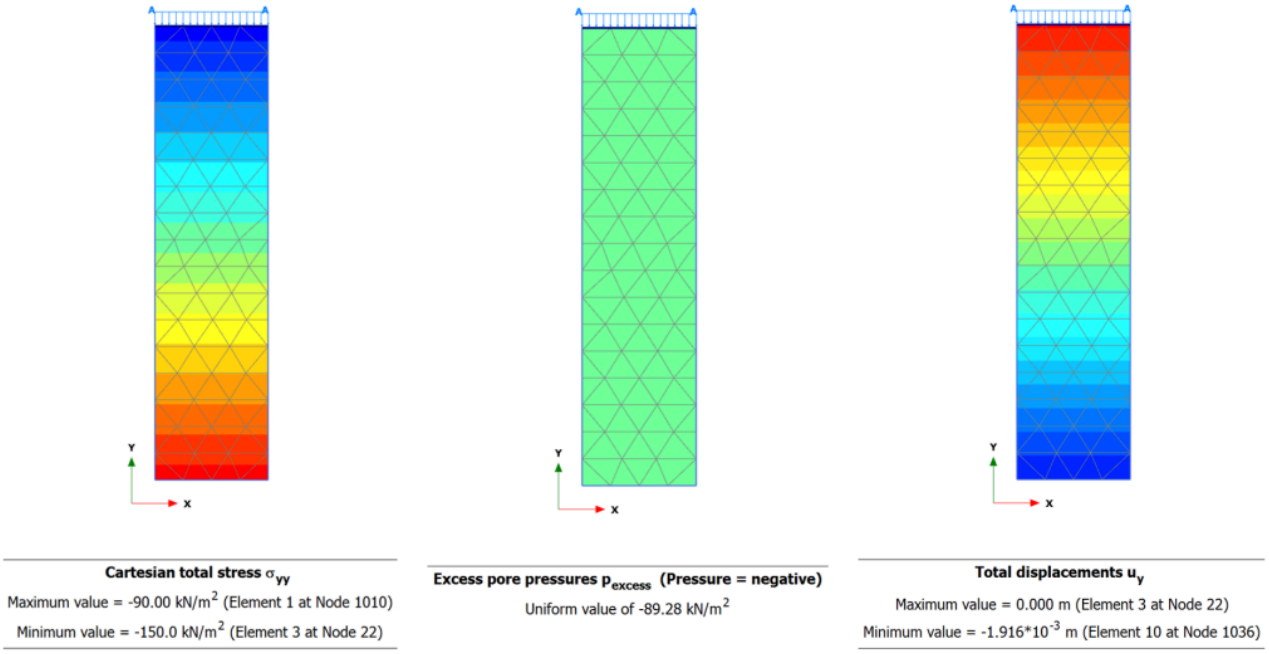

Figure 4.45. (Left) Total vertical stress, (middle) Excess pore pressure, and (right) Settlement contours immediately after the application of the external pressure, at the end of Step 2.

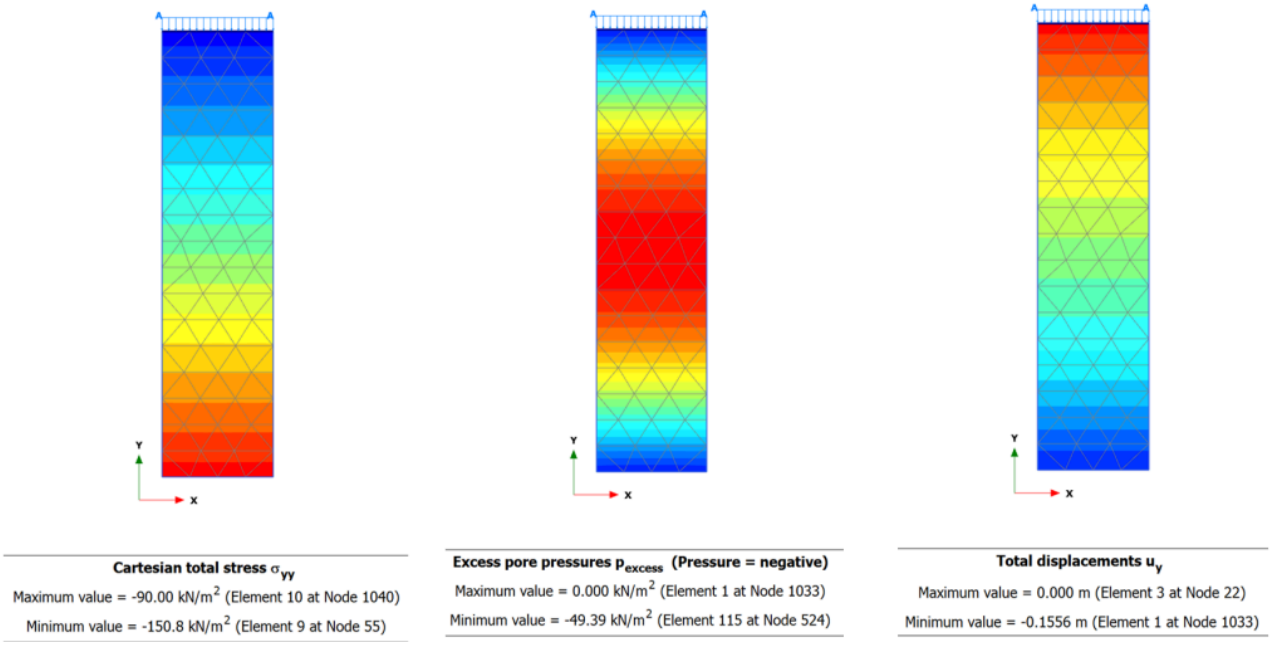

Figure 4.46. (Left) Total vertical stress, (middle) Excess pore pressure, and (right) Settlement contours at the end of Step 3, after t = 100 days.

Results at the end of Step 3, after t = 100 days, are presented in Figure 4.46, again in terms of total vertical stress, excess pore pressure distribution and settlement contours, for comparison. As expected, total stresses do not change. Excess pore water pressures have partly dissipated, but the maximum value at the middle of the sample is Δu = 49.4 kPa (Figure 4.47) which suggests that consolidation has not been completed yet (U < 100 %), and settlement has not attained its maximum value. Notice also in Figure 4.47 that excess pore pressure at the top and bottom boundary, where drainage is free, is zero.

If Step 3 is run for t = 1825 days (5 years), excess pore pressure will become practically zero along the full thickness of the clay (Figure 4.48a), which implies that consolidation has been completed, and the full primary consolidation settlement has developed (Figure 4.48b).

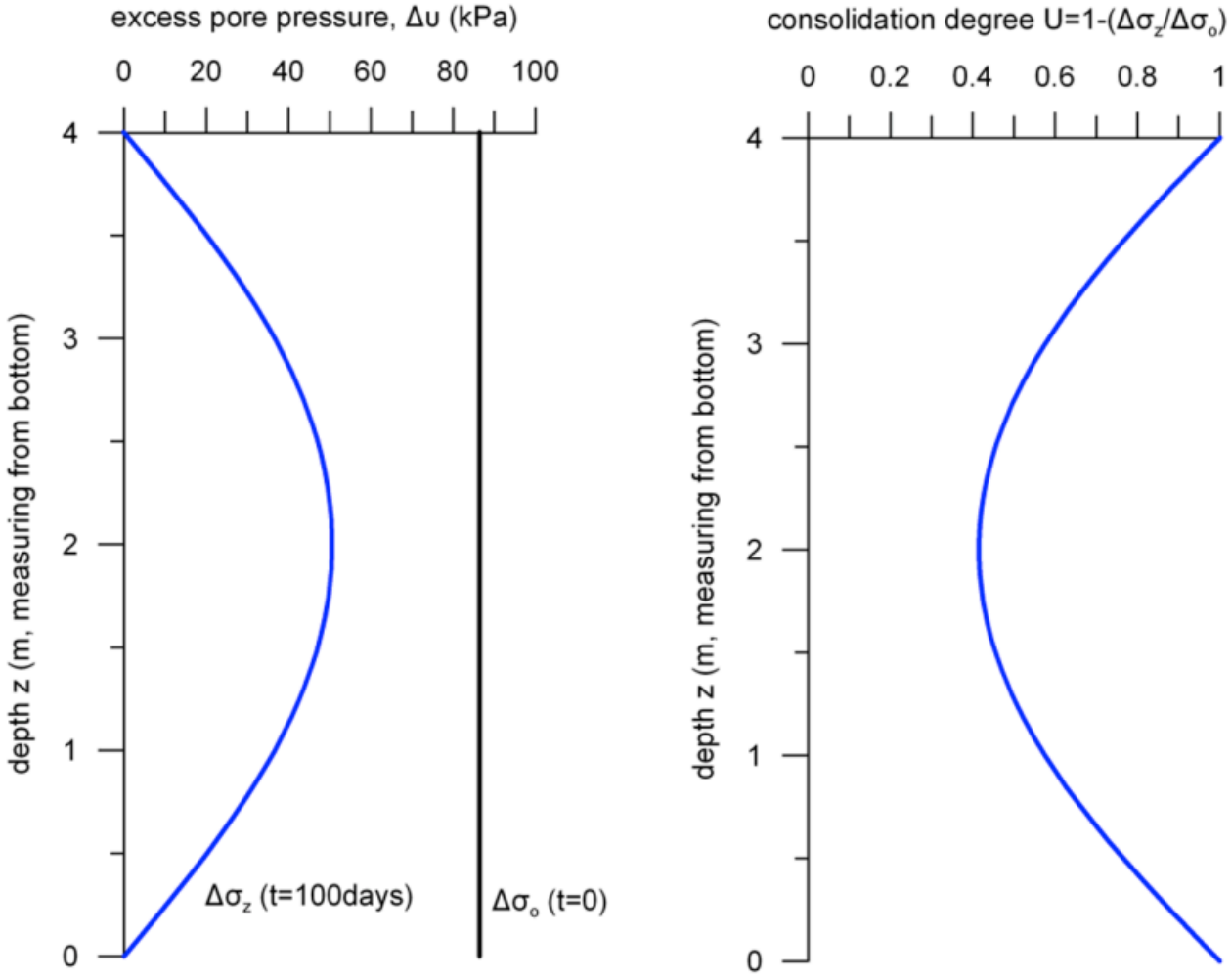

Figure 4.47. (Left) Excess pore pressure, and (right) Degree of consolidation profiles along the thickness of the clay layer at the end of Step 3, after t = 100 days.

Total stresses will of course remain unchanged. The degree of consolidation will be equal to $U \approx 100\%$ along the thickness of the soil layer. The value of settlement is, as expected, practically equal to the value computed analytically in Example 4.3 (ρ_{pc} = 240 mm).

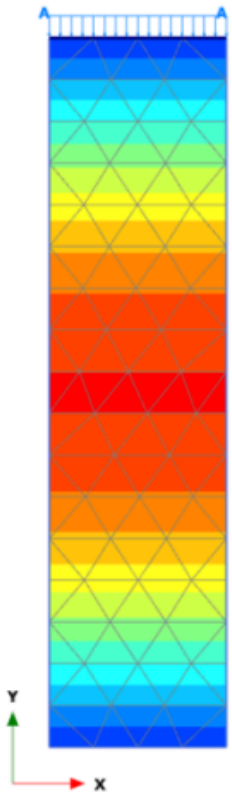

Excess pore pressures p_{excess} (Pressure = negative)

Maximum value = 0.000 kN/m^2 (Element 1 at Node 1033)

Minimum value = -0.2209 kN/m^2 (Element 118 at Node 534)

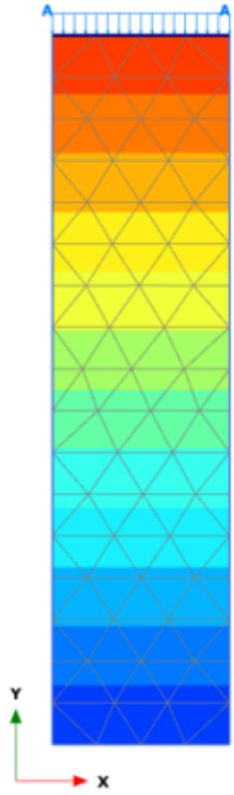

Total displacements u_y

Maximum value = 0.000 m (Element 3 at Node 22)

Minimum value = -0.2399 m (Element 1 at Node 1033)

Figure 4.48. (Left) Excess pore pressure, and (right) Settlement contours at the end of Step 3, after t = 1825 days.

EXAMPLE 4.7

Numerical simulation of 2-D consolidation

The approach embankment (transition from embankment to bridge) of the figure below is going to be founded on a compressible clay of thickness H = 5 m. Estimate the necessary time that the embankment should be left to settle before constructing the pavement layer, for its post-construction settlement to be less than 10 mm. Assume that the time required for the construction of the embankment is negligible.

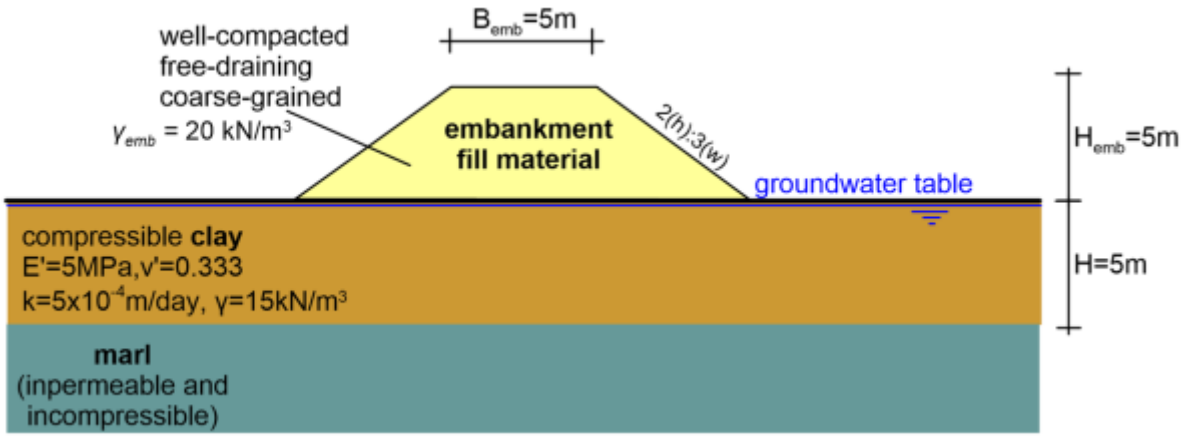

Example 4.7. Problem description and input parameters.

Answer:

The pressure applied on the subsoil from the embankment is non-uniform and its width, at least in the area of maximum embankment height, is comparable to the thickness of the compressible layer. The above suggest that the two-dimensional plane-strain consolidation problem must be simulated. Note that a closed-formed solution is not available for two-dimensional consolidation problems, and numerical methods (not necessarily the finite element method) are used to determine the excess pore water pressure and settlement evolution with time.

The problem is symmetric, with the axis of the embankment being the plane of symmetry. Given that we are not interested in the embankment stability conditions, instead of simulating the embankment itself, we will replace it with a distributed pressure (Figure 4.49). However, we can most certainly model the actual fill, as a separate geometry cluster comprising permeable (free-draining) linear elastic material with unit weight γ_{emb} = 20 kN/m^3. To obtain results similar to those with the model where the embankment is simulated as a pressure, we must assign very low stiffness and very high permeability to the material representing the fill, to approximate free dissipation of excess pore pressures from the body of the embankment, and flexible loading. Nevertheless, the stiffness of the fill material and its permeability will not have a particularly important effect on predicted settlements for the problem at hand.

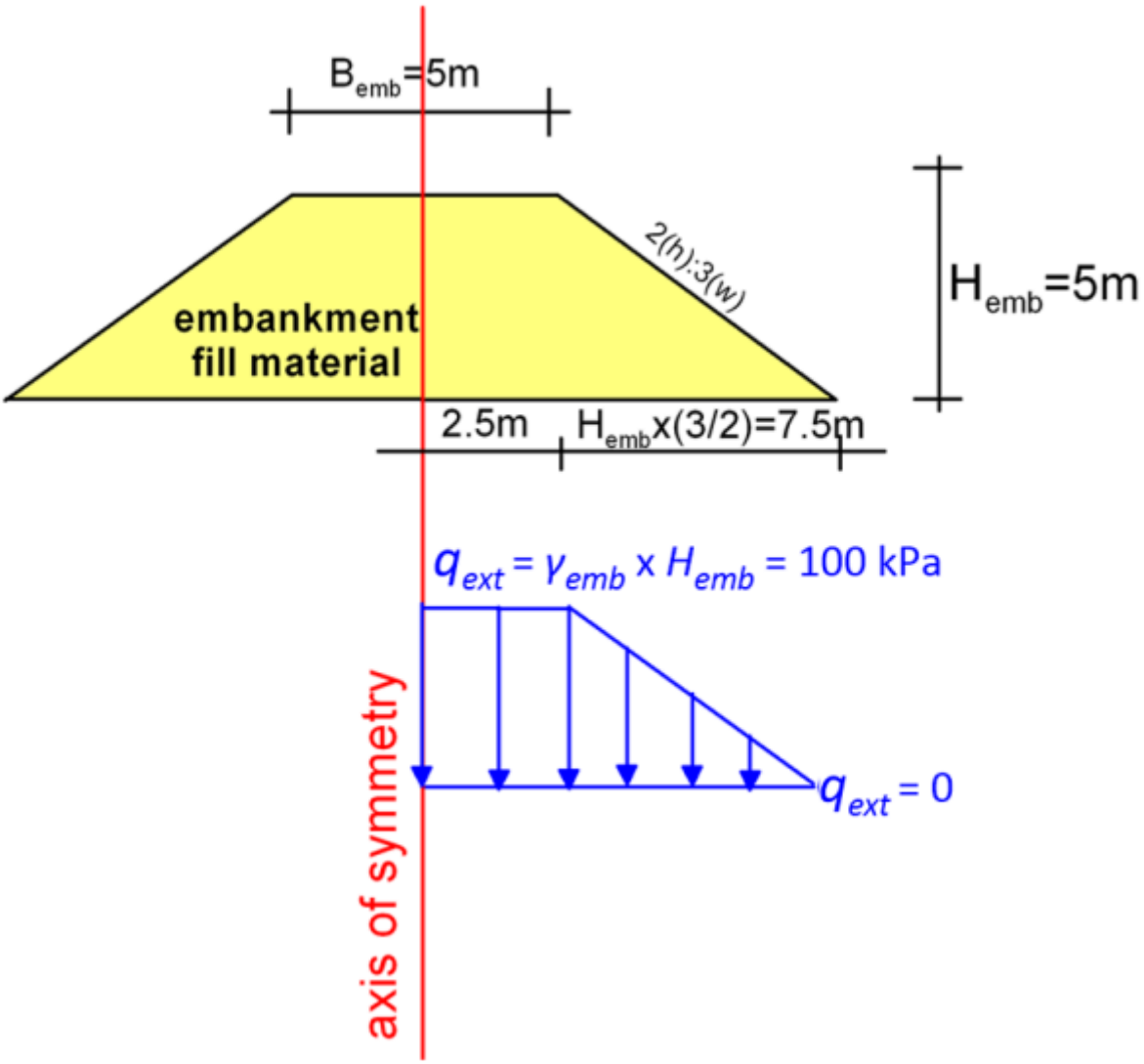

Figure 4.49. Estimation of equivalent pressure to simulate loading from the embankment.

"Standard fixities" will be applied as displacement boundary conditions. The marl formation is not simulated, and will be replaced by fixed displacements at the bottom of the clay layer, as in Example 4.6.

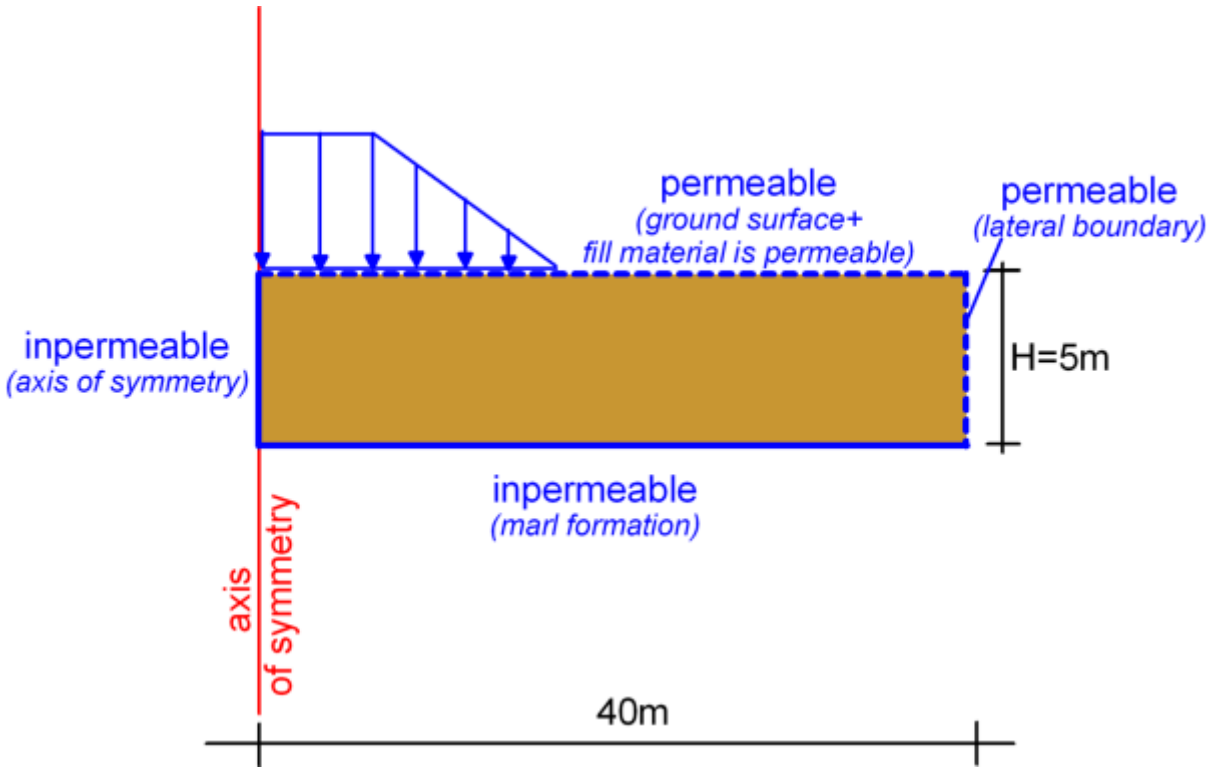

Figure 4.50. Permeability boundary conditions of 2-D problem (not in scale).

As far as drainage boundary conditions are concerned: The left lateral boundary is an axis of symmetry, thus no flow should be allowed, and an impermeable boundary should be considered. The right lateral boundary, which should be placed in sufficient distance from the embankment toe equal to about 3 times the half-width of the embankment, should be permeable, as the clay layer extents "infinitely" along the horizontal direction. This rule-of-thumb for determining the distance of the lateral boundaries from the area of interest must always be used with caution, and the sensitivity of the analysis model to the boundary conditions must always be checked by means of parametric analysis. Permeable boundary conditions must be applied to the ground surface too. The ground surface must be permeable along its full extent, as the embankment is constructed of free-draining material (Figure 4.50).

The undrained (A) linear elastic model is used to simulate clay behavior under the applied pressure, as in Example 4.6, allowing for the calculation of (excess) pore water pressures for plastic stages too. Soil compressibility is defined in terms of effective parameters i.e. the drained Young's modulus E' and Poisson's ratio v' as used as input, but the undrained stiffness parameters are calculated internally by PLAXIS. The permeability of the clay, k is also entered as a material parameter. Two distributed pressures are applied, a uniform and a triangular one, with the values and the widths presented in Figure 4.49.

The analysis consists of three stages:

- *Step 1: Initial phase.* The geostatic stresses and hydrostatic pore water pressures before the application of the external pressure are initialised with the "K0-procedure". Drainage boundary conditions and the water table level are defined, as in Figure 4.50.
- *Step 2: Sudden application of the loading.* A "Plastic" step is introduced, where the external pressure is instantaneously applied on the ground surface i.e., the time interval of this step is 0.0 days. This corresponds to instantaneous construction of the fill.
- *Step 3: Consolidation.* A "Consolidation" step follows the previous plastic step, where the analysis will continue until the degree of consolidation reaches 99%, and excess pore pressures developed during Step 2 will have practically fully dissipated. The loading option "Degree of Consolidation" is selected for that. *"Reset displacements to zero"* should not be active, so that the immediate settlement, which in that case is expected to be a considerable portion of total settlement, will be co-estimated.

Note that when the "Degree of Consolidation" option is used to define the end of the simulation, care must be taken to ensure that excess pore pressures in the area of interest (below the embankment) have dissipated and settlement has indeed stabilised. The reason for that is that PLAXIS calculates the average degree of consolidation across the simulated compressible layer, and significant pore pressure gradients may remain in the area of interest, even when the average degree of consolidation across the 40m-wide clay layer approaches $U = 100\%$. This reiterates the importance of carefully selecting the distance of the boundaries from the area of interest, instead of following rules-of-thumb without judgment.

In this particular example we assume for simplicity that the fill is placed "instantaneously". However, we can actually model staged construction of the fill in PLAXIS. This can be achieved by replacing the "Plastic" step 2 with a "Consolidation" step, of duration equal to the time required for the construction of the fill. In that case the pressure will not be applied instantaneously, but instead will be ramped-up to its final value, which will be reached at the end of the step. Assuming that the pressure increases linearly with time during the construction period will provide a more accurate estimate of pore pressures that will develop in soil *in situ*, which may be important if stability of the embankment during construction is assessed. Finally note that time has no physical meaning in "Plastic" steps, and is only used for presentation of analysis results. Even if a time value is entered as input for a plastic step, the entire pressure will be applied instantaneously in the beginning of the step, and held constant thereafter.

The deformed mesh at the area of the embankment at the end of Step 2, immediately after the application of the pressure, is presented in Figure 4.51. Notice that the immediate settlement due to the construction of the embankment is not negligible, and it reaches about $\rho_e = 22$ mm. As discussed in Chapter 4.4 soil deformation under short-term undrained conditions takes place without volume change (Figure 4.9), and soil heaves around the loaded area (Figure 4.51).

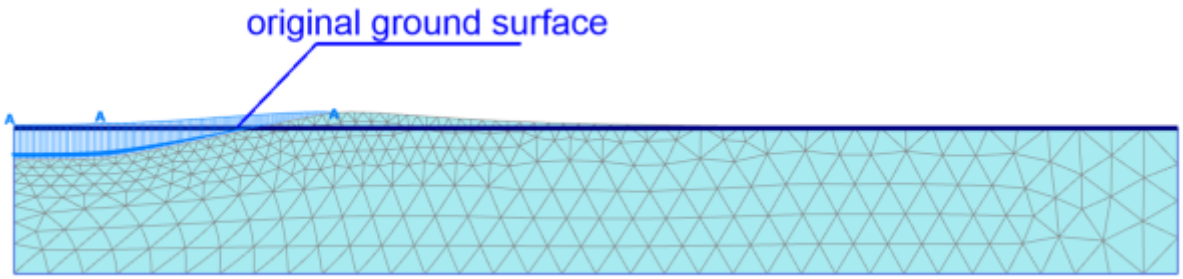

Figure 4.51. Settlement due to the pressure applied from the embankment immediately after its construction, at the end of Step 2 (deformations scaled x 50).

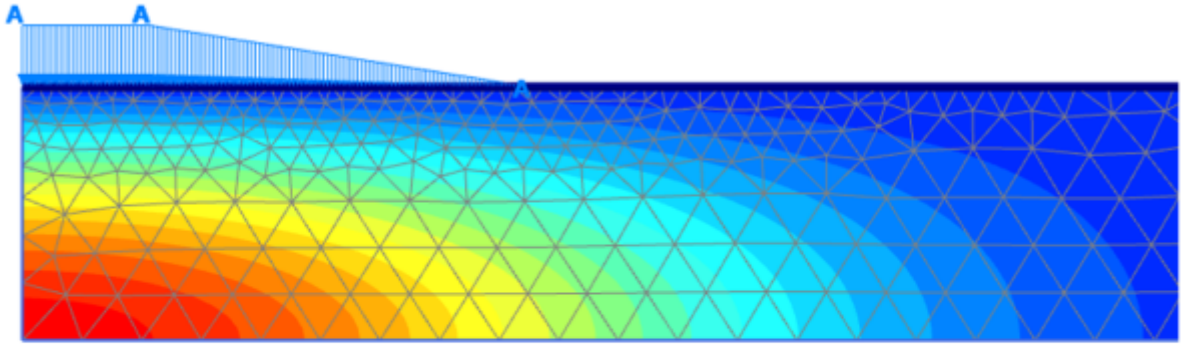

Excess pore pressures p_{excess} (Pressure = negative)

Maximum value = $6.832*10^{-3}$ kN/m^2 (Element 28 at Node 394)

Minimum value = -0.8798 kN/m^2 (Element 45 at Node 4531)

Figure 4.52a. Excess pore pressure contours, at the end of Step 3 (U = 99%).

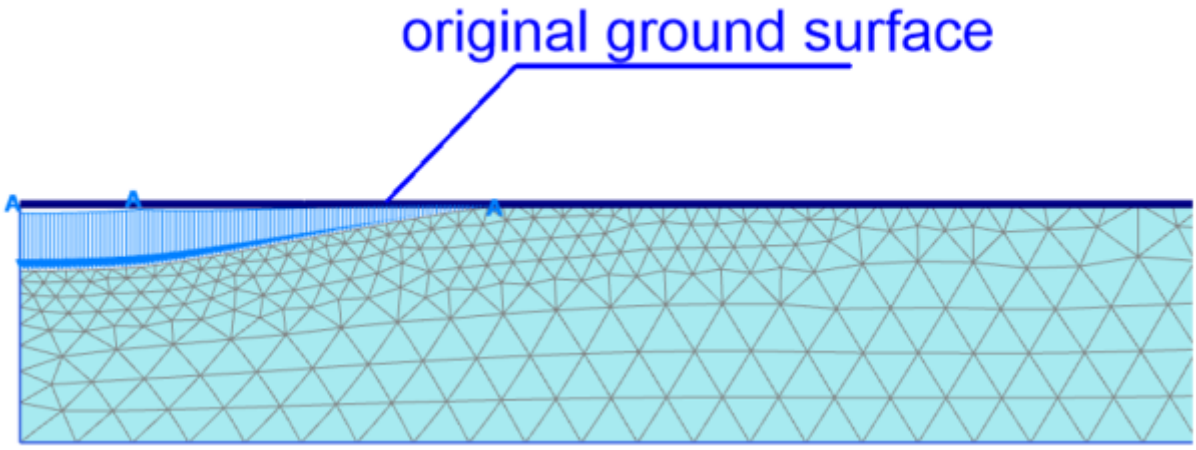

Figure 4.52b. Settlement (scaled x 50) at the area of the embankment, at the end of Step 3 (U = 99%).

At the end of Step 3, when the average degree of consolidation has reached U = 99%, excess pore pressures are practically reduced to zero, with its maximum value being Δu = 0.88 kPa below the axis of the embankment and near the impermeable marl layer boundary (Figure 4.52a). Total settlement of the soil surface has reached $\rho = \rho_e + \rho_{pc}$ = 70 mm, and soil heave is now negligible, as volume changes in long-term drained loading conditions.

The evolution of settlement with time is presented in Figure 4.53. Notice that part of settlement develops instantaneously, and is the immediate settlement calculated from Step 2, while primary consolidation settlement evolves with time. To find the necessary time that the embankment must be left to settle before constructing the pavement layers, we need to find from the settlement curve in Figure 4.53 the time when settlement reaches the final value of settlement minus the allowable post-construction settlement 70 mm – 10 mm = 60 mm (about 32 days).

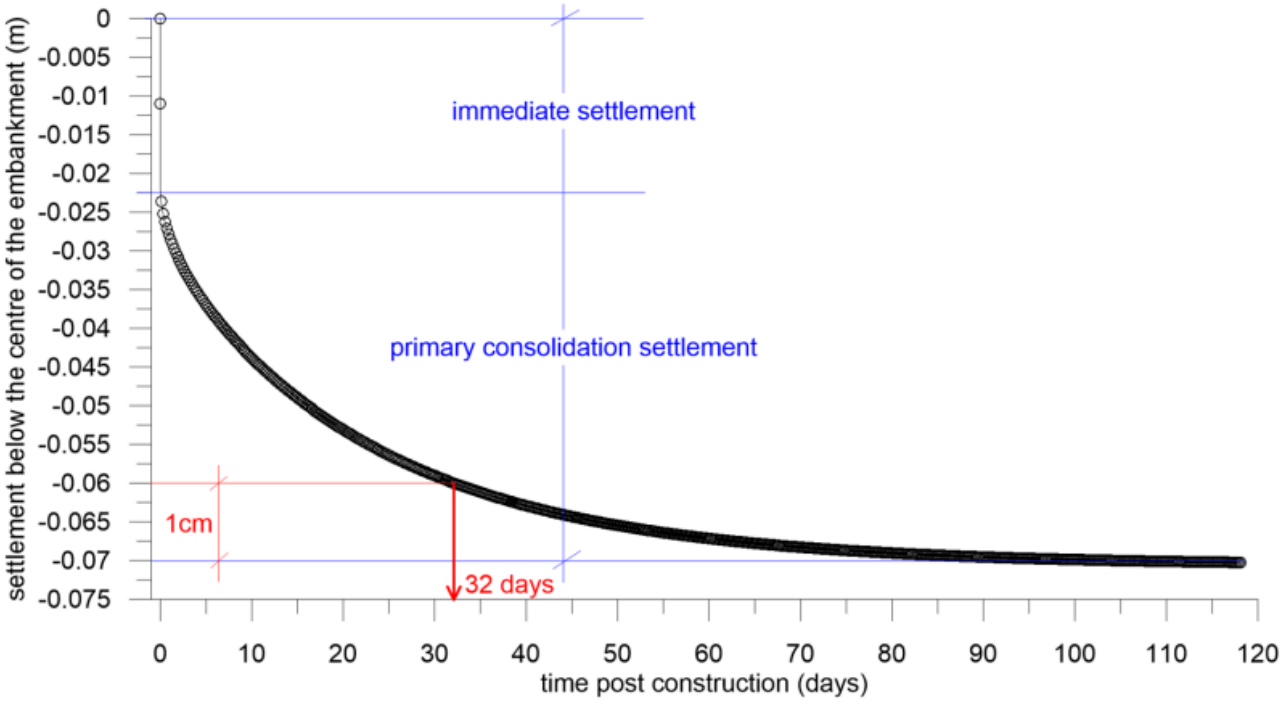

Figure 4.53. Evolution of embankment settlement with time.

EXAMPLE 4.8

The importance of boundary conditions

In this example we employ PLAXIS to validate the results of the simple, approximate method described in Section 4.5.4 for calculating immediate settlements of footings on linear elastic half-space. For that we will built two PLAXIS models, shown in Figure 4.54: A plane-strain one simulating a strip footing and an axisymmetric one simulating a circular footing.

Keep in mind that the method described in Section 4.5.4 does not work for strip footings, as it predicts that infinite settlement will occur (see Table 4.3). To confirm that, we start by building a model in PLAXIS with initial thickness 10 m, and run 5 simulations in total while increasing the thickness of the mesh from H = 10 m to H = 50 m, H = 100 m, H = 150 m and finally H = 200 m. Indeed, it appears that the more we increase H, the larger the settlement (settlements increase linearly) and settlement tends to infinity for an infinitely thick mesh.

However, results for a circular footing are rather puzzling. The analytical method yields an immediate settlement of 140 mm for the problem herein. Then we model the same problem in PLAXIS, starting with mesh thickness 10 m as shown in Figure 4.54, and again run multiple simulations while increasing H as above. Results of the first analysis for H = 10 m are relatively close to the analytical solution, as settlement from PLAXIS is about 170 mm. Keeping in mind that the solution is "approximate", a 30 mm difference is acceptable, especially if we consider that the analytical method is applicable to rigid footings and in PLAXIS we are modelling an infinitely flexible footing by means of a pressure applied at the surface of the model. But as we keep increasing H again to 200 m, settlement yet again increases linearly instead of reaching an asymptote, as expected. The gradient is not as steep as in the strip footing case (notice the linear fit of the numerical data), but at H = 200 m the PLAXIS settlement is already twice the analytical one, and we infer that it will reach 1.5 m if H was H = 2000 m. That's certainly not compatible with the analytical solution.

Is there a fundamental error in the analytical method, or there is an error in our numerical models?

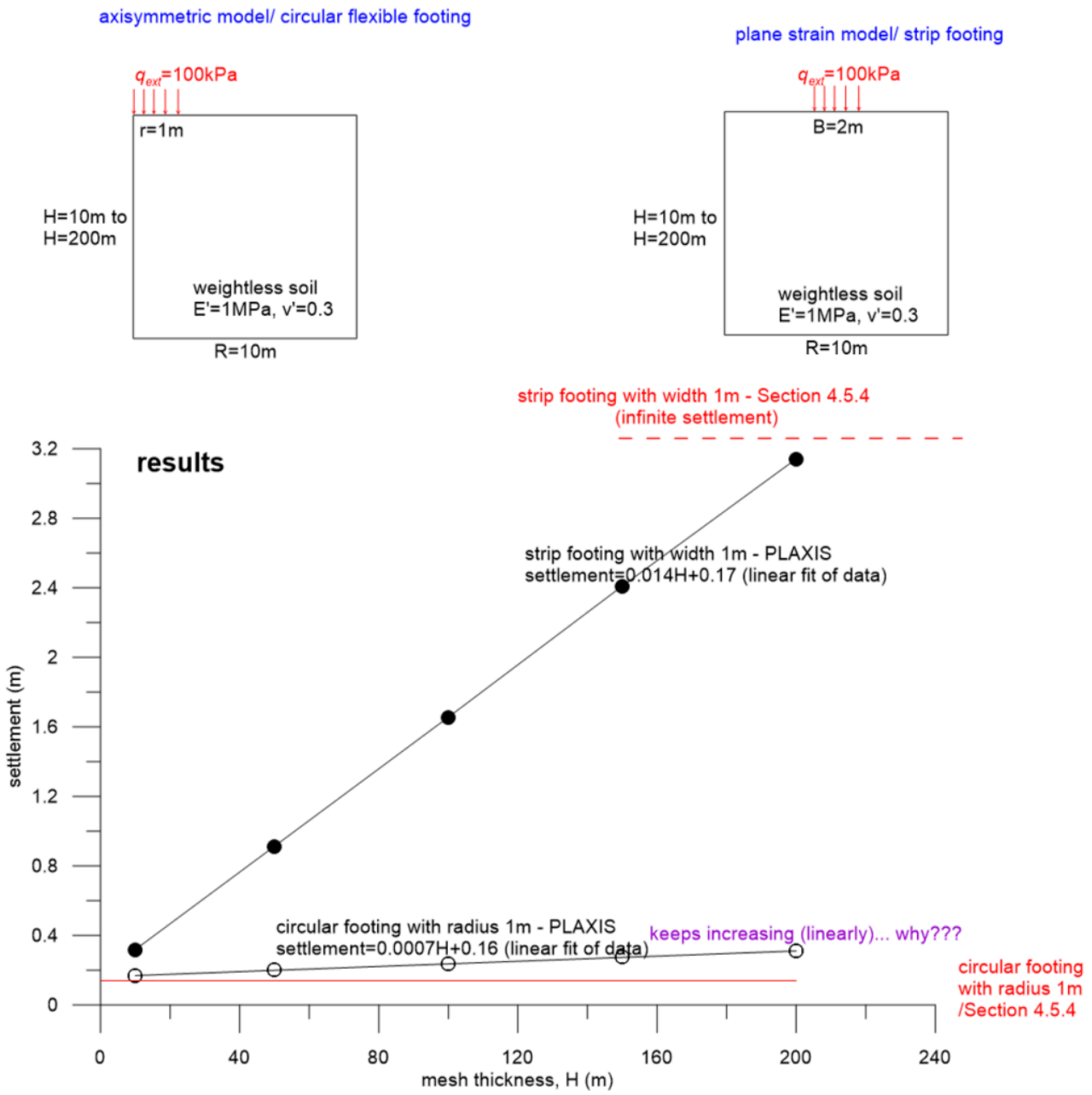

Figure 4.54. Evolution of footing settlement with increase in mesh thickness.

Answer:

Indeed, results presented in Figure 4.54 are flawed, but the error lies in the numerical solution, and not in the analytical results. The question mentions that we increase the thickness of the mesh from 10 m to 200 m, but does not mention anything about changing proportionally the mesh width, as seen in Figure 4.55.

When standard fixities are used in a numerical model i.e., the horizontal displacement is fixed at the lateral boundaries, we set the particular boundary to be an axis of symmetry. Therefore a "mirror" loading acts at a horizontal distance e.g., 8 m from the strip footing in Figure 4.55 and contributes to settlement (see also additional Example 3.2).

Correct (i.e. not compromised by boundary effects) results are depicted in Figure 4.56, and are obtained by increasing proportionally the mesh width to the mesh thickness. All other analysis parameters remain

unchanged. Notice that indeed settlement of a strip footing increases indefinitely as the mesh thickness increases, as intuitively expected for a plane-strain pressure acting on the top of a half-space (when the out-of-plane displacement is fixed to satisfy symmetry).

However, this is not the case for the circular footing, where settlement reaches an asymptote before the mesh thickness increases more than 40 m. In fact, the analytical solution is quite close to the numerical solution, and the above results verify its validity.

This rather crude example stresses out the importance of model boundary conditions in getting realistic results, and the need to carefully investigate the sensitivity of the solution to the boundary conditions (instead of relying on rules-of-thumb), to ensure that it is not compromised by errors introduced in the modelling stage. Analytical methods, such as the one described in Section 4.5.4 are invaluable for obtaining at least a first estimate of the expected solution.

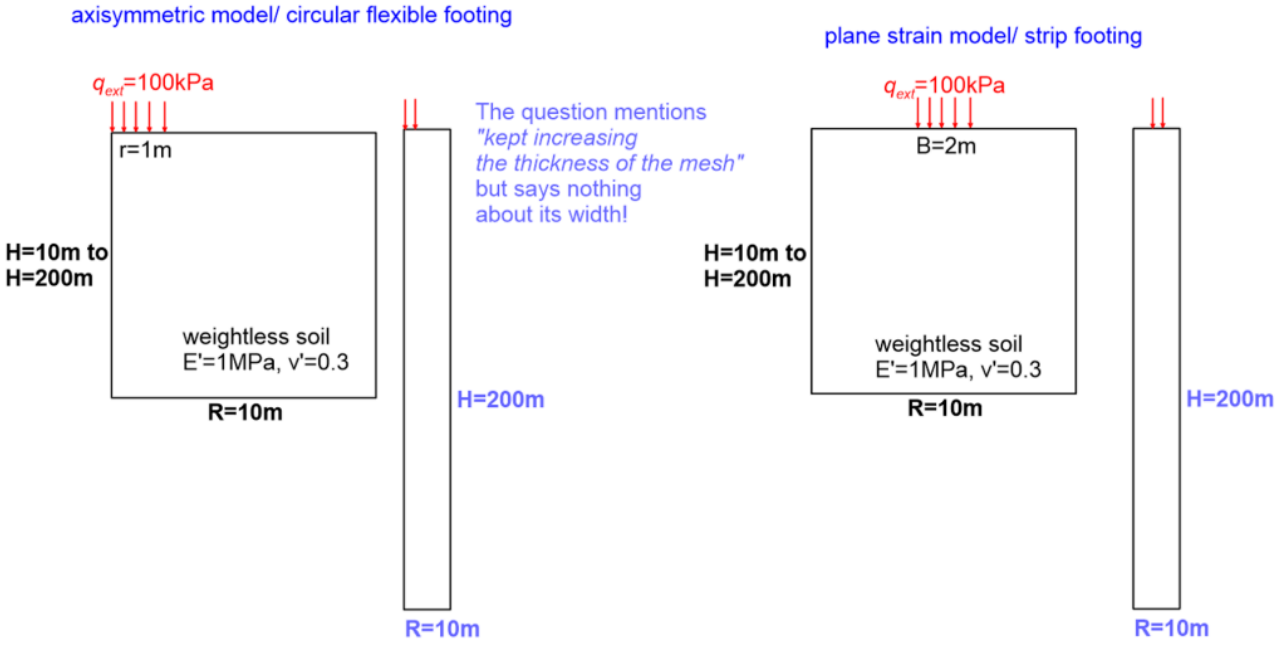

Figure 4.55. Simulated mesh dimensions for H = 200 m.

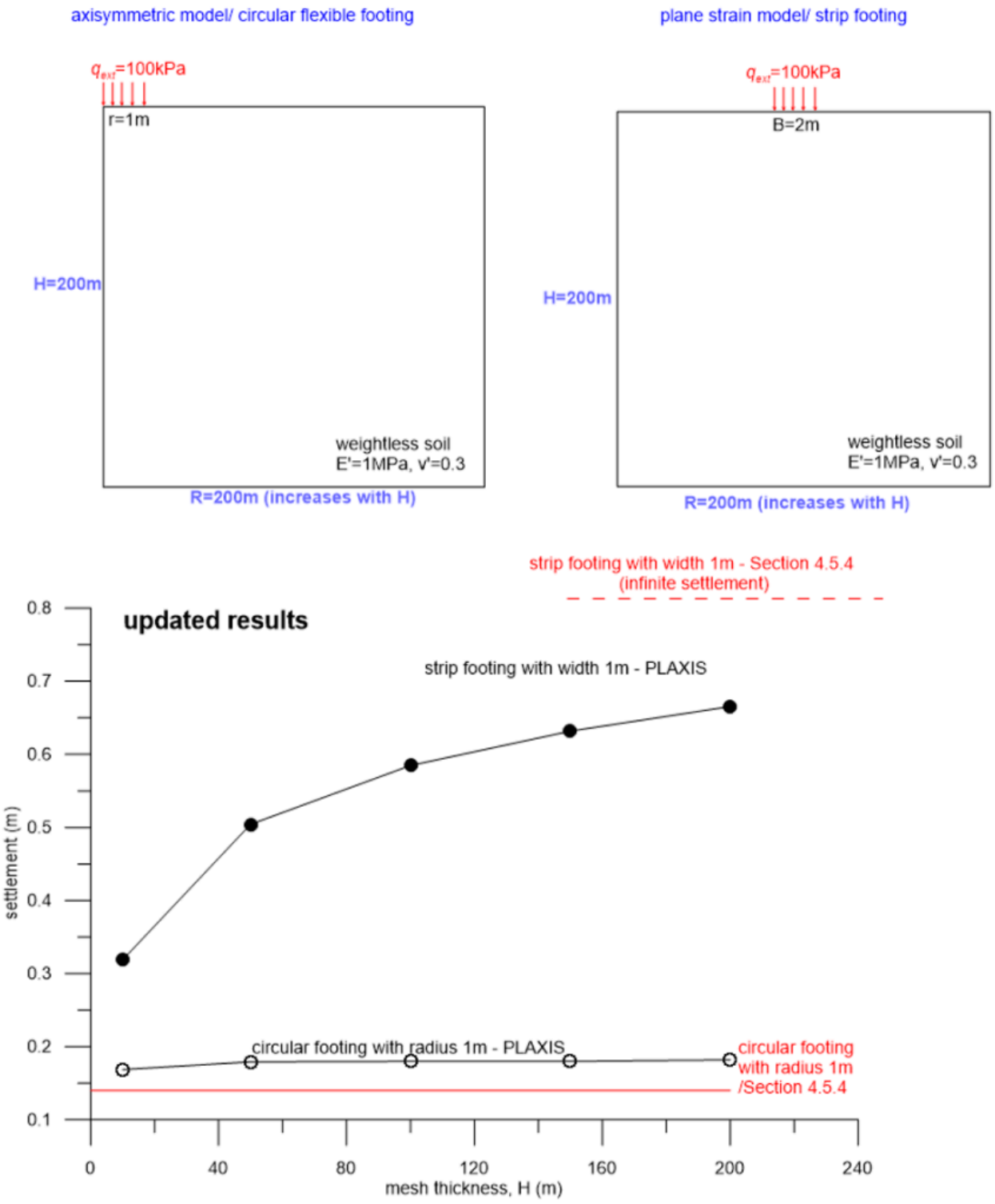

Figure 4.56. Evolution of footing settlement with increase in mesh thickness and mesh radius. Notice the vertical axis scale in comparison to Figure 4.55.

4.10 REFERENCES

1. Australian Standard AS2870. Residential slabs and footings.
2. Christian JT and Carrier WD (1978) Janbu, Bjerrum and Kjaernsli's chart reinterpreted. Canadian Geotechnical Journal, 15, 123-128.
3. Gazetas G, Tassoulas JL, Dobry R and O'Rourke MJ (1985). Elastic settlement of arbitrarily shaped foundations embedded in half-space. Géotechnique. Vol. 35(2), pp 339-346.
4. Lambe TW and Whitman RV (1969). Soil Mechanics. John Wiley & Sons, Inc.
5. Mitchell JK and Soga K (2005) Fundamentals of Soil Behavior. 3rd Edition, John Wiley & Sons, Hoboken.
6. Poulos HG, Carter JP and Small JC (2001). Foundations and retaining structures-research and practice. In: Proceedings, 15th International Conference on Soil Mechanics and Geotechnical Engineering, Istanbul, Turkey, Theme Lecture, Vol. 4, pp 2527-2606.
7. Skempton AW and Bjerrum L (1957). A contribution to the settlement analysis of foundation on clay. Géotechnique, Vol.7(4), pp 168-178.

4.11 ADDITIONAL PROBLEMS

4.11.1

The single-span bridge illustrated in the following figure is going to be founded on shallow square 6 m x 6 m footings, embedded at a depth equal to D_f = 2 m. The structural analysis of the bridge resulted in a maximum axial force on the bridge's piers under serviceability conditions equal to Q_w = 10 MN. The site investigation revealed a rather heterogeneous soil profile under the bridge, consisting of loose sand underneath the left abutment, and of medium-to-dense sand underneath the right abutment, featuring the compressibility parameters noted on the figure.

Ignoring the shear resistance developing at the wall-soil interface, calculate: a) the maximum uniform settlement of the critical pier, and b) the angular distortion of the bridge's foundation. Are these values tolerable, according to Poulos *et al.* (2001) criteria (Table 4.2)?

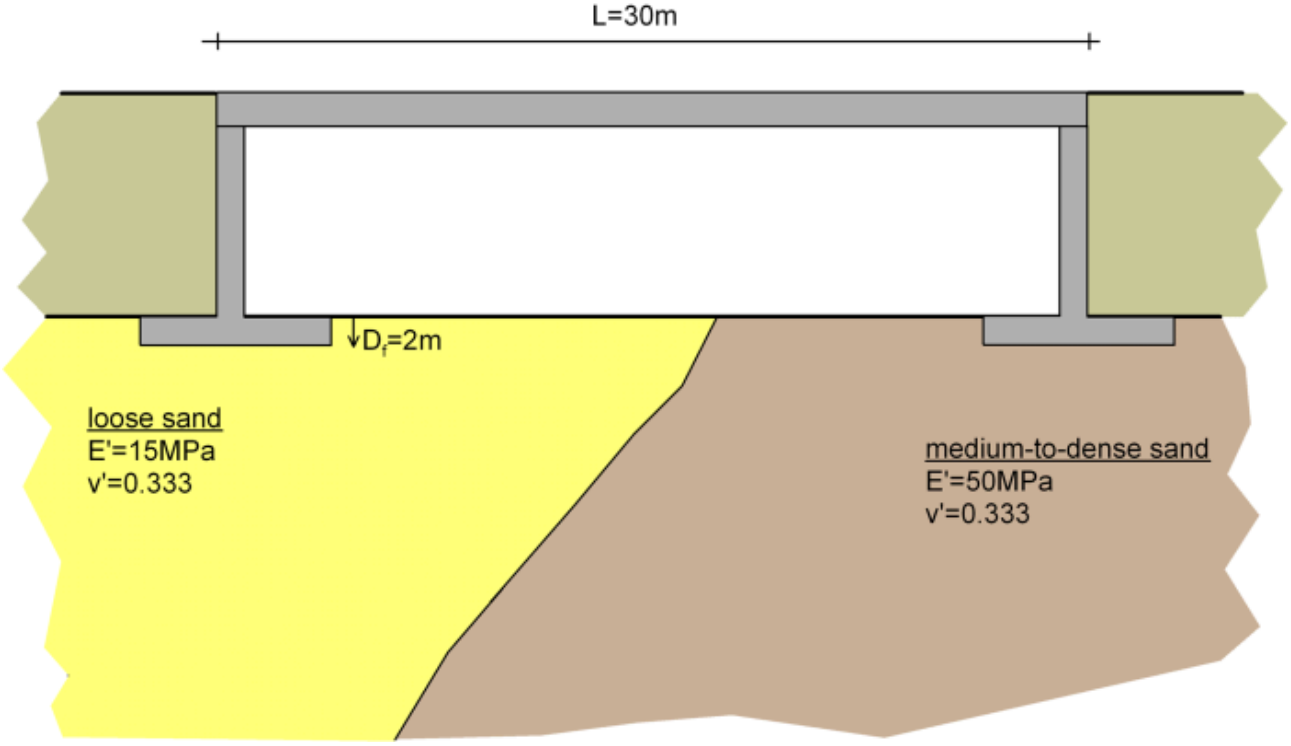

Additional problem 4.11.1. Problem description and input parameters.

Answer:

Critical pier settlement = 0.083 m

Angular distortion Δ/L=0.00193

Allowable total settlement = 100 mm>83 mm OK

Allowable angular distortion = 0.005>0.00193 OK

4.11.2

A wind turbine is going to be founded on the surface ($D_f = 0$) of a deep layer of homogeneous saturated clay, using a single circular footing. Triaxial laboratory tests on specimens of the foundation soil resulted to the following compressibility parameters: $E' = 10$ MPa, $\upsilon' = 0.333$. The maximum axial load on the foundation under serviceability conditions is, according to the Mechanical Engineer, equal to $Q_w = 5$ MN. Determine the minimum radius of the footing, so that its immediate settlement will not exceed 50 mm.

Answer:

R = 3.33 m

4.11.3

The subsoil at the bottom of a lake consists of a normally consolidated clay layer of thickness 5m, overlaying an incompressible layer of dense sand. Estimate the consolidation settlement of the bottom of the lake:

a. Due to an increase of the water level by 4m, and
b. Due to a subsequent desiccation of the lake, with the ground water level dropping at the level of the clay-sand interface.

Use the results of the oedometer test shown below, and assume the unit weight of the clay to be $\gamma = 18$ kN/m^3. For simplicity, do not divide the clay layer into sublayers.

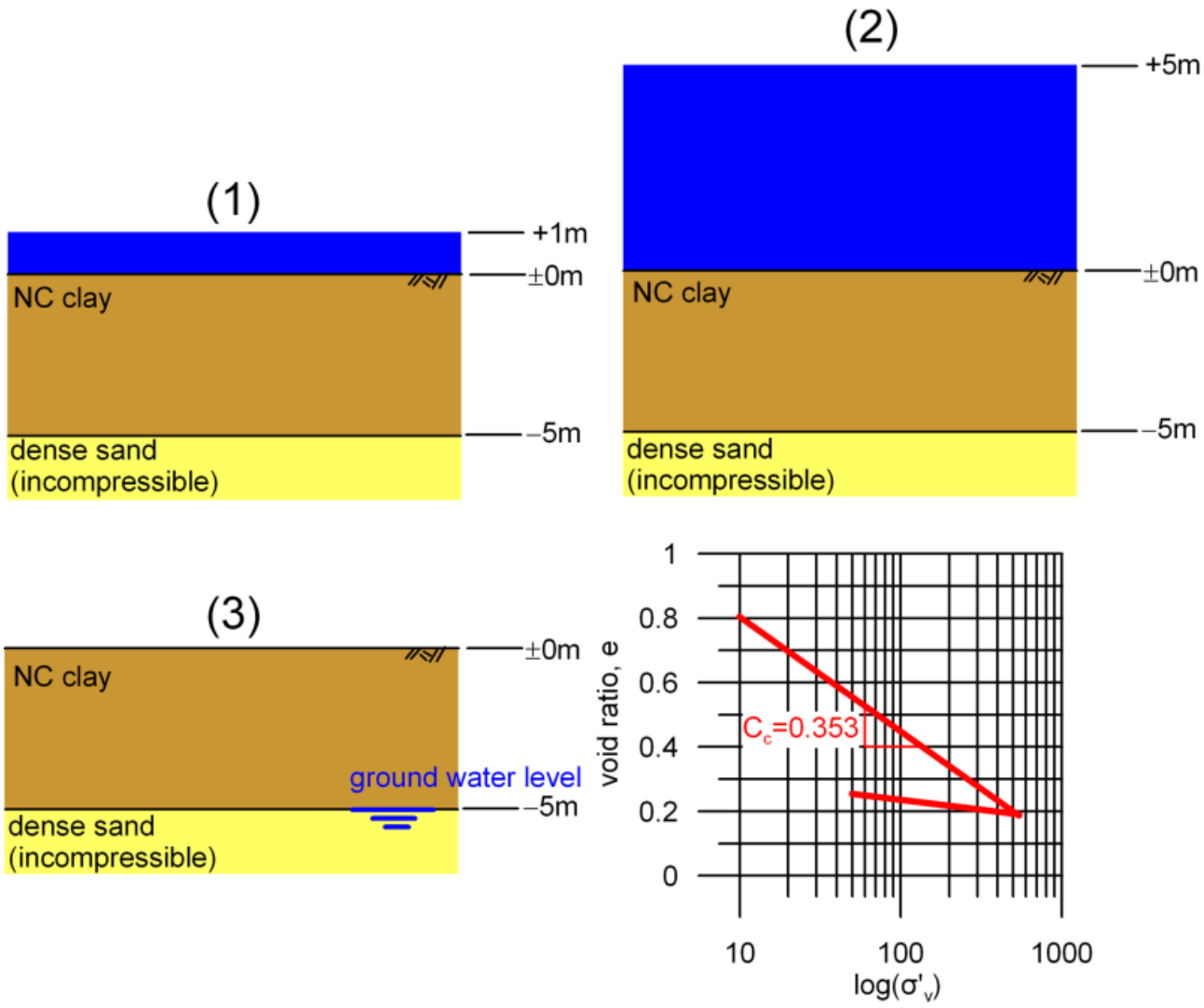

Additional problem 4.11.3. Problem description and input parameters.

Answer:

a. $\rho_{pc} = 0$
b. $\rho_{pc} = 0.33\ m$

4.11.4

A large cylindrical silo of diameter D = 30 m is going to be founded on a layer of soft saturated, normally consolidated clay of thickness 8 m, overlaying an incompressible layer of dense sand. The contact stress on the foundation of the silo is assumed uniform, and equal to q_{ext} = 160 kPa. Preliminary estimates indicated that ground improvement measures must be implemented to increase the bearing capacity of the clay layer, and reduce settlement. The cost-efficient method proposed for the improvement of the clay layer is its *preloading* via the construction of an extensive temporary embankment. Construction works will be implemented in 3 phases:

- Phase 1: Construction of a temporary embankment at the area of the foundation. The height of the

embankment will be 4 m, and the unit weight of the fill material will be $\gamma_{emb} = 20$ kN/m^3.

- Phase 2: Removal of the temporary embankment
- Phase 3: Construction of the silo

Assuming 1-D consolidation conditions, estimate the elevation of the ground surface at the foundation area, at the end of each construction phase. For simplicity, do not divide the clay layer into sublayers.

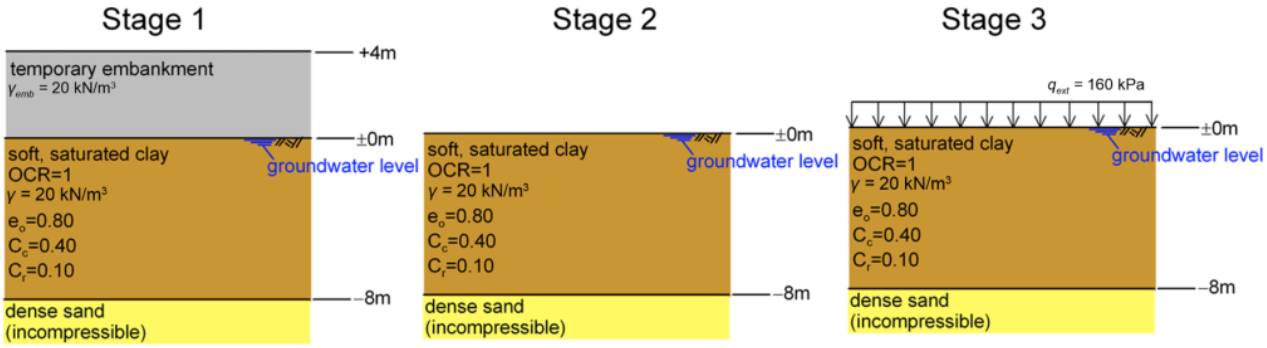

Additional problem 4.11.4. Problem description and input parameters.

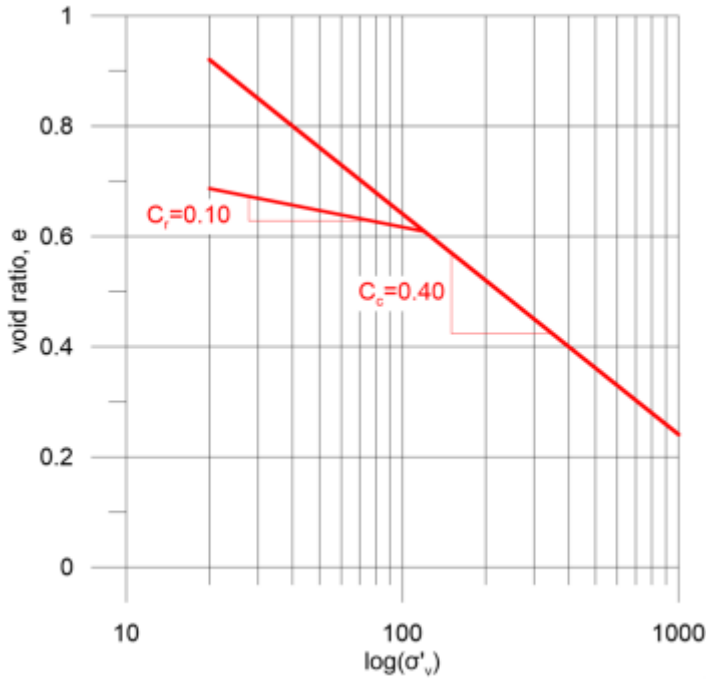

Additional problem 4.11.4. Oedometer test results.

Answer:

Initial level of ground surface : 0.0 m

At the end of stage 1: -0.848 m

At the end of stage 2: -0.636 m

At the end of stage 3: -1.24 m

5. BEARING CAPACITY OF SHALLOW FOUNDATIONS

5.1 INTRODUCTION TO PART 5

This Part is focused on applications of the theory of bearing capacity of *shallow* foundations i.e., footings which embedment depth is generally smaller than their plan view dimensions. Theoretical derivation of bearing capacity formulas for shallow footings is compendiously presented here, as it is covered in more detail in other textbooks. Emphasis of this Part is on design aspects viz. use of methods to design shallow foundations at the Ultimate Limit State together with *Load and Resistance Factor Design* (LRFD) concept inscribed in Australian Standards; practical considerations regarding modelling of the stress-strain behaviour of soils; analytical and numerical methods for predicting the collapse load of footings for common practical cases, based on laboratory and *in situ* test results.

5.2 SOME FUNDAMENTALS: LOAD AND RESISTANCE FACTOR DESIGN (LRFD) & SHEAR STRENGTH OF SOILS

5.2.1 General concepts

Geostructures are designed at the Ultimate Limit State to be able to safely carry a *collapse load*, without failure in the form of bearing capacity failure of shallow or deep foundations, rotational failure of slopes etc. Two design approaches are encountered in practice:

In the (perhaps now obsolete) conventional, *allowable stress design* (or *Limit State Design*) method, the collapse load is determined via analytical methods or numerical analyses, using appropriately factored material parameters. Accordingly, the collapse load or the load that a structure can safely carry at the Ultimate Limit State is divided by a *Factor of Safety* (F.S.) to obtain the allowable design load:

$$\text{Allowable design load} = \frac{\text{Collapse load}}{\text{F.S.}} \quad \textbf{(5.1)}$$

Values of the factor of safety depend on the nature of the problem, and are based on experience from previous projects. Thus, they are purely empirical.

Load and Resistance Factor Design, which forms the basis of design of foundations and soil-supporting systems with AS5100.3, but also with most modern geotechnical design codes from the United States and Europe, is based on reliability concepts and allows considering uncertainties in loads, soil resistance, method of analysis, and construction. The loads and action effects are multiplied by load factors (usually) greater than one, in different combinations, to determine the *design action load* S^*. The *ultimate geotechnical strength* R_{ug} (in the context of this Part it is the compressive loading that the geostructure can safely carry at the Ultimate Limit State) determined analytically or numerically, is multiplied by a *geotechnical strength reduction factor* φ_g (usually) less than one, to provide the *design capacity*. Design of any geostructure at the Ultimate Limit State must satisfy the following inequality:

$$\varphi_g R_{ug} \geq S^* \quad \textbf{(5.2)}$$

or, according to AS5100.3 for shallow footings:

> *"Footings subjected to vertical or inclined loads or overturning moments shall be proportioned such as the design bearing capacity is greater than or equal to the design action effect S^*"*

Note here that the load and strength reduction factors apply only to strength calculations. Settlement calculations are performed while considering serviceability load combinations, and no geotechnical strength reduction factors are applied on the calculated settlement value.

5.2.2 Establishment of the design action load

Apart from the usual loads and surcharges, which are defined in AS1170.0 and AS1170.1 and discussed

elsewhere, secondary loads must be considered for the design of geotechnical structures. These include loads resulting from vertical and lateral soil movement (e.g., negative skin friction due to consolidation, heave due to moisture changes in expansive soils), earth pressure loads, hydrostatic pressure loads and seepage forces, compaction pressures etc. Usual loads and load combinations for structural and geotechnical strength calculations can be found in AS1170.0 and AS1170.1 for structures other than bridges, and in AS5100.2 for bridges. Some of the most common ones are (the load factors are indicative):

- $S^* = [1.35G]$, considering permanent actions G only.
- $S^* = [1.2G, 1.5P]$, considering permanent actions G combined with imposed (live) actions P.
- $S^* = [1.2G, W, \xi P]$ considering permanent actions G combined with wind loads W and imposed actions ξP where ξ is a combination factor that accounts for the fact that all imposed loads will not act simultaneously with their maximum value.

Loads due to soil movement are considered as permanent loads (G) and introduced in the load combinations for *structural strength calculations only* (e.g., determining the necessary reinforcement of a footing or a pile). The factors are again indicative, and the reader is referred to the relevant standards.

- $1.2F_{nf}$ for negative skin friction due to consolidation.
- $1.5F_{es}$ for compressive and tensile loads resulting from vertical soil movements other than consolidation.
- $1.5F_{em}$ for bending moments, shear forces and axial loads resulting from lateral soil movements and heave.

Loads due to soil movement are not considered in *geotechnical strength calculations* e.g., the bearing capacity of shallow or deep foundations which are of interest here. The reasoning for that is discussed in Chapter 6.22, where negative skin friction effects on piles are introduced.

5.2.3 Estimation of the ultimate geotechnical strength

According to the Standards, the ultimate geotechnical strength R_{ug} shall be determined via well-established analytical or numerical methods, using unfactored *characteristic* values of geomaterial shear strength parameters.

Estimation of characteristic values of soil and rock parameters is based, as discussed in Part 1, on engineering judgment. AS5100.3 provides a more formal description of the factors that must be considered while determining characteristic shear strength parameters:

- Geological and geotechnical background information.
- The possible modes of failure.
- Results of laboratory and field measurements, taking into account the accuracy of the test method used.
- A careful assessment of the range of values that might be encountered in the field.
- The range of *in situ* and imposed stresses likely to be encountered in the field.
- The potential variability of the parameter values and the sensitivity of the design to this variability.
- The extent of the influence zone governing the soil behavior, for the limit state considered.
- The influence of workmanship on artificially placed or improved soils.
- The effects of construction activities on the properties of the *in situ* soil.

The quantity and quality of available data will most certainly affect the selection of characteristic soil parameters. When only a limited amount of tests of questionable reliability is available, it is prudent to consider a characteristic parameter value close to the lower bound of the values interpreted from the data. On the other hand, when sufficient high-quality, reliable data are available, it is reasonable to consider a characteristic value close to the median of the parameter values interpreted from the data.

5.2.4 Establishment of the geotechnical strength reduction factor

As discussed above, determination of the geotechnical strength reduction factor φ_g is based on reliability concepts considering uncertainties in the nature of loading, the determination of soil parameters from *in situ* and laboratory tests, the method used for the estimation of the ultimate geotechnical strength, and construction aspects. In more detail, according to AS5100.3, the following need to be considered for the estimation of the appropriate geotechnical strength reduction factor:

- Methods used to assess the geotechnical strength.
- Variations in soil conditions.
- Imperfections in construction.
- Nature of the structure and mode of failure.
- Importance of the structure and consequences of failure.
- Standards of workmanship and supervision of the construction.
- Loading variations and cyclic load effects.

Determination of the value of the geotechnical strength reduction factor for deep foundations by means of a risk assessment procedure is discussed in Part 6. For shallow footings, a range of values of φ_g is provided in the following Table 5.1, depending on the method of analysis used to determine the bearing capacity.

Table 5.1. Range of values of geotechnical strength reduction factor φ_g for shallow footings (AS5100.3).

Method of assessment of Ultimate Geotechnical Strength	Range of values of φ_g
Analysis using geotechnical parameters based on appropriate advanced *in situ* tests	0.50 to 0.65
Analysis using geotechnical parameters from appropriate advanced laboratory tests (see Chapters 5.4 and 5.5)	0.45 to 0.60
Analysis using CPT tests (see Chapter 5.8)	0.40 to 0.50
Analysis using SPT tests (see Chapter 5.7)	0.35 to 0.40

Selection of the appropriate value from the range provided in Table 5.1 is based on the guidelines presented in Table 5.2.

Table 5.2. Guidelines for determining the geotechnical strength reduction factor φ_g for shallow footings (AS5100.3).

Lower end of range	Upper end of range
Limited site investigation	Comprehensive site investigation
Simple methods of calculation	More sophisticated design method
Limited construction control	Rigorous construction control
Severe consequences of failure	Less severe consequences of failure
Significant cyclic loading	Mainly static loading
Foundation for permanent structures	Foundations for temporary structures
Use of published correlation for design parameters	Use of site-specific correlations for design parameters

Since this Part is devoted to shallow foundations subjected to compressive vertical or inclined loads, we will use

hereafter the term "bearing capacity q_f" to refer to the ultimate geotechnical strength in terms of stress, and the term "collapse load Q_f" to refer to the ultimate geotechnical strength in terms of force. The design capacity is defined as the collapse load multiplied by the geotechnical reduction factor $\varphi_g Q_f$.

Application of the Load and Resistance Factor Design concept for determining the ultimate geotechnical strength (bearing capacity/collapse load) of shallow footings with analytical and numerical methods and subsequently of their design capacity is presented in the following Examples 5.1 and 5.2. Before that, some of the fundamentals of the shear strength of soils are repeated, in the light of the Mohr-Coulomb failure criterion and its (arguably widespread) use for estimating the collapse load of shallow foundations in practice.

5.2.5 Drained and undrained shear strength of soils-The Mohr-Coulomb failure criterion.

In order to determine the collapse load by means of numerical analysis or analytical methods, we have to quantify soil's shear strength, and describe its non-linear response up to failure with a suitable *constitutive model*. The shear strength of soils is a subject discussed in detail in other textbooks, hence it is assumed that the reader is familiar with some essential concepts, such as laboratory soil tests, and emphasis is put here on practical aspects.

The simplest model used in practice to describe the response of soils up to failure and beyond is the elastic-perfectly plastic model obeying the Mohr-Coulomb failure criterion, referred to in the following as the *Mohr-Coulomb model* for brevity. The Mohr-Coulomb model is used to describe the real soil stress-strain response under different stress paths e.g., unconfined uniaxial compressive (UC) loading (Figure 5.1a) with an idealised elastic-perfectly plastic stress strain curve (Figure 5.1b), that is straightforward to define as it requires the minimum number of input soil parameters.

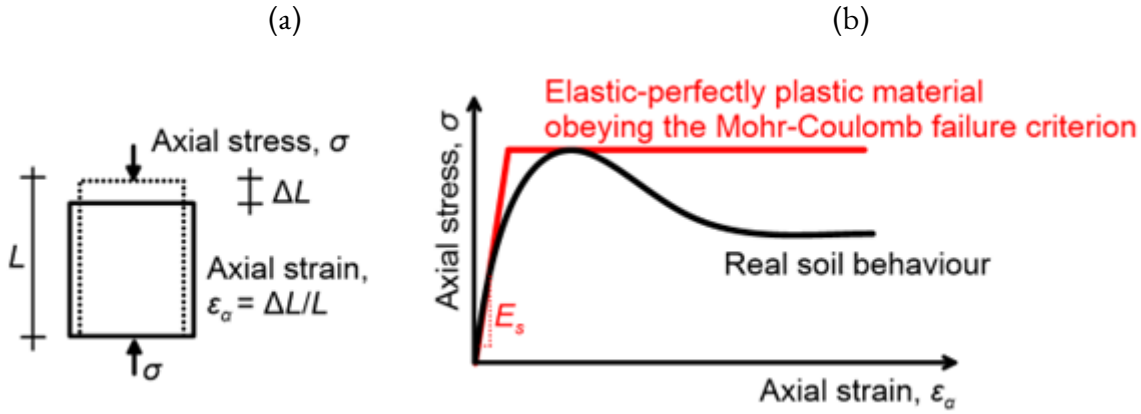

Figure 5.1. (a) Schematic of an unconfined compression test (b) Strain-strain curve.

It is reminded here that the stress state of any soil element can be described with Mohr's circle, depicted in Figure 5.2 for two-dimensional conditions.

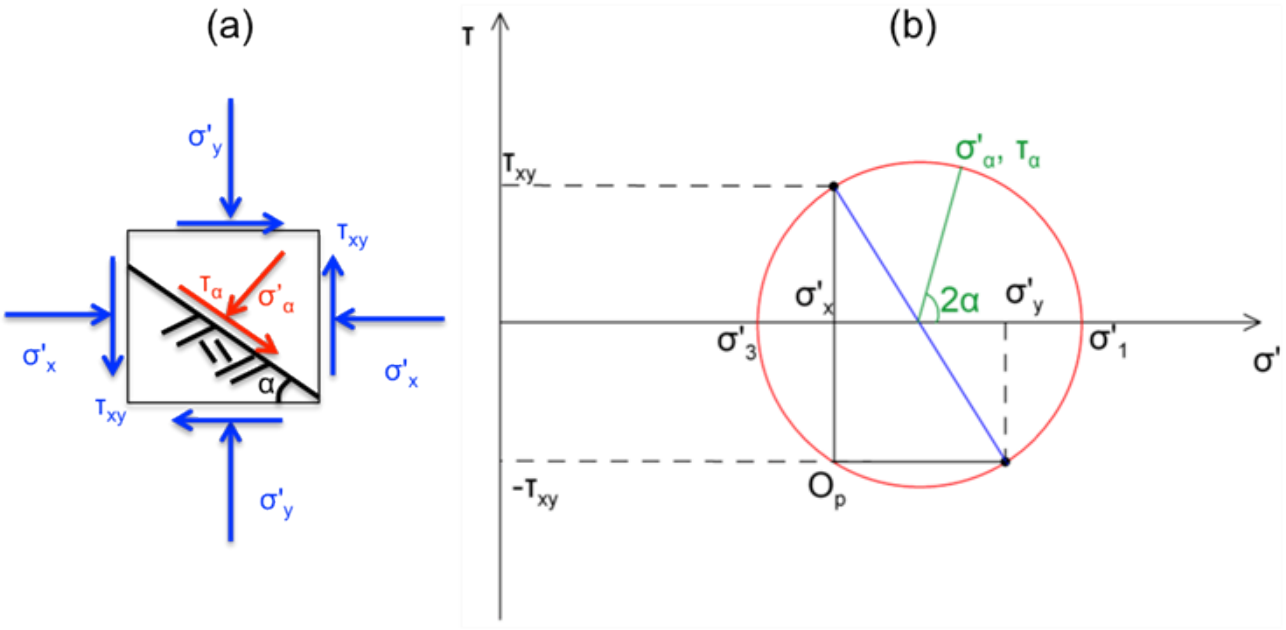

Figure 5.2. (a) Stress state of a soil element under general loading, and (b) the corresponding Mohr's circle for stresses.

The Mohr-Coulomb *failure criterion* suggests that the following inequality 5.3 is valid for all planes passing through the soil element in Figure 5.2, with the inclination of the plane defined by angle α:

(5.3) $\tau_\alpha \leq c' + \sigma'_\alpha \tan\varphi'$

As depicted in Figure 5.3, the Mohr-Coulomb failure criterion describes a line (envelope) in the σ'–τ effective normal stress-shear stress space. In effective stresses, this envelope is defined by the soil's effective cohesion c' and the friction angle φ'. Note that symbols φ' and φ are often used interchangeably, and both represent friction angle under effective stress. For any given stress state applied to the soil element, the Mohr's circle lies below the failure line (*feasible* area), or is tangent to it. In the first case the soil remains elastic, whereas in the second case the soil has reached failure (Figure 5.3).

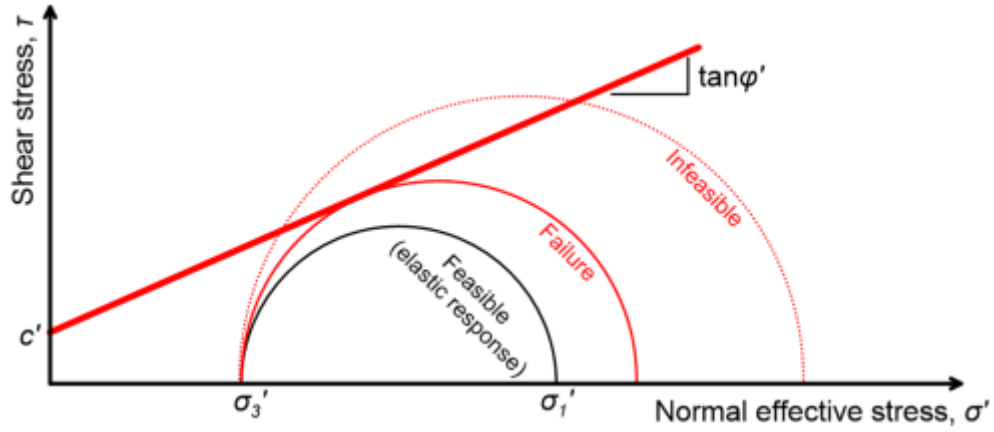

Figure 5.3. Mohr-Coulomb failure envelope for effective stress parameters.

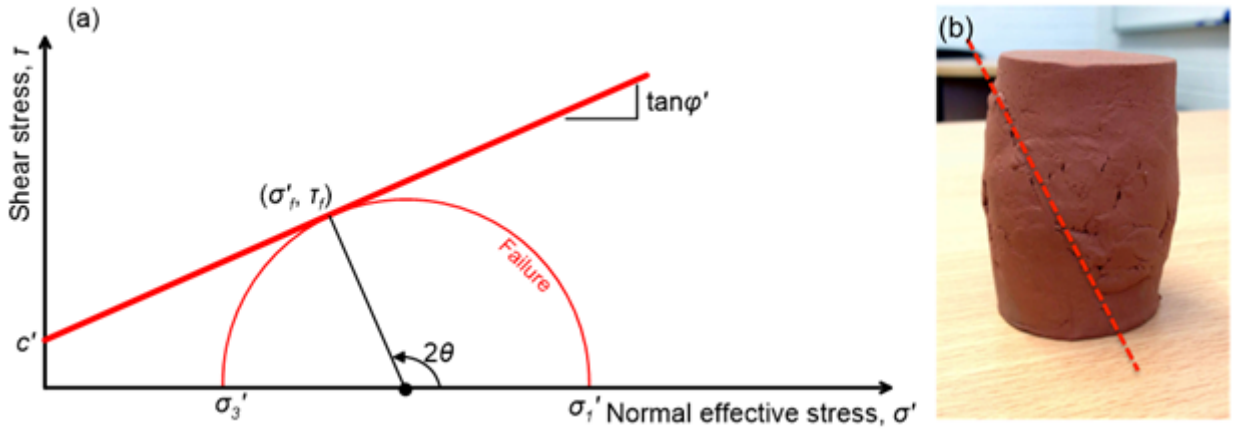

Figure 5.4. (a) Mohr-Coulomb circle at failure considering effective stress parameters (drained response) and (b) failure plane formed in an unconfined compression (UC) test.

Failure of the soil element takes place at a plane defined by angle θ, where the shear stress and the normal stress acting on this plane satisfy Eq. 5.4 (Figure 5.4):

(5.4) $$\tau_f = c' + \sigma'_f \tan\varphi'$$

When no excess water pore pressure develops in the soil upon loading, its response is called *drained*, and failure can be described with the effective stress parameters c', φ'. This type of response can be simulated in PLAXIS with the Mohr-Coulomb *Drained* soil model. Remember that the drained soil compressibility parameters (Young's modulus E', Poisson's ratio υ') must be used to quantify its linear elastic response up to failure. Properly using the Mohr-Coulomb model, which allows describing soil strength with only two (plus the dilation angle, as we will see later) parameters, requires understanding and appreciating the deficiencies of such a simplified approach. First of all, dilating soils such as dense sands will reach a peak strength during shearing, and their strength will drop to a residual value at relatively large strains (Figure 5.5). Depending on the selection of the friction angle φ' we can capture either the peak or the residual strength with the Mohr-Coulomb model-not both. Which one we will choose to capture depends on the nature of the problem.

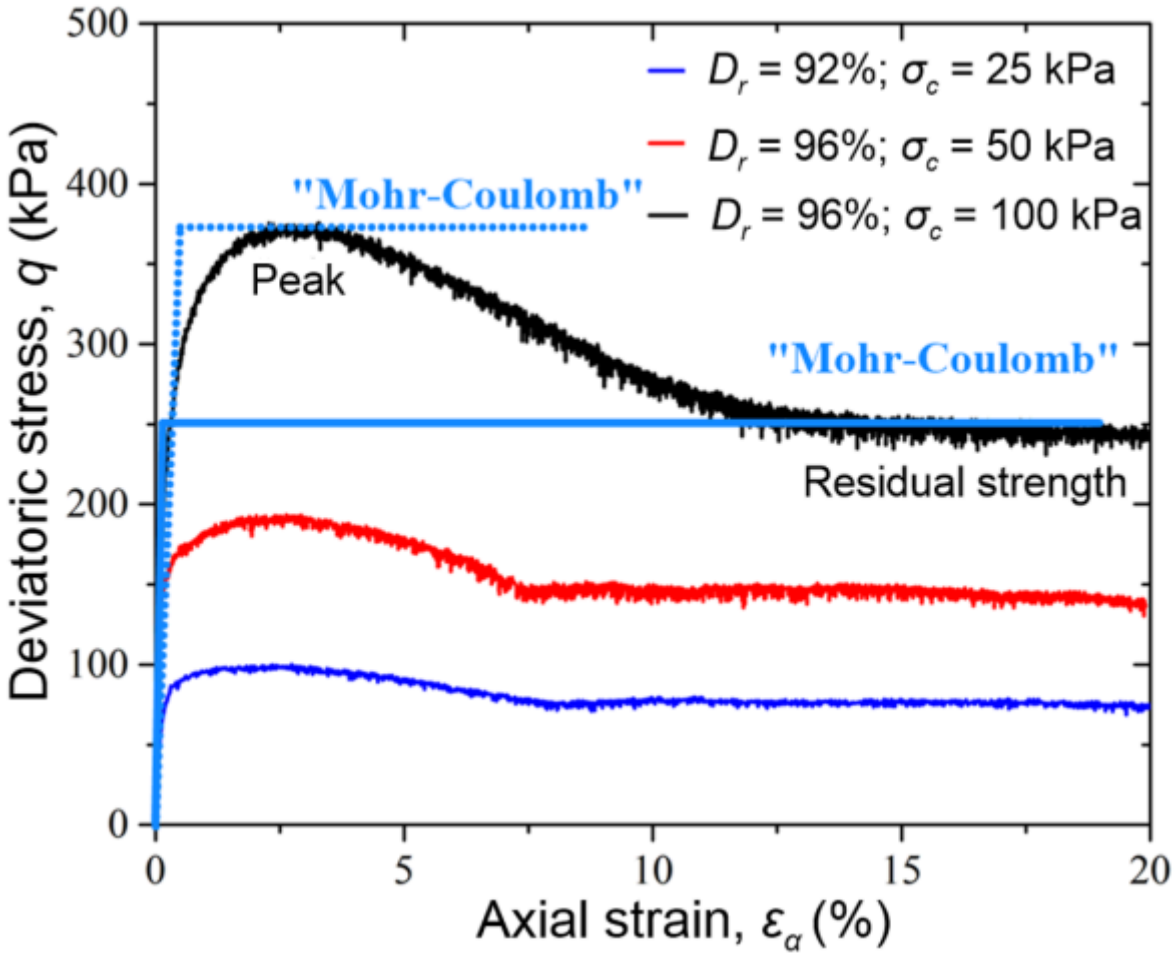

Figure 5.5. Deviatoric stress-axial strain curves obtained during the shearing stage of isotropically-consolidated (confining stress σ_C = 25, 50 and 100 kPa) triaxial compression tests on dense Stockton Beach sand samples.

Another important simplification introduced in the Mohr-Coulomb model is that the failure envelope in the σ'–τ space is a straight line (Figure 5.3). However, the failure envelope of real soils is not linear, in other words the friction angle φ' actually depends on the level of confining stress that the soil is being subjected to during shearing. As consequence, the Mohr-Coulomb shear strength parameters selected to estimate the collapse load must be compatible with the normal stress levels experienced by soil for the particular problem. To further delve into that, Figure 5.6a presents measurements obtained during four direct shear tests in dense dry Stockton Beach sand, a non-cemented silica sand that certainly has zero strength under zero normal stress or c' = 0. However, linear fitting of the test data by the direct shear testing device software to automatically obtain strength parameters yielded effective cohesion c' = 6.3 kPa. This is not an error, but a consequence of attempting to describe the sand failure envelope with two parameters (Figure 5.6b). The automatically calculated strength parameters will accurately describe Stockton Beach sand shear strength if the normal stress acting on shear planes are between 50 kPa and 250 kPa, but will result in erroneous predictions if e.g., the normal stress is significantly lower. As one would expect there exist material models (some of which implemented in PLAXIS) that incorporate non-linear failure criteria, thus are capable of quantifying soil strength across a wide range of normal stresses with a single set of parameters. However, description of such (more advanced) material models is beyond the scope of this Part.

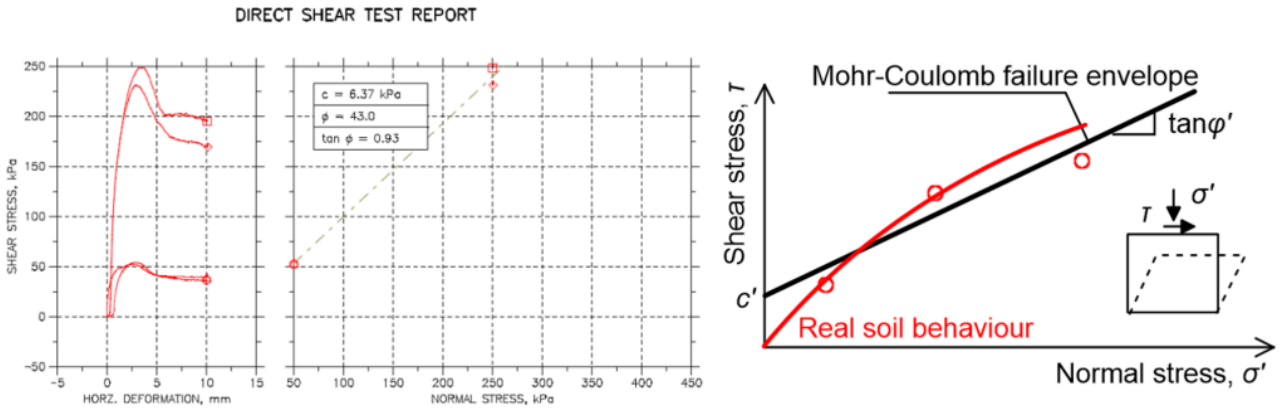

Figure 5.6. (Left) Shear stress-horizontal deformation and fitting Mohr-Coulomb failure envelope from four (4) direct shear tests on dense Stockton Beach sand (normal stress 50 and 250 kPa); (Right) Comparison of linear Mohr-Coulomb failure envelope and real (non-linear) soil failure envelope.

Excess pore pressure Δu may develop during and shortly after the application of external stresses on fine-grained soils exhibiting low permeability. This excess pore pressure should be accounted for the estimation of the effective normal stress acting on the failure plane. Considering explicitly the excess pore pressure that develops up to failure is not an easy task, and certainly the Mohr-Coulomb model, due to its simplicity, is not capable of providing realistic estimates. To tackle this problem, we resort to defining failure in terms of total (instead of effective) stresses. This concept is introduced in Figure 5.7 below, which presents results of two conceptual *undrained* triaxial tests on isotropically consolidated clay samples reconstituted from slurry (therefore normally consolidated at the end of Stage 1). During the undrained shearing Stage 2, excess pore pressure develops, and failure takes place at a deviatoric stress q less than the deviatoric stress that the sample would fail if sheared slowly enough that drained conditions would prevail, and effective stresses were equal to total stress ($\Delta u = 0$). As before, failure occurs when the effective stress circle becomes tangent to the Mohr-Coulomb failure line. In other words, soil still obeys the failure criterion defined in Eq. 5.1 and depicted in Figure 5.3.

To alleviate the need for calculating excess pore pressure, we can define failure through the Mohr's circle of total stresses which we know, as they are the externally applied stresses on the soil sample. The failure plane for total stress is horizontal, and intersects the shear stress axis at $S_u = q_{failure}/2 = (\sigma'_{1,failure}-\sigma'_{3,failure})/2 = (\sigma_{1,failure}- \sigma_{3,failure})/2$. We call the deviatoric stress at failure (divided by 2), S_u the *undrained shear strength* of the soil sample.

Note however that the undrained shear strength is not a fundamental material parameter, as it depends on the effective (pre)consolidation stress σ'_c, and the overconsolidation ratio OCR. This is clear in Figure 5.7, where a sample of the same soil isotropically consolidated at a higher stress (test 2) and thus featuring a lower void ratio (water content), fails under higher deviatoric stress, therefore will have a higher undrained strength.

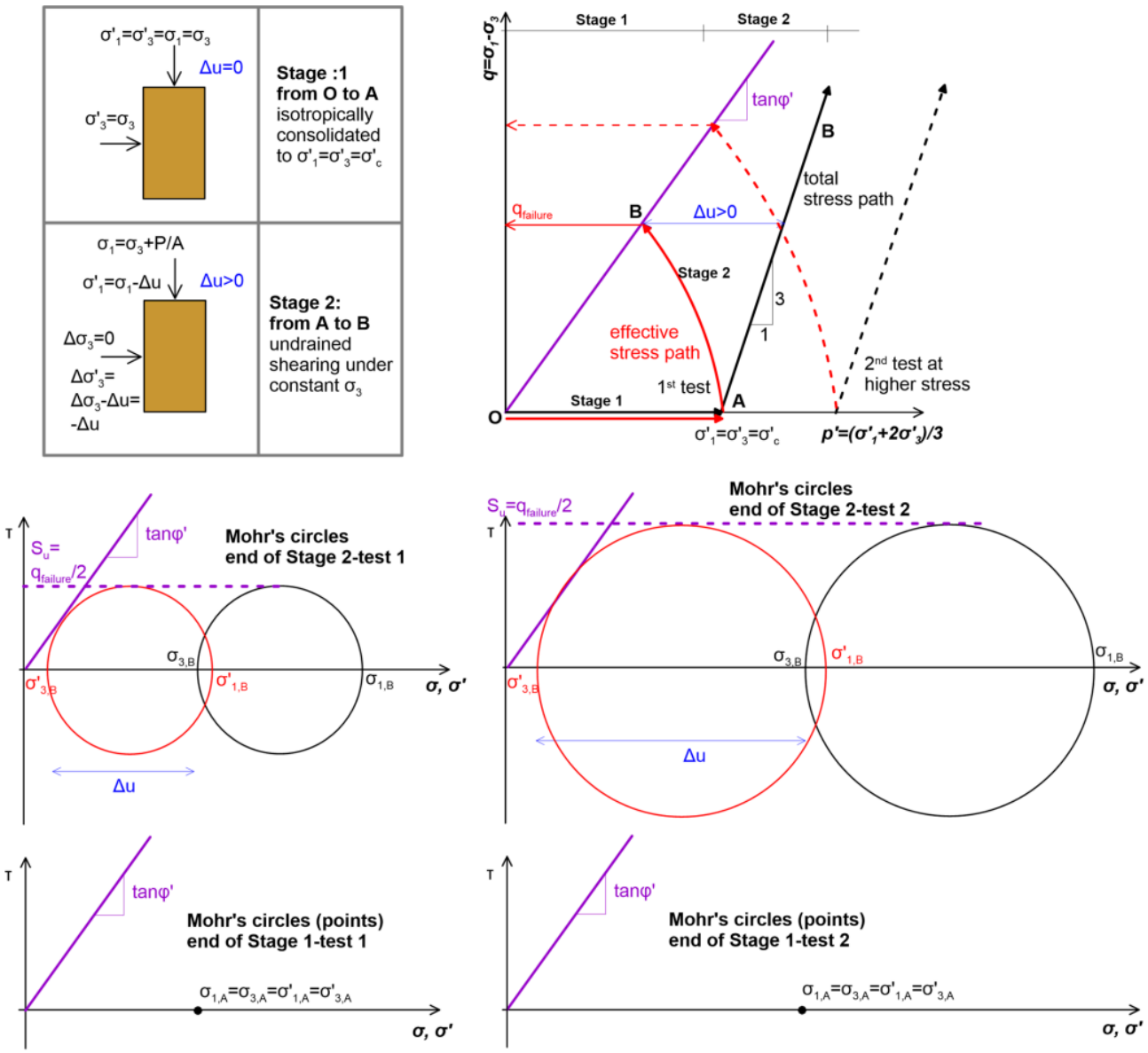

Figure 5.7. Schematic of isotropically consolidated undrained triaxial tests (CU) in two clay samples.

Some readers may erroneously associate the terms *drained* and *undrained* tests or soil behaviour with the presence of groundwater table, or even just drainage boundary conditions. However, the terms *drained* and *undrained* in soil mechanics context refer to the development or not of excess pore pressures in soil upon its loading, *in situ* or in the laboratory. Whether a soil will behave as drained or undrained *in situ* depends on its permeability and the rate of loading. It is reminded that soils above the groundwater table may still be saturated, and will develop excess pore pressures (will behave as undrained) after the application of an external loading, if their permeability is low. Bishop and Eldin (1950), who were among the first to use the terms undrained and drained, explain that undrained tests were referred to prior to 1949 as "immediate tests" in England and "quick tests" in the USA, Netherlands and Belgium since, owing to the low permeability of clay soils, the same result is obtained if the test is performed relatively quickly, even if drainage is not prevented during laboratory soil testing, because excess pore pressures cannot dissipate fast enough. Similarly, drained tests were referred to as "slow tests", since slow testing rate was required to ensure full dissipation of excess pore pressures, even when drainage is not prevented. However, the terms slow and fast can be misleading when dealing with soils of different permeabilities, and are not used anymore: For example an undrained test in clay may require several months to complete, while a drained test in sand may be completed in minutes.

There is a common misconception that the undrained shear strength does not depend on the level of stresses and is a material constant, which has its origins in the use of unconsolidated undrained triaxial

tests to quickly (as these tests are fast) determine the shear strength of samples in the laboratory. Indeed, when the sample is compressed quickly and is not allowed to consolidate (Figure 5.8) the effective stresses at the beginning of the shearing stage will remain the same, regardless of the level of applied confining (total) stress. Therefore, samples compressed at different levels of confining stress will fail at the same deviatoric stress as they will follow the same effective (but not total) stress path, hence exhibit the same undrained strength. In other words, Mohr circles under different total stress levels may be different, but the corresponding circles for effective stresses are all the same, and tangent to the effective stress failure envelope (Figure 5.8). This observation though is valid for unconsolidated undrained tests only. Note that an unconfined compression (UC) test that is performed under $\sigma_c = 0$ would result in the same undrained strength, and the soil sample would follow again the same effective stress path, despite total stresses being equal to zero. That is because the effective stresses are not zero, as they equilibrate the negative excess pore pressure $-u_r$ in the sample that develops due to capillary effects. This is the reason why a clay sample retrieved from a borehole appears to have "some strength" (and is often described as "cohesive", a term that has been avoided on purpose here) despite the total confining stress being equal to zero, and not because the soil has real cohesion due to cementation or natural fabric. The Mohr-Coulomb failure plane for total stresses is again horizontal (undrained friction angle $\varphi_u = 0$).

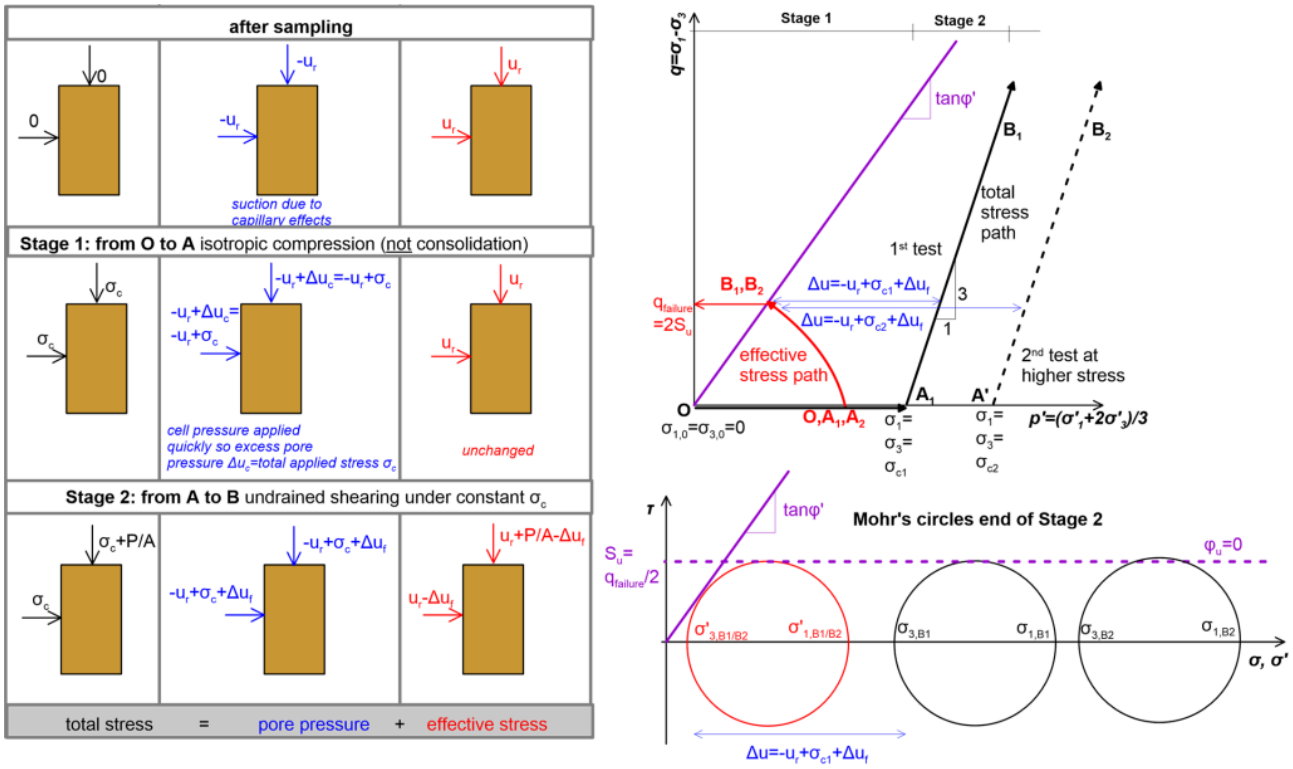

Figure 5.8. Schematic of unconsolidated undrained triaxial tests (UU) in two clay samples.

Some fundamental conclusions arise from this discussion, which are particularly important for modelling of failure of soils under undrained conditions:

- Soil fails under exactly the same "frictional sliding" mechanism, regardless of whether it is sheared under drained or undrained conditions.
- The undrained shear strength depends on the preconsolidation stress of soil, and is not a material parameter. The preconsolidation stress will increase with depth (as geostatic stresses increase), therefore the undrained strength will increase with depth even in uniform, normally consolidated soil. For a normally consolidated soil under geostatic stress $S_u/\sigma'_{z0} \approx 0.22$ or generally $S_u/\sigma'_c \approx 0.22$ where σ'_c is the preconsolidation stress. This is in line with Eq. 5.3 which suggests that the same soil will exhibit higher strength if found under higher confining normal stress.
- The undrained shear strength must be used to define failure together with total stresses only (total stress analysis). This response is simulated in PLAXIS with the Mohr-Coulomb *Undrained (C)* The undrained soil compressibility parameters (Young's modulus E_u, Poisson's ratio υ_u) must be considered together with this model to describe linear elastic response up to failure, and the

undrained shear strength S_u obtained from tests is provided as a model parameter. Certainly PLAXIS, as well as most geotechnical Finite Element Codes, allows considering a linear increase of undrained strength with depth along a particular soil layer by defining $S_{u,inc}$ (units: stress/unit depth) thus satisfying the described mechanisms.

It is perhaps clear from the above that soil strength (and the collapse load of foundations on it) depends on the loading conditions: drained or undrained. However, it also depends on the stress path that is followed to failure, as depicted in Figures 5.9 and 5.10. The stress path to failure is the field is rarely known (Figure 5.11) and therefore it is common to consider an average (or mobilised) shear strength.

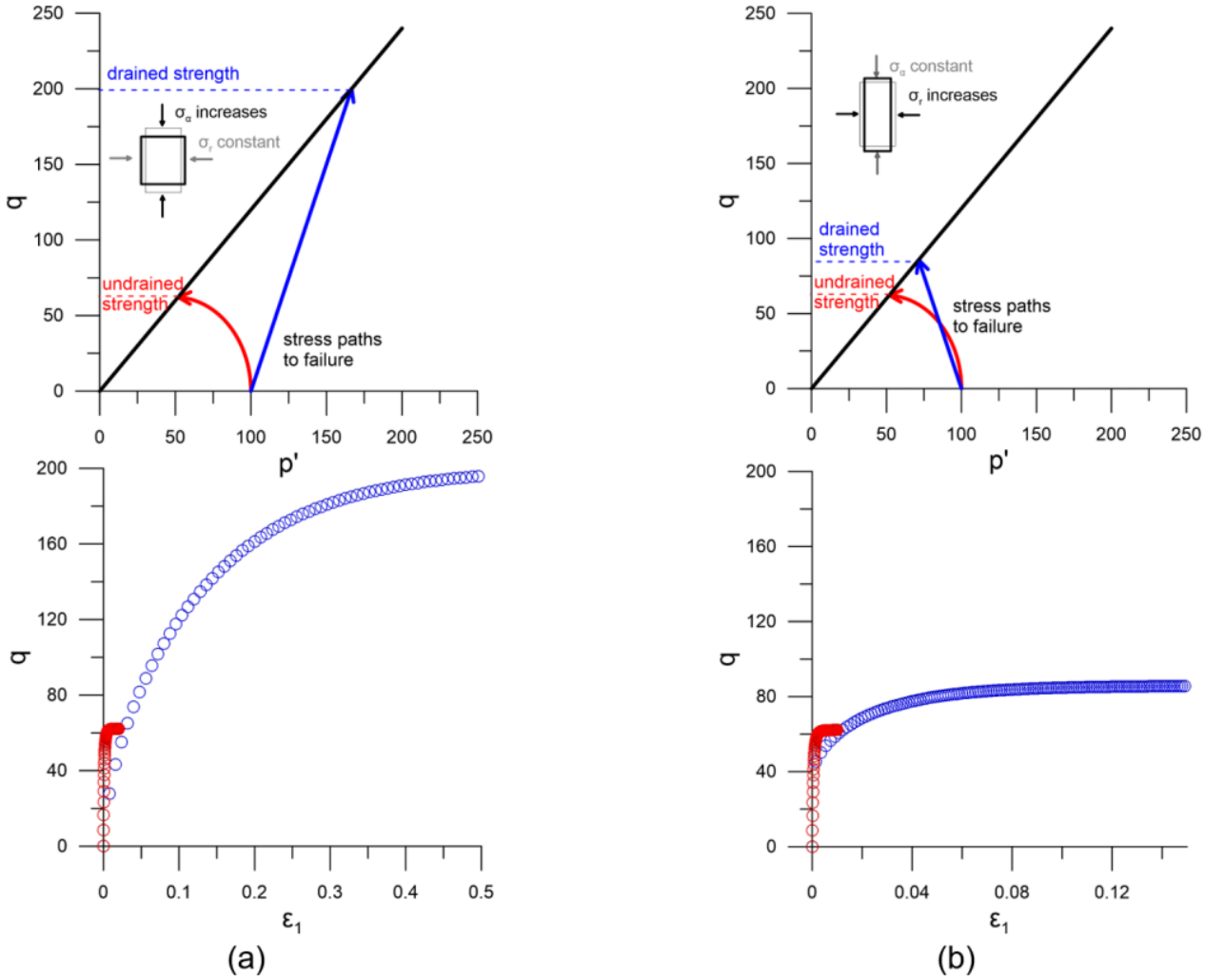

Figure 5.9. Simulated isotropically consolidated drained and undrained triaxial tests (CU) in (a) triaxial compression and (b) triaxial extension. Normally consolidated clay (OCR=1).

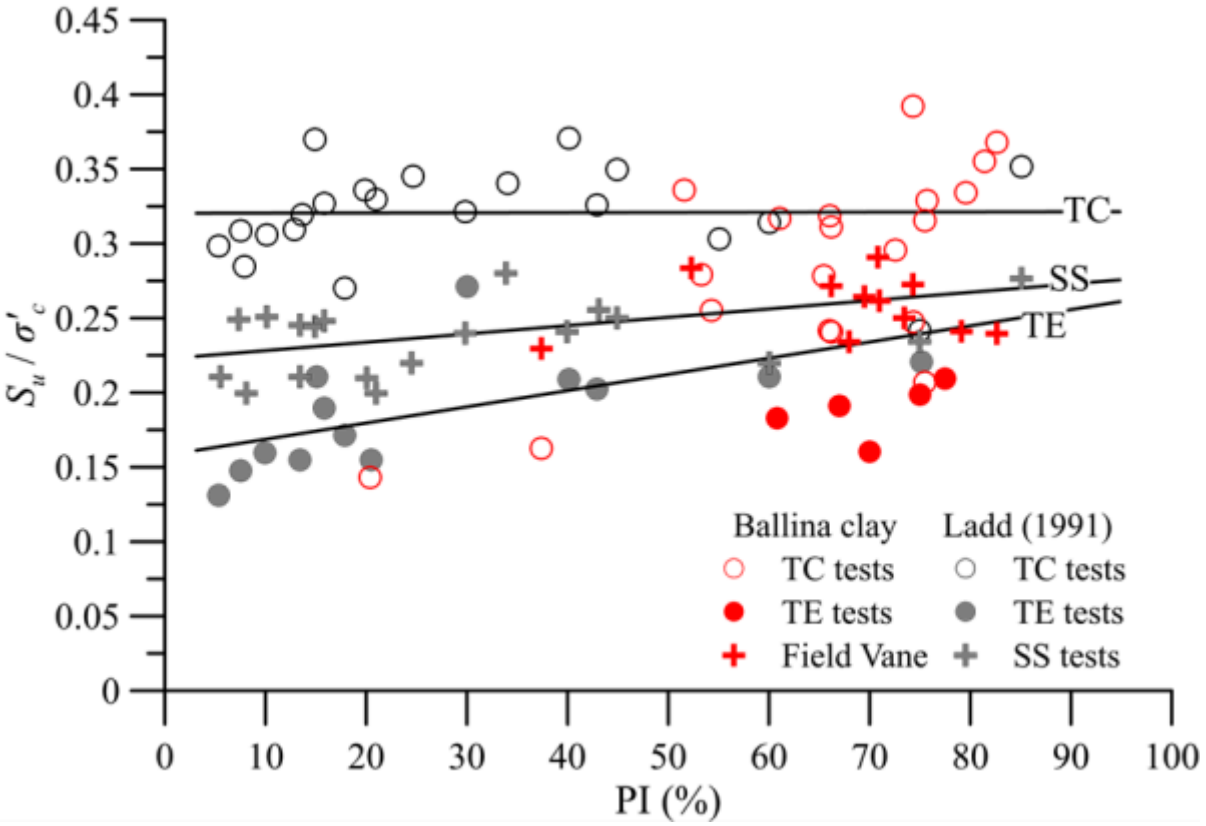

Figure 5.10. Undrained shear strength normalised against the preconsolidation stress from triaxial compression (TC), triaxial extension (TE), simple shear (SS) and field vane tests. Results from different clays around the world and Australia (Ballina clay) (Kouretzis et al. 2017).

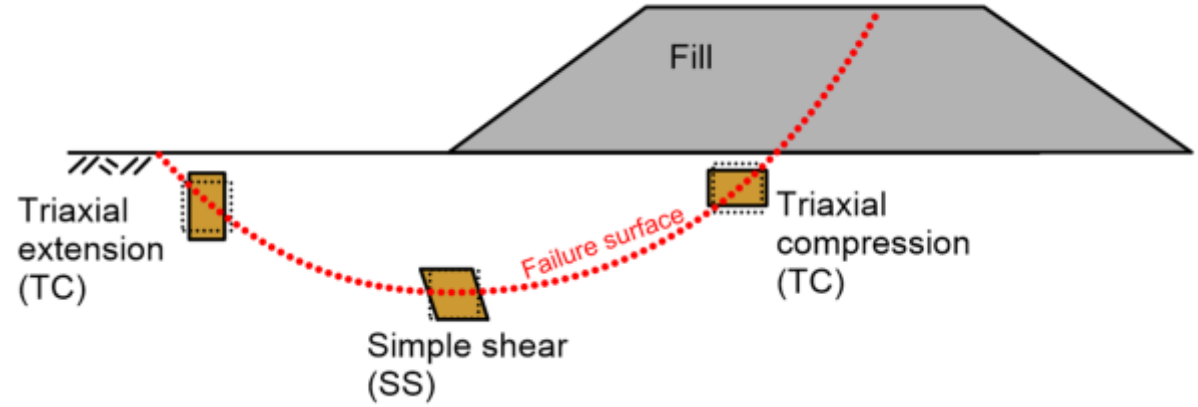

Figure 5.11. Stress paths to failure underneath an embankment.

On a similar note, Figures 5.7 to 5.9 all suggest that the shear strength under undrained loading conditions is consistently lower than the strength that the same soil will exhibit under drained conditions. This is true for contracting soils that develop positive excess pore pressures upon loading, such as normally or lightly-overconsolidated soft clays. However, this is not the case for soils exhibiting dilative response, such as overconsolidated clays, which will develop negative pore pressures (suction) when sheared under undrained conditions. This will result in their undrained strength being higher than the drained strength, as depicted in Figure 5.12 and described mathematically again by Eq. 5.3. In cases like these, both the short-term (undrained) and long-term (drained) collapse load must be calculated to identify the critical load case, as discussed in the following.

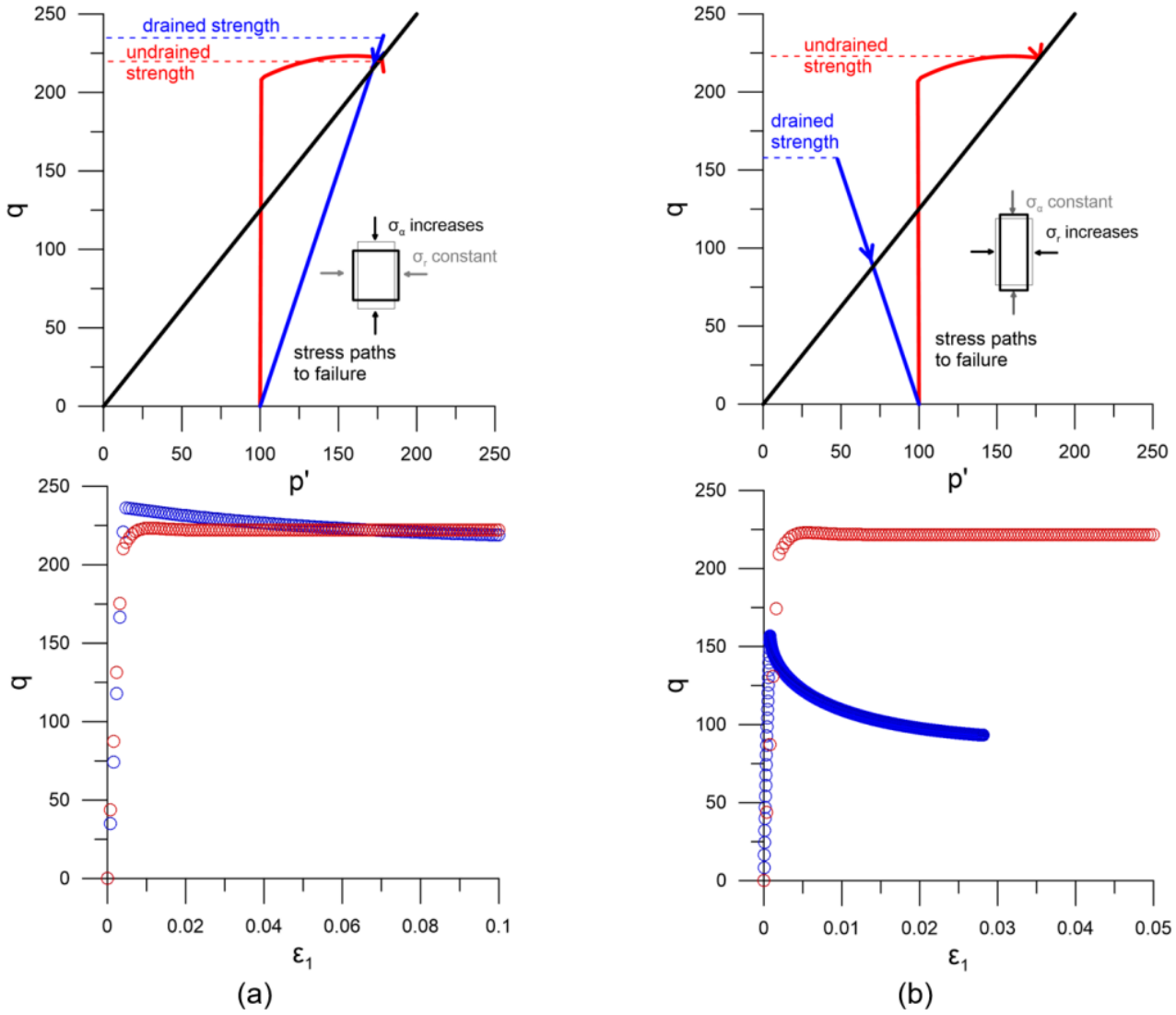

Figure 5.12. Simulated isotropically consolidated drained and undrained triaxial tests (CU) in (a) triaxial compression and (b) triaxial extension. Overconsolidated clay (OCR=5).

Finally, it is worth discussing briefly the effect of the flow rule used together with the Mohr-Coulomb *Drained* model on the estimation of the bearing capacity or the collapse load with numerical methods. The flow rule in the model controls the amount of volumetric deformation (volume change) that takes place at failure, via the dilation angle ψ, which depends on the level of confining stress; a dilative soil which volume tends to increase upon shearing, such as a dense sand (Figure 5.13), will behave as contractive if sheared under high confining stress. It was mentioned in Example 4.2 that consideration of non-associated flow rule ($\psi \neq \varphi'$) will result in more realistic estimates of volumetric deformation in soils, as also depicted below in Figure 5.13. This comes at the expense of complications related to localisation, mesh-dependency of the solution and possible convergence issues. On the contrary, it is widely accepted that adoption of associated flow will generally result in overestimation of the collapse load: Overestimating volumetric soil strains will result in overpredicting the normal stress acting on shear planes (particularly for problems with increased confinement, such as embedded foundations), and therefore the shear strength according to Eq. 5.3. A technique to avoid this, while still using associated flow in the analysis model by setting $\psi = \varphi'$ is to numerically estimate the collapse load while using an equivalent friction angle $\varphi^* = \psi^*$ and effective cohesion c^* calculated as (Davis, 1968):

(5.5) $$\tan \varphi^* = n \tan \varphi'$$

(5.6) $$c^* = nc'$$

(5.7) where $n = \dfrac{\cos\varphi' \cos\psi}{1 - \sin\varphi' \sin\psi}$

Keep also in mind that when using the Mohr-Coulomb *Undrained (C)* soil model we impose an associative flow rule, as $\psi = \varphi_u = 0$ ensures that no volume change takes place during undrained loading (Figure 5.13).

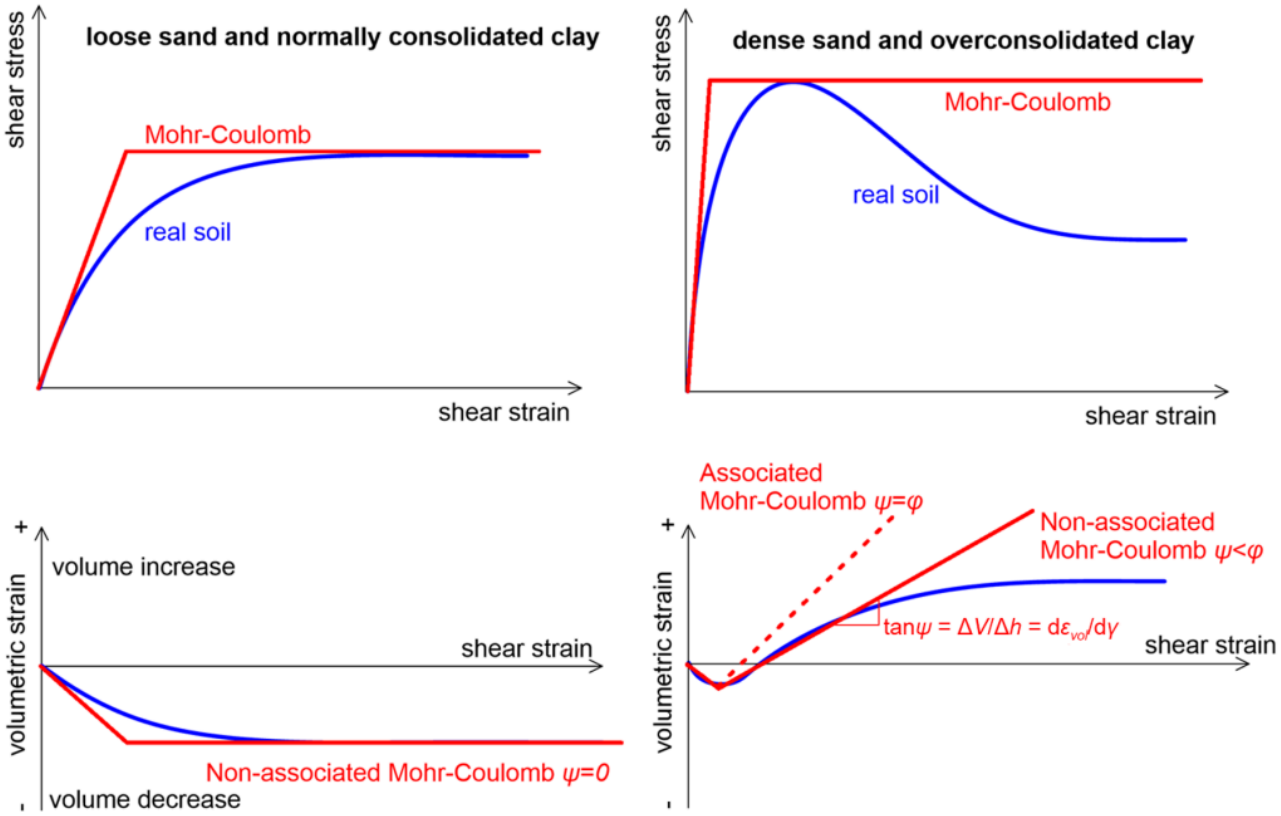

Figure 5.13. Soil behaviour and associated/non-associated Mohr-Coulomb models.

Summarising:

When excess water pore pressures do not develop upon loading of the soil, or have already dissipated (drained loading), as it will be the case for:

- Dry soils.
- Coarse-grained soils (sand, gravel) with high permeability.
- Saturated fine-grained soils (clay, silt) with low permeability, when we are interested in their *long-term behavior* e.g., long-term stability of an excavation or an embankment, after dissipation of excess pore pressures that developed during construction.

use the Drained Mohr-Coulomb model with effective shear strength and compressibility parameters (E', ν', c', φ', ψ). If the Mohr-Coulomb model is used together with an associate flow rule ($\psi = \varphi'$) to obtain the collapse load, it is recommended to use equivalent shear strength parameters from Eqs. 5.5-5.7.

When excess water pore pressure may develop upon loading of the soil (undrained loading), as it will be the case of:

- Saturated fine-grained soils (clay, silt) with low permeability, when we are interested in their *short-term behavior* e.g., collapse of a footing during and immediately after construction, or under dynamic loads; stability of an embankment during fill works, and immediately after construction.

use the Undrained (C) Mohr-Coulomb model with total shear strength and compressibility parameters (E_u, $\nu_u \approx 0.5$, S_u). The considered S_u value needs to properly account for the preconsolidation stress and of the overconsolidation ratio, as these cannot be computed automatically by PLAXIS with the particular soil model.

Note that for simplicity in the following examples we will consider generally the undrained shear strength to be constant, in line with the assumptions of most simple analytical solutions. However, the reader must understand that this by no means suggests that considering an appropriate undrained strength profile with depth is not required in practical problems.

EXAMPLE 5.1

Design of a circular footing according to AS5100.3 with analytical methods

A wind turbine is going to be founded on a shallow circular footing, on the surface of a saturated clay layer of practically infinite thickness, with the geotechnical properties shown in the figure below. The undrained shear strength of the clay has been determined from an adequate number of triaxial laboratory tests on undisturbed samples. Determine the minimum radius of the footing required to satisfy Ultimate Limit State requirements of AS5100.3. Assume that the footing is rigid and rough, and that imposed (live) loads are negligible.

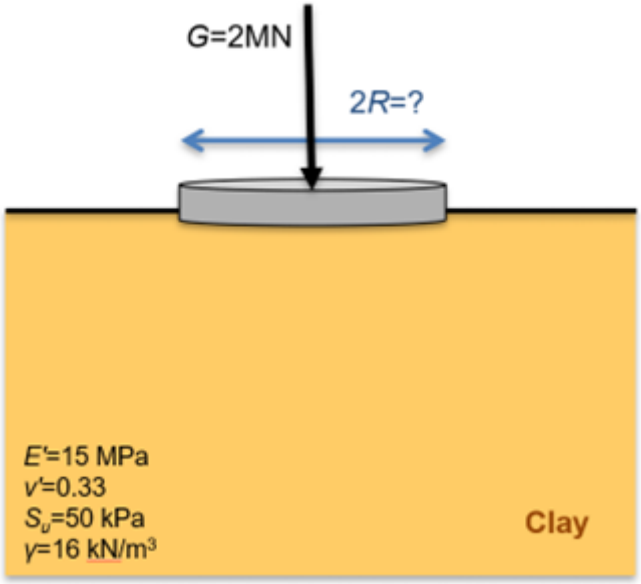

Example 5.1. Problem description and input parameters.

Answer:

The bearing capacity of a circular footing resting on a saturated clay layer under short-term, undrained loading conditions can be determined analytically, by assuming rigid plastic response of the soil. Derivation of the exact solution is provided elsewhere, while some fundamentals are discussed in Chapter 5.3. The ultimate geotechnical strength in terms of stress (bearing capacity), q_f is:

$$q_f = 5.14S_u + q_s \text{ for a strip footing}$$

$$q_f = 5.69S_u + q_s \text{ for a smooth circular footing}$$

$$q_f = 6.04S_u + q_s \text{ for a rough circular footing}$$

where S_u is the undrained shear strength of the clay layer, and q_s is the weight of the soil excavated to embed the footing $q_s = \gamma D_f$ (Figure 5.14). In the case at hand, where the footing rests on the top of the soil surface, it is $q_s = 0$. The other term in the above equations (e.g., $5.14S_u$) represents the bearing capacity in terms of stress of a footing resting on the soil surface and $N_{cu} = 5.14$ is the so-called *bearing capacity factor* for undrained loading, that depends on the shape of the footing, and on the soil-footing interface properties.

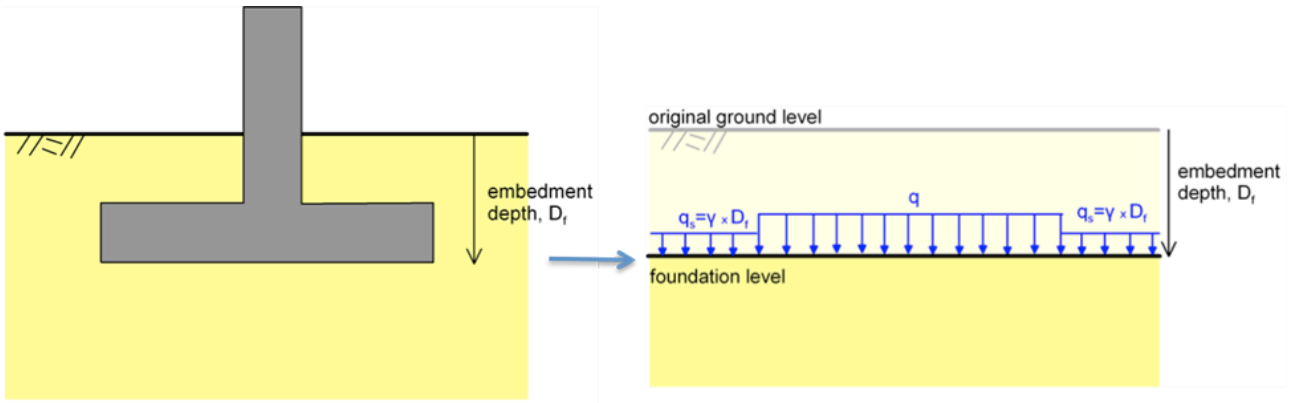

Figure 5.14. Replacement of the overburden soil by an equivalent stress q_s acting on the foundation level.

The design action load S^* for a load combination considering permanent action only is (AS1170.0):

$$S^* = 1.35G = 1.35 \times 2000 = 2700 \text{ kN}$$

The bearing of a rough circular footing on the ground surface, in terms of stress, is:

$$q_f = 6.04S_u = 6.04 \times 50 = 302 \text{ kPa}$$

Remember that the undrained shear strength to be used for the estimation of the ultimate geotechnical strength is always the characteristic value. Converting stress to force provides the collapse load Q_f:

$$R_{ug} = Q_f = q_f A_{footing} = q_f \pi R^2 = 942.5R^2 (\text{kN, radius R in meters})$$

As the characteristic value of the undrained shear strength has been determined from laboratory tests on undistrurbed samples, the appropriate range of the geotechnical strength reduction factor φ_g from Table 5.1 is φ_g = 0.45 to 0.60. Selecting conservatively the lower bound of the proposed range, Eq. 5.2 that provides the design capacity becomes:

$$\varphi_g R_{ug} \geq S^*$$

$$0.45 \times 942.5 \times R^2 \text{ (kN)} \geq 1.35 \times 2000 \text{ (kN)}$$

$$R \geq 2.52\text{m}$$

$$\text{Required footing diameter according to AS5100.3 } R \simeq 2.55\text{m}$$

EXAMPLE 5.2

Estimation of the short-term undrained collapse load with numerical methods

Use PLAXIS to confirm the value of the collapse load found analytically in Example 5.1 ($Q_f = 942.5 \times 2.5^2 = 5890$ kN). Repeat the comparison for the case where the embedment depth of the footing is $D_f = 2$ m.

Answer:

The radius of the footing has been estimated with the analytical method, so the geometry of the axisymmetric problem is fully defined (Figure 5.15a). Using PLAXIS, we can find the load-settlement curve for the particular footing diameter. The collapse load Q_f is the reaction for which settlement increases without any increase in the applied load (Figure 5.15b).

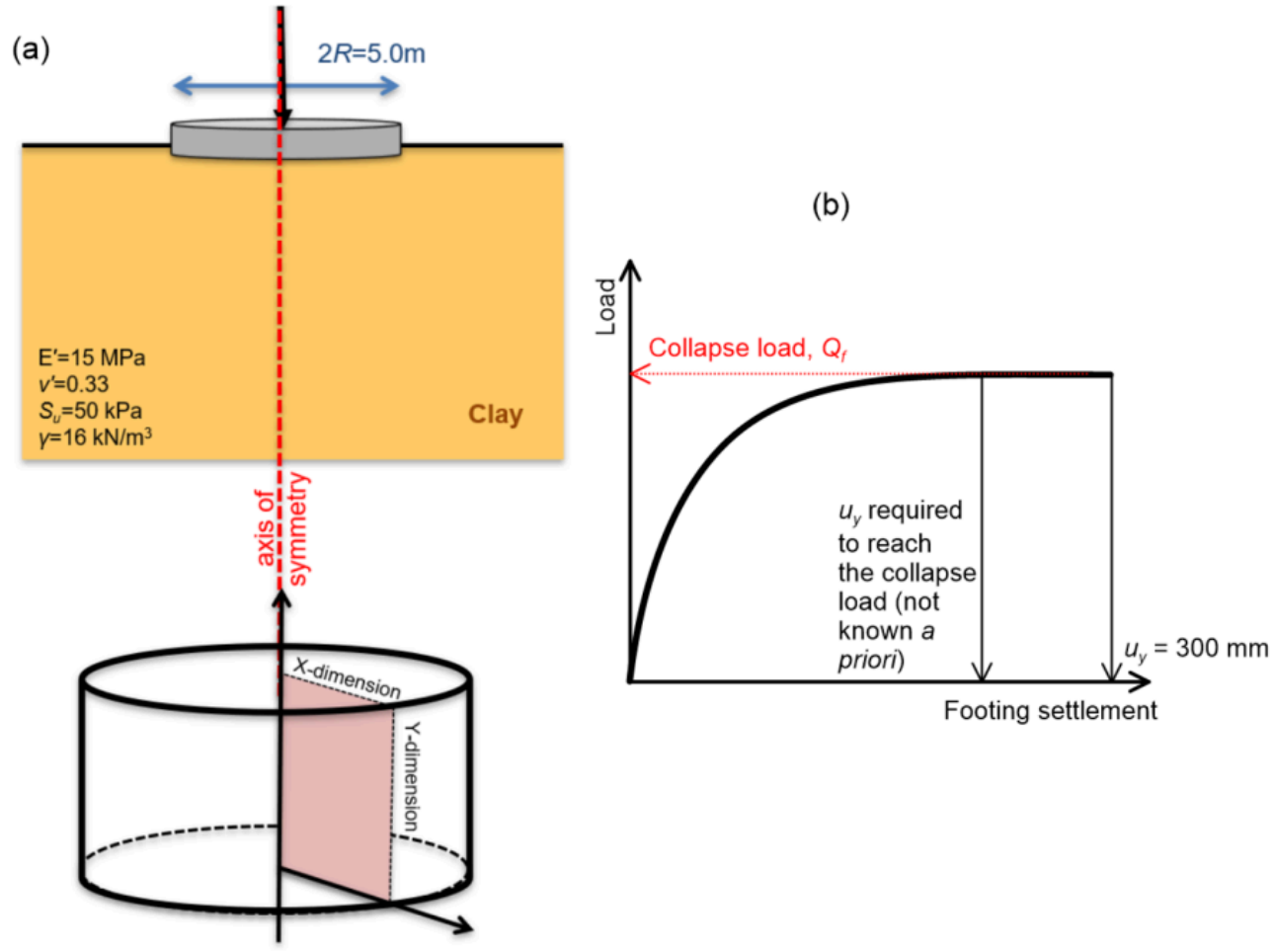

Figure 5.15. (a) Geometry of the axisymmetric problem and clay properties, and (b) load-settlement curve.

As we are interested in determining the short-term bearing capacity of a footing on clay, we have to consider undrained response according to Section 5.2.5, and perform a total stress analysis. Keep in mind that the

water table level does not play any role in a total stress analysis, as failure is defined in terms of total stresses. Employing the Undrained (C) Mohr-Coulomb model, we have to input the undrained shear strength provided in Figure 5.15 S_u = 50 kPa, as well as the undrained Young's modulus of the soil, calculated from Eq. 4.11 as:

$$E_u = \frac{3}{2\,(1+v')} E' = 16.88\ \text{MPa}$$

The undrained Poisson's ratio of the soil is automatically set by PLAXIS equal to $v_u \approx 0.5$, and accounts for the fact that no volume change takes place under undrained loading conditions i.e., the undrained bulk modulus of the soil $K_u = E_u/3(1\text{-}2v_u)$ is practically infinite. Note here that v_u cannot be taken equal to $v_u = 0.5$ in PLAXIS, and a value of e.g., $v_u = 0.495$ is used instead, to prevent a division-by-zero in the calculation of the bulk modulus.

A square 10 m x 10 m slice is used to simulate the problem, which should be more than enough to accommodate the failure surface that is expected to develop as the load on the footing approaches the collapse load. Recall that here our aim is to determine the maximum load that the footing can safely carry, not the settlement of the footing. Thus, the location of the bottom boundary can be within the influence depth of the applied pressure on the model surface, provided that the failure surface is accommodated within the soil slice. The settlement estimates in that case however will not be accurate, as a "shallow" fixed bottom boundary will lead to underestimation of settlement for a given applied pressure value.

The finite element mesh created while considering "medium" global coarseness is shown in Figure 5.16. A prescribed displacement is applied along the footing radius to simulate loading of a rigid and rough footing, as discussed in Example 4.2. The vertical displacement U_y should be enough to reach the collapse load i.e., the load-displacement curve should reach an asymptote (Figure 5.15b). A value of U_y = -0.30 m should be enough for that, for the particular compressibility parameters considered. Additionally U_x = 0.0 m along the radius of the rough footing.

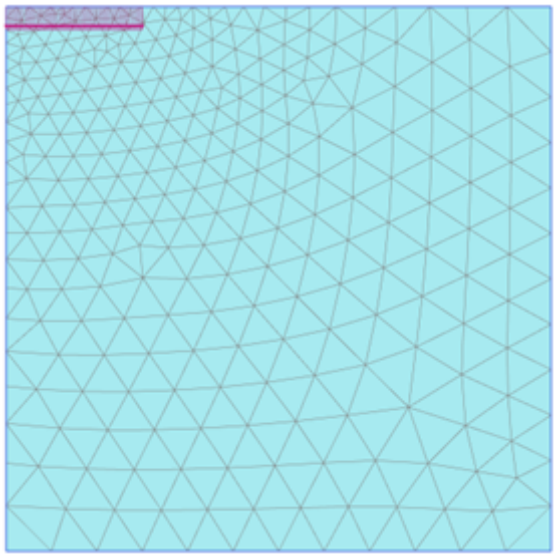

Figure 5.16. Finite element mesh and prescribed displacement to simulate loading of a rigid footing.

Analysis is performed in two stages: The "K_0 procedure" is used to initialise geostatic stresses, and subsequently the prescribed displacement simulating loading of the footing up to failure is activated in a single "plastic" loading step.

Results of the analysis are presented in Figure 5.17, in terms of shear strain increments developing in the

soil around the footing at failure, when the applied displacement has reached U_y = -0.30 m. Notice that the geometry of the failure surface that develops compares well will the log-spiral surface that was assumed while calculating analytically the bearing capacity.

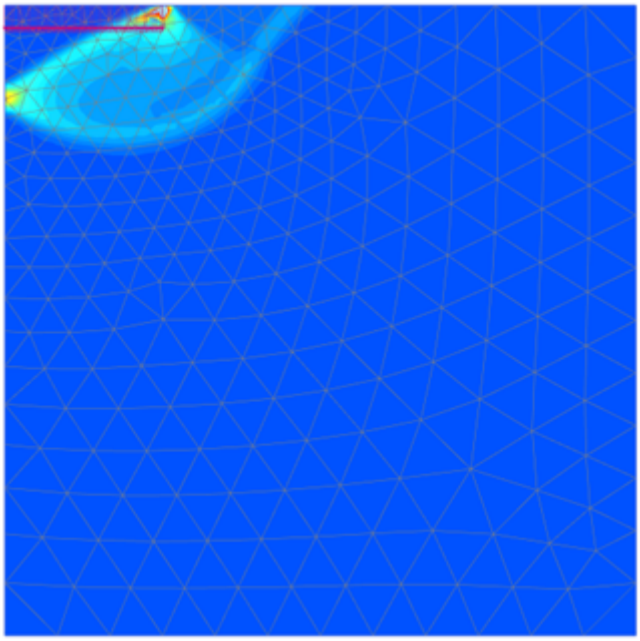

Figure 5.17. Shear (deviatoric) strain increments at failure.

The force-displacement curve can be obtained by considering a node at the footing axis, and plotting the reaction force F_Y versus the vertical displacement (settlement) of the same node U_y (Figure 5.18).

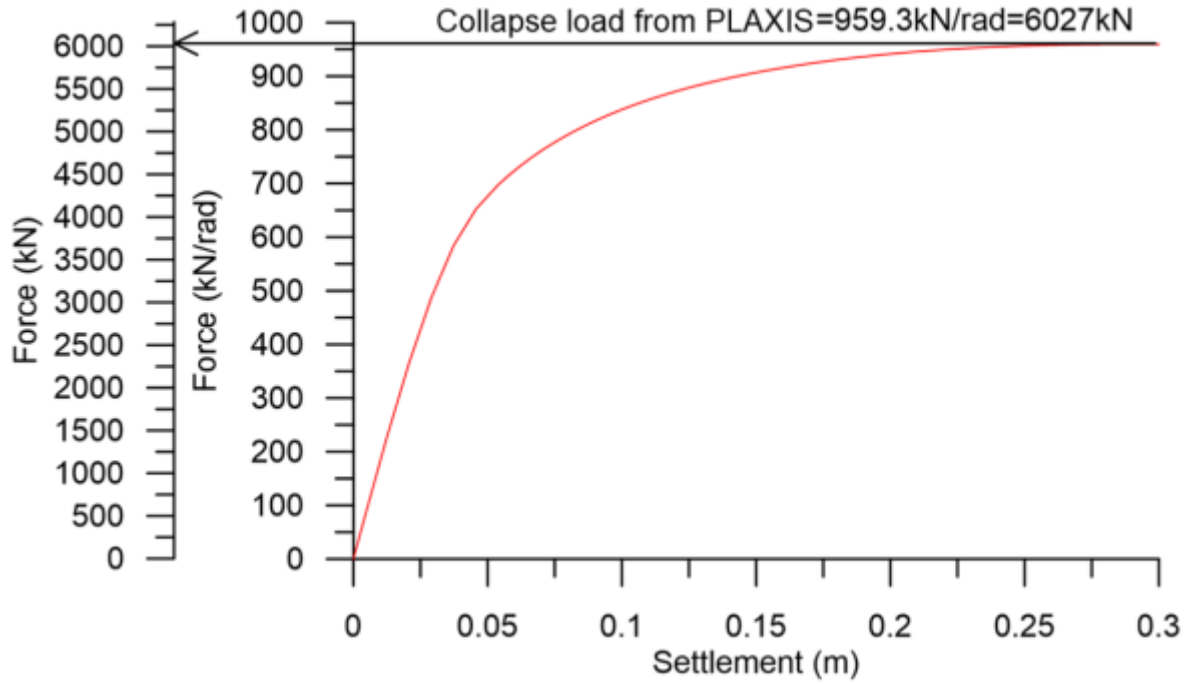

Figure 5.18. Load-settlement curve of the footing.

As discussed in Example 4.2, the reaction force is provided by PLAXIS in kN/rad, since we are simulating a "slice" of the problem of angle 1 rad (see also Figure 3.17). The total reaction force at failure, which

corresponds to the plateau of the curve, will be 959.3 kN/rad x 2π = 6027 kN, and the bearing capacity in terms of stress will be 6027/(πR^2) = 307 kPa; very close to the analytical solution from Example 5.1 (red continuous and dashed lines in Figure 5.19).

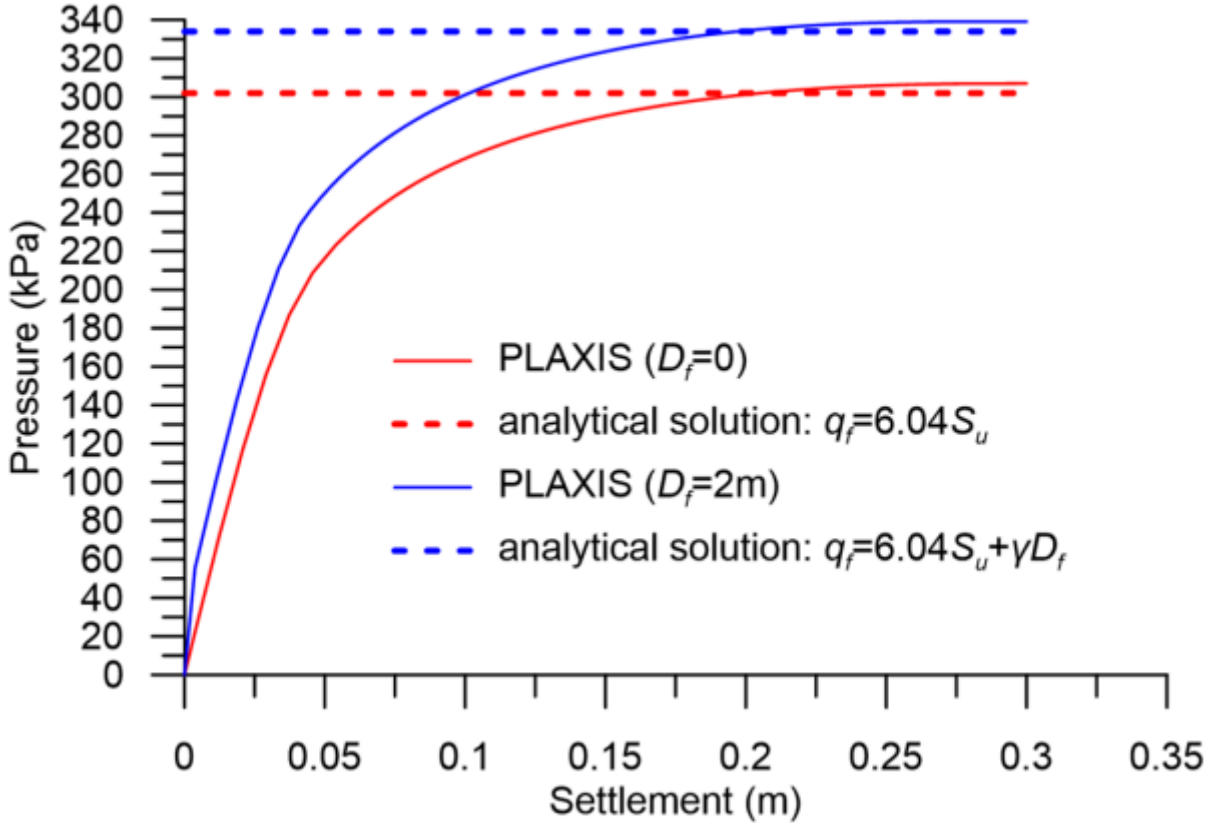

Figure 5.19. Comparison of analytically and numerically estimated bearing capacity for a footing laying on the ground surface (D_f = 0), and for a footing embedded at a depth D_f = 2 m.

A similar model is prepared for the case of the footing embedded at depth D_f = 2 m. To simulate the effect of embedment, we define two geometry clusters in PLAXIS, with the top cluster having a thickness equal to the embedment depth (Figure 5.20). Subsequently we apply a prescribed displacement to simulate loading of the footing at the foundation level, while outside the model area that corresponds to the footing, we apply a uniform pressure with magnitude equal to the weight of the excavated soil:

$$q_s = \gamma D_f = 16 \times 2 = 32 \text{ kPa}$$

where γ = 16 kN/m^3 is the unit weight of the excavated soil. Initialisation of geostatic stresses with the "K_0 procedure" is performed with both geometry clusters active, while the prescribed displacement and the uniform pressure q_s are not active. When the loading (prescribed displacement) is applied on the footing, at the subsequent plastic phase, the top cluster is deactivated. Deactivation of a geometry cluster in PLAXIS suggests that this part of the soil is excavated. At the same time, both the prescribed displacement and the pressure q_s are activated in the model. The soil pressure around the footing represents the non-excavated soil outside its perimeter (Figure 5.20). This is an efficient way of simulating footing embedment, and was also used for the derivation of the analytical expressions provided in Example 5.1. As one may notice from the results presented in Figure 5.19, again the numerically estimated bearing capacity in terms of stress q_f = 339 kPa compares well with the results of the analytical solution for a rough circular footing (blue continuous and dashed lines in Figure 5.19):

$$q_f = 6.04 S_u + q_s = 6.04 \times 50 + 16 \times 2 = 334 \text{ kPa}$$

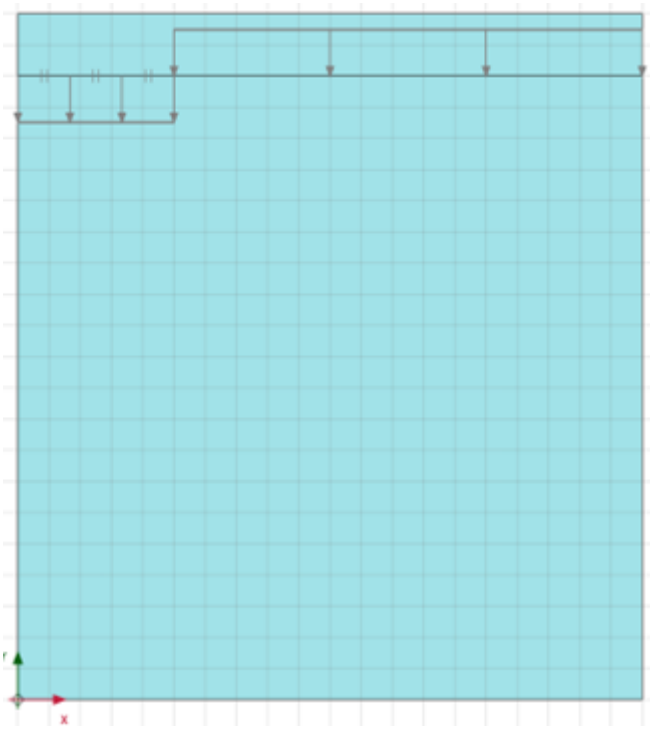

Figure 5.20a. Analyses stages for the simulation of an embedded footing, replacing soil with an equivalent pressure.

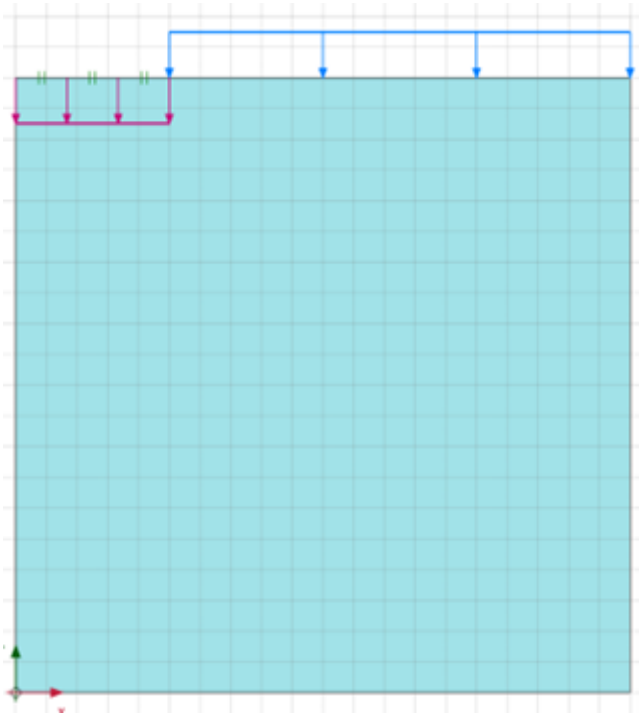

Figure 5.20b. Analyses stages for the simulation of an embedded footing, replacing soil with an equivalent pressure.

5.3 SOME FUNDAMENTALS OF THE BEARING CAPACITY OF SHALLOW FOUNDATIONS

With the term *bearing capacity* of a foundation we have defined the maximum pressure that the foundation can safely carry. For dilating soils that exhibit *softening behavior* (see Figure 5.5) failure corresponds to the peak shear stress, while for non-dilating (contractive) soils that exhibit *hardening behavior,* failure corresponds to the critical state shear stress, where shearing takes place under constant volume conditions. Sometimes, the *term failure load* is used to refer to the ultimate geotechnical strength in terms of force for contractive soils, and the term *collapse load* is used for dilating soils (Figure 5.21). Here we prefer to use the term collapse load Q_f to describe the ultimate geotechnical strength in terms of force for both dilating and contractive soils, as we use the Mohr-Coulomb failure criterion to quantify soil strength, and we do not differentiate between peak and residual strength (Figure 5.5). Keep in mind that the settlement associated with the design capacity may not be acceptable. Thus, apart from:

(5.8) $\varphi_g Q_f \geq S^*$

serviceability requirements must be taken into account for the proper design of a foundation.

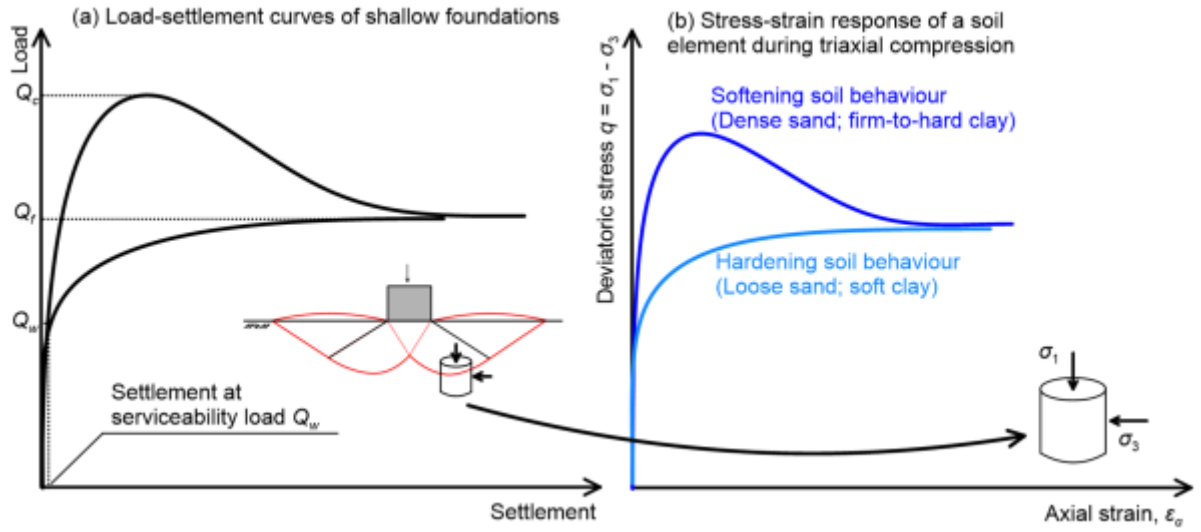

Figure 5.21. (a) Load-settlement curve of shallow foundations loaded up to failure, and (b) Stress-strain curve of a soil element located at the failure surface that is formed underneath the footing.

It is reminded here that settlement calculations are always performed with specific serviceability load combinations, in accordance with AS1170.0 and AS1170.1 for structures other than bridges, and in AS5100.2 for bridges. The geotechnical reduction factor φ_g does not apply when calculating settlement with the characteristic values of soil compressibility parameters, according also to AS5100.3.

Let's consider now the simplified case of a rigid strip footing resting on elastic-perfectly plastic soil (Figure

5.22). As the footing begins to settle upon load application, it "traps" a wedge of soil, which pushes its way downwards. According to our assumptions, initially the soil will respond elastically. It will be compressed vertically and extend laterally. Energy from the acting load is stored into the soil, as elastic energy.

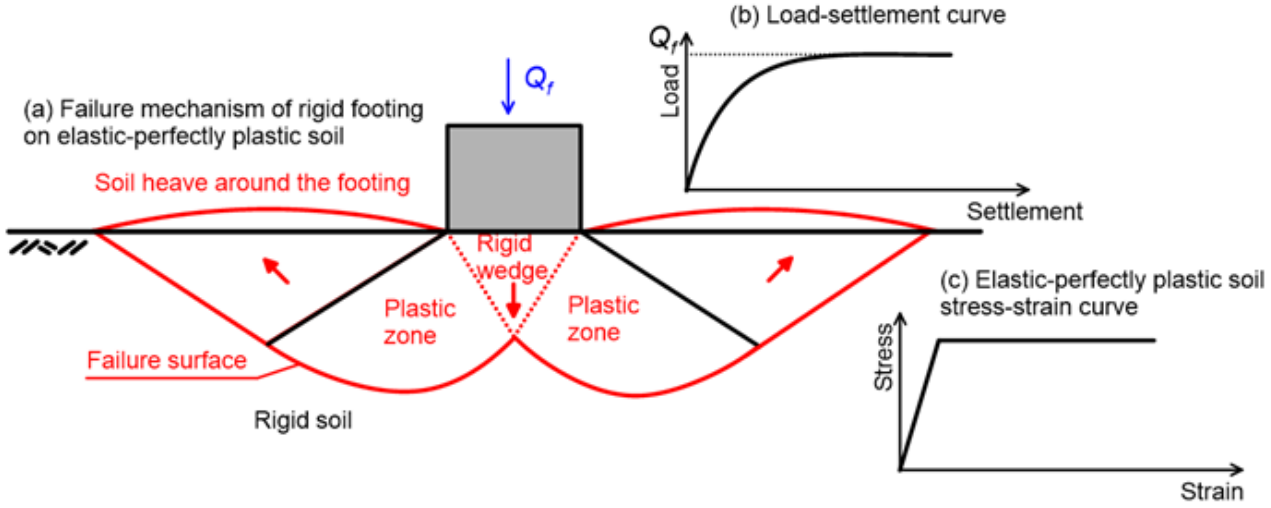

Figure 5.22. (a) Failure mechanism of a rigid footing on elastic-perfectly plastic soil, (b) Load-footing settlement curve, and (c) Stress-strain curve of elastic-perfectly plastic soil.

As the load increases, some regions of the soil will yield, forming plastic zones. Upon further increase of the load, plastic zones evolve to the ground surface around the footing, and appear with the form of heave (Figure 5.22a). There is an intermediate zone between elastic and perfectly plastic behavior, where the soil behaves as elasto-plastic material, and deformation is essentially only lateral. In reality, soil heave around the footing is influenced by the overburden pressure, and the strain-hardening ability of the material. If the footing is embedded into the soil and/or the material has a large potential to strain-harden, soil heave will be restrained and large lateral pressures will develop. In that case, a strain-softening material would behave as a strain-hardening material (we have mentioned earlier that dilatancy depends on the level of confining stress) pushing the plastic zone further into the soil mass, and the general failure mechanism depicted in Figures 5.23a and 5.23b may not fully develop (see Figures 5.23c-f).

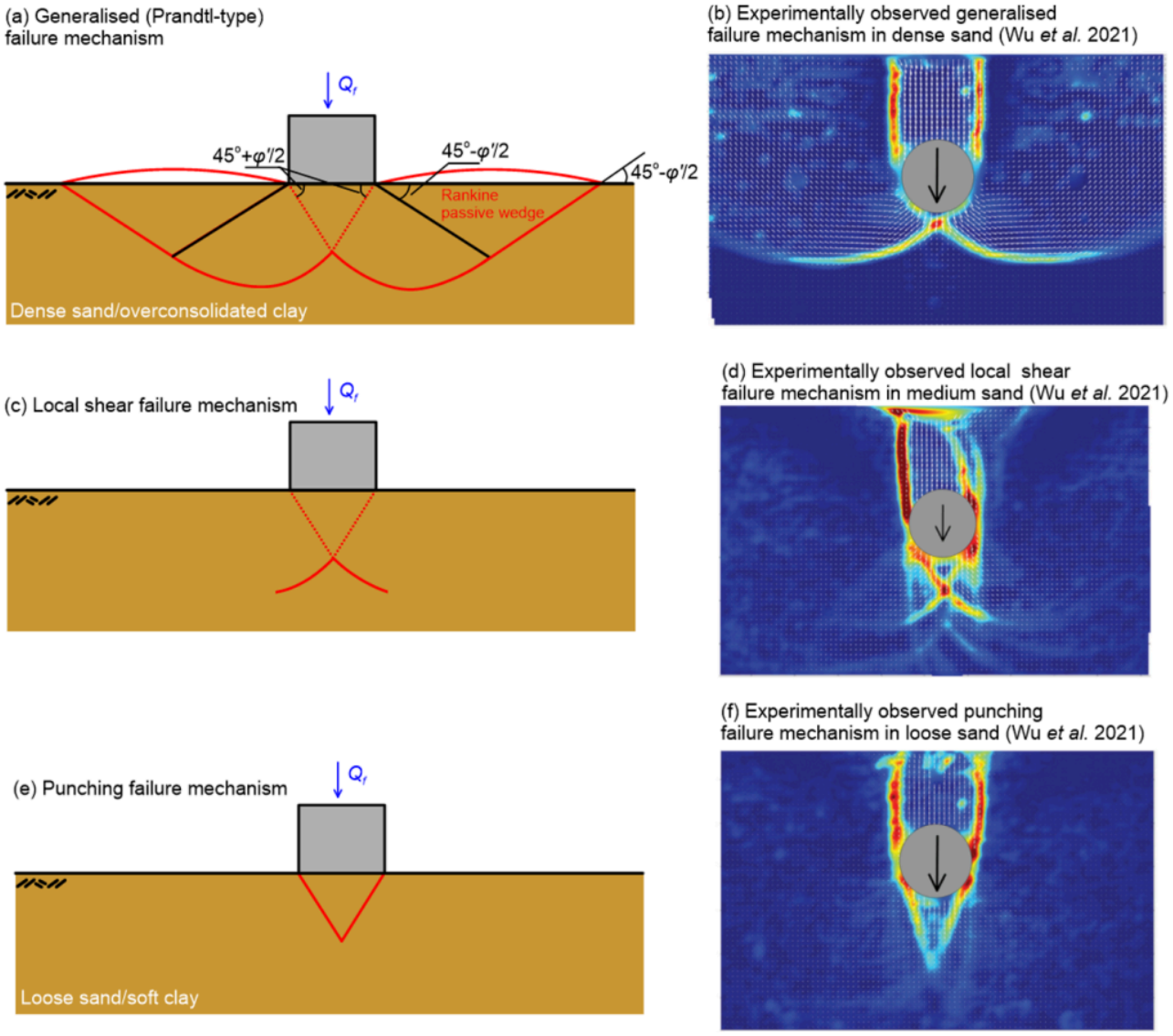

Figure 5.23. Different failure mechanisms: (left) Theoretical mechanisms, (right) Experimental observations by Wu et al. (2021).

Strictly speaking, for the estimation of the bearing capacity of a shallow footing we need to find a solution that satisfies the four general principles:

- Equilibrium.
- Stress-strain relations and failure criteria (e.g., the Mohr-Coulomb failure criterion described above).
- Compatibility of deformations.
- Stress and displacement boundary conditions.

It is not always possible to find a closed-form analytical solution that satisfies all the above. Instead, we can employ the limit theorems of plasticity to calculate *upper* and *lower* bound estimates of the bearing capacity. To use these theorems we assume that soil is rigid-plastic i.e., there is no elastic zone and deformations up to failure are zero (Figure 5.24a). Besides, we are not interested in calculating settlement at failure, which according to the definition of bearing capacity can be infinite. In some cases, the upper and lower bounds to the bearing capacity are the same, thus the calculated collapse load is the *exact* solution. The limit theorems are (Craig and Knappet 2012):

Lower bound theorem: If a state of stress can be found for which the failure criterion in not violated anywhere within the soil, and this state of stress is in equilibrium with the externally applied pressure and

internal soil stresses (geostatic stresses), then collapse cannot occur. The externally applied pressure is a lower bound estimate of the exact bearing capacity, as a more efficient stress distribution may exist, which may be in equilibrium with an external pressure of larger magnitude.

Upper bound theorem: Assume a kinematically admissible failure mechanism (that is a failure surface that is continuous and compatible with the boundary conditions). If during a displacement increment along this failure mechanism the work done by external pressures is equal to the dissipation of energy by the soil internal stresses (due to shearing), then collapse must occur. This system of external pressures is an upper bound estimate of the exact bearing capacity, as a more efficient mechanism may exist, that dissipates less energy, which might lead to failure under lower external pressures.

Let's see how these can be applied for the calculation of the bearing capacity of shallow foundations, by using the upper bound theorem to calculate an upper bound estimate of the bearing capacity q_f in terms of stress of a strip weightless footing resting on the surface of semi-infinite, homogenous, isotropic, weightless undrained soil (Figure 5.24b).

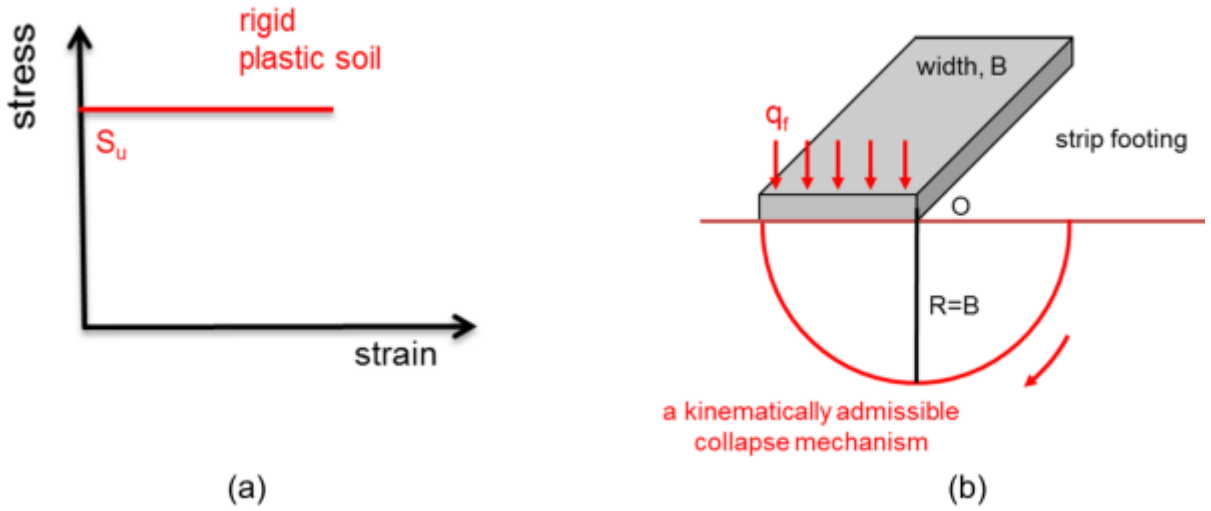

Figure 5.24. (a) Idealised rigid-plastic soil stress-strain relation (b) One possible kinematically admissible failure mechanism for a strip footing, that will lead to the calculation of an upper bound approximation of the bearing capacity.

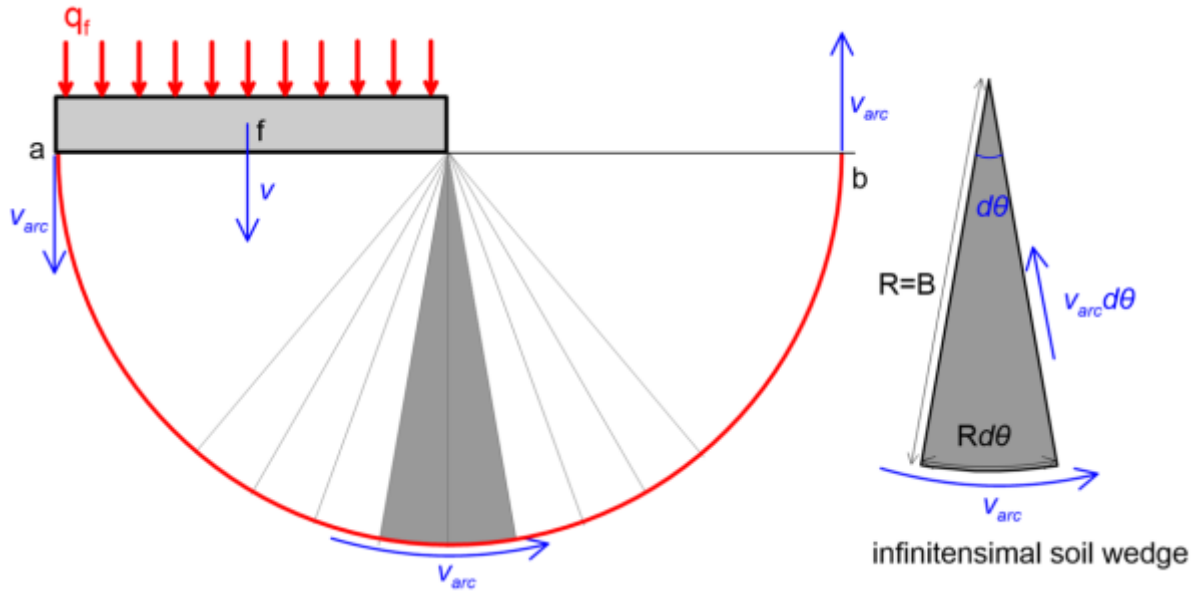

Figure 5.25. Slip velocities due to displacement increment and soil wedge geometry.

One possible and kinematically admissible failure mechanism comprises a circular arc of radius R equal to the width of the footing B, which center coincides with the edge of the footing. The work done by the pressure applied on the footing is equal to the force $q_f B$ multiplied by the relative velocity v during a displacement increment (Figure 5.25), therefore:

(5.9) $$W_{ext} = q_f B v = q_f R v$$

The energy dissipated due to shearing E_{shear} between the circular failure surface and the stationary soil is equal to the total shear resistance along the slip surface (undrained shear strength x length) multiplied by the relative velocity v_{arc}, therefore:

(5.10) $$E_{shear} = S_u \left(\theta R\right) v_{arc}$$

Where θ for the particular geometry is $\theta = \pi$. Note that the relative velocity around the edge of the circular arc is constant, and equal to $v_{arc} = v$, as the soil rotates relatively to O. However, we are not done yet with the calculation of internal energy, as we need to add the energy dissipated within the circular arc E_{int}, due to shearing occurring between soil wedges (Figure 5.25). The length of each wedge is equal to the radius R and the relative velocity is equal to $v_{arc} d\theta$ (so that the relatively velocity along the radius tends to zero as the wedge becomes infinitesimally small). Therefore, the internal energy dissipated due to shearing between wedges is:

(5.11) $$E_{int} = \int_0^{\theta} S_u R v_{arc} d\theta = \pi S_u R v_{arc}$$

And the total dissipated energy is:

(5.12) $$E_{tot} = E_{shear} + E_{int} = 2\pi S_u R v$$

If we equate this to the work of the external pressure (Eq. 5.9), we calculate the bearing capacity in terms of stress as:

(5.13) $$q_f = 2\pi S_u$$

The same result can be obtained by means of the limit equilibrium method. In that case we take moments about Point O in Figure 5.24. Moments due to normal forces acting on the arc about O are zero, since their line of action passes through O, therefore any shearing that takes place between wedges does not contribute to the moment equilibrium equation, which becomes:

(5.14) $$\left(q_f \times B\right) \times \frac{B}{2} = S_u \left(\pi R\right) R$$

and since $R = B$ it is again $q_f = 2\pi S_u$. Of course, as mentioned earlier, this is an upper bound to the exact bearing capacity. A more efficient mechanism (dissipating less energy) that is still kinematically admissible is the one shown in Figure 5.26, consisting of two rigid blocks a and b and an arc (or shear fan, as it is commonly called) of radius $R=B/\sqrt{2}$. The bearing capacity corresponding to this mechanism can be found similarly to the arc mechanism described above.

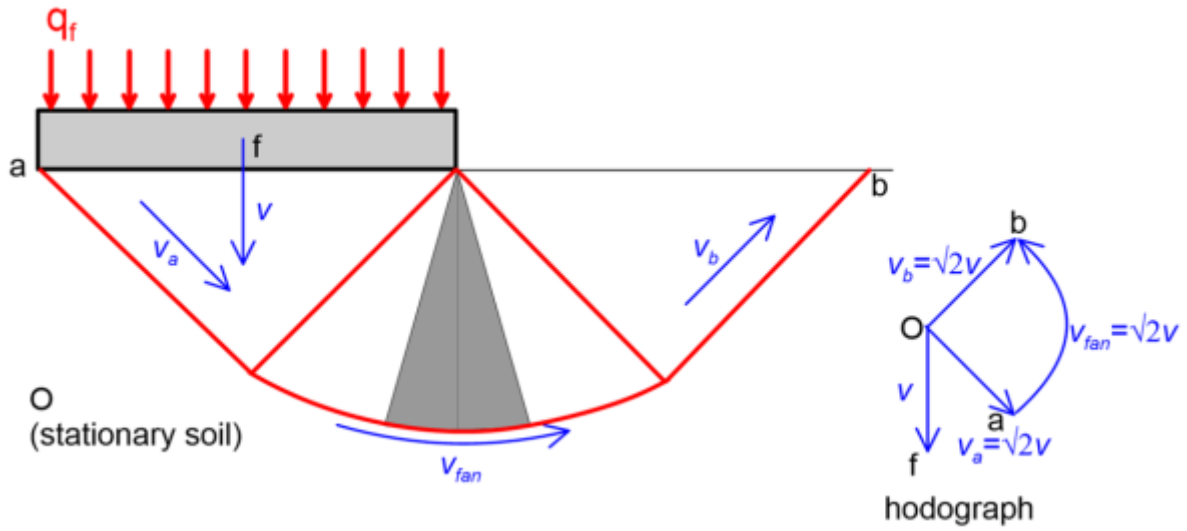

Figure 5.26. Refined failure mechanism and hodograph (velocity diagram).

The work done by the external forces is the same as in Eq. 5.9. The energy dissipated due to sliding of the rigid blocks relatively to the stationary soil, as well as sliding of the shear fan relatively to the stationary soil and shearing between its soil wedges is calculated in Table 5.3 below.

Table 5.3. Energy dissipated in the soil mass for the mechanism of Figure 5.26.

Failure line	Length of failure line	Relative velocity	Energy E_{shear} due to sliding relatively to stationary soil	Energy E_{int} due to shearing between soil wedges
a	$\frac{B}{\sqrt{2}}$	$\sqrt{2}v$	$S_u \frac{B}{\sqrt{2}} \sqrt{2}v = S_u B v$	0 (rigid)
Fan ($\theta = \pi/2$)	$R = \frac{B}{\sqrt{2}}$	$\sqrt{2}v$	$E_{shear} = S_u (\theta R) v_{fan} = \frac{\pi}{2} S_u \frac{B}{\sqrt{2}} \sqrt{2}v = \frac{\pi}{2} S_u B$	$\int_0^{\frac{\pi}{2}} S_u R v_{fan} d\theta = \frac{\pi}{2} S_u \frac{B}{\sqrt{2}} \sqrt{2}v = \frac{\pi}{2} S_u B v$
b	$\frac{B}{\sqrt{2}}$	$\sqrt{2}v$	$S_u \frac{B}{\sqrt{2}} \sqrt{2}v = S_u B v$	0 (rigid)
		Total:	$2 S_u B v + \pi S_u B v = (2 + \pi) S_u B v$	

Equating the total dissipated energy from Table 5.3 with the work done by the pressure acting on the footing yields the bearing capacity $q_f = (\pi+2)S_u$. This is equal to the exact bearing capacity for a strip footing without surface surcharge, because in this particular case we can find a lower bound solution equal to the upper bound solution. These calculations are omitted as they are beyond the scope of this Part. It should be further clarified here that the mechanism of failure below a strip footing subjected to a vertical pressure will be symmetric, as shown in Figure 5.27.

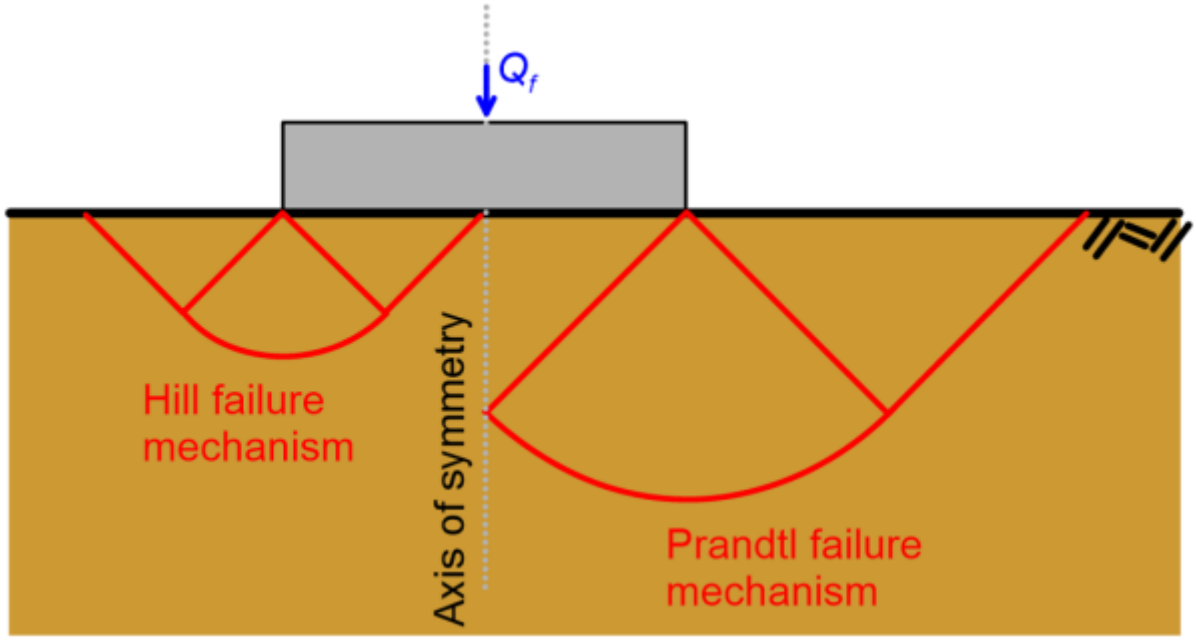

Figure 5.27. Hill- and Prandtl-type failure mechanisms for smooth and smooth/rough strip footings on undrained soil, respectively.

Application of limit analysis theorems suggests that two mechanisms are theoretically possible: the *Hill* mechanism where horizontal sliding takes place at the soil-footing interface (see also Figure 5.27), and the *Prandtl* mechanism which is valid also for rough footings, where no sliding takes place. Interestingly, both result in the same bearing capacity, suggesting that the bearing capacity of a strip footing on undrained homogeneous soil is independent of the properties of the soil-footing interface (unlike the case of a circular footing). In reality however, as the undrained strength increases with depth, the bearing capacity of a rough footing will be higher of that of a smooth footing, as the Prandtl-type mechanism mobilises a deeper soil mass, and the mobilised undrained strength will be higher.

The same concept can be employed for determining the bearing capacity of shallow footings under drained conditions, on *weightless* soil which strength is quantified via the effective parameters cohesion c' and friction angle φ' (Effective Stress Analysis). Note that to apply the upper and lower bound theorems, *soil must obey an associative flow rule* ($\psi = \varphi'$). A consequence of that is that correct application of these expressions requires entering the equivalent parameters c^*, φ^* (Eqs. 5.5-5.7), instead of the actual measured soil parameters. However, this notion is not further explored here, and instead conservative characteristic shear strength parameters are used in the examples, as often done in practice. In addition, since soil is assumed to obey the linear Mohr-Coulomb failure criterion, the friction angle φ' is independent of stress level.

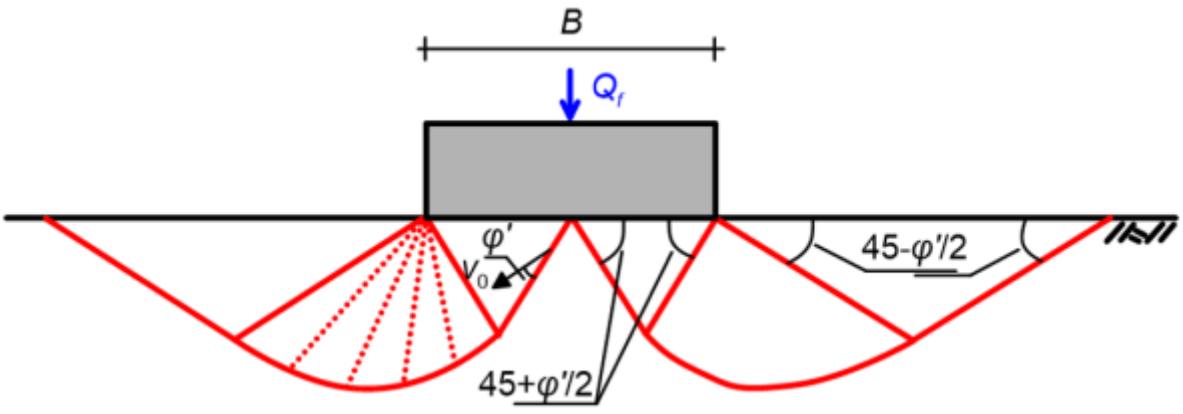

Figure 5.28a. Hill-type failure mechanisms for a footing on drained soil.

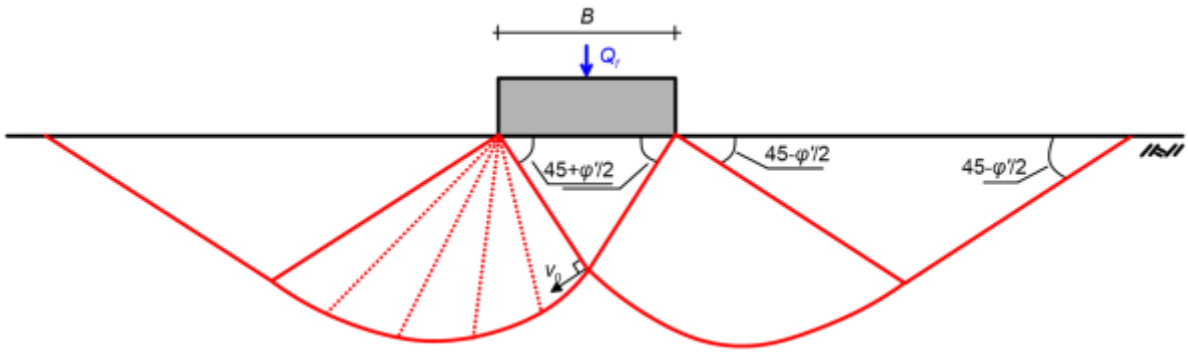

Figure 5.28b. Prandtl-type failure mechanisms for a footing on drained soil.

Equating the rate of external work and internally dissipated energy for half of the Hill mechanism shown in Figure 5.28a (as above) yields (Chen 2012):

$$\frac{1}{2}Q_f 2v_0 \cos\left(\frac{\pi}{4}+\frac{\varphi'}{2}\right) = c'\left(v_0\cos\varphi'\right)\left[\frac{B}{2\cos\left(\frac{\pi}{4}+\frac{\varphi'}{2}\right)}\right] + c'\left(v_0 e^{\frac{\pi}{2}\tan\varphi'}\cos\varphi'\right)\left[\frac{Be^{\frac{\pi}{2}\tan\varphi'}}{2\cos\left(\frac{\pi}{4}+\frac{\varphi'}{2}\right)}\right] + \frac{c'B\left(v_0\cot\varphi'\right)}{2\cos\left(\frac{\pi}{4}+\frac{\varphi'}{2}\right)}\left(e^{\pi\tan\varphi'}-1\right) \quad \textbf{(5.15)}$$

where Q_f is the collapse load and v_0 is the velocity of the rigid wedge below the footing. Similarly, for the Prandtl mechanism shown in Figure 5.28b (Chen 2012):

$$\frac{1}{2}Q_f v_0 \cos\left(\frac{\pi}{4}+\frac{\varphi'}{2}\right) = c'\left(v_0\cos\varphi'\right)\left[\frac{B}{4\cos\left(\frac{\pi}{4}+\frac{\varphi'}{2}\right)}\right] + c'\left(v_0\cos\varphi e^{\frac{\pi}{2}\tan\varphi'}\right)\left[\frac{Be^{\frac{\pi}{2}\tan\varphi'}}{4\cos\left(\frac{\pi}{4}+\frac{\varphi'}{2}\right)}\right] + \frac{c'B\left(v_0\cot\varphi'\right)}{4\cos\left(\frac{\pi}{4}+\frac{\varphi'}{2}\right)}\left(e^{\pi\tan\varphi'}-1\right) \quad \textbf{(5.16)}$$

Essentially, Eqs. 5.15 and 5.16 are the same. Notice that the geometry of both mechanisms depends on the friction angle of soil φ', and degenerates to the geometry shown in Figures 5.26 and 5.27 under undrained conditions, when $\varphi_u = 0°$. In that case the logarithmic spirals forming the shear fans degenerate to circular arcs. Eqs 5.15 and 5.16 can be written in a simpler form while including the effect of the overburden stress $q_s = \gamma D_f$ for footings embedded at a depth D_f as:

$$q_f = c'N_c + q_s N_q \quad \textbf{(5.17)}$$

where N_c, N_q are the *bearing capacity factors* provided from the Eqs. 5.18 and 5.19 and plotted in Figure 5.29 below. Note that the limit of N_c as φ tends to zero (or φ_u) is equal to $N_{cu} = (2+\pi)$, so in that case Eq. 5.17 provides the same collapse load for undrained weightless soil found earlier, since N_q also tends asymptotically to zero as friction angle approaches zero.

$$N_q = \tan^2\left(45^o + \frac{\varphi'}{2}\right)e^{\pi\tan\varphi'} \quad \textbf{(5.18)}$$

$$N_c = \left(N_q - 1\right)\cot\varphi' \quad \textbf{(5.19)}$$

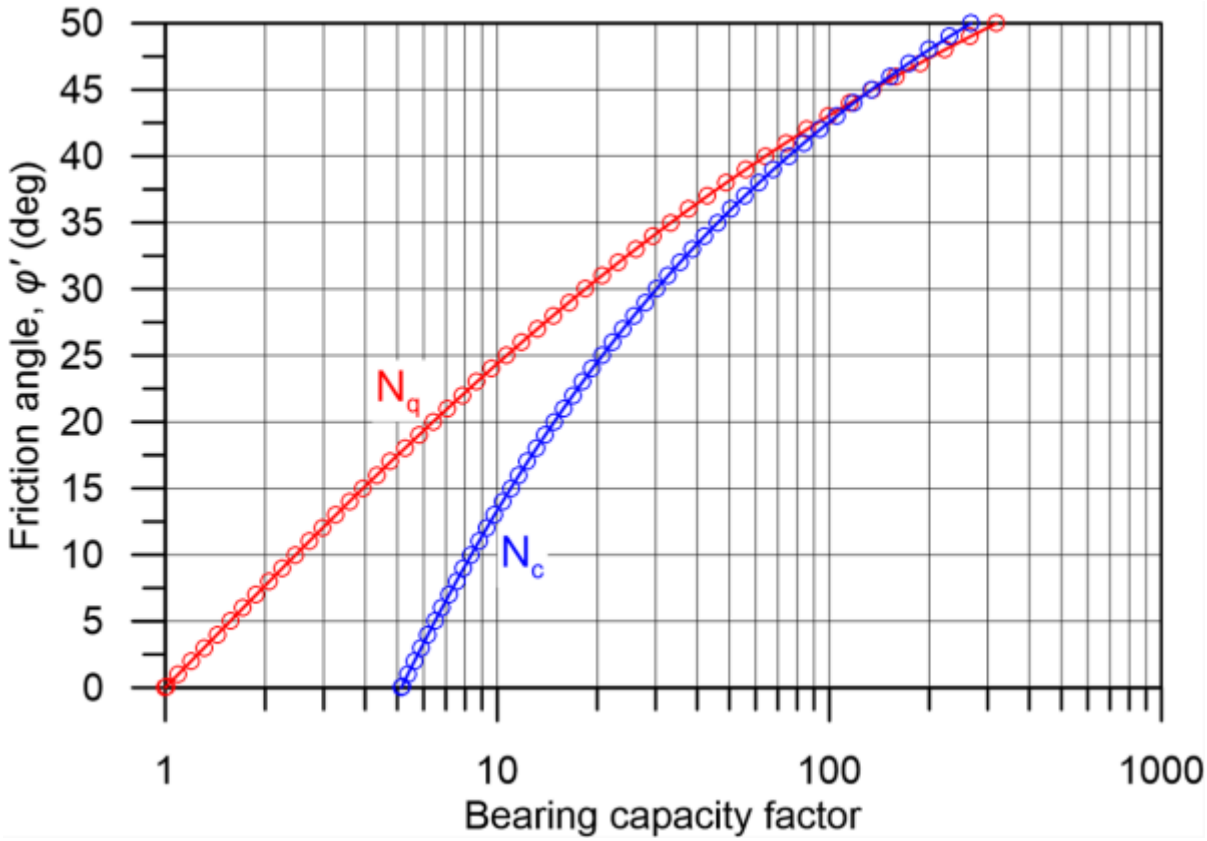

Figure 5.29. Bearing capacity factors plotted against the soil friction angle.

It is clear from the above expressions that the bearing capacity depends on whether soil response upon loading will be drained or undrained i.e., whether excess pore water pressures will develop. The following Table 5.4 summarises the type of expected soil behaviour as function of the soil grain size distribution and the scope of the analysis (long- or short-term). This table applies mainly to common, static loads. It is reminded that even sands, of high permeability, may develop excess pore pressures and behave as undrained if the rate of loading is sufficiently fast (e.g., during an earthquake).

A consequence of assuming a linear soil failure criterion, thus friction angle independent of confining stress levels, is that the bearing capacity factors N_q and N_γ are independent of the size of the foundation. Despite this not being true, and scale effects (i.e., the negative correlation of bearing capacity factors thus q_f in Eq. 5.17 to the dimensions of the foundation) on bearing capacity being documented in the literature, these are customarily ignored for common footing sizes encountered in practice.

Table 5.4. Selection of the appropriate equations for the estimation of the bearing capacity under static loads, depending on the soil type and loading scope.

Soil type	Analysis scope	Type of behaviour	Strength parameters
Sand (coarse-grained) or dry soils in general	Long-term or Short-term (no excess pore pressures due to high soil permeability and/or relatively slow loading rate)	Drained	c', φ' (ESA)
Saturated clay (fine-grained)	Long-term (after dissipation of excess pore pressures)	Drained	c', φ' (ESA)
	Short-term (during or immediately after construction; dynamic loads such as wind/wave action)	Undrained	S_u (TSA)
ESA: Effective Stress Analysis			
TSA: Total Stress Analysis			

5.4 COMMON BEARING CAPACITY EQUATIONS AND PRACTICAL CONSIDERATIONS

So far we have limited the discussion to idealised vertically-loaded strip and circular footings resting on the flat surface of semi-infinite, homogenous, isotropic, weightless soil. Under these assumptions we are able to derive exact solutions for the bearing capacity, but one may argue that these conditions, particularly weightless soil, are never met in practice. This is true, but we can use the above solutions together with correction factors for the effect of soil self weight, footing shape (for rectangular or square footings), load inclination and eccentricity, embedment conditions and groundwater table levels and estimate the design capacity required by AS 5100.3.

The *net* (i.e., not accounting for the contribution of overburden soil) bearing capacity (units: stress) equation for total stress analysis (TSA) under undrained conditions is:

(5.20) $$q = (5.14S_u)\, s_c d_c i_c b_c g_c$$

The net bearing capacity equation (units: stress) for effective stress analysis (ESA) under drained conditions is:

(5.21) $$q = [\gamma D_f\,(N_q - 1)]\, s_q d_q i_q b_q g_q + [0.5\gamma B' N_\gamma]\, s_\gamma d_\gamma i_\gamma b_\gamma g_\gamma$$

All symbols in the above equations will be introduced in the following. The above Eq. 5.20 conservatively disregards the beneficial contribution of soil cohesion c', which is unlikely to be important in coarse-grained materials and non-cemented clays. As it is discussed in Example 5.1, when the footing is embedded into the soil at a depth D_f, the bearing capacity is found by adding the weight of the excavated soil to the net bearing capacity q determined by Eqs. 5.20 and 5.21 as:

(5.22) $$q_f = q + \gamma D_f$$

Of course when a footing is not embedded in soil it is $q_f = q$. Note that when using AS5100.3 provisions for the design of the foundation, the geotechnical strength reduction factor φ_g must be applied only on the net bearing capacity q to obtain the design capacity as:

(5.23) $$(\varphi_g q + \gamma D_f) \times (\text{area of footing}) \geq S^*$$

or $\varphi_g R_{ug} \neq (\varphi_g q_f)$ x (area of footing). This is due to the fact that the uncertainties related to the weight of the excavated soil are considerably less than the uncertainties related to the shear failure developing in the soil below the footing.

Net bearing capacity Eqs. 5.20 and 5.21 include correction factors for the shape of rectangular or square footings (s), the effect of the embedment depth (d), the inclination of the load (i), the inclination of the base of the footing (b), the inclination of the foundation level (g) etc. Herein we focus on two of the most common cases of practical interest: i) a vertical load acting on a horizontal base footing resting on horizontal ground (Figure 5.22), and ii) an inclined load acting on a horizontal base footing resting on horizontal ground (Figure 5.30). In those cases, Eqs. 5.20 and 5.21 are simplified as follows:

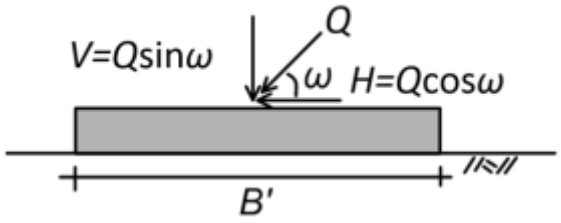

Figure 5.30. Inclined load acting on a horizontal base footing resting on horizontal ground.

Case (1) Vertical load on horizontal base footing resting on horizontal ground:

(5.24) Total Stress Analysis TSA : $q = (5.14 S_u)\, s_c d_c$

(5.25) Effective Stress Analysis ESA : $q = [\gamma D_f\,(N_q - 1)]\, s_q d_q + [0.5 \gamma B' N_\gamma]\, s_\gamma d_\gamma$

where: N_c, N_γ are *the bearing capacity factors*, accounting for the shear strength of soil; s_c, s_q, s_γ are the *shape factors;* d_c, d_q, d_γ are the *embedment factors;* γ is the unit weight of the foundation soil; B' is the effective footing width, defined in the following.

Case (2) Inclined load on horizontal base footing resting on horizontal ground:

(5.26) Total Stress Analysis TSA : $q = (5.14 S_u)\, i_c$

(5.27) Effective Stress Analysis ESA : $q = [\gamma D_f\,(N_q - 1)]\, i_q + [0.5 \gamma B' N_\gamma]\, i_\gamma$

where: N_c, N_γ are the bearing capacity factors, as above; i_c, i_q, i_γ are the *load inclination factors.*

The bearing capacity factors are employed in effective stress analyses, considering drained soil response, and depend on the friction angle of the soil. Factor N_q is provided from the exact solution for weightless c'–φ' soil (Eq. 5.18), considering the general failure mechanism depicted in Figures 5.23a and 5.28. On the other hand, there is no exact solution for soil with unit weight $\gamma > 0$ and various approximate expressions have been proposed for determining the corresponding bearing capacity factor N_γ, some of which are plotted in Figure 5.31. The expression that will be used mostly here is the one proposed by Meyerhoff (1963) for a rough footing:

(5.28) $N_\gamma = (N_q - 1)\tan(1.4\varphi')$

The expressions providing the shape and embedment factors both for total stress analysis (Eq. 5.24) and effective stress analysis (Eq. 5.25) are presented in Table 5.5, while the variation of the embedment factors d_c and d_q with the normalised embedment depth D_f/B is also depicted in Figure 5.32.

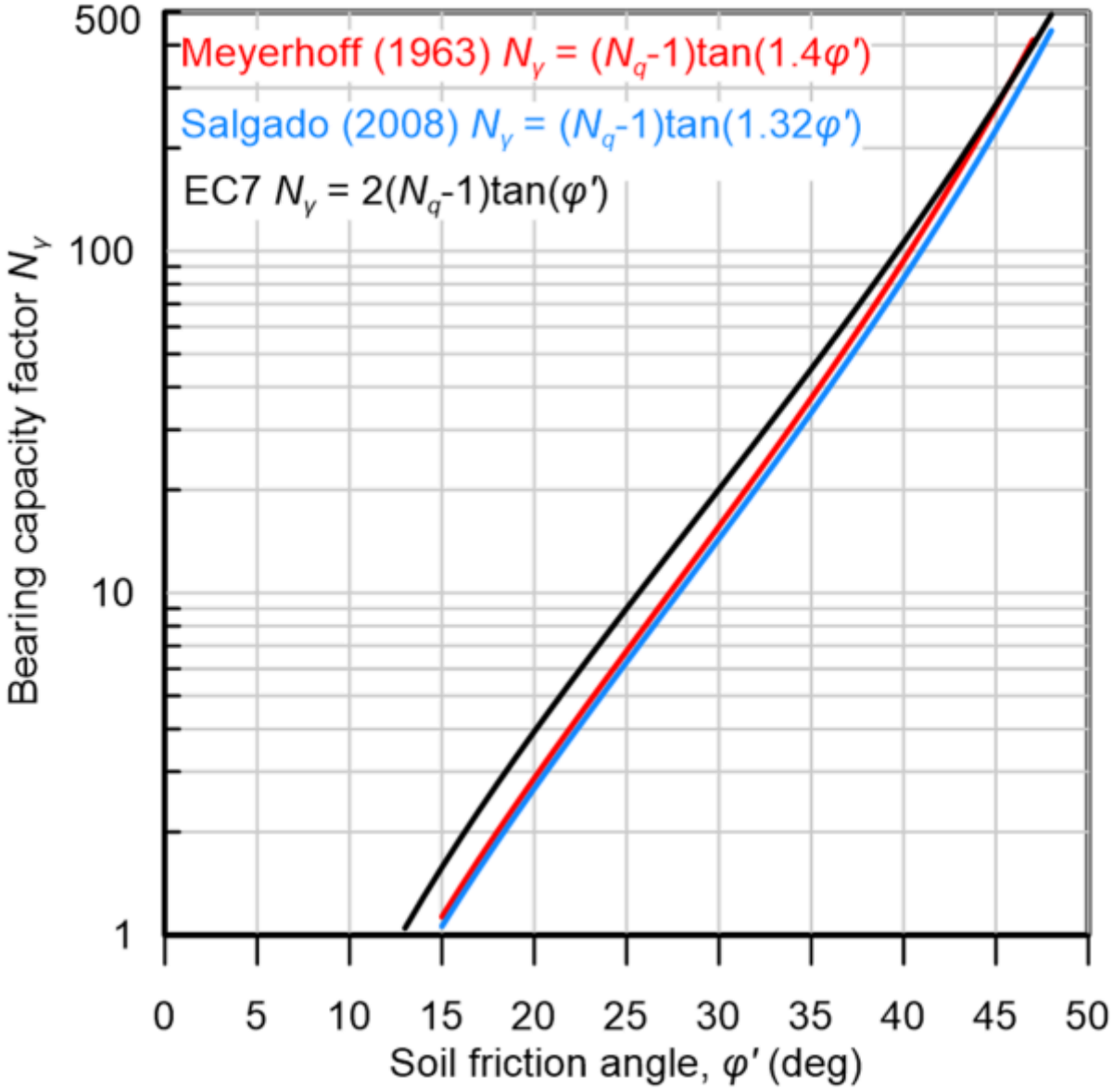

Figure 5.31. Variation of the bearing capacity factors with the friction angle of the soil.

Table 5.5. Shape and embedment factors for rectangular and square footings.

Total Stress Analysis (Eq. 5.24)	
s_c	$1 + 0.2\left(\frac{B'}{L'}\right)$
d_c	$1 + 0.33 \arctan\left(\frac{D_f}{B'}\right)$
Effective Stress Analysis (Eq. 5.25)	
s_q	$1 + \left(\frac{B'}{L'}\right)\tan\varphi'$
d_q	$1 + 2\tan\varphi'(1 - \sin\varphi')^2 \arctan\left(\frac{D_f}{B'}\right)$
s_γ	$1 - 0.4\left(\frac{B'}{L'}\right)$
d_γ	1

Note : $\arctan\left(\frac{D_f}{B'}\right)$ in rad

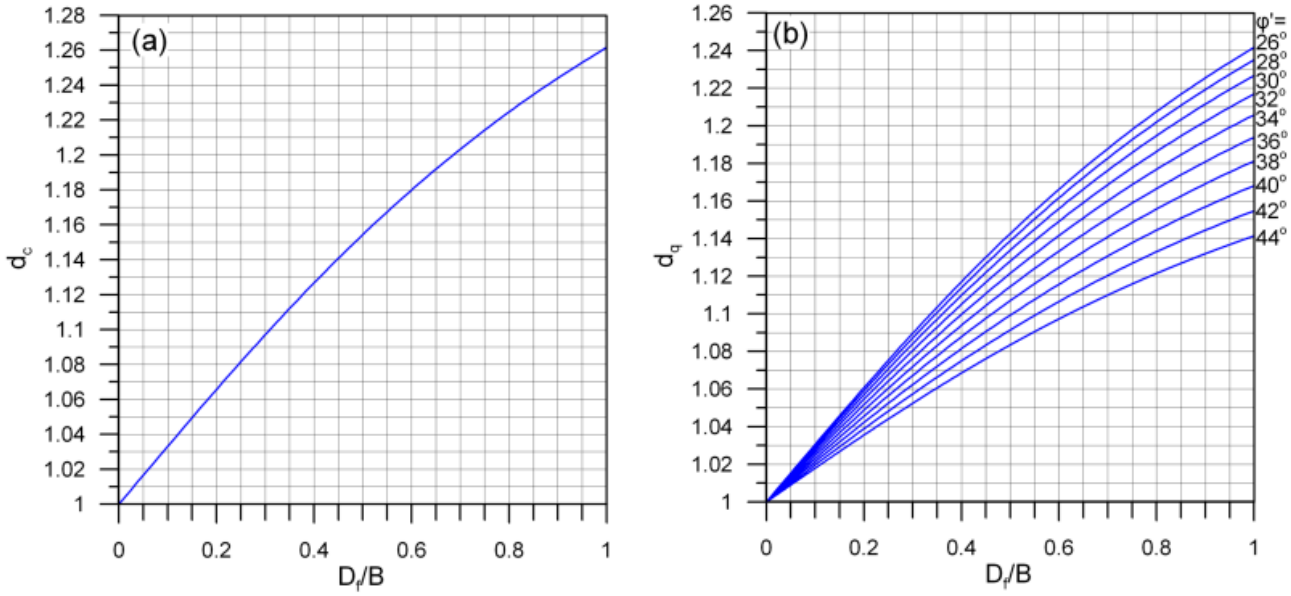

Figure 5.32. Variation of the embedment factors (a) d_c and (b) d_q with the normalised embedment depth D_f/B. B is the width of the footing and φ' is the friction angle.

The load inclination factors, to be used together with Eqs. 5.26 and 5.27 are provided in Table 5.6. These expressions are valid for a load inclined at the plane defined by B', as shown in Figure 5.30. Note that load inclinations factors are not to be used together with shape and embedment factors, so if e.g., an inclined load acts on an embedded footing, Eqs. 5.26 and 5.27 should be used.

Table 5.6. Load inclination factors.

Total Stress Analysis (Eq. 5.26)	
i_c	$1 - \frac{nH}{5.14 S_u B' L'}$
Effective Stress Analysis (Eq. 5.27)	
i_q	$\left(1 - \frac{H}{V}\right)^n$
i_γ	1

$$\text{Where}: n = \frac{\left(2 + \frac{B'}{L'}\right)}{\left(1 + \frac{B'}{L'}\right)}$$

In the above formulas for the net bearing capacity and the correction factors, the *effective width* B' and the *effective length* L' of the footing are used, instead of their actual dimensions. The footing dimensions are adjusted to their effective values when the location of the resultant load (load axis) does not coincide with the centroid (centre of area) of the footing, so as to align the load centre with the area centre (Figure 5.33). The distance from the centre of the area to the point of application of the vertical component of the resultant load is called *eccentricity, e*. Given the eccentricity of the load, the effective width of a strip footing is:

(5.29) $B' = B - 2e_b$

In the case of a rectangular footing, the same applies for the effective length:

(5.30) $L' = L - 2e_l$

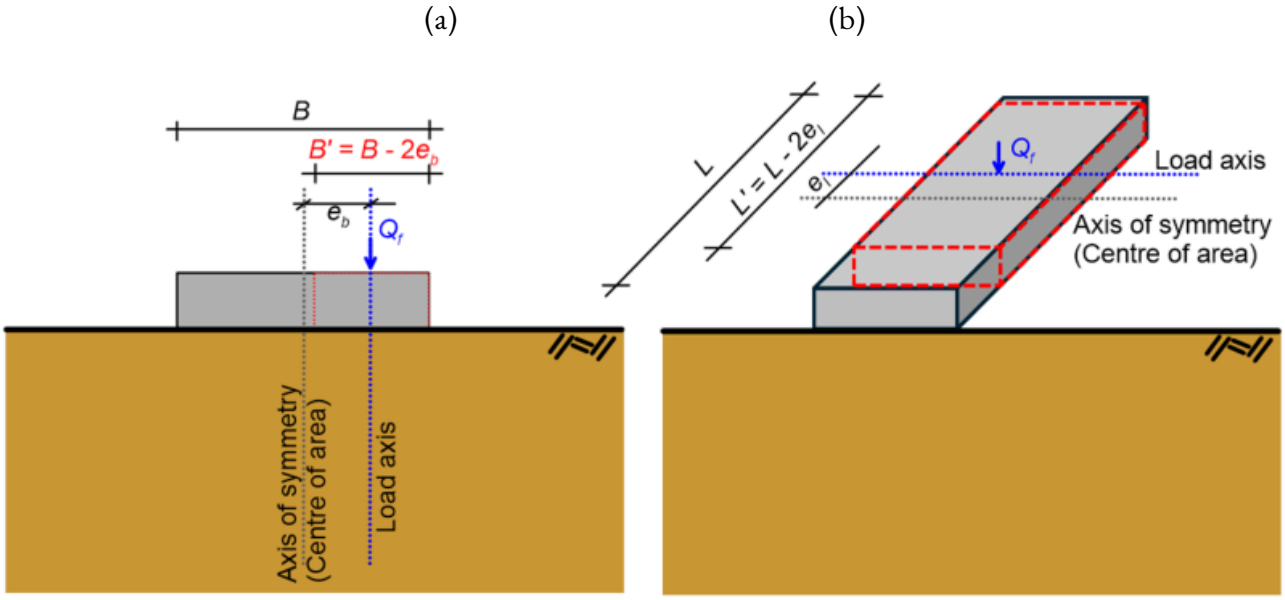

Figure 5.33. Definition of eccentricity (a) for a strip footing, along the footing width, and (b) for a rectangular footing, along the footing length.

Apart from the above, bearing capacity equations must be adjusted to account for groundwater effects, when performing an effective stress analysis under drained conditions. For that, we distinguish three cases, with respect to the elevation of the groundwater table relatively to the foundation level (Figure 5.34).

When the groundwater table is found below a depth B from the foundation level D_f (Case 1, Figure 5.34) no reduction of the bearing capacity is necessary, as we can assume that the failure surface will be contained in the soil above the groundwater table. When the groundwater is found at a level above $B+D_f$ from the ground surface, its effect on the bearing capacity of the footing is introduced in Eq. 5.25 as:

Case 2, Figure 5.34:

(5.31) $$q = [\gamma D_f\,(N_q - 1)]\,s_q d_q + [0.5\,\{\gamma z + (\gamma - \gamma_w)\,(B' - z)\}\,N_\gamma]\,s_\gamma d_\gamma$$

where z is measured from the foundation level of the footing.

Case 3, Figure 5.34:

(5.32) $$q = [\{\gamma z + (\gamma - \gamma_w)\,(D_f - z)\}\,(N_q - 1)]\,s_q d_q + [0.5\,(\gamma - \gamma_w)\,B' N_\gamma]\,s_\gamma d_\gamma$$

where in this case z is measured from the soil surface.

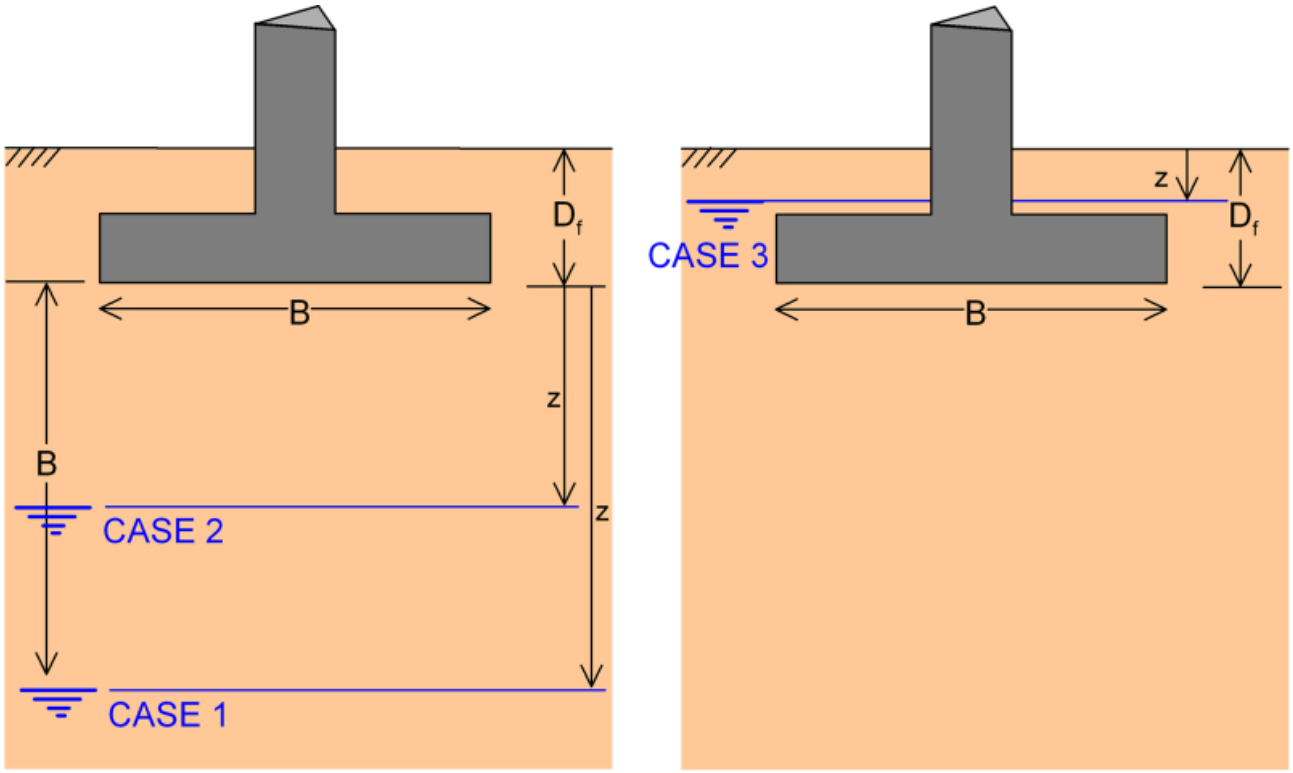

Figure 5.34. Groundwater effects on bearing capacity, distinguishing different cases with respect to the elevation of the groundwater table relatively to the foundation level.

The above Eqs. 5.31 and 5.32 were simplified on the basis of the assumption that soil above the groundwater table is saturated, so its unit weight is equal to the saturated unit weight $\gamma = \gamma_{sat}$. Moreover, γ_w is the unit weight of water $\gamma_w \approx 10$ kN/m^3.

Finally, one of the main assumptions that we make when using all the expressions presented above is that a general shear failure mechanism (Hill- or Prandtl- type) will develop when the footing is loaded to failure. However, as discussed earlier and depicted in Figure 5.23, other failure mechanisms may develop in e.g., medium-dense sands *(local shear mechanism,* Figure 5.23b*)* or very soft clays/loose sands *(punching mechanism,* Figure 5.23c).

Consider for example the problem of estimating the bearing capacity of a footing embedded in a trench, when the footing is separated by the trench walls by a gap with width m. This scenario is not compatible with the assumptions of the analytical solutions presented above, and we cannot know whether a generalised or a local shear failure will develop if the footing is loaded up to its collapse load. Certainly, if we neglect the existence of the gap and assume that a generalised failure surface will develop with the soil overburden contributing beneficially to the bearing capacity, we are not on the safe side.

To address this, for footings on loose-to-medium sands with relative density $D_r < 65\%$ and soft clays with undrained shear strength $S_u < 50$ kPa, where local shear failure is more likely to develop, it is proposed to use the bearing capacity expressions provided in this section while conservatively reducing the values of φ' and S_u to 2/3 of the characteristic value (Figure 5.35a, option 1):

(5.33) $$\varphi' = \arctan\left(\frac{2}{3}\tan\varphi'_{char}\right)$$

(5.34) $$S_u = \left(\frac{2}{3}\right) S_{u,char}$$

Alternatively, we can completely ignore the existence of the overburden, assuming therefore a localised failure mode (Figure 5.35a, option 2). The above are in agreement with field tests performed by Gaone *et al.* (2017) on footings on soft clay, and numerical simulation results obtained by the author (Figure 5.35b). For the particular tests, both options 1 and 2 provided reasonably accurate estimates of the measured collapse load.

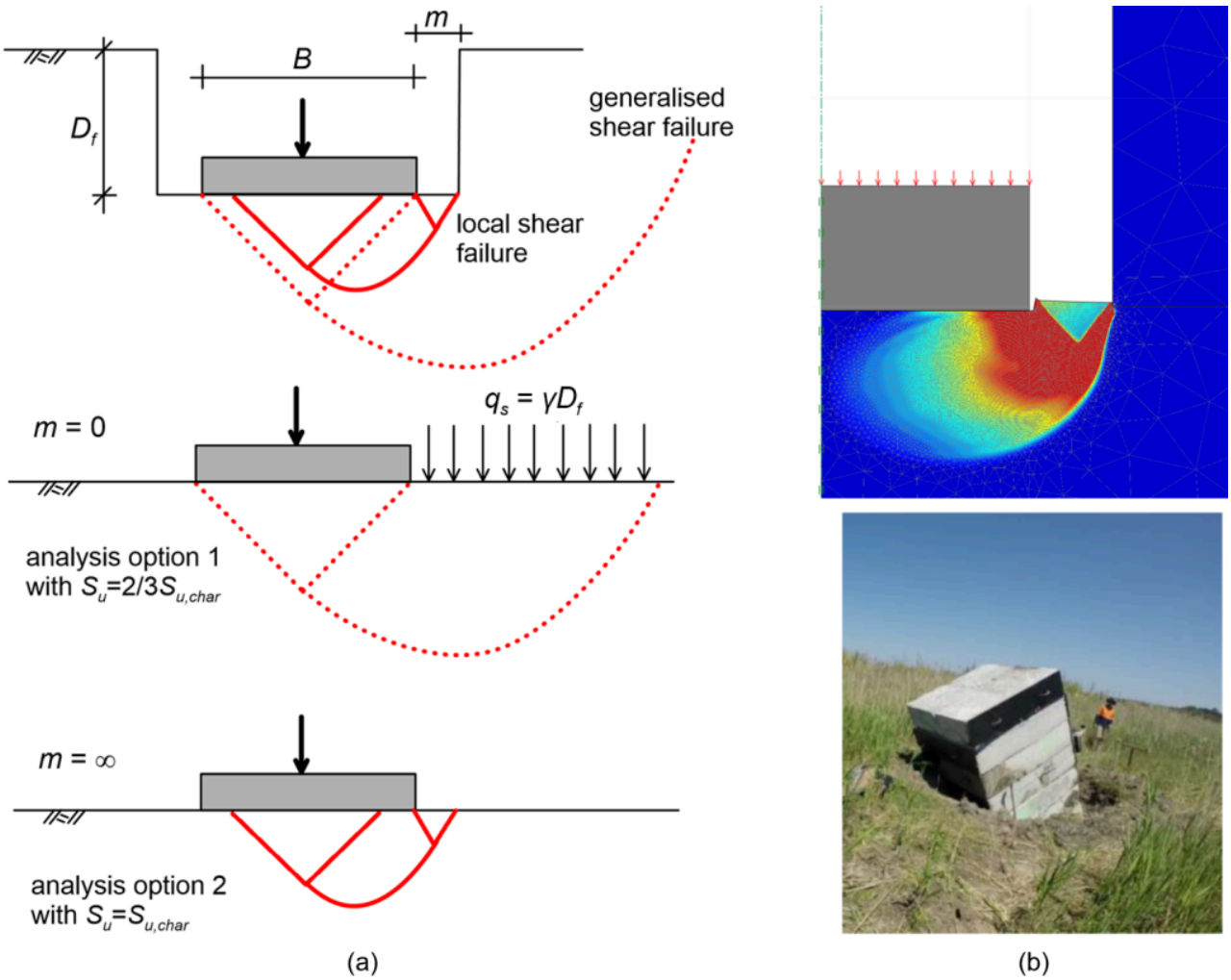

Figure 5.35. (a) Outline of the problem of bearing capacity of a rectangular footing embedded in a trench and different analysis options (b) failure surface obtained from numerical analysis and actual failure mode during a load test suggesting local failure (Gaone et al. 2018, Photograph reproduced with permission).

EXAMPLE 5.3

Estimation of the long-term and short-term design capacity of a rectangular footing according to AS5100.3 with the bearing capacity equations

A rectangular footing is embedded in a saturated normally consolidated clay layer. The shear strength parameters of the clay, depicted in the figure below, have been determined by means of triaxial laboratory tests on undisturbed samples. Estimate the design capacity of the footing under short-term and long-term loading conditions according to AS5100.3. Assume $\gamma = 15$ kN/m^3.

Answer:

As the design load acts at the center of area of the footing, no correction of the footing width and length to their effective values is necessary, thus $B' = B = 4$ m and $L' = L = 4$ m.

The saturated clay will behave as undrained in the short-term (before excess pore pressure generated by the loading dissipates), therefore we will employ TSA to determine the short-term bearing capacity (e.g., during construction), and from that the collapse load and the design capacity. Accordingly, we will use the ESA formulas to determine the long-term bearing capacity for drained conditions, when all excess pore pressures have dissipated e.g., during the service life of the project (Table 5.4).

The lower of short-term and long-term design capacities is the critical one, to be used for the design of the footing (that is if load and geotechnical reduction factors are the same during construction and during service, as we assume here). However, as the clay is normally consolidated, we can expect undrained loading to be critical (see Figure 5.9).

Since the load is not inclined, we will use the net bearing capacity equations 5.24 and 5.25 together with the shape and embedment correction factors and Eq. 5.23 to add the beneficial contribution of the overburden pressure. No groundwater table is present so a reduction of the long-term bearing capacity for groundwater effects is not required.

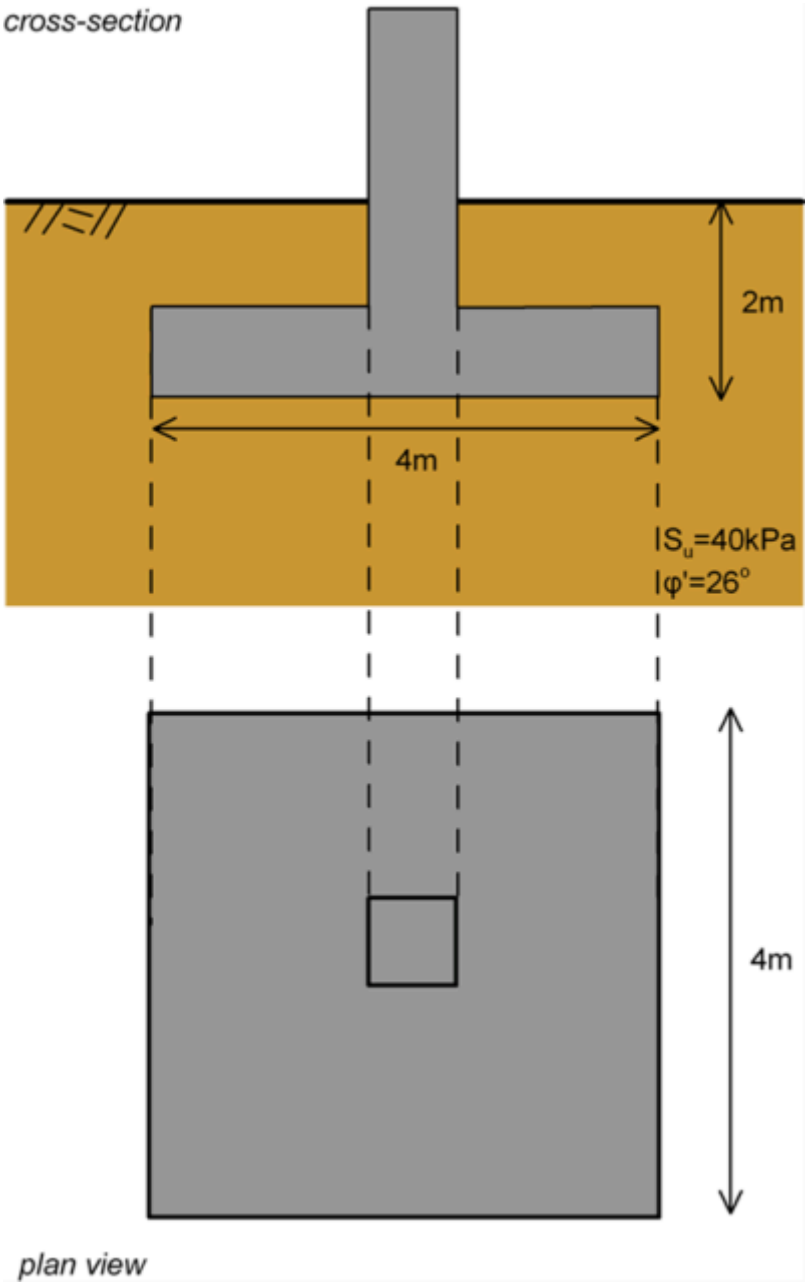

Example 5.3. Problem description and input parameters.

1. Short-term design capacity

We will use Eq. 5.24:

$$q = (5.14 S_u)\, s_c d_c$$

The shape, s_c and embedment, d_c factors for undrained conditions are calculated from Table 5.5 as:

$$s_c = 1 + 0.2\left(\frac{B'}{L'}\right) = 1.2$$

$$d_c = 1 + 0.33 \arctan\left(\frac{D_f}{B'}\right) = 1 + 0.33 \times 0.463 \text{ rad} = 1.153$$

Thus the short-term net bearing capacity is:

$$q = (5.14 S_u)\, s_c d_c = 284.4\ \text{kPa}$$

As the characteristic value of the undrained shear strength was determined from laboratory tests on undistrurbed samples, the appropriate range of the geotechnical strength reduction factor φ_g from Table 5.1 is φ_g = 0.45 to 0.60. Selecting conservatively the lower bound of the proposed range, the bearing capacity Eq. 5.23 accounting for embedment D_f = 2 m results to the design capacity of the footing (expressed in units of force) as:

$$\varphi_g q + \gamma D_f \geq S^*$$

$$0.45 \times 284.4 + 15 \times 2 \geq S^*$$

$$S^* \leq 158\ \text{kPa}$$

$$S^* \leq 158\ \text{kPa} \times (4 \times 4)\ \text{m}^2 = 2528\ \text{kN}$$

2. Long-term design capacity

We will use Eq. 5.25:

$$q = \left[\gamma D_f\, (N_q - 1)\right] s_q d_q + \left[0.5 \gamma B' N_\gamma\right] s_\gamma d_\gamma$$

The bearing capacity factors N_q and N_γ are calculated from Eqs. 5.18 and 5.28, respectively, as:

$$N_\gamma = (N_q - 1) \tan(1.4 \varphi') = 8$$

The shape s_q, s_γ and embedment d_q, d_γ factors for drained conditions are calculated from Table 5.5 as:

$$s_q = 1 + \left(\frac{B'}{L'}\right) \tan \varphi' = 1.487$$

$$s_\gamma = 1 - 0.4 \left(\frac{B'}{L'}\right) = 0.6$$

$$d_q = 1 + 2 \tan \varphi' (1 - \sin \varphi')^2 \arctan\left(\frac{D_f}{B'}\right) = 1.142$$

$$d_\gamma = 1$$

Thus the long-term net bearing capacity is:

$$q = \left[\gamma D_f\, (N_q - 1)\right] s_q d_q + \left[0.5 \gamma B' N_\gamma\right] s_\gamma d_\gamma$$

$$q = \left[15 \times 2\, (11.85 - 1)\right] \times 1.487 \times 1.142 + \left[0.5 \times 15 \times 4 \times 8\right] \times 0.6 \times 1$$

$$q = 696.7\ \text{kPa}$$

Using the same value for the geotechnical strength reduction factor φ_g = 0.45 as for the short-term loading case, the design capacity of the footing is again calculated as in terms of force:

$$\varphi_g q + \gamma D_f \geq S^*$$

$$0.45 \times 696.7 + 15 \times 2 \geq S^*$$

$$S^* \leq 343.5\,\text{kPa}$$

$$S^* \leq 343.5\,\text{kPa} \times (4 \times 4)\,\text{m}^2 = 5496.6\,\text{kN}$$

5.5 BEARING CAPACITY OF FOOTINGS ON LAYERED SOILS

5.5.1 Critical thickness of the surficial soil layer

One of the key assumptions of the common analytical solutions presented in Chapter 5.4 is that of uniform soil conditions, which is rarely the case in practice. When the geotechnical investigation reveals a non-uniform soil profile, we have to estimate whether the thickness of the top soil layer, measured below the embedment depth, is enough so that the failure surface will develop entirely inside it (Figure 5.36).

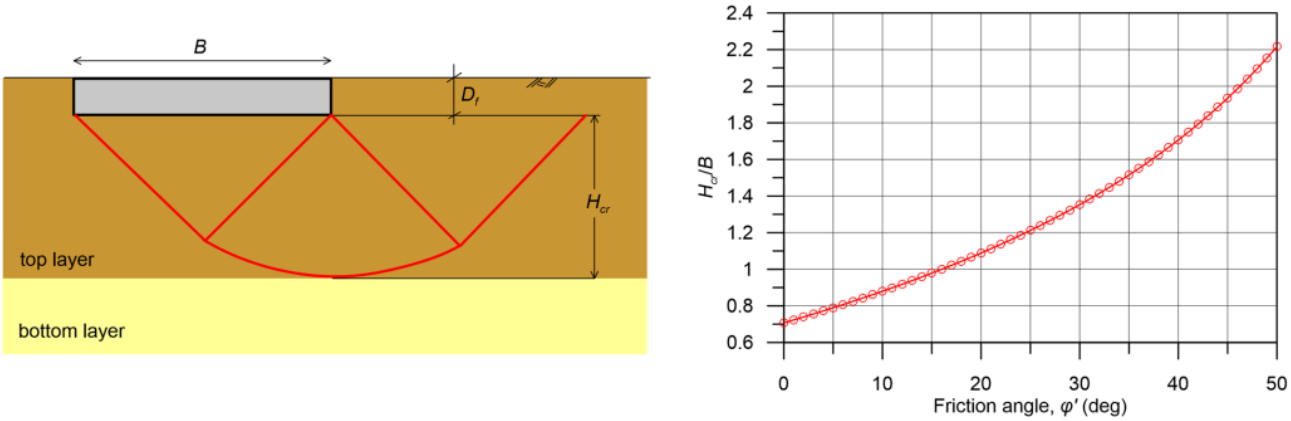

Figure 5.36. Definition of the critical thickness, H_{cr} for failure to develop within the surficial soil layer.

It is reasonable to assume that if the thickness of the soil layer below the foundation, H_{cr} is less than the depth that the Prandtl mechanism penetrates into the soil (Figure 5.26) the failure surface will be entirely contained in the top soil layer, and the subsoil can be considered as homogeneous for bearing capacity calculations.

(5.35) $$H_{cr} = \frac{B}{2\cos\left(45^o + \frac{\varphi'}{2}\right)} e^{(A\tan\varphi')}$$

Where $A = (45°+\varphi'/2)$ in rad.

Alternatively, the critical thickness H_{cr} can be calculated as (Budhu 2011):

(5.36) $$H_{cr} = \frac{3B\ln\left(\frac{q_{top}}{q_{bottom}}\right)}{2\left(1+\frac{B}{L}\right)}$$

where:

- q_{top} is the bearing capacity of the footing with the particular dimensions, resting on the surface of an infinitely deep layer with the properties of the *top* soil layer, and

- q_{bottom} is the bearing capacity of the footing with the particular dimensions, resting on the surface of an infinitely deep layer with the properties of the *bottom* soil layer.

If the thickness of the top soil layer measured below the embedment depth, H_{top} is less than the critical thickness, H_{cr}, there is no general analytical method to estimate the bearing capacity, except of course numerical methods. Some characteristic cases are examined in the following paragraphs.

5.5.2 Footing on a soft clay layer overlying a stiff soil formation

In the case where a thin soft clay formation is found near the ground surface, good engineering practice suggests excavating the soft clay layer, and replacing it with well-compacted coarse-grained fill material. Founding structures directly on soft clays with shallow foundation should be avoided, except light structures such as one-storey buildings.

Experimental results have shown that in the case of a footing resting on soft clay overlying a stiffer stratum, the mechanism of bearing capacity consists of lateral squeezing of the soft soil, as the footing "sinks" into the top layer. Tomlinson and Boorman (1995) proposed the following expressions to estimate bearing capacity in that case:

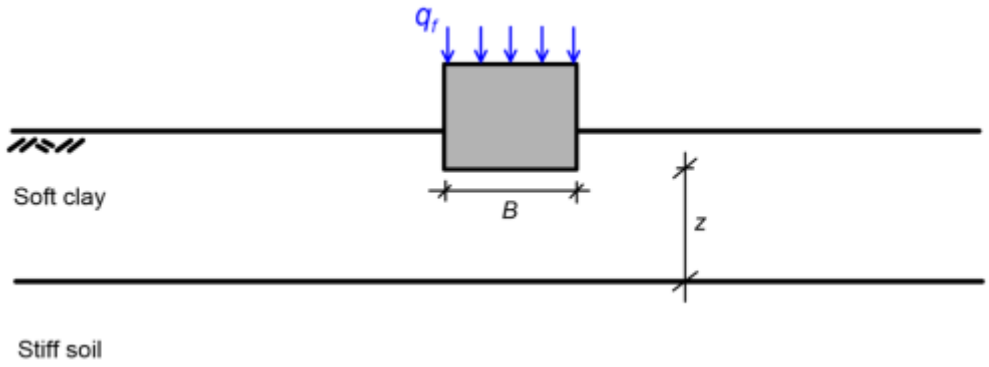

Figure 5.37. Footing on a soft clay layer overlying a stiff soil formation.

For circular/square footings:

$$\textbf{(5.37)}\ q_f = \left(\frac{B}{2z} + \pi + 1\right) S_u \text{ for } \frac{B}{z} \geq 2$$

For strip footings:

$$\textbf{(5.38)}\ q_f = \left(\frac{B}{3z} + \pi + 1\right) S_u \text{ for } \frac{B}{z} \geq 6$$

where z is defined in Figure 5.37 above. When $B/z < 2$ for circular/strip footings or $B/z < 6$ for strip footings (Figure 5.37), the expressions for homogeneous soil should be rather used.

5.5.3 Footing on stiff soil overlying a soft clay layer

This case could well correspond to the common problem of a footing resting on a foundation improvement layer made of well-compacted coarse-grained fill, overlying a soft subgrade. A *"punching"* failure mechanism may develop under these circumstances (Figure 5.38a).

A simplified method for estimating the bearing capacity of a footing of any shape resting on the surface of, or embedded in a stiff soil formation overlying a soft clay layer consists of the following steps: First, we estimate the bearing capacity of the footing while considering uniform soil with the properties of the top stiff soil layer, which must not be critical for the design.

Accordingly, we estimate using Eq. 5.24 the net bearing capacity q_{eq} of a hypothetical equivalent footing with the same shape and dimensions, embedded at a depth $D_{f,eq} = D_f+z$ equal to the thickness of the top stiff soil layer (Figure 5.38). Bearing capacity failure of the actual footing will be reached when the vertical stress $\Delta\sigma_z$ transferred from the actual footing to the interface of the stiff soil-soft clay layer (Figure 5.38b) becomes equal to q_{eq} i.e., $\Delta\sigma_z = q_{eq}$. The following approximate expressions can be used to calculate $\Delta\sigma_z$, while assuming 2:1 stress distribution (see Chapter 3.6):

For a rectangular footing:

$$\textbf{(5.39)}\ \Delta\sigma_z = q\left[\frac{BL}{(B+z)(L+z)}\right]$$

For a square/circular footing:

$$\textbf{(5.40)}\ \Delta\sigma_z = q\left[\frac{B}{(B+z)}\right]^2$$

For a strip footing:

$$\textbf{(5.41)}\ \Delta\sigma_z = q\left[\frac{B}{(B+z)}\right]$$

in the above expressions q is the net bearing capacity of the actual footing. Therefore substituting $\Delta\sigma_z = q_{eq}$ in the Eqs. 5.39 to 5.41 that corresponds to the actual footing shape will provide its net bearing capacity q. If the actual footing is embedded in soil, its bearing capacity will be $q_f = q + \gamma D_f$.

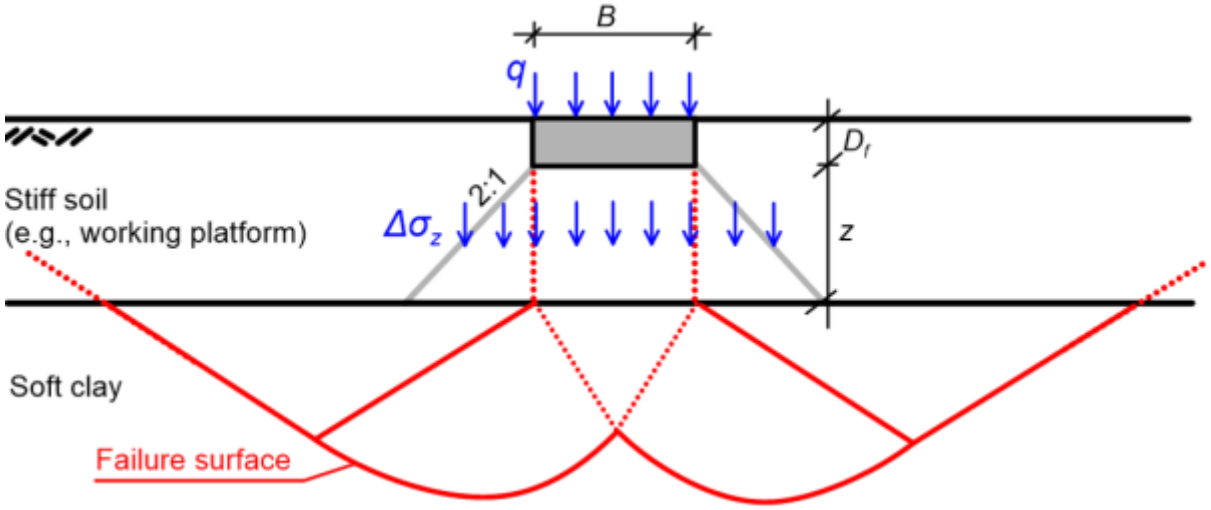

Figure 5.38a. Punching of a footing into the underlying soft clay layer.

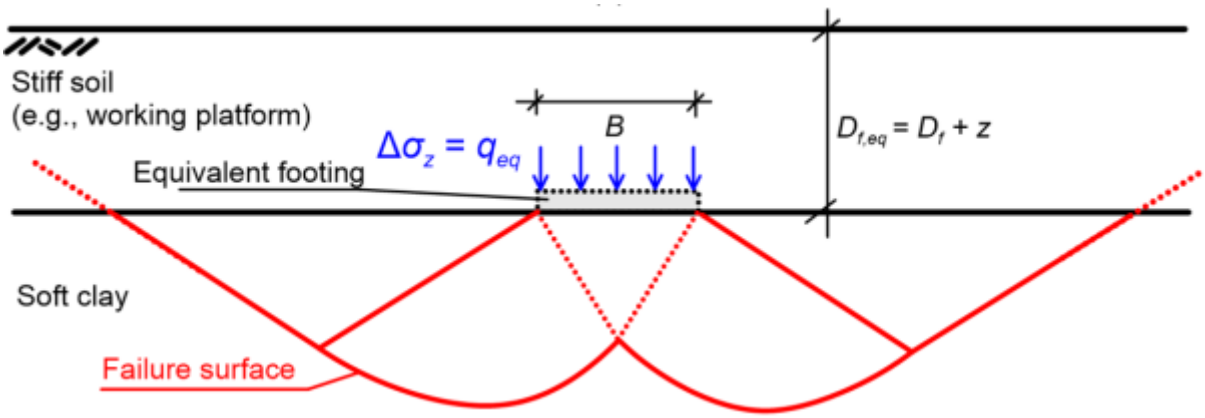

Figure 5.38b. Concept for estimating the bearing capacity accounting for the development of the failure surface inside the soft clay layer.

Note that the methodology described above conservatively ignores the shear resistance of the top layer, and the energy dissipated along the shear planes located with it. Another simplifying assumption is that the inclination of the shear planes relative to the vertical in the top layer is ignored i.e., the width of the equivalent, hypothetical footing is taken equal to the width of the real one. There are more refined methods in the literature that do not require introducing these assumptions, however their range of application is limited to specific footing geometries and soil types. Such a method has been developed by Salimi Eshkevari *et al.* (2019a) for estimating the bearing capacity of strip footings resting on the surface of a sand layer overlying a soft clay, which is relevant to the design of working platforms for tracked plants. Salimi Eshkevari *et al.* analysed the results of a series of Finite Element Limit Analyses and concluded to the following expression that provides the bearing capacity of a strip footing on a layered profile of sand over clay q_{fl}:

(5.42) $$q_{f,l}B = \gamma H^2 K_{sr} \tan\varphi' + N_{cu} S_u \left[B + 2H\tan\theta\right] + \gamma H^2 \tan\theta \leq qB$$

where B is the footing width, H is the thickness of the sand layer, γ is the unit weight of sand, φ' is the friction angle of sand, S_u is the undrained shear strength of the clay layer, $N_{cu} = 5.14$ is the bearing capacity factor for strip footings on undrained soil, q is the bearing capacity of a footing of width B resting on the surface of uniform sand, calculated according to Eq. 5.25. The angle θ that provides the inclination of the shear planes that will develop in the sand layer can be calculated as:

(5.43) $$\theta(\text{rad}) = \alpha \ln\left(\frac{S_u}{\gamma H}\right) + \beta$$

(5.44) $$\alpha = 0.039 \ln\left(\tan\varphi'\right) - 0.164$$

(5.45) $$\beta = 0.597 \ln\left(\tan\varphi'\right) - 0.051$$

Note that angle θ can be positive or negative. Thus, unlike the approximate method described above, the width $B+2H\tan\theta$ of the equivalent footing in Figure 5.38 can be greater, or less than the width of the actual footing B. Finally, the punching shear coefficient K_{sr}, that is correlated with the normal stress acting on the shear planes that will develop in the sand layer, is calculated as:

(5.46) $$K_{sr} = \delta\left(\frac{S_u}{\gamma H}\right) + 2$$

(5.47) $$\delta = -3.45\left(\tan\varphi'\right) + 8.693$$

5.5.4 Strip footings on layered sands

Estimation of the bearing capacity of strip footings resting on the surface of a relatively thin layer of dense sand overlaying a weak layer of loose sand underpins the design of working platforms for heavily loaded tracked piling rigs and cranes, on sites which loose sand deposits are found at the ground surface. Hanna (1981) was among the first to study this problem, and concluded to the following expression for estimating the bearing capacity in terms of stress when a punching failure mechanism develops:

(5.48) $$q_{f,l} = q_b + \gamma H^2 \frac{K_s \tan \varphi'_1}{B} - \gamma_1 H \leq q$$

where B is the footing width, H is the thickness of the top (dense) sand layer, γ_1 is the unit weight of the dense sand layer, φ'_1 is the friction angle of the dense sand layer, q_b is the bearing capacity of a footing of width B embedded at depth H in a uniform sand layer with the properties of the loose sand, calculated as:

(5.49) $$q_b = 0.5\gamma_2 B N_{\gamma 2} + \gamma_1 H N_{q2}$$

where γ_2 is the unit weight of the loose sand layer, while $N_{\gamma 2}$ and N_{q2} are the bearing capacity factors of the loose sand layer, featuring friction angle φ'_2, calculated according to Eq. 5.18 and Figure 5.31, respectively. Moreover, q in Eq. 5.48 is the bearing capacity of a footing of width B resting on the surface of uniform dense sand with friction angle φ'_1, calculated according to Eq. 5.25, and K_s is a punching shear resistance coefficient that depends on the friction angles of the two sand layers, and is provided in Figure 5.39.

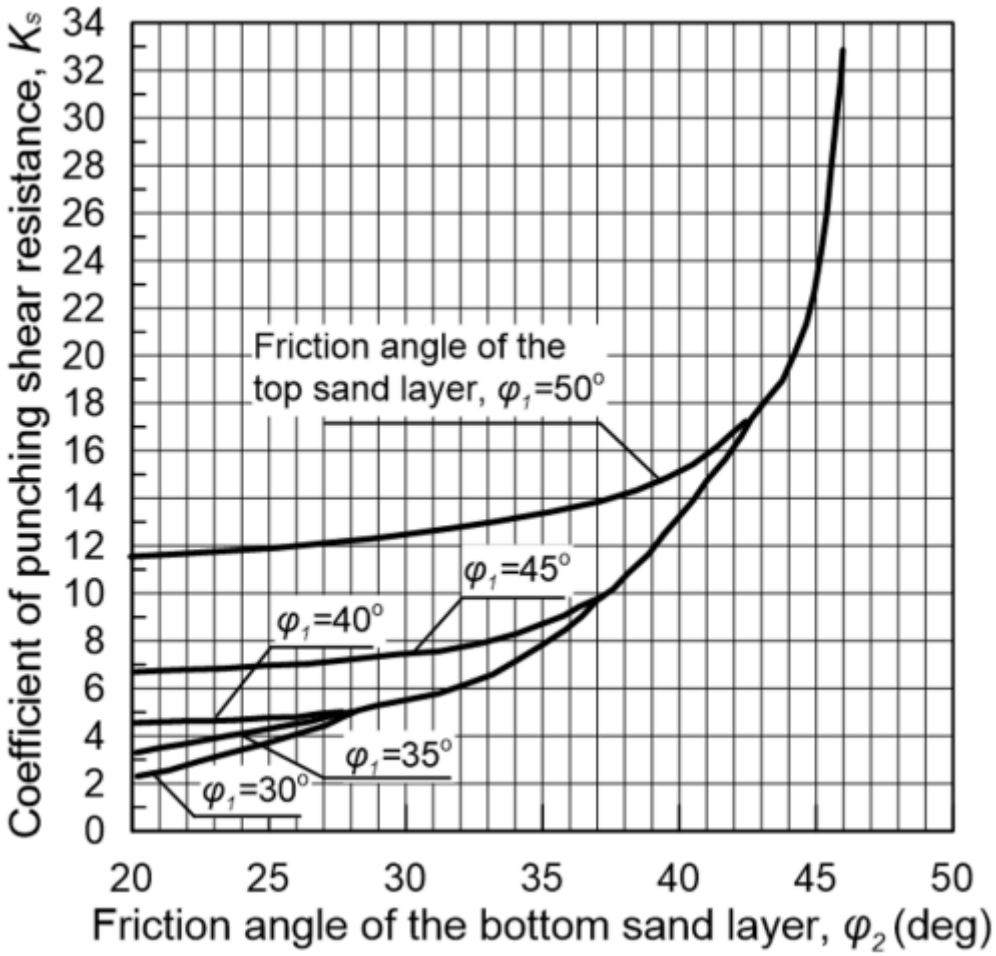

Figure 5.39. Determination of the coefficient of punching shear resistance K_s for strip footings on layered sand (after Hanna 1981).

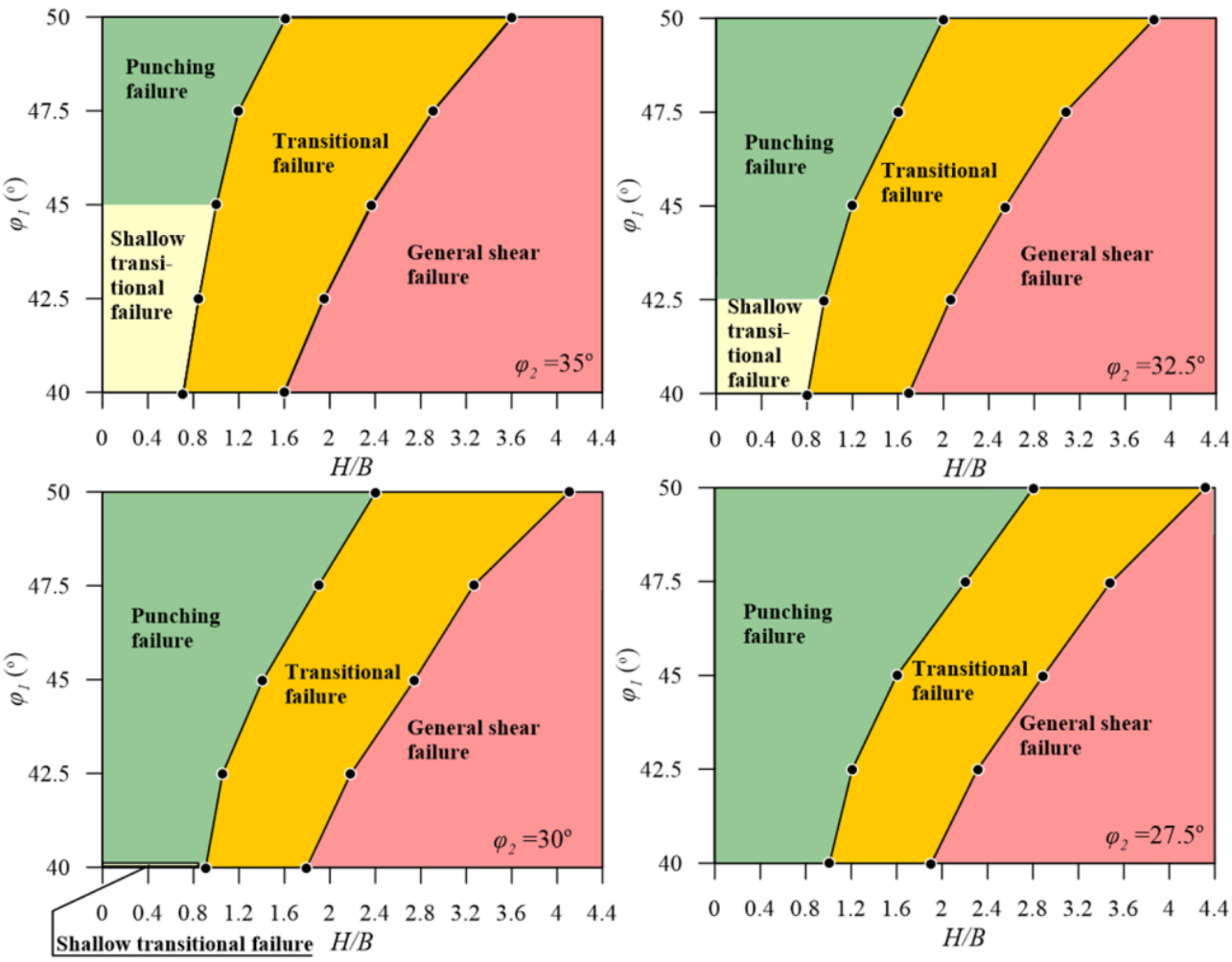

Figure 5.40. Failure mechanisms for strip footings on layered sand for different friction angles and dimensionless thickness *H/B* combinations (Salimi Eshkevari et al. 2019b).

An important assumption underlying Hanna's Eq. 5.48 is that a punching failure mechanism develops, irrespective of the relative strength of the two layers. Salimi Eshkevari *et al.* (2019b) have shown that the failure mechanism that will develop depends on the friction angles of the two layers, as well as the ratio of the thickness of the top dense sand layer over the width of the footing *H/B*. Using Figure 5.40 one can determine which failure mechanism will develop. Accordingly, Salimi Eshkevari *et al.* (2019b) proposed the following expression for calculating the bearing capacity of a strip footing resting on dense sand over loose sand, for the cases where a transitional (or shallow transitional) mechanism is expected to develop:

(5.50) $$q_{f,l} = 0.5\gamma_1 B N_\gamma^* \leq q$$

where the modified bearing capacity factor N_γ^* is given in Figure 5.41 for different values of φ'_1, φ'_2 and *H/B*. If Figure 5.40 suggests that a punching failure mechanism will develop, Salimi Eshkevari *et al.* recommended using Hanna's expression (Eq. 5.48) to determine the bearing capacity. Bearing capacity factor values in Figure 5.41 are applicable to the case where γ_1/γ_2 = 1.2, which is probably a reasonable approximation for most practical cases. Note also that Figure 5.41 covers only specific *H/B* ranges for which a transitional mechanism will develop. Finally, the upper bound to the bearing capacity factor N_γ^* (dashed lines in Figure 5.41) is the conventional bearing capacity factor N_γ, and indicates cases where the thickness of the top dense sand layer exceeds the critical thickness, thus a general shear failure mechanism will develop and $q_{fl} = q$.

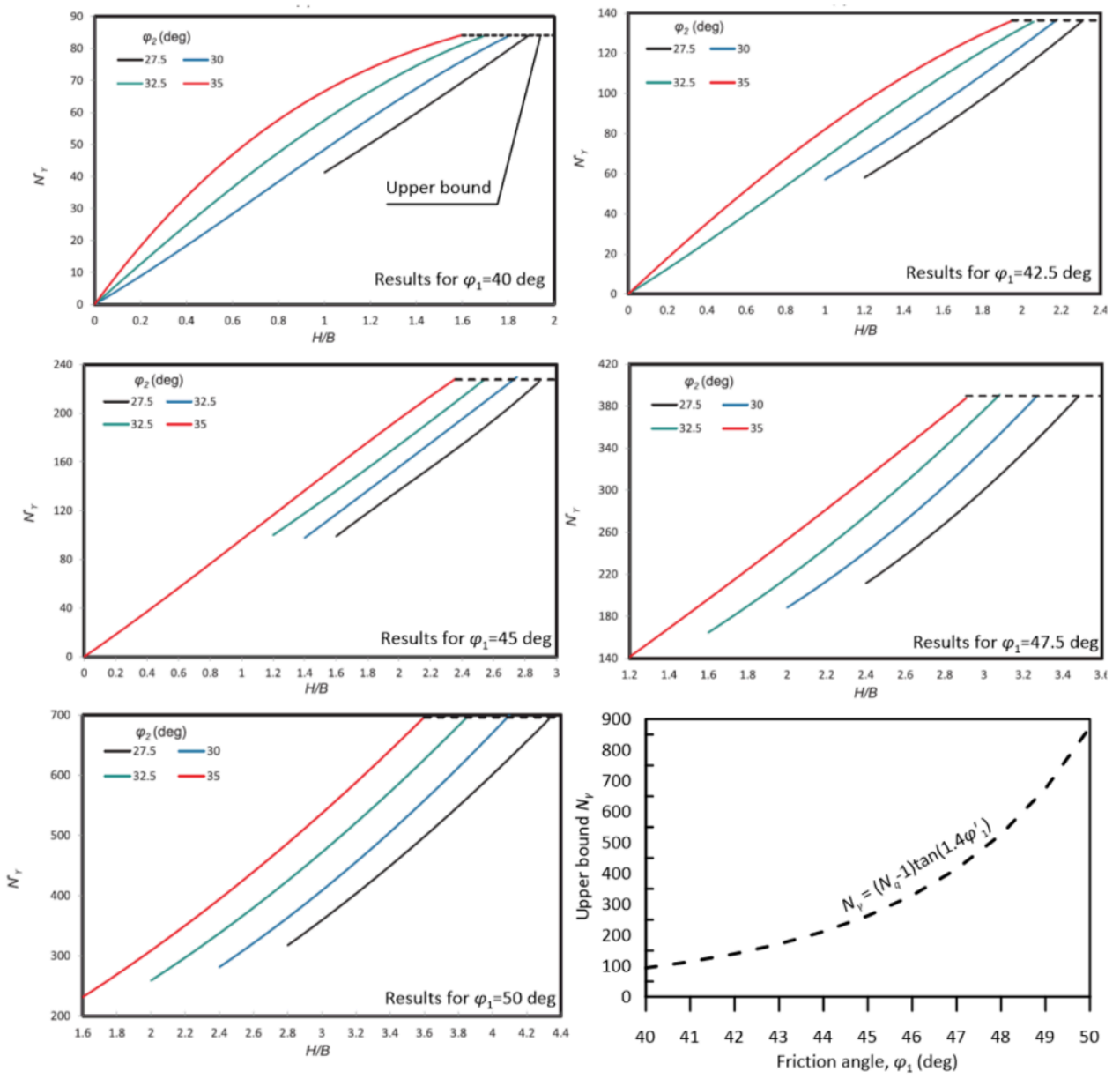

Figure 5.41. Modified bearing capacity factor N_γ^* for different values of φ'_1, φ'_2 and H/B (Salimi Eshkevari et al. 2019b) and upper bound bearing capacity factor N_γ for generalised failure according to Meyerhoff.

5.5.5 Footings on multi-layered soil profile

A lower-bound estimate of the bearing capacity of a footing resting on a multi-layered soil profile can be found by simply considering a homogeneous soil with the properties of the weakest layer, an approach that may lead to perhaps over-conservative results. Numerical methods are recommended for the treatment of such problems.

EXAMPLE 5.4

Design capacity of a footing resting on a two-layer formation according to AS5100.3

A strip footing, considered to be infinitely long for practical purposes, will be founded on the surface of a soft saturated clay layer. The undrained shear strength of the clay was measured in the laboratory to be S_u = 30 kPa. To increase the bearing capacity, the Geotechnical Engineer proposed to lay on top of the soft clay a 2m-thick layer of well-compacted coarse-grained material. Assuming a punching-type failure mechanism and vertical-only loading, estimate the design capacity of the footing under short-term conditions, according to AS 5100.3. The geotechnical strength reduction factor is equal to φ_g = 0.45.

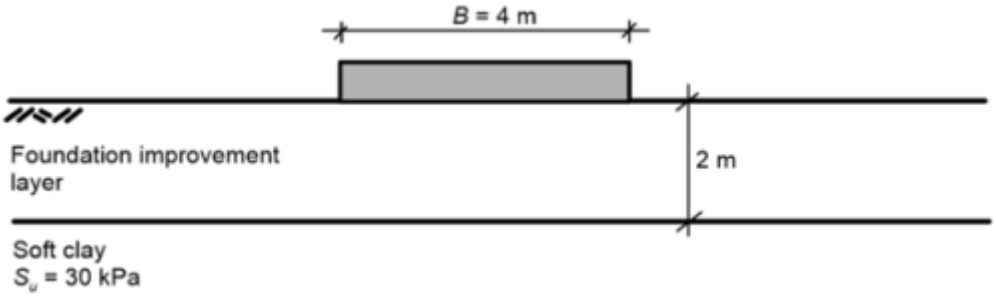

Example 5.4. Problem description and input parameters.

Answer:

We will consider only the punching failure mechanism here, and we will not estimate the design capacity considering uniform soil with the properties of the foundation improvement layer mentioned in Section 5.5.3, as it will not be critical. A well-compacted improvement layer will exhibit much higher shear strength, compared to the soft clay layer.

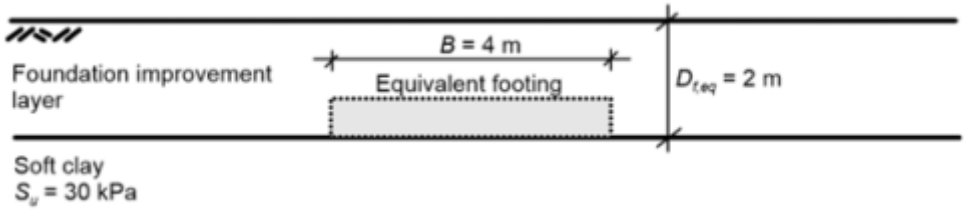

Figure 5.42. Geometry of the equivalent footing resting on the top of the soft clay layer.

First, following the simplified method presented in Section 5.5.3, we estimate the bearing capacity of a vertically loaded equivalent strip footing under short-term undrained conditions, assuming it is founded on the improvement layer-soft clay interface (Figure 5.42). The embedment depth of this equivalent footing is D_f = *2* m, its width is equal to the width of the real footing B = 4 m and its length is infinite L= ∞.

The short-term net bearing capacity of the equivalent strip footing q_{eq} is calculated from Eq. 5.24 as:

$$q_{eq} = (5.14 S_u)\, s_c d_c$$

While the shape, s_c and embedment, d_c factors can be calculated from Table 5.5 as:

$$s_c = 1 + 0.2\left(\frac{B'}{L'}\right) = 1.0 \text{ since } L = \infty$$

$$d_c = 1 + 0.33 \arctan\left(\frac{D_f}{B'}\right) = 1 + 0.33 \times 0.463 \text{ rad} = 1.153$$

and the short-term net bearing capacity of this equivalent footing is:

$$q_{eq} = (5.14 S_u)\, s_c d_c = 177.8 \text{ kPa}$$

The pressure q that must be applied on the real footing to transfer vertical stress at the improvement layer-soft clay interface equal to the net bearing stress of the equivalent footing q_{eq} is calculated from Eq. 5.41 as:

$$\Delta\sigma_z = q_{eq} = q\left[\frac{B}{(B+z)}\right] \Rightarrow q = \frac{(B+z)}{B} q_{eq} = \left(\frac{4+2}{4}\right) 177.8 = 266.7 \text{ kPa}$$

As application of the pressure q on the real footing results in shear failure developing into the soft clay layer, q will be equal to the net bearing capacity of the real footing. Moreover, as the real strip footing is constructed directly on the surface of the improvement layer, its design capacity in terms of load per running meter according to AS 5100.3 will be:

$$\varphi_g q + \gamma D_f \geq S^*$$

$$0.45 \times 266.7 + 0 \geq S^*$$

$$S^* \leq 120 \text{ kPa}$$

$$S^* \leq 120 \text{ kPa} \times (4 \times 1) \text{ m}^2 = 480 \text{ kN/running meter of footing}$$

Let's now estimate the design capacity again, using this time the method of Salimi Eshkevari *et al.* (2019a). For that we need two more parameters: The unit weight γ and the friction angle φ' of sand. We will assume here that γ = 20 kN/m^3 and φ' = 40 deg. The coefficients of Eq. 5.43 are calculated from Eqs. 5.44 and 5.45 as:

$$\alpha = 0.039 \ln(\tan 40^o) - 0.164 = -0.1708$$

$$\beta = 0.597 \ln(\tan 40^o) - 0.051 = -0.1557$$

and

$$\theta(\text{rad}) = (-0.1708) \ln\left(\frac{30}{20 \times 2}\right) - 0.1557 = -0.1065$$

In other words, the width of the equivalent footing is $B + 2H\tan\theta$ = 3.572 m < 4 m.

The coefficient δ required to calculate the punching shear coefficient K_{sr} is:

$$\delta = -3.45(\tan 40^o) + 8.693 = 5.798$$

Thus:

$$K_{sr} = \delta\left(\frac{S_u}{\gamma H}\right) + 2 = 6.348$$

The bearing capacity of the strip footing on sand over clay is calculated from Eq. 5.42 as:

$$q_{f,l} = \frac{1}{B}\left(\gamma H^2 K_{sr} \tan\varphi' + N_c S_u \left[B + 2H\tan\theta\right] + \gamma H^2 \tan\theta\right) = \frac{1}{4}\left(426.12 + 550.86 - 8.552\right) = 242\ \text{kPa}$$

Therefore, its design capacity in terms of load per running meter according to AS 5100.3 will be:

$$\varphi_g q_{f,l} + \gamma D_f \geq S^*$$

$$0.45 \times 242 + 0 \geq S^*$$

$$S^* \leq 108.9\ \text{kPa}$$

$$S^* \leq 108.9\ \text{kPa} \times (4 \times 1)\ \text{m}^2 = 435\text{kN/running meter of footing}$$

Observe that, while the results of the two method are generally compatible, the simplified method overestimates the bearing capacity in the problem at hand. That is because the width of the equivalent footing is not equal to the width of the actual footing, but rather it is shorter.

EXAMPLE 5.5

Design of shallow foundations at the Ultimate Limit State using numerical methods

A storage facility with dimensions 6 m x 30 m will be founded on a mat foundation i.e., a slab, that for practical purposes can be consider as an infinite strip footing. The embedment depth of the foundation cannot exceed D_f = 1 m, for practical reasons. The foundation subsoil consists of a medium stiff saturated clay layer, with the properties depicted in the figure below. Preliminary calculations resulted in short-term bearing capacity q_f = 180 kPa, which is lower than the ultimate limit state pressure provided by the Structural Engineer 200 kPa.

As the dimensions of the footing are fixed on the geometry of the facility, improvement measures must be implemented. The Geotechnical Engineer proposed the replacement of the clay with coarse-grained well-compacted material, as the most cost-effective ground improvement solution. Determine the minimum required thickness of the improvement layer to increase the bearing capacity to acceptable levels (q_f > 200 kPa), while taking into account the following:

- Consider for simplicity the unit weight of both the clay and the foundation improvement layer to be equal to γ = 18 kN/m^3.
- Do not apply any reduction factors on the shear strength of the geomaterials as per Eq. 5.33 and 5.34, nor a geotechnical strength reduction factor on the bearing capacity.
- Assume the footing to be rigid and rough.

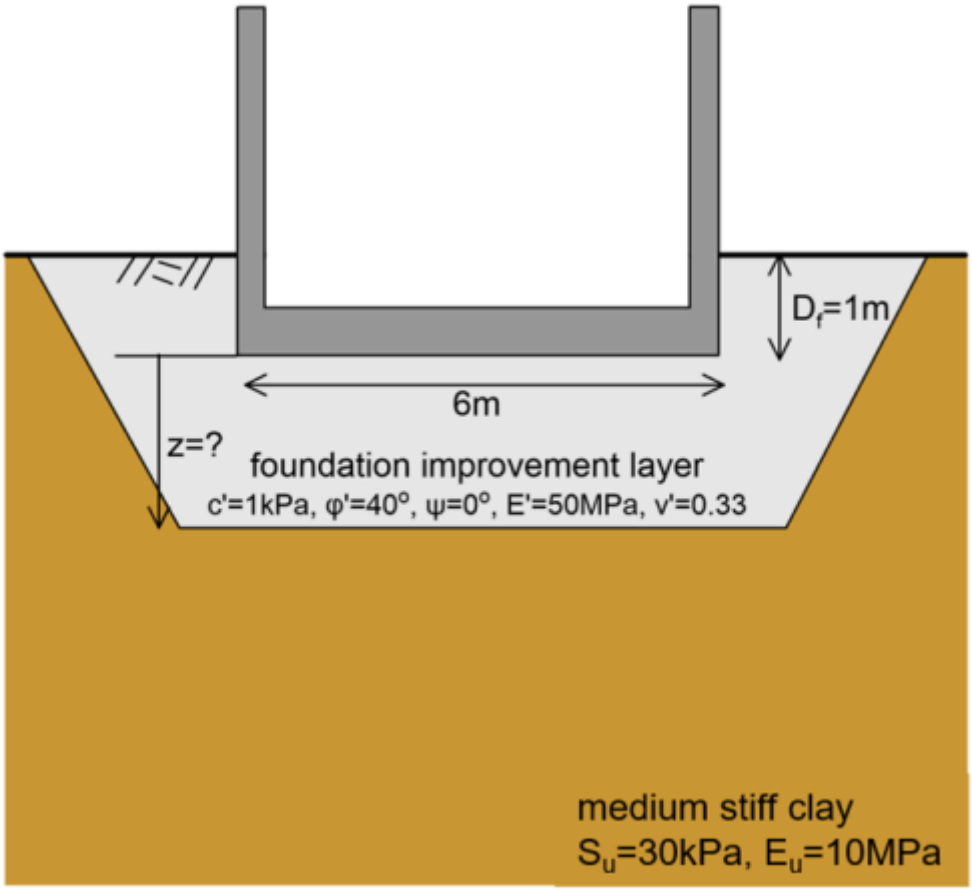

Example 5.5. Problem description and input parameters.

Answer:

Determining the optimum thickness of the foundation improvement layer is a trial-and-error procedure. We are seeking to find the thickness that will result in a bearing capacity slightly higher than 200 kPa (Figure 5.43); not too high, because that would mean that the solution is not economical.

We will thus assume different thickness for the improvement layer, considering rather crude increments of e.g., 0.5 m, and get the load-settlement curve from different PLAXIS models. Notice that employing Eq. 5.35 while assuming a friction angle for the foundation improvement layer $\varphi' = 40^{o}$ results in a critical thickness of the foundation improvement layer for the failure to be constrained in it:

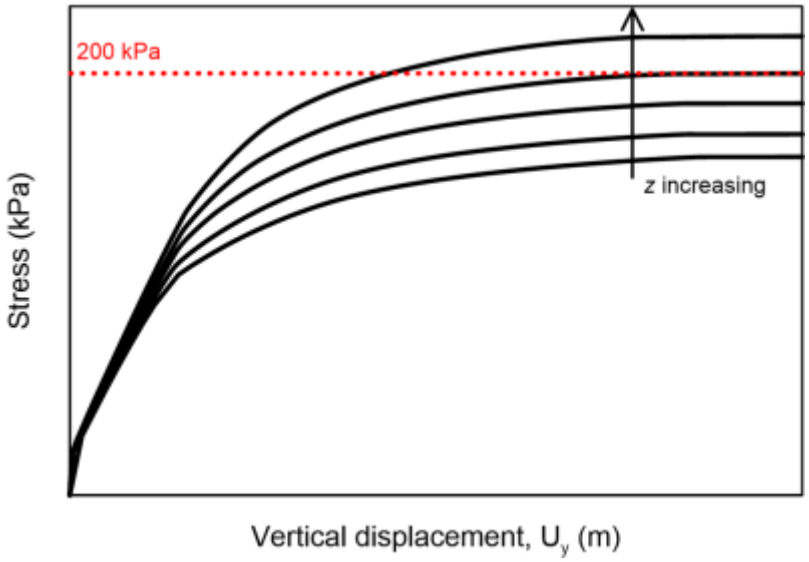

Figure 5.43. Load-displacement curves for varying foundation improvement layer thickness.

$$H_{cr} = \frac{B}{2\cos\left(45^o + \frac{\varphi'}{2}\right)} e^{(A\tan\varphi')}$$

$$\mathrm{A} = \left(45^o - \frac{\varphi'}{2}\right) = \left(45^o - \frac{40}{2}\right) = 0.436 \text{ rad}$$

$$H_{cr} = \frac{6}{2\cos\left(45^o + \frac{40^o}{2}\right)} e^{(0.436\tan 40^o)} = 7.1 \times 1.44 = 10.23 \text{ m}$$

This implies that we definitely have to consider the soft clay layer in our numerical model, and account for the possibility of punching failure, according to the mentioned in Section 5.5.3. We will simulate a plane-strain geometry of 20 m x 10 m, with the axis of the footing being an axis of symmetry (Figure 5.44). The top cluster of the geometry corresponds to the embedment depth (to be replaced by an equivalent pressure), the middle to the foundation improvement layer, and the bottom to the clay. The extent of the model should be enough to accommodate the complex failure surface illustrated in Figure 5.38a.

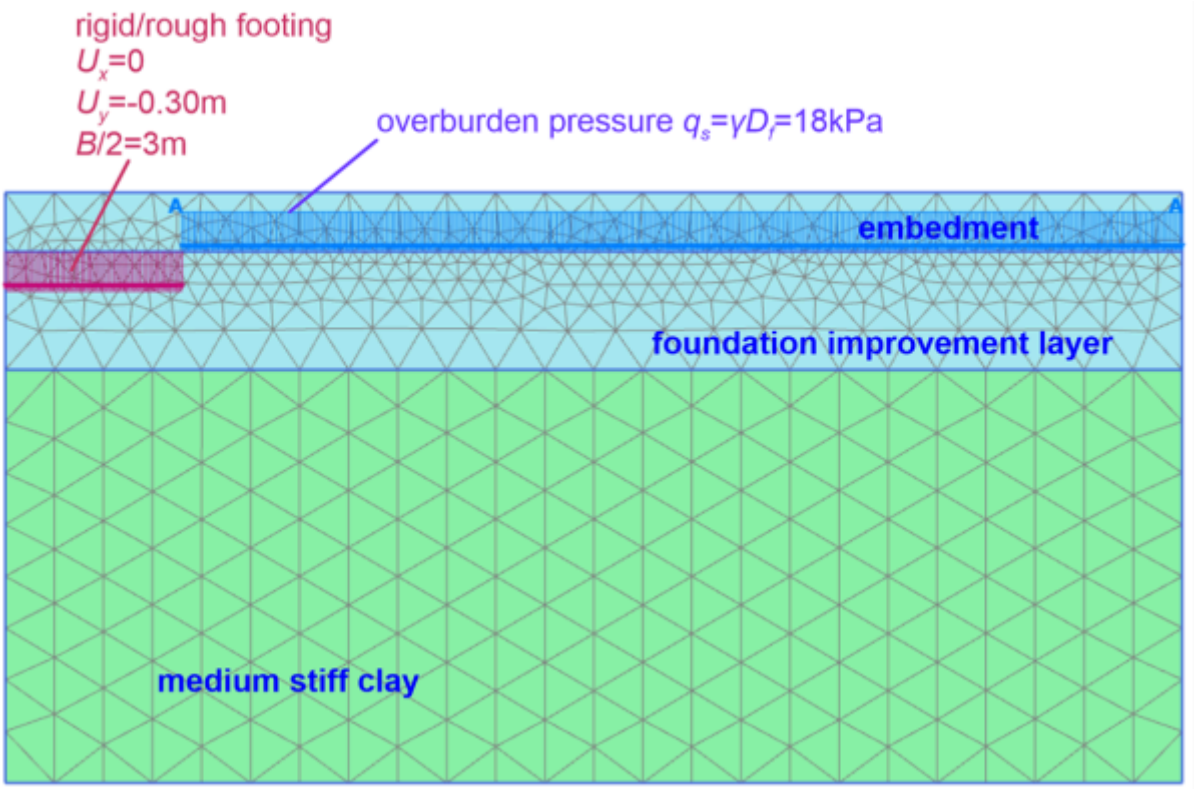

Figure 5.44. Indicative finite element mesh for the simulation of the problem. The thickness of the foundation improvement layer varies.

A prescribed displacement is applied to simulate the rigid and rough footing loading at the foundation level. As discussed in Example 5.2, the vertical displacement U_y should be enough to reach the collapse load i.e., U_y = -0.30 m. Additionally, applying U_x = 0.0 m along the width of the footing accounts for the rough interface i.e., no horizontal displacement is allowed to develop. To simulate embedment, we apply a uniform pressure outside the model area occupied by the footing, with magnitude equal to the weight of the excavated soil, as in Example 5.2:

$$q_s = \gamma D_f = 18 \times 1 = 18 \,\text{kPa}$$

We are seeking to determine the short-term bearing capacity. As presented in Table 5.4, the coarse-grained improvement material, which is usually a mixture of sand with gravels, will behave as drained, whereas the saturated fine-grained clay will behave as undrained under short-term loading conditions. As we are not interested in estimating excess pore pressure but only the bearing capacity, and no groundwater table is present, we will perform a total stress analysis TSA. For that we will use the Mohr-Coulomb *Drained* model to simulate the improvement material, and the Mohr-Coulomb *Undrained* (C) model to simulate soft clay's response (see also Example 5.2), with the shear strength and compressibility properties presented in the problem definition. Keep in mind that undrained or drained response refers to material behavior, so the same problem may include different materials behaving as drained or undrained under short term loads, depending on their properties.

The dilation angle of the improvement layer is assumed $\psi = 0^o$. We will use the Davis equivalent shear strength parameters c^* and φ^* (Eqs. 5.5-5.7) together with associative flow to model the response of this layer, and compare the outcomes to the analytical solution described in Section 5.5.3 to investigate whether the use of Davis parameters provides reasonable estimates of the bearing capacity. Eqs. 5.5-5.7 yield:

$$n = \frac{\cos\varphi \cos\psi}{1 - \sin\varphi \sin\psi} = \cos\varphi = 0.766$$

$$\tan\varphi^* = n \tan\varphi = 0.642 \Rightarrow \varphi^* = 32.7^o$$

$$c^* = nc' = 0.766 \text{ kPa}$$

where $n = \dfrac{\cos\varphi \cos\psi}{1 - \sin\varphi \sin\psi}$

The analysis is performed in two stages. During the initial stage before the construction of the footing, geostatic stresses are initialized with the "K_0 procedure", considering all the three clusters depicted in Figure 5.44 as active, whereas the prescribed displacement and the uniform pressure q_s are not active. When the prescribed displacement load is activated, at the subsequent plastic step, the top soil cluster is deactivated, as discussed in Example 5.2, and the pressure q_s is activated.

Results of the analysis for thickness of the foundation improvement layer z = 2 m are presented in Figure 5.45, in terms of the geometry of the developing failure surface. The shape of the failure surface depicted in Figure 5.45 is similar to the theoretical failure surface presented in Figure 5.38a, and suggests that "punching" of the footing indeed takes place, with failure developing within the soft clay layer.

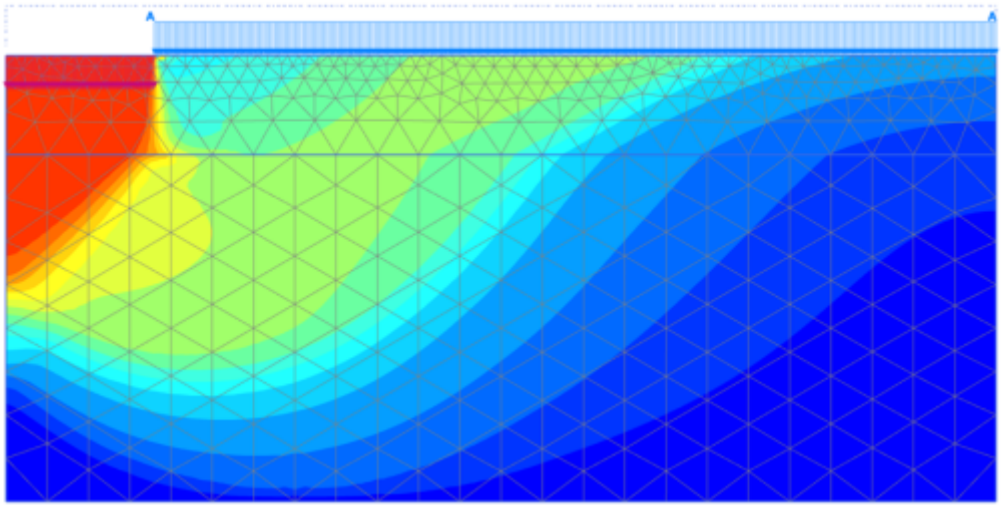

Figure 5.45a. Total displacement at failure, indicating the shape of the failure surface.

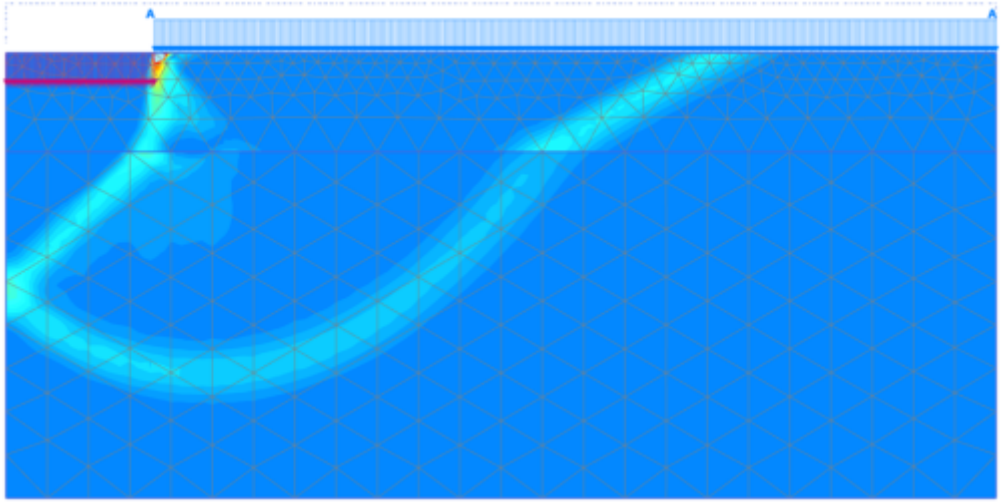

Figure 5.45b. Shear strain increment contours at failure, indicating the shape of the failure surface.

The force-settlement curve used to define the collapse load of the footing is presented in Figure 5.46. In a

plane-strain problem, the reaction force is provided in PLAXIS in kN/running meter of the strip footing. As we are simulating only half of the footing geometry, referring to the load-settlement curve of Figure 5.46 the bearing capacity will be:

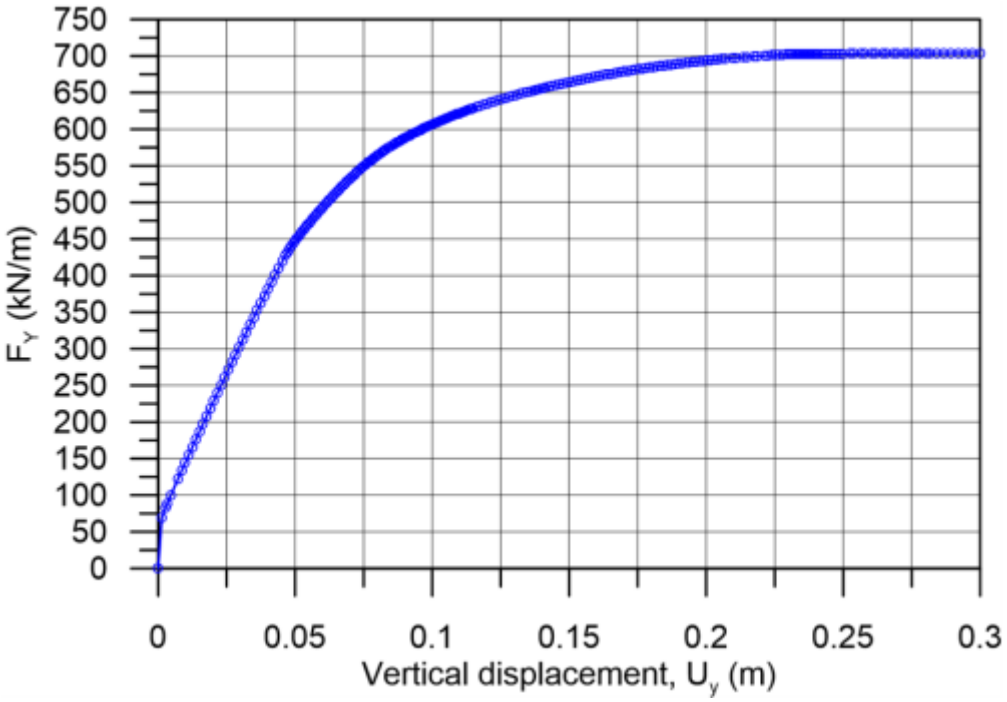

Figure 5.46. Force-displacement curve from the analysis for thickness of the foundation improvement layer z = 2m.

$$q_f = \frac{704}{(3 \times 1)} = 234.6 \text{ kPa}$$

thus higher than the ultimate limit state pressure (200 kPa). The total reaction force on the 6m-wide footing is equal to 2xF_Y =1408 kN/m.

Replacement of 2 m of clay below the foundation level with coarse-grained material resulted in ≈ 60 kPa increase in the bearing capacity (about 35%). Yet, it is considerably higher than the required bearing capacity of 200 kPa. The optimum improvement layer thickness that will result to bearing capacity marginally higher than the ultimate limit state pressure from the structure can be determined via a parametric analysis, trying different thickness z values, thus analyzing different model geometries.

From Figure 5.47, where the results of analyses for different z values are presented in terms of load-settlement curves, we conclude that an improvement layer with thickness z = 1 m is enough to increase the bearing capacity to 200 kPa.

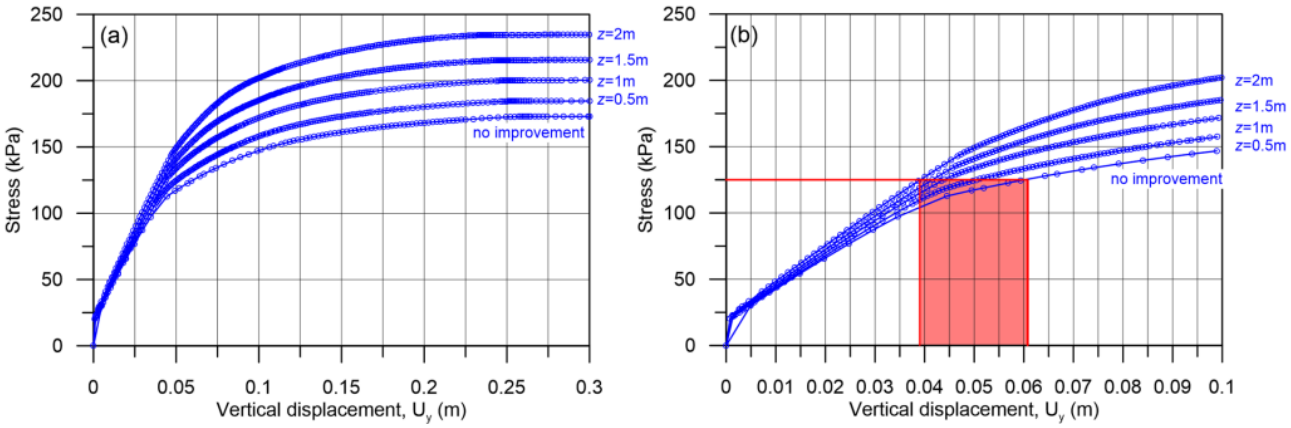

Figure 5.47. (a) Force-settlement curves resulting from the analyses for varying thickness of the foundation improvement layer, including the case where no ground improvement is applied, and (b) Detail of the load-settlement curves corresponding to serviceability stress levels.

Notice in Figure 5.47a that the bearing capacity develops for settlement values higher than about 0.20 m, a value that is (most probably) not acceptable under serviceability conditions. If we zoom into lower stress levels where serviceability stress is most likely to lie in (Figure 5.47b), we observe that the improvement layer plays a two-fold role: it increases the bearing capacity, but also reduces the settlement for a given applied pressure.

The same problem can be solved analytically too, using the approximate methodology presented in Section 5.5.3 and in Example 5.4 (see Additional Problem 5.10.1). Results of the analytical methodology, in terms of bearing capacity for variable thickness of the compressive layer, compare well with the numerical results (Figure 5.48), suggesting that i) the approximate methodology can be effectively used for practical problems, at least during preliminary design stages, and ii) use of the Davis effective shear strength parameters together with an associated flow rule yields comparable results.

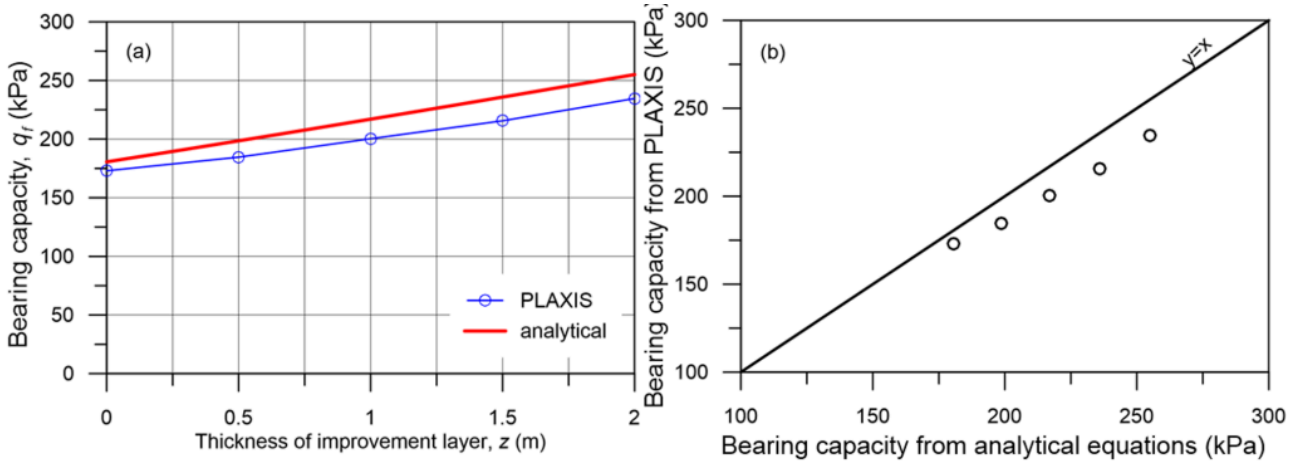

Figure 5.48. Comparison of bearing capacity values obtained with the approximate methodology (Additional Problem 5.10.1) for a footing on a stiff-over-soft soil layer, with the corresponding bearing capacity from PLAXIS analyses.

5.6 NUMERICAL MODELLING OF FOOTINGS RESTING ON THE SURFACE OF DRAINED SOIL

The numerical analysis results presented in Example 5.5 demonstrate that the use of equivalent strength parameters together with an associative flow rule provides reasonable estimates of the bearing capacity of foundations, while avoiding numerical instabilities that stem from using as input the actual friction angle and dilation angle of drained materials, and consequently of non-associative flow rule.

However, this is not the only potential source of numerical instabilities in simulations where we seek to estimate the bearing capacity of shallow foundations. Unlike undrained soils modelled with the Mohr-Coulomb *Undrained* material model, where shear strength does not depend on stress levels, drained soils modelled with the Mohr-Coulomb *Drained* material model will feature zero shear strength near the model surface if i) Their effective cohesion is set to be zero (see Figure 5.4), and ii) The footing is not embedded as it is in Example 5.5. Finite element codes have difficulty handling materials of zero strength, and the simulation may end prematurely (before the bearing capacity is reached) due to poor convergence. While using as input a nominal effective cohesion $c' \approx 1$ kPa to avoid modelling a material of zero strength near the surface where geostatic stresses are zero will certainly improve numerical stability, this is not always sufficient.

An alternative modelling strategy is illustrated in Figure 5.49: Instead of applying a prescribed displacement directly on the model surface (Model A) to obtain the force-displacement curve, as we did e.g., in Example 5.2, we apply the prescribed displacement on the top of a geometry cluster representing the footing (Model B). A weightless linear elastic material of very high stiffness is assigned to that cluster, to model a rigid footing. On the model surface we introduce a weightless thin crust, as another separate geometry cluster. To this cluster we assign a material of arbitrarily high cohesion ("infinite" strength) but also of very low stiffness, so that the stresses that will develop in this "dummy" crust will be extremely low, and will not contribute to a fictitious increase in the predicted bearing capacity. Notice that we still use Davis equivalent parameters φ^*, ψ^* for the actual soil, but we have considered its effective cohesion c' to be zero.

Results of the two model variants are presented in Figure 5.49, in terms of the predicted force-displacement curve. Observe that Model A failed to reach the collapse load, and the analysis ended prematurely with an error message. That is despite the fact that arc-length control was used to solve the system of non-linear equations, which can provide solution to problems where softening is expected, i.e., when the stiffness matrix is not always a positive definite through the analysis. On the other hand, Model B's analysis was completed successfully, and the collapse load can be inferred from the force-displacement curve. Notice also that, up to the analysis stage where Model A's analysis failed, both models produced identical results. This suggests that the introduced technique facilitates convergence, at no expense of model accuracy.

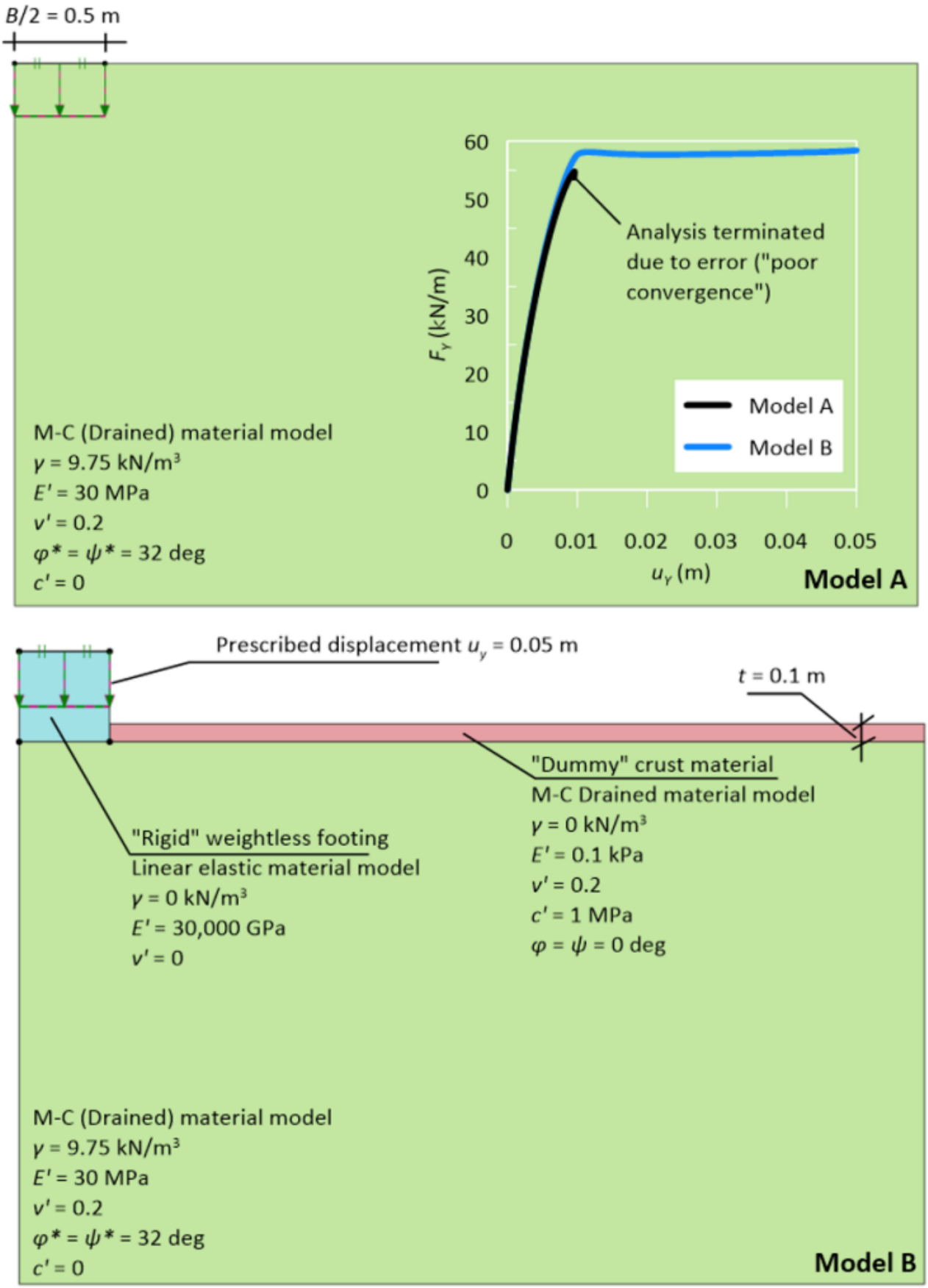

Figure 5.49. Modelling of a rigid and rough strip footing resting on the surface of drained soil. Model A: Applying a prescribed displacement directly on the model's surface; Model B: Applying a prescribed displacement on top of a "rigid" weightless cluster representing the footing, and introducing a "dummy" thin crust featuring very high cohesion and very low stiffness.

5.7 BEARING CAPACITY FROM STANDARD PENETRATION TEST (SPT) RESULTS

When coarse-grained soils are encountered during the geotechnical investigation, it is often extremely difficult to obtain undisturbed samples for determining their effective shear strength parameters in the laboratory. Hence, it is common practice to use directly results from *in situ* tests, like the Standard Penetration Test (SPT) together with empirical correlations, to determine the bearing capacity of footings resting on coarse-grained soils.

When using methodologies such as the one presented here (AASHTO 2012) we should consider the average SPT value for a depth 1.5B below the foundation base, corrected for overburden stress according to Chapter 1.5 as:

(5.51) $$N' = C_N N$$

where the overburden stress correction factor C_N is (Eq. 1.2):

(5.52) $$C_N = \sqrt{\frac{p_a}{\sigma'_{z0}}}$$

For footings on coarse-grained soils subjected to vertical loads of zero eccentricity, the AASHTO methodology provides the bearing capacity in terms of stress as:

(5.53) $$q_f = \frac{N'B}{5}\left(C_{w1}+C_{w2}\frac{D_f}{B}\right)\ (\text{ksf}) = 9.57N'B\left(C_{w1}+C_{w2}\frac{D_f}{B}\right)\ (\text{kPa})$$

where C_{w1}, C_{w2} are factors accounting for the depth of the groundwater table below the foundation level, and are provided in Table 5.7.

Table 5.7. AASHTO (2012) groundwater table factors.

Depth of water table below foundation level (m)	C_{w1}	C_{w2}
0	0.5	0.5
D_f	0.5	1.0
$1.5B + D_f$	1.0	1.0

In the above expressions, z is the depth to the groundwater table measured from the ground surface, B is the footing width, D_f is the embedment depth and σ'_{z0} is the effective geostatic vertical stress. Eq. 5.53 provides the pressure on the footing corresponding to a settlement less than 25 mm. Even when used for cases of embedded footings, the weight of the excavated soil γD_f should not be added to Eq. 5.53, as the latter provides directly the bearing capacity q_f.

An application of this method is provided in the following Example 5.6.

EXAMPLE 5.6

Design capacity from in situ tests: SPT

Estimate the design capacity of the footing shown below according to AS 5100.3, using directly the SPT measurements in the loose-to-medium sandy foundation soil.

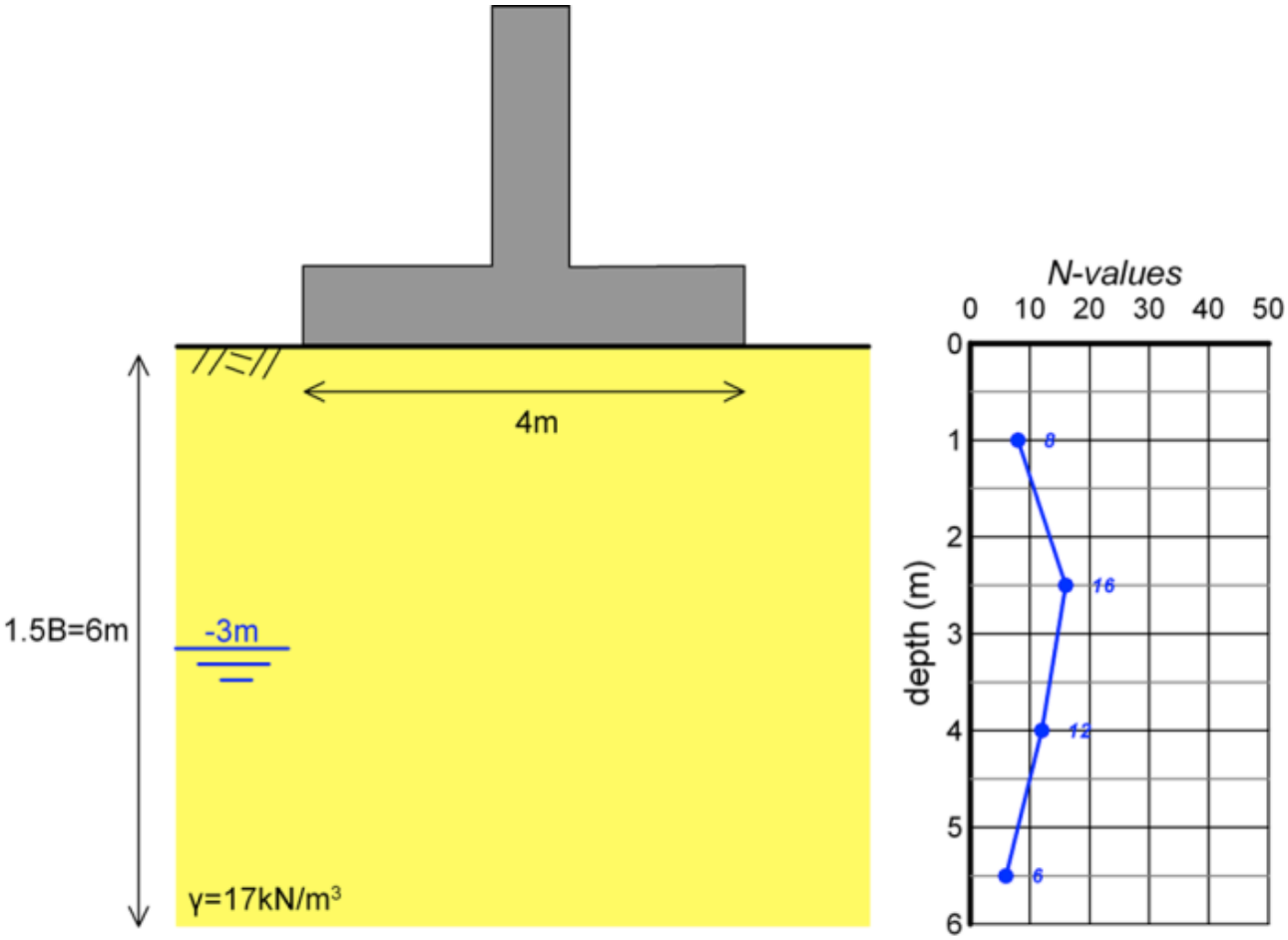

Example 5.6. Problem description and input parameters.

Answer:

Before applying Eq. 5.53 to estimate the bearing capacity, we must first find the corrected N' values for overburden stress, and the average corrected value N' over a depth $1.5B = 6$ m. Application of Eqs. 5.51 and 5.52 for calculating the overburden stress correction factor C_N and accordingly the average N' value for 6 m is presented in the table below.

Example 5.6. Calculation of average N' value.

Depth (m)	N	Total stress (kPa)	Pore pressure (kPa)	Effective stress (kPa)	C_N	$N' = NC_N$
1	8	17	0	17	2.373 2.0*	16
2.5	16	42.5	0	42.5	1.501	24
4	12	68	10	58	1.285	15.4
5.5	6	93.5	25	68.5	1.182	7.1
					$N'_{average}$	**15.62**

**Note: Use of C_N values higher than 2.0 is not recommended*

Substituting in Eq. 5.53 while taking the groundwater table factors C_{w1}, C_{w2} from Table 5.7 yields:

$$q_f = 9.57 N'_{average} B \left(1.0 + 1.0 \times \frac{0}{4}\right) = 598 \text{ kPa}$$

As the bearing capacity is determined from SPT test results, the appropriate range of the geotechnical strength reduction factor φ_g from Table 5.1 is $\varphi_g = 0.35$ to 0.40. Selecting conservatively the lower bound of the proposed range, the design capacity is determined in terms of stress as:

$$\varphi_g q_f \geq S^* \Rightarrow 0.35 \times 598 \geq S^* \Rightarrow S^* \leq 209 \text{ kPa}$$

5.8 BEARING CAPACITY FROM CONE PENETRATION TEST (CPT) RESULTS

Various empirical methods have been proposed in the literature to estimate the bearing capacity of shallow foundations directly from *in situ* cone penetration tests. One of the more recent ones was proposed by Eslaamizaad and Robertson (1996), who recommend calculating the bearing capacity in terms of stress of footings on coarse-grained soils as:

(5.54) $$q_f = K_\varphi q_{c,average}$$

where $q_{c,average}$ is the average cone resistance below the footing foundation level along a depth $z = B$. The shape conversion factor K_φ (from cone resistance to footing bearing resistance) ranges between $K_\varphi = 0.16$ to 0.30 depending on the ratio B/D_f, the shape of the footing and sand density and is given in Figure 5.50. However, given the uncertainties underlying this method it is recommended here to use Eq. 5.54 together with the lower bound value of the shape conversion factor $K_\varphi = 0.16$.

For fine-grained soils under undrained loading conditions, Eslaamizaad and Robertson (1996) proposed to calculate the bearing capacity in terms of stress as:

(5.55) $$q_f = K_{Su} q_{c,average} + \gamma D_f$$

where $q_{c,average}$ is again the average cone resistance over the influence depth defined above and K_{Su} ranges between $K_{Su} = 0.30$ to 0.60 depending on the ratio B/D_f, the shape of the footing and OCR. It is proposed again to conservatively use Eq. 5.55 with the lower bound value $K_{Su} = 0.30$.

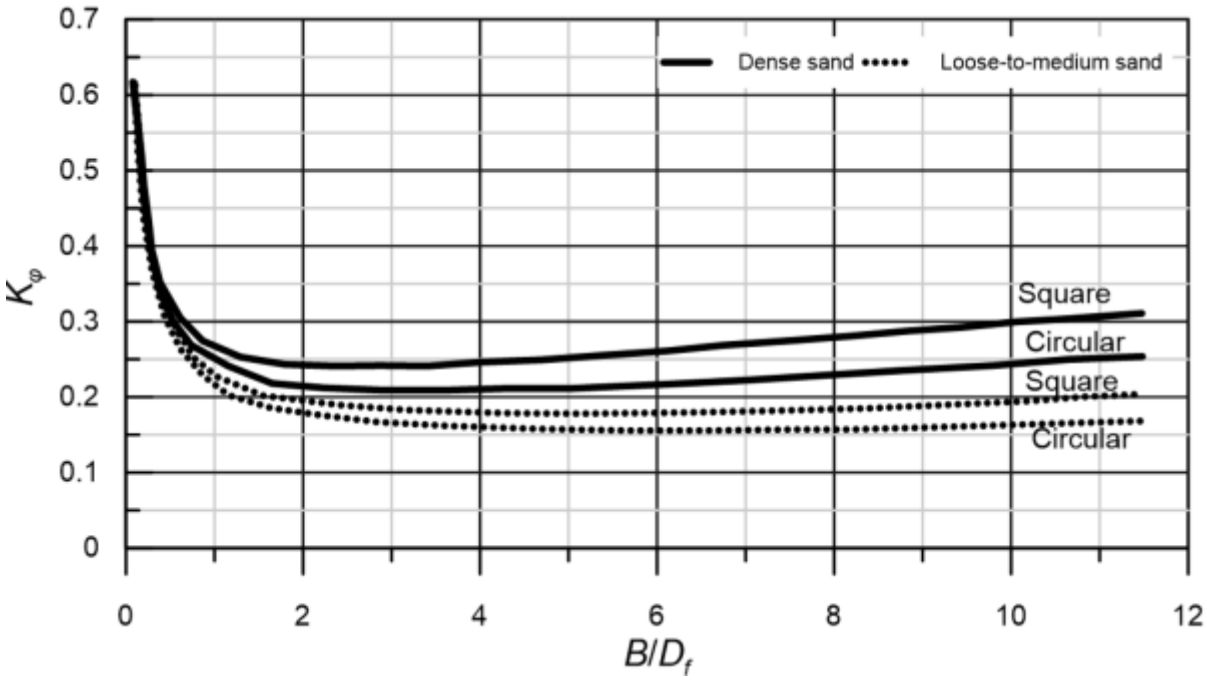

Figure 5.50. Conversion factor for determining the bearing capacity from the CPT cone tip resistance (after Eslaamizaad and Robertson 1996).

EXAMPLE 5.7

Design capacity from in situ tests: CPT

Estimate the design capacity of the strip footing shown below according to AS 5100.3-2, directly from CPT measurements. The foundation subsoil is classified as silty sand (SBT=5/6 from the soil behavior type chart of Figure 1.28).

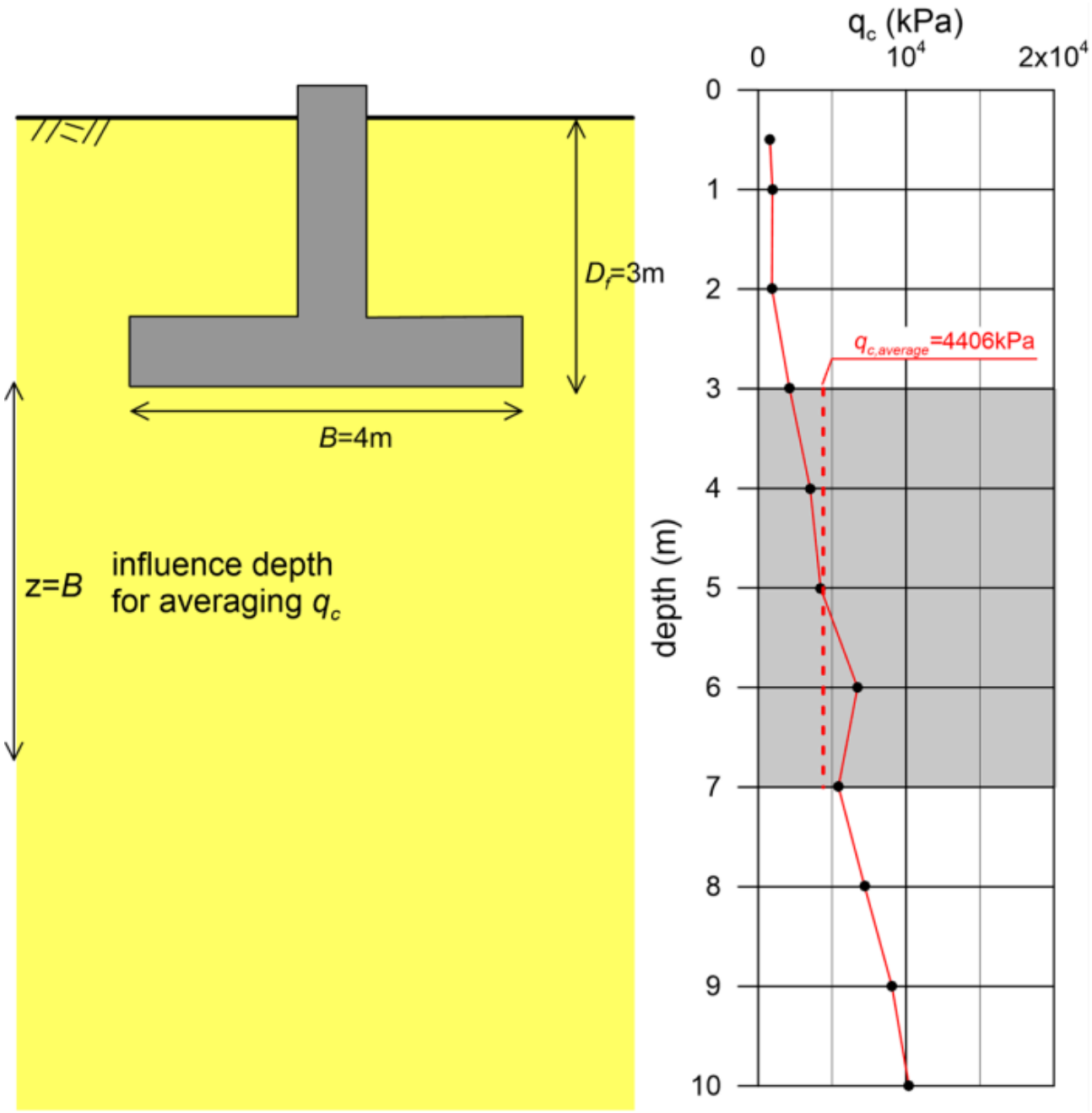

Example 5.7. Problem description and input parameters.

Answer:

The average cone resistance along a depth $z = B = 4$ m below the footing foundation level (-3m) is $q_{c,average}$ = 4.4 MPa (average of 5 values). Considering conservatively $K_\varphi = 0.16$ as per above, and substituting to Eq. 5.54 yields:

$$q_f = K_\varphi q_{c,average} = 700 \text{ kPa}$$

Note that the measured cone resistance in this sand is relatively low, and according to Table 1.8 the average N_{60} value along the influence depth is $N_{60} = (q_{c,average}/p_a)/3.0 = 14.6$ therefore the sand is classified as medium dense (Table 1.3).

As the bearing capacity is determined from CPT test results, the appropriate range of the geotechnical strength reduction factor φ_g from Table 5.1 is $\varphi_g = 0.40$ to 0.50. Selecting conservatively the lower bound of the proposed range, the design capacity in terms of stress in terms of force per running meter of the strip footing is determined as:

$$\varphi_g q_f \geq S^*$$

$$0.40 \times 700 \geq S^*$$

$$S^* \leq 280 \text{ kPa}$$

$$S^* \leq 280 \text{ kPa} \times (4 \times 1) \text{ m}^2 = 1120 \text{ kN/running meter of footing}$$

5.9 REFERENCES

1. American Association of State Highway and Transportation Officials (2012). AASHTO LRFD Bridge Design Specifications.
2. Australian Standard AS5100.3. Bridge design-Foundations and soil supporting structures.
3. Australian/New Zealand Standard AS1170.1. Structural design actions. Part 1: Permanent, imposed and other actions.
4. Australian/New Zealand Standard AS1170.0. Structural design actions. Part 0: General principles.
5. Australian Standard AS5100.2. Bridge design-Design loads.
6. Bishop AW and Eldin G (1950) Undrained triaxial tests on saturated sands and their significance in the general theory of shear strength. Géotechnique 2, 13-32
7. EC7 Eurocode 7: Geotechnical Design – Part 1: General Rules
8. Budhu M (2011). Soil mechanics and foundations. 3rd edition. John Wiley & Sons, Inc.
9. Chen WF (2012) Limit analysis and soil plasticity. Elsevier Scientific Publishing Company
10. Craig RF and Knappett JA (2012) Craig's soil mechanics. 8th edition. Taylor & Francis.
11. Davis EH (1968) Theories of plasticity and the failure of soil masses. In: Lee, IK (edt) Soil Mechanics: Selected Topics, 341-380, Butterworth, London.
12. Eslaamizaad S and Robertson PK (1996) Cone penetration test to evaluate bearing capacity of foundations in sands. In: Proc, 50th Canadian Geotechnical Conference, Ottawa, BiTech Publishers, 2, 755-764
13. Gaone FM, Gourvenec S and Doherty JP (2018) Large-scale shallow foundation load tests on soft clay – At the National Field Testing Facility (NFTF), Ballina, NSW, Australia. Computers and Geotechnics 93, 253-268.
14. Hanna AM (1981) Foundations on strong sand overlying weak sand. J Geotech Eng, 107(7), 915-927
15. Meyerhoff, G.G. (1963). Some recent research on the bearing capacity of shallow foundations. Canadian Geotechnical Journal, Vol. 1(1), pp 16-26.
16. Salgado R (2008) The engineering of foundations, McGraw-Hill New York
17. Salimi Eshkevari S, Abbo AJ and Kouretzis G (2019a) Bearing capacity of strip footings on sand over clay. Canadian Geotechnical Journal 56(5), 699-709.
18. Salimi Eshkevari S, Abbo AJ and Kouretzis G (2019b) Bearing capacity of strip footings on layered sands. Computers and Geotechnics 114, 103101.
19. Tomlinson MJ and Boorman R (1995). Foundation design and construction. Longman Scientific and Technical, Brunthill, Harlow, England.
20. Wu J, Kouretzis G and Suwal L (2021). Bearing capacity mechanisms for pipes buried in sand. Canadian Geotechnical Journal 58, 834-847

5.10 ADDITIONAL PROBLEMS

5.10.1.

Determine the minimum required thickness of the improvement layer for the problem presented in Example 5.5, while using the approximate methodology presented in Section 5.5.2 instead of PLAXIS.

Answer:

z ≈ 0.60 m

5.10.2.

A silo is going to be founded on a layer of saturated, normally consolidated clay, featuring the characteristic shear strength properties shown in the figure below, which were determined from laboratory triaxial tests. The foundation will be embedded at a depth D_f = 1 m. Groundwater table is found at -3.0 m below the ground surface.

Estimate the vertical load that can be carried by the silo's foundation at the Ultimate Limit State according to AS 5100.3, assuming only dead loads. Consider both short-term and long-term loading conditions.

Should the groundwater table rise to e.g. -2.0 m, what will be the effect on a) the short-term, and b) the long-term bearing capacity of the silo?

Note: Do not apply any reduction factors on the shear strength parameters of the clay (Eqs. 5.6 and 5.7) to account for the possibility of local shear failure.

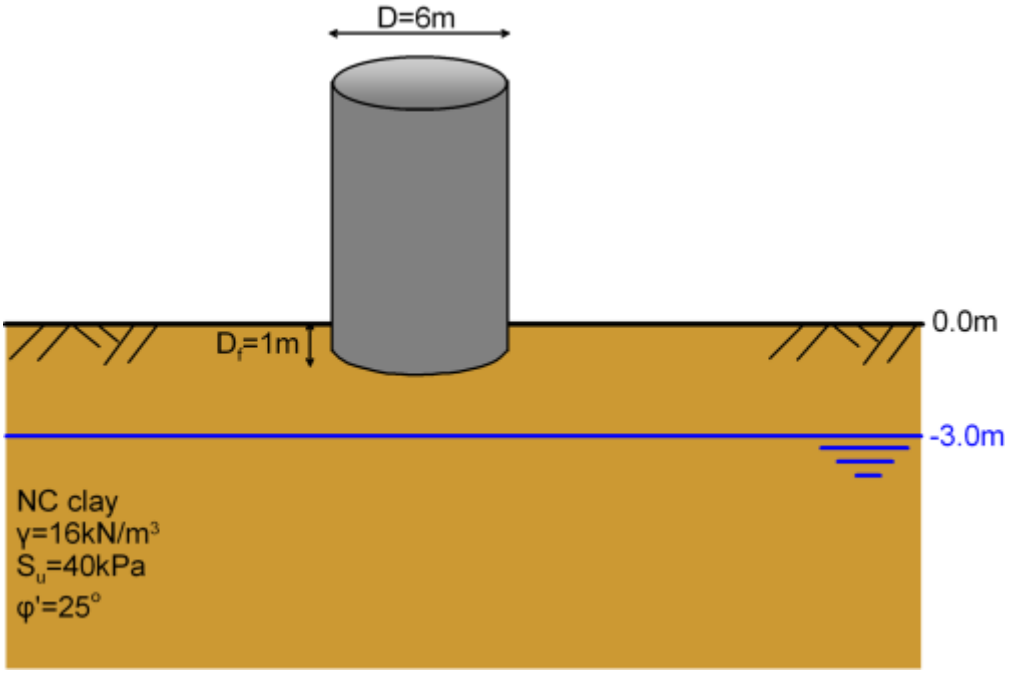

Example 5.10.2. Problem description and input parameters.

Answer:

Short-term vertical load G=2785 kN

Long-term vertical load G=3649 kN

6. PILE FOUNDATIONS

6.1 INTRODUCTION TO PART 6

There are situations where shallow foundations are proven inefficient or uneconomical for transferring loads from the structure to the subsoil. For example, bearing capacity and/or settlement calculations do not satisfy the relevant acceptance criteria, and any ground improvement methods (preloading, replacement of surficial soil with foundation improvement layer etc.) are either not effective, or too expensive. *Pile foundations*, which embedment depth is large compared to the width of the foundation, are designed to safely transfer the load from the structure through unsuitable subsoil layers to deeper, suitable bearing strata. In the following, some typical situations when deep foundations are used are compendiously described.

Case 1:

The surficial soil layers may feature low shear strength, or may be too compressible to carry the design vertical compressive load from the structure while satisfying shallow foundation bearing capacity and settlement requirements. Deep foundations are used to transfer the load to a stiff formation encountered at a "reasonable" depth, acting as *end-bearing* piles (Figure 6.1a). In the absence of a stiff formation at "reasonable" depth, which of course depends on the type of the structure, the load is transferred to the soft soil formation via soil resistance developing along the shaft (*friction* pile, Figure 6.1b).

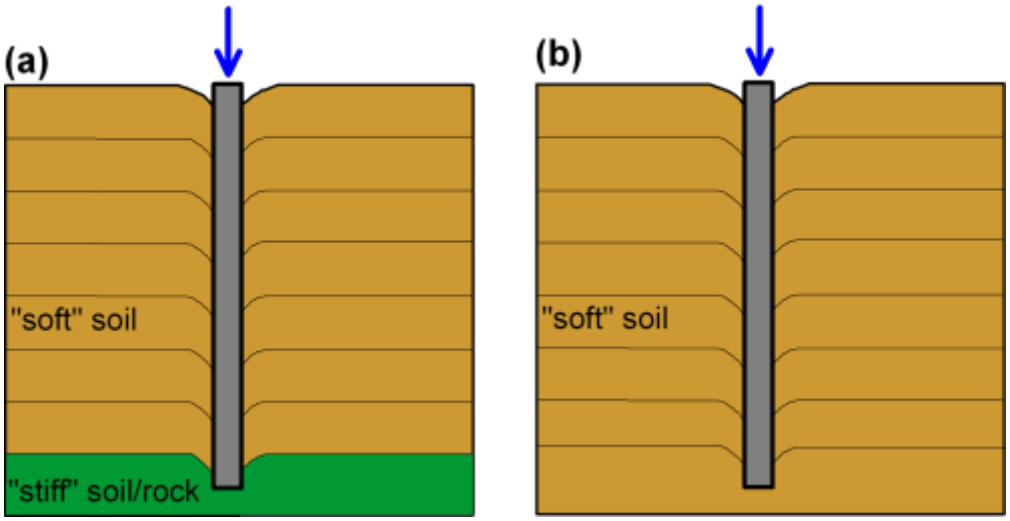

Figure 6.1. Typical pile cases: (a) End-bearing pile, and (b) Friction pile subjected to compressive vertical load.

Case 2:

Shallow foundations cannot efficiently transfer high lateral or uplift loads, and bending moments. On the other hand, pile foundations can resist uplift loads through shaft resistance (Figure 6.2a). Lateral loads and bending moments can be transferred by single piles through bending (Figure 6.2b), or by pile groups of vertical or sometimes battered piles, which lateral and bending stiffness is combined when connected with a *pile cap* (Figure 6.2c). Piles, and especially pile groups, are often used for the foundation of structures transferring significant lateral loads to their foundation, such as tall retaining walls supporting slopes or backfills (Figure 6.2d), highway signs, electricity poles, wind turbines etc.

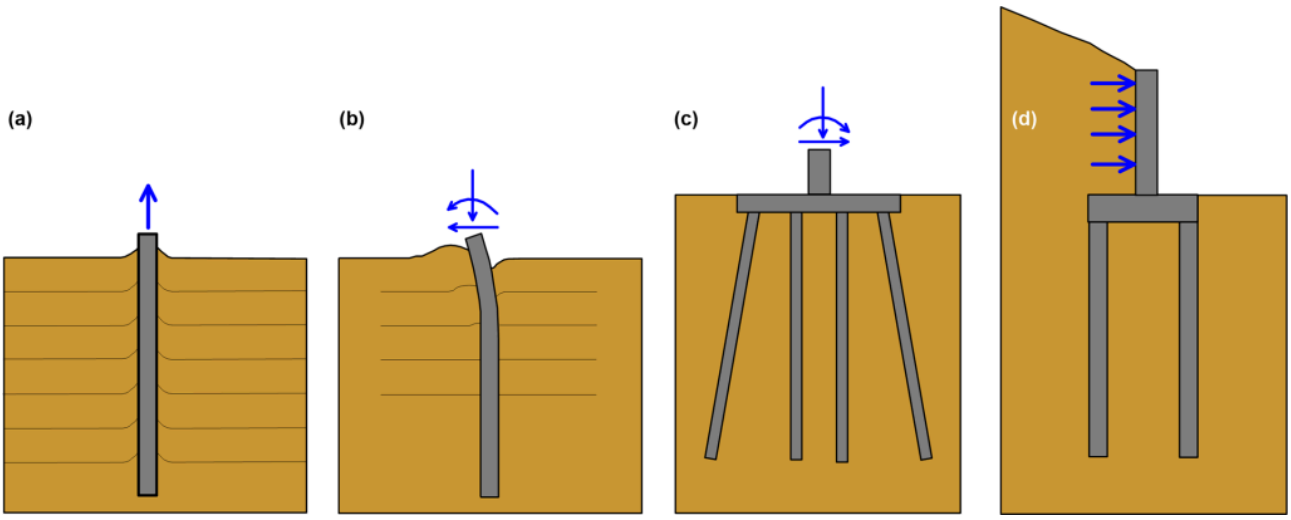

Figure 6.2. Typical pile cases: (a) Tension pile, (b) Laterally loaded single pile, (c) Pile group subjected to a combination of loads, and (d) Tall retaining wall subjected to high lateral earth pressure.

Case 3:

Scour around footings could result in loss of bearing resistance at shallow depths, and the foundation of a bridge pier must extend below the potential scour zone. Guidelines for bridges require that the design of the foundation should not consider the bearing resistance and lateral support above the level of expected scour. In that case, a pile foundation will transfer the loads from the bridge superstructure below the scour zone (Figure 6.3a).

Case 4:

Seismic liquefaction during a strong earthquake may result in sudden loss of the shear strength of loose saturated sands, and flow of the material in areas of non-horizontal ground surface (e.g., riverbanks). Liquefied sands offer significantly reduced support, thus loads must be transferred in deeper, competent layers (Figure 6.3b).

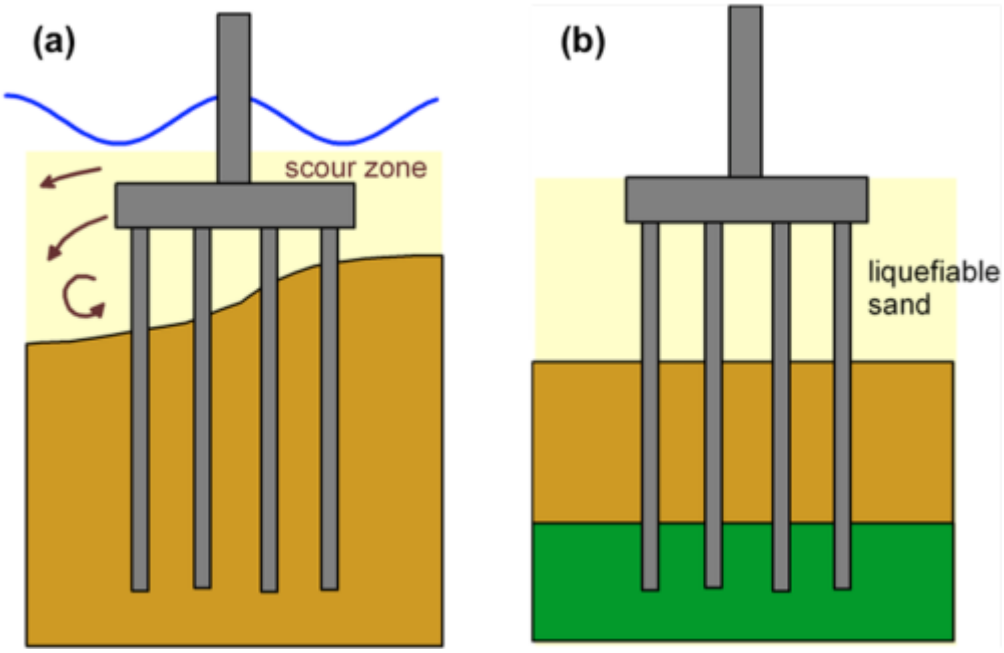

Figure 6.3. Typical pile cases: (a) Pile group transferring loads below the scour zone, and (b) Foundation in liquefiable soil.

Case 5:

In urban areas, deep foundations may be necessary for supporting structures adjacent to locations where future excavations are planned (Figure 6.4a), to avoid tilt and the requirement for future underpinning.

Case 6:

Pile foundations can be used in areas of expansive soils to resist undesirable seasonal movements. Loads, including uplift and downdrag are transferred to a deeper formation, which is not affected by moisture changes (Figure 6.4b).

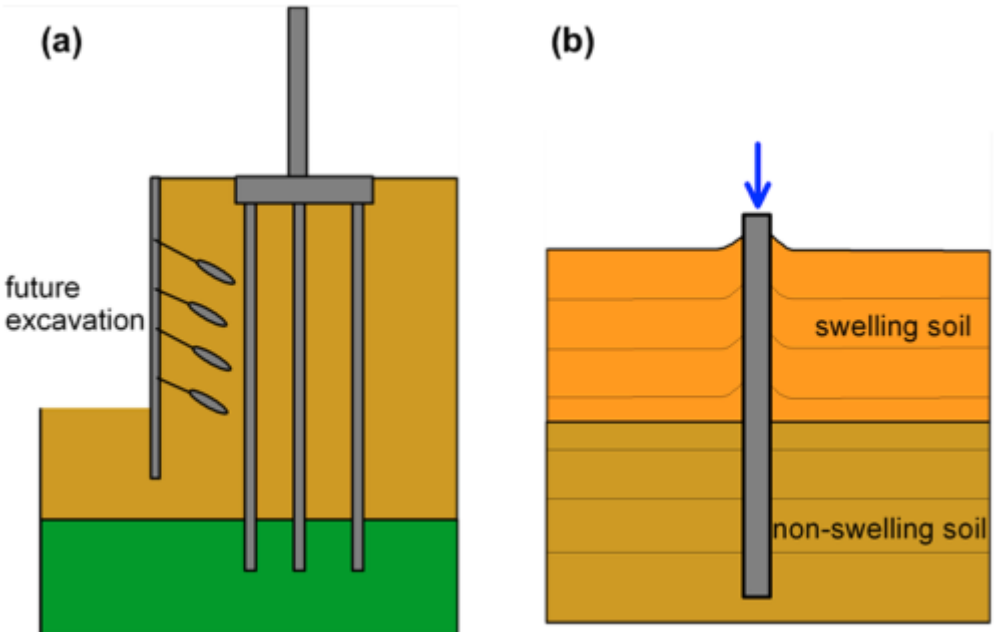

Figure 6.4. Typical pile cases: (a) Foundation of structures in areas of future excavations, and (b) Foundation of structures in expansive soils.

Apart from foundation of structures in the cases described above, piles are also used in a variety of geotechnical engineering applications, such as stabilisation of slopes or active landslide areas, as retaining elements for excavations etc. (Figure 6.5). The same (or similar) analysis methods, design guidelines and construction techniques apply.

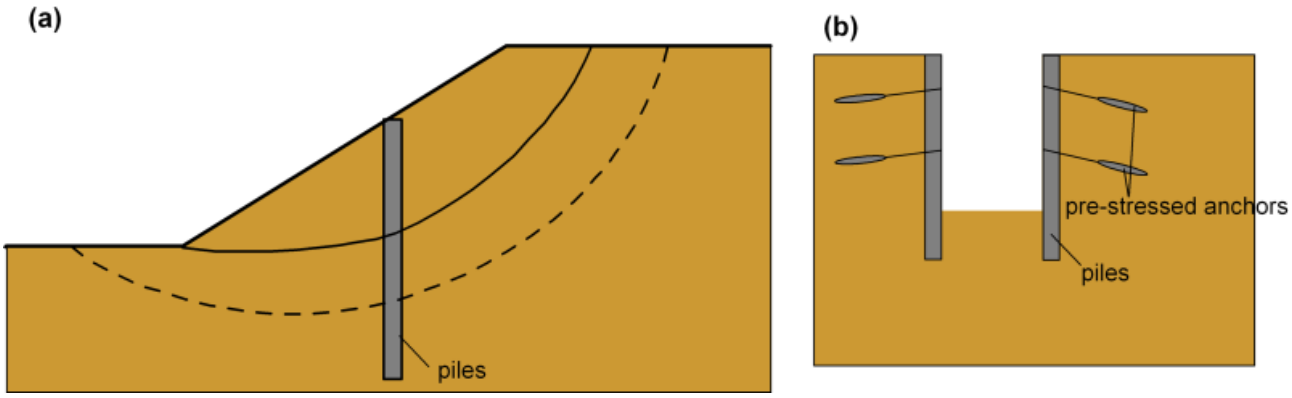

Figure 6.5. Other uses of piles: (a) slope stabilisation, (b) support of deep excavations.

6.2 COMMON PILE TYPES

Two main categories of piles can be identified, depending on their construction method:

- Displacement, *or driven piles* (Figure 6.6) displace and compact the ground through which they are installed, by nailing or screwing. Displacement piles may be installed by hammering, pushing, screwing etc.
- Non-displacement piles, *or drilled shafts, or bored piles* or *drilled piers* (Figures 6.6 and 6.7) are constructed by drilling and removing soil to form a cylindrical shaft into the ground (Figure 6.7). Subsequently a rebar cage is installed, and the void is filled with concrete. The sides of the excavated void may or may not be supported.

In this Part we will use the term *piles* to refer to driven piles and the term *drilled shafts* to refer mainly to non-displacement concrete piles that are cast *in situ*.

Furthermore, depending on the pile fabrication and installation method, displacement (driven) piles are subdivided in:

- Preformed piles: Steel (hollow or solid section), timber, reinforced or pre-stressed concrete sections, that are installed into the ground and left in position.
- Driven cast in place piles: Formed *in situ* by driving a tubular liner to form a void in the ground, which is then filled with concrete. The liner may be permanent or temporary.
- Screwed cast in place piles: Formed *in situ* by screwing a threaded tube into the ground, with concrete poured as the screw head is withdrawn.

Figure 6.6. Pile construction works (author's own photo).

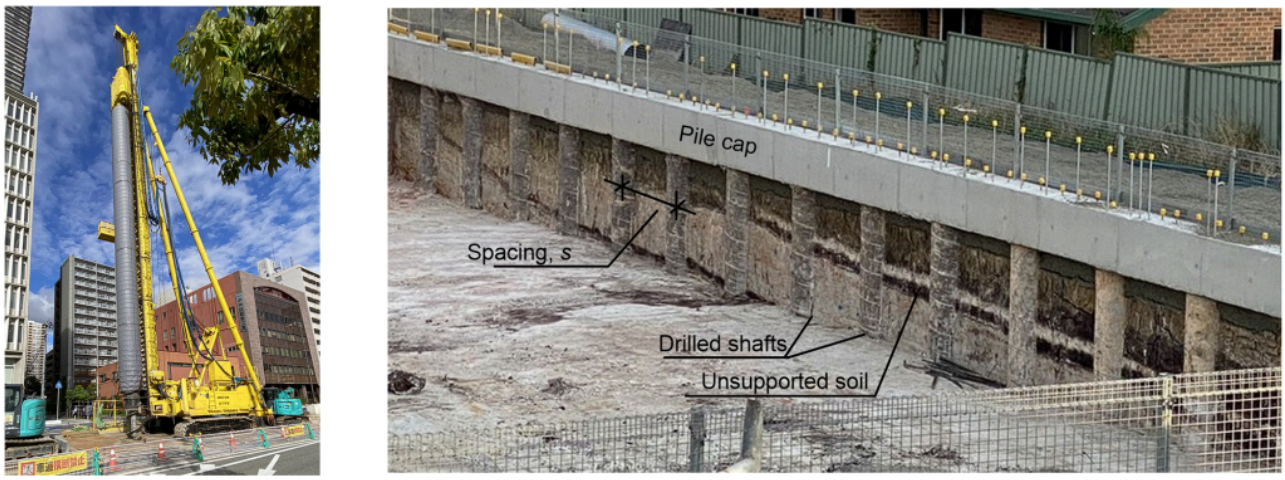

Figure 6.7. (a) Piling rig, (b) Retaining wall consisting of drilled shafts arranged in a pile row (author's own photos).

Depending on the pile installation method, non-displacement piles (drilled shafts) are subdivided into:

- Supported drilled shafts; when the excavated shaft is supported permanently (e.g. using steel liner) or temporary (e.g. using retractable liner or slurry)
- Unsupported drilled shafts; when the excavated void is not supported

A detailed classification of pile types according to AS2159 is presented in Figure 6.8.

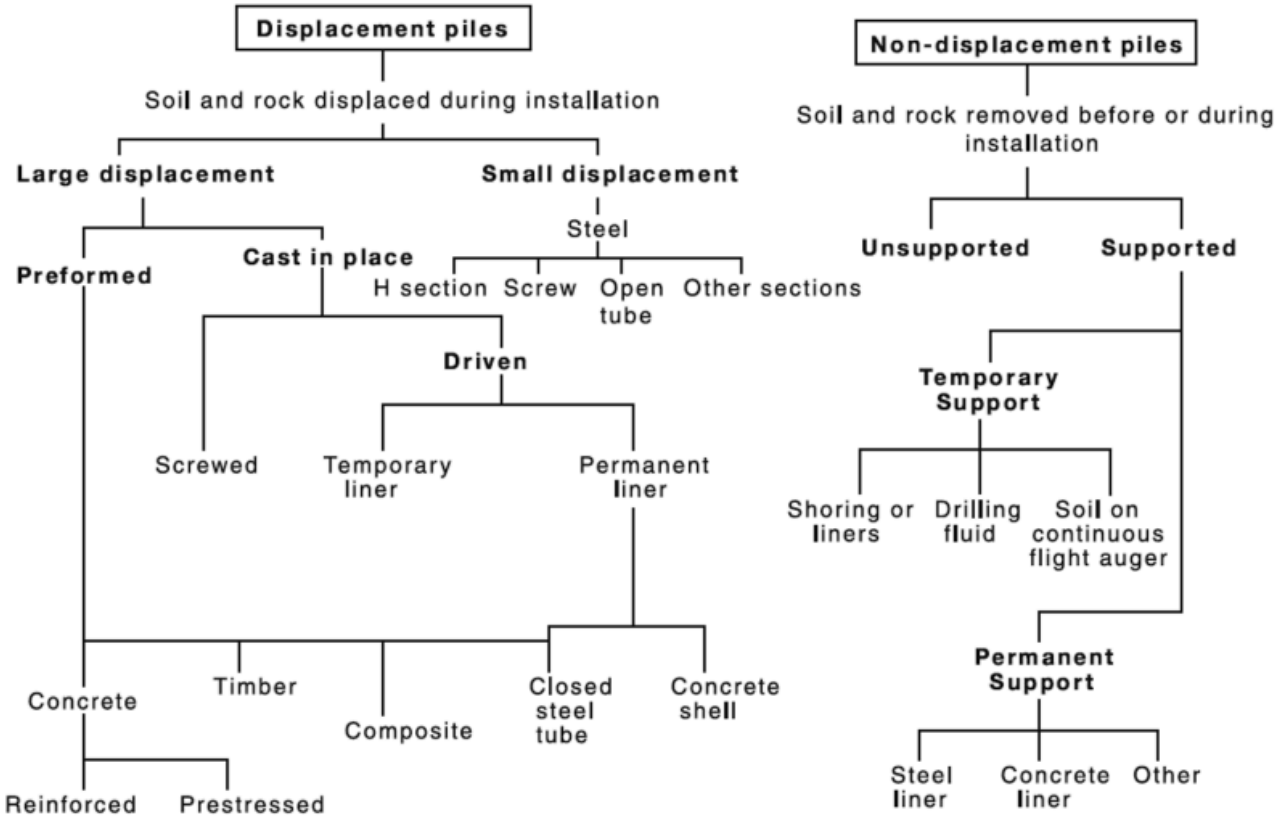

Figure 6.8. Classification of piles types according to AS2159.

Selection of the appropriate pile type for a specific project depends on the geotechnical and hydrogeological

conditions of the site, environmental restrictions, durability requirements as well as of course the available equipment and experience. For example, in loose sands driven piles are preferred, as drilled shafts will require some form of casing or slurry to support the walls of the shaft from caving in. A tapered pile section will develop the maximum skin friction when driven through loose sands. On the contrary, in a deep soft clay layer, a rough concrete pile will feature increased skin friction resistance and allow for faster dissipation of excess pore pressure that will develop during construction. Or, when the geotechnical investigation reveals the existence of boulders above the bearing stratum, a large diameter drilled shaft may be preferable, depending on the size of boulders.

6.3 INSTALLATION OF DRIVEN PILES

Driven piles are usually installed by means of an impact hammer. The pile type and hammer are selected while considering several factors such as the loads to be supported, tolerable noise and vibrations during construction, inspection requirements, available time, possible corrosion issues etc. Additional aspects should be also considered such the possible drift of piles during driving, which depends on the bending stiffness of the pile relatively to the stiffness of the soil, optimisation of the number or piles/of the pile length ratio etc.

Before pile driving commences, a continuous-flight auger may be used to pre-drill a small diameter hole, and facilitate driving through certain formations. The hammer is attached on the top of a crane, using leads to align the pile relatively to the hammer, and achieve verticality (Figure 6.9). Today, steam or pneumatic hammers are used in most projects, instead of simple drop hammers, to increase productivity.

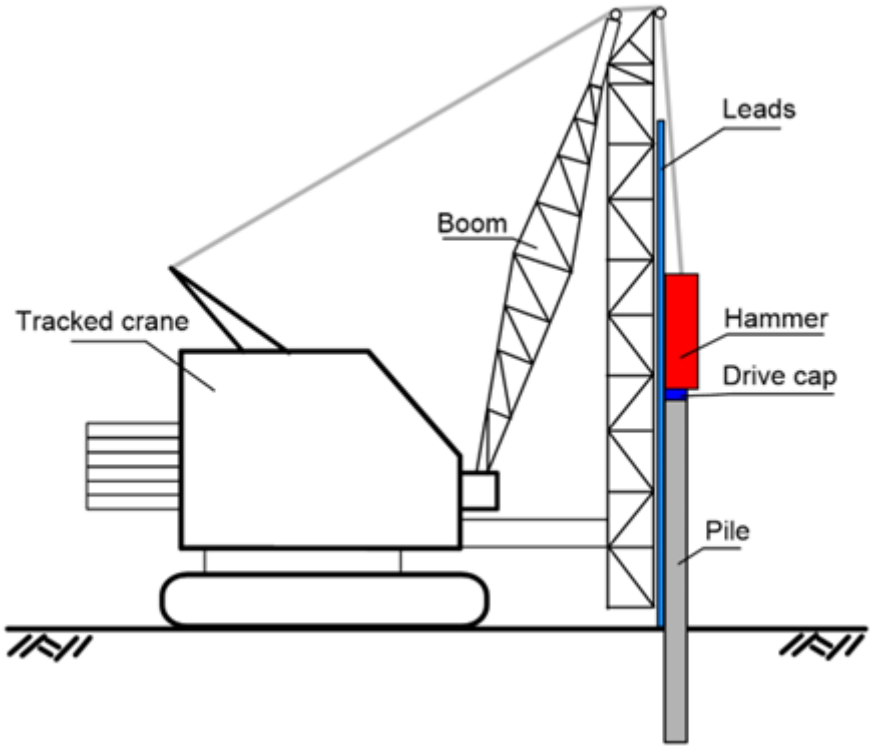

Figure 6.9. Key components of pile driving equipment.

6.4 CONSTRUCTION OF DRILLED SHAFTS

6.4.1 Dry construction (unsupported non-displacement piles)

In stable soils that will not cave in or deflect inward when the shaft is drilled to its full depth, such as stiff clay, the dry method of construction may be employed (Figure 6.10a). A temporary surface casing may be placed after excavation has advanced for a couple of meters, to prevent raveling of soil into the shaft, and act as a guide for drilling works. The pile may not be reinforced along its entire length: in some cases, the lower part of the pile may be constructed from unreinforced (plain) concrete, as bending stresses at that depth are low to negligible. The length of the pile requiring reinforcement, and the amount of rebars, will always be dictated by appropriate calculations.

6.4.2. Wet construction (supported non-displacement piles)

The wet method of construction (or slurry method, Figure 6.10b) is based on the use of slurry to fill the drilled shaft until excavation reaches the maximum depth. The rebar cage is placed directly into the fluid-filled shaft. The tremie concrete pouring method is used, to pour the concrete below the slurry level, so that the rising concrete displaces the slurry to the top, without washing out the cement content. The concrete mix design is of utmost importance for the successful application of the method.

6.4.3. Casing construction (supported non-displacement piles)

An alternative to the wet construction method when caving soils are encountered (e.g., loose saturated sands), is the casing method of construction (Figure 6.11). Casing of the shaft prevents cave in of the soil, and is used as a guide for drilling. After the shaft is filled with concrete, the casing is retracted (or in some cases is left *in situ*). The fluidity of the concrete is very important, so that the drilling fluid (slurry) will be ejected from the excavation, which must be completely filled with concrete. Care must be taken so that disposal of the slurry meets environmental standards.

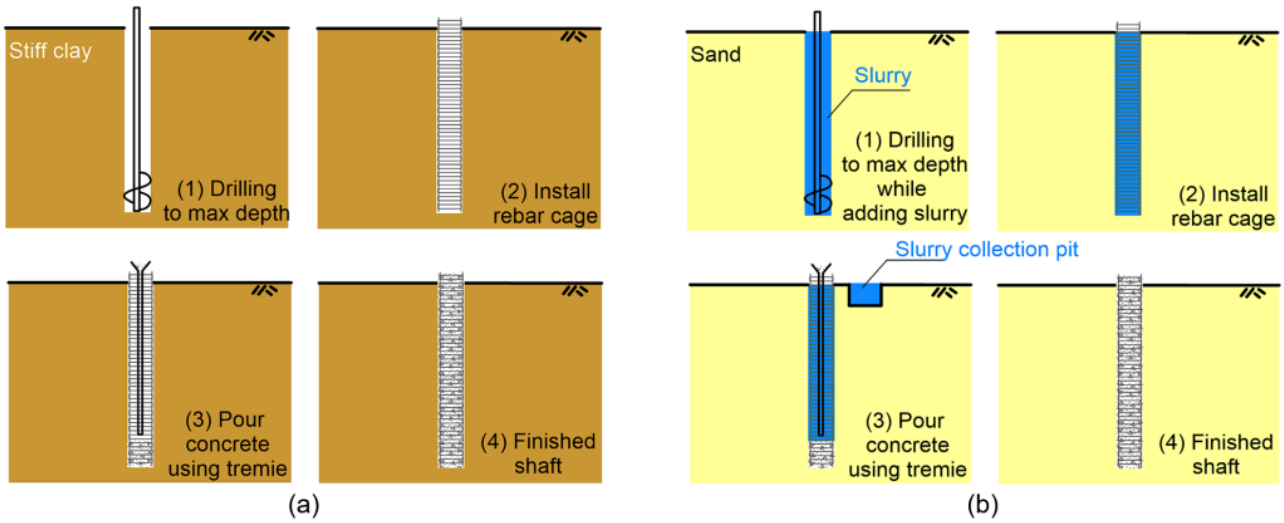

Figure 6.10. (a) Dry construction, and (b) Wet construction of a drilled shaft.

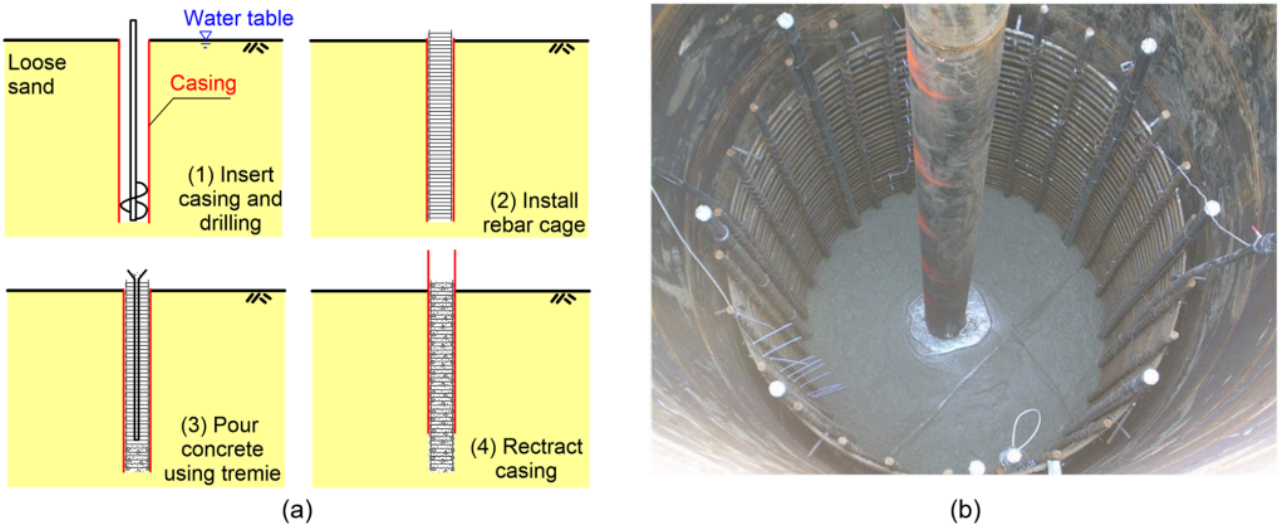

Figure 6.11. (a) Construction of a drilled shaft using casing and (b) Concrete pouring using tremie inside the shaft.

6.5 LOAD TRANSFER MECHANISMS

Piles are often classified according to the mechanism of transferring foundation loads to the subsoil. This classification does not refer to the properties of the pile itself (geometry, material, construction method) but rather to the subsoil and to the loading conditions:

- *Friction piles* in relatively homogeneous soil transfer vertical loads in the subsoil mainly via the development of skin friction along their surface (Figure 6.12a).
- *End-bearing piles,* which toe rests on a relatively stiff formation, compared to the above soft soil, transfer the vertical load mainly to the lower stiff formation (Figure 6.12b).

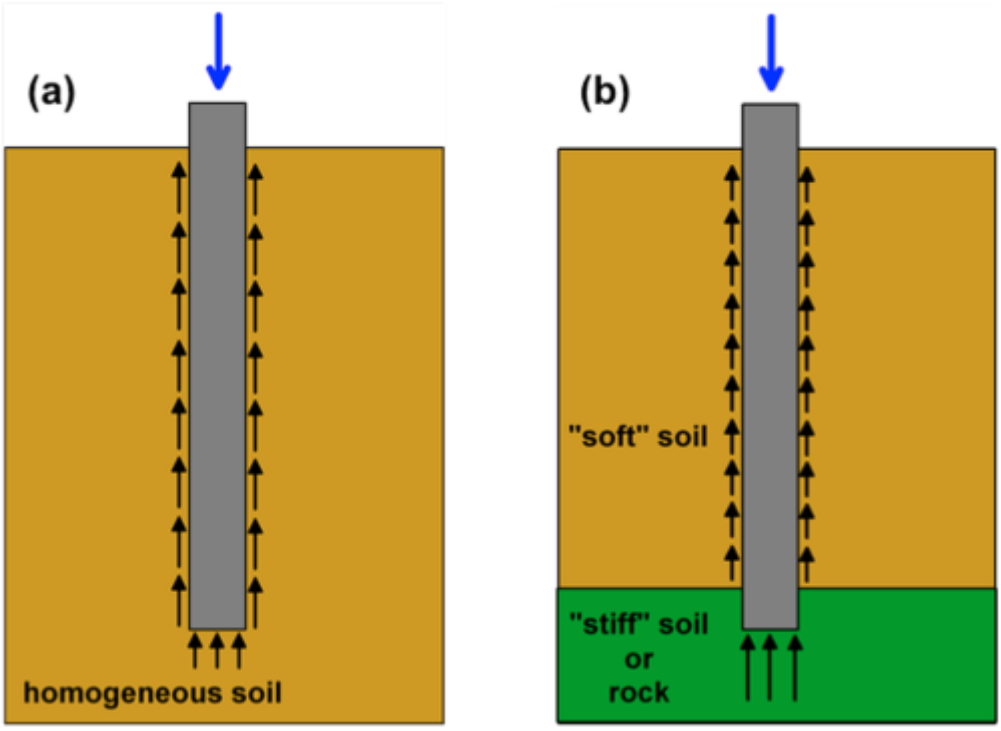

Figure 6.12. (a) Friction pile, and (b) End-bearing pile.

In practice, all piles act both as friction and end-bearing, and transfer loads via both skin (shaft) friction and end bearing resistance. The predominant mode of load transfer characterises them as *friction* or *end-bearing* piles: If the skin friction resistance Q_{sf} is greater than about 80% of the end bearing resistance Q_b, the pile is referred to as a friction pile, otherwise it is referred to as an end bearing pile. A special case is that of piles subjected to *negative skin friction* at their upper part, as a result of settlement of surficial soil layers. In that case the surficial soil layers impose a compressive load on the pile Q_{nf}, rather than contributing to its resistance (Figure 6.13a).

On the other hand, *laterally loaded piles* subjected to lateral forces and bending moments resist the applied loads though bending, and the development of passive earth pressures at the upper part of the pile (Figure 6.13b).

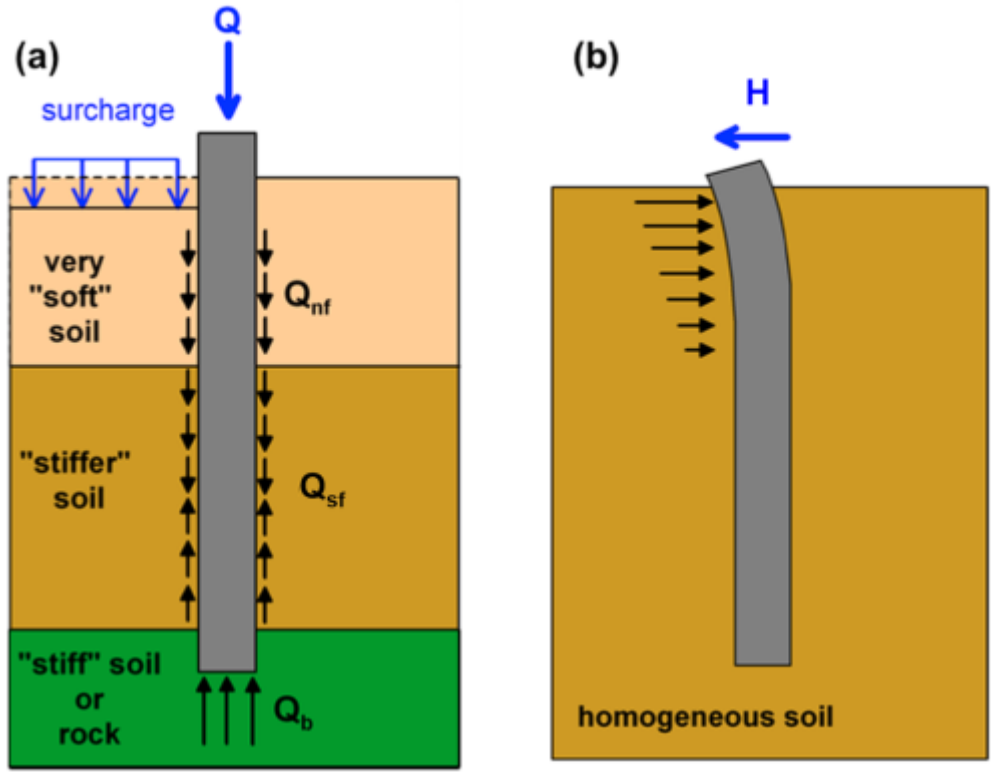

Figure 6.13. (a) Pile subjected to negative skin friction, and (b) Laterally-loaded pile.

6.6 PILE DRIVING EFFECTS

Pile driving imposes an impact load, and each hammer blow results in a stress wave that propagates through the pile, and into the soil. The resistance during driving (which can be measured during installation by recording the advancement of the pile head per hammer blow) can be used to infer the pile's collapse load, as discussed in later sections. The impact load is dynamic, thus excess pore water pressures will develop during pile driving in fine-grained soils, and soil deformation will take place under undrained conditions, without volume change (Figure 6.14a).

Pile driving is an imposed displacement problem: The soil adjacent to the pile shaft is subjected to radial compressive strains and shear strains, as it deforms to accommodate pile penetration, resulting in a stress state that is similar to undrained simple shear conditions. Thus, stresses in soil will depend on the properties of the variable soil layers, if the profile is not homogeneous. Note that pile installation will result in large soil strains, thus the ultimate soil resistance to pile driving will be associated with the residual shear strength of sensitive soils, rather than their peak strength.

Equilibrium of mass suggests that the volume of the soil displaced and remolded is equal to the volume of the pile, for closed-end piles. A zone of minimum radius of about $0.7D$, where D is the diameter of the pile, will be affected and soil in this zone will generally be less stiff than the original soil (Figure 6.14b).

After installation, excess pore pressures that (may) have developed in the disturbed zone due to the application of the additional stresses will begin to dissipate, and the soil will reconsolidate. During reconsolidation, two phenomena take place: a) as the volume of the soil decreases, negative skin friction will develop along the soil-pile interface, reducing its load capacity b) the effective stresses increase as pore pressures dissipate, increasing soil strength, and thus the pile's skin friction resistance. Given the fact that the effect of these two phenomena is antagonistic, we tend to ignore them when using simplified formulas for pile design.

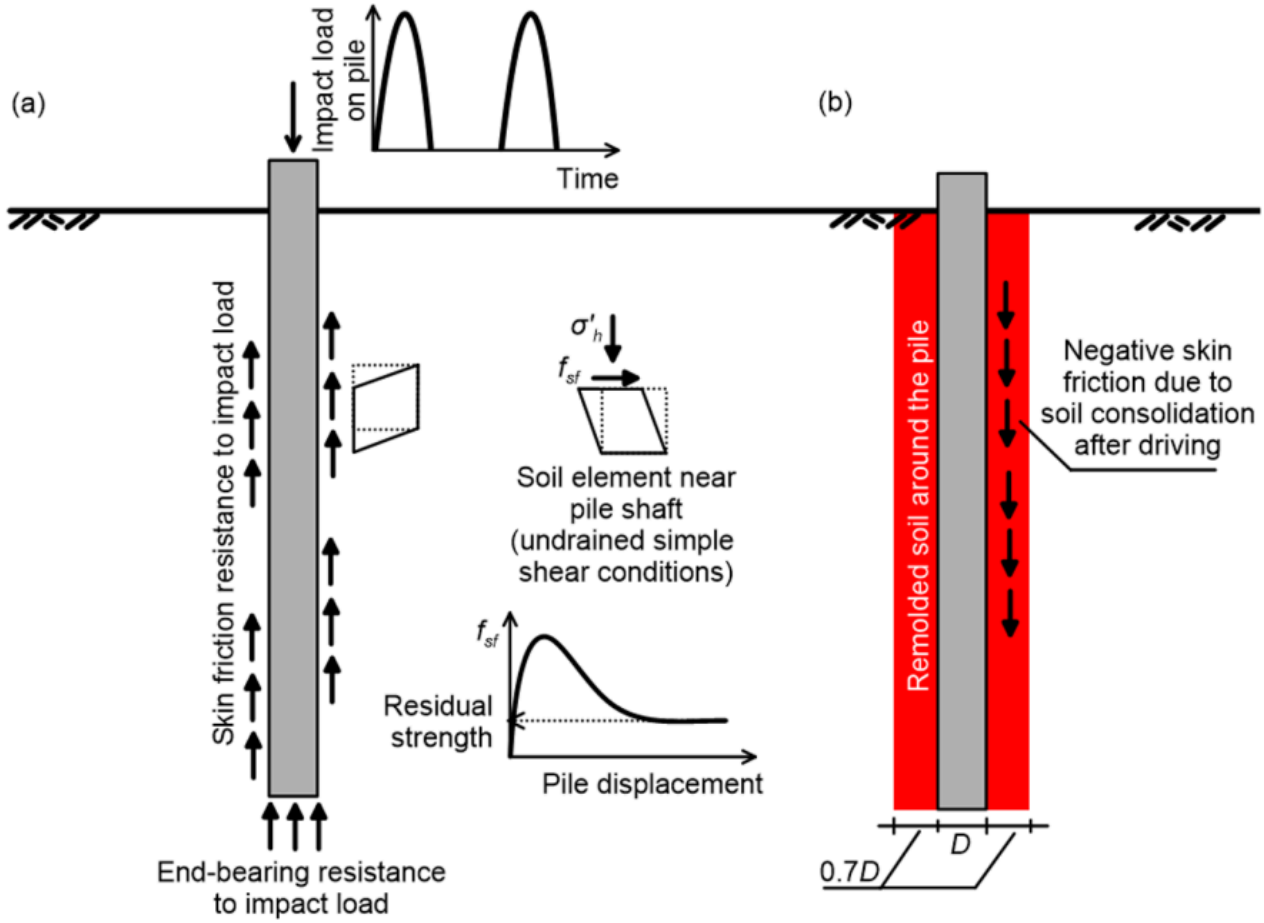

Figure 6.14. (a) Stresses developing along the shaft during pile driving, and (b) Disturbed soil zone around the shaft due to driving.

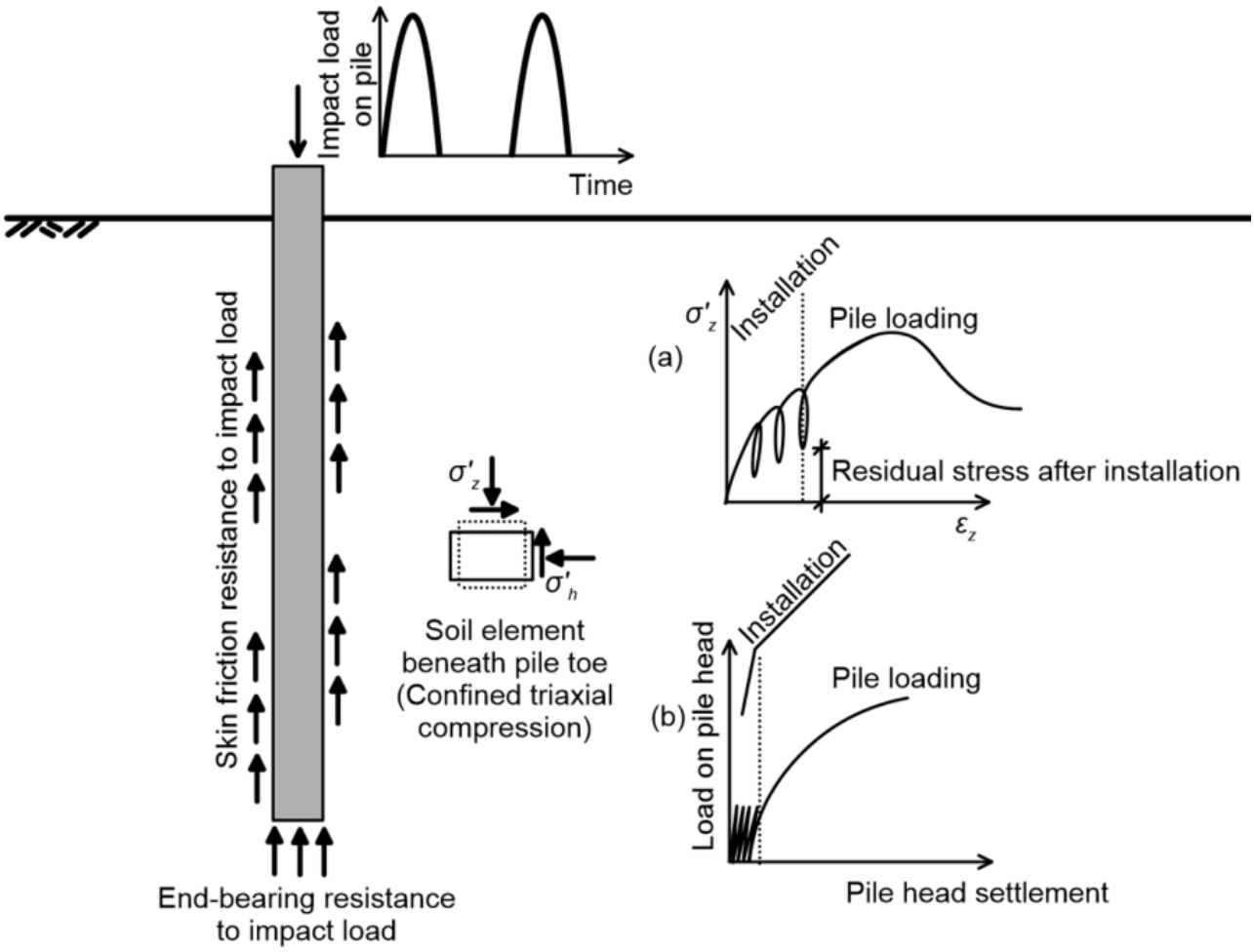

Figure 6.15. (a) Stress-strain curve of a soil element below the pile toe, and (b) Pile load-displacement curve.

Let's consider now a soil element below the pile toe (Figure 6.15a). During driving, this element will undergo a vertical compressive stress due to the axial load from the pile, and a shear stress, due to the difference between vertical and lateral stresses. Unlike soil elements along the pile shaft, a soil element below the pile's toe is severely confined laterally and vertically. If the pile is not pushed continuously into the soil, and installation involves impact loading-unloading-reloading, the stress-strain curve of the soil element will not be monotonic, as illustrated in Figure 6.15a.

As the soil below the pile toe is constrained vertically, due to the overburden pressure, but also radially, due to the lateral restrain imposed by the nearby soil, it undergoes a constrained mode of deformation. Consequently, after installation some residual stress will remain, despite a vertical load not being applied on the pile (Figure 6.15b), and the soil below the pile will not be in its original, geostatic stress state. This residual stress results from the restriction imposed on the soil by the weight of the pile and the negative skin friction acting at along the shaft, and is analogous to a preconsolidation stress. In other words, installation of the pile applies an apparent preconsolidation stress to the soil below the toe, which however cannot be straightforwardly determined.

If observations/measurements obtained during pile driving are used to indirectly estimate its collapse load, though pile driving formulas discussed in Chapter 6.17, one should bear in mind that the excess pore water pressures developing below the pile toe will result in additional resistance of piles penetrating into fine grained saturated soils, which may lead to over-estimating the long-term pile capacity. When installation stops, these excess pore pressures will gradually dissipate, leading to (some) pile settlement. However, if the pile toe is embedded into a highly overconsolidated clay or dense sand, negative excess pore pressures may develop due to their dilative response: Remember that dilating soils which are prone to volume contraction

tend to draw in water to compensate volume changes, resulting in negative pore pressure development under undrained loading conditions. This will lead to a temporary increase in effective stresses and a (temporary) increase in the soil strength.

6.7 PILES SUBJECTED TO AXIAL COMPRESSIVE LOADS - GENERAL CONCEPTS

After installation, the vertical load applied on the pile is transferred to the surrounding soil via skin friction and end-bearing mechanisms. The stress-strain response of a soil element below the pile toe will initially follow the loading curve (Figure 6.15a), which is analogous to the reloading curve of an over-consolidated soil from the oedometer test (see Figure 4.28). Note however that, unlike the oedometer test, the loading curve will not "exactly" match the installation curve, as installation loads are dynamic.

As we increase the vertical load applied on the pile head, a failure surface will gradually develop. Two possible pile failure mechanisms are presented in Figure 6.16a, assuming soil is rigid plastic material. These idealised failure mechanisms, which may develop when numerically simulating vertical loading of piles considering an elastic-rigid plastic material for the soil (Figure 6.16b), do not take into account neither the disturbance of soil around the shaft, nor the confined soil conditions below the pile toe. So actually they will not develop fully in practice, expect maybe in the case of a very short pile.

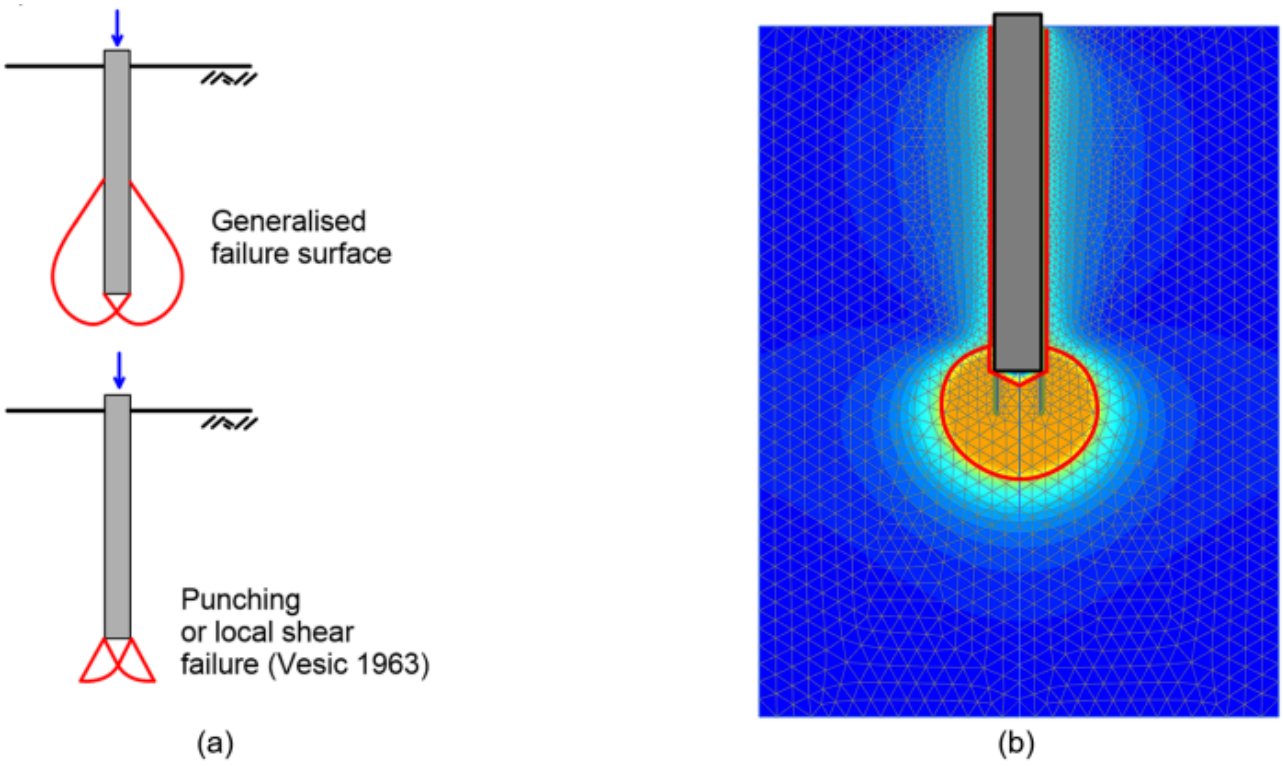

Figure 6.16. (a) Theoretical failure mechanisms of a pile subjected to axial compressive load, and (b) simulated pile failure mechanism in undrained soil.

In order for the full skin friction resistance to be mobilised, a vertical pile displacement of 2.5 mm to 10 mm is required. On the contrary, the full end-bearing resistance is mobilised at a much higher vertical displacement, between 10% and up to 30% of the pile diameter. This means that the full skin friction resistance will develop first, for a load lower than the collapse load, followed by the end-bearing resistance.

In practice, we can assume that the full end-bearing resistance develops when a failure mechanism similar

to that of shallow foundations is formed below the pile toe, and calculate the pile resistance by following the same concepts as for an embedded shallow footing. Due to the high degree of confinement under the toe, even over-consolidated clays or very dense sands will not exhibit a peak in their stress-strain response *("collapse load")* but will rather strain harden until intolerable settlements develop *("failure load").*

Following the nomenclature introduced in Part 5, we will use the term "collapse load Q_f" to refer to the ultimate geotechnical strength of piles (bearing capacity) in terms of force. The design capacity of piles is introduced in the next chapter.

6.8 LOAD AND RESISTANCE FACTOR DESIGN OF PILES SUBJECTED TO AXIAL COMPRESSIVE LOADS ACCORDING TO AS2159

According to AS2159, the *design capacity* of piles subjected to axial compressive loads is determined as the product of the ultimate geotechnical strength in axial compression (*collapse load* Q_f) and of the *basic geotechnical strength reduction factor* φ_{gb}. The term *basic* refers to designs which are not supported by pile loads tests-these are covered later in this Part. The product of the ultimate geotechnical strength in axial compression (collapse load) and the basic geotechnical strength reduction factor (i.e., the design bearing capacity) should be higher than the *design action load*, S^* resulting from Ultimate Limit State (ULS) load combinations. It is reminded that S^* is determined according to the provisions of the standard relevant to the specific structure e.g. AS1170.0 and AS1170.1 for structures other than bridges, and AS5100.2 for bridges.

(6.1) $\varphi_{gb} Q_f \geq S^*$

The basic geotechnical strength reduction factor φ_{gb} is determined via a risk assessment procedure, based on Table 6.1.

Table 6.1. Weighting factors and individual risk ratings for risk factors (AS2159).

Risk factor	Weighting factor (w_i)	Typical description of risk circumstances for individual risk rating (IRR)		
		1 (Very low risk)	3 (Moderate)	5 (Very high risk)
Site				
Geological complexity of site	2	Horizontal strata, well-defined soil and rock characteristics	Some variability over site, but without abrupt changes in stratigraphy	Highly variable profile of karstic features or steeply dipping rock levels or faults present on site, or combinations of these
Extent of ground investigation	2	Extensive drilling investigation covering whole site to an adequate depth	Some boreholes extending at least 5 pile diameters below the base of the proposed pile foundation	Very limited investigation with few shallow boreholes
Amount and quality of geotechnical data	2	Detailed information on strength and compressibility of the main strata	CPT probes over full depth of proposed piles or boreholes confirming rock as proposed founding level for piles	Limited amount of simple *in situ* testing (e.g. SPT) or index tests only
Design				
Experience with similar foundations in similar geological conditions	1	Extensive	Limited	None
Method of assessment of geotechnical parameters for design	2	Based on appropriate laboratory or *in situ* tests or relevant existing pile load test data	Based on site-specific correlations or on conventional laboratory or *in situ* testing	Based on non-site-specific correlations with (for example) SPT data
Design method adopted	1	Well-established and soundly based method or methods	Simplified methods with well-established basis	Simple empirical methods or sophisticated methods that are not well established
Method of utilising results of *in situ* test data and installation data	2	Design values based on minimum measured values on piles loaded to failure	Design methods based on average values	Design values based on maximum measured values on test piles loaded up only to working load, or indirect measurements used during installation, and not calibrated to static load tests
Installation				

Level of construction control	2	Detailed with professional geotechnical supervision, construction processes that are well established and relatively straightforward	Limited degree of professional geotechnical involvement in supervision, conventional construction procedures	Very limited or no involvement by designer, construction processes that are not well established or complex
Level of performance monitoring of the supported structure during and after installation	0.5	Detailed measurements of movements and pile load	Correlation of installed parameters with on-site static load tests carried out in accordance to AS2159	No monitoring

Note: The pile design shall include the risk circumstances for each individual risk category and consideration of all of the relevant site and construction factors.

More specifically: Each one of the risk factors of Table 6.1 is rated on a scale from 1 to 5 for the nature of the site, the available geotechnical information, pile design method and installation procedures, and an *individual risk rating* (IRR) is assigned to each one of the factors. The individual risk rating ranges from IRR = 1 for very low risk level to IRR = 3 for moderate risk level, up to IRR = 5 for very high risk level. Accordingly, the overall *average risk rating* (ARR) is determined as the weighted average of the product of all the *risk weighting factors* w_i times the IRR of each factor:

(6.2) $$\mathrm{ARR} = \frac{\sum (w_i \mathrm{IRR_i})}{\sum w_i}$$

An example application is provided in Table 6.2. For a given ARR value, the basic geotechnical strength reduction factor φ_{gb} is determined from Table 6.3, depending on the level of redundancy in the piling system. Systems with a high degree of redundancy would include large pile groups connected with stiff pile caps, pile raft foundations, and pile groups with more than 4 piles. Systems with low redundancy would include isolated heavily loaded piles, and piles set out at large spacing within a group.

Table 6.2. Estimation of the average risk rating ARR after AS2159.

Risk factor	w_i	$\mathbf{IRR_i}$	$w_i\mathbf{IRR_i}$
Geological complexity of the site	2	3	6
Extent of ground investigation	2	2	4
Amount and quality of geotechnical data	2	4	8
Experience with similar foundations in similar conditions	1	1	1
Method of assessment of geotechnical parameters for design	2	3	6
Design method adopted	1	2	2
Method of utilising results of *in situ* test data and installation data	2	2	4
Level of construction control	2	2	4
Level of performance monitoring of the supported structure during and after construction	0.5	5	2.5
Σw_i	14.5	$\Sigma w_i \mathrm{IRR_i}$	37.5

$$\mathrm{ARR} = \frac{\sum (w_i \mathrm{IRR_i})}{\sum w_i} = \frac{37.5}{14.5} = 2.58$$

Table 6.3. Basic geotechnical strength reduction factor φ_{gb} for different average risk ratings (AS2159).

Range of average risk rating, ARR	**Overall risk category**	φ_{gb} **for low redundancy systems**	φ_{gb} **for high redundancy systems**
ARR ≤ 1.5	Very low	0.67	0.76
1.5 < ARR ≤ 2.0	Very low to low	0.61	0.70
2.0 < ARR ≤ 2.5	Low	0.56	0.64
2.5 < ARR ≤ 3.0	Low to moderate	0.52	0.60
3.0 < ARR ≤ 3.5	Moderate	0.48	0.56
3.5 < ARR ≤ 4.0	Moderate to high	0.45	0.53
4.0 < ARR ≤ 4.5	High	0.42	0.50
4.5 < ARR	Very high	0.40	0.47

6.9 ULTIMATE GEOTECHNICAL STRENGTH OF PILES SUBJECTED TO AXIAL COMPRESSIVE LOAD UNDER UNDRAINED CONDITIONS (A-METHOD)

The *α–Method* is used to analytically estimate the short-term axial collapse load Q_f of piles installed in fine-grained saturated soils, when undrained loading conditions prevail i.e., before dissipation of excess pore pressures. Calculation of the collapse load with the *α–Method* is based on total stresses (Total Stress Analysis-TSA).

The ultimate geotechnical strength Q_f in terms of force is equal to the sum of the skin friction resistance Q_{sf} and the end-bearing resistance Q_b (Figure 6.17):

(6.3) $$Q_f = Q_{sf} + Q_b$$

If the self-weight of the pile is not included in the axial load combination provided by the Structural Engineer, it should be subtracted from the pile resistance, as:

(6.4) $$Q_f = Q_{sf} + Q_b - W_p$$

It must be noted here that the above Eq. 6.4 is rather conservative, because it does not take into account that soil is unloaded during pile construction. It would be reasonable to subtract from the ultimate strength of the pile $Q_{sf} + Q_b$ the weight of the pile *minus* the weight of the excavated soil. It is acknowledged though that this will not have significant impact on the design of piles.

Estimation of the skin friction resistance developing along the pile shaft is based on the simple Coulomb friction concept (Figure 6.17a). Under undrained conditions, the adhesion factor a_u is used to correlate the undrained shear strength of the soil, S_u to the skin friction resistance in terms of stress f_{sf} as:

(6.5) $$f_{sf} = a_u S_u$$

Of course, as discussed in Section 5.2.5, the real cohesion of the soil is usually zero, and the term “adhesion” refers merely to the fact that in a total stress analysis the interface friction is calculated independently of the level of normal stress acting on the interface, as pore pressures are not known.

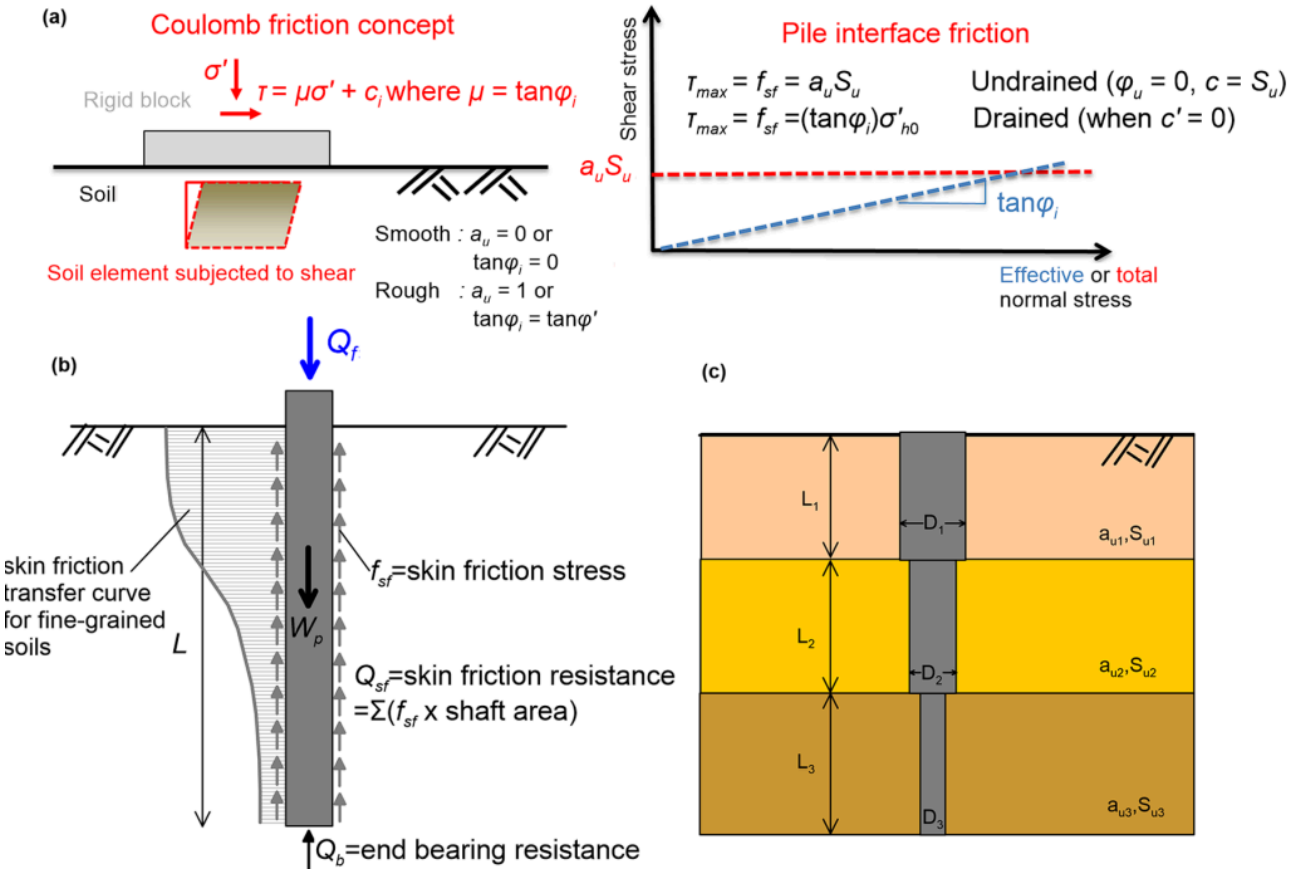

Figure 6.17. (a) Coulomb friction model used to estimate skin friction resistance of piles, (b) Skin friction resistance and end-bearing resistance of a pile subjected to vertical compressive load, and (c) Estimation of the skin friction resistance of a variable-diameter pile embedded in multi-layered soil.

Note that the interface strength generally is taken less or equal to the shear strength of its surrounding soil. While it has been proven experimentally that the strength of specially engineered interfaces can exceed the shear strength of soil, due to the development of a complex failure mode involving passive wedges, it is reasonable to consider that the adhesion factor a_u cannot exceed $a_u = 1$ (*rough* interface, Figure 6.17a). On the contrary, in the rather theoretical case where the pile-soil interface is perfectly *smooth* $a_u = 0$, and no friction resistance develops. According to the above, the skin friction resistance Q_{sf} (units: force) developing along the embedded length of the pile is calculated as the product of the skin friction stress times the surface area of the pile (Figure 6.17b). Specifically for a cylindrical pile of length L and diameter D in homogeneous soil featuring constant undrained strength S_u:

(6.6) $$Q_{sf} = a_u S_u \pi D L$$

or, when the undrained strength S_u varies with depth z as $S_u(z)$:

(6.7) $$Q_{sf} = \int_0^L (a_u S_u(z) \pi D)\, dz$$

In the more general case where a cylindrical pile of variable diameter is embedded in multi-layered soil consisting of n layers (Figure 6.17c), the skin friction resistance must be calculated separately for each soil layer. The sum of the skin friction resistance along each soil layer k will result to the total skin friction resistance of the pile:

(6.8) $$Q_{sf} = \sum_{k=1}^{n} a_{u,k} S_{u,k} \pi D_k L_k$$

Similarly, two soil sublayers must be considered if the pile diameter changes within the thickness of a soil sublayer with assumed constant undrained shear strength.

According to AS2159, the pile surface area from the ground surface level down to a depth equal to 1.5 pile diameters shall be assumed to be ineffective when estimating the appropriate pile length L values to calculate skin friction resistance, to account for severe soil disturbance during pile driving works.

Various methods have been proposed in the literature to estimate the adhesion factor a_u with some of the most commonly used ones presented in Figure 6.18a. Additionally, the nomographs proposed by Tomlinson (1987) are presented in Figure 6.18b, which should be conservatively used in the case where the pile toe is founded in a stiff soil layer, overlayed by a very soft clay layer (case (b), Figure 6.18b). Note that the undrained shear strength value S_u that will be used to estimate a_u and the skin friction resistance Q_{sf} must take into account the disturbance of soil around the shaft, as discussed earlier.

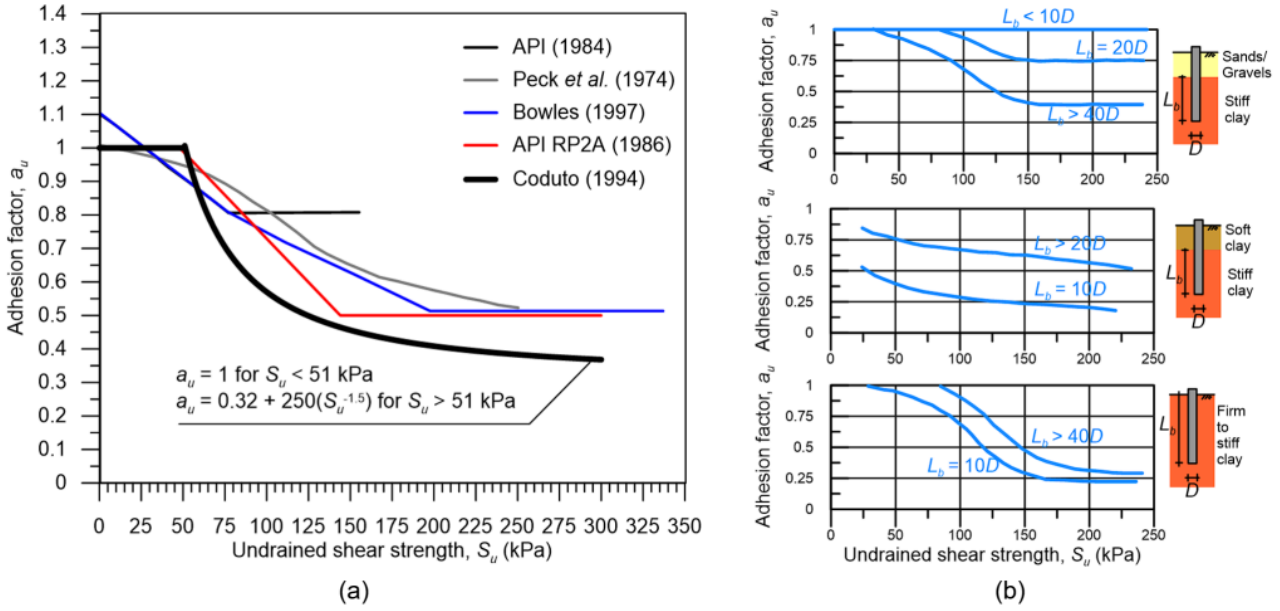

Figure 6.18. (a) Estimation of the adhesion factor according to API (1984), Peck et al. (1974), Bowles (1997), API (1986) and Coduto (1994), and (b) Estimation of the adhesion factor according to Tomlinson (after Tomlinson 1987).

Notice that the α-method will provide relatively high values of skin friction resistance for piles in soft-to-firm clay (S_u < 50 kPa), irrespective of pile roughness, as a_u depends only on soil's undrained strength. While there is sufficient field evidence to substantiate the selection of such high a_u values for piles driven in soft clays, it is perhaps prudent to consider soil's residual undrained strength in estimations of skin friction resistance, and conservatively ignore the gain in soil strength due to reconsolidation after pile driving. A discussion on challenges associated with predicting the skin friction resistance of piles with the α-Method is provided by Jardine *et al.* (2005) and a more rigorous method based on CPT measurements is presented in Section 6.12.7. The author recommends using the ICP method presented in Section 6.12.7 to, at least, evaluate predictions of skin friction resistance obtained with the α-method.

The end-bearing resistance Q_b (units: force) is estimated by analogy to the conventional methods for calculating the collapse load of shallow foundations under undrained loading conditions:

(6.9) $$Q_b = N_{cp} S_{u,b} A_b$$

where $S_{u,b}$ is the undrained shear strength of the soil layer below the pile toe, A_b is the area of the pile base, and N_{cp} is the bearing capacity factor for undrained conditions which accounts for the shape of the failure surface developing below the pile toe, and is taken equal to $N_{cp} = 9$ for $S_{u,b} > 25\text{kPa}$ and $N_{cp} = 6$ for $S_{u,b} \leq 25\text{kPa}$.

Notice that the bearing capacity factor N_{cp} is higher than the bearing capacity factor N_c for a circular smooth or rough footing on undrained soil, discussed in Part 5. This accounts for the difference in the

geometry of the failure surface that will develop below the pile's toe, as discussed earlier. It is also worth noting that Q_b of friction piles installed in clay is expected to be of the order of 20% of Q_{sf} (Jardine *et al.* 2005).

6.10 ULTIMATE GEOTECHNICAL STRENGTH OF PILES SUBJECTED TO AXIAL COMPRESSIVE LOAD UNDER DRAINED CONDITIONS (B-METHOD)

The *β–Method* is used to analytically estimate the short-term and long-term collapse load Q_f of piles installed in coarse-grained soils, and the long-term collapse load in fine-grained soils, under drained loading conditions, after excess pore pressures that will develop immediately after loading (careful, not installation) of the pile have dissipated. Calculation of the collapse load with the *β–Method* is based on effective stresses (Effective Stress Analysis-ESA). The concept introduced in the *α*-Method is followed here too i.e., skin friction and end-bearing resistance are considered separately, and the collapse load is calculated as the sum of the skin friction resistance and the end-bearing resistance of the pile (Eqs. 6.3-6.4).

The skin friction is estimated in terms of effective stress while considering again that the Coulomb friction law describes the shear resistance that develops at the soil-pile interface (Figure 6.17a). Ignoring soil cohesion, the frictional stress along the shaft f_{sf} is equal to the product of the lateral effective normal stress acting perpendicularly to the interface σ'_{h0}, multiplied by a friction coefficient μ equal to $\tan\varphi_i$, with φ_i being the interface friction angle as:

(6.10) $$f_{sf} = (\tan\varphi_i)\,\sigma'_{h0}$$

Assuming geostatic conditions (the subscript $_0$ refers to *in situ* conditions before installation of the pile), the lateral effective stress is calculated as:

(6.11) $$\sigma'_{h0} = K_0\sigma'_{z0}$$

so, the frictional stress can be re-written as:

(6.12) $$f_{sf} = (\tan\varphi_i)\,K_0\sigma'_{z0}$$

Replacing the product of the earth pressure coefficient at-rest K_0 and of the friction coefficient $\tan\varphi_i$ with a single factor β yields:

(6.13) $$f_{sf} = \beta\sigma'_{z0}$$

Notice that, as the vertical effective stress σ'_{z0} is not constant with depth, friction developing along the pile shaft is not uniform but rather increases with depth, while it depends also on groundwater table level.

Considering the general case of multiple layers n (Figure 6.19a) and, for simplicity, the effective stress acting at the middle of each drained layer k, the skin friction resistance (units: force) along a pile of variable circular cross-section will be calculated as:

(6.14) $$Q_{sf} = \sum_{k=1}^{n} \beta_k \sigma'_{z0,k} \pi D_k L_k$$

In the case of a deep uniform drained layer with groundwater table present (Figure 6.19b), a better approximation of the skin friction resistance will be obtained if we divide the foundation soil into sublayers, and estimate the effective stress at the middle of each sublayer.

Calculation of the β factor requires estimating the earth pressure coefficient at-rest K_0 and the friction coefficient $\tan\varphi_i$. The former can be estimated from the formula proposed by Jaky (1944):

(6.15) $$K_0 = (1 - \sin\varphi')\,\mathrm{OCR}^m$$

where OCR is the overconsolidation ratio, φ' is the friction angle of soil while the exponent m is often taken equal to m = 0.5. For normally consolidated clays (OCR = 1) and sands the above expression degenerates to:

(6.16) $$K_0 = (1 - \sin\varphi')$$

It is recommended to use Eq. 6.16 together with the critical state friction angle of soil, instead of the peak friction angle: K_0=1-sinφ_{cs} (Jaky, 1944). The interface friction angle is correlated with the friction angle of the soil, as:

(6.17) $$\varphi_i = \frac{\varphi'}{2} \text{ to } \frac{2\varphi'}{3}$$

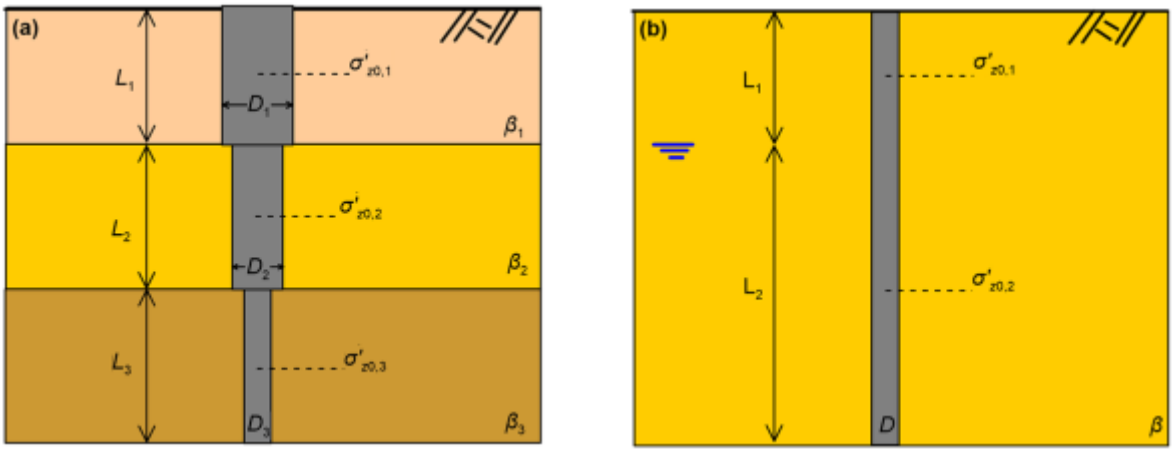

Figure 6.19. Estimation of the drained skin friction resistance (a) of a pile with variable cross-section in a non-uniform profile, and (b) of a pile with constant cross-section in a deep uniform layer, with groundwater table present.

The upper bound value of φ_i/φ' in Eq. 6.17 (see also Figure 6.17a) corresponds to a rather rough soil-pile interface, as the case of a concrete drilled shaft, while the lower bound value corresponds to a rather smooth soil-pile interface, as the case of a driven steel pile. Some further guidance on selecting appropriate φ_i values for piles driven in coarse-grained and fine-grained materials is provided in Chapter 6.12 (Figures 6.26 and 6.29).

While deriving the above expressions we have assumed that the normal stress acting at the soil-pile interface is equal to the geostatic stress σ'_{h0}, in other words the pile is "wished in-place" and any soil disturbance effects due to driving are ignored. This is not going to be the case in practice, and the normal stress acting at the soil-pile interface will not be equal to the *in situ* lateral soil stress. Owing to disturbance induced from pile construction, $K = \sigma'_h/\sigma'_{z0} < K_0$ for drilled shafts due to stress relief during boring, and $K > K_0$ for driven piles due to lateral stress increase during pile driving, where K is ratio of the normal stress acting at the soil-pile interface over the vertical geostatic effective stress. API RP2A (2000) suggests that, for driven piles, a value of σ'_h/σ'_{z0} =0.8 to 1.0 describes better the lateral stresses developing at the interface. More rigorous methods for estimating σ'_h are described in Chapter 6.12.

The friction angle of the soil around the pile will be also affected by pile driving, and generally will not be equal to the friction angle of the undisturbed soil, before pile construction. For example, friction angle of sand depends on its relative density. As pile driving will result in densification of a loose sand around the shaft, or perhaps to loosening of a dense sand (Figure 6.20) the friction angle may increase or decrease, respectively.

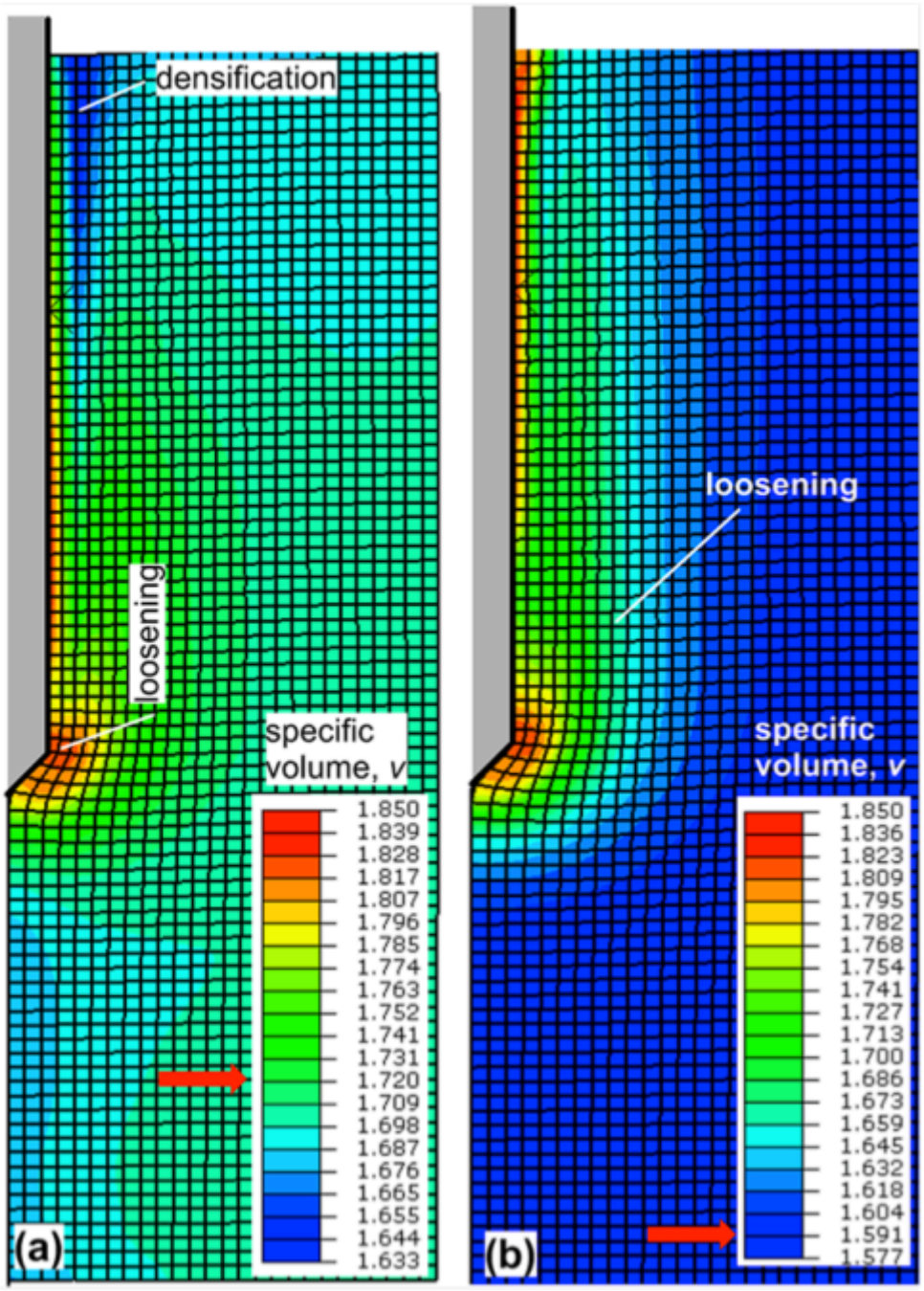

Figure 6.20. (a) Densification of loose sand, and (b) Loosening of dense sand during pile driving (Kouretzis et al. 2014).

The end-bearing resistance Q_b (units: force) is estimated similarly to the collapse load of shallow foundations under drained loading conditions (Figure 6.21a):

(6.18) $$Q_b = N_{qp}\sigma'_{z0,b}A_b$$

where $\sigma'_{z0,b}$ is the vertical effective stress at the level of the pile toe, A_b is the area of the pile base and N_{qp} is the bearing capacity factor for drained conditions. The bearing capacity factor can be estimated either with the exact expression for shallow footings established originally by Reissner (1924):

(6.19) $$N_{qp} = N_q = \tan^2\left(45^o + \frac{\varphi'}{2}\right)e^{\pi\tan\varphi'}$$

or, with the formula recommended in Janbu (1976), which takes into account the extent of the plastic zone developing below the pile toe, through the angle ψ_p:

(6.20) $$N_{qp} = \left(\tan\varphi' + \sqrt{1+\tan^2\varphi'}\right)^2 e^{2\psi_p \tan\varphi'}$$

with ψ_p in rad. According to Bowles (1997), ψ_p ranges from 60º in soft clays to 105º in dense sands and overconsolidated clays. As depicted in Figure 6.21b, adopting the formula proposed by Reissner (1924) will result in an average value of the end-bearing resistance, compared to the range of values resulting from application of the Janbu (1976) formula.

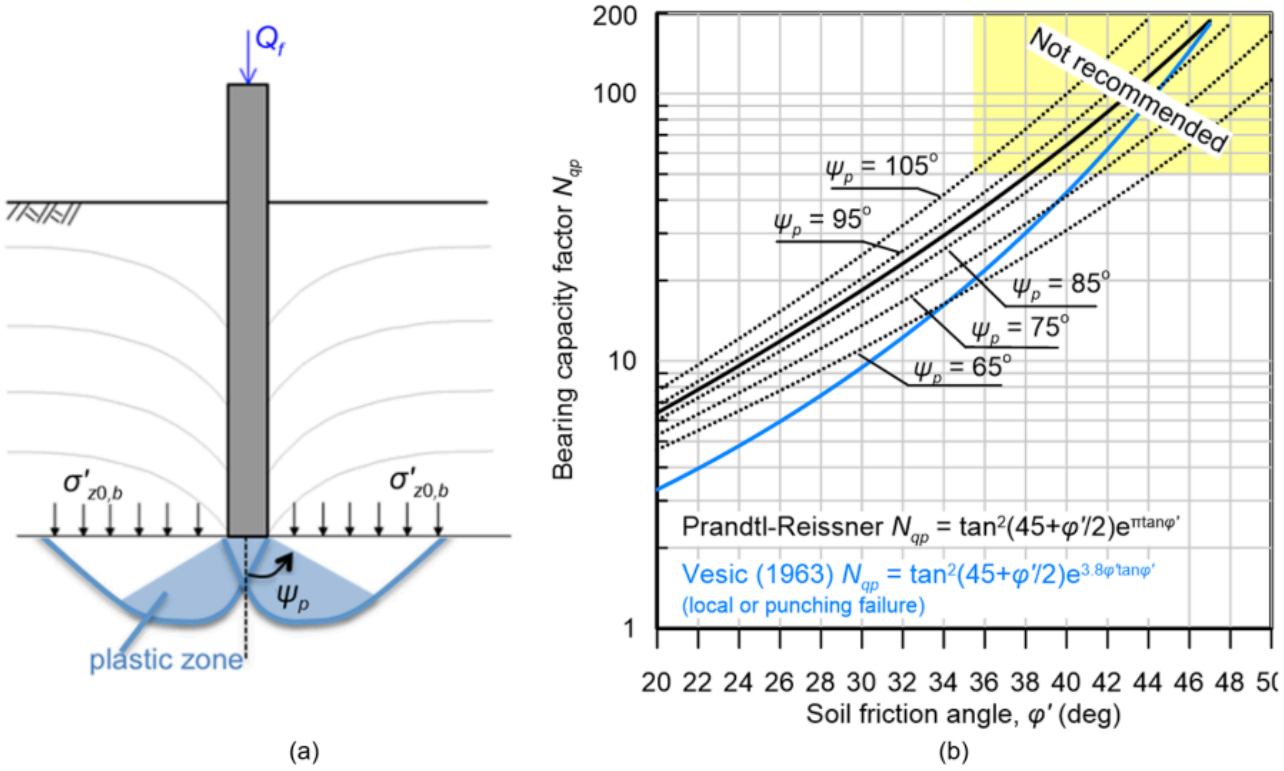

Figure 6.21. (a) End-bearing resistance estimation under drained conditions, and (b) Bearing capacity factors proposed by Reissner (1924), Janbu (1976) and Vesic (1963).

The following Table 6.4 provides typical values provided by API RP2A (2000) of interface friction angle φ_i, skin friction stress f_{sf}, drained bearing capacity factor N_{qp} and end-bearing resistance in terms of stress $q_{bf} = Q_b/(\sigma'_{z0,b}N_{qp})$. Values of f_{sf} in Table 6.4 must be consider as indicative, as the skin friction resistance depends on depth (and groundwater), and are perhaps applicable to relatively long piles. It is worth noting that the maximum recommended N_{qp} factor is of the order of $N_{qp} = 40 - 50$. The author agrees with API RP2A (and with Vesic, who proposed a formula for N_{qp} that accounts for the possibility of local or shear failure, Figure 6.21b) in the sense that while Eq. 6.19 and 6.20 may yield N_{qp} values higher than $N_{qp} = 50$, adopting such values for pile design is not recommended. Remember that the friction angle of soils depends on the confining stress. Therefore, considering that high confining stresses are present at the pile toe (Chapter 6.6), it is prudent to consider a relatively conservative value of N_{qp}.

Table 6.4. Recommended β-Method parameters for coarse-grained soils (API RP2A 2000).

Description	Density	φ_i (deg)	f_{sf} (kPa)	N_{qp}	$q_{bf} = \sigma'_{z0,b} N_{qp}$ (MPa)
Sand; Silt; Silty sand/Sandy silt	Very loose to medium	15	47.8	8	1.9
Sand; Silt; Silty sand/Sandy silt	Loose to medium	20	67.0	12	2.9
Sand; Silty sand	Medium to dense	25	81.3	20	4.8
Sand; Silty sand	Dense to very dense	30	95.7	40	9.6
Sand; Gravels; Gravelly sand; Sandy gravels	Dense to very dense	35	114.8	50	12.0

6.11 ULTIMATE GEOTECHNICAL STRENGTH OF PILES SUBJECTED TO AXIAL COMPRESSIVE LOAD FROM SPT TEST RESULTS

Given difficulties (and costs) associated with obtaining undisturbed coarse-grained soil samples for laboratory testing, as discussed in Chapter 5.7, the collapse load of piles in homogeneous coarse-grained soil can be estimated directly from SPT test results, skipping the intermediate step of interpreting characteristic values of soil parameters. While such methods are rather obsolete, and have been replaced by CPT-based methods described in the next section, the relevant formulas are provided below for completeness.

The skin friction resistance (units: force) is correlated to the average SPT value along the length of the pile $N_{60,\text{shaft}}$ as:

(6.21) $$Q_{sf} = (0.01 \text{ to } 0.02)\, p_a N_{60,shaft} \pi D L$$

The upper bound of Eq. 6.21 corresponds to driven piles, while the lower bound corresponds to drilled shafts.

In addition, the end-bearing resistance (units: force) is correlated to the average SPT value at the vicinity of the pile toe $N_{60,\text{toe}}$, considering blow counts about 6 to 10D above and 2 to 4D below the pile toe (Meyerhoff, 1976).

(6.22) $$Q_b = 0.4 p_a N_{60,toe} \frac{L}{D} \left(\pi \left(\frac{D}{2} \right)^2 \right) \leq 4 p_a N_{60,toe} \left(\pi \left(\frac{D}{2} \right)^2 \right)$$

In the above Eqs. 6.21-6.22 L is the length of the pile, D is its diameter and p_a is the atmospheric pressure, equal to p_a = 100 kPa. The pile length over which N_{60} are averaged to find $N_{60,\text{toe}}$ (from 6D to 10D above to 2D to 4D below the pile toe) covers the extent of the possible failure surface developing below the pile toe (Figure 6.22).

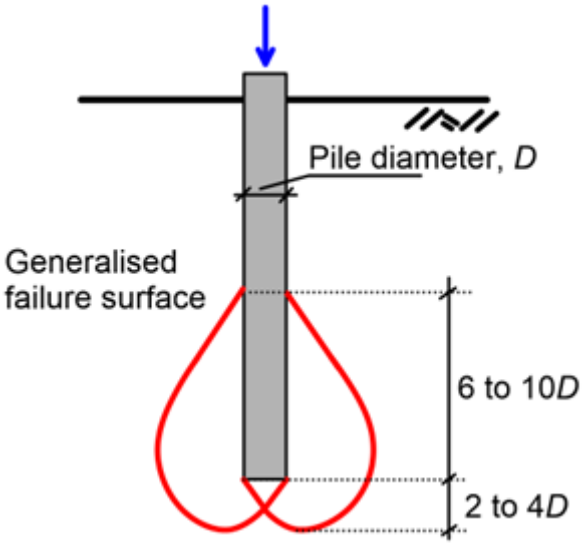

Figure 6.22. Geometry of a possible failure surface developing below the pile toe.

6.12 ULTIMATE GEOTECHNICAL STRENGTH OF PILES SUBJECTED TO AXIAL COMPRESSIVE LOAD FROM CPT TEST RESULTS

Initially, the cone penetration test was developed exactly for the estimation of the collapse load of driven piles, and several methodologies have been proposed for the estimating pile capacity on the basis of measurements obtained from CPT tests performed at the proposed pile location. Most of these methods are based on determining the collapse load as the sum of the skin friction resistance along the pile shaft and the end-bearing resistance at the pile toe, similar to the α– and β-Method. As consequence the two key quantities that the Geotechnical Engineer is called to calculate is the (depth-dependent) skin friction stress along the pile, and the end-bearing resistance in terms of stress. It is not the aim of this section to provide a critical analysis of different methods, and endorse one over the other. The interested reader is referred to Schneider *et al.* (2008), Lehane *et al.* (2005a) and various other publications for a discussion on the advantages and prediction capabilities of the methods. Here the most widely used methods are presented, in chronological order, starting with Schmertmann's method.

6.12.1 Schmertmann (1978) method for calculating the skin friction resistance

Despite being proposed almost 50 years ago, and the publication of several more refined methods since, Schmertmann's (1978) method for estimating the skin friction resistance is still applied in practice, perhaps owing to its simplicity as well as its consideration of different pile materials. According to Schmertmann, the skin friction resistance ΔQ_{sf} (units: force/unit pile length) of a pile segment with length dL can be correlated to the sleeve penetration resistance from a CPT test f_s measured at the same depth as:

(6.23) $$\Delta Q_{sf} = f_{sf}\,(\pi D)\,\Delta L = (\alpha' f_s)\,(\pi D)\,dL$$

where α' is a correction factor that depends on the material of the pile and the embedment ratio z/D for piles driven in coarse-grained soils, or the ratio of the CPT sleeve friction resistance over the atmospheric pressure f_s/p_a in fine-grained soils (Figure 6.23).

Instead of using the charts provided in Figure 6.23, one can use the following curve-fitting formulas for the estimation of the factor α':

For concrete piles in coarse-grained soils (Figure 6.23a):

(6.24) $$\alpha' = 1.85 - 0.1\left(\frac{z}{D}\right) + 0.0025\left(\frac{z}{D}\right)^2 - 0.259\times 10^{-4}\left(\frac{z}{D}\right)^3$$

For steel piles in coarse-grained soils (Figure 6.23a):

$$\alpha' = 3.88 - 0.482\left(\frac{z}{D}\right) + 0.0282\left(\frac{z}{D}\right)^2 - 0.718 \times 10^{-3}\left(\frac{z}{D}\right)^3 + 0.668 \times 10^{-5}\left(\frac{z}{D}\right)^4 \quad \textbf{(6.25)}$$

For concrete/timber piles in fine-grained soils (Figure 6.23b):

$$\alpha' = 1.28 - 1.473\left(\frac{f_s}{p_a}\right) + 0.839\left(\frac{f_s}{p_a}\right)^2 - 0.1634\left(\frac{f_s}{p_a}\right)^3 \quad \textbf{(6.26)}$$

For steel piles in fine-grained soils (Figure 6.23b):

$$\alpha' = 1.29 - 1.606\left(\frac{f_s}{p_a}\right) + 0.846\left(\frac{f_s}{p_a}\right)^2 - 0.159\left(\frac{f_s}{p_a}\right)^3 \quad \textbf{(6.27)}$$

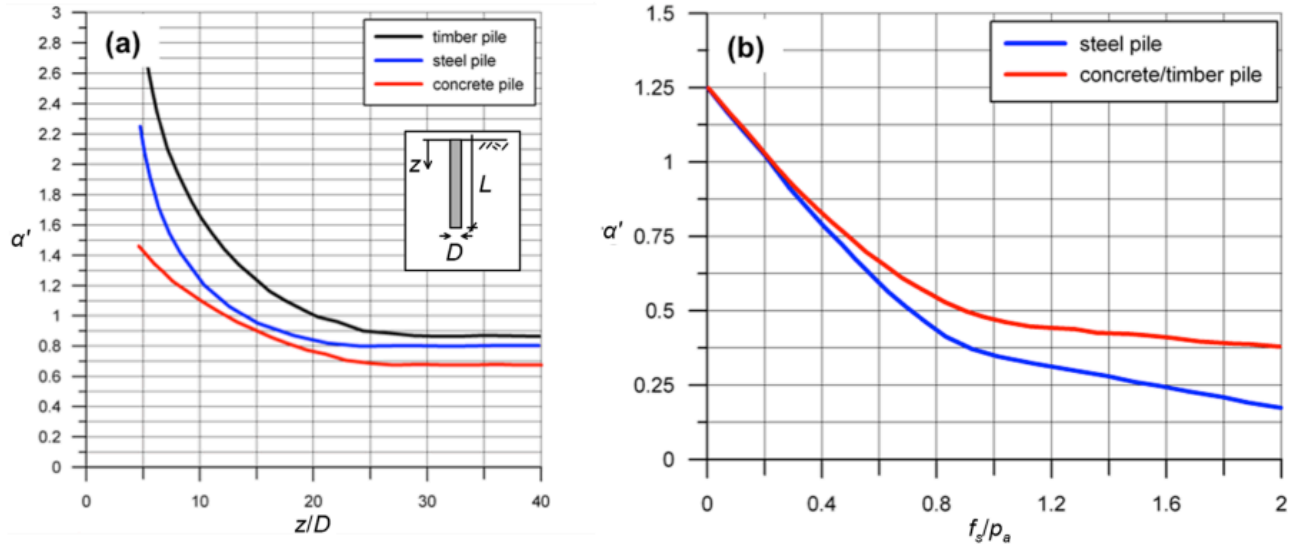

Figure 6.23. Correction factor α' for the estimation of the skin friction resistance from CPT test measurements for (a) coarse-grained soils, and (b) fine-grained soils, under short-term undrained loading conditions.

Accordingly, the total pile skin friction resistance is calculated as the sum of the unit friction resistance for all pile segments dL:

$$Q_{sf} = \int_0^L \alpha' f_s(z)\pi D dz \quad \textbf{(6.28)}$$

6.12.2 LCPC method (Bustamante and Gianeselli 1982)

Another widely used method is the one proposed by Bustamante and Gianeselli (1982), also know as the LCPC method. It is based on the statistical analysis of 197 pile load tests covering a wide range of soil conditions, and is applicable to both drilled shafts and driven piles.

The end-bearing resistance is estimated with the LCPC method as:

(6.29) $Q_b = q_{c(eq)} k_c A_b$

where $q_{c(eq)}$ is an equivalent average cone resistance in the vicinity of the pile toe from the CPT test, calculated as shown below; k_c is a bearing capacity factor from Table 6.5 or, according to Briaud and Miran (1992), can be assumed equal to $k_c = 0.6$ for clays and silts and $k_c = 0.375$ for sands; A_b is the area of the pile base.

The equivalent average cone resistance $q_{c(eq)}$ is estimated as illustrated in Figure 6.24 (Das 2007):

- Consider the cone tip resistance q_c (or q_t if a piezocone test has been performed and cone resistance has been corrected for pore pressure effects) within a range of $1.5D$ below the pile toe to $1.5D$ above the pile toe.
- Calculate the average value of the cone resistance $q_{c(av)}$ within this zone.
- Eliminate q_c values that are higher than $0.7q_{c(av)}$ and lower than $1.3q_{c(av)}$.
- Calculate $q_{c(eq)}$ by averaging the remaining q_c values.

Table 6.5. Bearing capacity factors k_c (after Bustamante and Gianeselli 1982, with modifications).

Soil type	Cone resistance q_c (MPa)	Factor k_c	
		Pile type I (drilled shafts)	Pile type II (driven piles)
Soft clay and mud	< 1	0.40	0.50
Moderately firm clay	1 to 5	0.35	0.45
Silt and loose sand	≤ 5	0.40	0.50
Firm to stiff clay and firm silt	> 5	0.45	0.55
Soft chalk	≤ 5	0.20	0.30
Medium dense sand/ sand-gravel mixture	5 to 12	0.40	0.50
Weathered to fragmented chalk	> 5	0.20	0.40
Dense to very sand/ sand-gravel mixture	> 12	0.30	0.40
Pile type I (Drilled shafts): Unreinforced drilled shafts; micropiles grouted under low pressure; cased drilled shafts; hollow auger drilled shafts, piers; barrettes			
Pile type II (Driven piles): Cast in-place screwed piles; driven precast piles; prestressed tubular piles; driven cast piles; jacked steel piles; micropiles grouted under high pressure; driven grouted piles (low pressure grouting); driven steel piles; driven rammed piles; jacked concrete piles; high pressure grouted piles of large diameter > 250 mm			

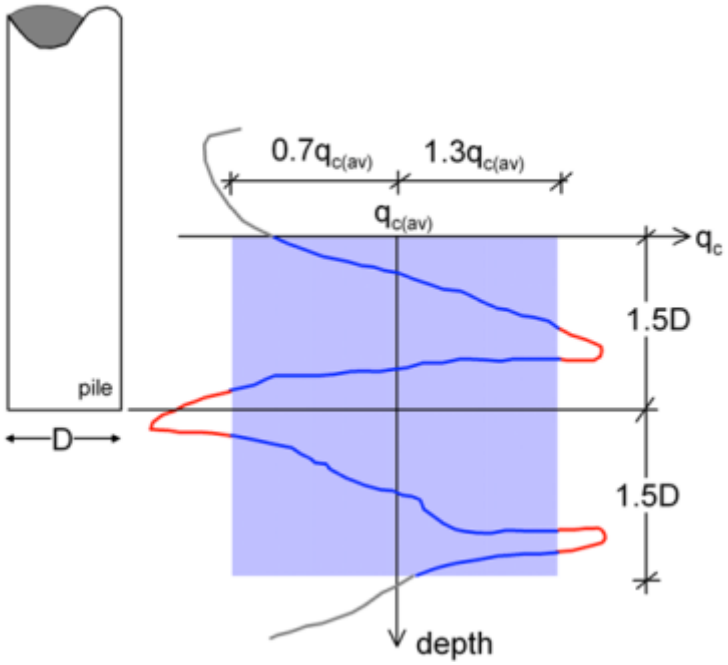

Figure 6.24. Estimation of the equivalent average cone resistance $q_{c(eq)}$ at the area of the pile toe.

In addition, the LCPC method can be used together with Eq. 6.23 and 6.28 to estimate the skin friction resistance (units: stress) from the distribution of the cone resistance q_c along the pile length as $f_{sf} = q_c/\alpha$, with the coefficient α (instead of α' in Eqs. 6.23 and 6.38) given in Table 6.6. Note that unlike the Schmertmann (1978) method described above, the LCPC method correlates the pile skin friction resistance to the cone tip resistance. Despite this being somewhat counterintuitive, it is considered an advantage by many due to difficulties in interpreting the CPT sleeve friction resistance f_s (Robertson and Kabal, 2022). As we will see in the next sections, this is followed by all modern methods.

Table 6.6. Skin friction resistance coefficient α (after Bustamante and Gianeselli 1982, with modifications).

Soil type	Cone resistance q_c (MPa)	Skin friction resistance coefficient α				Limiting value of skin friction resistance f_{sf} (kPa)					
		Pile type				Pile type					
		I		II		I		II		III	
		A	B	A	B	A	B	A	B	A	B
Soft clay and mud	< 1	30	30	30	30	15	15	15	15	35	–
Moderately firm clay	1 to 5	40	80	40	80	35 to 80*	35 to 80*	35 to 80*	35	80	≥ 120
Silt and loose sand	≤ 5	60	150	60	120	35	35	35	35	80	–
Firm to stiff clay and firm silt	> 5	60	120	60	120	35 to 80*	35 to 80*	35 to 80*	35	80	≥ 200
Soft chalk	≤ 5	100	120	100	120	35	35	35	35	80	–
Medium dense sand/ sand-gravel mixture	5 to 12	100	200	100	200	80 to 120*	35 to 80*	80 to 120*	80	120	≥ 200
Weathered to fragmented chalk	> 5	60	80	60	80	120 to 150*	80 to 120*	120 to 150*	120	150	≥ 200
Dense to very dense sand/ sand-gravel mixture	> 12	150	300	150	200	120 to 150*	80 to 120*	120 to 150*	120	150	≥ 200
Pile type IA: Unreinforced drilled shafts; hollow auger drilled shafts; micropiles grouted under low pressure; cast in-place screwed piles; piers; barrettes											
Pile type IB: Cased drilled shafts; driven cast piles											
Pile type IIA: Driven precast piles; prestressed tubular piles; jacked concrete piles											
Pile type IIB: Driven steel piles; jacked steel piles											
Pile type IIIA: Driven grouted piles (low pressure grouting); driven rammed piles											
Pile type IIIB: High pressure grouted piles of large diameter > 250 mm; micropiles grouted under high pressure											
* *Upper bound values apply to careful execution and minimum soil disturbance during construction*											

6.12.3 General about next generation CPT-based methods

More recently, the boom in construction of offshore facilities inspired among others the development of more rigorous (and perhaps less conservative) methods for the design of piles driven in silica sands and clays, including open-ended pipe piles for which soil plugging effects will be important. Some of the most popular of these methods, that rely heavily on CPT measurements, are compendiously presented in the following. The general form of the expression that provides the collapse load Q_f of a pile of constant diameter D is:

(6.30) $$Q_f = Q_{sf} + Q_b - W_p = \pi D \int f_{sf}(z)dz + \left(\frac{\pi D^2}{4}\right) q_{bf} - W_p$$

where $f_{sf}(z)$ is the depth-dependent skin friction resistance (units: stress), q_{bf} is the end-bearing resistance at the pile toe (units: stress) and W_p (units: force) is the weight of the pile, defined earlier. In this section we cover closed-end and open-ended (where soil plugging effects are important) piles subjected to axial compressive loads: estimation of the ultimate geotechnical strength or collapse load in tension is covered later in this Part.

6.12.4 FUGRO-05 method for piles in coarse-grained soils

The FUGRO-05 method (Kolk *et al.* 2005) has been developed by Fugro Engineers BV, a consulting firm with long experience in the design of offshore foundations. The skin friction resistance f_{sf} is calculated from the cone resistance q_c, similar to the LCPC method, as:

(6.31) $$f_{sf} = 0.08 q_c \left(\frac{\sigma'_{z0}}{p_a}\right)^{0.05} \left(\frac{h}{R^*}\right)^{-0.9} \text{for} \frac{h}{R^*} \geq 4$$

(6.32) $$f_{sf} = 0.08 q_c \left(\frac{\sigma'_{z0}}{p_a}\right)^{0.05} (4)^{-0.9} \left(\frac{h}{4R^*}\right)^{-0.9} \text{for} \frac{h}{R^*} < 4$$

where σ'_{z0} is the vertical effective geostatic stress (again, the subscript $_0$ refers to *in situ* conditions before installation of the pile) at depth z, p_a is the atmospheric pressure, while the remaining geometrical parameters are defined in Figure 6.25.

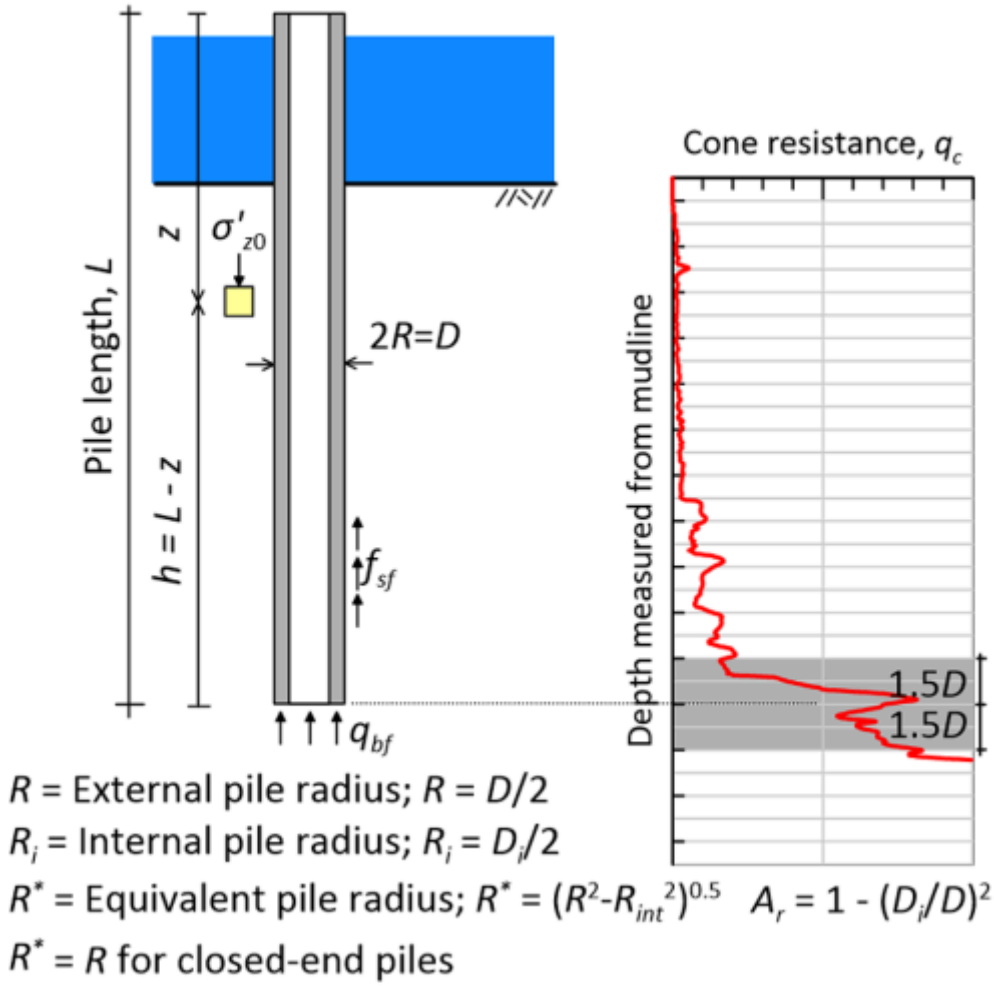

Figure 6.25. Parameters introduced in the estimation of the compressive collapse load of offshore piles in sand with CPT-based methods.

The end-bearing resistance at the pile toe q_{bf} (units: stress) is calculated from the average cone resistance at the pile toe, $q_{c(av)}$ which is determined according to Figure 6.24 as the average cone resistance over ± 1.5D from the pile toe (see also Figure 6.25):

$$\textbf{(6.33)}\quad \frac{q_{bf}}{p_a} = 8.5\left(\frac{q_{c(av)}}{p_a}\right)^{0.5} A_r$$

where the area ratio A_r is calculated as (Figure 6.25):

$$\textbf{(6.34)}\quad A_r = 1 - \left(\frac{D_i}{D}\right)^2$$

For solid piles it is of course A_r = 1. Note that the FUGRO method does not account for soil plug effects on the end-bearing resistance.

6.12.5 Imperial College ICP-05 method for piles in coarse-grained soils

The ICP-05 Method (Jardine *et al.* 2005) has been established from the analysis of field measurements obtained with the Imperial College Pile, a densely-instrumented kit developed at Imperial College, UK. For piles subjected to axial compressive load, the skin friction resistance (units: stress) f_{sf} is calculated as:

(6.35) $$f_{sf} = \sigma'_{hf} \tan \varphi_{i,cs} = (\sigma'_{he} + \Delta\sigma'_{rd}) \tan \varphi_{i,cs}$$

Whilst Eq. 6.35 features the same form as Eq. 6.10, the parameters introduced are different, and account for installation effects. First, instead of the peak interface friction angle φ_i, the skin friction resistance is correlated to the interface friction angle at constant volume (or at critical state) $\varphi_{i,cs}$, measured at large relative displacements when shearing at the soil-pile interface takes place under constant volume. This allows considering that slippage will take place along the soil-pile interface when the collapse load of the pile is reached, thus dilating sands will have reached their residual strength (see Figure 5.5). In lack of interface shear tests, Figure 6.26 can be used to obtain an estimate of $\varphi_{i,cs}$ as function of the median grain size of sand D_{50}.

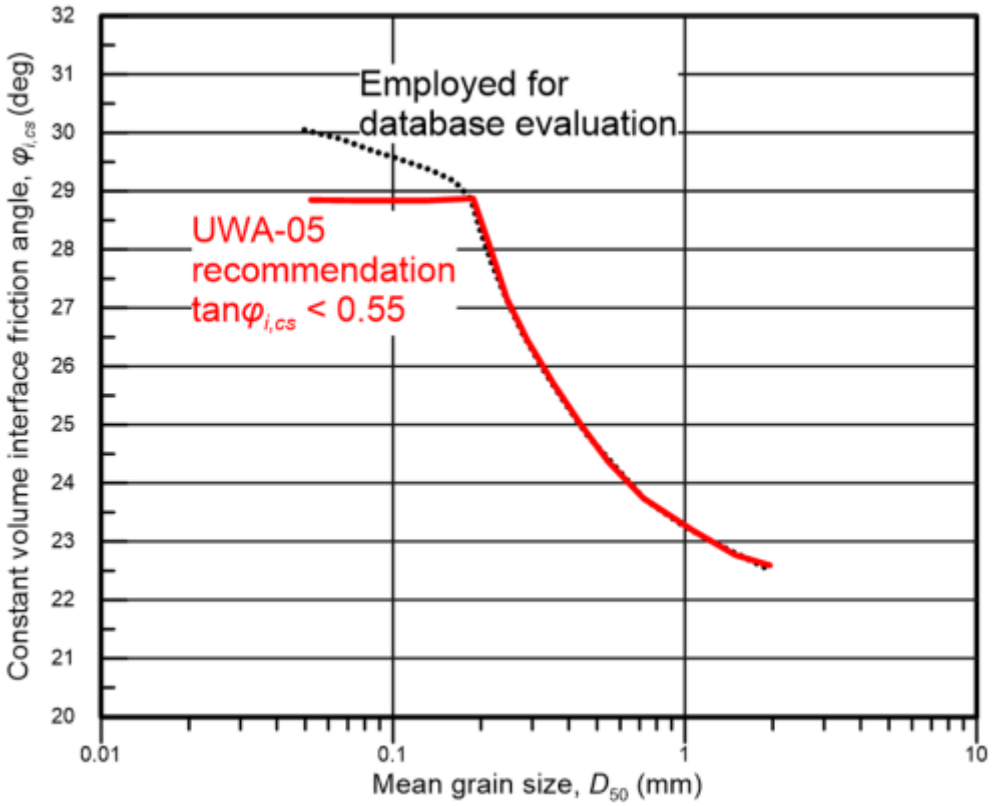

Figure 6.26. Variation of interface friction angle at constant volume $\varphi_{i,cs}$ with median grain size D_{50} (after Lehane et al. 2005). UWA-05 method does not recommend using $\tan\varphi_{i,cs}$ values higher than 0.55.

In addition, Eq. 6.35 correlates skin friction resistance with the normal effective stress acting at the soil-pile interface *when the collapse load is reached* (or the pile fails) σ'_{hf}, and not the *in situ* geostatic horizontal effective stress σ'_{h0} as β-Method does. The normal effective stress at the soil-pile interface σ'_{hf} is calculated as the sum of the normal effective stress acting at the interface after pile installation and equalisation of pore pressures σ'_{he}, and the change in the normal stress acting at the interface that takes place during axial loading of the pile $\Delta\sigma'_{rd}$. This change in normal stress takes place as the pile expands radially when compressed, and is related to dilation at the soil-pile interface. σ'_{hf} is correlated to cone resistance q_c as:

(6.36) $$\sigma'_{hf} = 0.029 q_c \left(\frac{\sigma'_{z0}}{p_a}\right)^{0.13} \left[\max\left(\frac{h}{R^*}, 8\right)\right]^{-0.38}$$

where all the symbols are defined in Figure 6.25. The change in normal stress during pile loading $\Delta\sigma'_{rd}$ is calculated on the basis of cavity expansion theory as:

(6.37) $$\Delta\sigma'_{rd} = 2G\left(\frac{\Delta r}{R}\right)$$

where Δr is the interface dilation, which can be taken equal to $\Delta r = 0.02$ mm for slightly rusted steel piles, and G is the shear modulus of soil. Lehane *et al.* (2005) recommend using the low strain shear modulus G_0 together with Eq. 6.37, as soil deformations in the vicinity of the pile shaft are small. Monzon (2006) proposes to estimate G_0 from CPT measurements using a modified version of the expression of Baldi *et al.* (1989):

(6.38) $$G_0 = q_c 1504.1 \left(\frac{q_c}{\sigma'_{z0}}\right)^{-0.7503}$$

For *closed-end piles*, the end-bearing resistance at the pile toe q_{bf} (units: stress) that develops when pile head displacement reaches about 10% of the pile's diameter D is calculated again from the average cone resistance at the pile toe, $q_{c(av)}$ as:

(6.39) $$q_{bf} = q_{c(av)} \max\left[1 - 0.5 \log \frac{D}{D_{CPT}}, 0.3\right]$$

where $D_{CPT} = 35.7$ mm is the standard cone diameter. Eq. 6.39 implies that the maximum pile diameter for which the formula works is of the order of $D = 0.9$ m, thus its use for larger piles is not recommended.

For *open-ended pipe piles*, the ICP-05 method employs different formulas for the calculation of q_{bf}, depending on whether the pile is completely plugged as consequence of arching (Figure 6.27c), or unplugged i.e., when soil coring takes place and there is relative movement between soil trapped inside the pile and the internal pile shaft (Figure 6.27a).

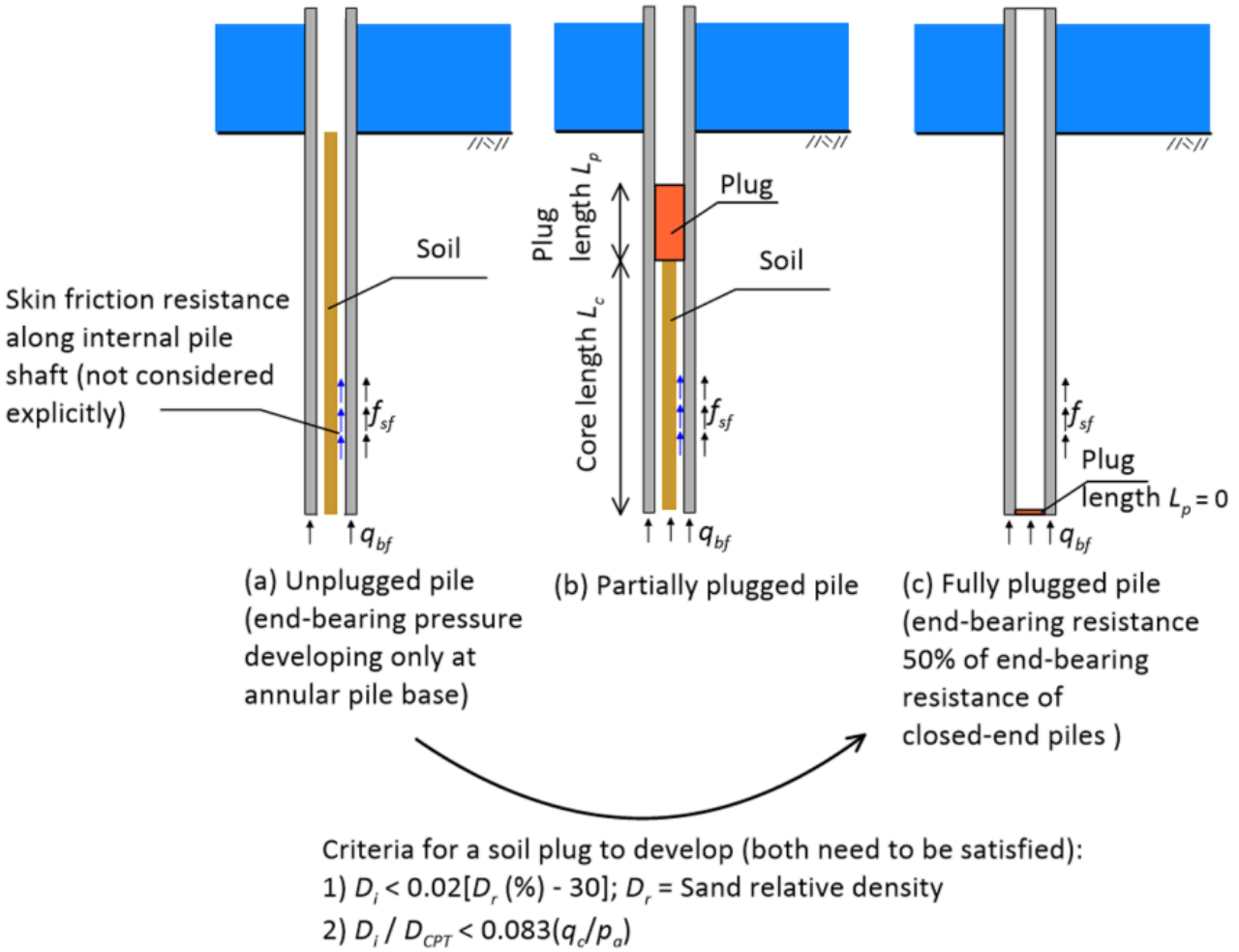

Figure 6.27. Soil plugging in open-ended pile piles driven in sand.

An empirical criterion to determine whether there sufficient arching for the formation of a full plug will develop (Figure 6.27c) is show in Figure 6.27, and both conditions must be satisfied. If the criterion is satisfied, the end-bearing resistance will be 50% of the resistance calculated with Eq. 6.39, but no less than the end-bearing resistance that will develop at the annual pile base i.e.:

(6.40) $$q_{bf} = q_{c(av)} \max\left[0.5 - 0.25 \log \frac{D}{D_{CPT}}, 0.15, A_r\right]$$

where the pile's area ratio A_r is defined in Eq. 6.34.

If the plugging criterion is not satisfied, then the pile should be considered as unplugged (Figure 6.27a) and the limiting end-bearing pressure is calculated as:

(6.41) $$q_{bf} = q_{c(av)} A_r$$

Note that the contribution of internal skin friction is not introduced explicitly into the calculation of the collapse load.

6.12.6 UWA-05 method for piles in sand

The UWA-05 method has been developed in the University of Western Australia by Lehane *et al.* (2005b), who reviewed the FUGRO-05, ICP-05 as well as the NGI-05 methods (not covered here for brevity), and subsequently established a unified set of recommendations which they tested against numerous pile load tests.

Calculation of the skin friction resistance f_{sf} (units: stress) that develops during axial compressive loading is based on the same concept as the ICP-05 method, and the same expression Eq. 6.35. However, calculation of the normal effective stress at the soil-pile interface at failure σ'_{hf} with the UWA-05 method is based on the following expression:

(6.42) $$\sigma'_{hf} = 0.03 q_c (A_{r,eff})^{0.3} \left[\max\left(\frac{h}{D}, 2 \right) \right]^{-0.5}$$

where $A_{r,eff}$ is the effective area ratio, that depends on the so-called *Incremental Filling Ratio IFR*. *IFR* is a parameter that accounts for the displacement experienced by soil in the vicinity of the toe of open-ended piles during pile driving, when full or partial soil plugging (Figure 6.27) takes place during pile driving. As such $A_{r,eff}$ is defined as:

(6.43) $$A_{r,eff} = 1 - IFR \left(\frac{D_i}{D} \right)^2$$

and the *IFR* is quantified as the increase in plug length with respect to the increase in pile's driven length:

(6.44) $$IFR = \frac{\Delta L_p}{\Delta L}$$

where ΔL_p is the increment of soil plug length L_p corresponding to a small increment of the driven pile length ΔL (Figure 6.27). Fully plugged and fully coring modes correspond to *IFR* = 0 and *IFR* = 1 respectively, while intermediate values correspond to partially plugged piles. Eq. 6.43 requires as input the *IRF* corresponding to the final $20D$ of pile penetration which, in lack of site-specific data, can be approximated as:

(6.45) $$IFR = \min\left[1, \left(\frac{D_i}{1.5} \right) \right]^{0.2} \quad (D_i \text{ in meters})$$

The change in normal stress during pile loading $\Delta\sigma'_{rd}$ is calculated again with Eq. 6.37. Note that Lehane *et al.* (2005b) recommend the following expression, instead of Eq. 6.38, for calculating G_0 to be used together with Eq. 6.37:

(6.46) $$G_0 = q_c 185 (Q')^{-0.7}$$

Where:

(6.47) $$Q' = \frac{\left(\frac{q_c}{p_a} \right)}{\left(\frac{\sigma'_{z0}}{p_a} \right)^{0.5}}$$

is a dimensionless expression for cone resistance that has been introduced in Part 1.

The UWA-05 method does not differentiate the calculation of the end-bearing resistance at the pile toe q_{bf} (units: stress) for open and closed-end piles, as plugging effects are introduced by means of the filing ratio.

The end-bearing resistance at the pile toe q_{bf} associated with pile head displacement about 10% of the pile's diameter D is calculated as function of an alternative form of the average cone resistance at the pile toe, $q_{c(avD)}$ as:

(6.48) $$q_{bf} = q_{c(avD)} \left(0.15 + 0.45 A_{rb,eff}\right)$$

Instead of correlating q_{bf} to the average cone resistance at the pile toe $q_{c(av)}$, Lehane *et al.* (2005b) recommend using the more complex "Dutch" averaging method described in Figure 6.28, and calculate $q_{c(avD)}$ instead. The effective area ratio $A_{rb,eff}$ is equal to $A_{rb,eff} = 1$ for closed-ended or fully-plugged piles, and can be calculated with the expression found in Figure 6.28. The *Final Filling Ratio FFR* in Figure 6.28 is the incremental filling ratio measured during the last stages of pile driving, and can be approximated again with Eq. 6.45.

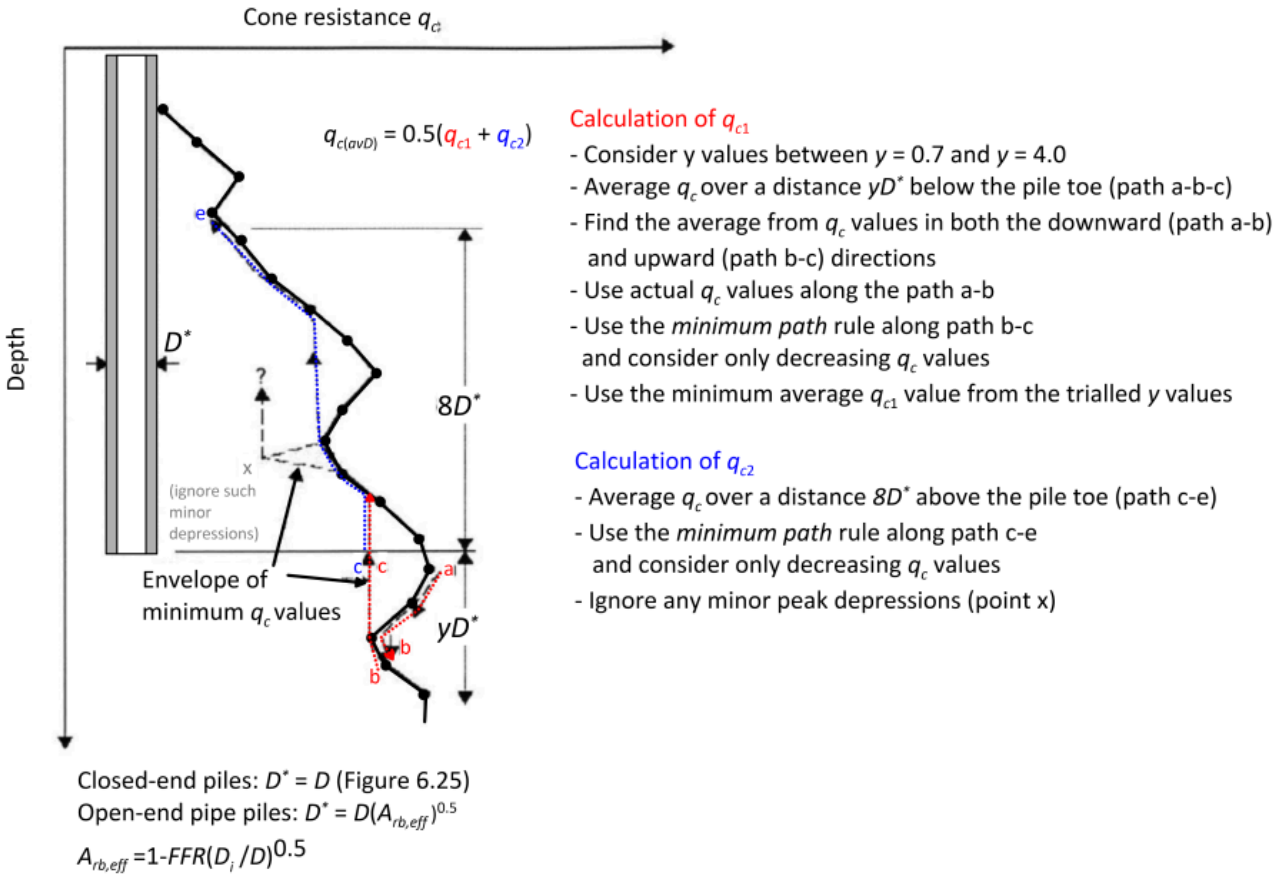

Figure 6.28. Calculation of $q_{c(avD)}$ with the Dutch averaging method (after Lehane *et al.* 2005).

6.12.7 ICP method for piles in fine-grained soils

The last CPT-based method for predicting the collapse compressive load of piles that is presented in this Chapter is the method developed by researchers at the Imperial College, UK (Jardine *et al.* 2005) on the basis on field tests with the Imperial College Pile ICP installed in clay-type soils. We refer to this as CPT-based method, despite the fact that the predicted skin friction resistance is independent of the cone resistance, but rather is function of the overconsolidation ratio, clay sensitivity, the geostatic vertical effective stress, and of course of the soil-pile interface friction angle.

The general formula Eq. 6.30 applies to this method too, and the expressions used to obtain the skin

friction resistance f_{sf} and end-bearing resistance q_{bf} for piles driven in fine-grained soils are presented in the following. It must be stressed that, although the method provides a single expression for the short-term and long-term skin friction resistance, unlike the α-Method it is not based on total stress analysis but rather on effective stress principles. However, the effect of pore pressures that will develop during pile loading is accounted for, via the loading factor K_f/K_c.

The skin friction resistance is calculated with an expression similar to Eq. 6.35, as:

$$\textbf{(6.49)}\quad f_{sf} = \sigma'_{hf} \tan\varphi_{i,f} = \left(\frac{K_f}{K_c}\right) \sigma'_{he} \tan\varphi_{i,f}$$

where σ'_{hf} is the normal stress acting at the soil-pile interface at failure, while σ'_{he} is the normal stress acting at the soil-pile interface prior to pile loading and after equalisation of stresses induced during pile installation. $\varphi_{i,f}$ in Eq. 6.49 is the interface friction angle at failure, and should be taken between the peak interface friction angle $\varphi_{i,peak}$ and the residual $\varphi_{i,residual}$, which are both provided in Figure 6.29 as function of the plasticity index of clay PI. Of course a conservative approach is to consider $\varphi_{i,f} = \varphi_{i,residual}$.

For closed-end piles, the normal stress σ'_{he} acting at the soil-pile interface after equalisation is provided as function of the vertical *in situ* effective stress at the particular depth and a factor K_c as:

$$\textbf{(6.50)}\quad \sigma'_{he} = K_c\sigma'_{z0} = \sigma'_{z0}\left[2.2 + 0.016\mathrm{OCR} - 0.87\Delta I_{vy}\right]\mathrm{OCR}^{0.42}\left[\max\left(\frac{h}{R}, 8\right)\right]^{-0.20}$$

where OCR is the overconsolidation ratio, or (more rigorously, since stresses are not always vertical) the yield stress ratio YSR = $\sigma'_{vy}/\sigma'_{z0}$; $\Delta I_{vy} = \log_{10}S_t$ is the logarithm of the clay's sensitivity (Section 1.8.3); h/R is the normalised distance from the pile toe, defined in Figure 6.25. It is reminded here that for common clays that do not develop brittle shear bands upon shearing $(S_u/\sigma'_{z0}) = (S_u/\sigma'_{z0})_{NC}\mathrm{YSR}^{0.85}$ where S_u/σ'_{z0} is the undrained shear strength ratio in triaxial compression. Finally, the loading factor K_f/K_c in Eq. 6.49 accounts for the reduction in the normal stress acting at the soil-pile interface during loading of the pile, and it is taken equal to $K_f/K_c = 0.8$.

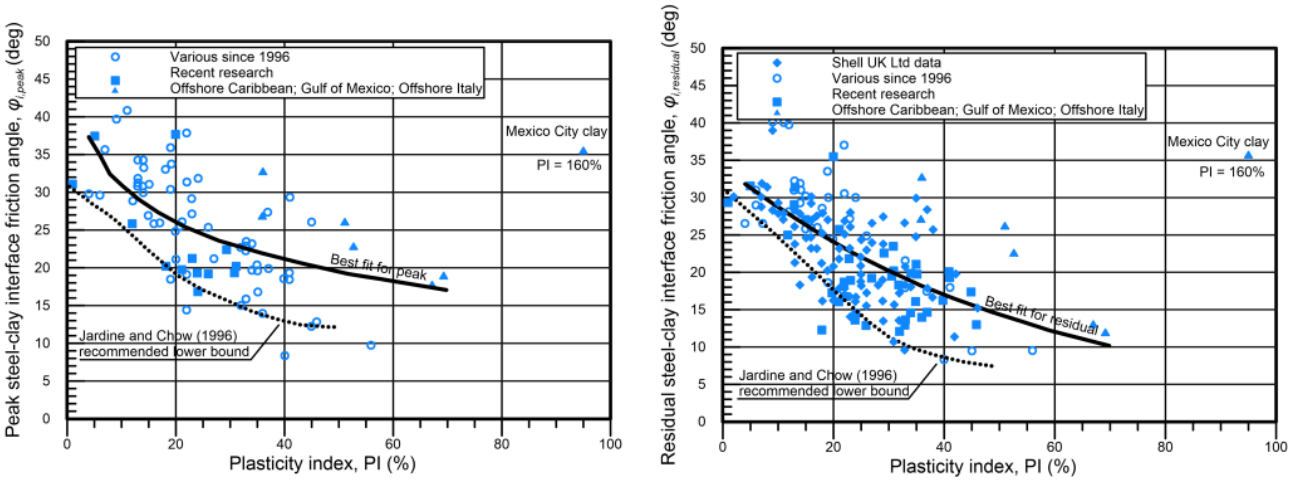

Figure 6.29. (a) Peak and (b) residual soil-steel pile interface friction angle, determined via ring shear tests (after Jardine *et al.* 2005).

For open-ended piles, the normal stress σ'_{he} in Eq. 6.50 should be evaluated while considering the equivalent radius R^* in Figure 6.25.

For *closed-end piles*, the end-bearing resistance at the pile toe q_{bf} (units: stress) that develops when pile head displacement reaches about 10% of the pile's diameter D is calculated again from the average cone resistance at the pile toe, $q_{c(av)}$ as:

$$\textbf{(6.51)}\quad q_{bf} = 0.8q_{c(av)} \text{ for short-term conditions (undrained loading)}$$

(6.52) $q_{bf} = 1.3q_{c(av)}$ for long-term conditions (drained loading)

where the average cone resistance at the pile toe $q_{c(av)}$ is determined according to Figure 6.24 as the average cone resistance over ± 1.5D from the pile toe (see also Figure 6.25).

For *open-ended pipe piles*, the ICP method employs different formulas for the calculation of q_{bf}, depending if the pile is completely plugged or unplugged. The criterion that must be satisfied for plugging to occur under static loading is:

(6.53) $$\left[\frac{D_i}{D_{CPT}} + 0.45\left(\frac{q_c}{p_a}\right)\right] < 36$$

where D_{CPT} = 35.7 mm is the standard cone diameter. If the criterion is satisfied then q_{bf} is estimated to be half the resistance from Eqs. 6.51 and 6.52, or:

(6.54) $q_{bf} = 0.4q_{c(av)}$ for short-term conditions (undrained loading)

(6.55) $q_{bf} = 0.65q_{c(av)}$ for long-term conditions (drained loading)

If the criterion is not satisfied then coring will occur, and the limiting end-bearing pressure will develop only on the annular area of steel. In this case:

(6.56) $q_{bf} = q_{c(av)}A_r$ for short-term conditions (undrained loading)

(6.57) $q_{bf} = 1.6q_{c(av)}A_r$ for long-term conditions (drained loading)

where the area ratio A_r is defined in Eq. 6.34. As in the case of piles in sand, the contribution of internal skin friction is not introduced explicitly into the calculation of the collapse load.

6.13 DESIGN OF DRILLED SHAFTS SOCKETED IN SOFT ROCK TO RESIST AXIAL COMPRESSIVE LOADS

Methods developed for the design of piles founded in soil are not appropriate (i.e., will probably result in particularly conservative designs) if used to design drilled shafts which toe is socketed into even relatively soft rock, such as the sandstone/siltstone formations encountered along the East Coast of Australia. As such, design of drilled shafts socketed in soft rock in practice is performed using custom methods, such as the method of Rowe and Armitage (1987a), which has been used successfully for the design of numerous projects in Australia. Rowe and Armitage's method is based on satisfying a design settlement criterion when the drilled shaft is subjected to a factored axial compressive load at its head, and ensuring that collapse (bearing capacity failure) under the same axial load will be avoided. Therefore, there is no clear differentiation between Serviceability Limit State (SLS) and Ultimate Limit State (ULS), as the method had originally been developed to be used together with traditional partial safety factors (limit state design). Here the method is adapted to conform with AS2159 requirements. Note that the following are applicable to rockmass without significant presence of weak seams. If this is the case, the reader is referred to the original publications of Rowe and Armitage for the expressions required to adjust the method. However, the general concepts described in the following remain the same.

It should be noted that the method of Rowe and Armitage, and the associated "design charts" presented in the following, have resulted from numerical analyses of a single pile subjected to an axial compressive load. Hence, instead of using the provided charts etc., one can attempt to replicate Rowe and Armitage simulations, and design the drilled shaft on the basis of project-specific numerical simulations. For the model to be able to successfully simulate the behaviour of socketed drilled shafts, it is critical that the shear resistance at the shaft-rock interface is modelled properly, and the parameters recommended in Rowe are Armitage have been validated against numerous tests on sandstone/siltstone formations. Rowe and Armitage have used an elastic-perfectly plastic failure criterion for the interface, and account for degradation of interface strength with increasing relative displacement, as well as (degrading) dilation angle to account for interface roughness. Details on the model are provided in Rowe and Armitage (1987b).

6.13.1 Design of a fully socketed drilled shaft

If the drilled shaft is not recessed i.e., the interface between the shaft and the rock is fully bonded (Length $L_e = 0$, Figure 6.30) and there are no weathered seams along the wall of the socket, the design method is as follows:

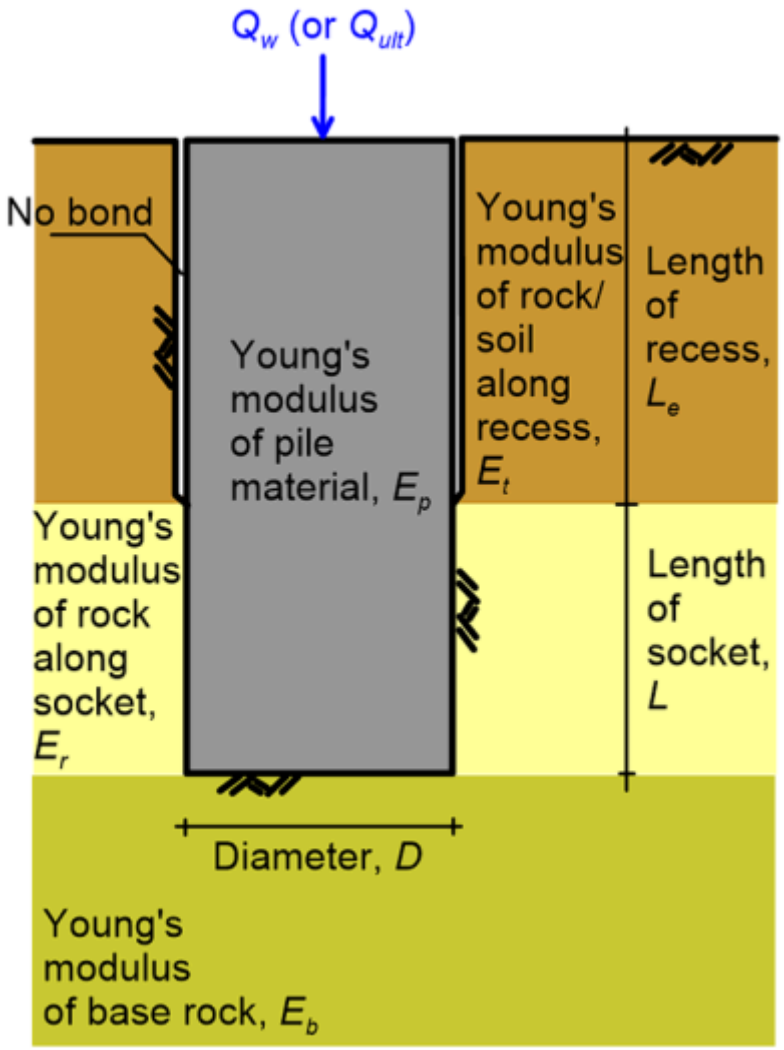

Figure 6.30. Schematic of a recessed drilled shaft (pier) socketed in rock (after Rowe and Armitage 1987).

Step 1:

We first determine the design parameters. These include an initial estimate of the pile diameter D, the design settlement ρ_D, which depends on the requirements of the project, the modulus of the drilled shaft E_p, which depends on concrete properties, and the *characteristic* value of the unconfined compressive strength of rock cores σ_c, from the interpretation of unconfined compressive (UCS) tests on rock samples. Point Load test results can be used to supplement UCS test data, however the Geotechnical Engineer must appreciate the uncertainties associated with using point load test data to estimate the unconfined compressive strength, and factor these uncertainties in the selection of the characteristic σ_c value. In addition, the design axial compressive load at the ULS ($Q_{ult} = S^*$) and the serviceability axial compressive load (Q_w) acting on the pile head must be estimated, using AS1170 provisions and appropriate load factors for Q_{ult}. Note that usually the settlement criterion will govern the design, and not the ULS collapse load criterion. Since SLS axial compressive loads calculated according to AS1170 are not factored, the maximum acceptable settlement value must be prudently selected, to account for the probability of exceedance of the predicted settlement through the design life of the project.

Step 2:

Estimate the characteristic value of the side shear resistance that can develop at the shaft-rock interface τ_d

and the *characteristic* values of the rockmass Young's modulus E_b underneath the shaft toe and along the length of the socket E_r. Note that the symbol τ_d is used here to denote side shear resistance developing on piles in rock, instead of the symbol f_{sf} used in the previous sections to denote skin friction resistance of piles in soil, despite both being shear stresses at the interface between a pile and its surrounding medium. In lack of site-specific data, the following expressions by Rowe and Armitage (1984) can be used to estimate the abovementioned parameters from the characteristic value of the unconfined compressive strength of rock cores σ_c (in MPa).

(6.58) $\tau_d = 0.45\sqrt{\sigma_c}\ (\text{MPa})$ for regular clean sockets (roughness R1-R3: Table 6.7)

(6.59) $\tau_d = 0.60\sqrt{\sigma_c}\ (\text{MPa})$ for clean rough sockets (roughness R4: Table 6.7)

(6.60) $E_b, E_r = 215\sqrt{\sigma_c}\ (\text{MPa})$

Step 3:

Calculate the dimensionless socket length L/D required for the entire serviceability load to be carried by side shear:

(6.61) $$\left(\frac{L}{D}\right)_{\max} = \frac{Q_w}{(\pi D^2 \tau_d)}$$

Table 6.7. Roughness classification (Pells *et al.* 1980).

Roughness class	Description
R1	Straight, smooth-sided socket, grooves or indentations less than 1 mm deep
R2	Grooves of depth 1 to 4 mm, width greater than 2 mm, at spacing 50 to 200 mm
R3	Grooves of depths 4 to 10 mm, width greater than 5 mm, at spacing 50 to 200 mm
R4	Grooves or undulations of depth greater than 10 mm, width greater than 10 mm, at spacing 50 to 200 mm

The subscript $_{\max}$ in the above Eq. 6.61 denotes the dimensionless socket length required for all the load to be carried by side shear i.e., no load is to be transferred to the shaft's toe.

Step 4:

Calculate the design settlement influence factor I_d:

(6.62) $$I_d = \frac{\rho_D E_r D}{Q_w}$$

Step 5a:

We can now select the length of the socket L (see Figure 6.30) required to achieve the target design settlement influence factor, while allowing for slip at the shaft-rock interface i.e., a percentage of the serviceability load Q_w transferred to the toe of the shaft. This requires calculating first the dimensionless moduli E_p/E_r and E_b/E_r and selecting the appropriate design chart from Figures 6.31 to 6.35. Accordingly, we draw a straight line that connects the coordinates (L/D = 0, Q_{bw}/Q_w = 100%) and ($L/D = (L/D)_{max}$, Q_{bw}/Q_w = 0) i.e., the red line drawn indicatively in Figure 6.31. Here Q_{bw} is the serviceability load

transferred to the toe of the shaft, expressed as a percentage of the serviceability load applied at the head Q_w. The intersection of that straight line with the curve corresponding to the I_d value calculated from Eq. 6.62 provides: i) The design dimensionless length $(L/D)_{design}$, from which the required pile length to satisfy the settlement criterion is calculated, and ii) The design load ratio (Q_{bw}/Q_w)design that provides the load transferred to the toe of the shaft under serviceability conditions.

Step 5b:

It is not guaranteed that an intersection of the straight line connecting (L/D = 0, Q_{bw}/Q_w = 100%) and ($L/D = (L/D)_{max}$, Q_{bw}/Q_w = 0) and of the curve corresponding to the I_d value calculated from Eq. 6.62 can be found. In this case we need to check first if the drilled shaft can be designed so that no slip occurs at the shaft-rock interface under serviceability conditions (elastic design). This is achieved by selecting first the appropriate chart from Figures 6.36 and 6.37 and drawing a horizontal line on the elastic settlement factor I charts for $I = I_d$ i.e., the red line drawn indicatively in Figure 6.36. If this line intersects the E_p/E_r curve corresponding to the particular shaft, the drilled shaft can be designed elastically, and the required dimensionless pile length $(L/D)_{design}$ can be read from the same figure (see Figure 6.36). Next, the percentage of the serviceability load transferred to the toe $(Q_{bw}/Q_w)_{design}$ can be estimated from the elastic load distribution charts, as presented indicatively in Figure 6.36.

Step 5c:

If no intersection point can be found between the horizontal line $I = I_d$ and the E_p/E_r curve, then the pile must be re-designed, by changing the selected diameter D (or the settlement criterion).

Step 6:

Following the design of the pile to satisfy the serviceability criterion, we must now check that the pressure at the toe of the shaft does not exceed the allowable value at the ultimate limit state. The end bearing stress at the toe of the shaft is calculated as:

(6.63) $$q_b = \frac{\left(\frac{Q_{bw}}{Q_w}\right)_{design} Q_{ult}}{\left(\frac{\pi D^2}{4}\right)}$$

An important assumption underlying the above Eq. 6.63 is that the percentage of the load transferred at the toe remains the same under both SLS and ULS conditions. This may not be the case e.g., if the pile has been designed elastically for serviceability conditions. As such we should calculate the load ratio $(Q_b/Q)_{design}$ under ULS conditions by repeating Steps 3-5 while considering Q_{ult} instead of Q_w in the denominator and an appropriate settlement value e.g., $\rho=(Q_{ult}/Q_w)\rho_D$. The axial stress at the toe of the shaft must be lower than the unconfined compressive strength of rock, multiplied by the geotechnical reduction factor:

(6.64) $$q_b \leq \varphi_{gb}\sigma_c$$

The above criterion intends to ensure that no significant yielding will take place in the rock underneath the shaft toe. In addition to that, the end-bearing resistance at the base of the shaft q_{bf} must not exceed 2.5 times the factored unconfined compressive strength $\varphi_{gb}\sigma_c$:

(6.65) $$q_{bf} \leq 2.5\varphi_{gb}\sigma_c$$

The factor 2.5 in Eq. 6.65 resulted from field tests on socketed piles, and is the base pressure when yield of the drilled shaft was observed as a change in the shape of the load-displacement curve. The limiting end-bearing pressure q_{bf} is calculated as:

(6.66a) $$q_{bf} = \frac{Q_{ult}}{\left(\frac{\pi D^2}{4}\right)} - 4f\frac{L}{D}\tau_d \text{ when } \frac{Q_{ult}}{\left(\frac{\pi D^2}{4}\right)} \geq 4f\frac{L}{D}\tau_d$$

(6.66b) $$q_{bf} = 0 \text{ when } \frac{Q_{ult}}{\left(\frac{\pi D^2}{4}\right)} \leq 4f\frac{L}{D}\tau_d$$

The factor f in Eq. 6.66 intends to ensure that even when the rock-shaft friction mobilised in the field is less than the value assumed in the design τ_d, there will be sufficient margin of safety against collapse. Rowe and Armitage recommend to take $f = 0.3$ i.e., to assume that only 30% of the expected shear resistance is mobilised. Both Eqs 6.64 and 6.65 must be satisfied for the design to be acceptable.

6.13.2 Design of a recessed drilled shaft

Rowe and Armitage recommend to initially completely ignore the contribution of the surficial layers (length L_e where no bond exists at the shaft-rock interface, Figure 6.30) to the axial capacity of recessed drilled shafts, and design the shaft according to the steps 1-6 above. This approach will produce a reasonably accurate design if the drilled shaft is designed so that slip at the socketed shaft length-rock interface takes place i.e., if an intersection point can be established in the charts presented in Figures 6.31 to 6.35. Elastic shortening of recessed piles may contribute significantly to their settlement. Therefore, the elastic shortening of the recess, calculated using theory of elasticity while considering the recessed section of the pile as 1-D rod as $\rho_s = 4L_eQ_w/(\pi D^2E_p)$, must be subtracted from ρ_D when calculating the design settlement influence factor for recessed piles, I_d in Step 4.

However, if an intersection point could not be established, and the shaft is designed to perform elastically following step 5c, ignoring the contribution of the surficial layers may be too conservative. In this case, the contribution of the recessed part of the drilled shaft to the axial capacity can be accounted for in the design as follows: After having calculated the design dimensionless length $(L/D)_{design}$ from step 5a, calculate the settlement reduction factor $(RF)_\rho$ from Figures 6.38 to 6.40 as function of the parameters L/D, L_e/D, E_t/E_r and E_p/E_r (see Figure 6.30 for definitions). Subsequently adjust the design settlement influence factor I_d as:

(6.67) $$I_d^* = \frac{I_d}{(\mathrm{RF})_\rho}$$

and repeat step 5b using the adjusted value of the settlement influence factor I^*_d. During repeating step 5c a new value of $(L/D)^*_{design}$ will be calculated, therefore $(RF)_\rho$ may have to be calculated again and the process may have to be iterated until convergence is achieved.

Notice from Figure 6.40 that if the recess consists of (relatively soft) soil layers i.e., the ratio of E_t/E_r attains values significantly lower than unity, then the settlement reduction factor $(RF)_\rho$ attains values close to unity i.e., the contribution of shaft resistance along the part of the pile in soil to reducing settlement of the drilled shaft will be trivial.

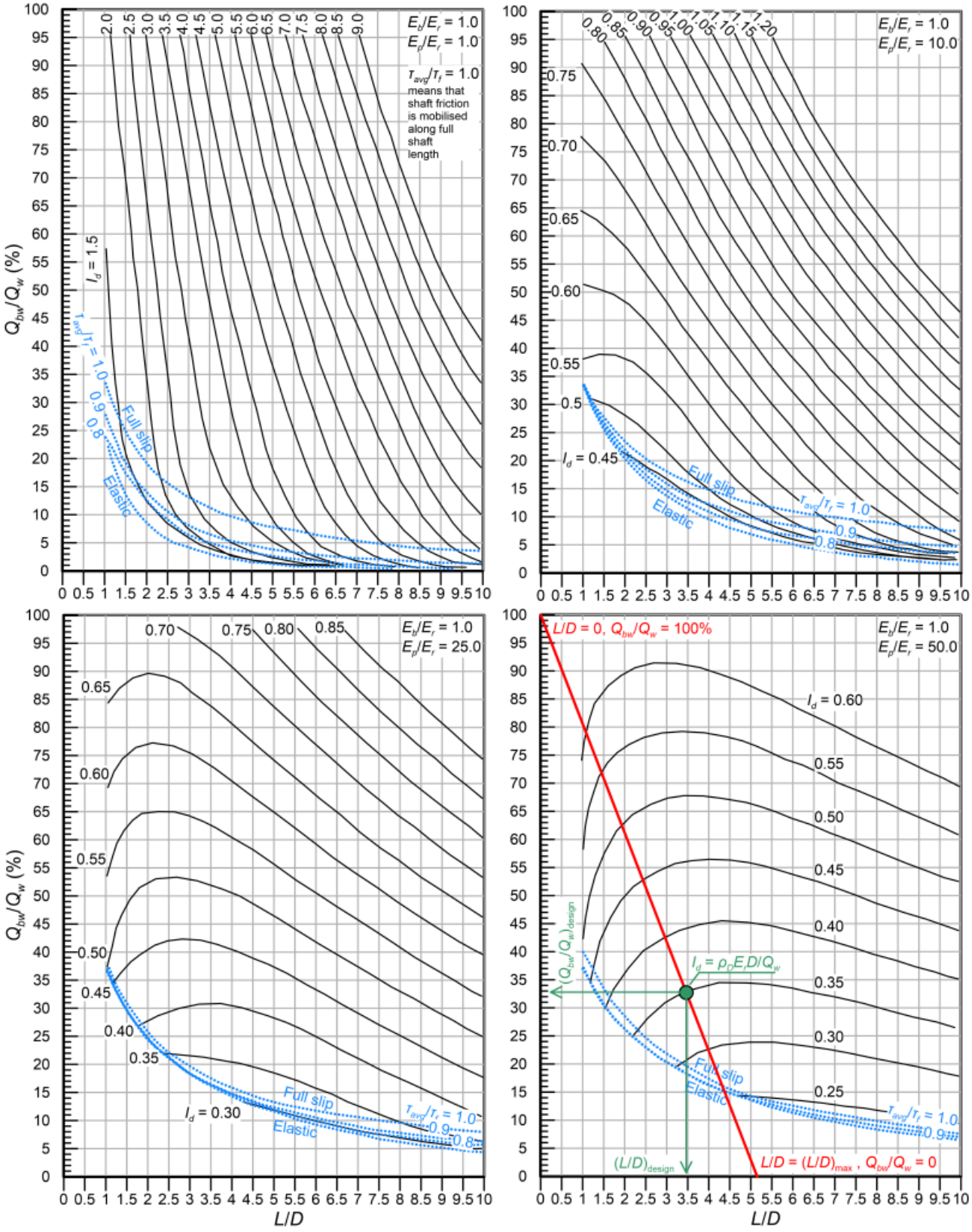

Figure 6.31. Calculation of settlement influence factor I_d for fully socketed drilled shafts. Results for E_b/E_r = 1 and E_p/E_r = 1, 10, 25 and 50 (after Rowe and Armitage 1984).

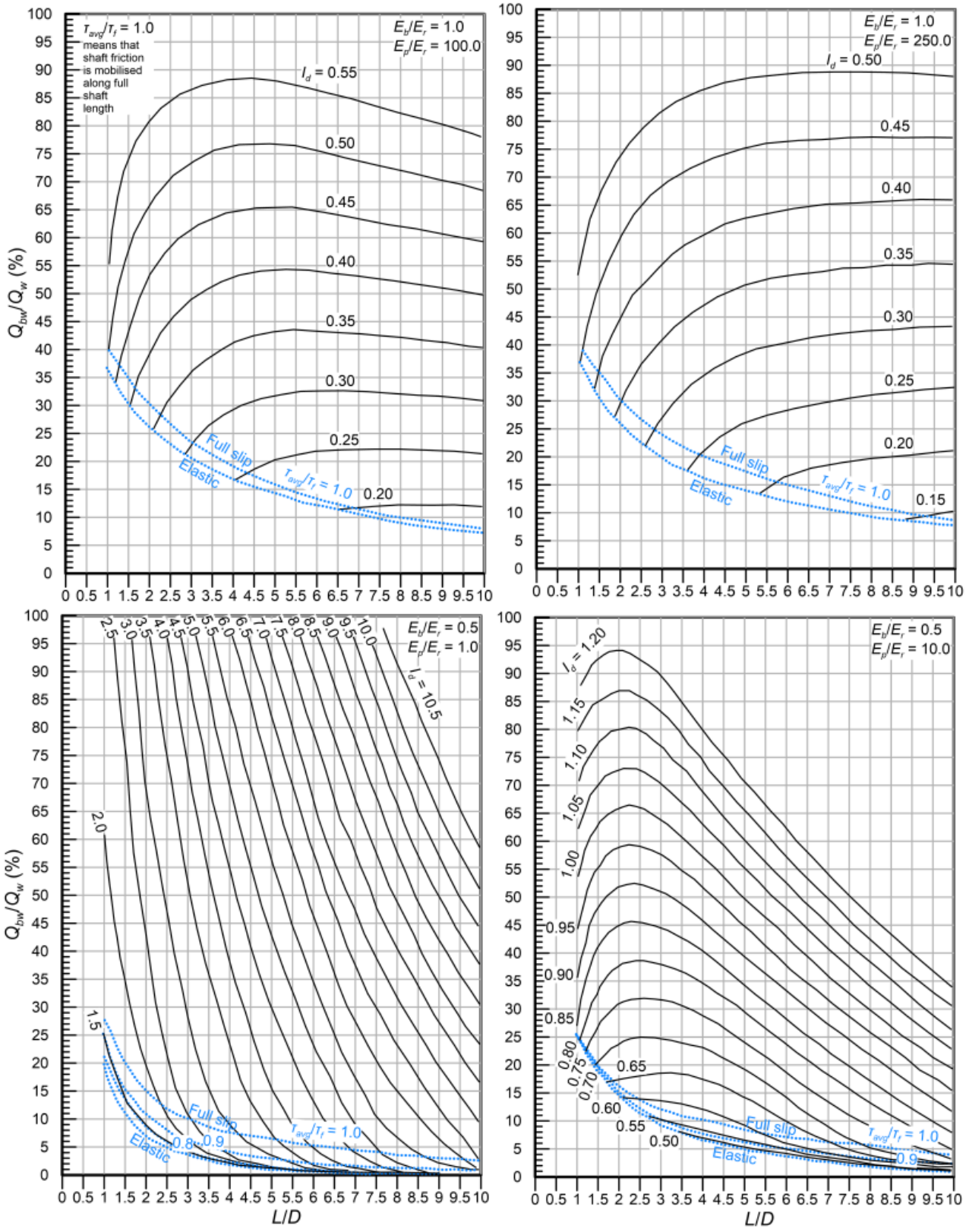

Figure 6.32. Calculation of settlement influence factor I_d for fully socketed drilled shafts. Results for E_b/E_r = 1 and E_p/E_r = 100, 250; E_b/E_r = 0.5 and E_p/E_r = 1, 10 (after Rowe and Armitage 1984).

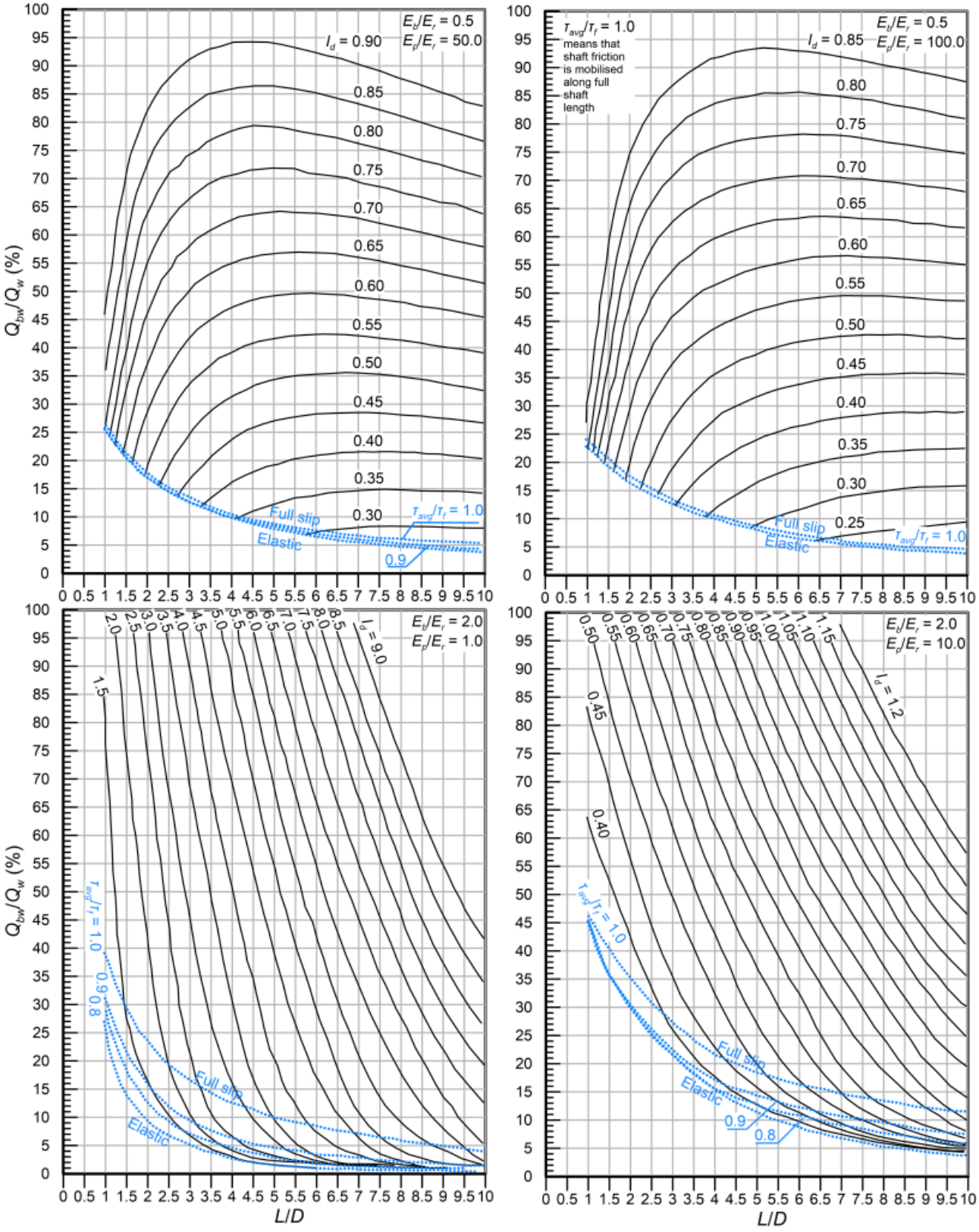

Figure 6.33. Calculation of settlement influence factor I_d for fully socketed drilled shafts. Results for E_b/E_r = 0.5 and E_p/E_r = 50, 100; E_b/E_r = 2 and E_p/E_r = 1, 10 (after Rowe and Armitage 1984).

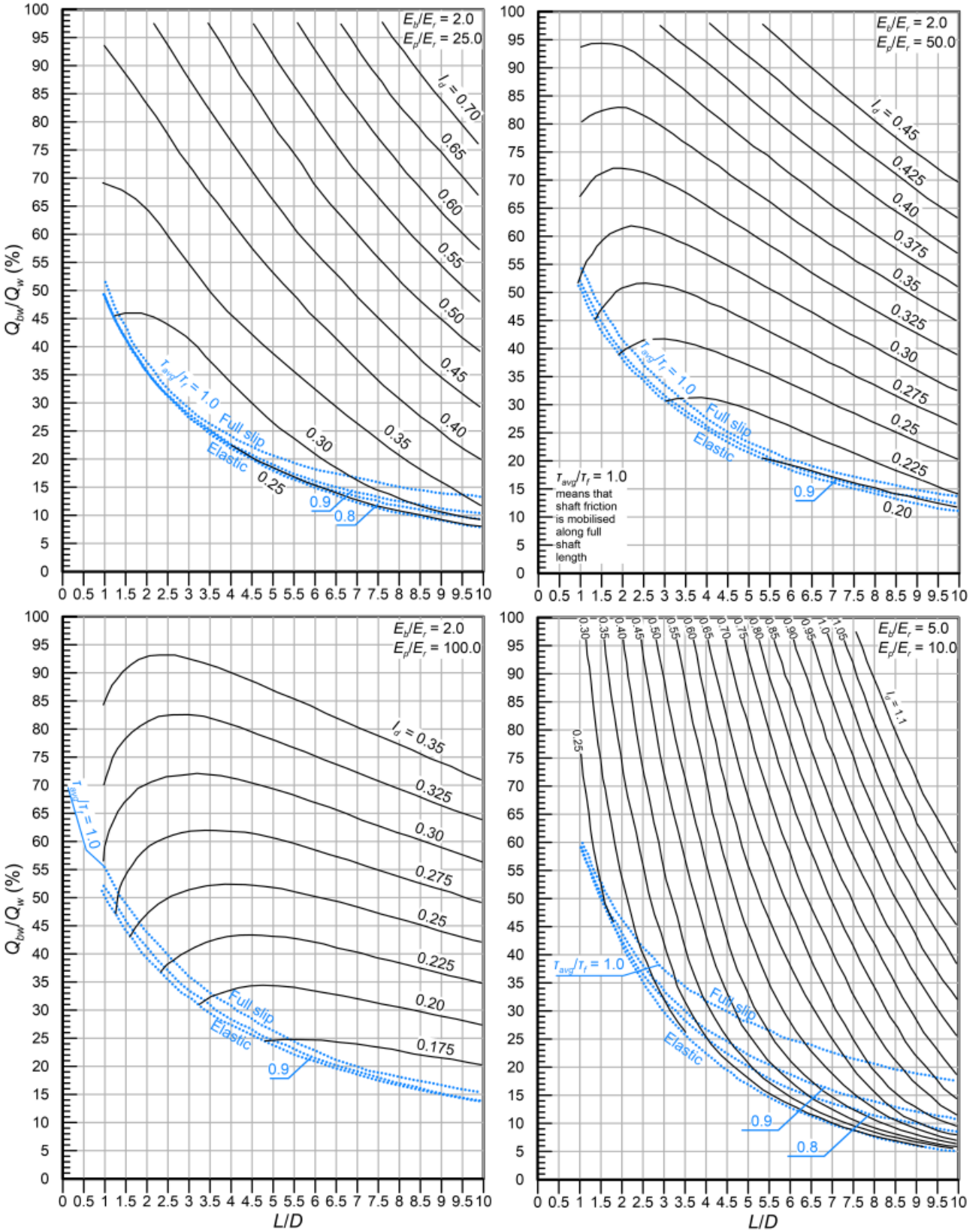

Figure 6.34. Calculation of settlement influence factor I_d for fully socketed drilled shafts. Results for E_b/E_r = 2 and E_p/E_r = 25, 50, 100; E_b/E_r = 5 and E_p/E_r = 10 (after Rowe and Armitage 1984).

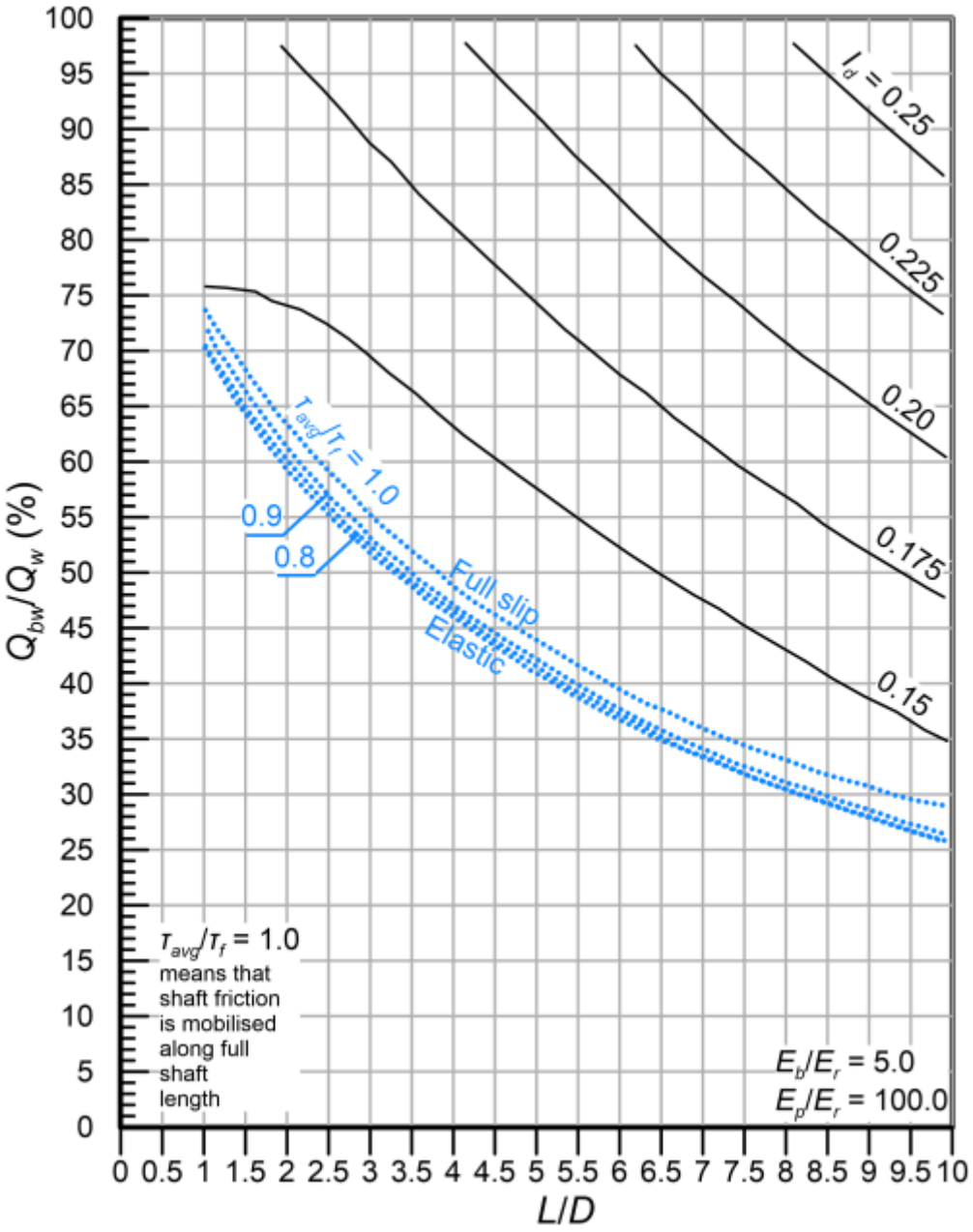

Figure 6.35. Calculation of settlement influence factor I_d for fully socketed drilled shafts. Results for E_b/E_r = 5 and E_p/E_r = 100 (after Rowe and Armitage 1984).

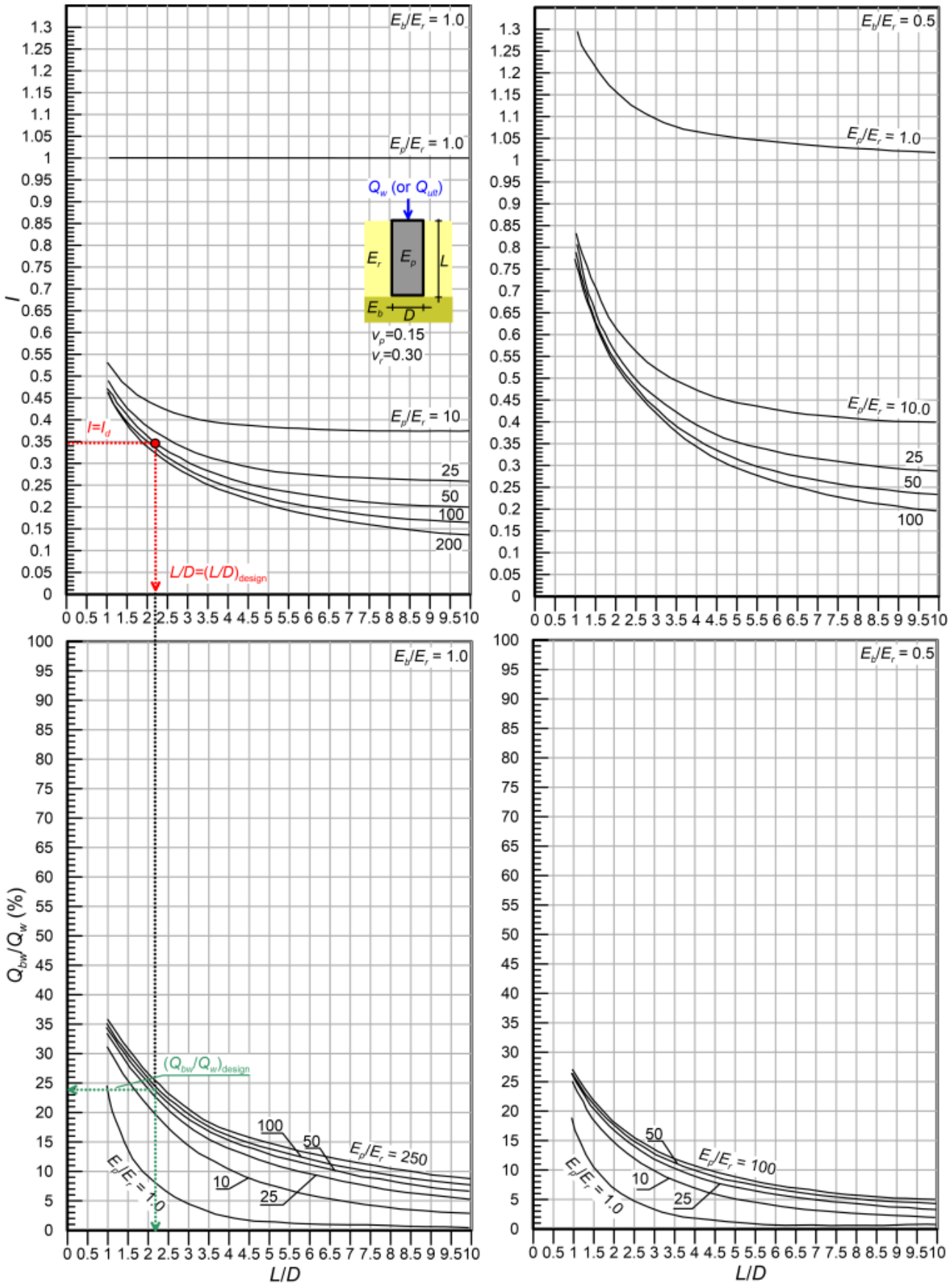

Figure 6.36. Calculation of elastic settlement influence factor *I* (top) and elastic load distribution (bottom) for fully socketed drilled shafts. Results for E_b/E_r = 1 and E_b/E_r = 0.5 (after Rowe and Armitage 1984).

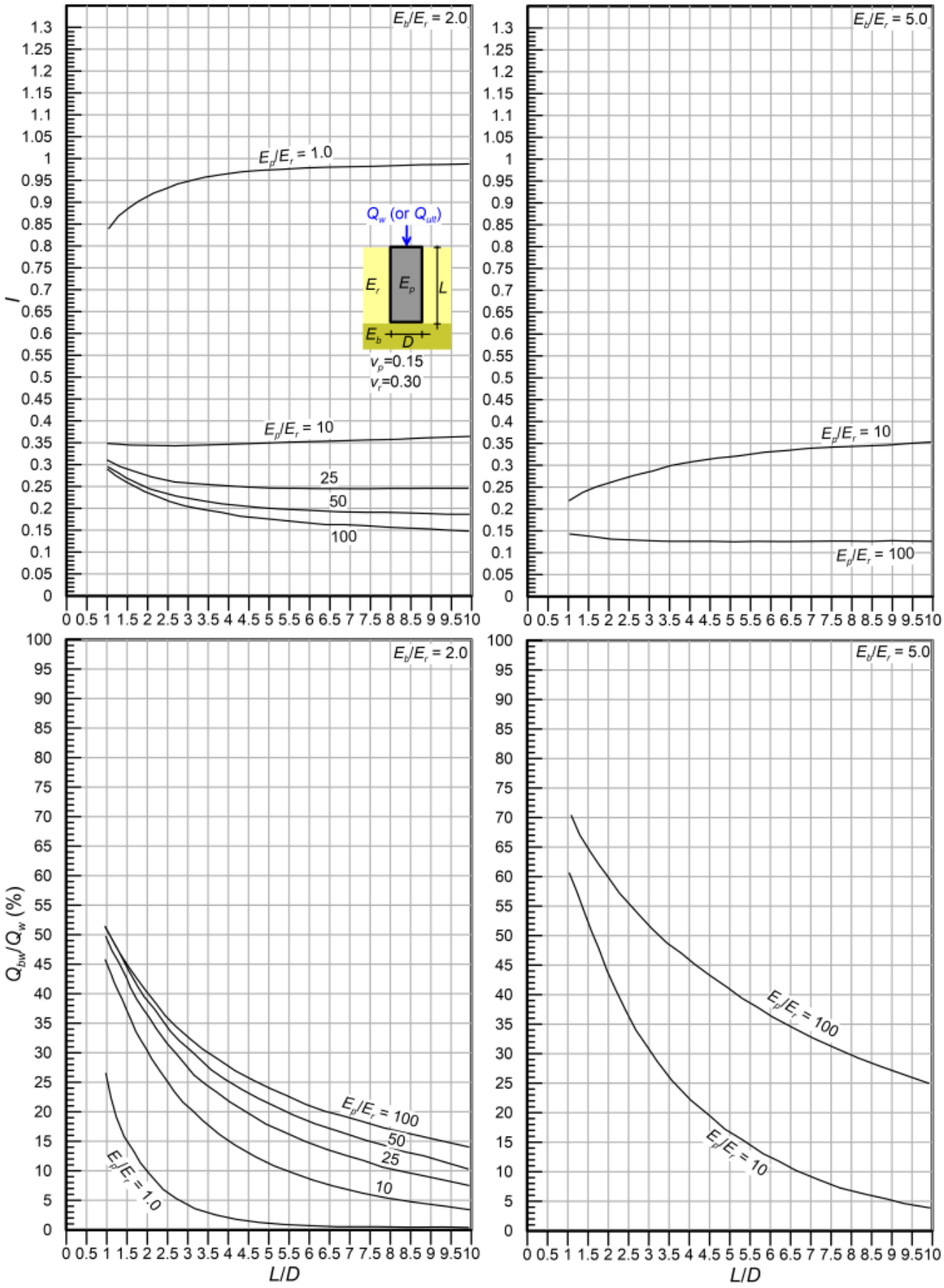

Figure 6.37. Calculation of elastic settlement influence factor *I* (top) and elastic load distribution (bottom) for fully socketed drilled shafts. Results for E_b/E_r = 2 and E_b/E_r = 5 (after Rowe and Armitage 1984).

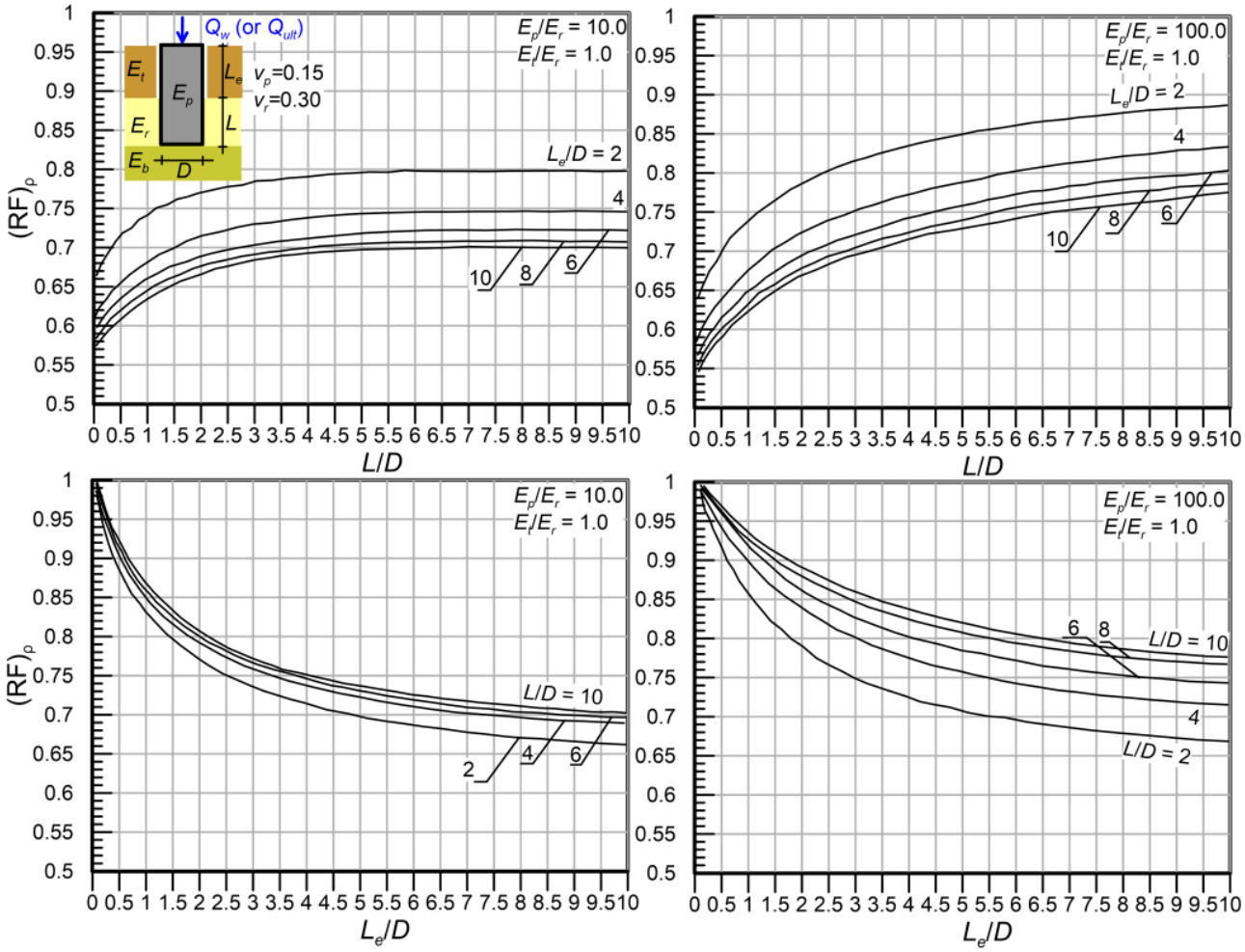

Figure 6.38. Reduction factors for a recessed socket as function of the dimensionless lengths L/D and L_e/D. Results for E_t/E_r = 1 and E_p/E_r = 10 and 100 (after Rowe and Armitage 1984).

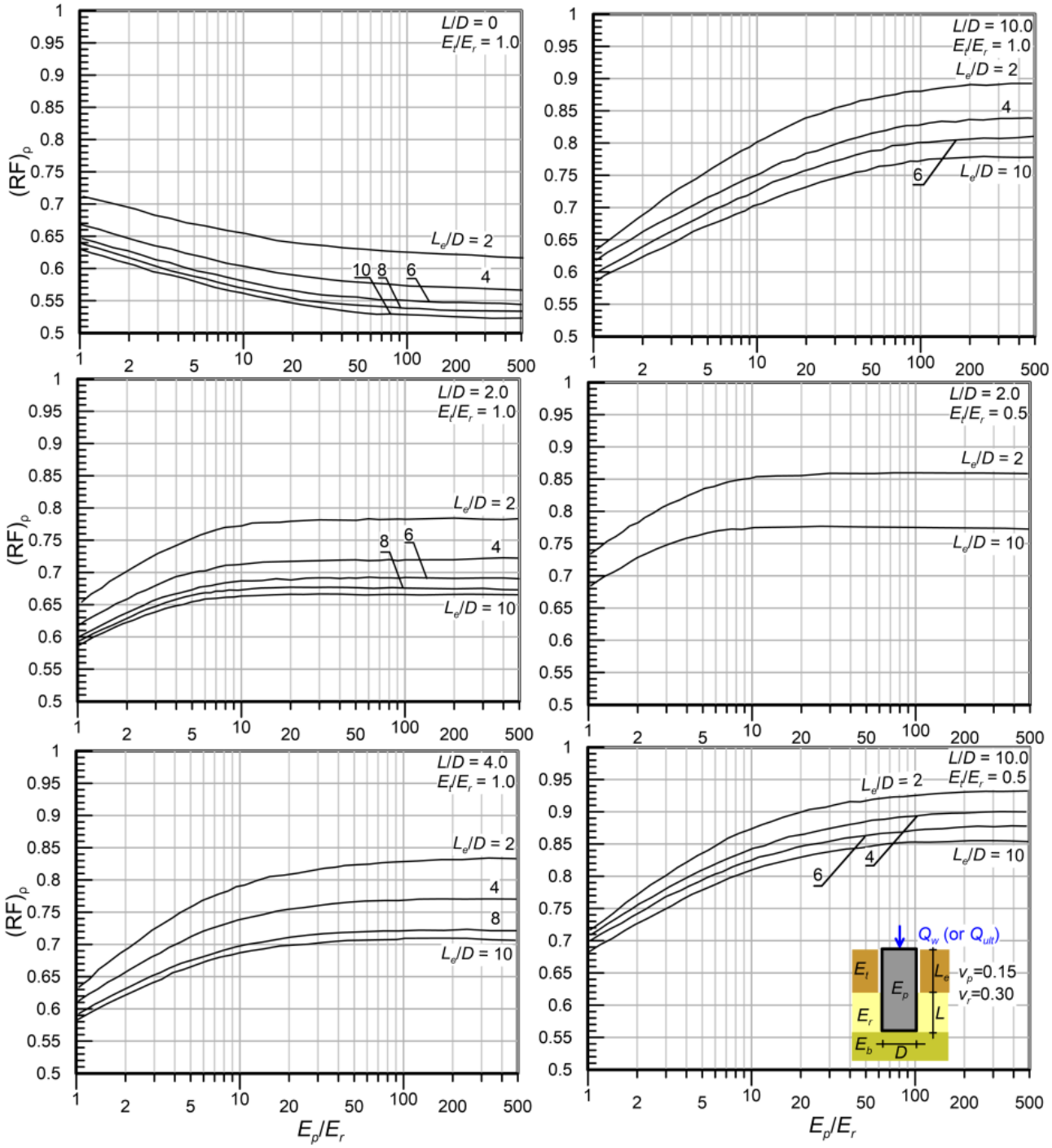

Figure 6.39. Reduction factors for a recessed socket as function of the dimensionless shaft modulus E_p/E_r. Results for L/D = 0 to 10 and E_t/E_r = 1 and 0.5 (after Rowe and Armitage 1984).

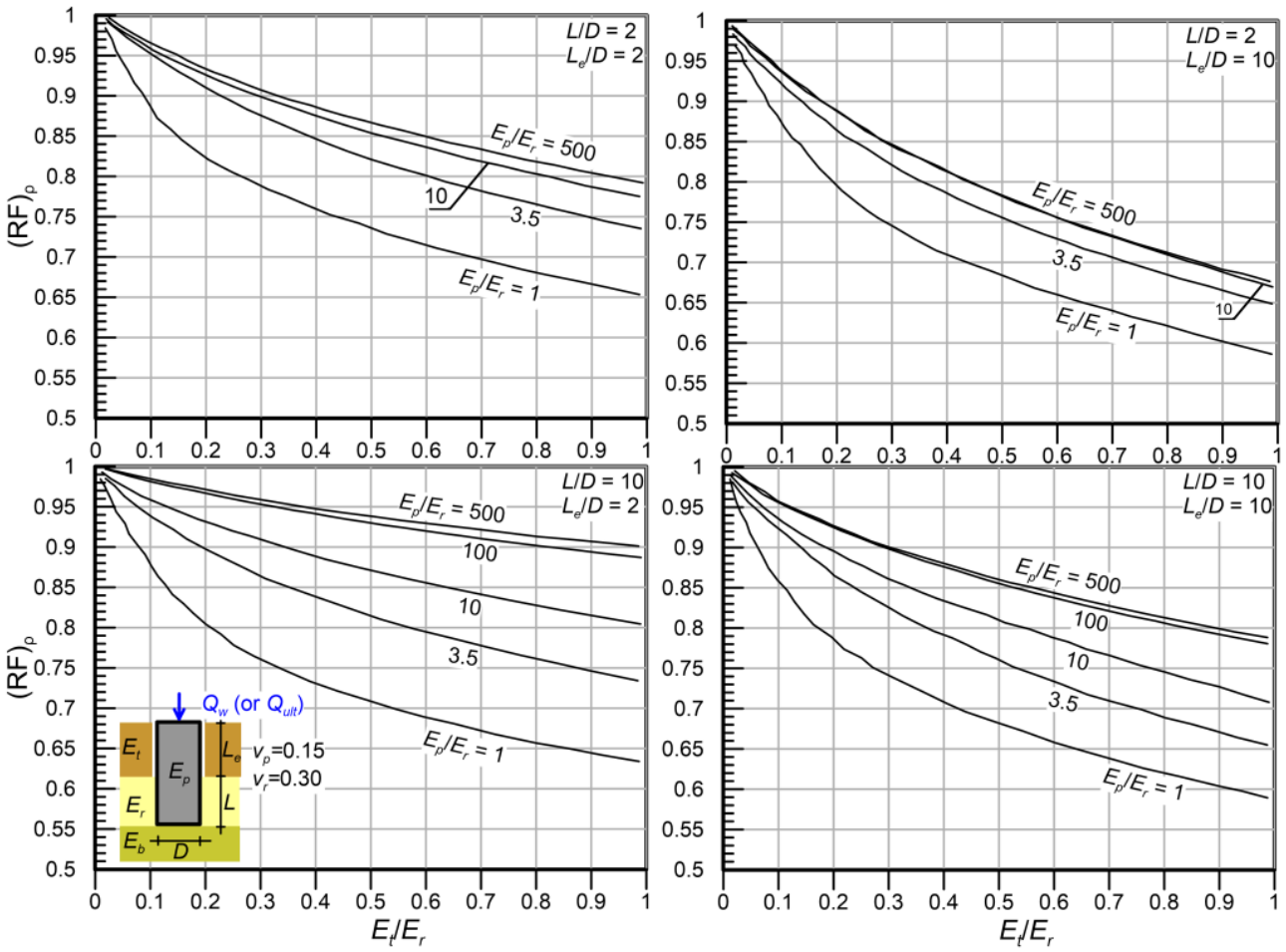

Figure 6.40. Reduction factors for a recessed socket as function of the dimensionless rock modulus E_t/E_r. Results for L/D = 2 and 10 and L_e/D = 2 and 10 (after Rowe and Armitage 1984).

6.14 ULTIMATE GEOTECHNICAL STRENGTH OF DRILLED SHAFTS SUBJECTED TO AXIAL COMPRESSIVE LOADS

The general concept for estimating the collapse load of driven piles under drained and undrained loading conditions using analytical formulas (α– and β-Method) can be applied for the estimation of the collapse compressive load of drilled shafts too. However, the factors employed in the calculation of the skin friction resistance and the end bearing resistance with the α-Method and the β-Method may have to be modified, to account for the soil disturbance during excavation of drilled shafts.

6.14.1 Estimating the ultimate geotechnical strength of drilled shafts with the α-Method

For the estimation of the adhesion factor a_u for drilled shafts, the formula proposed by O'Neil and Reese (1999) and depicted in Figure 6.41 should be used for drilled shafts. Observe that it provides significantly more conservative values compared to the corresponding Figure 6.18 for driven piles.

In addition, the bearing capacity factor N_{cp} employed in the estimation of the end-bearing resistance under undrained loading conditions with Eq. 6.9 is replaced by the factor N^*_{cp}:

(6.68) $$N^*_{cp} = 1.33\,[\ln(I_r) + 1]$$

where I_r is the *rigidity index* of the soil, equal to $I_r = G/S_u = E_u/3S_u$. When undrained triaxial tests are not available for the estimation of the shear G or of the undrained Young modulus of the soil E_u, one may obtain the values from Table 6.8, using linear interpolation for intermediate values.

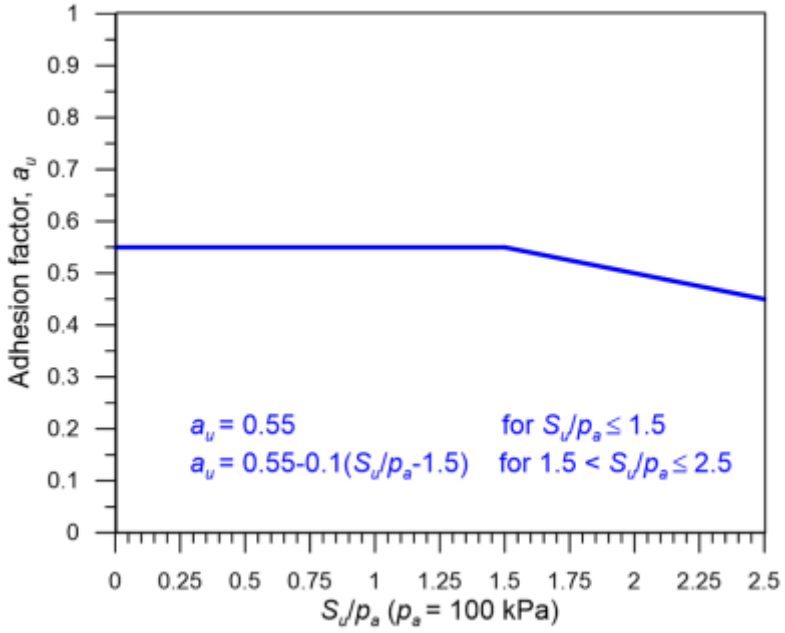

Figure 6.41. Estimation of the adhesion factor for drilled shafts according to O'Neill and Reese (1999).

Table 6.8. Rigidity index I_r and bearing capacity factor N^*_{cp} correlation with the undrained shear strength (Reese *et al.* 2006).

Undrained shear strength, S_u (kPa)	I_r	N^*_{cp}
25	50	6.53
50	150	7.99
100	250	8.67
200	300	8.91

6.14.2 Estimating the ultimate geotechnical strength of drilled shafts with the β-Method

Generally, the formulas for driven piles can be applied as-is for drilled shafts too. Reese *et al.* (2006) proposed specific formulas for estimating the skin friction resistance and end-bearing resistance of drilled shafts installed in coarse-grained soils on the basis of SPT test data. More specifically, the factor β for medium-to-dense sands with uncorrected SPT blow count $N_{60} > 15$ can be estimated as (Figure 6.42):

(6.69) $$\beta = 1.5 - 0.245\sqrt{z} \text{ and } 0.25 \leq \beta \leq 1.2$$

while for loose-to-medium sands with uncorrected SPT blow count $N_{60} < 15$:

(6.70) $$\beta = \frac{N_{60}}{15}\left[1.5 - 0.245\sqrt{z}\right]$$

and for gravels:

(6.71) $\beta = 2.0 - 0.25z^{0.75}$ and $0.25 \leq \beta \leq 1.8$

where z is the depth measured from the ground surface. The skin friction resistance estimated with this method must be limited to $f_{sf} = \beta\sigma'_{z0} < 200$ kPa, arguably a quite high value if we consider Table 6.4 and the fact that construction of drilled shafts will result in release of stresses in sand. The author would recommend considering a more conservative cap on the skin friction resistance calculated with the above formulas, in line with Table 6.4.

As far as the end-bearing resistance q_{bf} is concerned, Reese *et al.* (2006) recommend the following formula:

(6.72a) $L \geq 10$ m use $q_{bf} = 57.5N_{60} \leq 2900$ kPa

(6.72b) $L < 10$ m use $q_{bf} = 57.5\left(\frac{L}{10}\right)N_{60} \leq 290L$ kPa

It is reminded that the end-bearing resistance (units: force) of closed-end piles of diameter D is calculated from the end-bearing resistance (units: stress) as:

(6.73) $Q_b = q_{bf}\pi\left(\frac{D}{2}\right)^2$

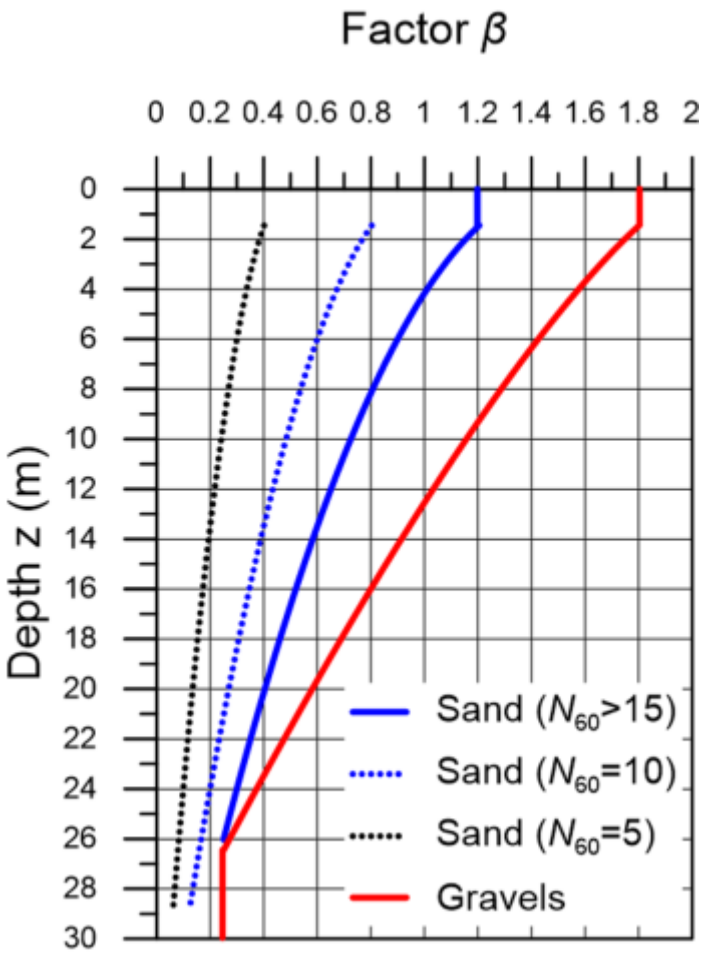

Figure 6.42. Estimation of β factor for drilled shafts in coarse-grained soils according to Reese et al. (2006).

6.15 ULTIMATE GEOTECHNICAL STRENGTH OF PILES SUBJECTED TO AXIAL TENSILE LOADS

In the simplest yet most common case of a pile without an enlarged base, its resistance to uplift axial loads is directly estimated as the sum of the skin friction resistance and the dead weight of the pile:

(6.74) $Q_{f,t} = Q_{sf,t} + W_p$

If the α-method or the ICP method is used to determine the pile's tensile collapse load $Q_{f,t}$, the skin friction resistance developing during uplift of piles installed in soft fine-grained soils is assumed to be equal to the friction resistance in compression, and is estimated with the formulas presented in Chapter 6.9 (α-method) and Section 6.12.7 (ICP method for piles in fine-grained soils).

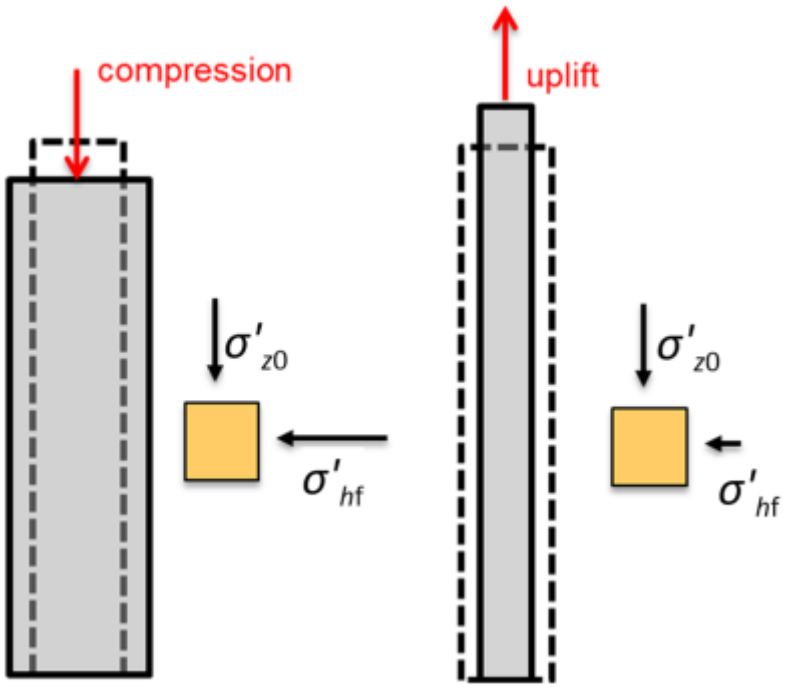

Figure 6.43. Reduced interface normal stress during pile uplift.

Under drained conditions, the skin friction resistance to pile uplift $f_{sf,t}$ is reduced due to the Poisson effect (Figure 6.43), which results in lower confining stress at the side of the shaft and thus reduced friction compared to f_{sf} (Reese *et al.*, 2006, AS 2159). In that case, the skin friction stress developing at the interface to resist tensile an axial load may be computed as:

(6.75) $f_{sf,t} = \psi_t f_{sf}$

where the reduction factor ψ_t is given by the formula (Reese *et al.*, 2006):

(6.76a) $\psi_t = 1 - 0.2 \log\left(\frac{100D}{L}\right)\left[1 - 8n + 25n^2\right]$

(6.76b) where $n = v_p \tan\left[\varphi_i \left(\frac{L}{D}\right)\left(0.385\frac{E_{s,aver}}{E_p}\right)\right]$

where φ_i is the interface friction angle; $E_{s,aver}$ is the average Young modulus of the soil along the pile; E_p is the Young modulus of the pile's material; v_p is the Poisson ratio of the pile's material; L is the pile's length; D is the pile's diameter.

The reduction factor ψ_t estimated from Eq. 6.76 ranges from 0.75 to 0.85 for typical piles, and can be conservatively taken equal to 0.75. The above formulas were originally proposed for coarse-grained soils, but can be used conservatively for fine-grained soils under long-term uplift loading.

The ICP-05 method for piles in coarse-grained soils, presented in Section 6.12.5 can also be used to estimate the skin friction resistance $f_{sf,t}$ developing in piles subjected to axial tensile loads. For *closed-end* cylindrical piles Eq. 6.35 that provides the skin friction stress becomes:

(6.77) $f_{sf,t} = (0.8\sigma'_{he} + \Delta\sigma'_{rd}) \tan\varphi_{i,cs}$

i.e., the normal stress acting at the soil-pile interface after equilibration is reduced by 20%, which is comparable with Eq. 6.76 and the recommended ψ_t values.

For *open-ended* pipe piles Jardine *et al.* (2005) recommend further reducing $f_{sf,t}$ by another 10%, as:

(6.78) $f_{sf,t} = 0.9\,(0.8\sigma'_{he} + \Delta\sigma'_{rd}) \tan\varphi_{i,cs}$

EXAMPLE 6.1

Estimation of the design bearing capacity of a pile according to AS2159 using the α-Method and the ICP method

Determine the short-term design bearing capacity of the single cylindrical pile driven in a uniform clay layer, according to AS 2159 provisions. For the specific problem, assume a basic geotechnical strength reduction factor φ_{gb} equal to $\varphi_{gb} = 0.60$. Ignore the weight of the pile.

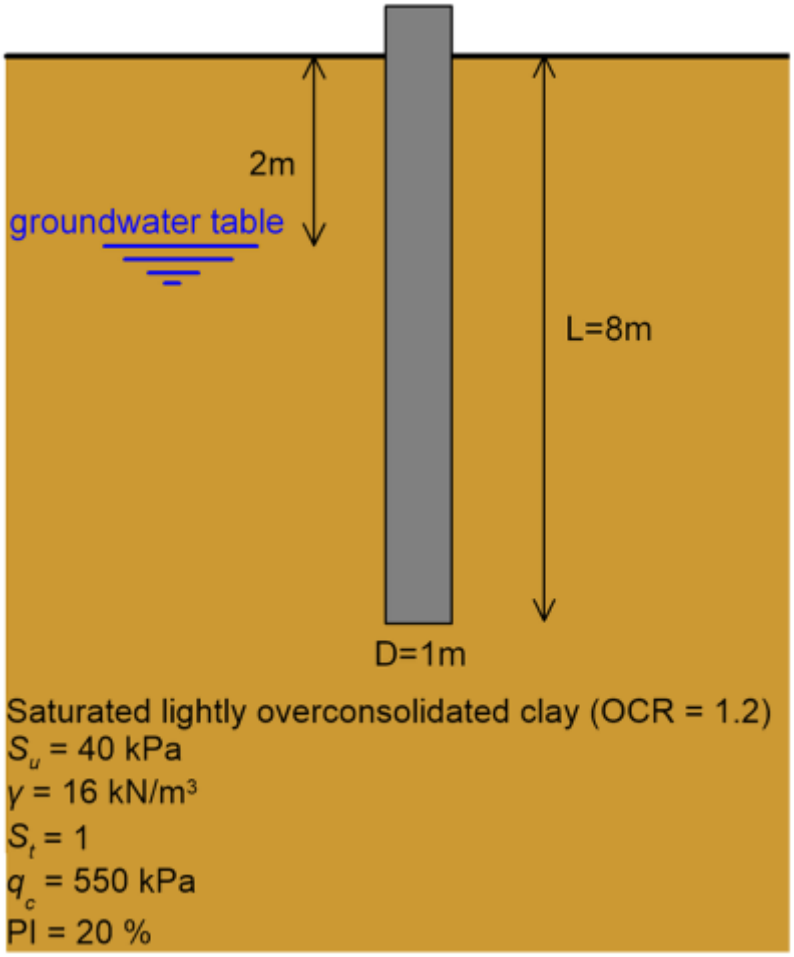

Example 6.1. Problem description and input parameters.

Answer:

Since the problem is asking us to find the design bearing capacity, we will consider that the pile is loaded with axial compressive load. A saturated clay layer will behave as undrained under short-term loading. The pile bearing capacity will be determined first using the α-Method, employing a total stress analysis (TSA). Remember that during a total stress analysis, the groundwater table level does not affect the calculations. In fact, the only soil parameter required by the α-method is the undrained shear strength S_u.

1. Estimation of the skin friction resistance, Q_{sf} with the α-method:

Following Tomlinson (1987) for L/D = 8 and uniform clay with S_u = 40kPa (Figure 6.18b), the adhesion

factor is estimated to be a_u = 0.95. Alternatively, according to Coduto (1994) (Figure 6.18a) for a uniform clay with S_u=40 kPa it is a_u = 1.00. We will estimate the skin friction resistance while adopting the slightly more conservative value a_u = 0.95. Following AS2159, the first $1.5D$ meters of the pile shaft will not contribute to the skin friction resistance, thus Eq. 6.6 yields:

$$Q_{sf} = a_u S_u \pi D \left(L - 1.5D\right) = 0.95 \times 40 \times \pi \times 1 \times (8 - 1.5) = 776 \text{ kN}$$

2. Estimation of the end bearing resistance, Q_b with the α-method:

Using Eq. 6.9 for S_u > 25 kPa:

$$Q_b = N_{cp} S_{u,b} A_b = 9 \times 40 \times \pi \left(\frac{D}{2}\right)^2 = 282.7 \text{ kN}$$

As the skin friction resistance is higher than 80% of the end-bearing resistance, the pile is classified as *friction pile.*

3. Estimation of the design bearing capacity $\varphi_{gb} Q_f$ with the α-method:

Since we seek to estimate the design bearing capacity (i.e., pile subjected to axial compressive loads) the collapse load (ultimate geotechnical strength) of the pile is the sum of its skin friction and end-bearing resistance:

$$Q_f = Q_{sf} + Q_b = 1059 \text{ kN}$$

According to AS2159, the design bearing capacity of the pile is calculated as:

$$\varphi_{gb} Q_f = 0.60 \times 1059 = 635 \text{ kN}$$

Notice that the skin friction resistance of this pile contributes approximately 73% of total strength, which is expected for friction piles in clay. Nevertheless, the skin friction resistance predicted with TSA is f_{sf} = 0.95 x 40 = 38 kPa is quite high. Let's repeat the calculations using this time the ICP method (Section 6.12.7).

4. Estimation of the skin friction resistance, Q_{sf} with the ICP method:

We will estimate first the skin friction resistance with Eq. 6.49. For that we need to know the interface friction angle at failure $\varphi_{i,f}$. Let's assume conservatively that the residual friction angle will govern the skin friction resistance. From Figure 6.29 and for PI = 20 % we obtain from the best fit line $\varphi_{i,f} = \varphi_{i,residual}$ = 25 deg. At the middle of the pile (h/R = 4/0.5 = 8, Figure 6.25) the geostatic vertical effective stress is:

$$\sigma'_{z0} = 16 \times 2 + (16 - 10) \times 2 = 44 \text{ kPa}$$

and the normal stress acting at the soil-pile interface prior to pile loading σ'_{he} is calculated from Eq. 6.50 as:

$$\sigma'_{he} = K_c \sigma'_{z0} = 44 \left[2.2352\right] 1.2^{0.42} [8]^{-0.20} = 70 \text{ kPa}$$

Therefore the skin friction resistance from Eq. 6.49 is:

$$f_{sf} = \left(\frac{K_f}{K_c}\right) \sigma'_{he} \tan \varphi_{i,f} = 0.8 \times 70 \times 0.466 = 26.1 \text{ kPa}$$

Compare f_{sf} calculated with the ICP method (26.1 kPa) and the f_{sf} calculated with the α-method: there is important difference, suggesting that the α-method, which is based on TSA, provides relatively high values of skin friction resistance, compared with the ICP method which is based on ESA principles (undrained strength is not an input parameter) and explicitly accounts for installation effects. The skin friction resistance predicted with the ICP method is accordingly calculated as:

$$Q_{sf} = f_{sf}\pi D\,(L - 1.5D) = 26.1 \times \pi \times 1 \times (8 - 1.5) = 533\ \text{kN}$$

5. Estimation of the end bearing resistance, Q_b with the ICP method:

For closed-end piles and short-term loading conditions, the end-bearing resistance in terms of stress q_{bf} is calculated from Eq. 6.51, as function of the average cone resistance. Here we are considering for simplicity constant cone resistance q_c = 550 kPa (compatible with undrained strength of S_u = 40 kPa according to the interpretation methods presented in Part 1). Therefore the end bearing resistance is:

$$q_{bf} = 0.8q_{c(av)} = 440\ \text{kPa}$$

and the end-bearing resistance in terms of force is calculated from Eq. 6.30 as:

$$Q_b = \left(\frac{\pi D^2}{4}\right) q_{bf} = 345.6\ \text{kN}$$

Notice that Q_b calculated with the ICP method (345.6 kN) is only slightly higher compared to that calculated with the α-method. Jardine *et al.* (2005) discuss that indeed the ICP method provides comparable end bearing resistance values to the α-method.

6. Estimation of the design bearing capacity $\varphi_{gb}Q_f$ with the ICP method:

As before, the collapse load (ultimate geotechnical strength) of the pile is the sum of its skin friction and end bearing resistance:

$$Q_f = Q_{sf} + Q_b = 878.6\ \text{kN}$$

According to AS2159, the design bearing capacity of the pile is calculated as:

$$\varphi_{gb}Q_f = 0.60 \times 878.6 = 527.1\ \text{kN}$$

The conclusion from this exercise, where the design bearing capacity calculated with the ICP method is 17% lower compared to that calculated with the α-method is that simplified methods (which require only one input parameter i.e., the undrained shear strength) do not always provide conservative predictions.

EXAMPLE 6.2

Estimation of the design bearing capacity of a single pile according to AS2159 using the α- and β-Methods - Multilayered soil profile case

Determine the design bearing capacity of the concrete pile shown below, according to AS2159 provisions, using the simplified α– and β-Methods. For the specific problem, assume a basic geotechnical strength reduction factor φ_{gb} equal to $\varphi_{gb} = 0.52$. Ignore the weight of the pile.

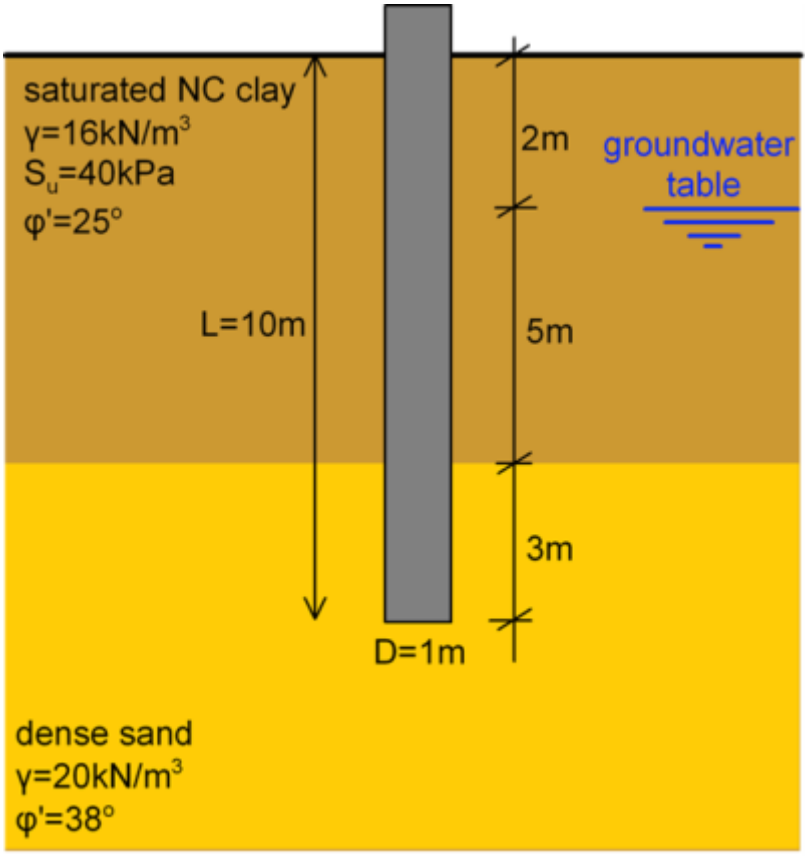

Example 6.2. Problem description and input parameters.

Answer:

Since the problem is asking us to find the design bearing capacity, we will consider that the pile is loaded with axial compressive load. The design bearing capacity of the pile must be determined both under short-term and long-term loading conditions, in order to establish the critical design bearing capacity. The top clay layer will behave as undrained under short-term loading, and as drained under long-term loading. On the other hand, the bottom dense sand layer will behave as drained under both long-term and short-term loading.

1. Estimation of the ultimate geotechnical strength under short-term conditions

    1.1 Estimation of the skin friction resistance, Q_{sf}:

Clay layer (α-Method): According to Coduto (1994) (Figure 6.18a) for a uniform clay with S_u = 40 kPa it is a_u = 1.00. Moreover, following AS 2159, the first 1.5D meters of the pile shaft will not contribute to the friction resistance of the part of the pile embedded in the clay layer (Eq. 6.6):

$$Q_{sf,clay} = a_u S_u \pi D\,(L - 1.5D) = 1.0 \times 40 \times \pi \times 1 \times (5.5) = 691\ \text{kN}$$

Dense sand layer (β-Method): First, we have to calculate the vertical effective stress at the middle (z = 8.5 m) of the sand layer σ'_{z0}:

$$\sigma'_{z0} = \sigma_{z0} - u = (7 \times 16 + 1.5 \times 20) - 6.5 \times 10 = 77\ \text{kPa}$$

In order to find the β factor, we estimate the earth pressure coefficient at-rest K_0 as (Eq. 6.16):

$$K_0 = 1 - \sin\varphi' = 0.384$$

and the interface friction angle φ_i, which for a concrete pile with rough surface will be equal to 2/3 of the friction angle of the sand layer φ' (Eq. 6.15):

$$\varphi_i = \frac{2\varphi'}{3} = 25.33^o$$

Given the above, the β factor is calculated as (Eqs. 6.12-6.13):

$$\beta = K_0 \tan\varphi_i = 0.181$$

and the skin friction resistance in terms of force of the part of the pile embedded in the dense sand layer will be equal to (Eq. 6.11):

$$Q_{sf,sand} = \beta \sigma'_{z,0} \pi D L = 0.181 \times 77 \times \pi \times 3 = 132\ \text{kN}$$

It is interesting to note that the skin friction resistance in terms of stress f_{sf} at the middle of the sand layer is f_{sf} = 13.93 kPa. Considering the recommended values in Table 6.4, this is quite low, especially if we consider that the skin friction resistance in the overlying clay layer is f_{sf} = 40 kPa. However, observe that we have used the *in situ* lateral earth pressure in the calculations from Eq. 6.16. Had we followed API RP2A recommendations and considered K = 0.8 to 1 to account for installation effects, we would have calculated $f_{sf} = K\tan\varphi_i\sigma'_{z0}$ = 1.0×0.473×77 = 36 kPa, which is considerably higher. This is an example where simplified methods, not accounting for installation effects, can provide over-conservative predictions.

1.2 Estimation of the end bearing resistance, Q_b

The pile toe is embedded in the dense sand layer, thus we will use Eq. 6.19 for drained loading conditions. First, we have to estimate the vertical effective stress at the pile toe level (z = 10m) $\sigma'_{z0,b}$:

$$\sigma'_{z0,b} = \sigma_{z0,b} - u = (7 \times 16 + 3 \times 20) - 8 \times 10 = 92\ \text{kPa}$$

For the estimation of the bearing capacity factor N_{qp} we will use Eq. 6.19:

$$N_{qp} = N_q = \tan^2\left(45^o + \frac{\varphi'}{2}\right) e^{\pi \tan\varphi'} = 48.9$$

The calculated N_{qp} value is quite high, still within the recommended zone of Figure 6.21. The end bearing resistance is calculated as:

$$Q_b = N_{qp}\sigma'_{z0,b}A_b = 48.93 \times 92 \times \pi \times \left(\frac{1}{2}\right)^2 = 3535\ \text{kN}$$

Note that if we use the expression recommended by Janbu (Eq. 6.20) to estimate the bearing capacity factor

while considering a rational range of ψ_p values $\psi_p = 75^o$ to 85^o we calculate bearing capacity factors ranging between $N_{qp} \approx 32$ to 42 and the corresponding end-bearing resistance will be $Q_b \approx 2312$ to 3034 kN. These values are compatible with the recommended N_{qp} values in Table 6.4.

1.3 Ultimate geotechnical strength (collapse load) under short-term conditions

The collapse load is the sum of the pile's skin friction resistance along the clay and the sand layer, and its end bearing resistance:

$$Q_f = Q_{sf,clay} + Q_{sf,sand} + Q_b = 691 + 132 + 3535 = 4358 \text{ kN}$$

Notice that the over-conservative prediction of $Q_{sf,sand}$ had little effect on the collapse load (about 5%), which is governed by the end bearing resistance of the pile's toe in sand.

2. Estimation of the ultimate geotechnical strength under long-term conditions

2.1 Estimation of the skin friction resistance, Q_{sf}:

Clay layer (β-Method): We can divide the clay layer into two sublayers; one with thickness 2 m above the ground water table, and one with thickness 5 m below the groundwater table.

For the first sublayer (above the groundwater table):

vertical effective stress at the middle (z = 1.0 m) of sublayer 1 $\sigma'_{z0,1}$:

$$\sigma'_{z0,1} = \sigma_{z0,1} - u_1 = 1 \times 16 - 0 = 16 \text{ kPa}$$

lateral earth pressure coefficient (Eq. 6.15):

$$K_0 = (1 - \sin\varphi')\,\text{OCR}^{0.5} = (1 - \sin 25^o) \times 1^{0.5} = 0.577$$

Interface friction angle φ_i for a rough concrete pile (Eq. 6.15):

$$\varphi_i = \frac{2\varphi'}{3} = 16.66^o$$

β factor (Eqs. 6.12-6.13):

$$\beta_1 = K_0 \tan\varphi_i = 0.577 \times 0.299 = 0.172$$

For the second sublayer (below the groundwater table):

vertical effective stress at the middle (z = 4.5 m) of sublayer 2 $\sigma'_{z0,2}$:

$$\sigma'_{z0,2} = \sigma_{z0,2} - u_2 = 4.5 \times 16 - 2.5 \times 10 = 47 \text{ kPa}$$

and $\beta_2 = K_0 \tan\varphi_i = 0.577 \times 0.299 = 0.172$

Using Eq. 6.14, the total skin friction resistance of the clay layer will be:

$$Q_{sf,clay} = \beta_1 \sigma'_{z0,1} \pi D\,(L_1 - 1.5) + \beta_2 \sigma'_{z0,2} \pi D L_2 =$$
$$= 0.172 \times 16 \times \pi \times 1 \times (2 - 1.5) + 0.172 \times 47 \times \pi \times 1 \times 5 = 131 \text{kN}$$

Note that if we considered the clay layer as a single layer, and calculated the vertical effective stress at its middle (z = 3.5 m), we would calculate a total skin friction resistance $Q_{sf,clay}$ = 122 kN.

If we assume the same ICP parameters for clay as in Example 6.1 (S_t = 1, φ_i = 25 deg) we would calculate according to the ICP method at the middle of the clay layer:

$$\sigma'_{z0} = \sigma_{z0} - u = (2 \times 16 + 1.5 \times 6) - 1.5 \times 10 = 26\,\text{kPa}$$

$$\sigma'_{he} = K_c \sigma'_{z0} = 26\,[2.216]\,1.0^{0.42}[13]^{-0.20} = 34.5\,\text{kPa}$$

$$f_{sf} = \left(\frac{K_f}{K_c}\right)\sigma'_{he}\tan\varphi_{i,f} = 0.8 \times 34.5 \times 0.466 = 12.86\,\text{kPa}$$

$$Q_{sf,clay} = f_{sf}\pi D\,(L - 1.5D) = 12.86 \times \pi \times 1 \times (7 - 1.5) = 222\,\text{kN}$$

Therefore, unlike Example 6.1., here the ICP method provides considerably higher skin friction resistance for the clay layer, noting though that the ICP method is based on ESA concepts, and does not differentiate between long-term and short-term skin friction resistance.

As far as the skin friction resistance of the part of the pile embedded into the sand layer, it will be essentially the same as under short-term conditions:

$$Q_{sf,sand} = 132\,\text{kN}$$

2.2 Estimation of the end-bearing resistance, Q_b:

The same applies for the end-bearing resistance of the pile toe embedded in sand: it will be the same as under short-term conditions:

$$Q_b = 3535\,\text{kN}$$

2.3 Ultimate geotechnical strength (collapse load) under long-term conditions, Q_f:

The collapse load is the sum of the long-term pile's skin friction resistance along the clay and the sand layer, and its end-bearing resistance:

$$Q_f = Q_{sf,clay} + Q_{sf,sand} + Q_b = 131 + 132 + 3535 = 3789\,\text{kN}$$

3. Estimation of the design bearing capacity, $\varphi_{gb}Q_f$:

It appears that in this case, the long-term loading is critical, as it results in the lowest pile ultimate bearing capacity. The design bearing capacity according to AS2159 is calculated as:

$$\varphi_{gb}Q_f = 0.52 \times 3789 = 1970\,\text{kN}$$

This is due to the long-term skin friction resistance in the clay layer being lower that the short-term skin friction resistance, and appears to be counterintuitive: As discussed in Part 5, we would expect the short term loading to be critical. However, comparisons with the ICP method have demonstrated that the α-method appears to be overestimating the skin friction resistance for soft-to-firm clays, and at the same time the β-method appears to be underestimating the skin friction resistance. Indeed, pile test results (Fellenius 1991) indicate that for clays and silts, the factor β usually ranges between 0.25 and 0.40 depending on their friction angle, as shown in Figure 6.44. In this example we have calculated $\beta = 0.172$ for the clay layer with $\varphi' = 25$ deg, while the ICP method provides $\beta = f_{sf}/\sigma'_{z0} = 12.86/26 = 0.49$.

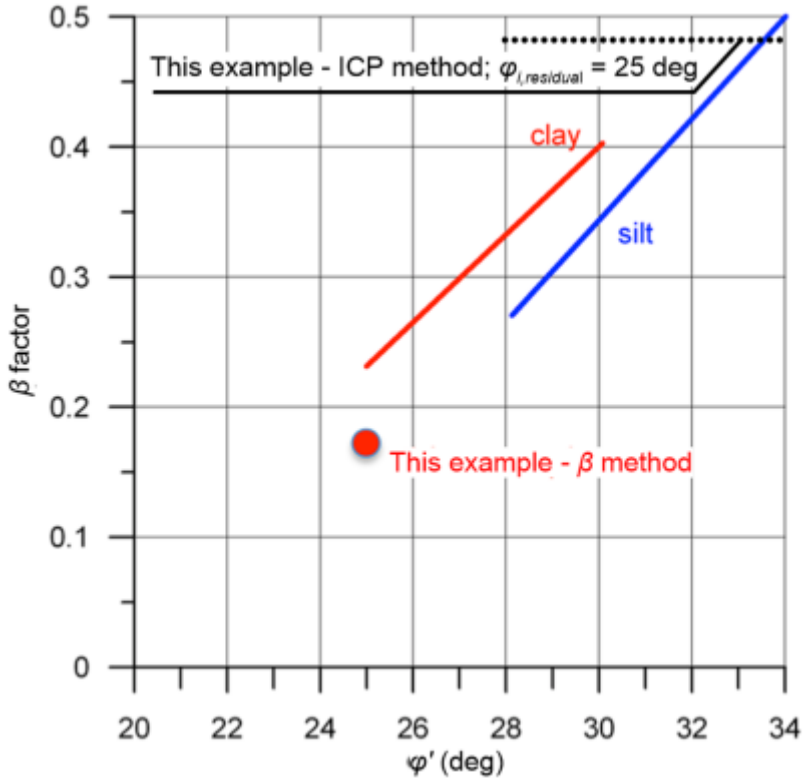

Figure 6.44. Comparison of results with β factor for clays and silts estimated according to Fellenius (1991).

EXAMPLE 6.3

Numerical estimation of the ultimate geotechnical strength of a single pile in homogeneous soil, considering undrained behaviour

Determine the load-displacement curve (*compliance curve*) of the pile shown below, up to a maximum pile head vertical displacement equal to 30% of the diameter of the pile.

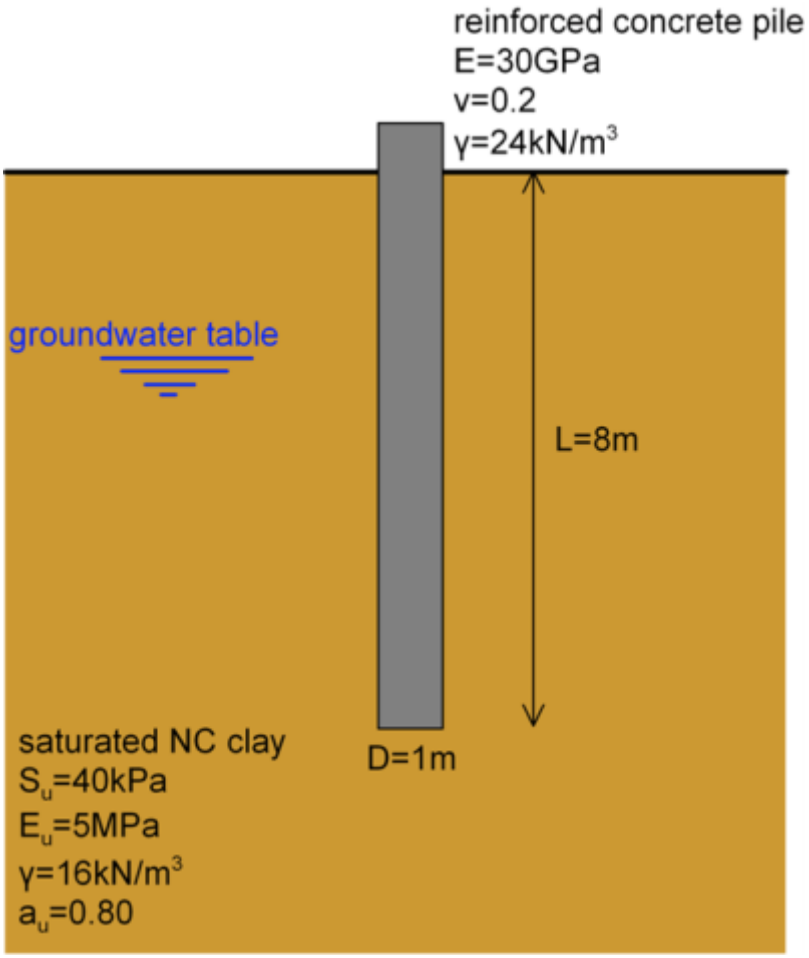

Example 6.3. Problem description and input parameters.

Answer:

Installation of the pile is not going to be simulated, although this would be possible, but with a more complex numerical model. It is perhaps clear that, as the vertical load on the pile increases, shear stresses f_{sf} develop at the soil-shaft interface, and eventually some slippage will develop, as illustrated in Figure 6.45. Following the development of slippage at the soil-pile interface, stresses are being transferred to the pile toe, and reach the end bearing resistance q_{bf} at a vertical pile head displacement $u_{y,f}$ that is taken between 0.1 and 0.3D (Figure 6.45). It has been mentioned earlier that modern CPT-based method associate the development of the end bearing resistance with a pile head displacement about $u_{y,f}$ = 0.1D. Here we will explore, among others, how much the collapse load of the pile (the reaction at the corresponding

displacement value, taken from the load-displacement curve) increases if we take the pile head displacement at failure $u_{y,f}$ to be $0.3D$, instead of $0.1D$. It is reminded that analytical formulas (α– and β-method) assume that soil is rigid-plastic, hence pile head displacement at failure has no physical meaning.

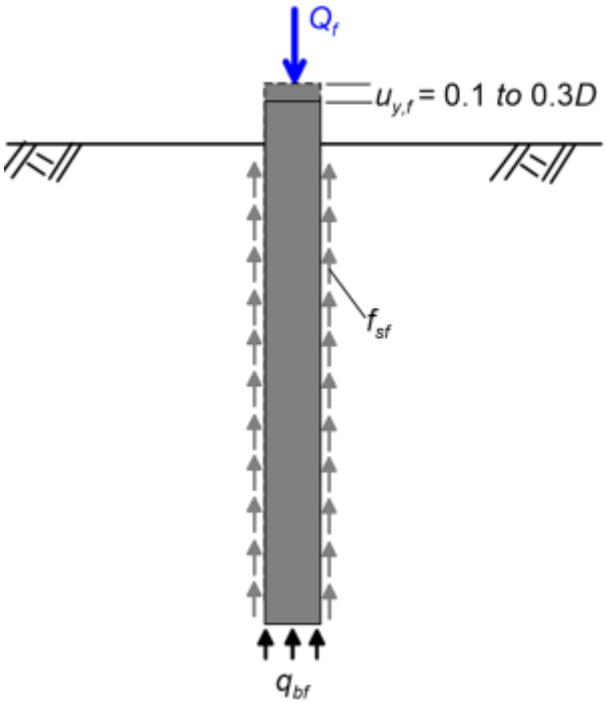

Figure 6.45. Illustration of the stresses developing along a pile subjected to axial compressive load.

When applying the α-method formulas, we used the conceptual model depicted in Figure 6.17 to determine the skin friction resistance at the pile-shaft interface, assuming that the full friction at the interface has mobilised:

$$f_{sf} = a_u S_u$$

In PLAXIS, and other numerical codes, *interfaces* are used to model soil-pile interaction. An interface describes the contact between two different model entities e.g. the soil and a pile, a retaining wall or a tunnel, and sometimes the interface of two different soil layers. The roughness of the interface, and thus the maximum shear stress that can develop along the interface before slippage occurs, is introduced in PLAXIS via the *interface strength reduction factor* (R_{int}). The contact interface model implemented in PLAXIS is based on the Coulomb friction criterion.

Considering again a rigid block resting on a surface, as in Figure 6.17, we can estimate the maximum shear stress at the interface when slip occurs as:

$$\tau_{\max} = \sigma' \tan \varphi_i + c_i$$

where φ_i and c_i is the friction angle and the cohesion of the interface, and are associated with the drained c' and φ' or undrained S_u shear strength properties of the soil layer, as:

$\tan \varphi_i = R_{\text{int}} \tan \varphi'$ and $c_i = R_{\text{int}} c'$ under drained conditions, or

$S_{u,i} = R_{\text{int}} S_u$ under undrained conditions

for the pile problem at hand it is:

$$\tau_{\max} = f_{sf} = R_{\text{int}} S_u = a_u S_u$$

so $R_{\text{int}} = a_u$

Each interface is assigned a *virtual thickness,* an imaginary dimension related to the average element size with the *virtual thickness factor*. The default PLAXIS value of 0.1 will provide reliable results for most problems. Interface elements are created by PLAXIS when an interface is defined, connecting the two adjacent regions (Figure 6.46).

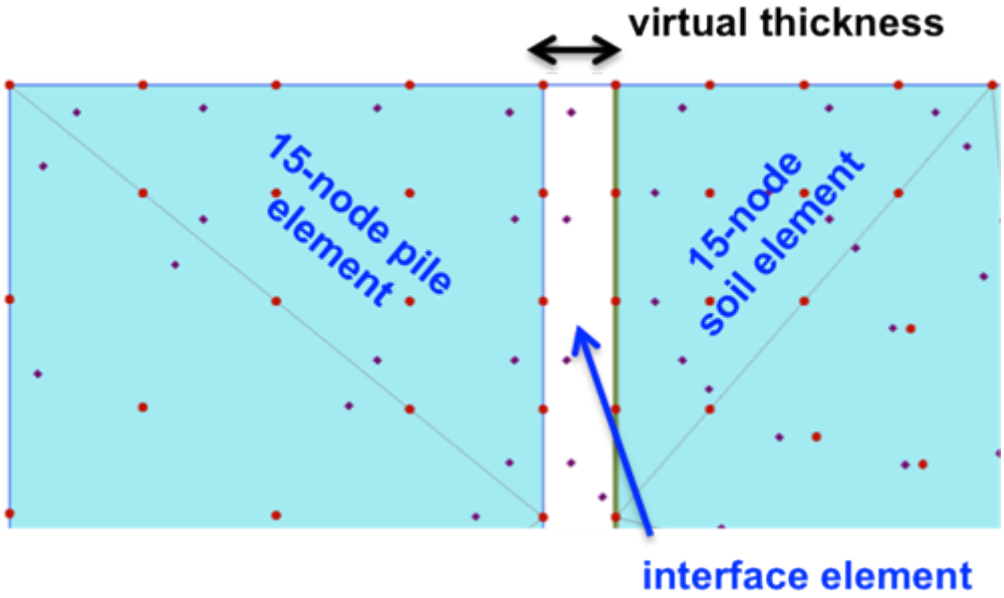

Figure 6.46. Interface elements at the soil-pile interface.

The axisymmetric finite element mesh is presented in Figure 6.47, with the axis of symmetry being the pile vertical axis. An area of dimensions 6 m x 16 m is discretised with a "medium coarse" mesh. A uniform prescribed displacement $u_{y,f}$ is applied on the head of the pile, equal to $0.30D$ = 0.3 m, in order to obtain the compliance (load-displacement) curve of the pile.

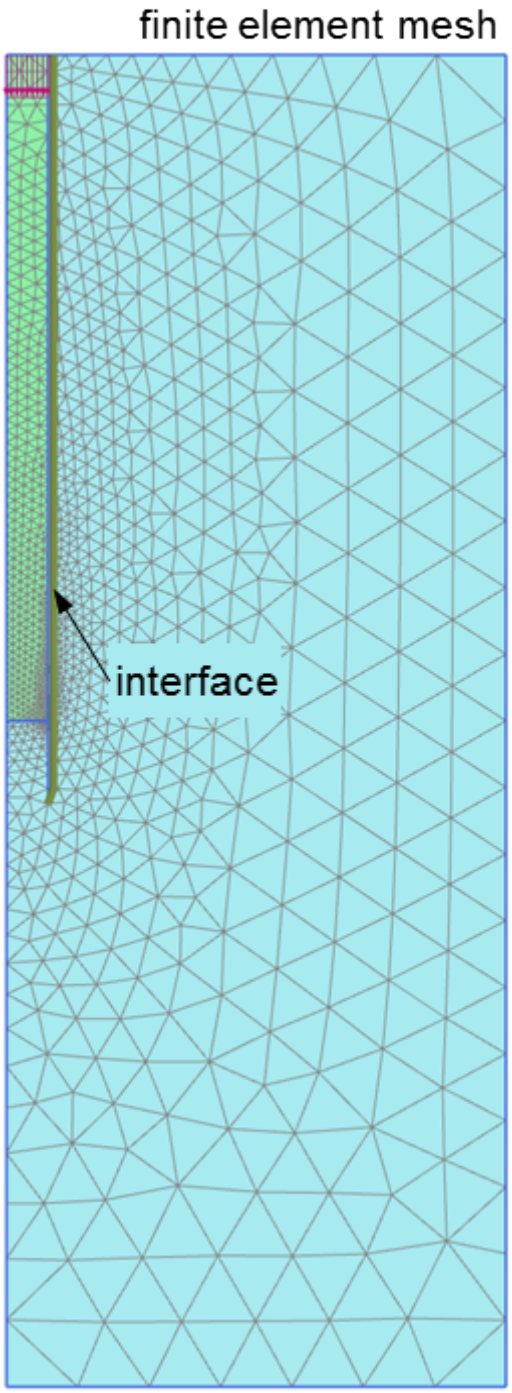

Figure 6.47. Finite element mesh including interface elements. Notice the mesh refinement around the pile edge resulting from meshing the model while assigning the much stiffer linear elastic material at the pile cluster.

The clay is simulated as an Undrained (C) Mohr-Coulomb material (Example 5.2), and a total stress analysis is performed. The interface reduction factor $R_{int} = a_u = 0.8$ is introduced to PLAXIS as a property of the soil material that interacts with the pile. A linear-elastic material is used to simulate the pile, with Young's modulus E_p = 30 GPa and Poisson's ratio $\upsilon_p = 0.2$. Note here that we can introduce the weight of the pile in the calculations, by assigning a proper unit weight to the pile's material. Following Section 6.9, in PLAXIS simulations we do take into account unloading of soil during pile construction, because

we assign the pile material to the soil column during Stage 2 of the analysis. Therefore, additional loading of soil associated with the self-weight of the pile results from the different in the unit weight of the soil column (γ = 16 kN/m^3) and of the pile column (γ = 24 to 25 kN/m^3 for reinforced concrete pile).

The analysis is performed in 3 stages:

1. *Initial stage (before the construction of the pile)* Calculate initial geostatic stresses before the construction of the pile with the "K_0 procedure", by associating both geometry clusters with the clay material. Interfaces and loads are not active.
2. *Plastic stage 1 (construction of the pile)* The material of the geometry cluster corresponding to the pile is switched to the linear elastic material described above, and interfaces are activated. This simplified procedure implies that the soil around the pile is not disturbed from its construction i.e., the pile is "wished in-place".
3. *Plastic stage 2 (loading of the pile)* The displacement on the pile head is activated, and the analysis is run until it reaches the desired value.

As in Example 6.1, while performing a total stress analysis (TSA) the groundwater table level will not affect the calculations, and does not need to be simulated.

A detail of the deformed mesh and of the plastic points near the area of the pile toe are plotted in Figure 6.48. Notice that slippage at the soil-pile interface develops, resulting in yielding of the soil elements around the shaft, while a failure zone develops below the pile toe.

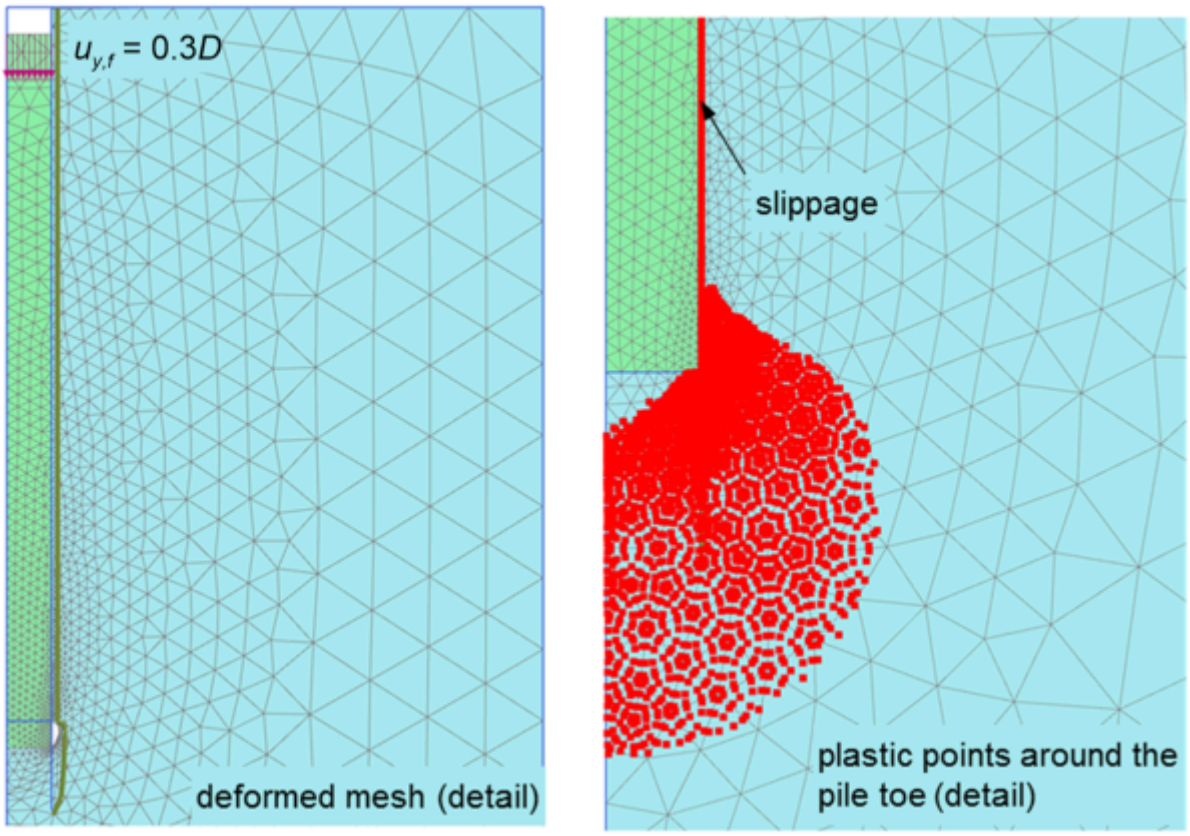

Figure 6.48. Deformed finite element mesh and plastic points developing around the pile toe.

The problem here is solved parametrically, for different clay undrained Young's modulus values E_u ranging from E_u = 1 MPa to E_u = 10 MPa (Figure 6.49) and different a_u values ranging from a_u = 0 to a_u = 1.0 (Figure 6.50). Additional analyses were also performed to identify the effect of separation at the soil-pile interface on the results (Figure 6.51), comparing the load-displacement curve that resulted from a model where no separation was allowed at the interface (no interface elements were employed), with the load-

displacement curve that resulted from a model where a "rough" interface was considered ($a_u = R_{int} = 1.0$). The ultimate geotechnical capacity was also estimated via the α-method formulas, and analytical results are compared to the numerical ones.

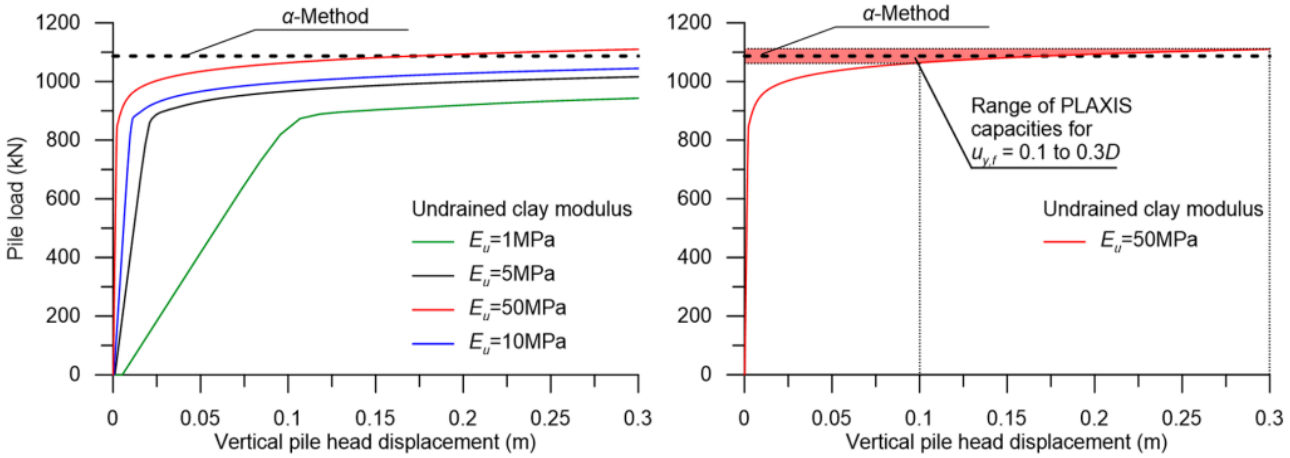

Figure 6.49. (Left) Effect of the soil compressibility on the load-displacement curve, (right) Effect of nominal vertical pile head displacement at failure on predicted ultimate geotechnical strength.

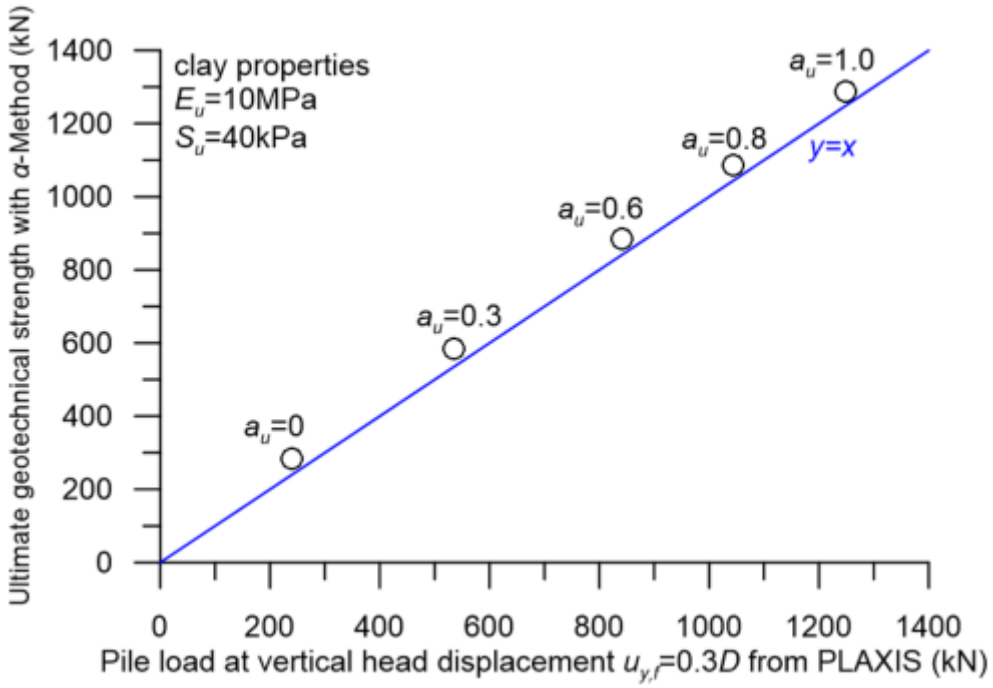

Figure 6.50. Comparison of analytical and numerical results for different a_u values.

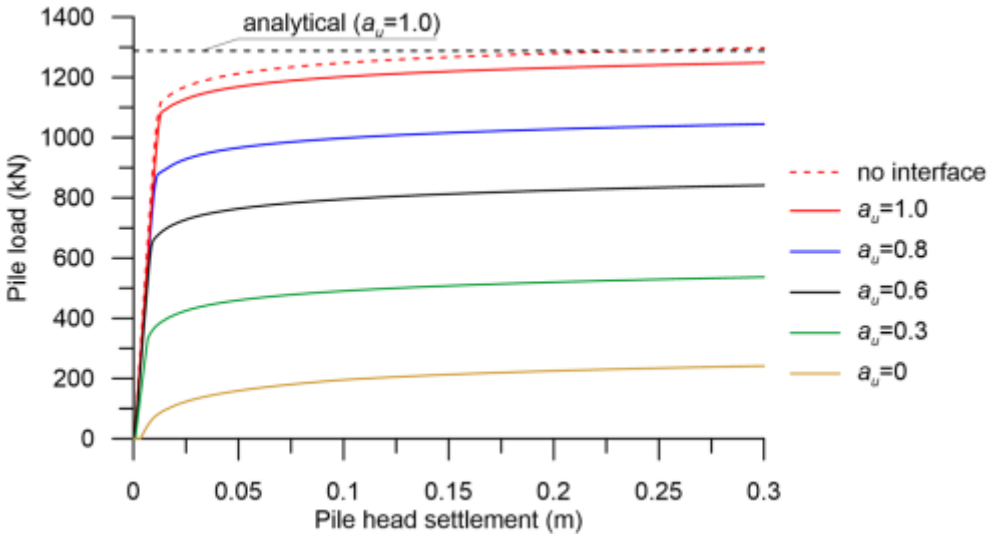

Figure 6.51. Load-displacement curves for different a_u values. The effect of separation at the interface is depicted by comparing the curve for a_u = 1.0 with the curve that results from an analysis without interface.

Results presented in the above figures suggest that numerical results from PLAXIS compare well with the predictions of the α-method. It is also verified that, as discussed before, that the *collapse load* of the pile cannot be straightforwardly identified: the load on the pile continues to increase until non-tolerable settlements develop. In the rather theoretical case where the clay layer features a very low Young's modulus, compared to its undrained shear strength, settlements will increase to intolerable levels well before the ultimate load is applied (Figure 6.49 – E_u = 1 MPa). Nevertheless, for higher E_u values the sensitivity of the predicted ultimate geotechnical strength of piles in clay to the nominal pile head vertical displacement at failure $u_{y,f}$ is not particularly important (Figure 6.49).

One could argue, on the basis of the above results, that the α-method provides very reasonable estimates of the pile's skin friction resistance under undrained conditions, therefore ICP (and other modern methods) are unnecessarily conservative. There is a caveat though. First, we have not modelled installation effects with PLAXIS, hence we did not account for soil disturbance during pile driving in our numerical model. Second, PLAXIS uses the same Coulomb model to calculate interface shear stresses, thus skin friction resistance, as the α-method. Since R_{int} is taken equal to a_u, skin friction estimates obtained with both methods will be very similar. Therefore the author recommends to carefully select the R_{int} parameter when seeking to predict the ultimate geotechnical strength with PLAXIS, ideally using methods as the ICP one for guidance.

EXAMPLE 6.4

Numerical estimation of the ultimate geotechnical strength of a single pile in multilayered soil

Determine the short-term and long-term load-displacement curve of the pile shown below, up to a maximum vertical pile head displacement of 30% of the diameter of the pile.

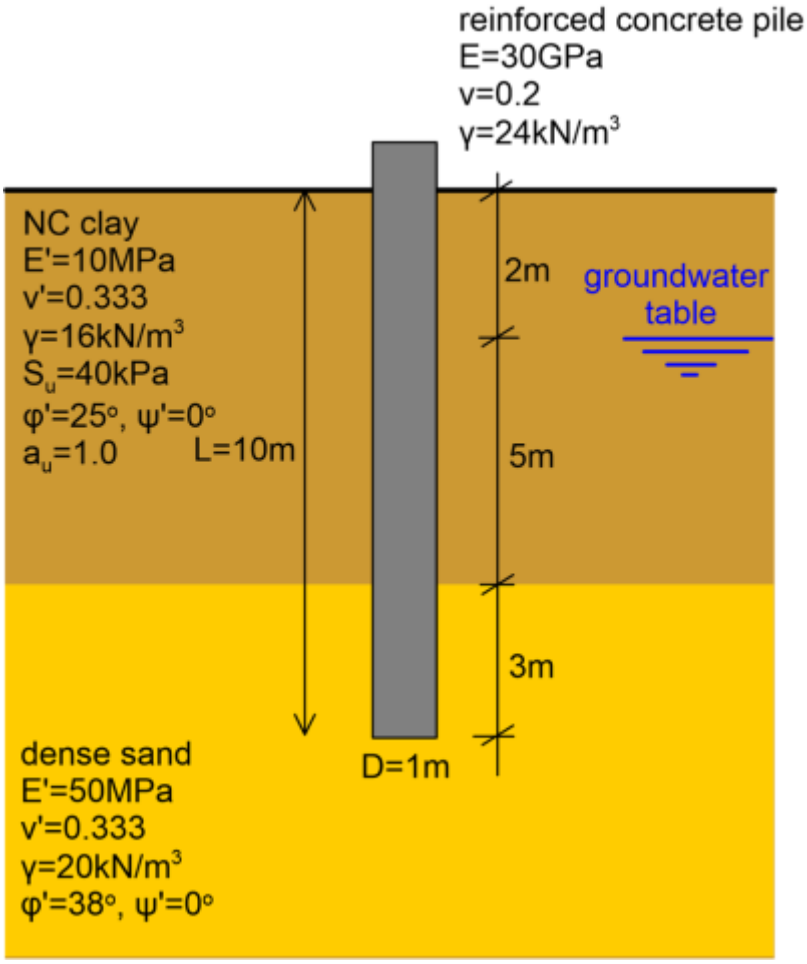

Example 6.4. Problem description and input parameters.

Answer:

The general concept described in Example 6.3 regarding the simulation of soil-pile interaction applies in this problem too. Note however that when considering drained loading conditions, for the clay layer under long-term loading and for the sand layer under both short-term and long-term loading, the interface strength reduction factor R_{int} will depend on the friction angle of the soil. For a concrete pile, where the interface friction angle φ_i is assumed to be equal to 2/3 of the soil friction angle φ':

$$R_{\text{int}} = \frac{\tan\varphi_i}{\tan\varphi'} = \frac{\tan\left(\frac{2}{3}\varphi'\right)}{\tan\varphi'}$$

$R_{\text{int},sand} = 0.606$; $R_{\text{int},clay} = 0.642$

Geostatic effective stresses must be calculated, as an effective stress analysis (ESA) is performed when considering drained material behavior and groundwater is present. We can use the Undrained (B) Mohr-Coulomb material to simulate undrained clay response under short-term loading conditions, which allows for direct input of the undrained shear strength S_u while estimating effective stresses too. Notice that the *drained* Young's modulus E' and Poisson's ratio v' must be used in tandem with the Undrained (B) Mohr-Coulomb model. However, since here we are not interested in excess pore pressure development, using the Undrained (C) Mohr-Coulomb model for the clay will essentially yield the same results.

Under long-term loading conditions on the other hand, both clay and sand response are simulated with the Drained Mohr-Coulomb model, assuming non-associated flow ($\psi = 0°$) as per the brief. Although the effective cohesion of the normally consolidated clay and dense sand is equal to zero ($c' = 0$), a small value of cohesion ($c' = 1$ kPa) is considered with the Drained Mohr-Coulomb model, for numerical stability reasons. A linear-elastic material is used to simulate the pile, with Young's modulus $E_p = 30$ GPa and Poisson's ratio $v_p = 0.2$.

As in the Example 6.3, the analysis is performed in 3 stages:

1. *Initial stage (before the construction of the pile)* Calculate initial geostatic stresses before the construction of the pile, by associating all geometry clusters with the original soil material. This means that two separate geometry clusters must be defined for the pile, connected at the interface of the soil-sand layers (Figure 6.52). Interfaces and loads are not active during this stage. Note that also PLAXIS uses Eq. 6.16 for the estimation of the lateral earth pressure coefficient K_0 and the lateral geostatic stresses.
2. *Plastic stage 1 (construction of the pile)* The material of the geometry cluster corresponding to the pile is switched to the linear elastic material described above, and interfaces are activated. This simplified procedure implies that the soil around the pile is not disturbed from its construction i.e., the pile is "wished in-place".
3. *Plastic stage 2 (loading of the pile)* The prescribed vertical displacement $u_{y,f} = 0.3D$ on the pile head is activated, and the analysis is run until it reaches the desired value.

Here, the groundwater table level must be explicitly introduced during the definition of the analyses stages. Geostatic effective stresses can be checked with hand calculations. Note that when we are using the Undrained (C) Mohr-Coulomb model for the clay, PLAXIS cannot compute effective stresses in this particular layer. However, as friction resistance in the clay layer does not depend on the effective stress level, the results will be essentially correct.

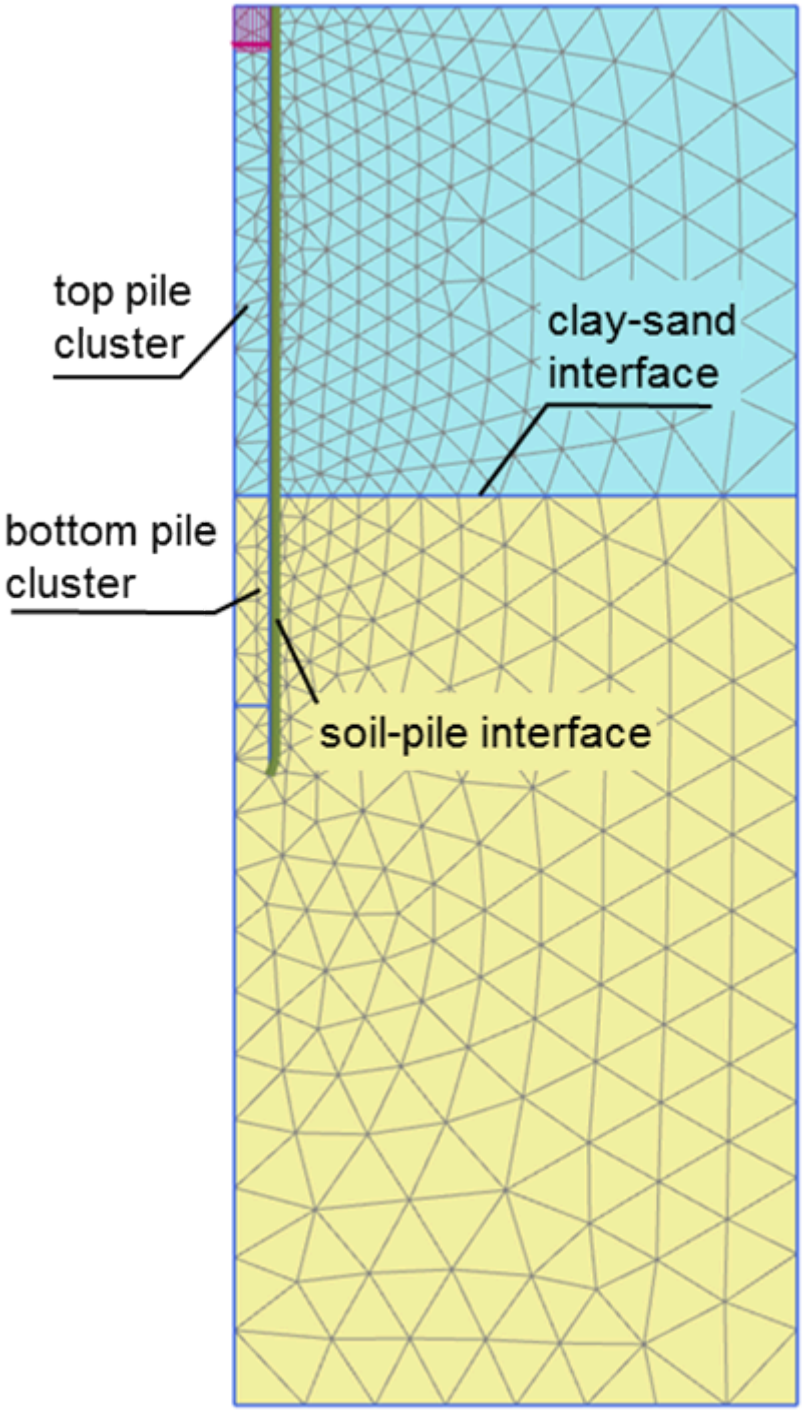

Figure 6.52. Finite element mesh including interface elements. A 10 m x 20 m "medium coarse" mesh is used, and the model is meshed while assigning soil materials to the pile clusters.

The load-displacement curves obtained from both the short-term and long-term analyses are presented in Figure 6.53, while the results of the short-term analysis are compared to the ultimate geotechnical strength estimated via the analytical α– and β-Method formulas in Figure 6.54. The upper bound of the collapse load was obtained while considering Eq. 6.20 and ψ_p = 85º for the bearing capacity factor N_{qp}, and the lower bound while considering ψ_p = 75º. The resulting bearing capacity factors are compatible with the recommendations in Table 6.4. Notice in Figure 6.53 that, as expected, the difference between the short-term and long-term response is solely due to the increased shaft friction under short-term conditions: when the maximum shaft friction resistance is reached, for a relative low pile displacement according to the mentioned in Chapter 6.7, the two load-displacement curves become parallel. As in the Example 6.2,

long-term response is found to be critical for the design of the pile. As explained in Example 6.3, this is not a surprise: PLAXIS uses the same Coulomb model as the α– and β-methods to calculate interface shear stresses, and installation effects are customarily ignored i.e., the normal stress acting at the soil-pile interface is taken equal to the geostatic horizontal stress. Therefore, the simplifications introduced in the estimation of skin friction resistance in the α– and β-methods are carried over to PLAXIS, as it is based on the same interface strength model.

Finally, notice in Figure 6.53 that, unlike Example 6.3, here the selected nominal vertical pile head displacement associated with the collapse load has profound impact on the predicted value of the later. That is because the pile toe is now embedded in drained material (sand), which shear strength depends on the confining stress. As settlement of the pile upon loading results in the development of significantly high confining stresses under its toe, the limiting end-bearing pressure increases significantly as pile head settlement progresses and this is reflected to the load-displacement curve.

In such cases it is advised to carefully select the nominal vertical pile head displacement at failure, if a numerical model is used to estimate the collapse load: the nominal vertical pile head displacement at failure $u_{y,f}$ should be the vertical pile head displacement that will result in failure of the structure supported by the pile, at the ultimate limit state.

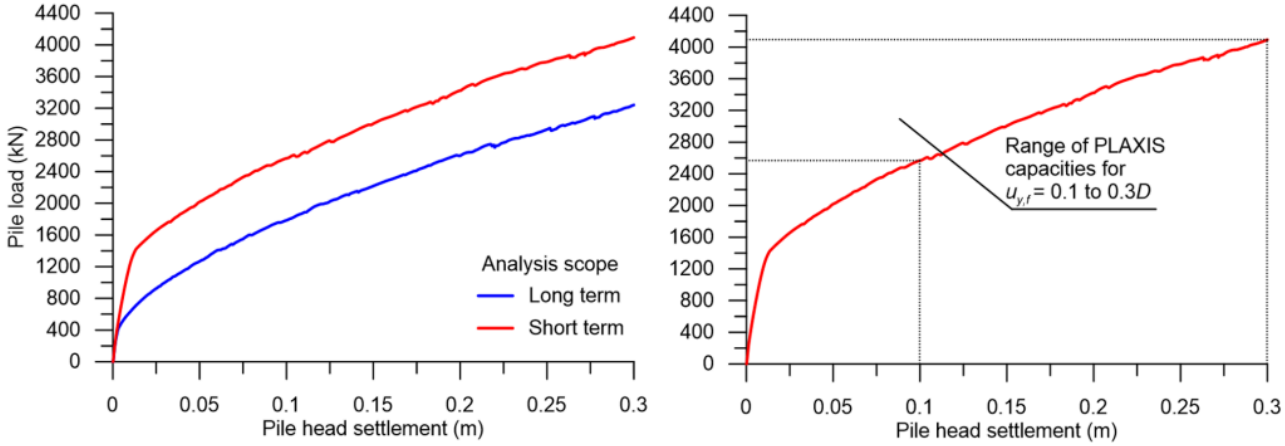

Figure 6.53. (Left) Comparison of short-term and long-term load-displacement curves, (right) Effect of nominal vertical pile head displacement at failure on predicted ultimate geotechnical strength.

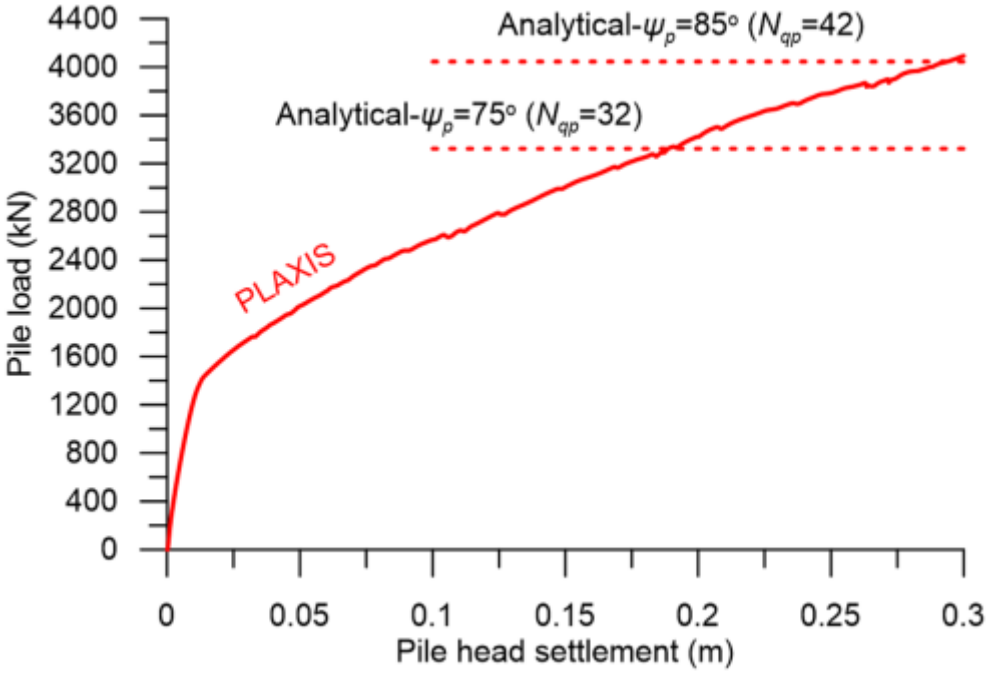

Figure 6.54. Comparison of analytical and numerical results for the short-term load case.

EXAMPLE 6.5

Estimation of the ultimate geotechnical strength of a pile subjected to axial compressive load based on SPT test results

Determine the ultimate geotechnical strength Q_f of the pile shown below. The pile is subjected to axial compressive load and is embedded in homogeneous sand. Use the SPT-based method (Chapter 6.11) and the SPT results provided below. Ignore the weight of the pile in the calculations.

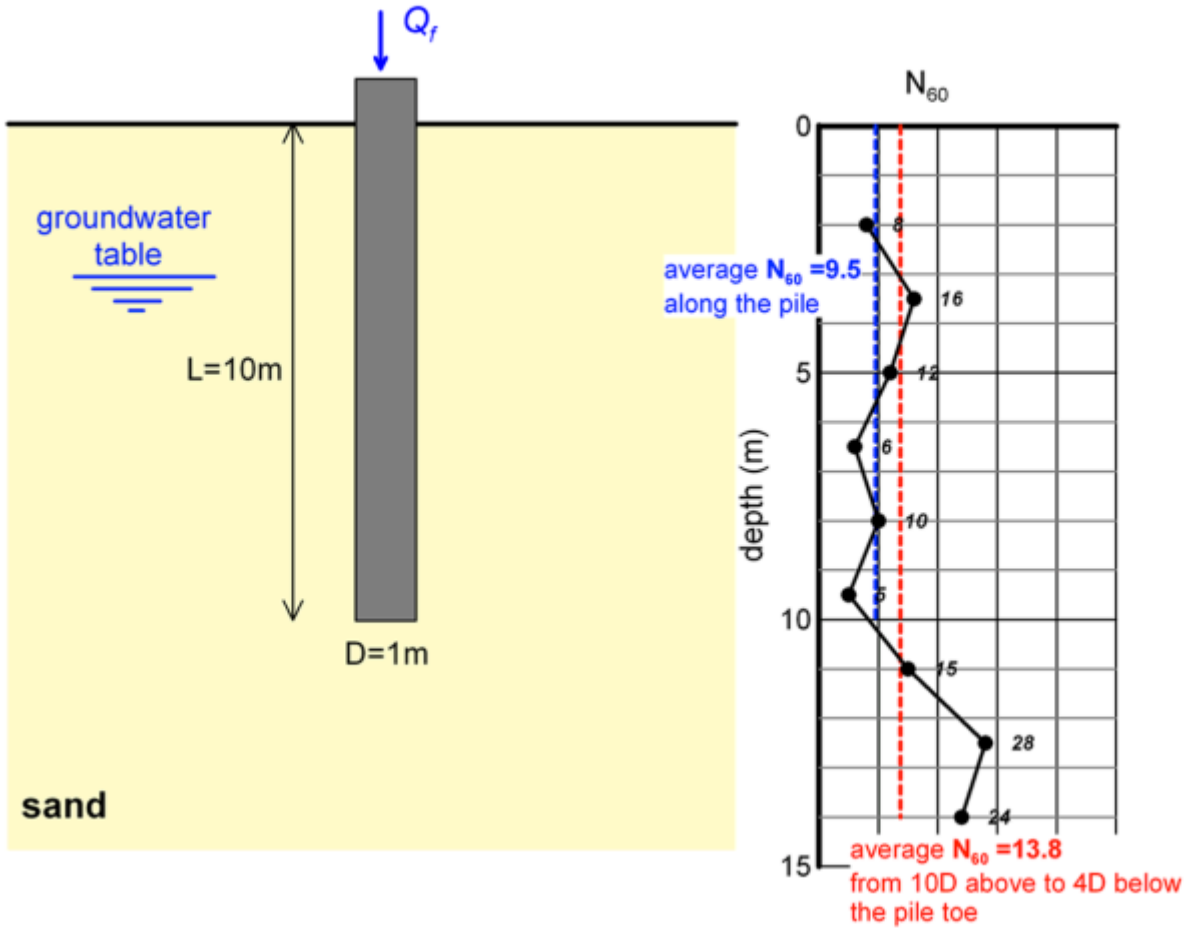

Example 6.5. Problem description and input parameters.

Answer:

1. Calculation of skin friction resistance, Q_{sf}:

We will use the upper bound of Eq. 6.21. for driven piles. The average SPT value along the length of the pile $N_{60,shaft}$ is equal to $N_{60,shaft}$ = 9.5, thus:

$$Q_{sf} = 0.02 p_a N_{60,shaft} \pi D L = 0.02 \times 100 \times 9.5 \times \pi \times 1 \times 10 = 597 \text{ kN}$$

2. End-bearing resistance, Q_b:

For the estimation of the end-bearing resistance, we have to find the average SPT value at the vicinity of the pile toe, considering blow counts about $10D$ = 10m above and $4D$ = 4m below the pile toe (Chapter 6.11). As depicted from the figure above, the average SPT value to be considered for the estimation of the end-bearing resistance is $N_{60,\text{toe}}$ = 13.8. Substituting in Eq. 6.22:

$$Q_b = 0.4 p_a N_{60,toe} \frac{L}{D} \left(\pi \left(\frac{D}{2} \right)^2 \right) = 0.4 \times 100 \times 13.8 \times \frac{10}{1} \times \left(\pi 0.5^2 \right) =$$

$$4335 \text{ kN} \leq 4 p_a N_{60,toe} \left(\pi \left(\frac{D}{2} \right)^2 \right) = 4335 \text{ kN}$$

3. Ultimate geotechnical strength, Q_f:

The ultimate geotechnical strength of the pile is again the sum of its skin friction and end-bearing resistance:

$$Q_f = Q_b + Q_{sf} = 4932 \text{ kN}$$

Notice that considering the full extent of the possible failure surface from Figure 6.22 to get the average N_{60} value implies that toe failure for this short pile with L/D=10 will reach the soil surface. This is probably unrealistic, yet it is a conservative assumption, as generally N_{60} values increase with depth.

While using similar methodologies that are based on non-site specific correlations, care must be taken so that appropriate, conservative risk ratings are introduced during the estimation of the average risk rating after AS2159.

EXAMPLE 6.6

Estimation of the ultimate geotechnical strength of a pile subjected to axial compressive load based on CPT test results

Estimate the ultimate geotechnical strength Q_f of the driven concrete pile shown below. The pile is subjected to axial compressive load and is embedded in a layered profile comprising both fine-grained and coarse-grained layers. Use CPT-based methods of Schmertmann (1978) and Bustamante and Gianeselli (1982) (Chapter 6.12) together with the CPT results provided below. Ignore the weight of the pile in the calculations.

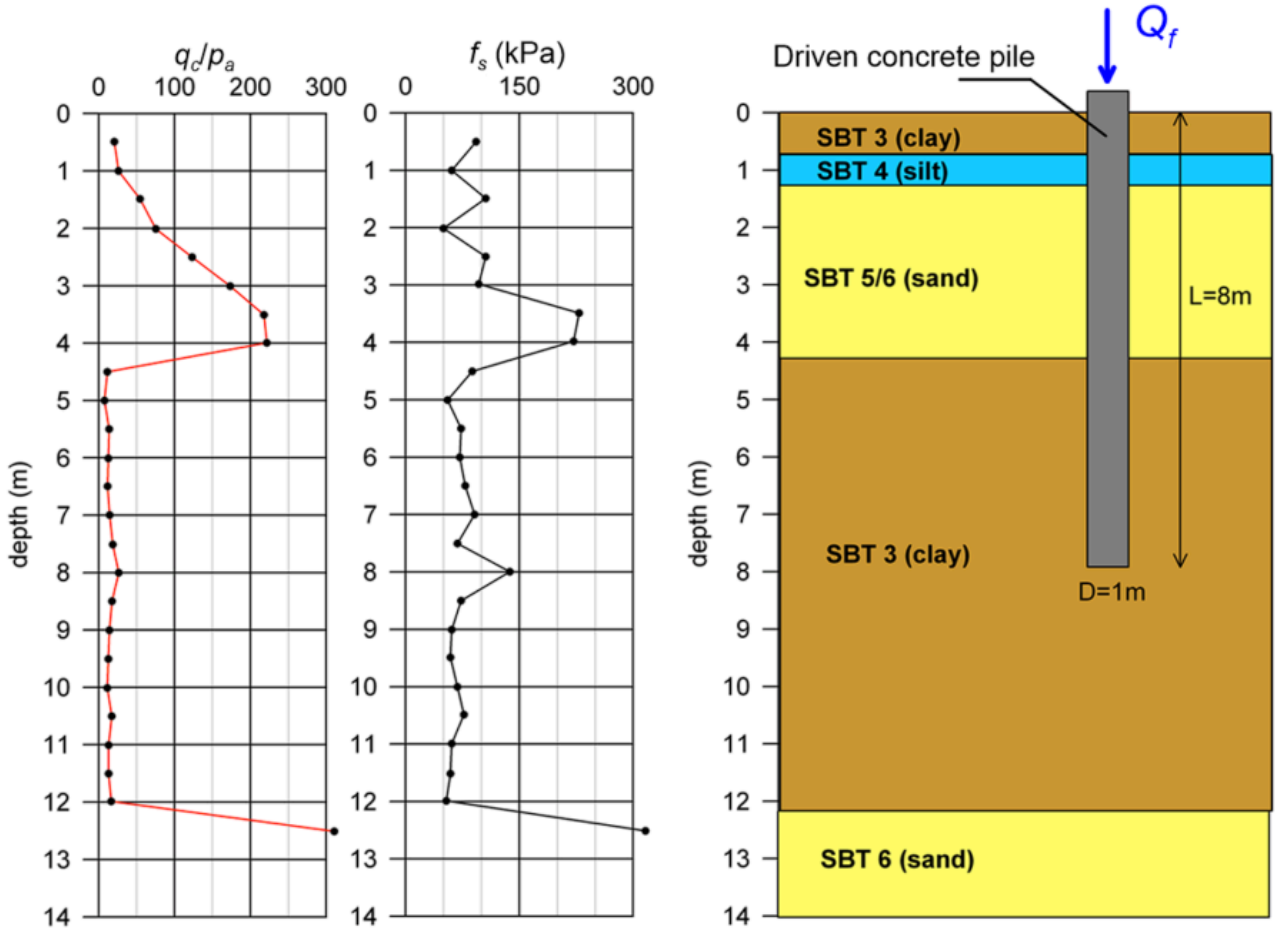

Example 6.6. Problem description and input parameters.

Answer:

As discussed in Chapter 6.12, the correction factor α' used in Schmertmann's method in the determination of the skin friction resistance Q_{sf} of the pile depends on the nature of the surrounding soil (coarse-grained or fine grained). Thus, before proceeding with the estimation of the skin friction resistance, the soil behavior types SBT encountered along the length of the pile must be determined, according to the mentioned in Chapter 1.7.

1. Calculation of skin friction resistance Q_f using the method proposed by Schmertmann (1978):

1.1 Skin friction resistance along pile shaft embedded in sand (SBT 5/6):

For the part of the concrete pile that is embedded into sand, the variation of the correction factor α' with depth z is determined with the aid of Eq. 6.24 (Figure 6.55):

$$\alpha' = 1.85 - 0.1\left(\frac{z}{D}\right) + 0.0025\left(\frac{z}{D}\right)^2 - 0.259 \times 10^{-4}\left(\frac{z}{D}\right)^3$$

The sand layer is divided into sublayers, the thickness ΔL of which depends on the frequency of sleeve friction resistance f_s measurements from the CPT test.

The unit friction resistance of each sublayer ΔQ_f is then estimated with Eq. 6.23 (Figure 6.55):

$$\Delta Q_{sf} = f_{sf}\,(\pi D)\,\Delta L = (\alpha' f_s)\,(\pi D)\,dL$$

and summed to find the skin friction resistance of the pile that develops along the part of the shaft embedded in the sand layer, $Q_{sf,sand}$.

Alternatively, we can use the Bustamante and Gianeselli's method to estimate $Q_{sf,sand}$. In that case the skin friction resistance along each sublayer is calculated as $f_{sf} = q_c/\alpha$ where the coefficient α is provided by Table 6.6 for sand with $q_c > 12$ MPa (generally $q_c/p_a > 120$ in the provided data indicating dense sand) and driven precast concrete piles (Category IIA) to be $\alpha = 150$. The limiting value of f_{sf} is from Table 6.6 $f_{sf} < 120$ kPa. Using the provided q_c values we calculate $Q_{sf,sand} = 823$ kN. There is significant difference between the results of the two methods, and is attributed only partly to the Bustamante and Gianeselli's method imposing a limiting value to f_{sf}, as the f_{sf} is exceeded in merely two sublayers.

1.2 Skin friction resistance along pile shaft embedded in clay (SBT3) and silt (SBT4):

A similar procedure is followed for the part of the pile embedded into the fine-grained clay/silt layers. In that case, the correction factor α' depends on the sleeve friction resistance, and is provided from Eq. 6.26 for concrete piles (Figure 6.56):

$$\alpha' = 1.28 - 1.473\left(\frac{f_s}{p_a}\right) + 0.839\left(\frac{f_s}{p_a}\right)^2 - 0.1634\left(\frac{f_s}{p_a}\right)^3$$

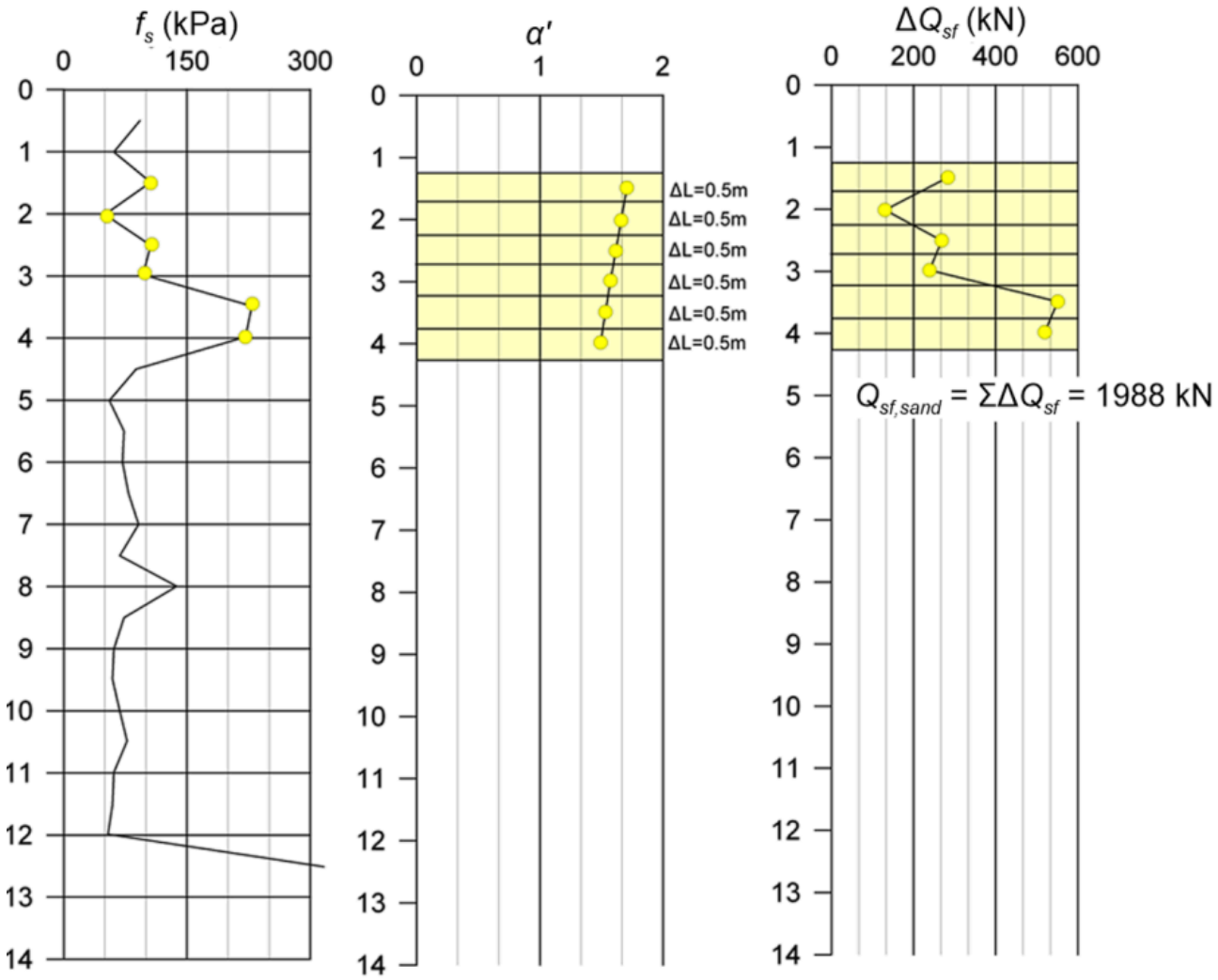

Figure 6.55. Calculation of pile's skin friction resistance along the sand layer (SBT5/6).

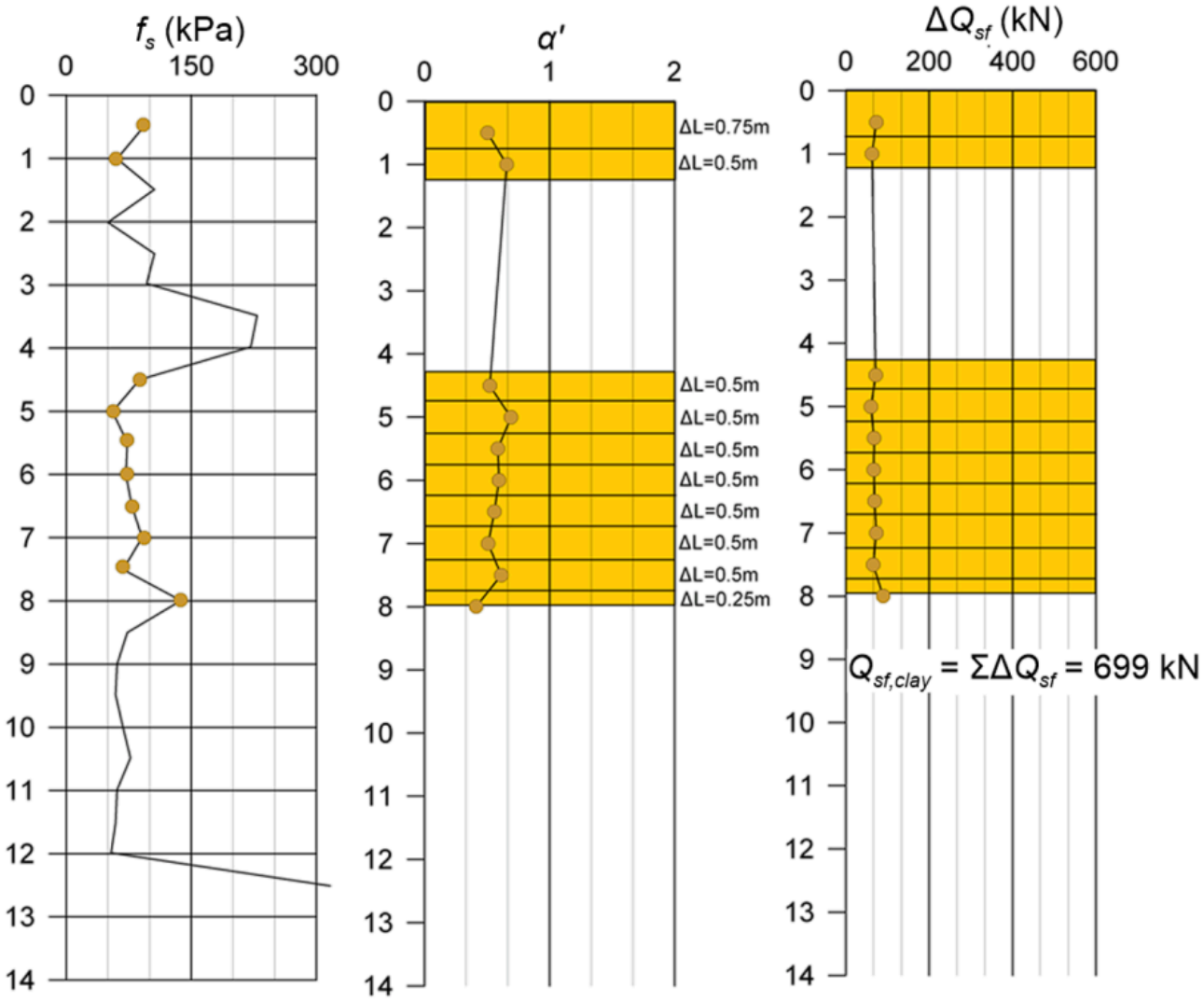

Figure 6.56. Calculation of the pile's skin friction resistance along the clay (SBT3) and silt (SBT4) layers.

Dividing again into sublayers we can estimate the unit skin friction resistance with Eq. 6.23, and the total friction resistance developing along the part of the pile embedded in fine-grained soil, $Q_{sf,clay}$ (Figure 6.56).

Again we will use the Bustamante and Gianeselli's method to estimate $Q_{sf,clay}$, for comparison purposes. Skin friction resistance along each sublayer is again calculated as $f_{sf} = q_c/\alpha$ where the coefficient α for clay with q_c = 1 to 5 MPa (firm to stiff clay) and driven precast concrete piles (Category IIA) to be α = 40. The limiting value of f_{sf} is from Table 6.6 f_{sf} < 35 kPa. Using the provided q_c values we calculate $Q_{sf,clay}$ = 499 kN. Again, there is a significant difference between the results of the two methods.

While this comparison is based on fictitious CPT data, therefore one may argue that the differences between the two methods may have been exaggerated (the total skin friction resistance estimated with Schmertmann's method is Q_{sf} = 2700 kN, and the total skin friction resistance estimated with Bustamante and Gianeselli's method is Q_{sf} = 1322 kN i.e., less than half) its purpose in not to endorse one method over the other. Instead, its purpose is to inform the reader about the uncertainties associated with estimating the ultimate geotechnical strength with empirical methods. This is the reason why careful selection of risk ratings AS2159 is required, particularly when using legacy methods to estimate the design bearing capacity of piles.

2. End-bearing resistance, Q_b:

In order to apply the LCPC method and use Eq. 6.29 to estimation the end bearing resistance of the pile, we must first estimate the equivalent average cone resistance $q_{c(eq)}$, following the procedure described in Chapter 6.12:

- Consider the cone tip resistance q_c within a range of $1.5D$ = 1.5 m below the pile toe to $1.5D$ = 1.5 m above the pile toe (Figure 6.57b) and calculate the average value of $q_{c(av)}$ = 1648 kPa within this zone.
- Eliminate q_c values that are higher than $0.7q_{c(av)}$ and lower than $1.3q_{c(av)}$ (Figure 6.57c) and calculate $q_{c(eq)}$ = 1482 kPa by averaging the remaining q_c values.

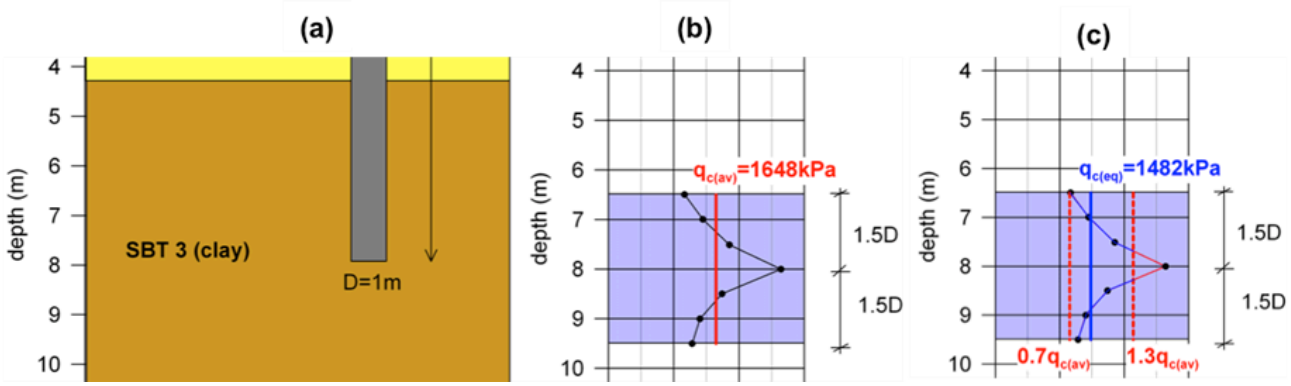

Figure 6.57. (a) Detail of the pile toe area, (b) Calculation of $q_{c(av)}$, and (c) Calculation of $q_{c(eq)}$.

Furthermore, as the pile toe is embedded in clay, the empirical bearing capacity factor to be introduced in Eq. 6.29 is k_b = 0.6 according to Briaud and Miran (1991). Substituting in Eq. 6.29 yields:

$$Q_b = q_{c(eq)} k_c A_b = 1482 \times 0.6 \times \pi \times \frac{D^2}{4} = 698 \text{ kN}$$

We can perform a sanity check here, if we consider that the undrained strength of clays is correlated to the cone resistance with Eq. 1.16 as:

$$S_u = \frac{q_t - \sigma_z}{N_{kt}} = \frac{1482 - \sigma_z}{N_{kt}}$$

If we take an average N_{kt} value N_{kt} = 15 and an estimate of the total vertical stress at -8 m i.e. σ_z = 16 x 8 = 128 kPa we calculate at the base of the pile $S_{u,b}$ = 90 kPa, which is reasonable for a stiff clay. Using Eq. 6.9 to calculate the end bearing resistance with the α-method we obtain:

$$Q_b = N_{cp} S_{u,b} A_b = 9 \times 90 \times \pi \times \frac{D^2}{4} = 636 \text{ kN}$$

Such "sanity checks" are particularly important, when empirical methods are employed for the design of piles.

3. Ultimate geotechnical strength, Q_f:

The collapse load of the pile is the sum of its skin friction resistance along the clay/silt and the sand layers, and end-bearing resistance:

$Q_f = Q_b + Q_{sf,sand} + Q_{sf,clay} = 698 + 1988 + 699 = 3385$ kN (using Schmertmann's method to calculate Q_{sf})

$Q_f = Q_b + Q_{sf,sand} + Q_{sf,clay} = 698 + 823 + 499 = 2020$ kN (using Bustamante and Gianeselli's method to calculate Q_{sf})

6.16 STATIC PILE LOAD TESTS

6.16.1 General

Static load testing is a "direct" method for determining the ultimate geotechnical strength of piles. A pile load test is practically a full-scale experiment to determine the load-settlement (or load-uplift, for tension tests) curve of an actual pile installed in the project site, in order to verify the design capacity and predicted pile settlements, or to optimise the design of the rest of the piles to be constructed.

During a pile load test, the pile head is loaded according to a predetermined loading sequence described in relevant standards (Table 6.9) and the movement at the pile head (and perhaps at some points along the pile shaft, using strain gauges or metallic rods in tubes called telltales) is recorded (Figure 6.58).

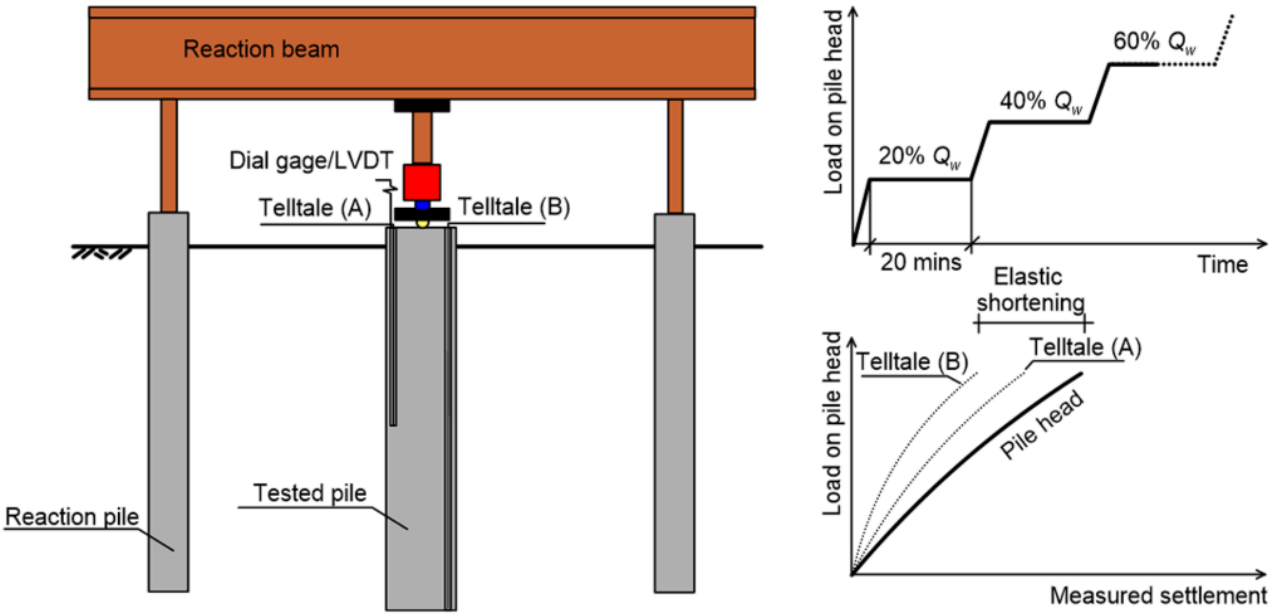

Figure 6.58. Outline of a compression static pile load test following AS2159 loading sequence.

Table 6.9. Compression static test procedure according to AS2159.

	Load	Minimum load duration
Stage S1 (proof and ultimate tests): Loading to serviceability load Q_w	20% Q_w	20 min
	40% Q_w	20 min
	60% Q_w	20 min
	80% Q_w	20 min
	100% Q_w	4 hrs
Stage S2 (proof and ultimate tests): Unloading from serviceability load Q_w	30% Q_w	10 min
	0% Q_w	20 min
Stage G1 (proof and ultimate tests): Loading to estimated collapse load Q_f	30% Q_f	20 min
	40% Q_f	20 min
	50% Q_f	20 min
	60% Q_f	20 min
	70% Q_f	20 min
	80% Q_f	20 min
	90% Q_f	20 min
	100% Q_f	1 hr
Stage U1 (ultimate tests only): Loading to *in situ* collapse load $Q_{f,test}$	110% Q_f	20 min
	Further increments of 10% Q_f	20 min each increment
	$Q_{f,test}$ or maximum available test load	Hold only if $Q_{f,test}$ exceeds the maximum available test load
Stage U2 (ultimate tests only): Unloading from in situ collapse load $Q_{f,test}$	0	10 min
Stage G2 (proof and ultimate tests): Unloading from estimated collapse load Q_f	Loading decrements of 20% Q_f	10 min each decrement
	100% Q_f	10 min
	80% Q_f	10 min
	60% Q_f	10 min
	40% Q_f	10 min
	20% Q_f	10 min

The load-settlement curve (or *compliance curve*) is plotted, and the collapse load and/or corresponding settlements at different test stages are determined by properly interpreting the results.

A pile load test is performed:

- To minimise risks by confirming the suitability of deep foundations to support the design action load without exceeding the allowable settlement, especially in projects of high geotechnical risk.
- To optimise design and construction procedures during the early stages of a project.
- To satisfy regulatory agency requirements.

Although static pile load tests are costly and time consuming, they may ultimately result in significant savings, as "in depth" project-specific knowledge of the behaviour of the pile-soil system may lead to reduction of necessary pile lengths, and to the adoption of a higher geotechnical reduction factor φ_g. Dynamic pile load tests are faster but, in the author's view, more cumbersome to interpret and are not covered in this Part.

6.16.2 Description of test procedures

The axial load is applied on the pile by stacking sandbags or, more usually these days, by jacking against a reaction beam and reaction piles (Figure 6.59). Instead of reaction piles, anchors or a weighted platform may be used. Working piles may be used as reaction piles to carry the tension load, provided that:

- As illustrated in Figure 6.59, the centre-to-centre spacing between the reaction piles and the loaded pile will not be less than the greater of 5 times the test pile diameter, and 2.5 m (AS2159).
- Measures are implemented to ensure that any permanent displacement of the reaction piles will not affect their load carrying performance in serviceability and ultimate limit state conditions.

Calibrated load cells are used to measure the applied load, while the jack load should also be recorded from a pressure gauge. A spherical bearing plate is placed between the hydraulic jack and the reaction beam, to minimise eccentricities. The pile displacement and any rotation or tilt of the pile head are monitored either by a survey leveling system, or by 3 or more dial gauges or position sensors (LVDT's) in conjunction with a reference frame, that is independent of the reaction system and the test pile. Often, the leveling system is used as back-up of dial gauges or LVDT's.

Dial gauges or LVDT's should preferably have a minimum of 75 mm of travel and a precision of 0.025 mm (less than 0.1% of the pile diameter and 0.1 mm, according to AS2159).

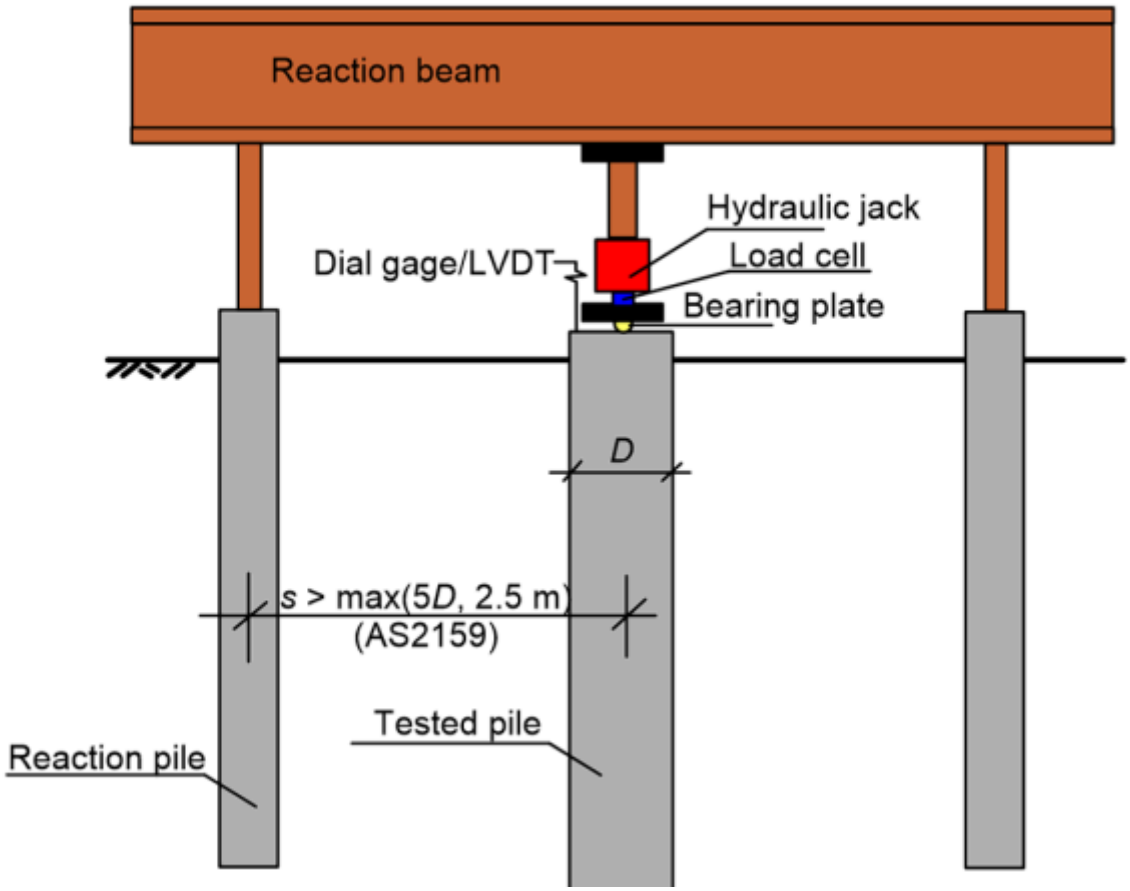

Figure 6.59. Pile load test setup and AS2159 spacing requirements.

6.16.3 Proof and ultimate static load tests

Based on the objectives of the load test, pile load tests are classified into:

- *Proof tests,* where we seek to measure the settlement of the pile head under the serviceability load Q_w, and confirm that the pile is able to carry a vertical load equal to the estimated (by means of the methods described earlier in this Part) collapse load Q_f without developing excessive pile head settlement.
- *Ultimate tests,* where we seek to find the ultimate geotechnical strength (collapse load) $Q_{f,test}$ of the pile *in situ*.

As it is perhaps clear from the above, proof tests can be performed on working piles too, while ultimate tests are performed on sacrificial piles that are loaded up to failure.

When *negative skin friction* is not expected, the following maximum test loads Q_{max} are applied on the pile's head (Figure 6.60):

For a proof load test to measure the settlement under serviceability conditions:

$Q_{max} = Q_w$ where Q_w is the design serviceability load

For proof load test to verify the design geotechnical strength:

$Q_{max} = Q_f = S^*/\varphi_g$, where S^* is the design action compressive load, or

$Q_{max} = Q_{f,t} = 1.2S_t^*$, where S_t^* is the design action tensile load

For an ultimate load test:

$Q_{max} = Q_{f,test}$ or $Q_{f,t,test}$ which is the ultimate geotechnical strength (collapse load) of the pile as assessed *in situ*, from pile tests. This load must be estimated in advance, while sufficient allowance must be made in all aspects of the test setup, including the structural strength of the pile required to exceed this estimate.

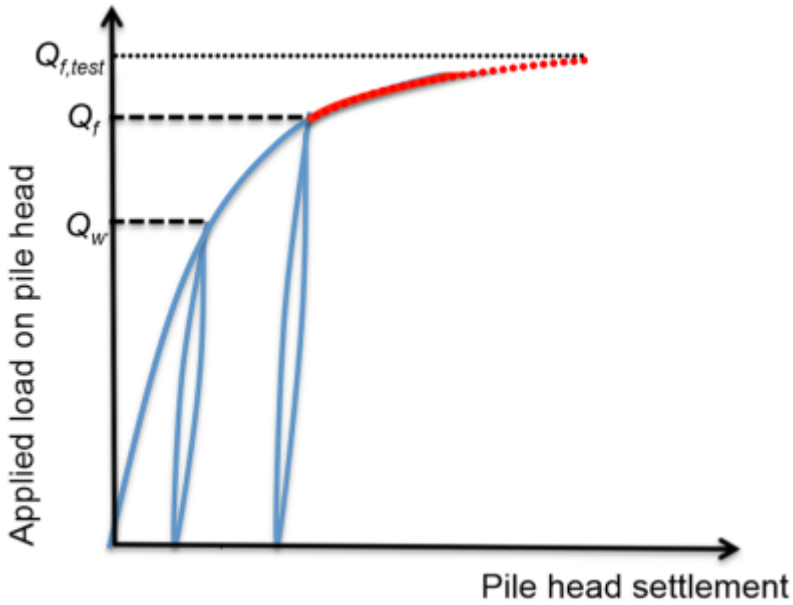

Figure 6.60. Compliance curve of proof and ultimate compressive static pile load tests.

The load on the pile head must be applied in specific increments, according to the test procedure (Figure 6.61 and Table 6.9). Following application of each load increment, the load shall be sustained at a constant magnitude until the rate of pile head settlement is less than 0.5 mm per 15 min, commencing 5 min after applying any load increase. The minimum holding time specified in AS2159 is listed in Table 6.9. Both pile loading and unloading must comply with the minimum load duration.

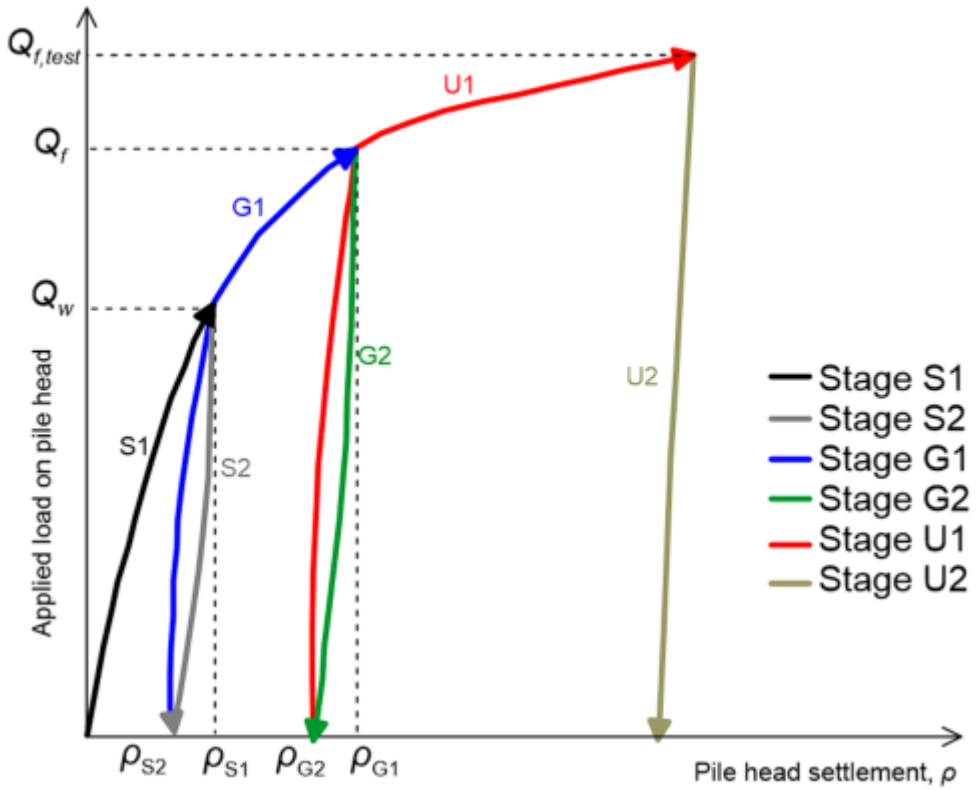

Figure 6.61. Compliance curve following the test procedure described in AS2159.

Successful proof tests must satisfy certain *acceptance criteria* related to the pile head settlement at the end of the loading and unloading stages S1-S2 and G1-G2 (Table 6.10). If these criteria are not met, the design bearing capacity must be reassessed.

Various methods have been proposed for the definition of the *in situ* collapse load from ultimate tests $Q_{f,test}$ as it is rarely explicitly identifiable from the load-displacement curve: It has been mentioned earlier that piles rarely develop a "brittle" plunging failure mode, and usually harden until unacceptable settlements develops (see Chapter 6.7). According to AS2159, the *in situ* ultimate geotechnical strength $Q_{f,test}$ of the pile is the greater of:

- The maximum pile load which can be sustained for a period of 10 min, and
- The pile load corresponding to the maximum settlement that would cause failure of the structure (*not* the maximum allowable settlement of the structure, which corresponds to serviceability conditions).

In the absence of project-specific values of the maximum allowable settlement, this shall be considered to be equal to $0.05D$ for driven piles and $0.1D$ for drilled shafts.

Table 6.10. Compression load test acceptance criteria according to AS2159.

Stage	Load at the end of stage	Pile head settlement at the end of stage (mm)
S1	Q_w	$\left(\frac{Q_w L}{E_p A_p}\right) + 0.01D$
S2	*0*	$\max\left(0.01D; 5\text{ mm}\right)$
G1	Q_f	$\left(\frac{Q_f L}{E_p A_p}\right) + 0.05D + 10$
G2	*0*	$0.05D + 10$
D is the pile diameter; L is the pile length; A_p is the area of the pile's section; E_p is the Young's modulus of the pile's material		

Alternatively, one case use the *"offset limit"* method proposed by Davisson (1972) (FHWA 2006). As illustrated in Figure 6.62a, the elastic shortening of the pile head under the *in situ* collapse load $Q_{f,test}$ is estimated as:

(6.79) $$\rho_{short} = \frac{Q_{f,test} L}{E_p A_p}$$

For piles with diameter D < 0.60 m the failure load is the one that results in a pile toe settlement equal to:

(6.80) $$\rho_f = \rho_{short} + 0.381 + \frac{D}{120}\left(\text{units}: \text{ cm}\right)$$

For piles with diameter D > 0.60 m the failure load is the one that results in a pile toe settlement equal to:

(6.81) $$\rho_f = \rho_{short} + \frac{D}{30}\left(\text{units}: \text{ cm}\right)$$

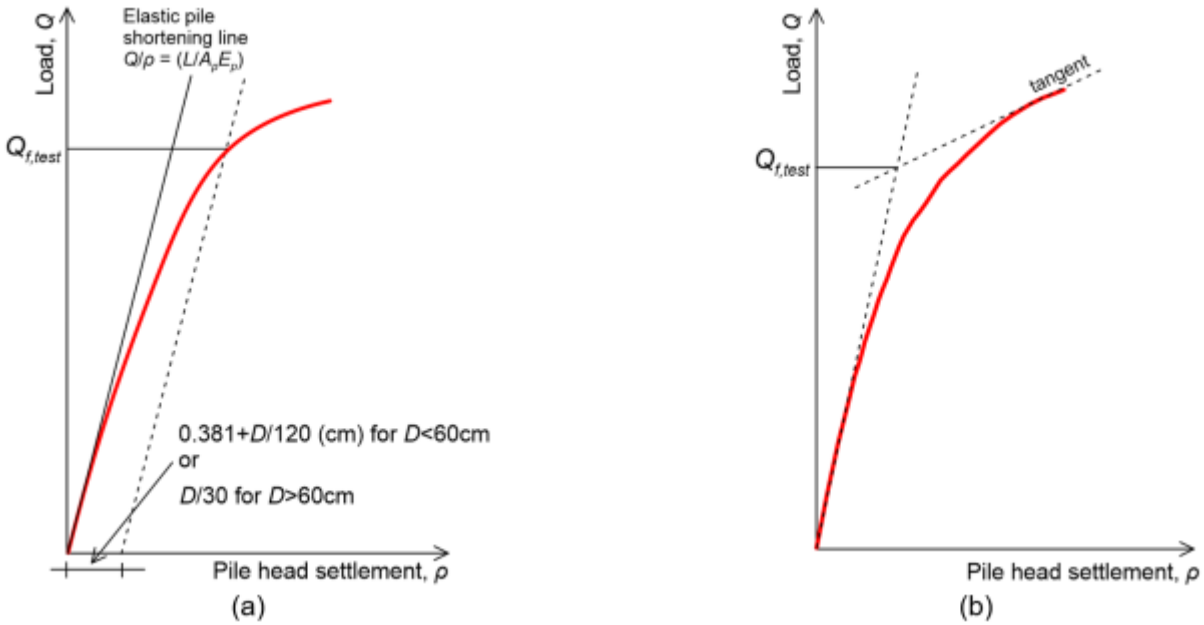

Figure 6.62. Alternative methods for determining the ultimate geotechnical strength of piles from ultimate tests: (a) offset limit method, and (b) double tangent method.

For drilled shafts, the graphical *double tangent* method can be used (Figure 6.62b) to determine $Q_{f,test}$. The load-displacement curve is plotted, and the *in situ* collapse load $Q_{f,test}$ is defined at the intersection of the tangent lines of the initial and final part of the curve. When applying this method one should bare in mind that the elastic shortening of the pile ($Q_{f,test}L/E_pA_p$) is not considered. Thus, the *in situ* collapse load of short piles may be over-estimated, and the *in situ* collapse load of long piles may be under-estimated, if the elastic shortening of the pile (Eq. 6.79) is significant.

6.16.4 Geotechnical strength reduction factor φ_g according to AS2159 accounting for pile load test results.

As discussed earlier, when static pile load tests are performed to verify *in situ* the design assumptions, AS2159 allows for the adoption of a higher value for the *geotechnical strength reduction factor* φ_g. The basic geotechnical strength reduction factor φ_{gb} derived via the risk assessment procedure described in Chapter 6.8, is increased as:

(6.82) $$\varphi_g = \varphi_{gb} + (\varphi_{tf} - \varphi_{gb})\, K \geq \varphi_{gb}$$

where φ_{tf} = 0.9 for static load tests, and

(6.83) $$K = \frac{1.33p}{p + 3.3} \leq 1$$

with p (%) being the percentage of total piles tested that meet the acceptance criteria listed in Table 6.10. When a systematic pile load testing campaign is performed, the above procedure will lead to substantial increase of the strength reduction factor: For example, if proof load tests are performed in 1 every 20 working piles (p = 5%), and all piles meet the acceptance criteria, the geotechnical strength reduction factor can be increased from e.g. φ_{gb}=0.56 to

(6.84) $$\varphi_g = 0.56 + (0.9 - 0.56)\left(\frac{1.33 \times 5}{5 + 0.33}\right) = 0.832$$

6.17 PILE DRIVING FORMULAS

An alternative method for determining the collapse load of driven piles *in situ* is to correlate it with the energy required to drive the pile into the soil. Several equations have been proposed for this and are implemented in pile driving equipment software to verify whether a pile has reached the required ultimate geotechnical strength Q_f when driven at the pre-determined depth (or determine the penetration depth where the required Q_f is reached).

One of the earliest equations is the *Engineering News (EN) Record formula*, which was derived in 1888 by AM Wellington, editor of the Engineering News Record, to measure the capacity of light-weight timber piles on the basis of work-energy theory (Lawton et al. 1986):

$$\textbf{(6.85)}\ Q_{f,test} = \frac{n_1 W_R h}{s_p + C_1}$$

where W_R is the weight of the hammer; h is the height of fall; s_p is the pile penetration depth per blow, taken as the average value obtained from the last few driving blows; C_1 is a constant, equal to C_1 = 25 mm for drop hammers and C_1 =2 .5 mm for steam hammers; n_1 is a constant depending on the hammer efficiency, provided in Table 6.11.

Table 6.11. Typical values for the n_1 factor (Budhu 2011).

Hammer type	n_1
Drop hammer	0.75-1.0
Single-acting hammer	0.75-0.85
Double-acting hammer	0.85
Diesel hammer	0.85-1.0

The EN formula has been modified several times over the years, to account for developments in driving technology. A more recent version of Eq. 6.85 is (Michigan State Highway Department 1965):

$$\textbf{(6.86)}\ Q_{f,test} = \left(\frac{E_{EN} W_R h}{s_p + C}\right) \times \left(\frac{W_R + n_{EN}^2 W_p}{W_R + W_p}\right)$$

where E_{EN} is the efficiency of the hammer, from Table 6.12; C = 2.54 mm (s and h in mm too); W_p is the weight of the pile; n_{EN} is the coefficient of restitution between the hammer and the pile tip, provided in Table 6.13.

Table 6.12. Typical values for the E_{EN} factor (Michigan State Highway Department 1965).

Hammer type	E_{EN}
Single and double-acting hammer	0.70-0.85
Diesel hammer	0.80-0.90
Drop hammer	0.70-0.90

Table 6.13. Typical values for the n_{EN} factor (Michigan State Highway Department 1965).

	n_{EN}
Cast-iron hammer and concrete piles (without cap)	0.40-0.50
Wood cushion on steel piles	0.30-0.40
Wooden piles	0.25-0.30

6.18 PILE GROUP EFFECTS ON ULTIMATE GEOTECHNICAL STRENGTH

In most practical cases, except of some special structures such as lighting poles or wind turbines, multiple piles arranged in groups are used for the foundation of structures. Piles are arranged in square, rectangle, circular groups, or in pile rows and their heads are connected via a reinforced concrete *pile cap* of adequate thickness (Figure 6.63).

Piles groups feature considerable lateral stiffness, which renders them the most efficient foundation solution when large lateral loads or bending moments must be transferred to the subsoil due to e.g., seismic or wind actions or lateral earth pressures.

Additionally, pile groups have the capacity to carry high vertical loads, although the load capacity of a pile group is not necessarily equal to the load capacity of a single pile multiplied by the number of piles in the group. The *pile group efficiency,* n_g is defined as the ratio of the ultimate geotechnical strength of a group of n piles, $Q_{f,group}$ to the sum of the ultimate geotechnical strength of the individual piles comprising the group, Q_f. In most common cases where all piles in the group feature the same ultimate geotechnical strength:

(6.87) $$n_g = \left(\frac{Q_{f,group}}{nQ_f} \right)$$

The pile group efficiency n_g can be higher or lower than 1, meaning that the bearing capacity of the pile group can be less or greater than the sum of the capacities of the individual piles. Pile group efficiency $n_g < 1$ is possible in piles driven into soft clay/silt or dense sand/dense gravel formations, while group efficiency $n_g > 1$ can be attained when piles are driven into loose sand/loose gravel formations, due to densification of soil around the piles during driving (see for example Figure 6.20). To achieve pile group efficiencies higher than unity, the centre-to-centre spacing of the piles in the group must be dense, generally $s < 3D$ (Figure 6.63). However, installation of piles with such dense spacing is not recommended, due to constructability issues. According to AS2159, spacing $s < 2.5D$ is not recommended, unless *"an analysis of interaction effects indicates that overall pile group performance is not adversely affected".* When $s > 3D$, the piles perform essentially as individual under vertical compressive loads ($n_g = 1$), and the bearing capacity of the pile group can be taken as equal to the sum of capacities of individual piles.

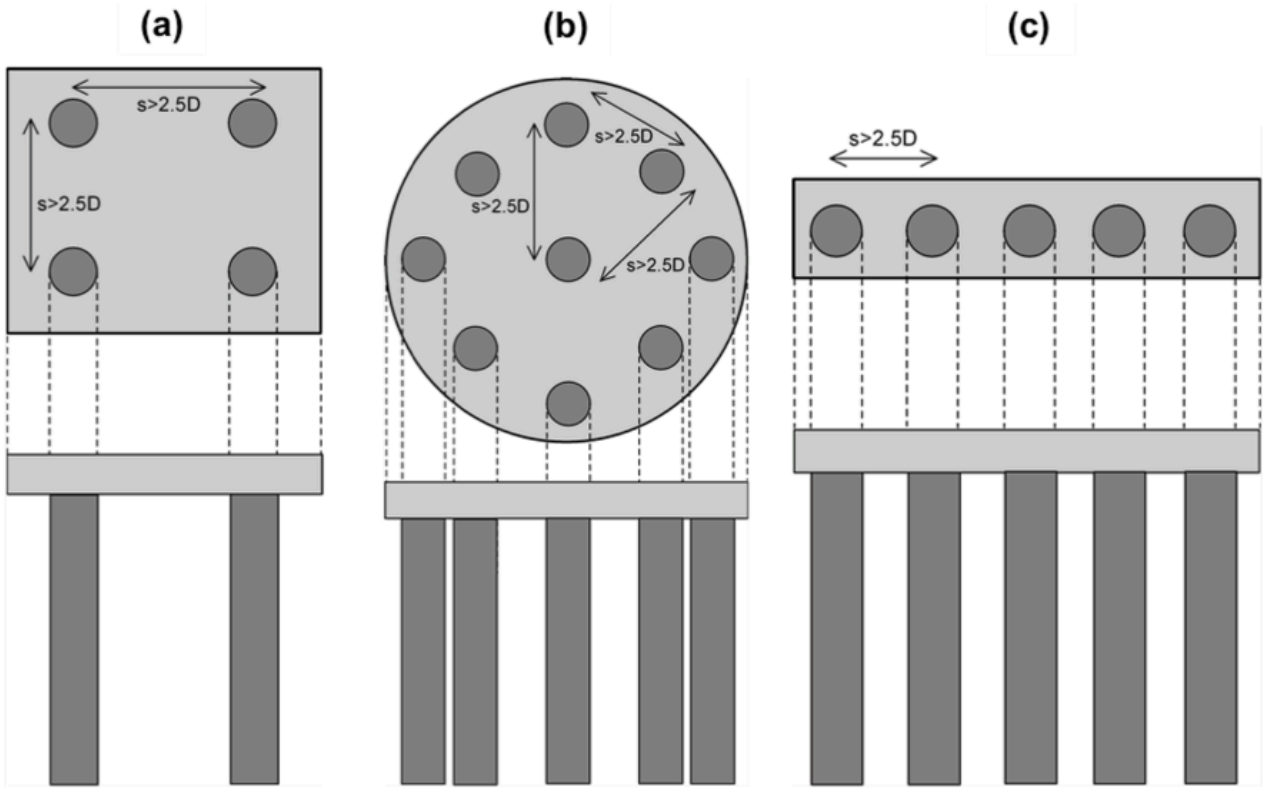

Figure 6.63. Piles arranged in (a) square group, (b) circular group, and (c) pile row (figures not in scale).

Figure 6.63d. Piles arranged in pile row.

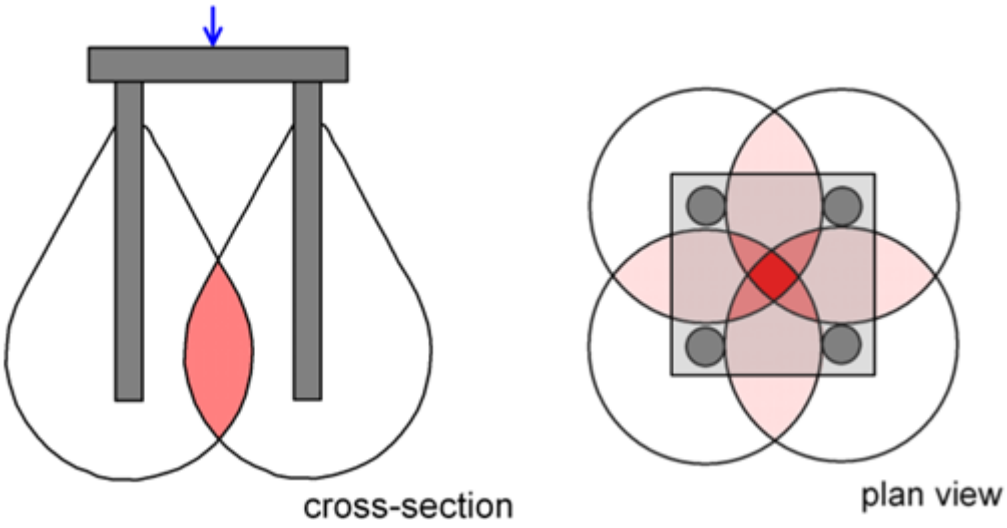

Figure 6.64. Overlapping of stress zones in a closely-spaced pile group.

In fine-grained soils, pile group efficiency $n_g < 1$ may need to be considered, to account for overlapping zones of shear deformation in the soil surrounding the piles (Figure 6.64). FHWA (2006) recommends:

- If the pile cap is in firm contact with the ground, consider $n_g = 1$.
- If the pile cap is not in firm contact with the ground as in the case of e.g., an offshore platform foundation, and the undrained shear strength of the fine-grained foundation soil is $S_u < 100$ kPa, a group efficiency $n_g = 0.7$ should be considered in the calculation when the center-to-center pile spacing is $s = 3D$. When the spacing is greater than $s = 6D$, $n_g = 1$ can be considered. Linear interpolation can be used to obtain n_g for intermediate spacing values:

$$\textbf{(6.88)}\quad n_g = 0.1\left(\frac{s}{D}\right) + 0.4 \leq 1$$

- As above, spacing s should not be less than $s < 3$

Note that pile driving operations can result in generation of excess pore pressures, that could lead to *temporary* pile group efficiencies of $n_g = 0.4$ to 0.8 immediately after construction. As excess pore pressures dissipate, the efficiency will increase to its normal value. If the foundation will be loaded with the full load shortly after its construction, this effect must be taken into account while determining the ultimate geotechnical of the pile group.

When estimating the ultimate geotechnical strength of a pile group, the possibility of a general, *block-type* failure mode must be also considered, as described in AS2159. When the pile spacing is generally small, the pile group may fail as a block containing the piles and the soil between them (Figure 6.65a). This type of failure can occur in pile groups installed in fine-grained soils, but also in pile groups founded in a layer of dense coarse-grained soil of limited thickness, when it is underlain by a soft fine-grained layer.

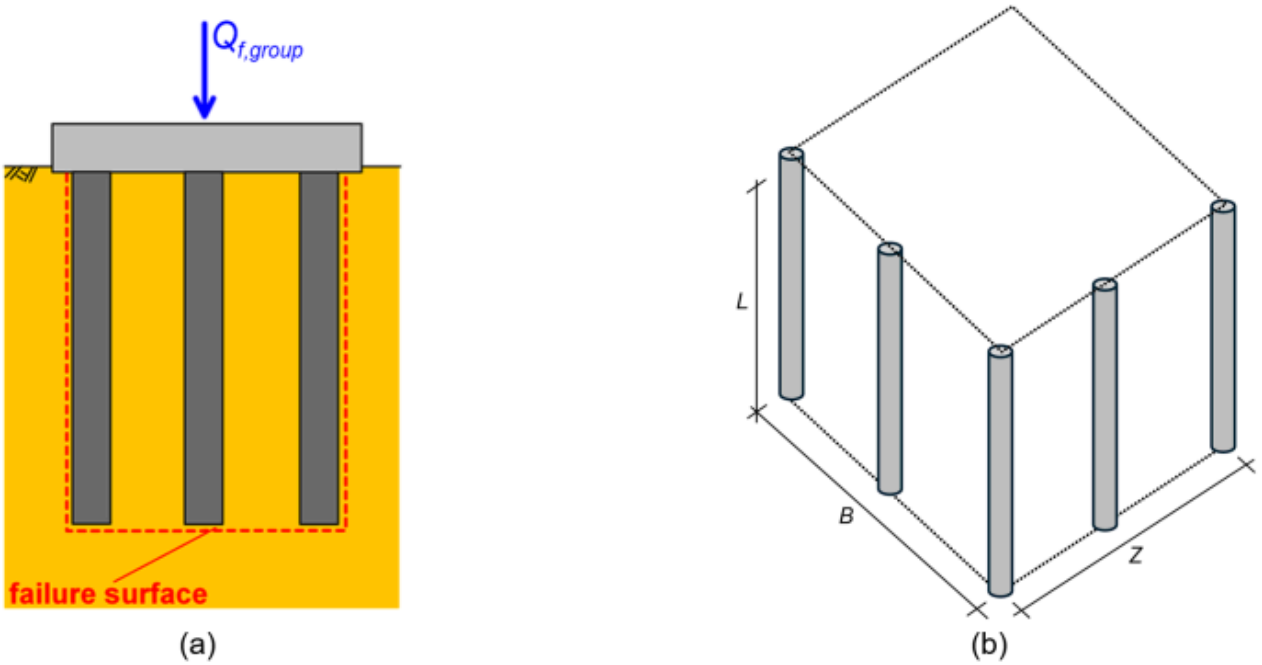

Figure 6.65. (a) Block-type failure of pile group in fine-grained soil, and (b) 3-D pile group arrangement.

The ultimate geotechnical strength of a pile group against block failure is estimated as:

(6.89) $$Q_{f,group} = S_{u,ave}\left[2L\left(B+Z\right)\right] + N_{cp}S_{u,b}\left(BZ\right)$$

where B is the width of the pile group (Figure 6.65b); Z is the length of the pile group (Figure 6.65b); L is the length of the piles; $S_{u,ave}$ is the average undrained shear strength of the soil along the length L; $S_{u,b}$ is the average undrained shear strength at the base of the pile group up to a depth of $2B$ below the pile toe level; N_{cp} is the bearing capacity factor for undrained conditions defined in Chapter 6.9.

EXAMPLE 6.7

Estimation of the design bearing capacity of a pile group

An offshore pole is going to be founded on a pile group consisting of 4 cylindrical piles, with the geometry shown in the figure below. Determine the short-term design bearing capacity of the pile group, according to AS 2159 provisions, For the specific project, assume a basic geotechnical strength reduction factor φ_{gb} equal to $\varphi_{gb} = 0.60$.

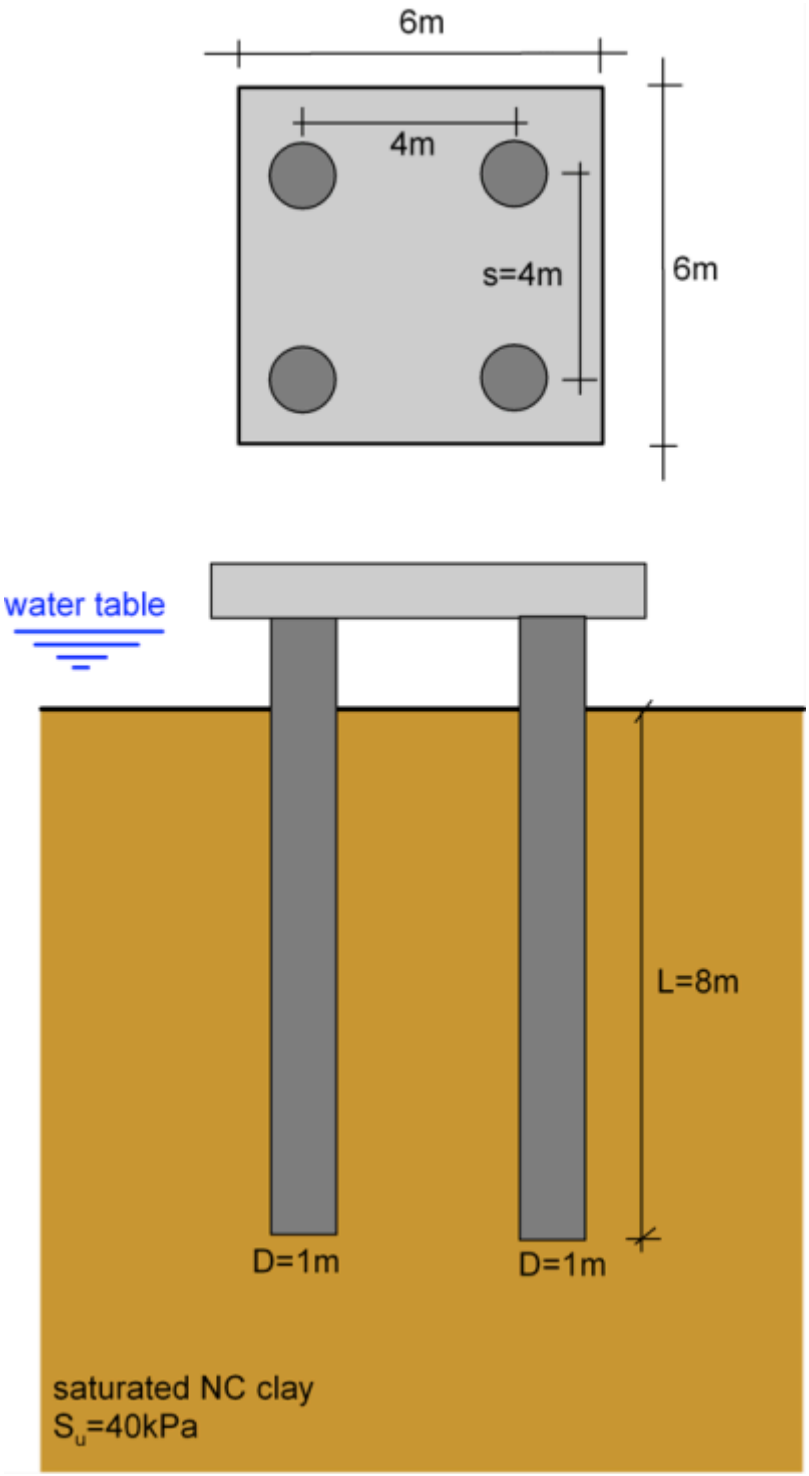

Example 6.7. Problem description and input parameters.

Answer:

In the Example 6.1 we have determined the ultimate geotechnical strength of each single pile with the α-Method as:

$$Q_f = Q_{sf} + Q_b = 1059 \text{ kN}$$

1. Ultimate geotechnical strength of pile group considering efficiency, n_g:

According to FHWA (2006), pile group efficiency n_g for cases where the pile cap is not in firm contact with the ground and s/D = 4 m/1 m =4 (Eq. 6.88) is:

$$n_g = 0.1\left(\frac{s}{D}\right) + 0.4 = 0.8$$

Therefore the ultimate geotechnical strength of pile group considering is (Eq. 6.87):

$$Q_{f,group} = n_g\left(nQ_f\right) = 0.8 \times 4 \times 1059 = 3389\ \text{kN}$$

2. Ultimate geotechnical strength of pile group for block-type failure:

We will apply Eq. 6.89, considering B = 4 m and Z = 4 m i.e., the dimensions of the pile group, not the pile cap (Figure 6.65b). Also, as for the calculation of the skin friction resistance of a single pile, the first $1.5D$ meters of the pile shaft will not contribute to the friction resistance:

$$Q_{f,group} = S_{u,ave}\left[2L\left(B+Z\right)\right] + N_{cp}S_{u,b}\left(BZ\right) = 40\left[2\left(8-1.5\right)\left(4+4\right)\right] + 40 \times 9 \times \left(4 \times 4\right) = 9920\ \text{kN}$$

Observe that the ultimate geotechnical strength for block-type failure is grossly larger than the ultimate geotechnical strength considering failure of individual piles, even when pile group efficiency $n_g < 1$ is applied to the latter. This does not come as surprise: Block-type failure can, by definition, be critical only for very dense pile spacings, when the area of the pile group $(B \times Z) + 2(B \times L) + 2(Z \times L)$ is smaller than the surface area of the individual piles.

3. Design bearing capacity of pile group

The design bearing capacity $\varphi_{gb}Q_{f,group}$ is:

$$\varphi_{gb}Q_{f,group} = 0.60 \times 3389 = 2033\ \text{kN}$$

6.19 IMMEDIATE SETTLEMENT OF SINGLE PILES

State-of-practice methods for predicting settlement of single piles (driven piles or drilled shafts) are still very much based on simplified mathematical models of piles and their surrounding soil. Predictions of such models for typical pile/soil parameter combinations are often compiled by authors of relevant publications into "design charts", to relieve users from the onerous task of programming the rather convoluted expressions. The vast majority of such mathematical models are based on the theory of elasticity, and as such require adopting a series of assumptions, the main of which is that both pile and soil behave as linear elastic, and no separation (slippage) takes place at the soil-pile interface. Comparison of model predictions with measurements obtained during field tests has proven that these assumptions are reasonably accurate under serviceability conditions, when the load acting on the pile head is relatively low, and non-linearity effects can be ignored. Of course today it is relatively straightforward to numerically model a single pile subjected to an axial compressive load (see Examples 6.3 and 6.4), thus obtain direct estimates of settlement without being limited to specific combinations of parameters for which the design charts have been prepared for, while non-linear soil behaviour and slippage at the soil-pile interface can certainly be accounted for even in simple models. This however has not rendered simplified methods obsolete.

It is important to keep in mind that, as settlement is estimated while considering serviceability loads, we may assume that the full serviceability load Q_w is transferred through skin friction when the skin friction resistance Q_{sf} is higher than the serviceability load:

(6.90) $$\text{if } Q_w < Q_{sf} \text{ then } Q_{sfw} = Q_w \text{ and } Q_{bw} = 0$$

If the serviceability load Q_w is higher than the available skin friction resistance Q_{sf}, then we can effectively assume that the load transferred along the pile shaft through friction under serviceability conditions Q_{sfw} is equal to the skin friction resistance Q_{sf}. The remaining of the load Q_{bw} is transferred to the pile toe:

(6.91) $$\text{if } Q_w > Q_{sf} \text{ then } Q_{sfw} = Q_{sf} \text{ and } Q_{bw} = Q_w - Q_{sf}$$

In other words, the skin friction resistance of the pile is fully mobilised before any load is transferred to its toe.

As the serviceability load is transferred from a pile to the soil predominantly via friction at the soil pile-interface, with little change in the normal stress, the bulk of settlement of a single pile will develop immediately after the load is applied *(immediate, or elastic settlement).* Consolidation settlement is of the order of 15% of the total settlement for individual piles driven through saturated clay, and generally is not explicitly calculated.

The methods presented in the following for the calculation of immediate settlement of single piles consider compressible piles, hence elastic shortening ρ_s is inherently considered in the analysis.

6.19.1 Estimation of settlement of compressible friction piles in homogeneous soil

Poulos (1989) describes elasticity-based solutions for predicting settlement of a single cylindrical friction

pile embedded in a homogeneous elastic soil layer of infinite thickness. Under these conditions, settlement of a single friction pile ρ_e (the subscript $_e$ refers to elastic settlement, that will develop immediately after application of the load) can be calculated as:

$$\textbf{(6.92)}\ \rho_e = \frac{Q_w}{E_s D} I_s$$

where Q_w is the serviceability load applied at the pile head, D is the diameter of the pile and E_s is the Young's modulus of the soil layer. The factor I_s, which actually is the inverse of the dimensionless vertical stiffness of the pile head (vertical stiffness = axial load/vertical settlement Q/ρ), can be estimated from Figure 6.66. It depends on the ratio of the Young's modulus of the pile E_p over the (drained E' or undrained E_u depending on the soil type) Young's modulus of the soil E_s. Note that the original solutions by Poulos consider undrained incompressible soil (Poisson's ratio $\upsilon_s = 0.5$) therefore, strictly speaking, Figure 6.66 is applicable only to piles in clay and $E_s = E_u$. However, it is common to use this chart for piles in drained soil too, as the effect of the Poisson's ratio of soil on pile settlement is not particularly prominent. This is demonstrated later in this Chapter.

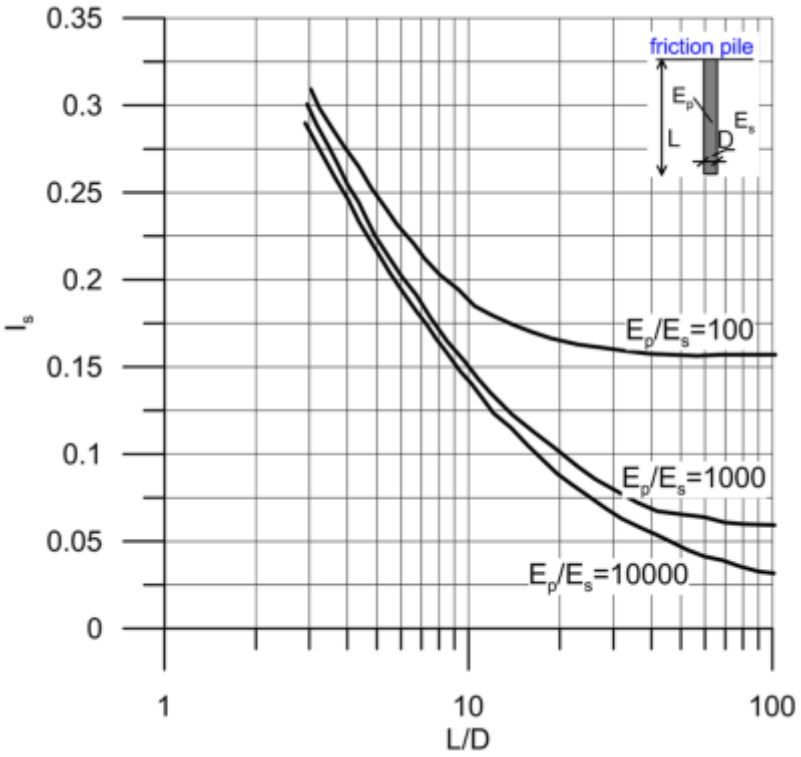

Figure 6.66. Pile head stiffness factor I_s for estimating settlement of a friction pile in homogeneous soil of infinite thickness (after Poulos 1989).

Note here that in case the pile is not solid (i.e., is a hollow cylindrical pipe pile), the moduli ratio or relative pile material stiffness $K_p = E_p/E_s$ should be calculated as:

$$\textbf{(6.93)}\ K_p = \frac{E_p}{E_s}\left(\frac{\text{Area of pile section}}{\frac{\pi D^2}{4}}\right)$$

In the special case of a solid pile it is $K_p = E_p/E_s$. In lack of a more accurate (and equally simple) solution, if the soil's Young modulus is not uniform along the length of the pile, a weighted average can be used together with Eq. 6.92 as (Figure 6.67):

(6.94) $$E_{s,av} = \frac{E_{s,1}L_1 + E_{s,2}L_2 + E_{s,3}L_3 + \ldots}{L_1 + L_2 + L_3 + \ldots}$$

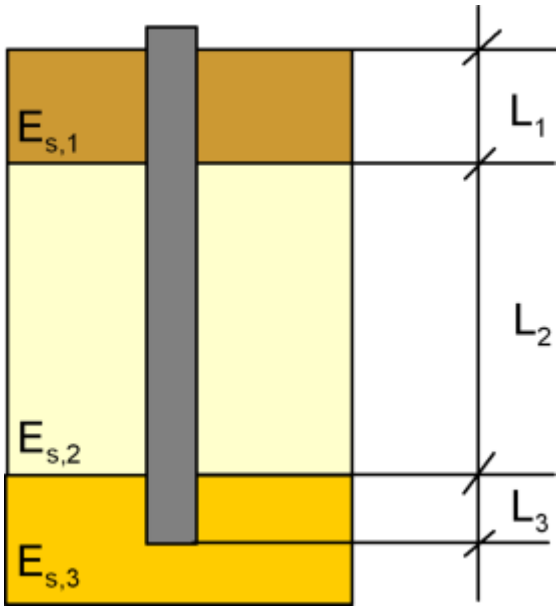

Figure 6.67. Estimation of a weighted average soil Young's modulus, to be used in pile settlement calculations.

Cases where considering a weighted average soil modulus is reasonable and cases where it can lead to important error in the estimation of settlement are discussed in the following.

6.19.2 Estimation of settlement of compressible friction piles in homogeneous soil of finite thickness

One important drawback of the method presented above is that the thickness of the foundation stratum is assumed infinite. This cannot be the case in practice, thus Poulos' method will result in overestimating settlement if the bedrock is found at relatively shallow depth. A rigorous elasticity method applicable to cylindrical friction piles embedded in a homogeneous soil layer of finite thickness has been recently proposed by Zheng *et al.* (2023). A schematic of the problem considered by Zheng *et al.* is shown in Figure 6.68. The friction pile features diameter D and length L and is embedded in a soil layer of finite thickness H. The method explicitly accounts for the Poisson's ratio of soil, and is applicable to both drained (e.g., soil Poisson's ratio $\upsilon_s = 0.3$ and soil modulus $E_s = E'$) and undrained conditions (soil Poisson's ratio $\upsilon_s = 0.5$ and soil modulus $E_s = E_u$).

Figures 6.69 and 6.70 provide the dimensionless pile head stiffness $Q_w/E_sD\rho_e$ as function of the Poisson's ratio of soil υ_s, the moduli ratio E_p/E_s or K_p for non-solid piles (Eq. 6.93), the pile slenderness L/D and the dimensionless thickness of the soil layer H/D. When $H/D = inf$ Figures 6.69 and 6.70 provide identical results to the Poulos (1989) method. Comparison of Figures 6.69 and 6.70 confirms that the Poisson's ratio of soil does not significantly affect pile settlement, as stated earlier.

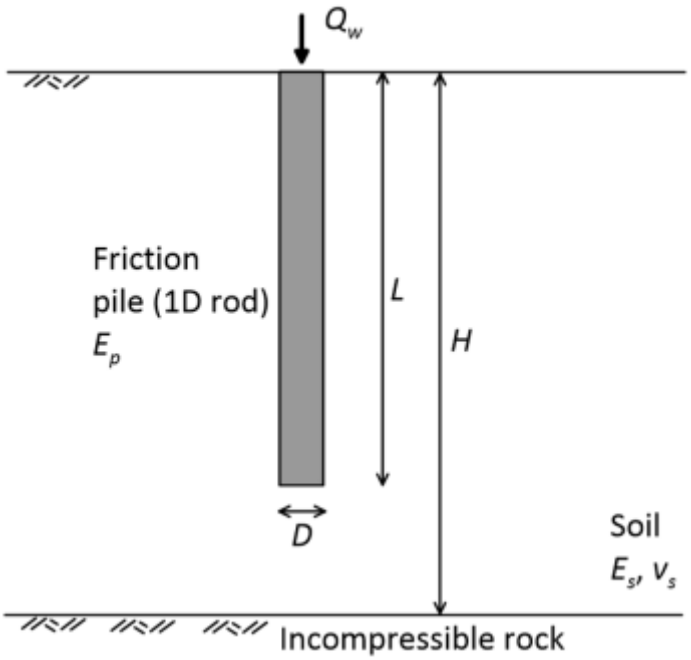

Figure 6.68. Schematic of a cylindrical friction pile embedded in a soil layer of finite thickness, underlain by incompressible bedrock.

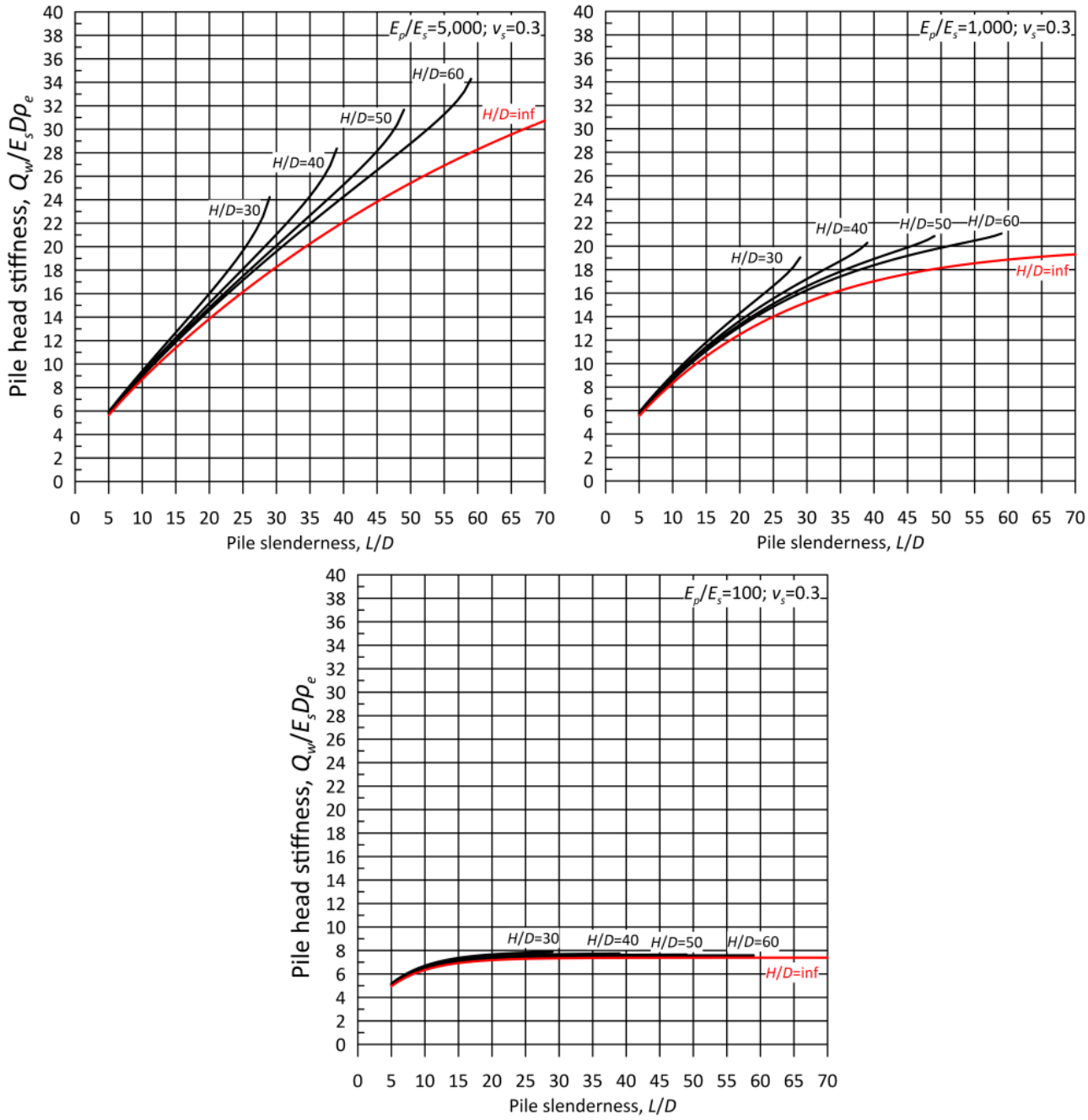

Figure 6.69. Pile head stiffness of a friction pile embedded in a soil layer of finite thickness. Results for soil Poisson's ratio v_S = 0.3 (Zheng *et al.* 2023).

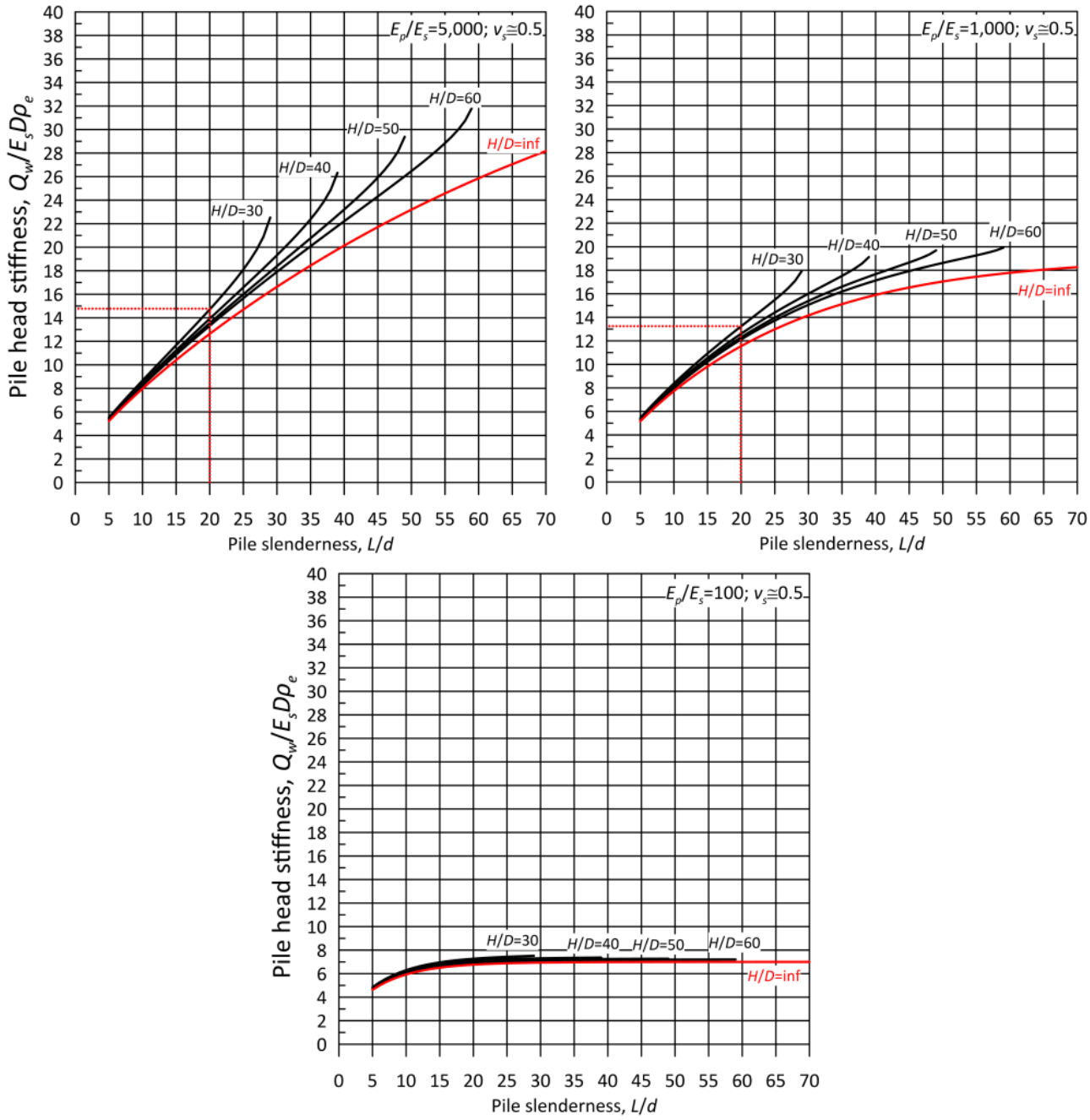

Figure 6.70. Pile head stiffness of a friction pile embedded in a soil layer of finite thickness. Results for soil Poisson's ratio v_S = 0.5 (Zheng *et al.* 2023).

6.19.3 Estimation of settlement of compressible end bearing piles in homogeneous soil

Poulos and Davis (1991) describe a method for calculating settlement of end-bearing compressible cylindrical piles embedded in a uniform elastic soil layer of thickness equal to the pile length L, underlaid by rigid end-bearing stratum (bedrock).

If the end-bearing stratum is much stiffer than the overlying soil layer (Young's modulus of the bedrock E_b is much larger than the Young's modulus of the soil layer around the pile shaft E_s) then we can use

Figure 6.71 to estimate the pile head stiffness factor I_b, and subsequently the elastic settlement of a single end bearing pile ρ_e for given serviceability load Q_w. The curves plotted in Figure 6.71 correspond to the two extreme values of soil Poisson's ratio $\upsilon_s = 0.5$ and $\upsilon_s = 0$. Again, the effect of soil Poisson's ratio on pile settlements is not particularly prominent.

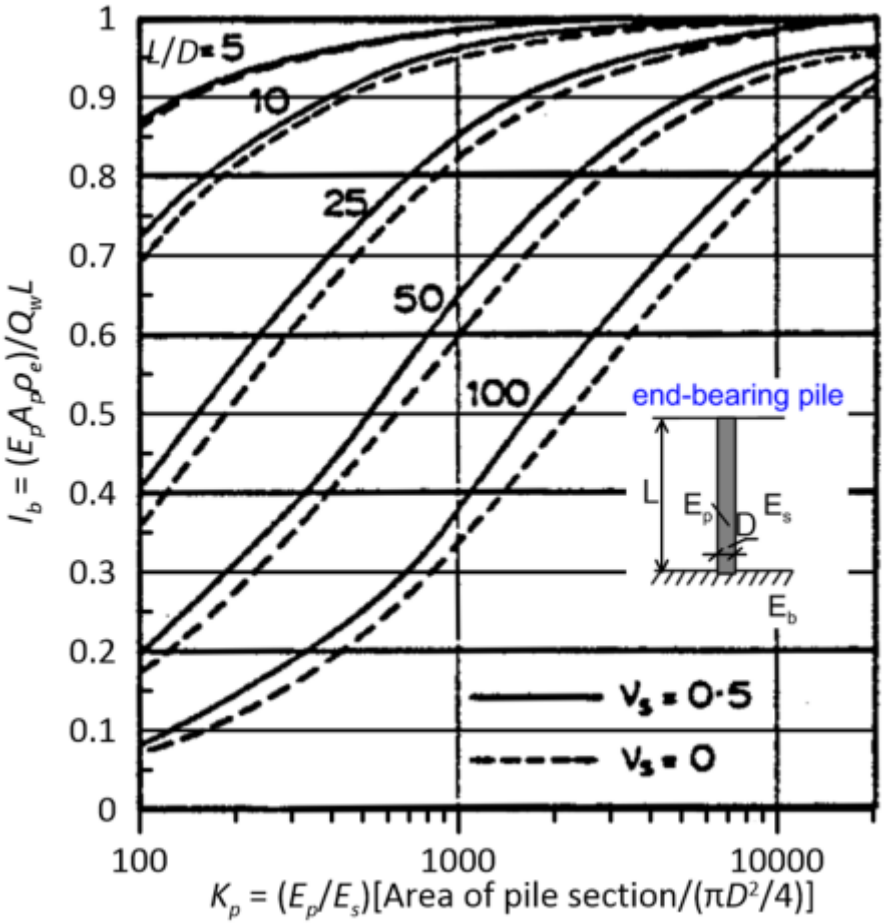

Figure 6.71. Pile head stiffness factor I_b for estimating settlement of an end-bearing pile in homogeneous soil underlaid by rigid bedrock (after Poulos and Davis 1991).

The compressibility of the bedrock will have an effect on the predicted settlement of end-bearing piles, particularly for short piles (low L/D values) when significant portion of the serviceability load will actually be transferred to the pile toe. Figure 6.72 below presents the effect that the stiffness of the bedrock has on end bearing pile settlement. To compute the settlement of an end bearing pile on the basis on Figure 6.72, we assume first that the total load is transferred through shaft friction, and estimate the pile settlement $\rho_{e,friction}$ as:

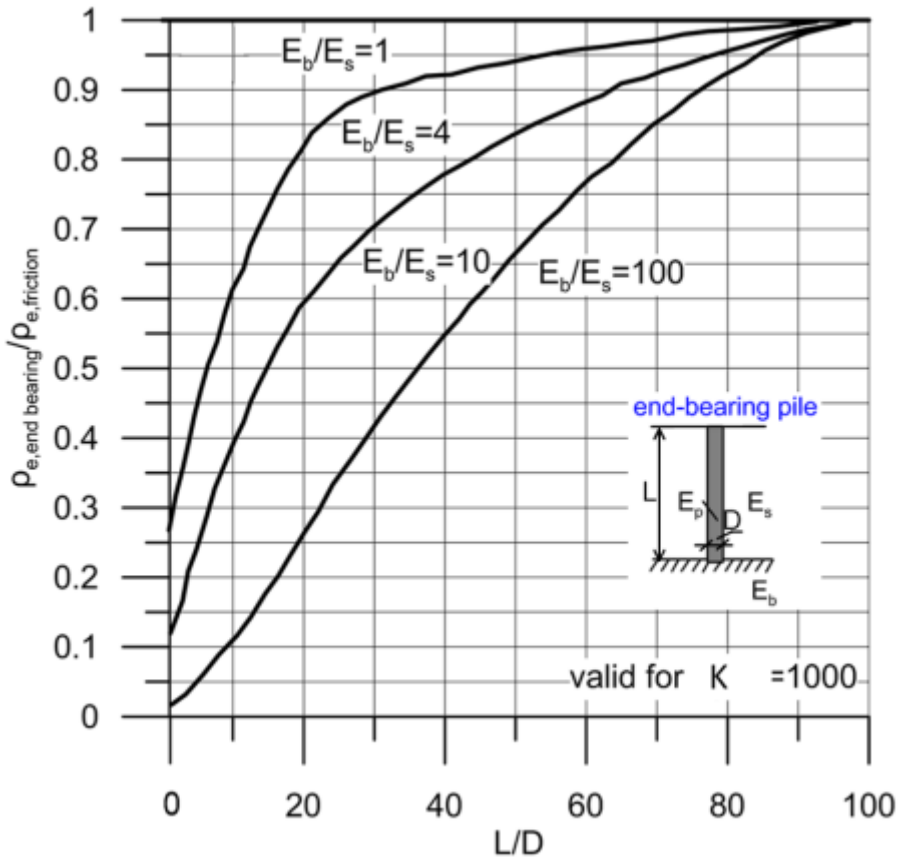

Figure 6.72. Relative settlement of end-bearing pile and friction pile. Results for relative pile stiffness K_p = 1000 (after Poulos 1989).

(6.95) $$\rho_{e,friction} = \frac{Q_w}{E_s D} I_s$$

where I_s is read from Figure 6.66. Then, using Figure 6.72, we can estimate the settlement of the end bearing pile, as a function of the pile slenderness *(L/D)* and the ratio of the Young's modulus of the end bearing layer E_b over the Young's modulus of the overlying soil layer(s) E_s. Figure 6.72 presents results for typical relative pile stiffness K_p = 1000.

Notice in Figure 6.72 that the settlement of slender piles (L/D > 50) is not influenced significantly by the compressibility of the bearing stratum. In other words, if we seek to reduce the settlement of a relatively long pile, it is preferable to increase its diameter or stiffness, rather than increasing its length to found its toe on a deep, stiff layer.

6.19.4 Estimation of settlement of compressible end bearing piles in layered soil

It has been discussed earlier that estimating settlement of a pile in layered soil with methods developed for uniform soil conditions along the pile shaft may lead to inaccurate predictions, even when a weighted average soil modulus in considered in the analysis. This problem has been tackled by Zheng *et al.* (2024), who developed an elasticity method for predicting settlement of end bearing piles resting on rigid bedrock (E_b = infinite) driven through soil that consists of two soil layers that feature different properties. The problem they considered is depicted in Figure 6.73.

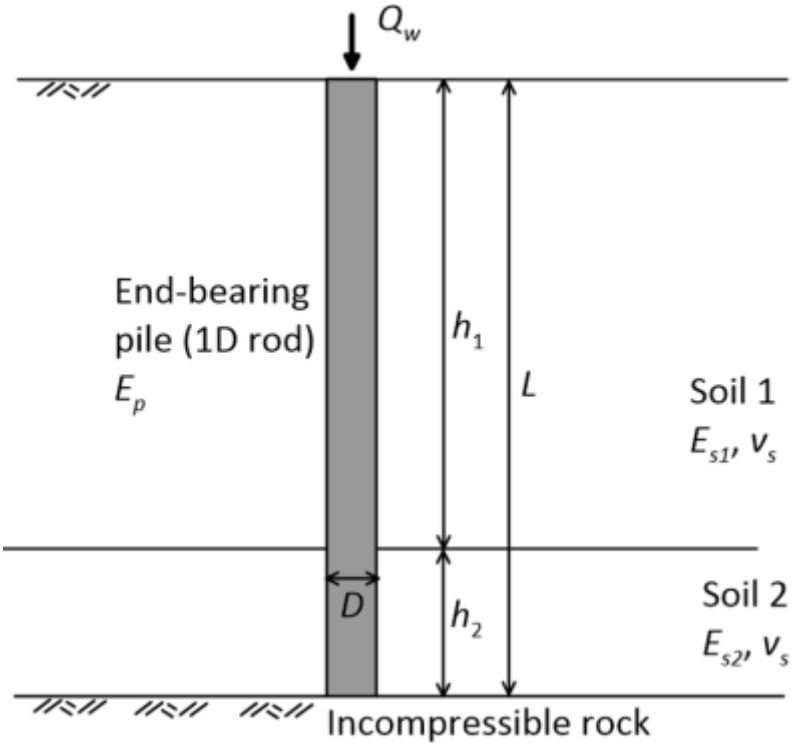

Figure 6.73. Schematic of a cylindrical end-bearing pile embedded in layered soil, underlain by incompressible bedrock.

Zheng *et al.* produced charts that provide the dimensionless pile head stiffness $Q_w/E_pD\rho_e$ as function of the modulus of the pile E_p, the moduli of the soil layers E_{s1} and E_{s2}, pile slenderness L/D, and the thickness of the soil layers h_1 and h_2. These charts are presented in Figures 6.74 and 6.75, and can be used to directly estimate settlement of end-bearing piles for any serviceability load Q_w. The results presented in the mentioned figures demonstrate that the role of top layer to pile head stiffness (thus pile settlement) is more important than the role of the bottom layer. Thus, using a weighted average soil modulus (Eq. 6.94) together with homogeneous soil models may lead to inaccurate settlement predictions when the surficial soil layer is stiffer than the underlying soft soil. On the other hand, considering a weighted average soil modulus may be a reasonable approximation if soil stiffness increases with depth, for example for piles in sand.

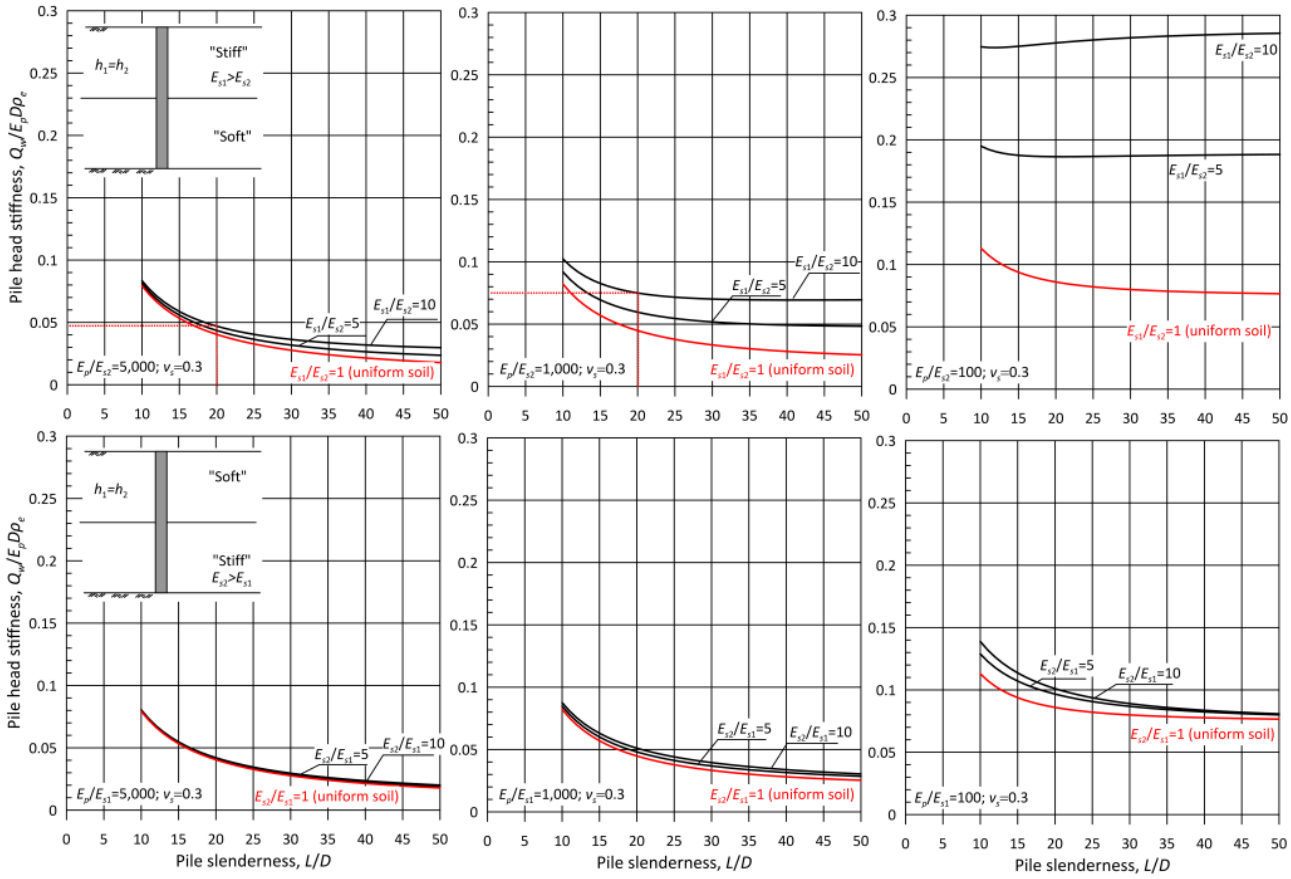

Figure 6.74. Head stiffness of an end-bearing pile embedded in two soil layers of equal thickness $h_1 = h_2$. Results for soil Poisson's ratio $v_S = 0.3$ (Zheng *et al.* 2024).

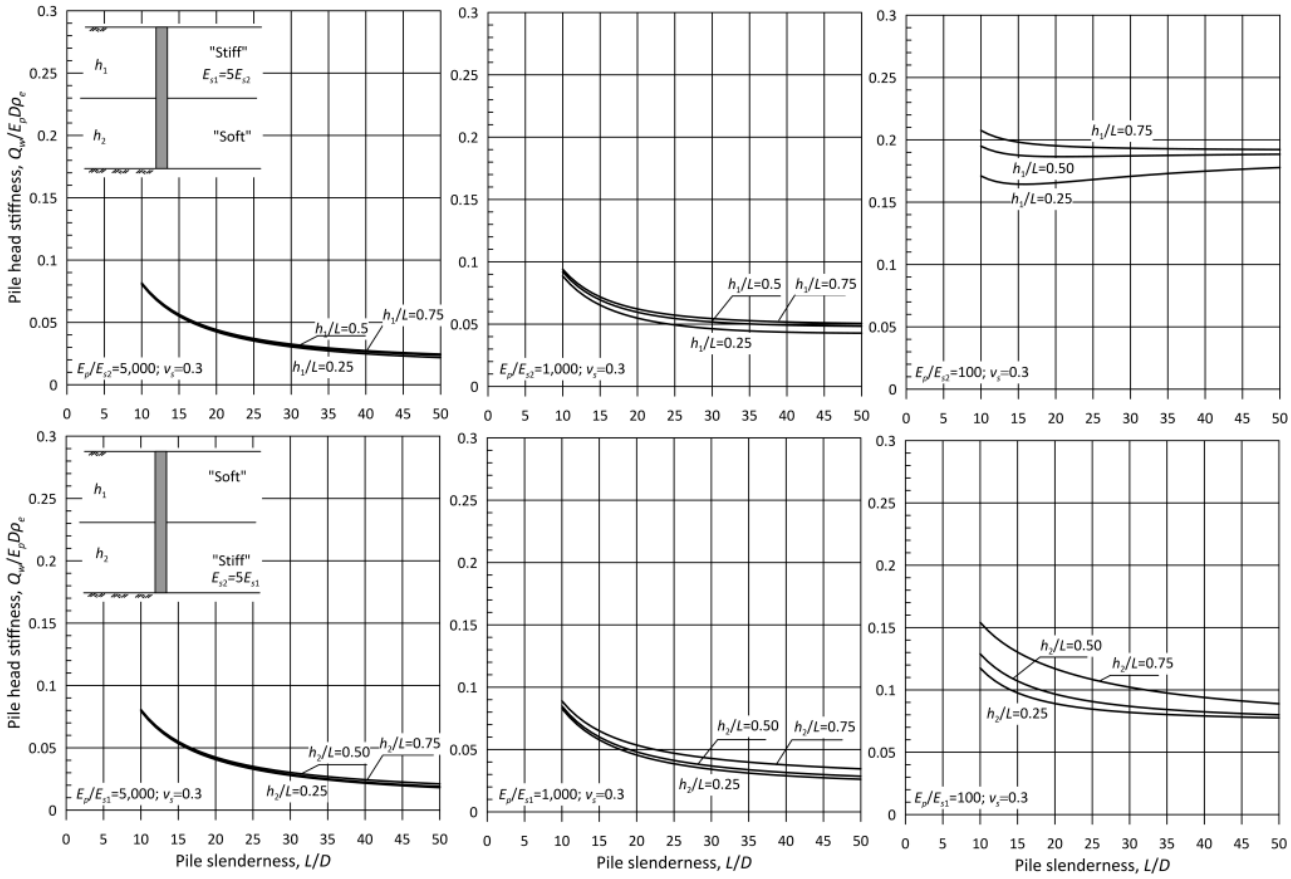

Figure 6.75. Head stiffness of an end-bearing pile embedded in two soil layers of varying thickness. Results for "stiff" crust ($E_{S1}=5E_{S2}$, top) and "soft" crust ($E_{S2}=5E_{S1}$, top) and soil Poisson's ratio v_S = 0.3 (Zheng *et al.* 2024).

EXAMPLE 6.8

Calculation of settlement of a friction pile in homogeneous soil

Calculate the immediate settlement of the driven solid concrete pile shown in the figure below, using i) the method of Poulos (1998) for friction piles in infinitely deep soil and ii) the method of Zheng *et al.* (2023) for friction piles in a soil layer of finite thickness.

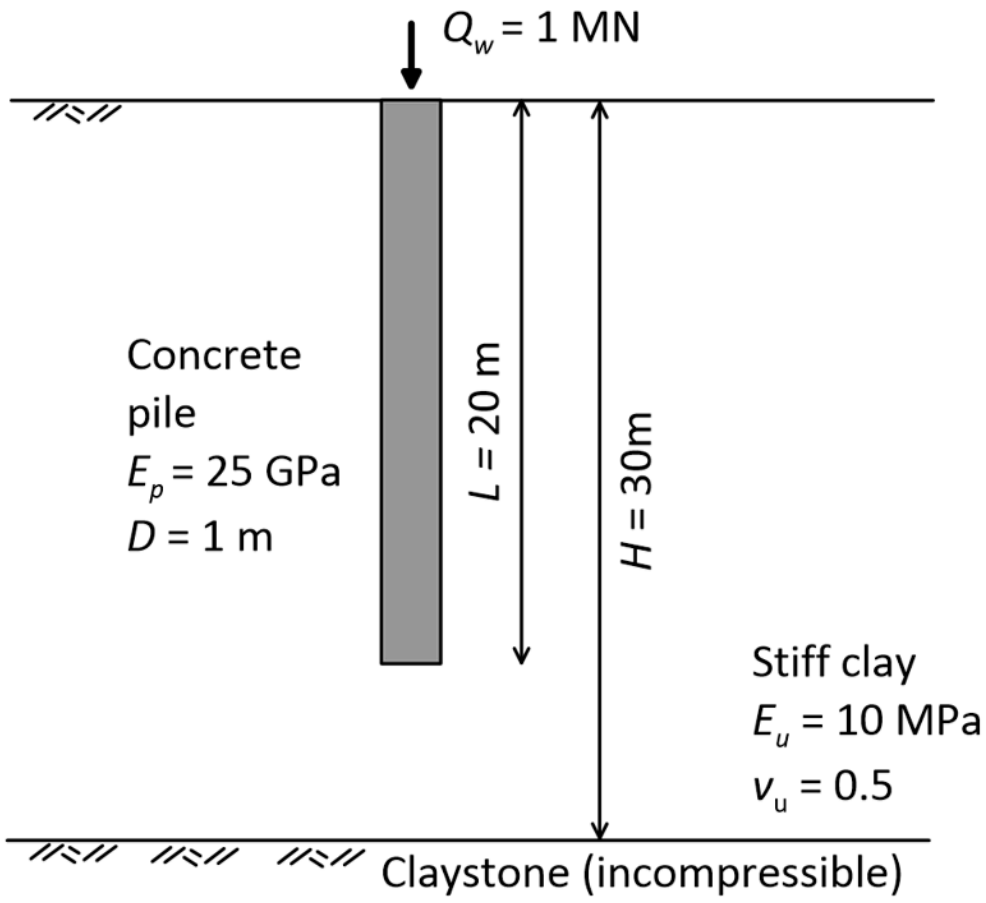

Example 6.8. Problem description and input parameters.

Answer:

1. Calculation of settlement according to Poulos (1998):

First, we estimate the pile head stiffness factor I_s from Figure 6.66. For $K_p = E_p/E_s$ (solid pile) = 25,000/10 = 2500 and $L/D = 20$ it is $I_s \approx 0.095$ (see Figure below).

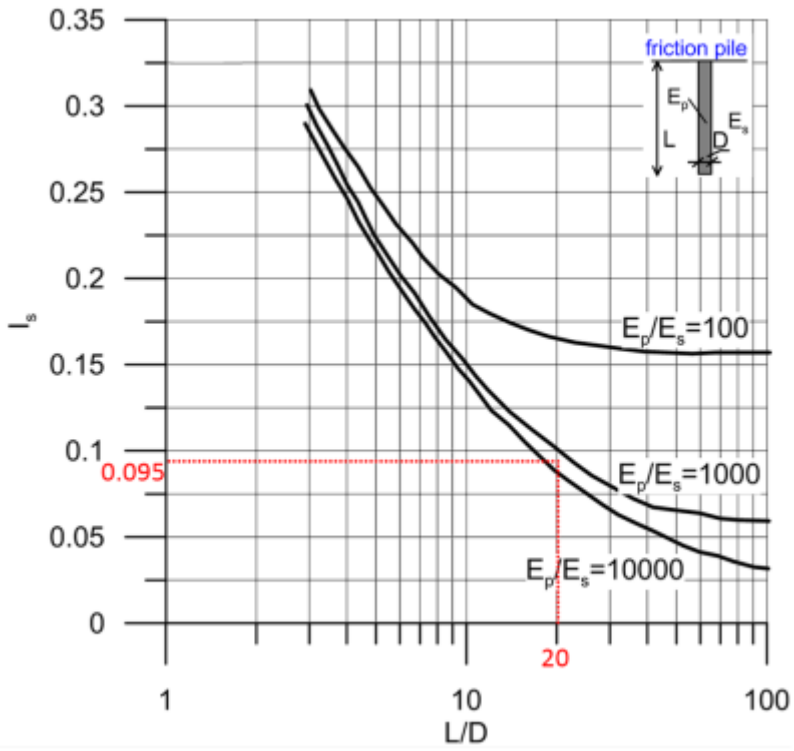

Example 6.8. Calculation of I_s.

Thus, from Eq. 6.92 it is:

$$\rho_e = \frac{Q_w}{E_s D} I_s = \frac{1000}{10000 \times 1} 0.095 = 9.5 \text{ mm}$$

2. Calculation of settlement according to Zheng *et al.* (2023):

We estimate the pile head stiffness from Figure 6.70, which presents results for υ_s = 0.5. For $K_p = E_p/E_s$ (solid pile) = 5000, H/D = 30 and L/D = 20 it is $Q_w/E_s D\rho_e \approx 14.8$ while for $K = E_p/E_s$ = 1000, H/D = 30 and L/D = 20 it is $Q_w/E_s D\rho_e \approx 13.2$ (see Figure below).

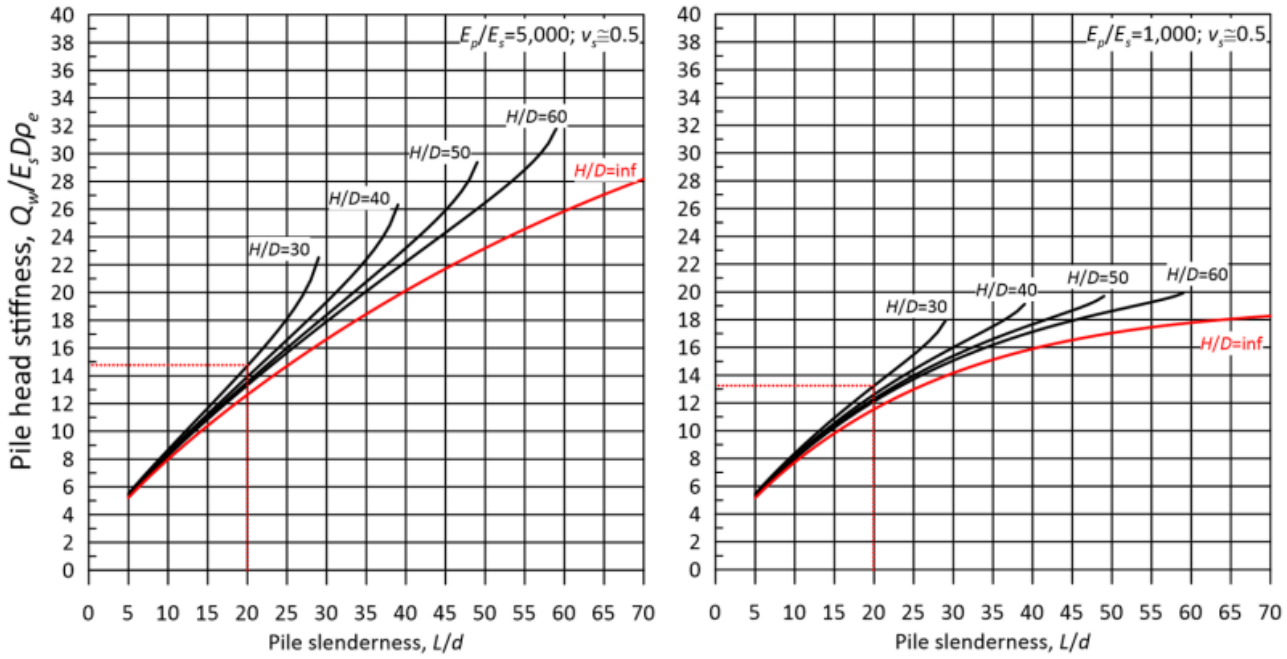

Example 6.8. Calculation of pile head stiffness.

Using linear interpolation we can obtain:

$$\frac{\frac{Q_w}{E_s D \rho_e} - 13.2}{K_p - 1000} = \frac{14.8 - 13.2}{5000 - 1000}$$

$$\frac{\frac{Q_w}{E_s D \rho_e} - 13.2}{2500 - 1000} = 0.0004$$

$$\frac{Q_w}{E_s D \rho_e} = 13.8$$

Therefore the settlement ρ_e is:

$$\rho_e = \frac{1000}{13.8 \times 10000 \times 1} = 7.2 \text{ mm}$$

i.e., as expected, lower than that calculated using the method of Poulos because the method of Zheng *et al.* accounts for the actual thickness of the soil layer.

EXAMPLE 6.9

Calculation of settlement of an end-bearing pile in layered soil

Calculate the immediate settlement of the driven solid concrete pile shown in the Figure below, using i) the method of Poulos and Davis (1991) for end-bearing piles in uniform soil underlaid by rigid bedrock (claystone) and ii) the method of Zheng *et al.* (2023) for end-bearing piles in two-layered soil underlaid by rigid bedrock. Repeat the calculation, this time considering that instead of rigid claystone, the bedrock consists of hard alluvial clay with E_b = 55 MPa.

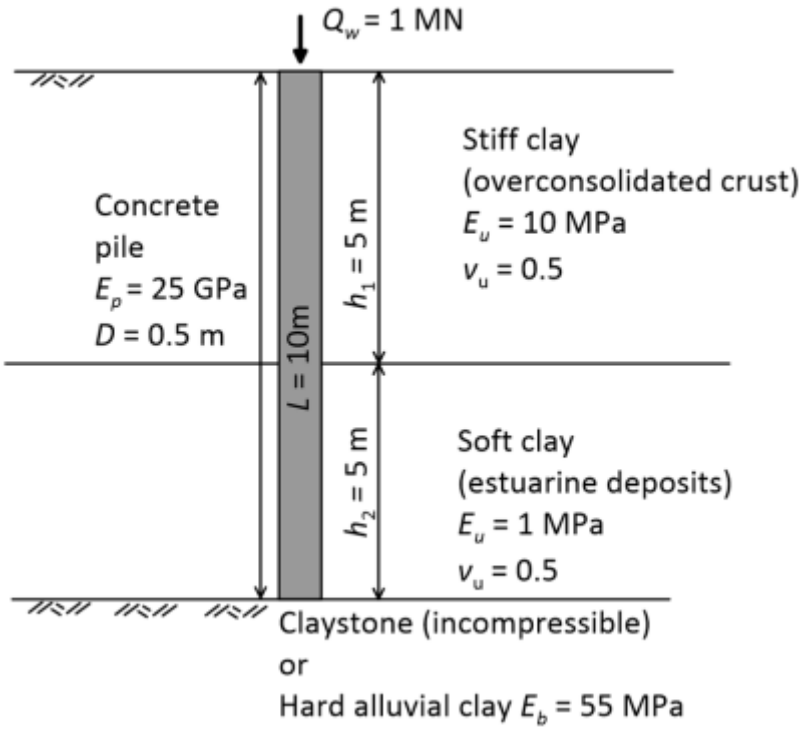

Example 6.9. Problem description and input parameters.

1. Calculation of settlement according to Poulos and Davis (1991) for E_b = *inf*:

We estimate the pile head stiffness factor I_b from Figure 6.71 using a weighted average soil modulus from Eq. 6.94 equal to E_s = 5.5 MPa. For $K_p = E_p/E_s$ (solid pile) = 25,000/5.5 = 4,545 and L/D = 20 it is $I_b \approx$ 0.98 (see Figure below).

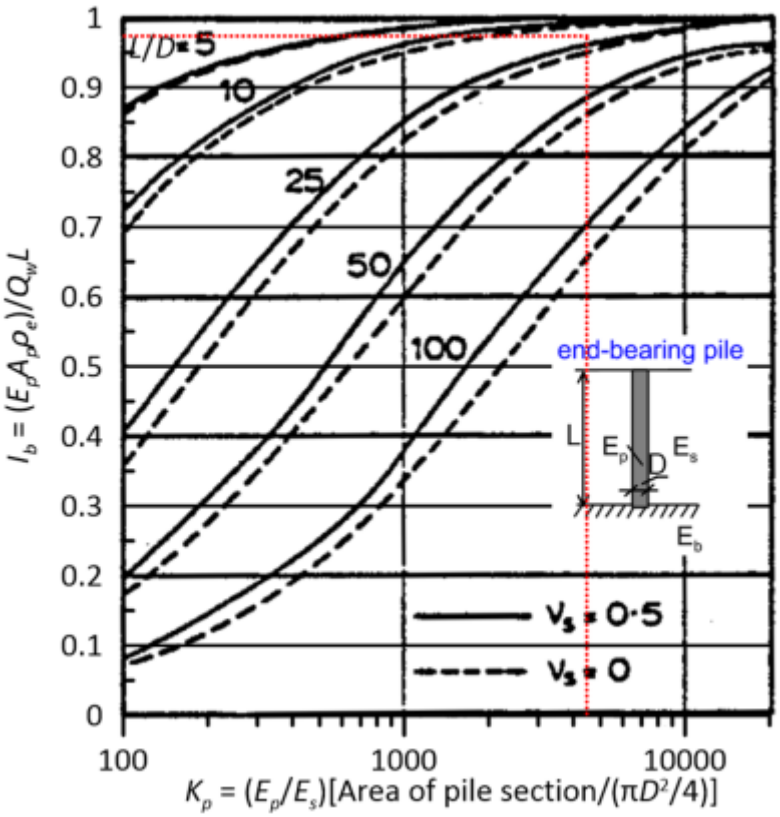

Example 6.9. Calculation of I_b.

Therefore settlement of the end-bearing pile is equal to:

$$\frac{E_p A_p \rho_e}{Q_w L} = I_b = 0.98$$

$$\rho_e = 0.98 \times \frac{1000 \times 10}{25000000 \times \left(\frac{\pi 0.5^2}{4}\right)} = 1.99 \text{ mm}$$

2. Calculation of settlement according to Zheng *et al.* (2024) for $E_b = inf$:

In lack of charts for soil Poisson's ratio $\upsilon_s = 0.5$, we will use the chart of Figure 6.74 to estimate the pile head stiffness $Q_w/E_p D\rho_e$. Since here $E_p/E_{s2} = 25{,}000$ we will use the chart for the nearest K_p value of $K_p = E_p/E_{s2}$ (solid pile) = 5,000 and $E_{s1}/E_{s2} = 10$, $L/D = 20$. As shown below, we obtain $Q_w/E_p D\rho_e \approx 0.048$.

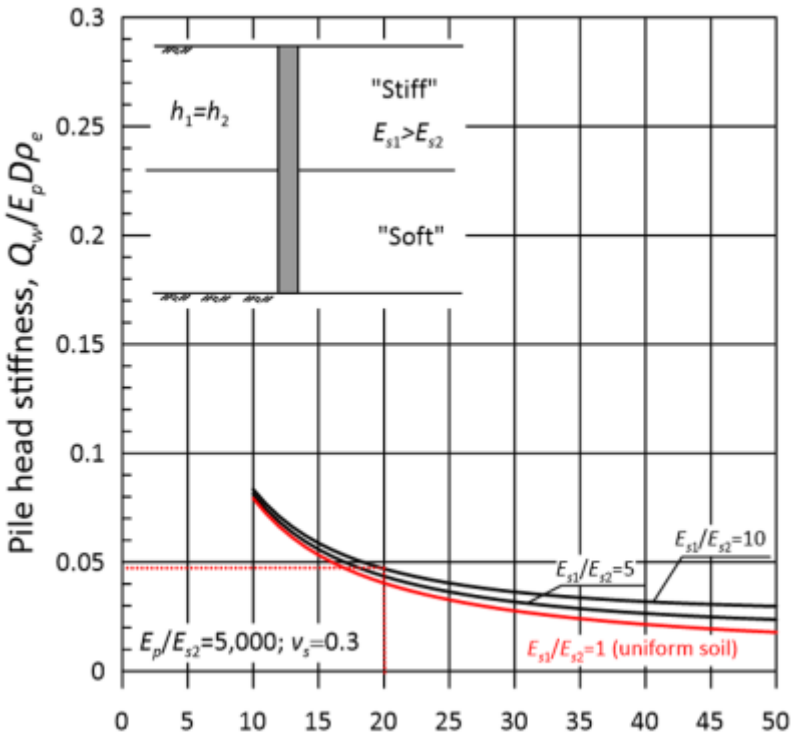

Example 6.9. Calculation of pile head stiffness.

Therefore pile settlement is estimated to be:

$$\rho_e = \frac{Q_w}{E_p D \times 0.048} = \frac{1000}{25000000 \times 0.5 \times 0.048} = 1.66 \text{ mm}$$

This settlement value is lower to that computed with the method of Poulos and Davis, which requires using a weighted average soil modulus if the pile is driven in layered soil.

3. Calculation of settlement for hard alluvial clay bedrock (E_b = 55 MPa) :

We first consider the pile as friction pile, and obtain the factor I_s from Figure 6.66. For $K_p = E_p/E_s$ (solid pile) = 25,000/5.5 = 4,545 and L/D = 20 it is $I_s \approx 0.09$.

Thus, from Eq. 6.95 it is:

$$\rho_{e,friction} = \frac{Q_w}{E_s D} I_s = \frac{1000}{5500 \times 0.5} 0.09 = 32.7 \text{ mm}$$

We can now refer to Figure 6.72 and estimate the settlement of the end-bearing pile, as function of $\rho_{e,friction}$ while considering pile slenderness L/D = 20 and E_b/E_s = 55/5.5 = 10. Note that the particular figure presents results for K_p = 1000, therefore will provide an upper bound of settlement as here K_p = 4,545.

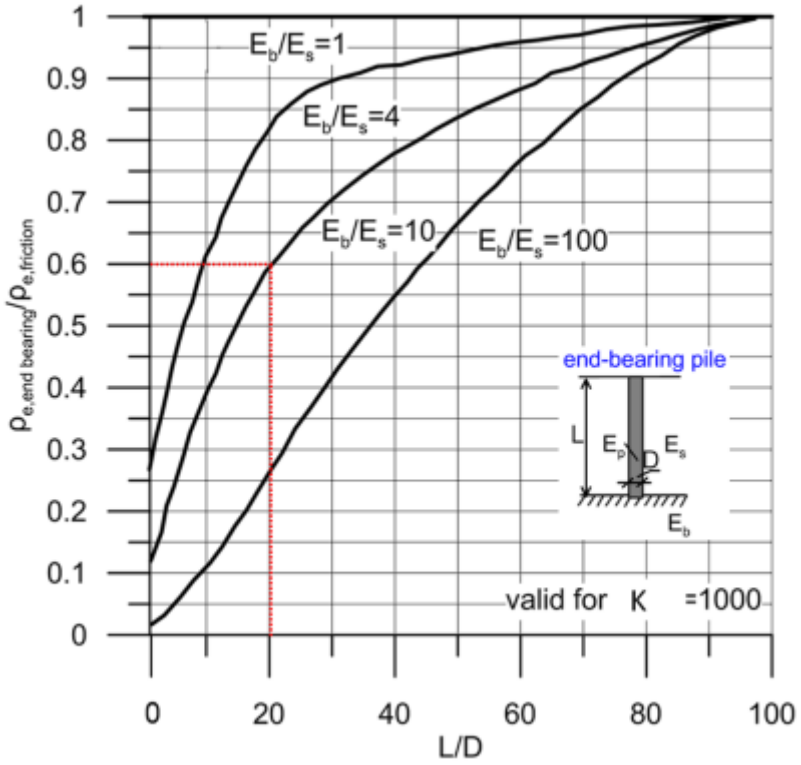

Example 6.9. Calculation of $\rho_{e,end\ bearing}/\rho_{e,friction}$.

The above figure suggests that $\rho_{e,friction}/\rho_{e,end\ bearing} = 0.6$, therefore $\rho_e = 0.6 \times 32.7 = 19.6$ mm.

It is clear from the above that: i) Considering a weighted average modulus may result in overestimating settlement when the surficial layer (crust) is stiffer than the bottom layer (soft soil), and ii) Assuming that the bedrock is incompressible can result in significantly underestimating settlement of relatively short piles (low L/D values), when the ratio of Young's modulus of the bedrock over the Young's modulus of the soil layer is $E_b/E_s = 10$, or less.

6.20 IMMEDIATE SETTLEMENT OF PILE GROUPS

Interaction between piles in a group and stress overlapping (Figure 6.64) tends to affect pile settlements, so the settlement of a pile group subjected to axial compressive load is not equal to the settlement of a single pile carrying the same average load. Pile group settlement is generally influenced by the spacing between the piles, the number of piles in the group, and the slenderness ratio *L/D*. Two families of methods for predicting settlement of a pile group consisting of arbitrary number of piles are presented in the following.

6.20.1 Approximate methods for piles connected with a rigid cap

To calculate settlement of a group of piles spaced at $s/D > 2.5$ (s is the centre-to-centre pile spacing) and connected with a *rigid* cap, a first-order approximation is to assume that the vertical compressive load acting at the cap is distributed equally among all piles in the group. In that case we can use the following formula to get an estimate of the settlement of the piles, which of course will settle uniformly (Fleming *et al.* 1985).

(6.96) $$\frac{\text{settlement of pile group}}{\text{settlement of single pile at the same average load}} = R_s = n^{\Phi}$$

where n is the number of piles in the group and the factor Φ ranges between 0.4 and 0.6 (Figure 6.76).

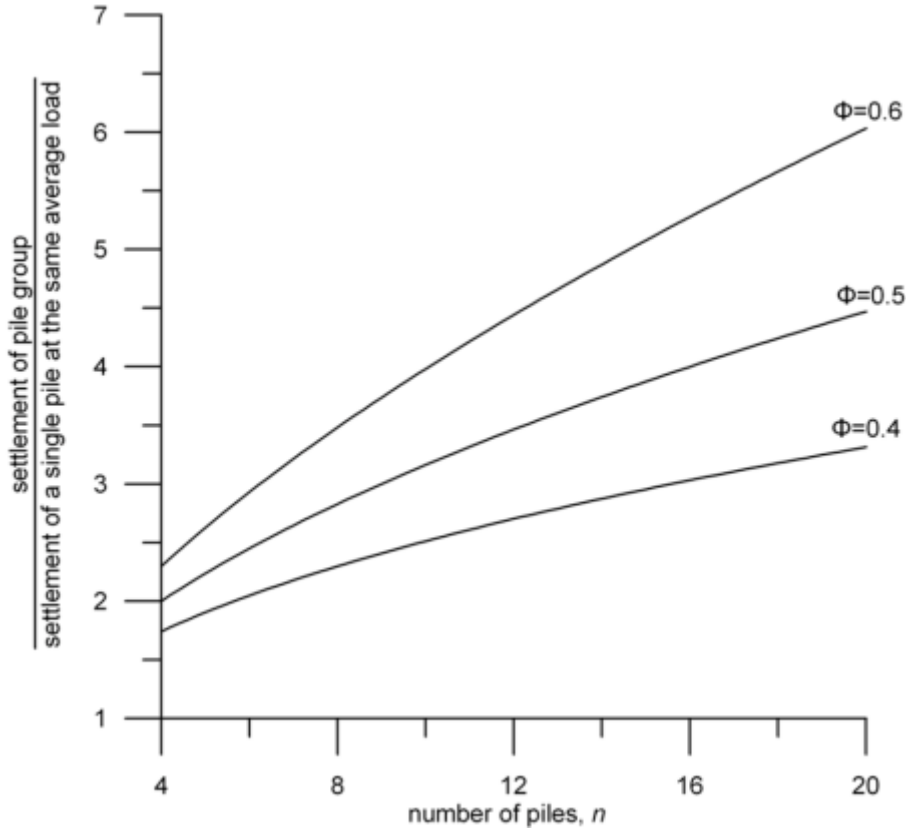

Figure 6.76. Ratio of the settlement of a pile group over the settlement of a single pile at the same average load, according to Fleming *et al.* (1985).

According to Poulos (1989), comparisons with pile load tests suggest that Eq. 6.96 provides reasonable results for $\Phi = 0.5$. Values of the factor R_s for common pile groups comprising 8-to-16 piles lie in the range of $R_s = 2.8$ to 4, suggesting that settlement of pile groups can be considerable, compared to settlement of individual piles.

Alternatively, the *equivalent pier method* can be used (Poulos, 1993). In this method, the pile group is replaced by a pier of similar length to the piles of the group, featuring an equivalent diameter, D_e:

(6.97) $$D_e = (1.13 \text{ to } 1.27)\sqrt{A_G}$$

where A_G is the plan area of the pile group, including the soil between the piles. The lower value of D_e applies to predominantly end-bearing piles, while the upper value should be considered for friction piles. Accordingly, the methodology for single piles is followed, assuming the pier is working as a single pile. Generally, both the Fleming *et al.* (1985) and the equivalent pier methods will result to comparable pile group settlement estimates.

6.20.2 Elasticity method for piles connected with flexible or rigid cap, accounting for load distribution

The are several solutions in the literature that can be used to predict the settlement and the distribution of axial loads in floating and end-bearing groups of piles, that require little computational effort-at least for static loads. These are based on certain important assumptions, such as elastic soil behaviour, no

slippage at the soil-pile interface or incompressible soil (soil Poisson's ratio v_s = 0.5). Nevertheless, it has been demonstrated in the literature (e.g. Poulos and Mattes 1971) that, despite their simplicity, elasticity-based methods can provide reasonably accurate estimates of pile group behaviour in the field, as under serviceability conditions non-linearity effects are not particularly important.

Many of the mentioned solutions used in practice are based on the interaction factor α_i (or its variants), first conceived by Harry Poulos and his co-workers at the University of Sydney:

(6.98) $$\alpha_i = \frac{\text{additional settlement due to adjacent pile(s)}}{\text{settlement of a pile under its own load}}$$

For a two-pile group consisting of friction or end-bearing identical piles, elastic settlement of a pile that accounts for group effects ρ_i can be calculated while considering pile-to-pile interaction as:

(6.99) $$\rho_i = (1 + \alpha_i)\,(\text{settlement of pile under its own load})$$

where the elastic settlement of the pile under its own load (ρ_e) can be calculated using the elasticity-based methods described in the previous Chapter 6.20.

The interaction factor α_i for a two-pile group is given by the charts prepared by Poulos (1968) and Poulos and Mattes (1971) and presented in Figures 6.77 and 6.78, for floating and end-bearing pile groups embedded in undrained soil (v_s = 0.5) respectively. In these charts K_p is the pile stiffness factor, as piles are considered as elastic 1D rods (i.e., are not rigid), and is calculated according to Eq. 6.93.

The two-pile group interaction factors can be used to obtain the settlement and load distribution in a pile group consisting of arbitrary number of identical circular piles connected with rigid or flexible cap, by exploiting the principle of elastic superposition. The settlement of any pile i in a group of k identical piles is:

(6.100) $$\rho_i = \rho_1 \sum_{\substack{j=1 \\ j \neq k}}^{k} (Q_j a_{i,ij} + Q_{w,i})$$

where: ρ_1 is the elastic settlement of a single pile under unit load, $\alpha_{i,ij}$ is the interaction factor for spacing s between piles i and j (from Figure 6.77 or Figure 6.78), $Q_{w,i}$ is the serviceability load on pile i, and $Q_{w,j}$ is the serviceability load on pile j. Casting the above equation for all piles in a group results in a system of linear equations, that can be solved if we consider:

1. Equilibrium of forces

(6.101) $$Q_{w,group} = \sum_{j=1}^{k} Q_{w,j}$$

where $Q_{w,group}$ is the total axial compressive load acting on the pile cap for serviceability conditions.

2. Equal settlement of all piles, if they are connected with a rigid pile cap, or

3. Equal load on all piles, if they are connected with a flexible pile cap, thus the load will be distributed uniformly.

It is reminded here that this method does not account for the (additional) settlement of the compressible soil layer underneath the toe of floating piles groups. This needs to be calculated separately according to the mentioned in the next section.

Application of the method is demonstrated in the worked example that follows. Note that his method is not applicable to piled rafts i.e., we assume that no load is transferred to soil through the pile cap.

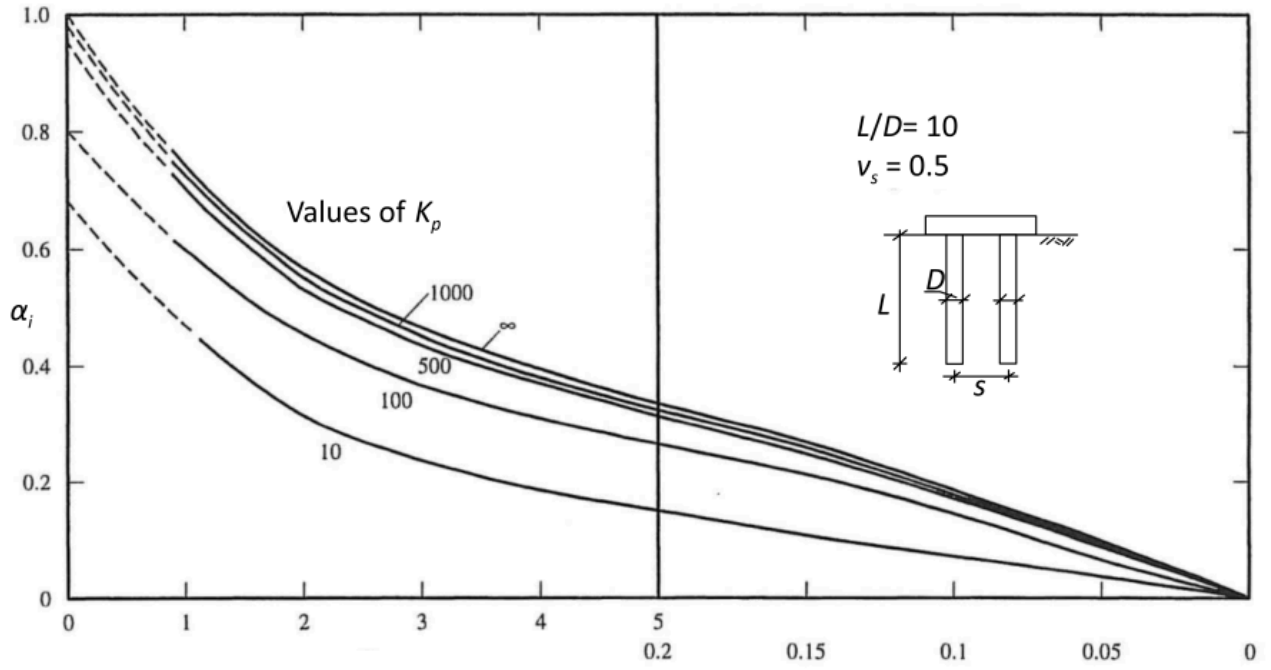
L/D= 10
v_s = 0.5
Values of K_p
1000
∞
500
100
10
α_i
D
L
s
0
0.2
0.4
0.6
0.8
1.0
1
2
3
4
5
0.2
0.15
0.1
0.05
0

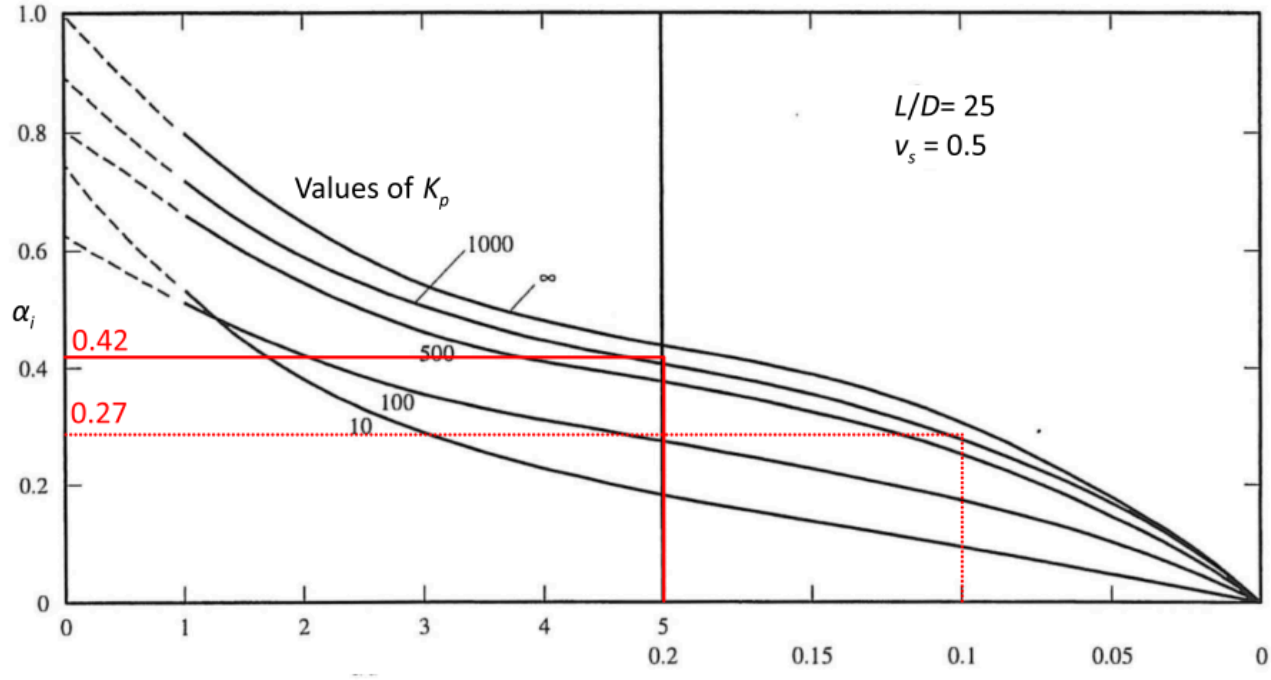
L/D= 25
v_s = 0.5
Values of K_p
1000
∞
500
100
10
α_i
0.42
0.27
0
0.2
0.4
0.6
0.8
1.0
1
2
3
4
5
0.2
0.15
0.1
0.05
0

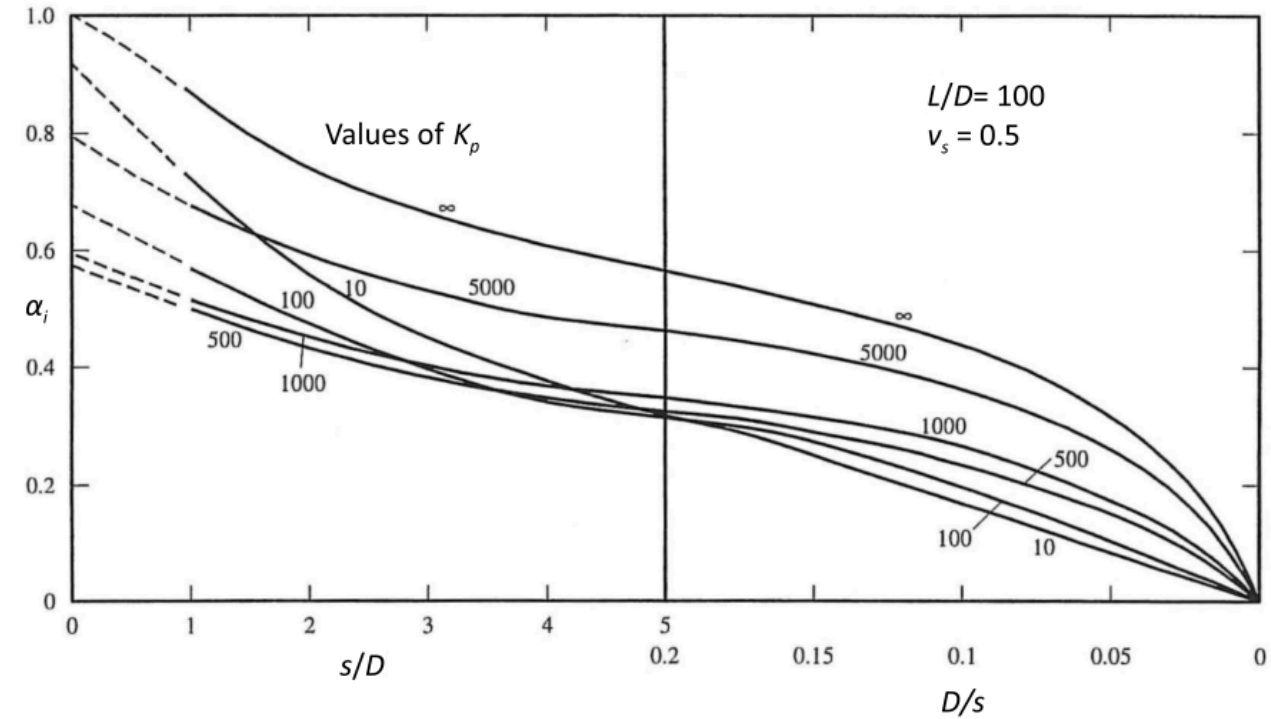
L/D= 100
v_s = 0.5
Values of K_p
∞
5000
1000
500
100
10
α_i
s/D
D/s
0
0.2
0.4
0.6
0.8
1.0
1
2
3
4
5
0.2
0.15
0.1
0.05
0

Figure 6.77. Interaction factor α_i for floating two-pile group; L/D = 10, 25 and 100 (after Poulos and Mattes 1971).

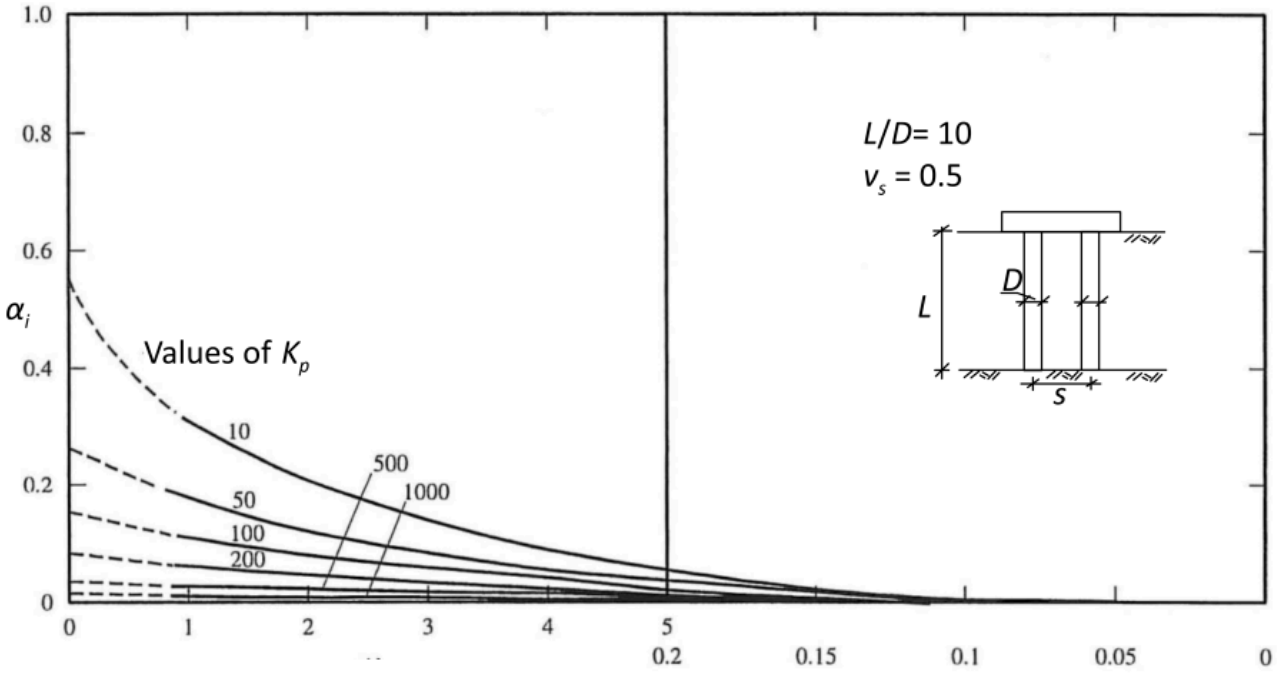
L/D= 10
v_s = 0.5
D
L
s
α_i
Values of K_p
10
50
100
200
500
1000
0
0.2
0.4
0.6
0.8
1.0
0
1
2
3
4
5
0.2
0.15
0.1
0.05
0

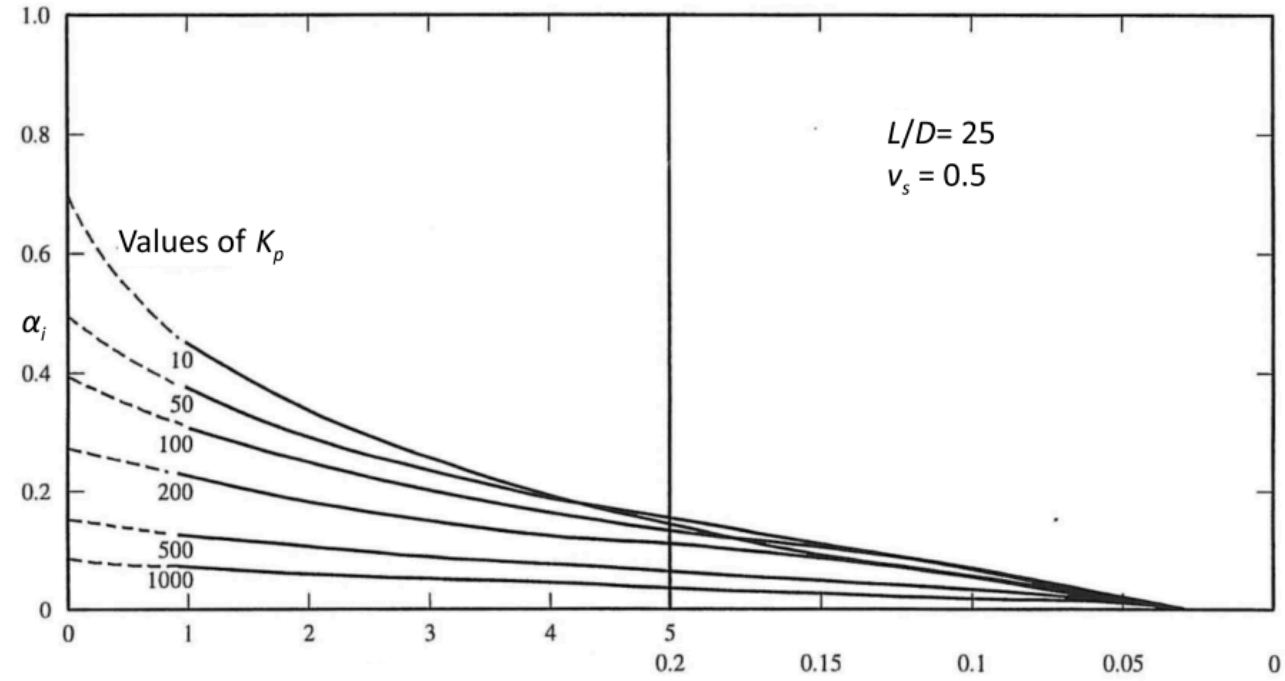
L/D= 25
v_s = 0.5
Values of K_p
α_i
10
50
100
200
500
1000
0
0.2
0.4
0.6
0.8
1.0
0
1
2
3
4
5
0.2
0.15
0.1
0.05
0

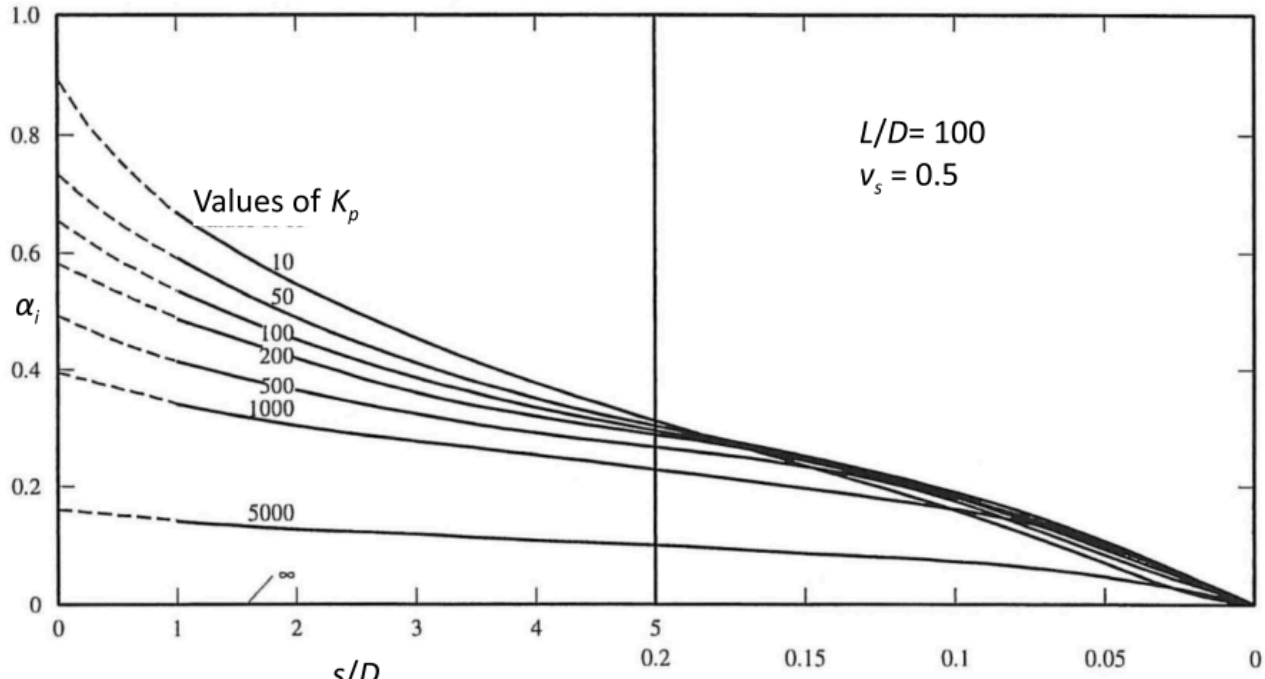
L/D= 100
v_s = 0.5
Values of K_p
α_i
10
50
100
200
500
1000
5000
∞
0
0.2
0.4
0.6
0.8
1.0
0
1
2
3
4
5
0.2
0.15
0.1
0.05
0
s/D

Figure 6.78. Interaction factor α_i for end bearing two-pile group; L/D = 10, 25 and 100 (after Poulos and Mattes 1971).

EXAMPLE 6.10

Calculation of settlement of a group of piles connected with rigid and flexible pile cap

Consider the floating pile group depicted in the figure below, consisting of six concrete piles of diameter D = 300 mm driven into a deep clay layer. The group is subjected to a vertical compressive load $Q_{w,group}$ = 3000 kN. A load test was performed on a single pile, and resulted in settlement of 15 mm under load 500 kN. The ratio of the Young's modulus of the pile over the Young's modulus of the clay is E_p/E_s = 2000. Determine the immediate settlement of the pile group if i) the pile cap is rigid, and ii) the pile cap is flexible.

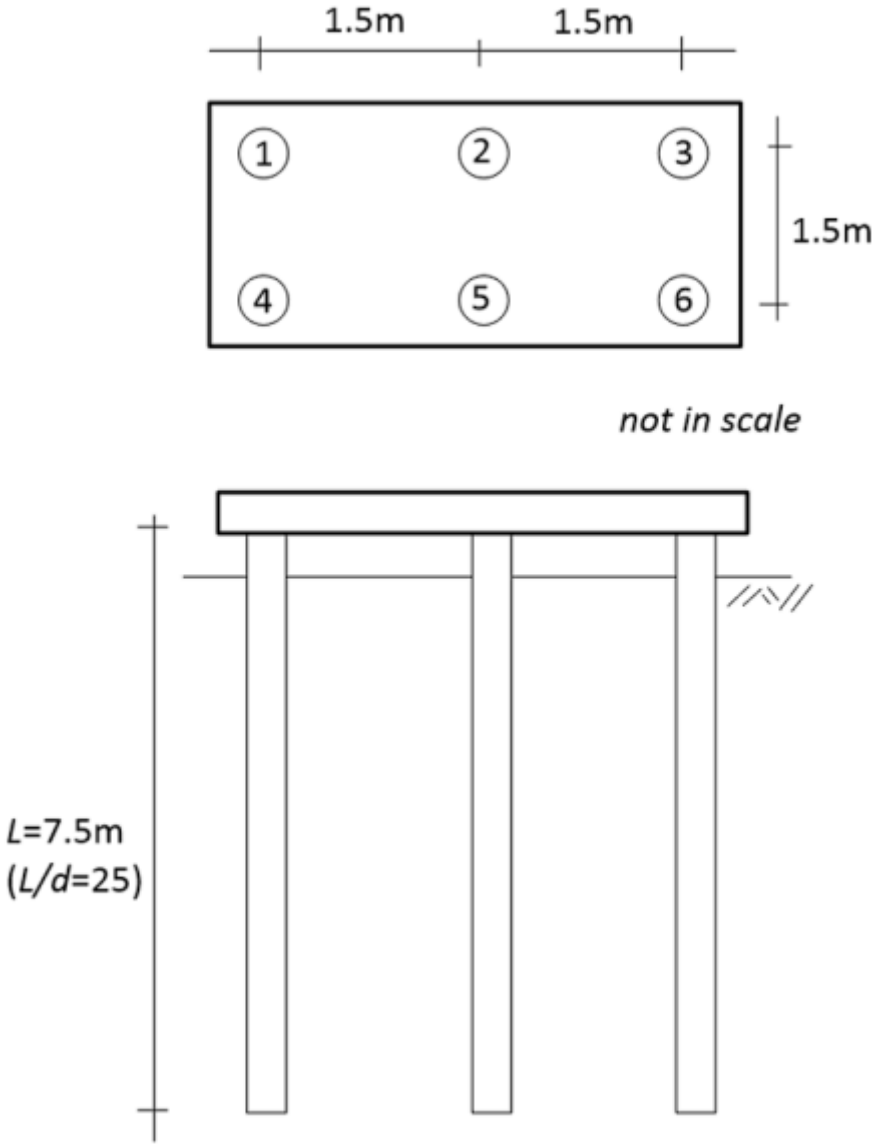

Example 6.10. Problem description and input parameters.

We need first to determine the pile stiffness factor K_p from Eq. 6.93. Since the piles are solid it is $K_p = E_p/E_s$ = 2000.

Corner piles 1, 3, 4 and 6 will behave identically, and we will call them Pile Type A. Mid piles 2 and 5 will also behave identically, and we will call them Pile Type B. We will also denote the serviceability load on piles A is B as Q_A and Q_B, respectively.

We can find the interaction factors $\alpha_{i,ij}$ from the chart in Figure 6.77 for L/D = 25, interpolating between K_p = 1000 and K_p =∞. We need interaction factors for two piles types: Pile Type A (e.g. for Pile 1) and Pile Type B (e.g. for Pile 2).

Interaction factors α_{ij}

PIle *j*	Pile 1 (Pile type A)		Pile 2 (Pile type B)	
	s/D	$\alpha_{i,ij}$	*s/D*	$\alpha_{i,ij}$
1	0	–	5	0.42
2	5 (i.e., 1500 mm/ 300 mm)	0.42	0	–
3	10	0.27	5	0.42
4	5	0.42	7.07	0.35
5	7.07	0.35	5	0.42
6	11.2	0.25	7.07	0.35

We can now cast Eq. 6.100 for all piles. It is:

Settlement of pile 1 (and all Type A piles), ρ_A:

$$\rho_A = \rho_1 \left[Q_A \left(0.27 + 0.42 + 0.25\right) + Q_B \left(0.42 + 0.35\right) + Q_A\right] \rightarrow \frac{\rho_A}{\rho_1} = 1.94P_A + 0.77P_B$$

Settlement of pile 2 (and all Type B piles), ρ_B:

$$\rho_B = \rho_1 \left[Q_A \left(0.42 + 0.42 + 0.35 + 0.35\right) + Q_B \left(0.42\right) + Q_B\right] \rightarrow \frac{\rho_B}{\rho_1} = 1.54P_A + 1.42P_B$$

In addition, the force equilibrium Eq. 6.101 is:

$$Q_{w,group} = 3000 = 4Q_A + 2Q_B$$

We have three equations, with four unknowns, the two settlements and the two loads acting on each pile type. So we need one more equation.

Case 1: Piles connected with a rigid pile cap

In this case the extra equation results from considering that the settlement of all piles will be the same, therefore $\rho_A/\rho_1 = \rho_B/\rho_1$. In addition, settlement of a pile under unit load ρ_1 is ρ_1 = 15/500 = 0.03 mm/kN. As such:

$$1.54Q_A + 1.42Q_B = 1.94Q_A + 0.77Q_B \rightarrow \frac{Q_A}{Q_B} = 1.625$$

and

$$3000 = 4Q_A + 2Q_B$$

$$\rightarrow Q_B = 352.9 \text{ kN}$$

$$\rightarrow Q_A = 573.5 \text{ kN}$$

As expected, when the pile cap is rigid the corner piles are carrying larger axial loads, relatively to the mid piles.

$$\frac{\rho_A}{\rho_1} = \frac{\rho_B}{\rho_1} = 1.94Q_A + 0.77Q_B = 1384.32 \text{ kN}$$

$$\rightarrow \rho_A = \rho_B = 41.5 \text{ mm}$$

Note that for a six-pile group (n = 6) and Φ = 0.5 Eq. 6.96 yields R_s = 2.44. In other words, the simplified method of Flemming *et al.* predicts that settlement of each pile, carrying load 3000/6 = 500 kN, will be 500 x 0.03 x 2.44 = 36.6 mm. The advantage of this, more rigorous, method, apart of course of considering the distribution of the vertical load on piles, is that it does not require assuming a value for the factor Φ.

Case 2: Piles connected with a flexible pile cap

If the piles are connected with a flexible pile cap, we can assume that they will all be carrying the same vertical load. Therefore our fourth equation is $Q_A = Q_B$ = 500 kN. Accordingly:

$$\frac{\rho_A}{\rho_1} = 1.94Q_A + 0.77Q_B = 1355 \text{ kN}$$

$$\rightarrow \rho_A = 40.65 \text{ mm}$$

$$\frac{\rho_B}{\rho_1} = 1.54P_A + 1.42P_B = 1480 \text{ kN}$$

$$\rightarrow \rho_B = 44.4 \text{ mm}$$

Notice that there is some differential settlement between piles connected with a flexible cap, with the mid piles 2 and 5 (Piles B) settling, as expected, more. This differential settlement may be important, and should be considered in the design of the pile group.

6.21 CONSOLIDATION SETTLEMENT OF PILE GROUPS

When a pile group consisting of friction piles is embedded in, or rests above a soft clay layer, it may transfer compressible stresses to the subsoil below the pile toe sufficient to cause substantial consolidation settlement, that must be added to the group settlement calculated using the methods described in Chapter 6.20.

A simplified procedure to estimate this settlement is based on the assumption that the total serviceability load transferred by the pile group $Q_{w,group}$ is acting at a depth equal to $(2/3)L$ below the pile cap (Figure 6.79), and is distributed in the underlying soil following a 2:1 stress distribution (Das 2007, Budhu 2011).

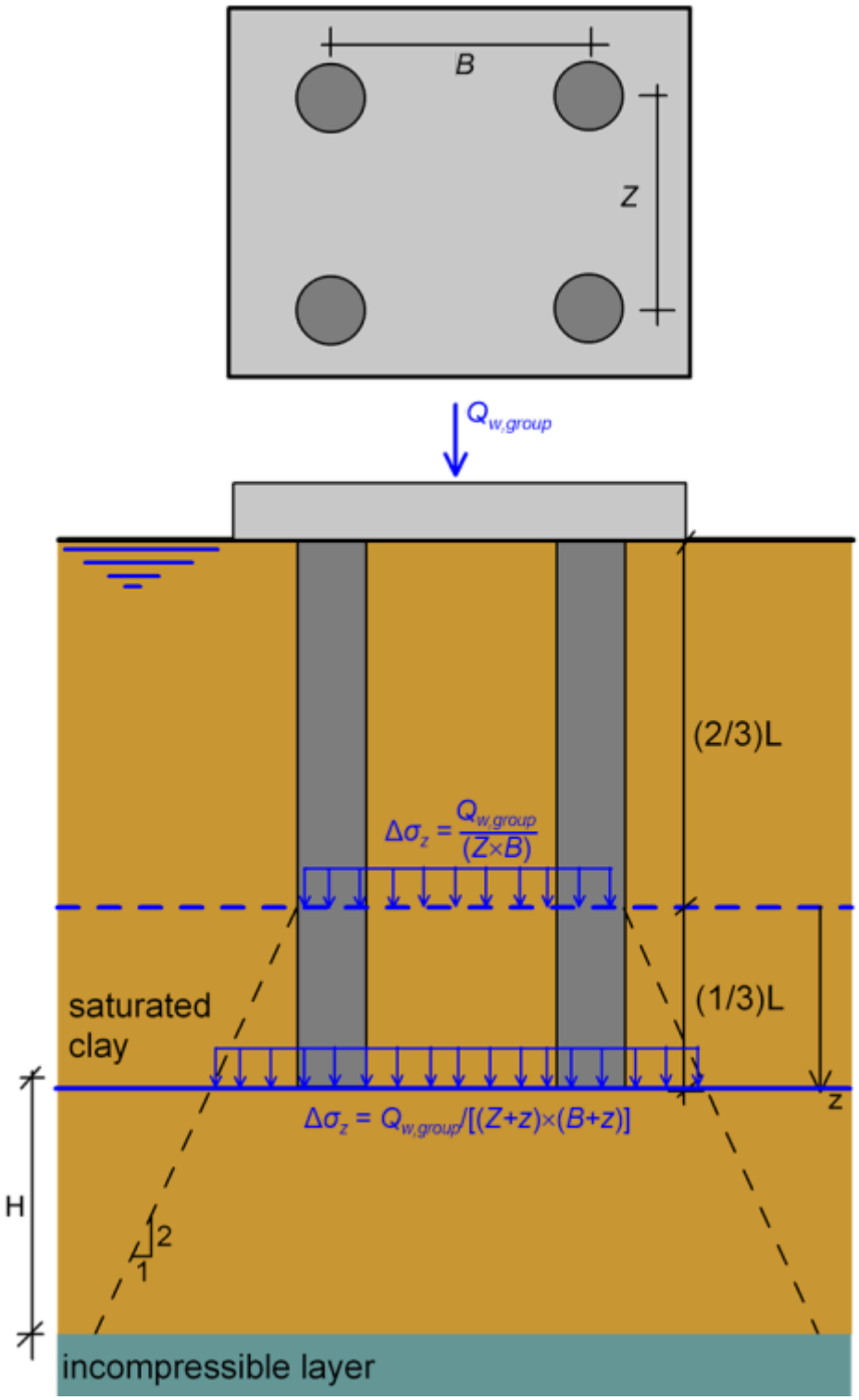

Figure 6.79. Additional stress distribution for the estimation of the consolidation settlement of a pile group.

Under this assumption, the increase in the vertical stress in the clay layer is calculated as (see also Chapter 3.6):

(6.102) $$\Delta\sigma_z = \frac{Q_{w,group}}{(Z+z)\,(B+z)}$$

where Z and B are the dimensions of the pile group, depicted in Figure 6.79, and z is measured from the level where the total load is assumed to act (at $2/3L$ from the surface).

Following the estimation of the distribution of $\Delta\sigma_z$ with depth along the compressible layer of thickness $H+(1/3)L$ (Figure 6.79) we can estimate its consolidation settlement using the 1D (or 2D if the thickness of the compressible layer is comparable to the pile cap dimensions) linear or non-linear consolidation methods described in Part 4. Note that settlement of the soil layers above a depth equal to $(2/3)L$ are not considered.

6.22 NEGATIVE SKIN FRICTION EFFECTS

Let's consider the case where a load is applied on the ground surface in the vicinity of a pile, or a pile group, after the construction of the piles has been completed. A common case where these conditions are met in practice is the construction of a bridge approach embankment, which follows the construction of the bridge foundation (Figure 6.80).

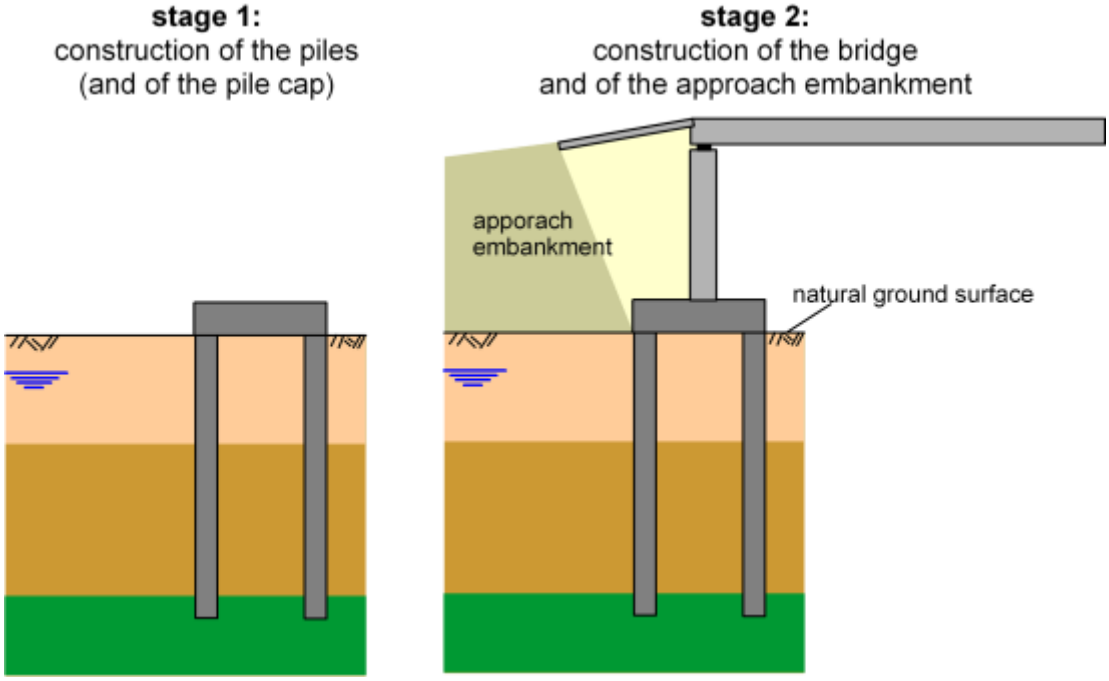

Figure 6.80. Staged bridge construction resulting in the development of negative skin friction in the abutment piles.

The approach embankment will impose a surcharge on the soil, and the soil adjacent to the pile will begin to settle. If the magnitude of the surcharge, or the compressibility of the surficial soil layers, is high the soil around the pile will settle more than the pile settles while transferring the axial compressive load from the superstructure.

Remember that skin friction develops on the pile shaft to resist the relative vertical displacement of the pile resulting from the load imposed on its head, Q. For the sake of generality we will drop the subscript $_w$ in this chapter and refer to the load on the pile head as Q although, as discussed later, negative skin friction is a serviceability problem, and pile settlement due to negative skin friction must be estimated while considering the serviceability load acting at the pile's head. Along the pile length where $\rho_{pile} < \rho_{soil}$, the developing skin friction will have an opposite sign, compared to the skin friction at the lower part of the pile *(negative skin friction)*. Thus, instead of contributing to the pile resistance, the friction along the upper part of the pile will add to the external load (Figure 6.81):

(6.103) $$Q + Q_{nf} = Q_b + Q_{sf}$$

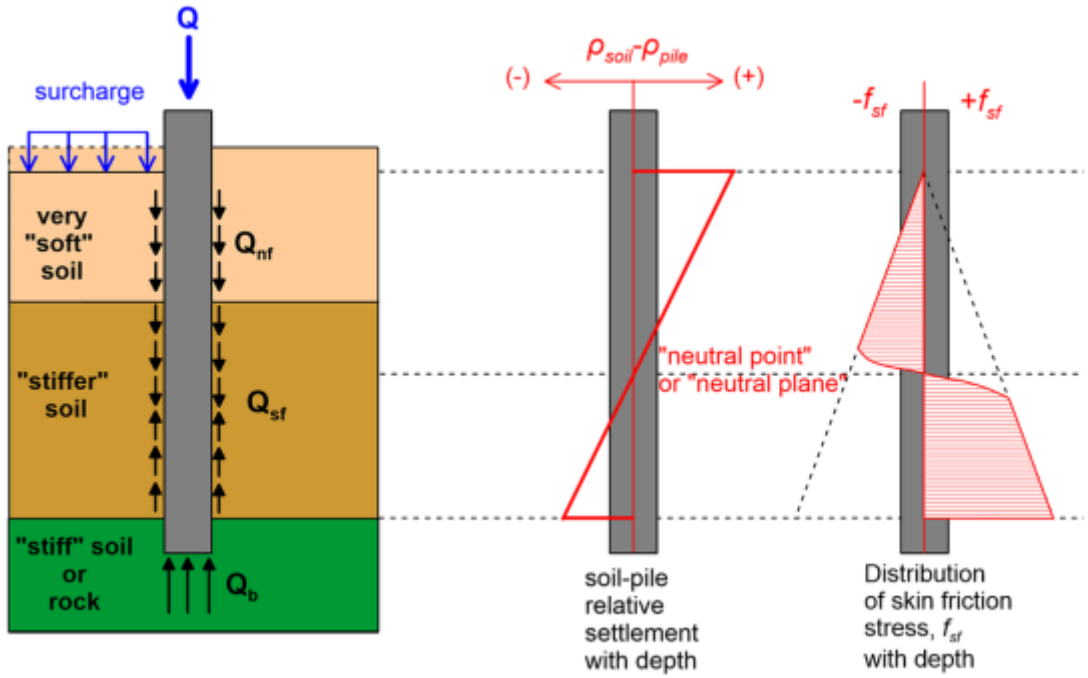

Figure 6.81. Soil-pile relative displacements and skin friction stress distribution with depth.

If we plot the distribution relative soil-pile displacement $\rho_{soil}-\rho_{pile}$ along the pile shaft, we will find the point where the relative displacement becomes zero, or $\rho_{pile} = \rho_{soil}$. This point is called the *"neutral point"* or *"neutral plane"*. Above the neutral plane skin friction stresses are negative, adding to the external load, and below the neutral plane friction stresses are positive, and contribute to pile resistance (Figure 6.81).

Estimation of the location of the neutral plane is necessary for the estimation of the negative and positive friction load and resistance of the pile, respectively. This is not a straightforward process, as it depends on a number of parameters.

Provided that the soil strength increases with depth, as in most common cases, the neutral plane will be found somewhere below the mid-point of the pile, if the external load applied at the pile head is zero (Q = 0). In the extreme case where the pile toe is founded directly on a practically incompressible layer of rock, the neutral plane will be located at the elevation of the bedrock (Figure 6.82a). In the case of a friction pile in uniform soil, which shear strength increases linearly with depth, the neutral plane will lie near the lower third of the pile (Figure 6.82b), if the pressure transferred to the pile toe is negligible, which is reasonable under serviceability conditions.

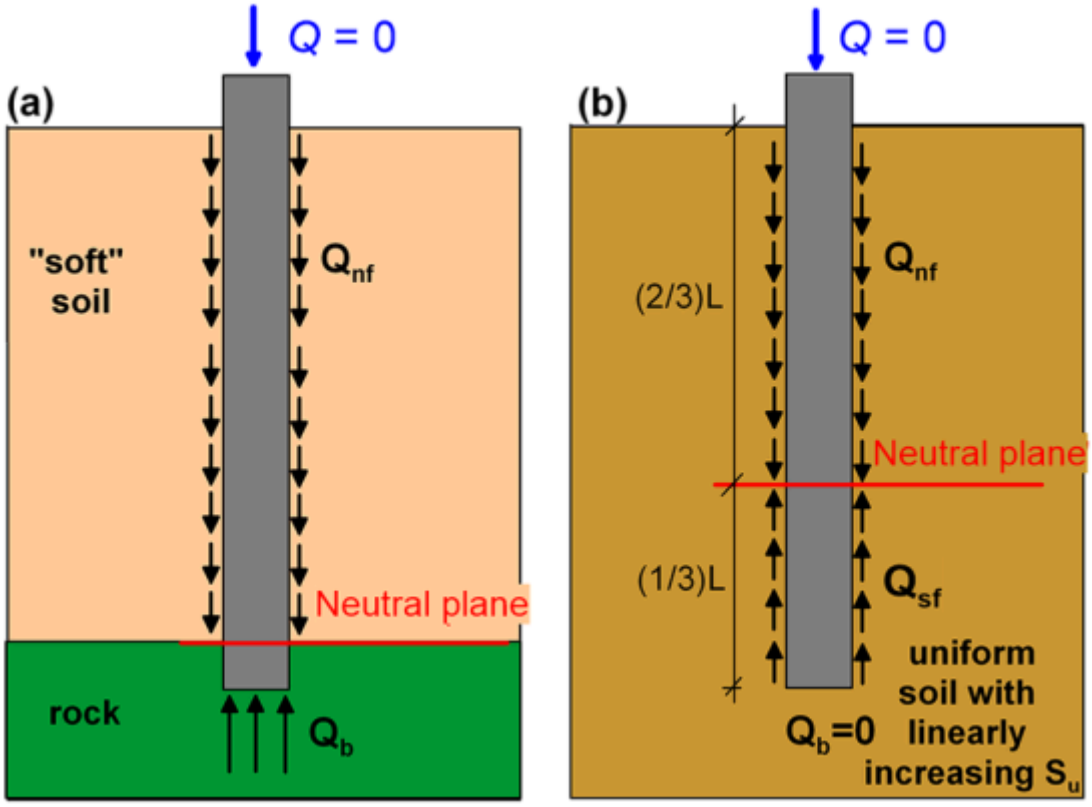

Figure 6.82. Location of neutral plane for (a) an end-bearing pile founded on bedrock, and (b) a friction (floating) pile, *before the application of any load Q on the piles.*

However, the above are valid if no vertical load is applied on the pile. Following the application of an axial compressive load at the pile head Q, the pile will settle further. Consequently, the neutral plane will move up, and the magnitude of the *dragload*, defined as the sum of the negative skin friction shear stresses along the interface, is reduced. In other words, negative skin friction also depends on the load applied on the pile under serviceability conditions. As depicted in Figure 6.83, the location of the neutral plane is found at the intersection of two load distribution curves (Fellenius, 1984):

- of the *forcing load distribution curve*, which is drawn from the pile head downwards, starting from the applied axial compressive load Q, and adding the load due to negative skin friction Q_{nf}, with the latter taken as acting along the entire length of the pile.
- of the *resistance load distribution curve*, which is drawn from the pile toe upwards, starting from the value of the end bearing resistance Q_b, and adding the resistance due to positive skin friction Q_f, with the latter taken again as acting along the entire length of the pile. Note that under serviceability conditions Q_b can be considered to be zero, as it is not at all certain that sufficient pressure has been transferred to the pile toe.

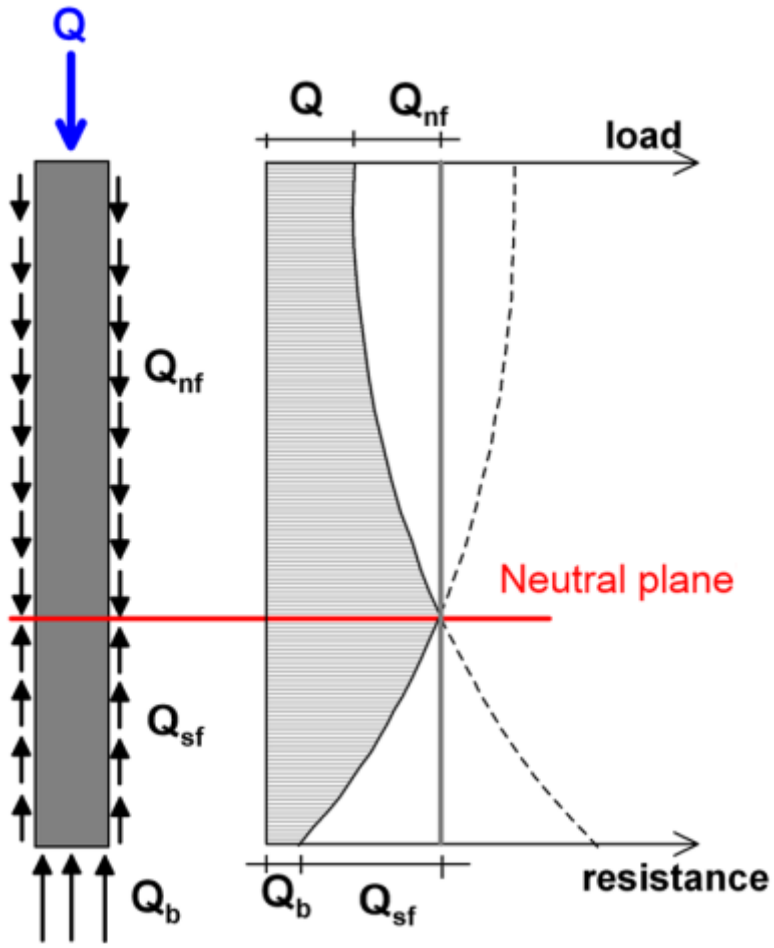

Figure 6.83. Determination of the neutral plane according to Fellenius (1984).

While drawing the abovementioned curves, the skin friction resistance must be estimated while considering drained soil behavior (β-method or ICP method, Chapter 6.10 and Section 6.12.7), as excess pore pressure at the end of consolidation will have dissipated.

Some key points that must be taken into account while considering negative skin friction effects:

- The structural capacity of the pile to resist axial compressive forces must be checked at the location of the neutral plane. Generally, the axial capacity of the cross-section will be higher than the sum of the serviceability load and the negative skin friction, and this check should not be critical.
- The dragload must not be included in the consideration of the ultimate geotechnical strength i.e., the load applied on the pile head should not be reduced by any portion of the dragload: In the Ultimate Limit State, when the collapse load is reached, the pile will move downwards along its entire length, and negative skin friction is eliminated. In that case, the neutral point will be found at the pile head. Of course, if settlement of the pile head due to negative skin friction is large enough to cause failure of the superstructure, then the ULS criteria will not be met. However, in that case settlement of the pile under serviceability conditions will not be acceptable either.
- *Negative skin friction is rather a settlement problem.* Consider the problem depicted in Figure 6.84, where a pile is installed in a two-layer profile consisting of a consolidating layer 1 and a non-consolidating layer 2. The neutral plane will be found at a depth z_{np} which may be larger than the thickness of layer 1 ($z_{np} > L_1$, Option 1, Figure 6.84), or smaller ($z_{np} < L_1$, Option 2, Figure 6.84). Poulos *et al.* (2001) recommend calculating the depth of the neutral plane with the Fellenius (1984) method outlined above. Accordingly, settlement of the pile head (which should be calculated for serviceability conditions) is estimated as the larger of: i) The elastic compression of the portion of the pile embedded in layer 1 (Length L_1, Figure 6.84) *plus* the settlement of the portion of the pile embedded in layer 2. The latter can be calculated using the methods described in Chapters 6.20 and

6.21, while considering a pile of length L_2 (Figure 6.84) equal to the thickness of layer 2 and compressive load equal to $Q = Q_w + Q_{nf}$; ii) The free-field movement of the soil at the level of the neutral plane $\rho_{s,np}$ (Figure 6.84). This settlement is calculated with conventional methods (Part 4), ignoring the existence of the pile. While this is not mentioned in Poulos *et al.* (2001) the author recommends adding to the free-field movement of the neutral plane $\rho_{s,np}$ the elastic shorting of a portion of the pile with length z_{np}. This may or may not be important.

- Inclined (battered) piles should be avoided in areas where negative skin friction development is expected, as large soil settlement will induced excessive bending of inclined piles.

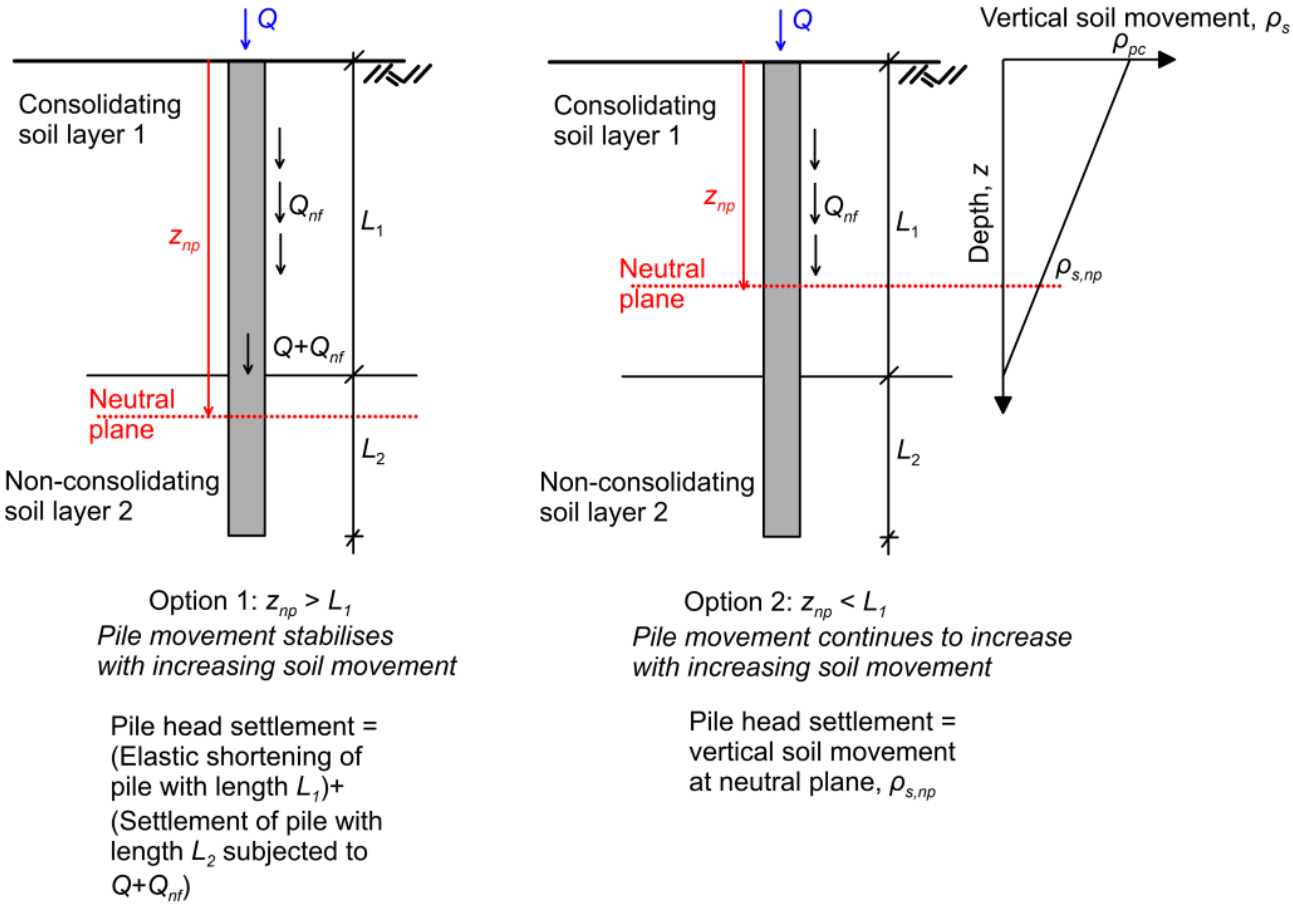

Figure 6.84. Simplified method to determine pile head settlement due to negative skin friction (after Poulos *et al.* 2001).

There are several methods to reduce negative skin friction effects, such as (FHWA 2006):

- Reduction of the soil settlement e.g., by preloading soil or implementing other soil improvement methods, or even using lightweight fill material (EPS geofoam) for the core of the approach embankment.
- Treatment of the piles with a friction reducer, such as bitumen or plastic wrap. This method will work only for drilled shafts.
- Use pile sleeves to prevent direct contact between the soil and the pile.
- Alter the construction sequence, so that no consolidation settlement takes place after the construction of the piles.

Concluding, negative skin friction will develop whenever differential settlement develops between the soil surrounding the pile, and the pile itself, regardless of the cause of settlement. Thus, in cases where consolidation settlement is possible due to e.g., lowering of the water table as a result of groundwater overpumping (Chapter 4.2), construction of an adjacent foundation that will impose additional stresses in the soil or seismic liquefaction, the possibility of the development of negative skin friction must be examined.

EXAMPLE 6.11

Numerical simulation of negative skin friction effects: estimation of the elevation of the neutral plane for different applied load levels

After construction of the drilled shaft of the figure, the area around the shaft is backfilled, and a uniform surcharge of magnitude 160 kPa is applied on the ground surface. Assuming for simplicity that the total settlement is equal to the immediate settlement, determine the location of the neutral plane:

a. Before any load is applied on the shaft,
b. If a vertical load equal to about 10% of the long-term collapse load is applied on the pile, and
c. If the pile is loaded up to its long-term collapse, defined as the load resulting to shaft head displacement $u_{y,f}$ equal to $0.3D$.

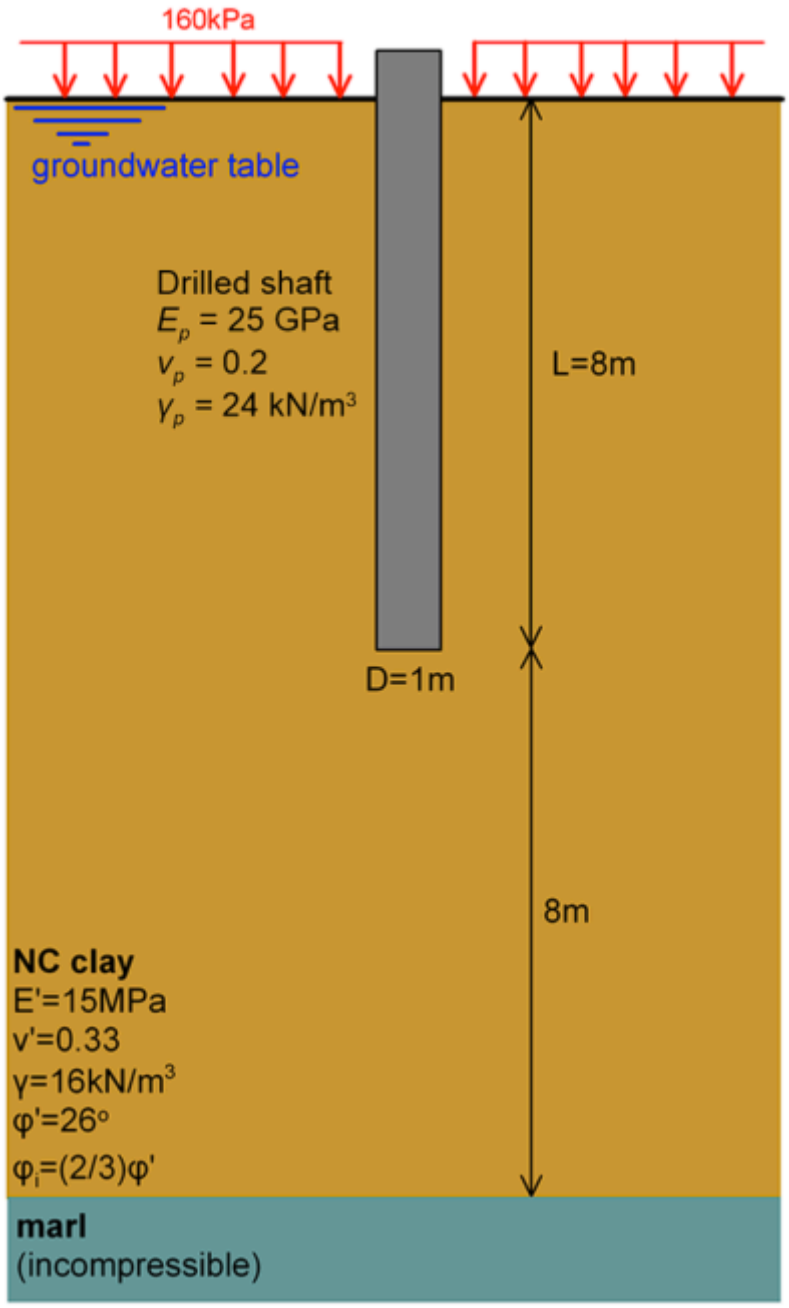

Example 6.11. Problem description and input parameters.

Answer:

This simplified problem is used to "visualise" the concept of the negative skin friction and of the neutral plane, described in Chapter 6.22, and follows the same general concepts of numerical simulation of piles subjected to vertical loads developed in Examples 6.3 and 6.4. Note that in practice negative skin friction effects on piles is a three-dimensional problem, as an approach embankment will not apply a uniform surcharge on the surface of the soil surrounding the pile. Nevertheless, we consider a simplified axisymmetric version of the problem here, as the aim of this example is to demonstrate to the reader how the elevation of the neutral plane changes as the axial load applied on the pile head increases.

The response of the clay will be simulated as drained, employing the Drained Mohr-Coulomb model, as we assume that excess pore pressures will have dissipated, and settlement due to the application of the surcharge will have been completed, before any load is applied on the shaft. Although the cohesion of the normally consolidated clay is assumed equal to zero ($c' = 0$), a small value of cohesion ($c' = 1$ kPa)

is considered with the Drained Mohr-Coulomb model, for numerical stability reasons. A linear-elastic material is used to simulate the shaft, with Young's modulus E_p = 25 GPa and Poisson's ratio v_p = 0.2. The interface strength reduction factor R_{int} for a concrete drilled shaft under long-term load conditions is defined as:

$$R_{\text{int}} = \frac{\tan \varphi_i}{\tan \varphi'} = \frac{\tan\left(\frac{2}{3}\varphi'\right)}{\tan \varphi'} = 0.642$$

where $\varphi' = 26^o$.

The considered model geometry and the finite element mesh are presented in Figure 6.85.

The analysis is performed in 4 stages:

1. *Initial stage (before the construction of the shaft)* Calculate initial geostatic stresses with the "K_0 procedure", while associating all geometry clusters with the original soil material.
2. *Plastic stage 1 (construction of the shaft)* The material of the geometry cluster corresponding to the shaft is switched to the linear elastic material described above, and interfaces are activated.
3. *Plastic stage 2 (application of the surcharge)* A uniform pressure of q = 160 kPa is applied on the top of the mesh, but not on the shaft head.
4. *Plastic stage 2 (loading of the shaft)* An imposed displacement of maximum magnitude $0.3D$ = 0.3m is applied at the head of the shaft. Results during intermediate analysis stages are saved too.

Note that, as an effective stress analysis is performed, the groundwater table level must be explicitly introduced during the definition of the analyses stages.

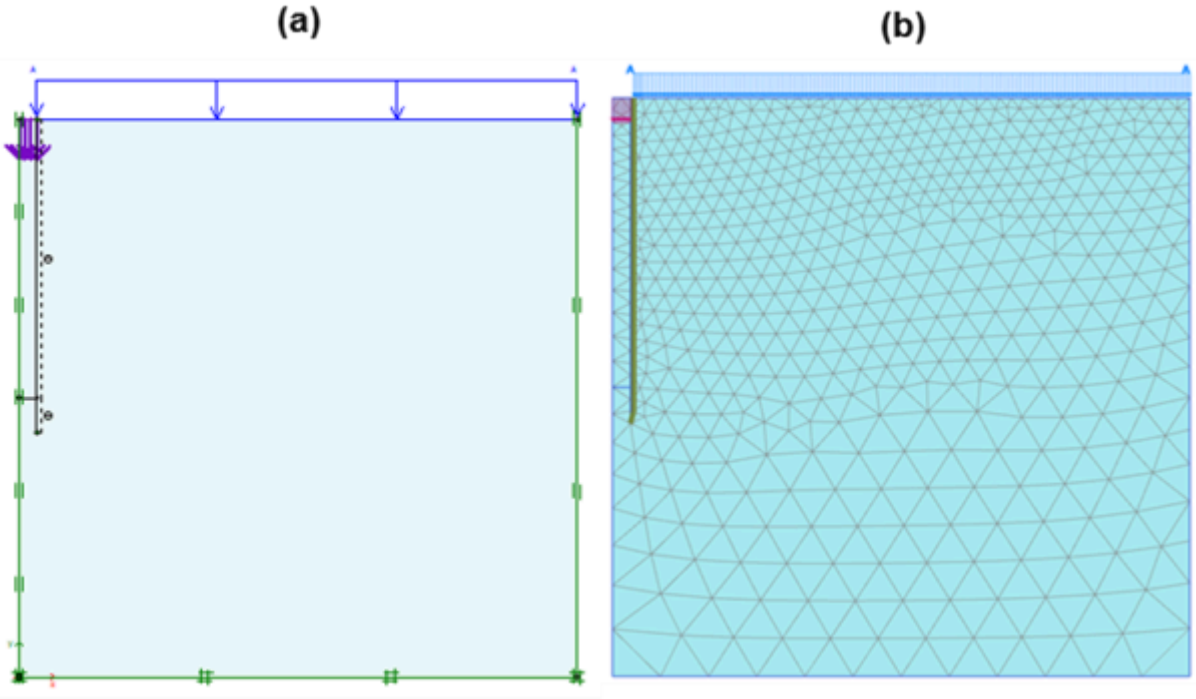

Figure 6.85. (a) Model geometry and (b) Finite element mesh.

Snapshots of the deformed mesh are presented in Figure 6.86, after the application of the surcharge, and after loading the shaft up to failure. As expected, application of the surcharge results to some settlement of the shaft, although no load is applied on its head (see also Figure 6.87a). On the contrary, as the shaft is loaded up to its collapse load, its head settles more than the surrounding soil.

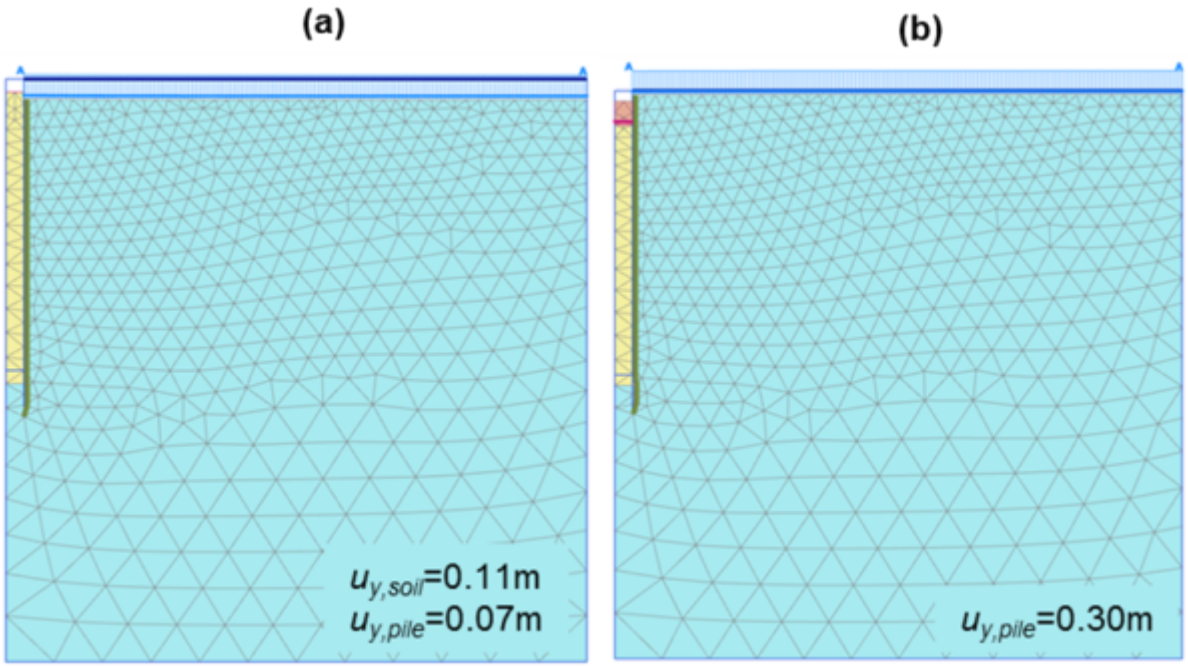

Figure 6.86. Deformed mesh (a) at the end of plastic stage 2, after the application of the surcharge (magnified 5 times), and (b) at the end of plastic stage 3, after loading the shaft up to the failure load (true scale). The vertical displacement of the soil surface $u_{y,soil}$ and of the shaft's head $u_{y,pile}$ at each stage are also reported.

The location of the neutral plane can be found by plotting the shear stress along the soil-pile interface, as illustrated in Figure 6.87b. The neutral point is located initially, when zero load is applied at the pile head, at a depth equal to $0.75L$ from the head, quite close to the theoretical value of $0.66L$ which applies for linearly increasing shear strength of clay with depth (as it will be the case for drained loading). As a vertical load is applied on the shaft head, the neutral plane moves upwards, and negative skin friction stresses are reduced. When the collapse load is reached, as expected, negative stresses at the interface vanish, the neutral plane is now located at the pile head, and the full length of the shaft contributes to the resistance by developing positive skin friction. This demonstrates that negative skin friction is a settlement, rather than a resistance problem.

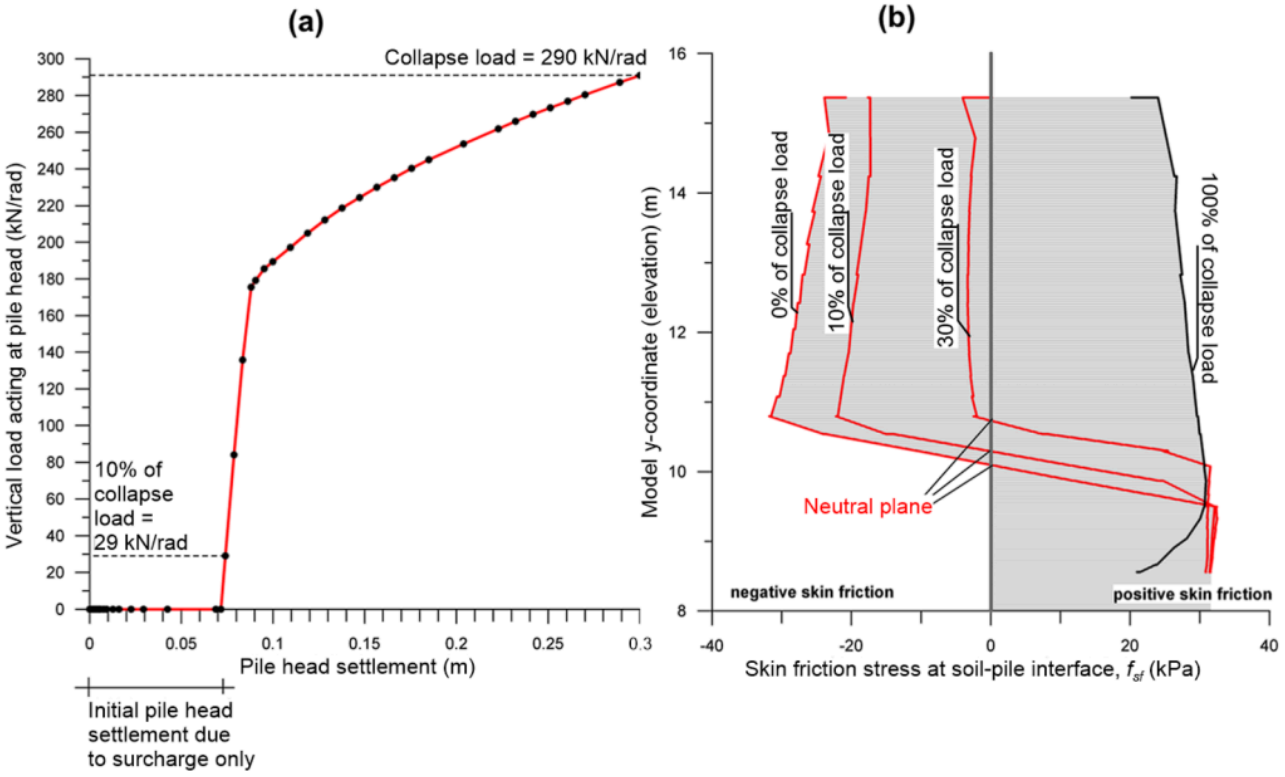

Figure 6.87. (a) Load-settlement curve, and (b) Skin friction along the soil-pile interface for increasing vertical load.

Further to that, it is interesting to compare the load-settlement curve of Figure 6.87a with the load-settlement curve that would result from an additional analysis, without applying a surcharge load (Figure 6.88). Clearly, the surcharge has a beneficial effect on the bearing capacity of the shaft, as it results in increased vertical, and consequently lateral effective stresses along the shaft length, thus in increased skin friction resistance (Eq. 6.12-6.13).

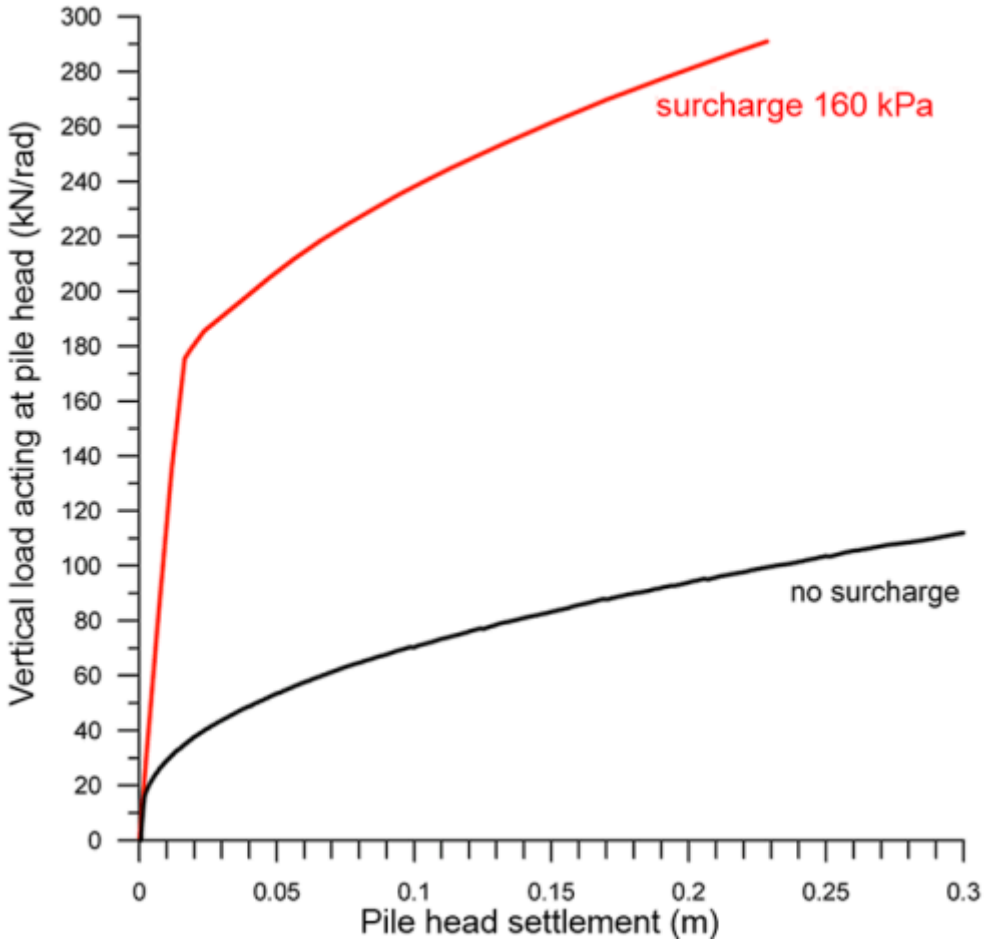

Figure 6.88. Shaft load-settlement curve with and without surcharge loading.

6.23 LATERAL LOADING OF PILES – GENERAL CONSIDERATIONS

One of the main advantages of pile foundations, compared to shallow footings, is their ability to sustain high lateral forces and bending moments (Figures 6.2b-6.2d) due to seismic actions, wind pressure, vehicle acceleration and braking loads, wave loads etc. Design of piles to resist lateral loads is a soil-structure interaction problem, where the response of the superstructure, the pile and the soil must be jointly considered.

Development of methodologies for the design of piles against lateral loads has its origins back in the 1950's, when exploitation of offshore resources commenced. Most of the methods are based on the interpretation of measurements obtained during full-scale experiments on instrumented piles subjected to static and cyclic lateral loads. Lateral load tests on piles, especially cyclic load tests are less common, as they are much more expensive than compressive static load tests discussed in Chapter 6.16, and they are performed only in special projects.

After installation of the pile, the horizontal ground stresses developing around its cross-section can be assumed uniform, and are often taken equal to the geostatic earth pressure at-rest as e.g., in the β-Method described in Chapter 6.10 (Figure 6.89). As the pile deflects under the application of a lateral load H by y, the distribution of stresses changes: the soil stresses applied at the front side of the pile increase *(passive earth pressure state)* and the soil stresses applied at the back side of the pile decrease *(active earth pressure state)*.

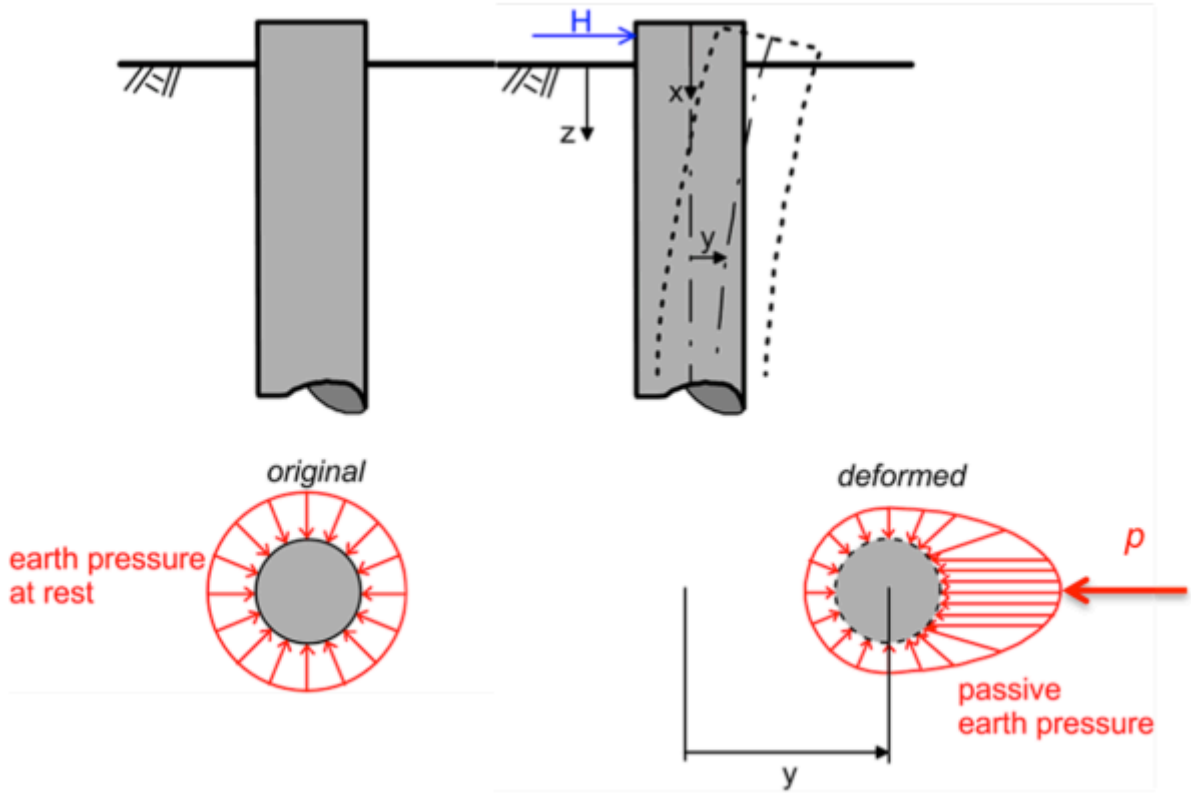

Figure 6.89. Distribution of lateral soil stresses on a pile before and after lateral deflection (after Reese and van Impe, 2001). Soil resistance to pile lateral movements is equal to the sum of the normal stress from the soil acting on the pile section.

The soil-related parameter governing the design of a pile under lateral loading is the *reaction modulus p/y* defined as the reaction p from the soil at a point along the pile, divided by the deflection of the pile at the same point y. The reaction, or soil resistance p results from integration of stresses along the cross-section (Figure 6.89), and its dimensions are force per unit length along the pile.

The reaction p is a function of the soil and pile properties, the depth below the ground surface z, and the deflection of the pile, y. Notice that in reality, the magnitude of the soil resistance varies significantly with pile deflection: the p-y curve is actually non-linear (Figure 6.90). However, an equivalent linear approximation of the p-y curve is often used in design, particularly for serviceability analysis where pile deflection is of interest, and soil-pile interaction is described by a single parameter: the slope of the idealised curve, or the coefficient of subgrade reaction K_h (Figure 6.90).

When a pile is subjected to a combination of lateral force and bending moment at its head (Figure 6.91), the following must be ensured via proper engineering calculations and checks:

- The lateral capacity of the soil must not be exceeded.
- Displacements and rotations of the pile head must not affect the serviceability of the structure.
- The developing axial force and bending moment must not exceed the structural strength of the pile cross-section.

Non-linear (or equivalent linear) p-y curves can be introduced in a simple beam-spring finite element model, to determine pile deformation and internal forces under a combination of loads (Figure 6.91). This method is described later in this Part, as it is widely used in practice. Instead of applying the loads directly on the pile head, the superstructure (e.g. bridge pier) may be modeled too, to account for soil-pile-superstructure interaction effects (Figure 6.92a). Of course, more elaborate 3-D models of the pile embedded into the soil system may be used for the most accurate simulation of the soil-pile system response (Figure 6.92b), but their use is limited to special projects or for research purposes.

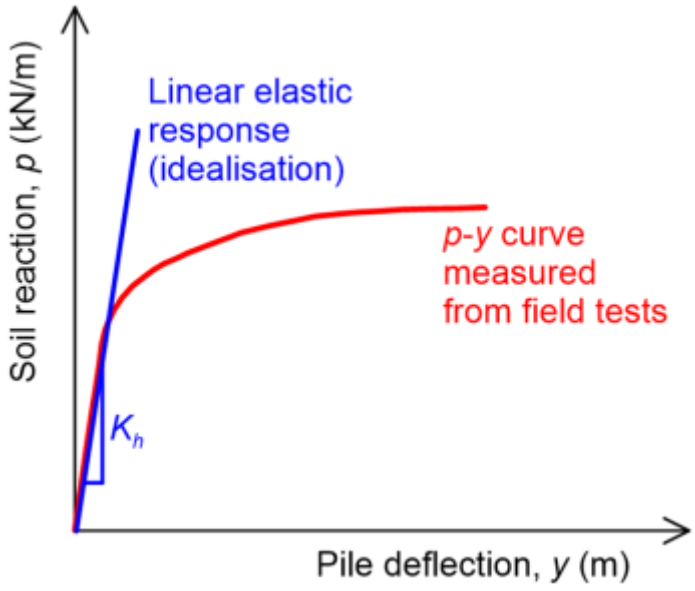

Figure 6.90. Typical force-deflection (p-y) curve and idealized linear response.

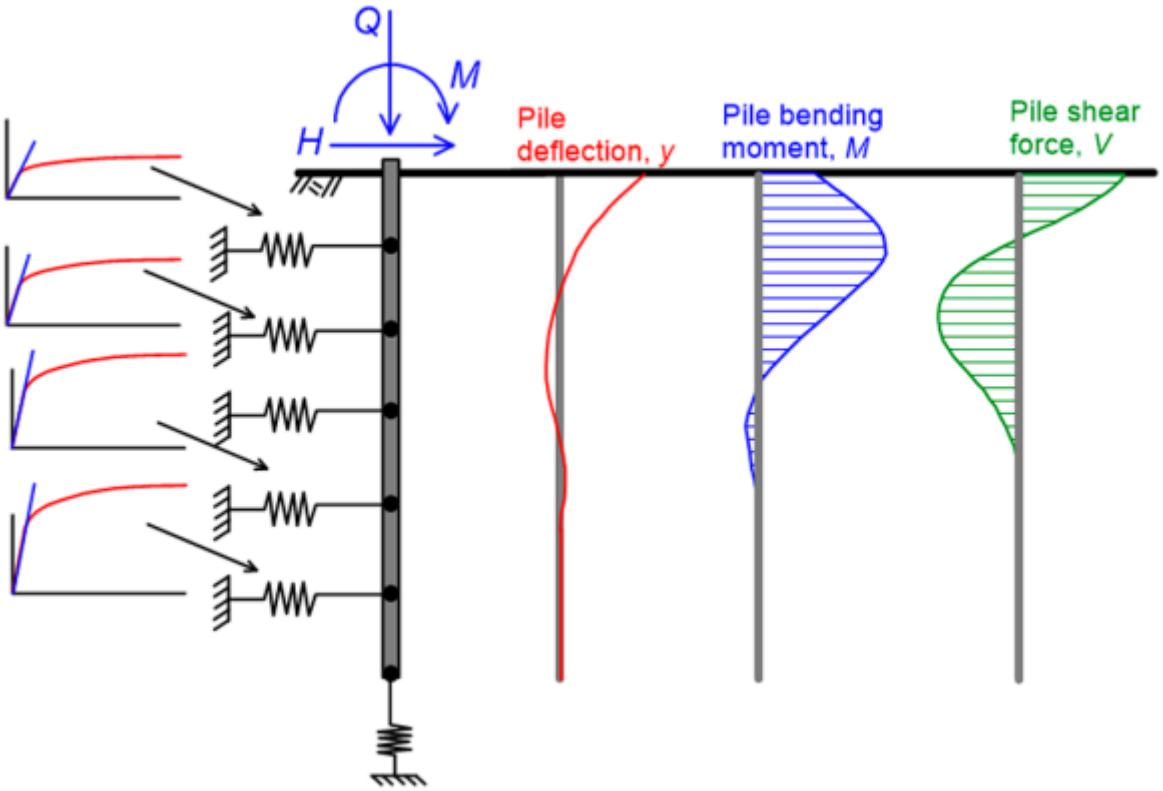

Figure 6.91. Beam-spring finite element model to determine deformation and internal forces of a single pile subjected to a combination of external loads applied on its head.

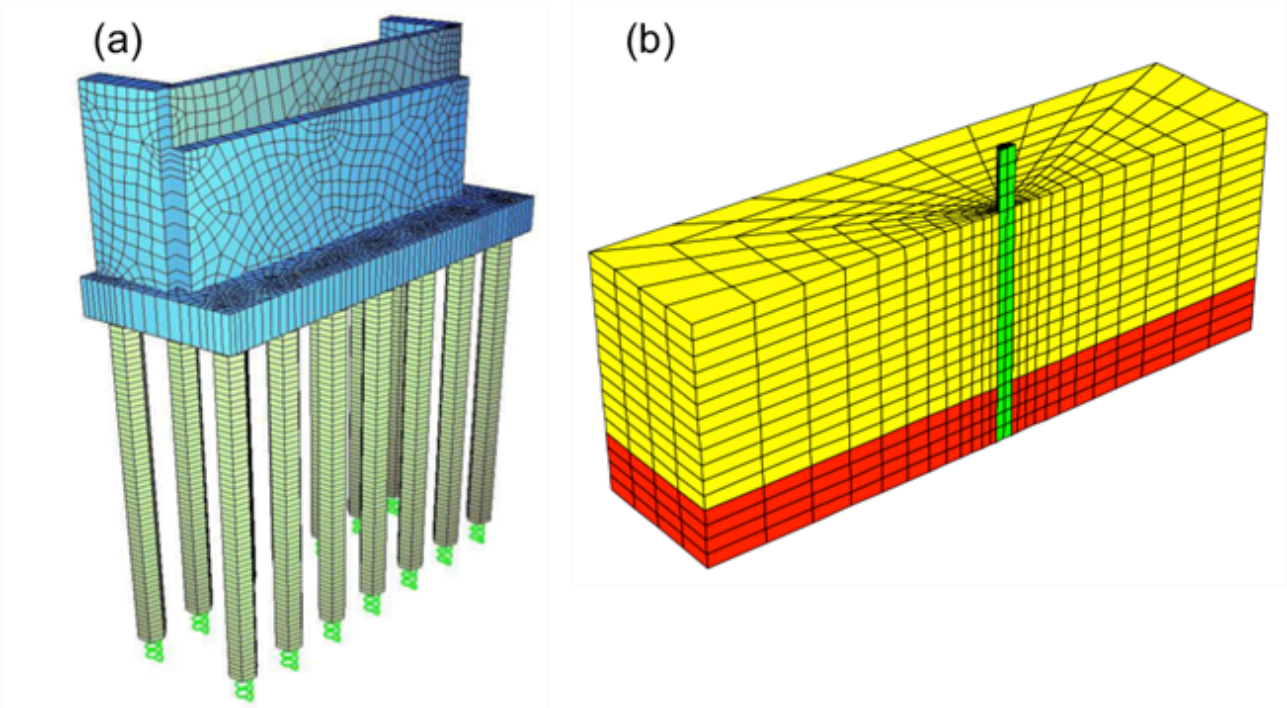

Figure 6.92. (a) Pile-superstructure model and (b) Full 3-D soil-pile model.

As described in the following paragraphs, simpler methods that do not require the use of a computer

may be also applied, at least to obtain a first-order estimate of the pile response. According to AS2159, the ultimate geotechnical strength (collapse lateral load, H_f) of a pile subjected to lateral loading shall be determined as the minimum of the following two values:

- The ultimate geotechnical strength for *"short pile"* failure (Figure 6.93a), developing when the ultimate reaction from soil is mobilised uniformly along the entire length of the pile (*soil fails first*). The later is assumed to translate or rotate as a rigid body, depending on the fixity conditions at its head. The ultimate soil reaction per unit length of a pile in undrained perfectly-plastic soil been calculated by Randolph and Houslby (1984) using the upper and lower bound plasticity theorems described in Part 5. For "smooth" soil-pile interface (see Chapter 6.9) the exact plasticity solution for the ultimate reaction is $p_f = 9.14 S_u D$, while for "rough" soil-pile interface $p_f = 11.94 S_u D$ (Figure 6.93b).
- The ultimate geotechnical strength for *"long pile"* failure (Figure 6.94), developing when the structural strength of the pile section is reached at some point along the pile shaft, and a plastic hinge is formed before the ultimate soil reaction is mobilised along the entire length of the pile (*pile fails first*).

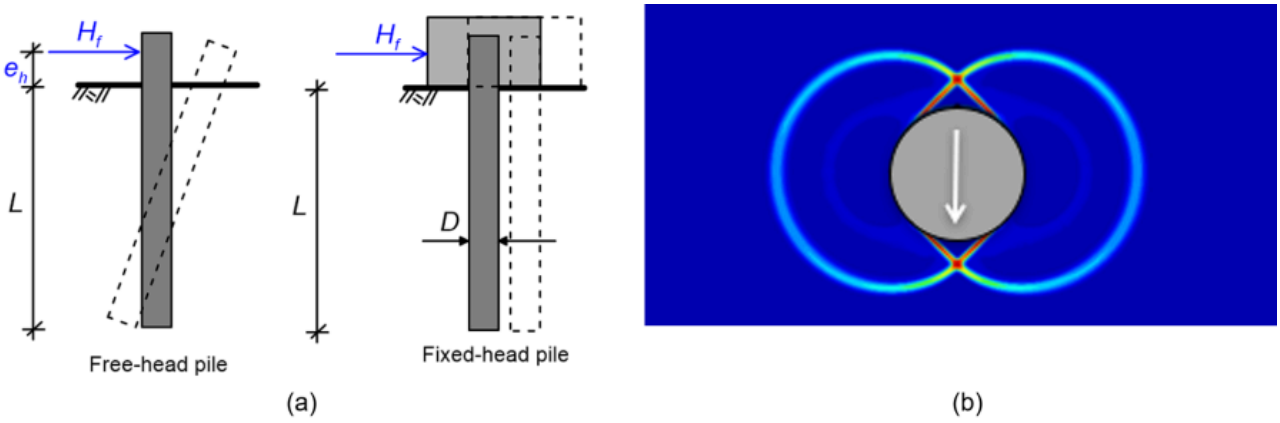

Figure 6.93. (a) "*Short pile*" failure mode, and (b) Plane-strain horizontal section of a rigid pile translating laterally in undrained soil; the energy dissipation contours depict the shape of the failure surface mobilised when the ultimate soil reaction is reached.

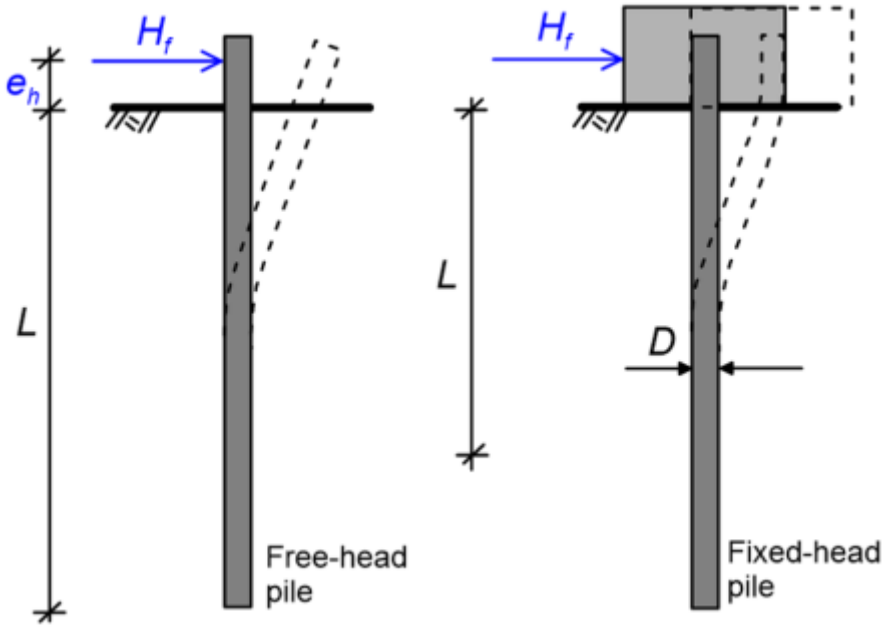

Figure 6.94. "*Long pile*" failure mode.

The type of failure that will eventually develop depends on the relative rigidity of the pile, compared to the surrounding soil. A method that appropriately considers both "short pile" and "long pile" failure modes was develop by Broms (1964a,b, 1965), based on the following assumptions: a) Rigid pile and *uniform*, perfectly plastic soil, for the estimation of the ultimate geotechnical strength and associated pile bending moment, and b) Linear elastic soil, for the estimation of pile deflection under the serviceability load. Broms developed different solutions for uniform soil and both undrained and drained loading conditions, but not for layered soil profiles. Notice that the response of the pile depends also on the fixity conditions at its head (Figures 6.93–6.94).

Although it is based on a number of simplifying assumptions, Broms method can be useful for the initial selection of the pile cross-section and length, and can act as springboard for more detailed finite element analyses. It must be noted that since lateral loads on piles often act for a short period of time (seismic, wave, wind, vehicle loads), low permeability soils such as clay are almost exclusively treated as undrained.

It is worth concluding this section by noting that, while in AS2159 there is no mention of a "preferable" failure mode, in the author's view piles generally should not be designed to fail with a "short" failure mode: The redundancy of the soil-pile system is zero if the ultimate lateral reaction of soil is reached along the full length of the pile, and failure will result in excessive pile lateral displacement and perhaps collapse of the supported structure. On the other hand, plastic hinge(s) that will develop in a soil-pile system that has been designed to fail with a long failure mode will feature some over-capacity, and catastrophic collapse will probably be avoided.

6.24 BROMS METHOD – PILES IN UNDRAINED SOIL

6.24.1 Short free-head piles

Calculation of the ultimate geotechnical strength (collapse lateral load) of a pile subjected to lateral load H at its head, and of the maximum bending moment M_{max} developing along the pile, is based on static equilibrium considerations (Figure 6.95). The ultimate soil reaction (Figures 6.95, 6.96) is taken equal to $p_f = 9S_uD$, and is compatible with the exact solution of Randolph and Housbly (1984) mentioned above, if we assume conservatively that the soil-pile interface is smooth.

While considering equilibrium, the reaction on the pile from soil developing near the soil surface (length equal to $1.5D$) is ignored, because a wedge of soil can move up and outwards when the pile is deflected. Based on that, the ultimate geotechnical strength H_f can be determined from Figure 6.96 as a function of the pile geometry, the elevation of load resultant e_h, and the undrained shear strength of the fine-grained soil, assumed constant with depth. Furthermore, the point along the pile where the maximum bending moment will develop (zero shear force) will be at distance f (units: length) from the surface (Figure 6.95):

(6.104) $$f = \frac{H_f}{9S_uD}$$

Having calculated the collapse lateral load H_f and f, the maximum bending moment that will develop on the pile M_{max} is calculated as:

(6.105) $$M_{max} = H_f\,(e_h + 1.5D + 0.5f)$$

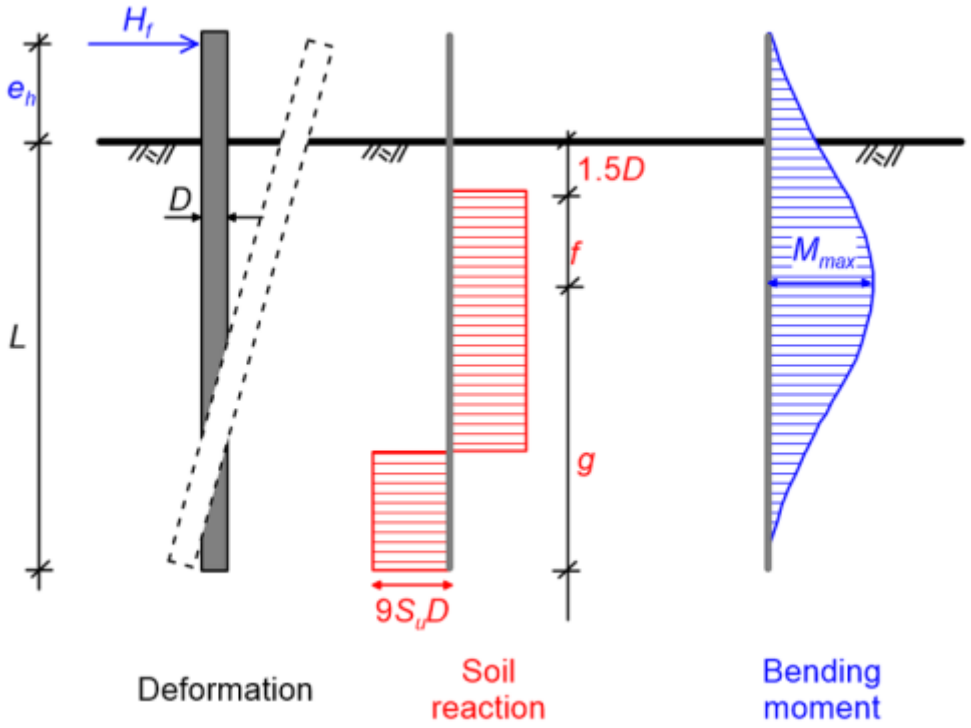

Figure 6.95. Deformation mode of a short pile unrestrained against rotation, and corresponding soil reaction and bending moment diagrams – Undrained soil.

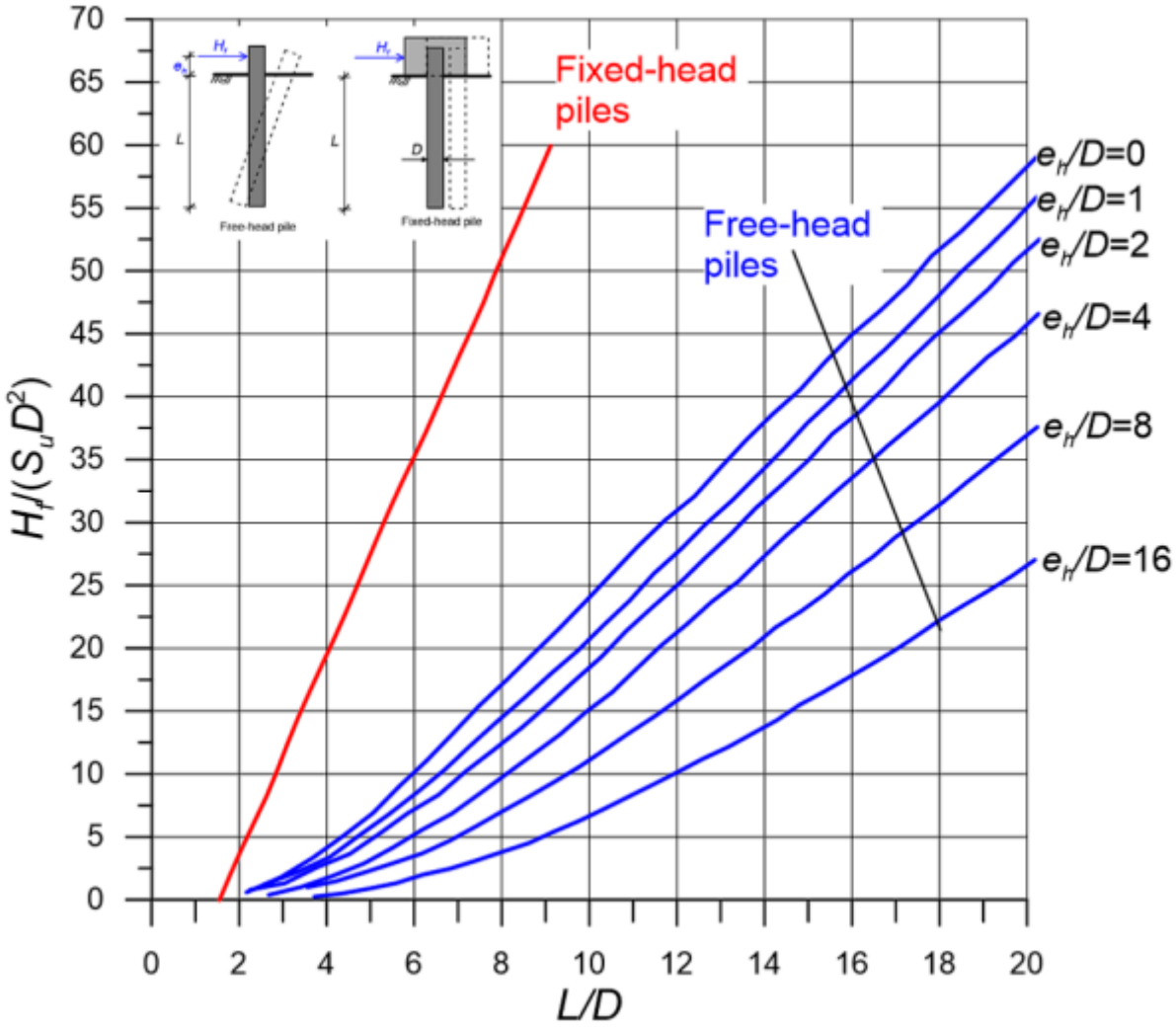

Figure 6.96. Estimation of the normalised collapse lateral load H_f of short piles in undrained soil.

6.24.2 Short fixed-head piles

The same procedure is followed for fixed-head piles too, assuming that the ultimate soil reaction develops along the full length of the pile, with the exception of the top 1.5 diameters, where it is customarily ignored (Figure 6.97).

The ultimate lateral load H_{ult} results from the need to satisfy static equilibrium, and can be either found using Figure 6.96, or directly as:

(6.106) $$H_f = 9S_uD\left(L - 1.5D\right)$$

Similarly, the maximum bending moment M_{max} that will develop at the head of the pile, at the connection with the rigid cap, is estimated as:

(6.107) $$M_{\max} = 4.5S_uD\left(L^2 - 2.25D^2\right)$$

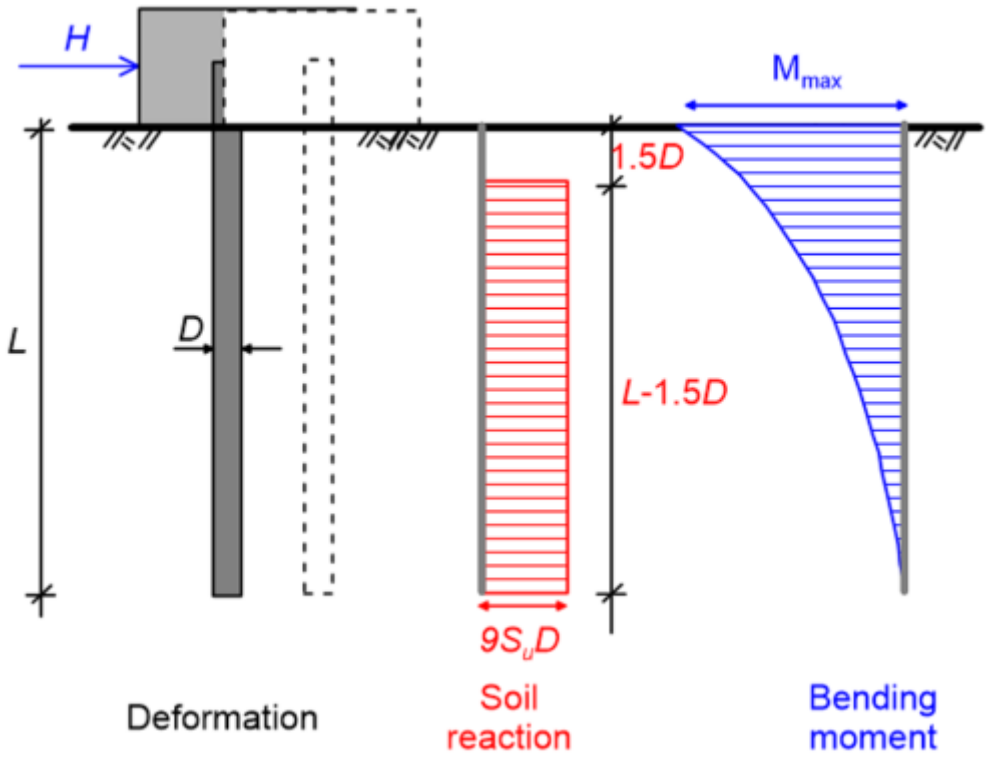

Figure 6.97. Deformation mode of a short pile restrained against rotation, and corresponding soil reaction and bending moment diagrams – Undrained soil.

6.24.3 Long free-head piles

Long failure mode corresponds to cases where the passive resistance from the soil along the pile length is very high, and before it is full mobilised, the maximum bending moment along the pile will became equal to the plastic (yield) bending moment, M_y of the pile's section. Failure will occur with the formation of a plastic hinge at the point where the maximum bending moment develops (Figure 6.98), at a depth equal to $1.5D+f$ where f is calculated from Eq. 6.104. The collapse lateral load, H_f is determined from Figure 6.99, or directly as:

(6.108) $$H_f = \frac{M_y}{(e_h + 1.5D + 0.5f)}$$

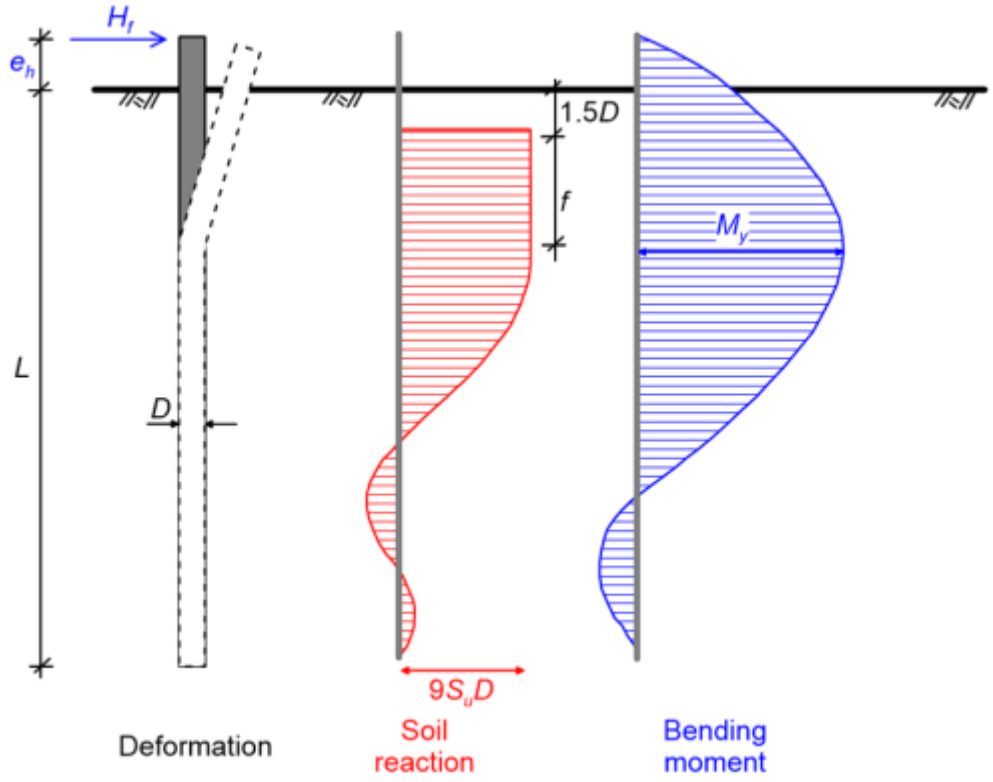

Figure 6.98. Deformation mode of a long pile unrestrained against rotation, and corresponding soil reaction and bending moment diagrams – Undrained soil.

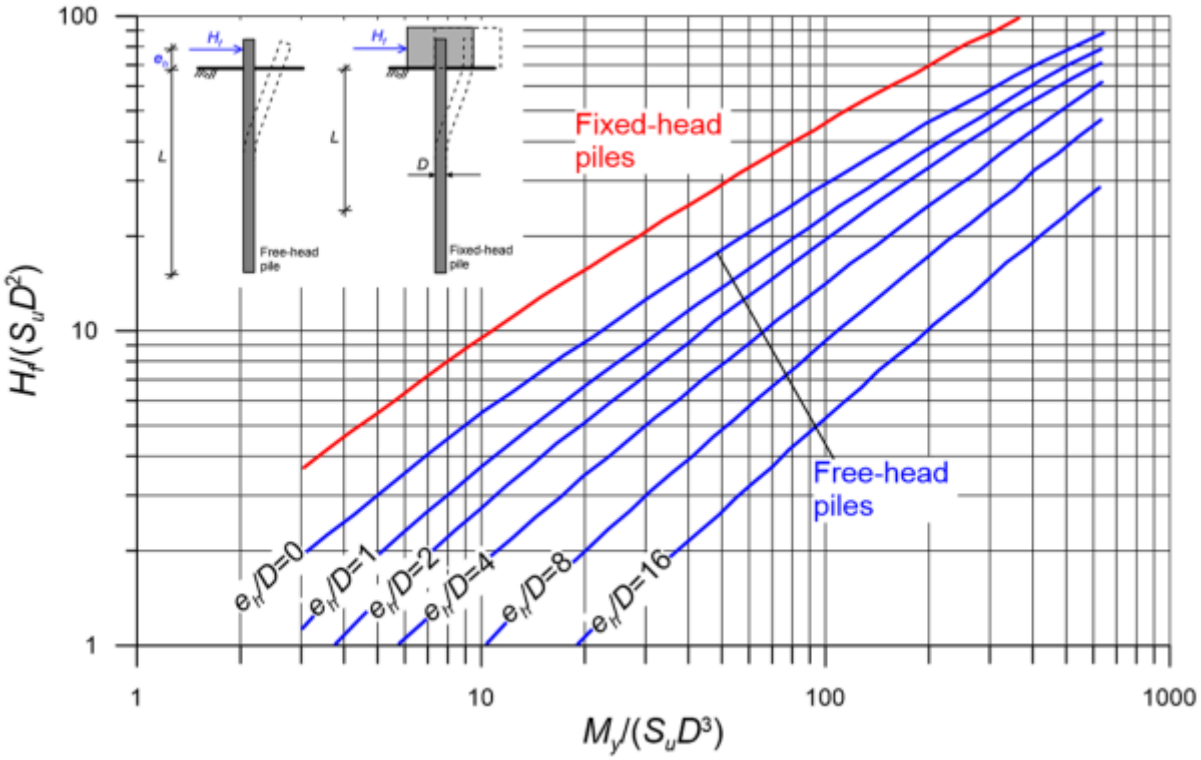

Figure 6.99. Estimation of the normalised collapse lateral load H_f of long piles in undrained soil.

The plastic moment, that develops when stresses over the entire cross-section of the pile reach the yield

stress of the material, depends on the material properties, the geometry of the cross-section as well as the axial force on the pile, for concrete piles. The plastic moment of some typical cross-section geometries for homogeneous pile material (e.g., steel) are provided in Table 6.14.

Table 6.14. Plastic (yield) moment of characteristic cross-sections. In the provided expressions, σ_y is the yield stress of the homogeneous cross-section material.

	Plastic moment, M_y
Rectangular cross-section, with width b and height h.	$\left(\frac{bh^2}{4}\right)\sigma_y$
Circular cross section, with diameter D	$\left(\frac{D^3}{6}\right)\sigma_y$
Hollow circular cross section with external diameter D_{ext} and internal diameter D_{int}	$\left(\frac{D_{ext}^3 - D_{int}^3}{6}\right)\sigma_y$

For design purposes, both the *short pile* and the *long pile* failure modes must be considered, to find the critical, minimum collapse load. To determine whether the pile will fail as a *short pile* or as a *long pile* first, one should start with the expressions in Section 6.24.1 for a short pile. If the resulting maximum bending moment is larger than the yield moment, the formulas for long pile failure must be used, as they will result in lower collapse lateral load.

6.24.4 Long fixed-head piles

As in the case of long free-head piles, the plastic (yield) bending moment, M_y will be reached before the ultimate soil reaction is mobilised along the full length of the pile. Failure will occur with the formation of two plastic hinges (Figure 6.100): One at the connection of the pile with the cap, where the pile is fixed against rotation, and a second at the point where the maximum bending moment develops, at a depth equal to $1.5D+f$ where f is calculated from Eq. 6.104. The collapse lateral load, H_f is determined from Figure 6.99, or directly as:

(6.109) $$H_f = \frac{2M_y}{(1.5D + 0.5f)}$$

There is however an *intermediate* case: A plastic hinge may develop at the head of the pile only, when the bending moment reaches there M_y. Then the ultimate lateral load will be:

(6.110) $$H_f = \frac{M_y + 2.25S_uD(L - 1.5D - f)^2}{(1.5D + 0.5f)}$$

and the bending moment at a depth equal to $1.5D+f$:

(6.111) $$M_{max} = 2.25S_uD(L - 1.5D - f)^2$$

Note that in that case M_{max} is lower than the plastic moment $M_{max} < M_y$. For given soil undrained strength and pile section properties, the critical failure mode (long, short, intermediate) that will result in the lowest lateral load depends on the length of the pile.

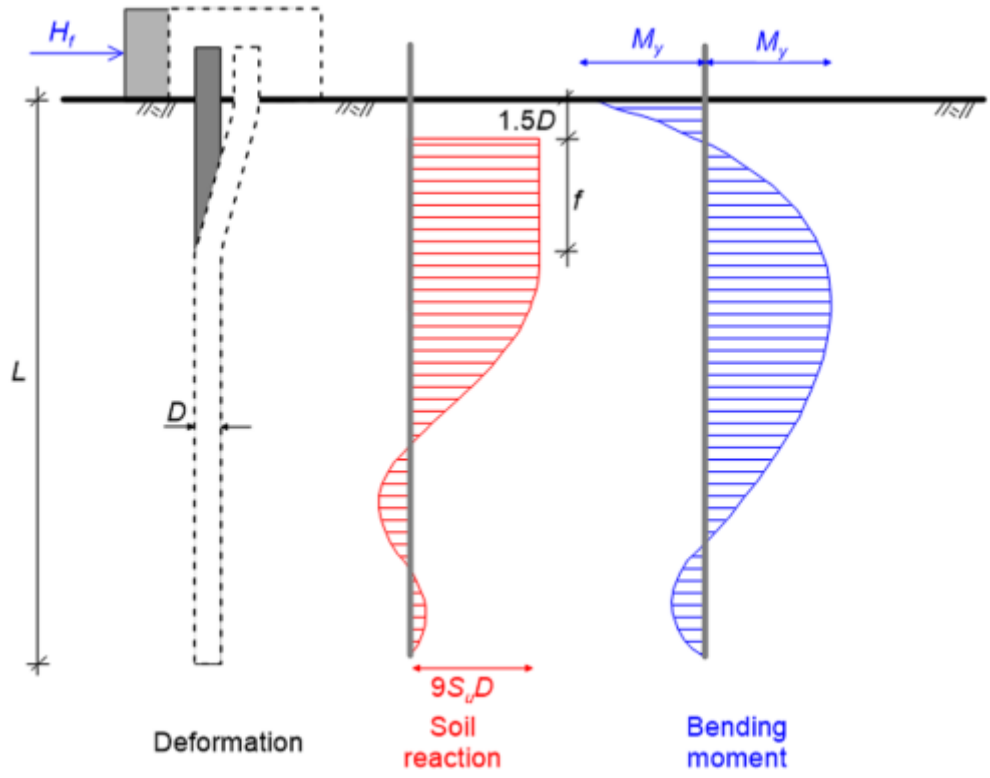

Figure 6.100. Deformation mode of a long pile restrained against rotation, and corresponding soil reaction and bending moment diagrams – Undrained soil.

6.24.5 Pile lateral deflection

For the calculation of the pile head deflection $y(0)$ at serviceability conditions, soil is assumed to behave as linear elastic material (see Figure 6.90). Besides, good design practice suggests that piles should be designed so that soil strains under serviceability lateral loads remain low. In line with Figure 6.90, a key parameter for the estimation of the lateral deflection of piles is the slope of the linear p–y curve K_h, which is referred to as *coefficient of subgrade reaction* or *soil reaction modulus* (units: stress/unit length).

A limitation of Brom's method is that K_h must be estimated by means of empirical formulas. A more rigorous solution that forgoes this requirement is presented later in this Part. For *overconsolidated clays,* we can assume for simplicity that K_h is not depth-dependent, and can be estimated as:

(6.112) $$K_h = \frac{E_u}{D}$$

where E_u is the undrained Young's modulus of clay, which should be compatible with the level of the applied strain due to the lateral soil displacement. Alternatively, Davidson (1972) proposed to estimate K_h as a function of the undrained shear strength of clay, as:

(6.113) $$K_h = 67\frac{S_u}{D}$$

Some typical coefficient of subgrade reaction values for overconsolidated clays are listed in Table 6.15.

Table 6.15. Typical coefficient of subgrade reaction values for stiff-to-hard over-consolidated clays.

	Undrained shear strength range		
	100 < S_u < 200 kPa	**200 < S_u < 400 kPa**	**S_u > 800 kPa**
Range of K_h values (kN/m^3)	12000 to 24000	24000 to 48000	48000 to 96000
Recommended K_h value (kN/m^3)	18000	36000	73000

The coefficient of subgrade reaction generally increases with depth, z in *normally consolidated clays*. For simplicity, we can assume linear increase of K_h with z, as:

(6.114) $$K_h = n_h \frac{z}{D}$$

where n_h is a factor that ranges between n_h = 350 to 700 kN/m^3. Alternatively, Eq. 6.113 can be used for normally consolidated clays too, with some conservatism. The increase of undrained shear strength with depth can be introduced in Eq. 6.113, hence considering the increase of K_h along the pile length in the calculations.

Note that the above formulas for the estimation of the coefficient of subgrade reaction, as well as the typical values, apply to static, monotonic lateral loads. For dynamic loads with a low number of loading cycles (e.g., seismic loads) one should adopt a higher value of $K_{h,dynamic}$=2 to 3K_h.

According to Broms, the coefficient of subgrade reaction should be estimated as the average over a depth 0.5βL, where β is:

(6.115) $$\beta = \left(\frac{K_h D}{4 E_p I_p} \right)^{0.25}$$

where I_p is the moment of inertia of the pile's cross-section, and E_p the Young's modulus of the pile material. Given the value of K_h and factor β from Eq. 6.115, Figure 6.101 can be used to estimate the lateral deflection of free-head and fixed-head piles due to a serviceability lateral load, H_w. As discussed before, the provided coefficient of subgrade reaction modulus values, and the methodology for estimating pile displacements are valid for a working load that is one-third up to one-half the collapse lateral load of the pile, H_f.

Finally, it should be noted that free-headed piles will rotate as well as deflect upon application of a lateral load. A method for calculating pile head rotation is presented later in this Part.

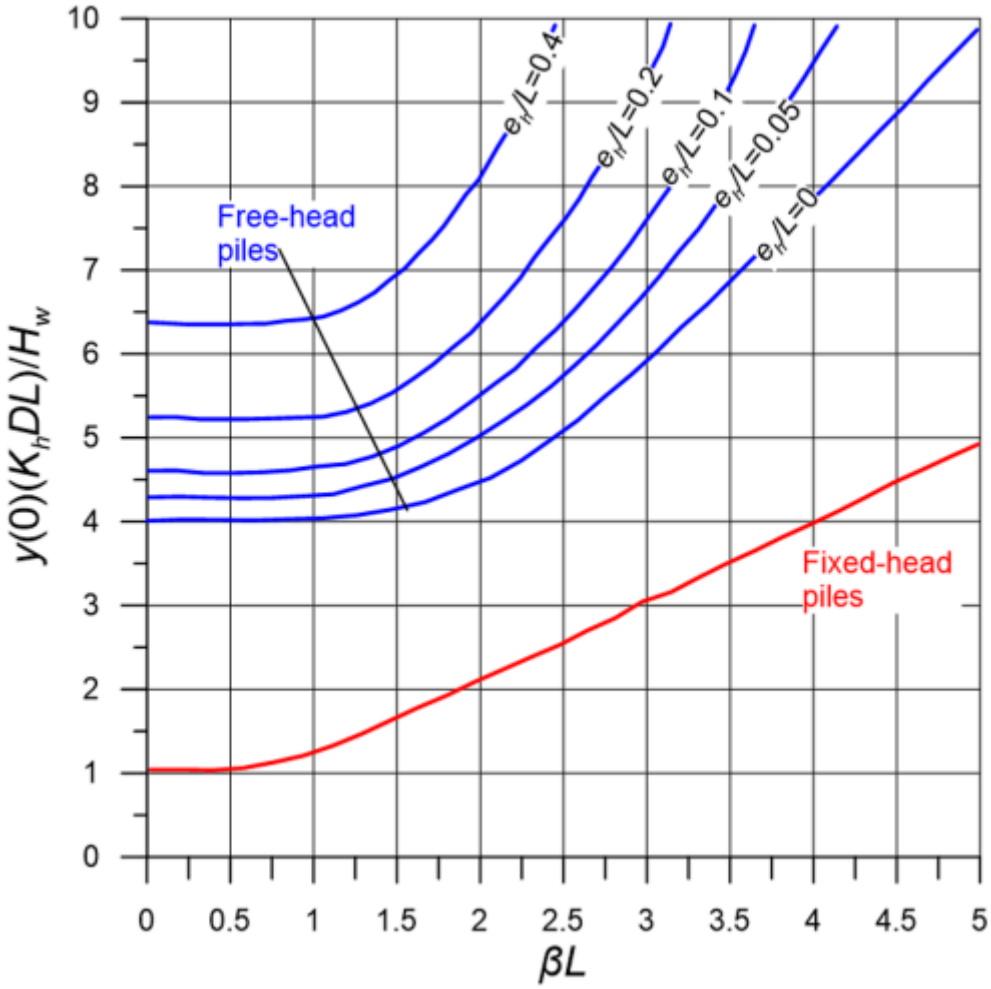

Figure 6.101. Estimation of pile head deflection $y(0)$ for piles in undrained soil.

EXAMPLE 6.12

Calculation of the ultimate geotechnical strength and of the pile head deflection of a laterally loaded pile driven in undrained soil

A steel pipe pile of external diameter D_{ext} = 0.4 m and internal diameter D_{int} = 0.39 m is driven through a layer of uniform, stiff overconsolidated clay with undrained shear strength S_u = 100 kPa. The design yield strength of the pile's steel material is σ_y = 450 MPa, and the Young's modulus of the steel material is E_p = 210 GPa. The necessary pile length to safely carry the vertical load is L = 10 m. Assuming the pile is connected with a rigid cap *(fixed-head),* determine the collapse lateral load H_f, and the deflection of the pile's head at a serviceability load equal to half the collapse lateral load $H_w = H_f/2$.

Answer:

Both *long* and *short* pile failure must be considered to determine the collapse lateral load, according also to AS2159. To do that, we must first estimate the yield moment M_y of the pile's section, which is the maximum moment that the pile's section can carry before a plastic hinge is formed. For a hollow pipe pile and homogeneous material, the plastic moment is estimated from Table 6.14 as:

$$M_y = \left(\frac{D_{ext}^3 - D_{\text{int}}^3}{6}\right)\sigma_y = \left(\frac{0.4^3 - 0.39^3}{6}\right)450000 = 351 \text{ kNm}$$

We will start by applying the short-pile equations. If the resulting maximum pile moment M_{max} is higher than the yield moment (351 kNm), the long-pile equations should be used instead, as they will result in a lower collapse load. For the case herein, the collapse lateral load considering short-pile failure is (Eq. 6.106):

$$H_f = 9S_u D_{ext}\left(L - 1.5D_{ext}\right) = 9\times 100\times 0.4\times\left(10 - 1.5\times 0.4\right) = 3384 \text{ kN}$$

and the maximum moment corresponding the ultimate lateral load (Eq. 6.107):

$$M_{\max} = 4.5S_u D_{ext}\left(L^2 - 2.25D_{ext}^2\right) = 4.5\times 100\times 0.4\times\left(10^2 - 2.25\times 0.4^2\right) = 17935 \text{ kNm} > M_y$$

It is thus clear that the pile will develop a plastic hinge before a short-pile failure mode fully develops, and the long-pile equations must be used instead. The collapse later load considering long-pile failure is given by substituting Eq. 6.104 into Eq. 6.109 as:

$$H_f = \frac{2M_y}{\left(1.5D_{ext} + 0.5\dfrac{H_f}{9S_u D_{ext}}\right)} = \frac{2\times 351}{1.5\times 0.4 + 0.5\left(\dfrac{H_f}{9\times 100\times 0.4}\right)}\$$

$$H_f = 527.03 \text{ kN}$$

However, we have to further check whether the collapse lateral load that will result while considering intermediate pile failure is not lower than 527.03 kN. Employing Eq. 6.110 and substituting f from Eq. 6.104 yields:

$$H_f = \frac{M_y + 2.25 S_u D_{ext}\left(L - 1.5D - \dfrac{H_f}{9 S_u D_{ext}}\right)^2}{\left(1.5D + 0.5\dfrac{H_f}{9 S_u D_{ext}}\right)}$$

The above equation can be solved for H_f, and results in H_f = 1333.6 kN > 527.03 kN, which means that long pile failure is critical. Indeed, if we substitute H_f in Eq. 6.111 for the bending moment that will develop at a depth $1.5D+f$:

$$M_{\max} = 2.25 S_u D_{ext}\left(L - 1.5D_{ext} - \frac{H_f}{9 S_u D_{ext}}\right)^2 = 2.25 \times 100 \times 0.4 \times \left(10 - 1.5 \times 0.4 - \frac{527.03}{9 \times 100 \times 0.4}\right)^2 = 5668\ \text{kNm} > M_y$$

which implies that two plastic hinges will be formed along the pile.

The pile head displacement for the working lateral load $H_w = H_f/2$ = 263.5 kN will be estimated while calculating the modulus of subgrade reaction according to Davidson (1972) as:

$$K_h = 67\frac{S_u}{D_{ext}} = 16750\ \text{kN/m}^3$$

In order to use Figure 6.101, we must first estimate the factor β from Eq. 6.115:

$$\beta = \left(\frac{K_h D_{ext}}{4 E_p I_p}\right)^{0.25}$$

where:

$$I_p = \pi\left(\frac{D_{ext}^4 - D_{\text{int}}^4}{64}\right) = 0.000121\ \text{m}^4$$

is the moment of inertia of the hollow pile's cross-section, and

$$\beta = \left(\frac{16750 \times 0.4}{4 \times 210 \times 10^6 \times 1.21 \times 10^{-4}}\right)^{0.25} = 0.50$$

Considering the curve for fixed-head piles of Figure 6.101 and βL = 5, we obtain:

$$y(0) = 5\left(\frac{H_w}{K_h D_{ext} L}\right) = 5\left(\frac{263.5}{16750 \times 0.4 \times 10}\right) = 0.019\text{m}$$

6.25 BROMS METHOD – PILES IN DRAINED SOIL

6.25.1 Short free-head piles

As in the case of piles in undrained soil, determination of the ultimate geotechnical strength and of the maximum bending moment developing on piles under drained loading conditions is based on static equilibrium considerations (Figure 6.102), while accounting for the rotation boundary conditions at the pile head. The ultimate soil reaction, developing at the pile toe, is calculated while assuming that the earth pressure acting on the pile is equal to three times the Rankine passive pressure. Further assuming that the ultimate soil reaction decreases linearly to zero at the ground surface, the ultimate soil reaction p_f per unit pile length at a depth z below the soil surface (units: force/length) is calculated as:

(6.116) $$p_f = 3D\gamma z K_P$$

Where:

(6.117) $$K_P = \tan^2\left(45° + \frac{\varphi'}{2}\right)$$

is Rankine's passive earth pressure coefficient, γ is the unit weight of the soil, and φ' is its friction angle. Accordingly, the collapse lateral load H_f can be either determined from Figure 6.103, or directly as:

(6.118) $$H_f = \frac{1}{2}\gamma K_P L^3 \left(\frac{D}{e+L}\right)$$

Given the collapse lateral load H_f, the maximum bending moment that will develop on the pile M_{max} is calculated as:

(6.119) $$M_{\max} = H_f\,(e_h + f) - \frac{1}{2}K_P\gamma D f^3$$

where f (units: length) defines the location where the maximum bending moment will develop along the pile:

(6.120) $$f = \left(\frac{2H_f}{3\gamma D K_P}\right)^{0.5}$$

The above formulas must be used together with the submerged unit weight of the soil, if the groundwater table level is relatively high.

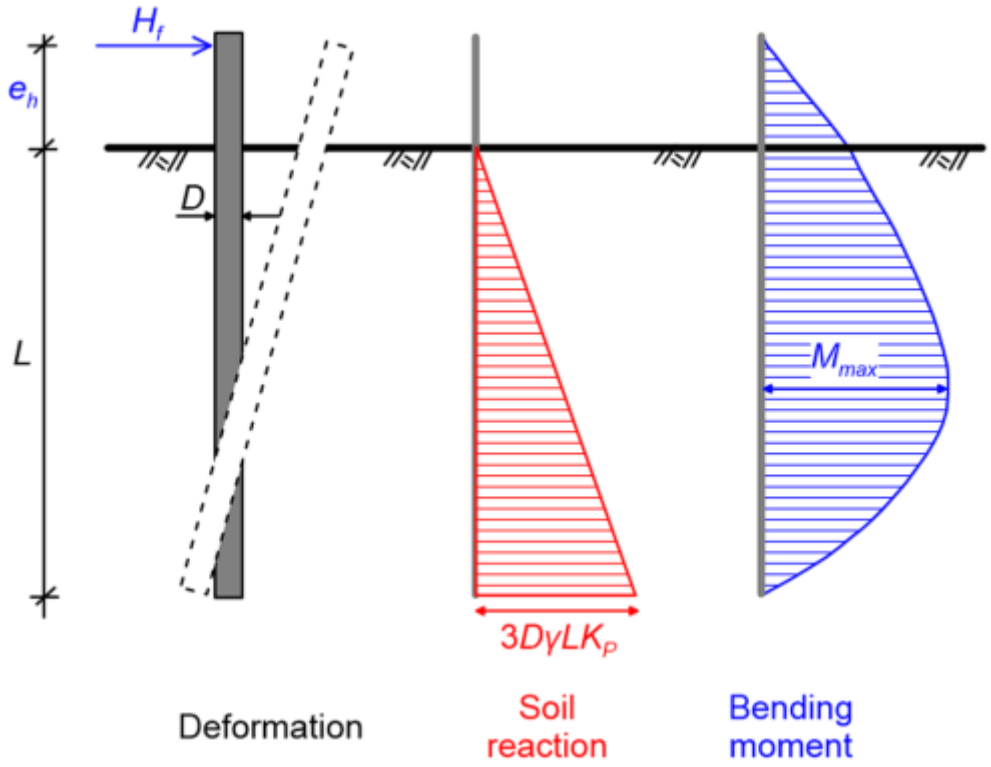

Figure 6.102. Deformation mode of a short pile unrestrained against rotation, and corresponding soil reaction and bending moment diagrams – Drained soil.

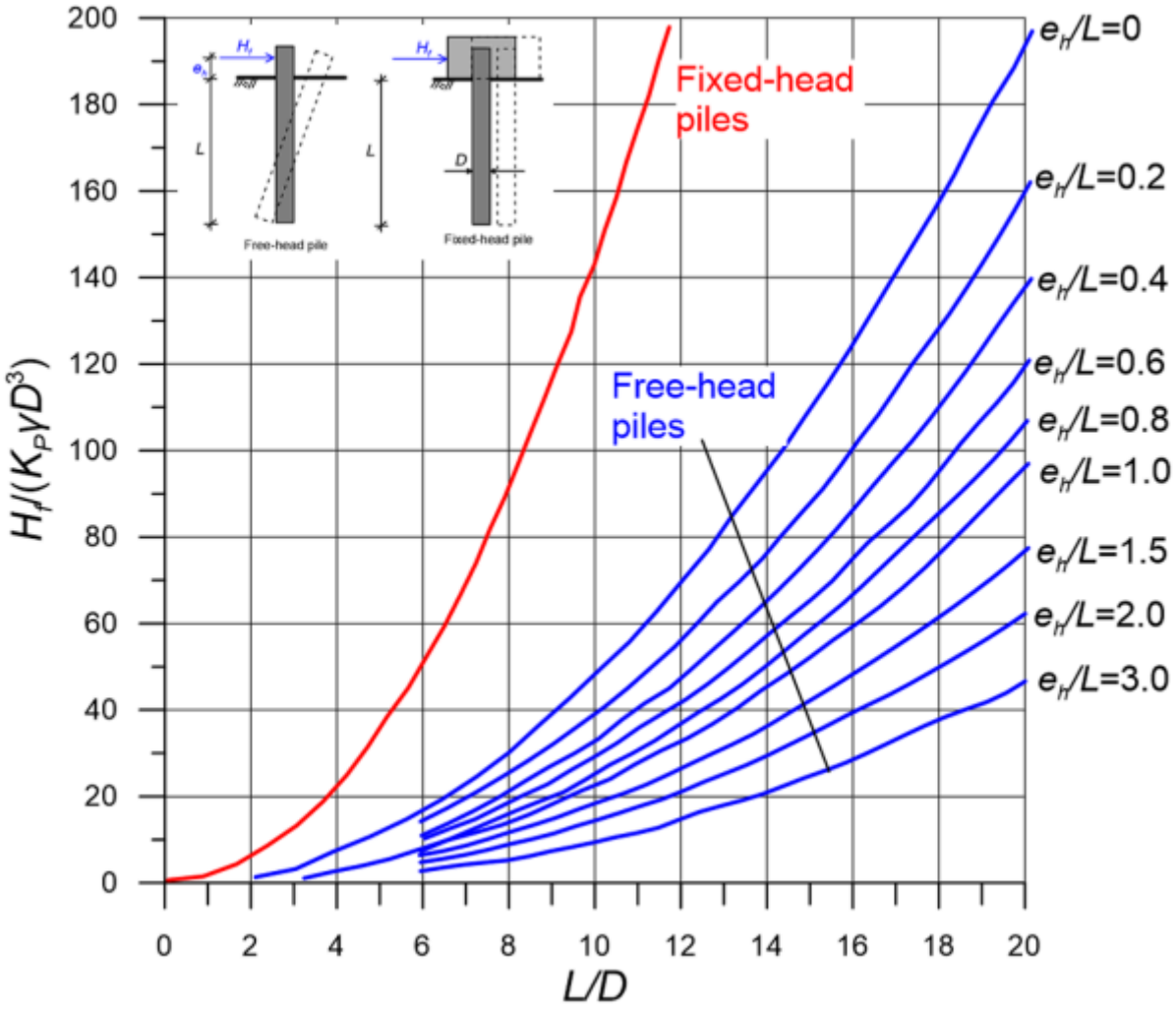

Figure 6.103. Estimation of the normalised collapse lateral load H_f of short piles in drained soil.

6.25.2 Short fixed-head piles

The same procedure is followed for fixed-head piles too, that translate as a rigid body, assuming again that the ultimate lateral reaction p_f develops at the pile toe and is calculated while assuming that the earth pressure acting on the pile equal to three times the Rankine passive pressure (Figure 6.104).

The collapse lateral load H_f can be either found using Figure 6.103, or directly via static equilibrium considerations as:

(6.121) $$H_f = \frac{3}{2}\gamma K_P L^2 D$$

The maximum bending moment M_{max} that will develop at the head of pile, at the connection with the rigid cap, is estimated with the following Eq. 6.122, using again the submerged unit weight of the soil, if applicable:

(6.122) $$M_{max} = \gamma K_P L^3 D$$

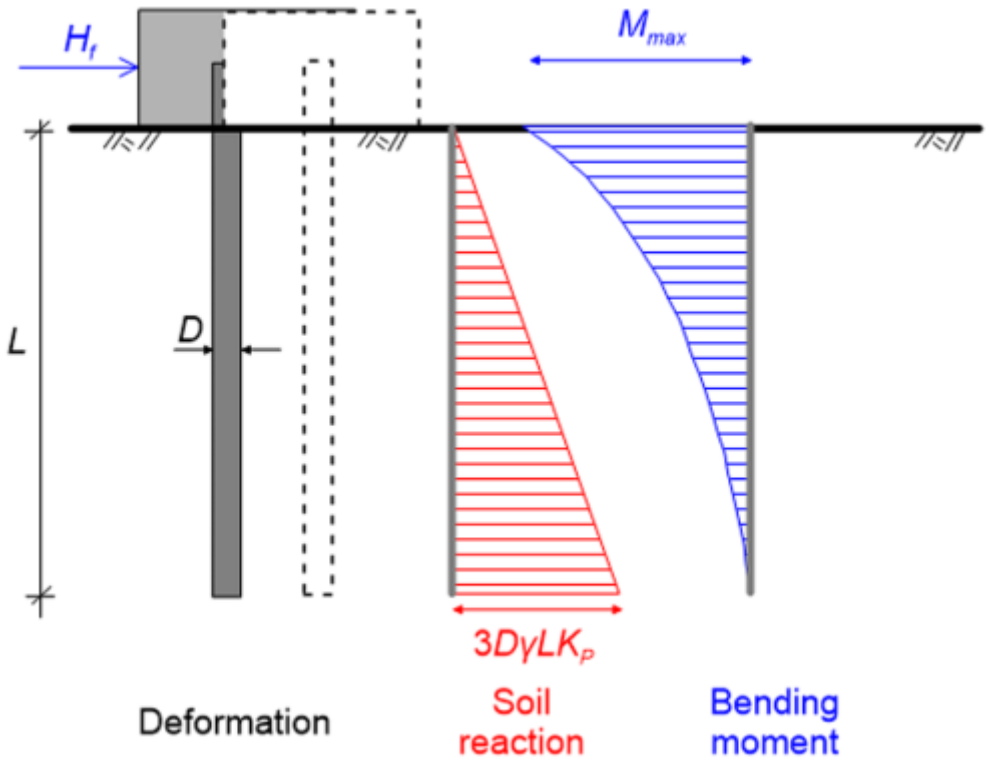

Figure 6.104. Deformation mode of a short pile restrained against rotation, and corresponding soil reaction and bending moment diagrams – Drained soil.

6.25.3 Long free-head piles

As in the case of long piles driven through undrained soil, the ultimate soil reaction that can theoretically develop along the pile length is very high. Therefore, before the ultimate soil reaction is mobilised along the entire pile length, a plastic hinge will develop at depth f given by Eq. 6.120 where the maximum bending moment becomes equal to the yield moment of the pile's section, M_y (Figure 6.105). The collapse lateral load, H_f is determined from Figure 6.106, or directly as:

(6.123) $$H_f = \frac{M_y}{e_h + 0.544\sqrt{\frac{H_f}{\gamma K_P D}}}$$

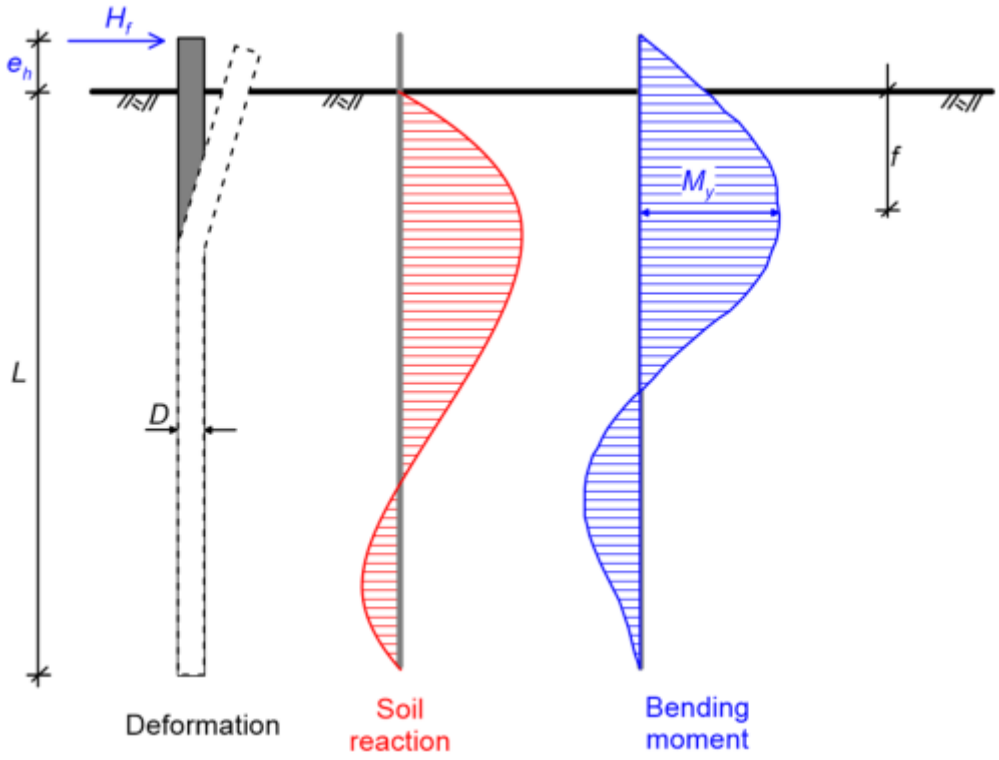

Figure 6.105. Deformation mode of a long pile unrestrained against rotation, and corresponding soil reaction and bending moment diagrams – Drained soil.

As in the case of piles in undrained soil, both the *short pile* and the *long pile* failure modes must be considered, to find the critical, minimum collapse load that the pile can carry. To determine whether the pile will fail as a *short pile* or as a *long pile* first, one should start again with the expressions in Section 6.25.1 for a short pile. If the resulting maximum bending moment is larger than the yield moment, the formulas for long pile failure must be used, as they will yield lower collapse lateral load.

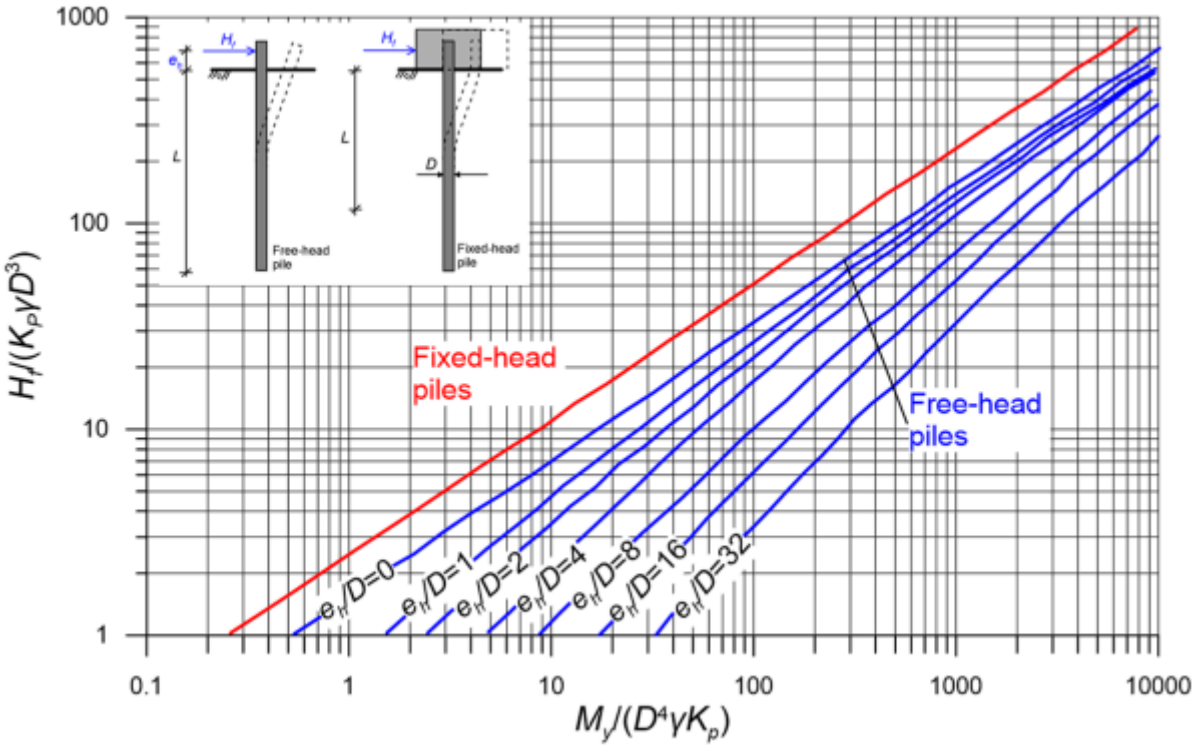

Figure 6.106. Estimation of the normalised collapse lateral load H_f of long piles in drained soil.

6.25.4 Long fixed-head piles

As for long free-head piles, the plastic (yield) bending moment, M_y will be reached before the ultimate soil reaction is mobilised along the full length of the pile. Similarly to the case of a pile driven through undrained soil, failure will occur with the formation of two plastic hinges (Figure 6.107): one at the connection of the pile with the cap, where the pile is fixed against rotation, and a second at the point where the maximum bending moment develops, at a depth f calculated from Eq. 6.120. The collapse lateral load, H_f is determined from Figure 6.106, or directly as:

(6.124) $$H_f = \frac{2M_y}{0.544\sqrt{\frac{H_f}{\gamma K_P D}}}$$

Piles of *intermediate* length will fail by developing a single plastic hinge at their head. The collapse lateral load in that case will be:

(6.125) $$H_f = \frac{M_y}{L} + \frac{1}{2}\gamma D K_P L^2$$

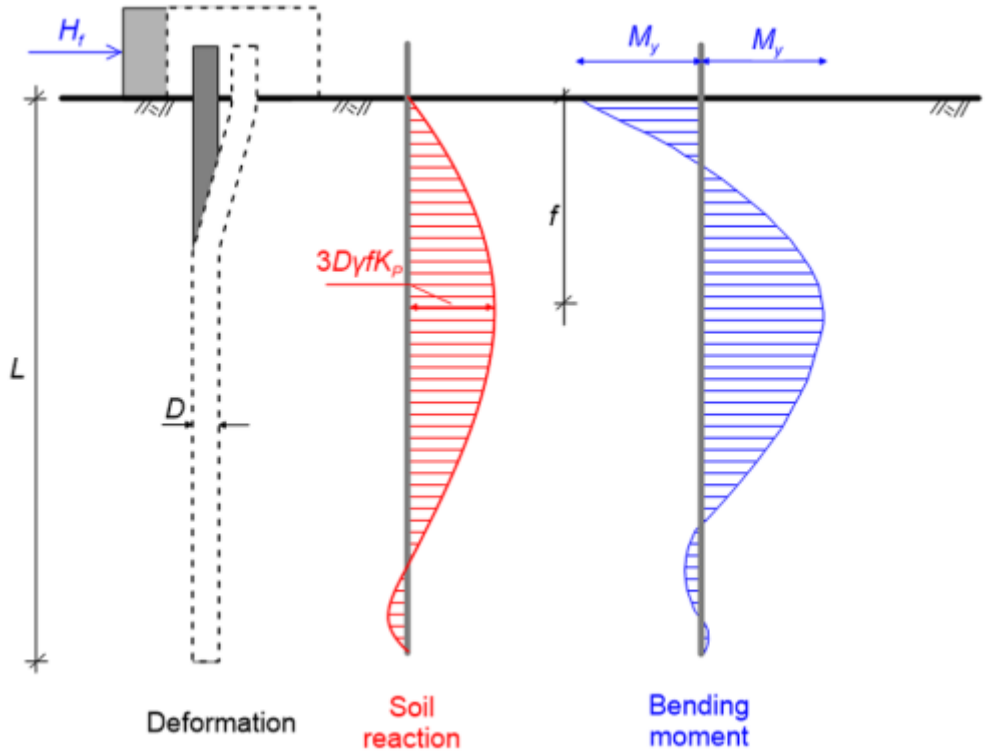

Figure 6.107. Deformation mode of a long pile restrained against rotation, and corresponding soil reaction and bending moment diagrams – Drained soil.

6.25.5 Pile lateral deflection

For the reasons explained in Section 6.24.5, calculation of the pile head deflection $y(0)$ under the serviceability load is based again on the assumption of linear elastic soil behavior. This assumption is reasonable when the working lateral load that is one-third up to one-half the collapse lateral load of the pile.

Brom's method to estimate lateral deflection of piles in drained soil requires again the estimation of a coefficient of subgrade reaction, via empirical formulas. The coefficient of subgrade reaction K_h (units: stress/unit length) of piles driven through *sands* is taken to increase linearly with depth, as in Eq. 6.114:

(6.126) $$K_h = n_h \frac{z}{D}$$

Where the factor n_h depends on the density of the sand. Some typical values of the factor n_h are presented in Table 6.16.

Table 6.16. Typical factor n_h values for sands above and below the ground water table.

	Sand relative density, D_r		
	D_r < 50%	**50% < D_r < 75%**	**D_r >75%**
n_h for dry or moist sand (kN/m^3)	1800 to 2200	5500 to 7000	15000 to18000
n_h for submerged sand (kN/m^3)	1000 to 1400	3500 to 4500	9000 to 12000

Note that these typical n_h values are applicable to static, monotonic lateral loads. For dynamic loads with a low number of loading cycles (e.g., seismic loads) one should adopt again a higher value of $K_{dynamic}$=2 to 3K_h.

Given the value of K_h, Figure 6.108 can be used to estimate the lateral deflection of free-head and fixed-head piles due to a serviceability lateral load, H_w. The term η is calculated as:

(6.127) $$\eta = \left(\frac{n_h}{E_p I_p} \right)^{0.20}$$

where I_p is the moment of inertia of the pile's cross-section, and E_p the Young's modulus of the pile material. This method provides only lateral pile head deflection, and not pile head rotation, that will develop in free-head piles.

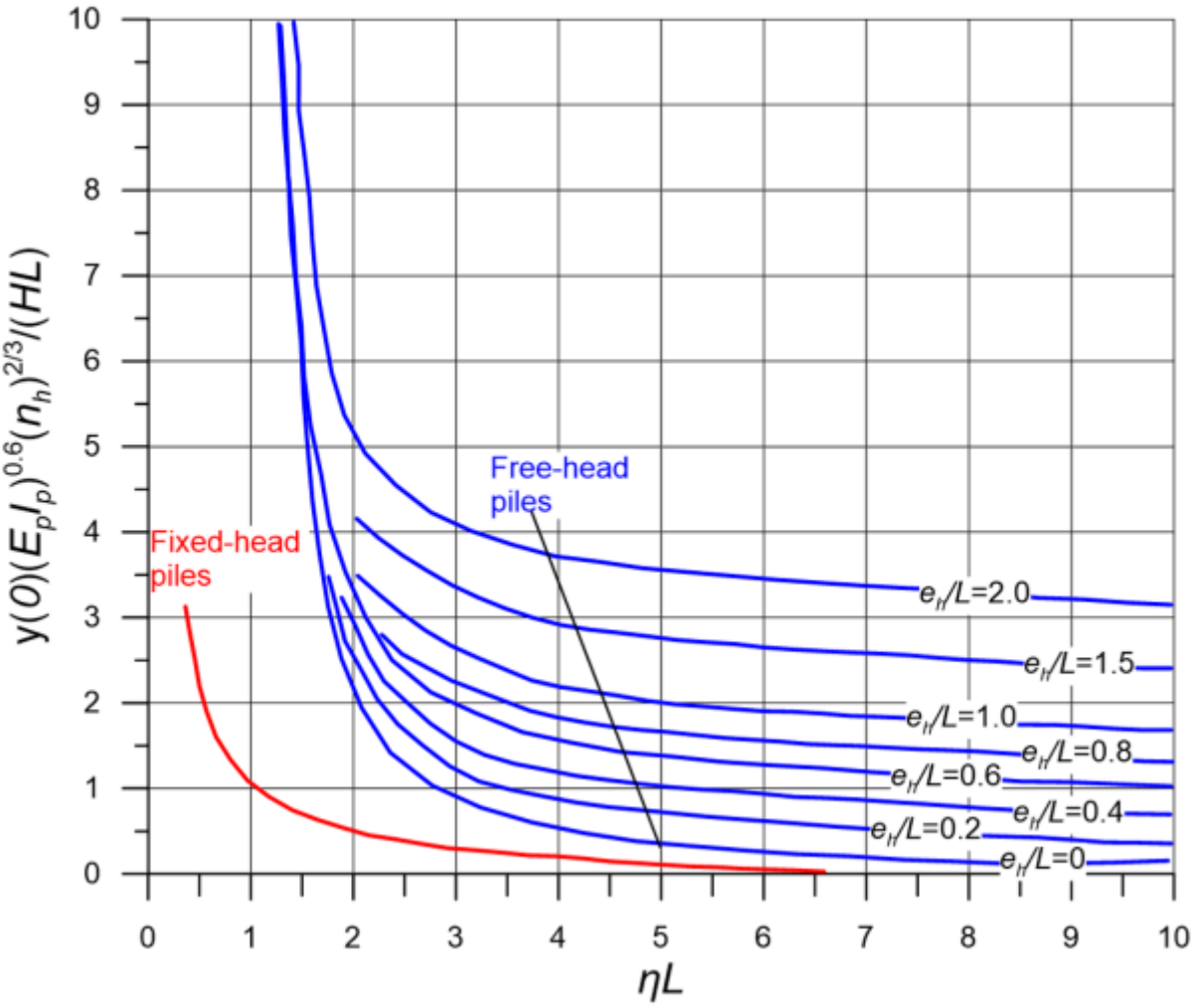

Figure 6.108. Estimation of pile head deflection $y(0)$ for piles in drained soil.

EXAMPLE 6.13

Calculation of the ultimate geotechnical strength and of the pile head deflection of a laterally loaded pile driven in drained soil

A steel pipe pile of external diameter D_{ext} = 0.4 m and internal diameter D_{int} = 0.39 m is driven through a layer of uniform, dry loose-to-medium sand with friction angle φ' = 33° and unit weight γ =18 kN/m^3. The design yield strength of the pile's steel material is σ_y = 450 MPa, and the Young's modulus of the steel material is E_p = 210 GPa. The necessary pile length to safely carry the vertical load is L = 10 m. Assuming the pile is connected with a rigid cap *(fixed-head),* determine the collapse lateral load H_f, and the deflection of the pile's head at a serviceability load equal to half the collapse lateral load $H_w = H_f/2$.

Answer:

Both *long* and *short* pile failure must be considered to determine the collapse lateral load, according to AS2159 (Example 6.12). In the previous Example 6.12, we have found that the yield moment of the pile's section to be M_y = 351 kNm.

As in the case of the pile driven in clay under undrained conditions, the solution starts by applying the short-pile equations. If the resulting maximum pile moment is higher than the yield moment, the long-pile equations are used instead. For the case herein, the collapse lateral load considering short-pile failure is (Eq. 6.121):

$$H_f = \frac{3}{2}\gamma K_P L^2 D_{ext}$$

with the Rankine passive pressure coefficient being:

$$K_P = \tan^2\left(45° + \frac{\varphi'}{2}\right) = 3.39$$

substituting:

$$H_f = \frac{3}{2}\gamma K_P L^2 D_{ext} = \tfrac{3}{2} \times 18 \times 3.39 \times 10^2 \times 0.4 = 3661.2\,\text{kN}$$

and the maximum bending moment corresponding that collapse load (Eq. 6.122) is:

$$M_{\max} = \gamma K_P L^3 D_{ext} = 18 \times 3.39 \times 10^3 \times 0.4 = 24408\,\text{kNm} > M_y$$

The pile cannot sustain the maximum bending moment that is calculated while considering short-pile failure. It will develop a plastic hinge before the lateral load reaches 3661.2 kN, and the long-pile equations must be used instead. The collapse later load considering long-pile failure is given by solving Eq. 6.124:

$$H_f = \frac{2M_y}{0.544\sqrt{\dfrac{H_f}{\gamma K_P D_{ext}}}} = \frac{2 \times 351}{0.544\sqrt{\dfrac{H_f}{18 \times 3.39 \times 0.4}}}$$

which yields H_f = 343.8 kN.

However, we have to further check whether the collapse lateral load that will result while considering intermediate pile failure from Eq. 6.125 is not lower than 343.8 kN:

$$H_f = \frac{M_y}{L} + \frac{1}{2}\gamma D_{ext} K_P L^2 = \frac{351}{10} + \frac{1}{2} \times 18 \times 0.4 \times 3.39 \times 10^2 = 1255.5 \text{ kN}$$

Thus the long pile failure mode is critical, as it results in the lower collapse lateral load.

The pile head displacement for the working lateral load $H_w = H_{ult}/2 = 171.9$ kN will be estimated while assuming the n_h factor to be $n_h = 5500$ kN/m^3 from Table 6.16 i.e., the lower bound for medium-dense dry sand.

In order to use Figure 6.108, we must first estimate the factor η from Eq. 6.127:

$$\eta = \left(\frac{n_h}{E_p I_p} \right)^{0.20}$$

where:

$$I_p = \pi \left(\frac{D_{ext}^4 - D_{\text{int}}^4}{64} \right) = 0.000121 \text{ m}^4$$

is the moment of inertia of the hollow pile's cross-section, and

$$\eta = \left(\frac{5500}{210 \times 10^6 \times 1.21 \times 10^{-4}} \right)^{0.20} = 0.736$$

Considering the curve for fixed-head piles of Figure 6.108:

we conclude that:

$$y(0) \frac{(E_p I_p)^{0.6} n_h^{\frac{2}{3}}}{HL} = 0.01 \text{ or } y(0) \approx 0$$

6.26 RIGOROUS ELASTICITY METHOD FOR ESTIMATING PILE DEFORMATIONS

As previously mentioned, Brom's method for estimating pile head deflection requires estimating the coefficient of subgrade reaction K_h by means of empirical formulas. As such, the method is inherently approximate. A rigorous method for estimating the deflection but also the rotation of the head of a single pile has recently been developed by Zheng *et al.* (2024). Their formulation is based on modelling soil as elastic Tajimi-type medium, and ignoring possible slippage or separation at the soil-pile interface, therefore is applicable mainly to serviceability conditions. Zheng *et al.*'s method allows estimating the swaying K_{hh}, rocking K_{rr} and swaying-rocking $K_{rh} = K_{hr}$ components of the head stiffness of a single floating pile embedded in elastic soil of finite thickness (Figure 6.109a).

It is reminded that the swaying stiffness K_{hh} is the lateral load H_w that, when applied to the head of a pile results in head deflection $y(0) = 1$ (Figure 6.109b). The rocking stiffness K_{rr} is the bending moment M_w that, when applied to the head of a pile results in head rotation $\omega(0) = 1$ (Figure 6.109b). The swaying-rocking stiffness K_{rh} is the bending moment that will develop to a pile with fixed head rotation $\omega(0) = 0$ when the pile is subjected to unit displacement at its head $y(0) = 1$, considering the sign convention in Figure 6.109b. The swaying-rocking stiffness K_{hr} is the lateral force that will develop to a pile with fixed head displacement $y(0) = 0$ when the pile is subjected to unit rotation at its head $\omega(0) = 1$, considering the sign convention in Figure 6.109b. Moreover, it is $K_{rh} = K_{hr}$.

Using Zheng *et al.*'s method to calculate the stiffness components allows establishing the stiffness [**K**] and compliance [**S**] matrixes of the pile, as:

(6.128a) $$\begin{bmatrix} H_w \\ M_w \end{bmatrix} = [\mathbf{K}] \begin{bmatrix} y(0) \\ \omega(0) \end{bmatrix} = \begin{bmatrix} K_{hh} & K_{hr} \\ K_{rh} & K_{rr} \end{bmatrix} \begin{bmatrix} y(0) \\ \omega(0) \end{bmatrix}$$

(6.128b) $$\begin{bmatrix} y(0) \\ \omega(0) \end{bmatrix} = [\mathbf{S}] \begin{bmatrix} H_w \\ M_w \end{bmatrix} = [\mathbf{K}]^{-1} \begin{bmatrix} H_w \\ M_w \end{bmatrix}$$

It is reminded that the stiffness and compliance matrixes are independent of the load conditions, and of any restrains imposed to pile head deflection or rotation. The charts provided in Figure 6.110 allow calculating directly the components of the stiffness matrix for soil with Poisson's ratio $\nu_s = 0.3$ and different values of the pile-soil moduli ratio E_p/E_s, the slenderness of the pile L/D and the dimensionless thickness of the foundation soil layer H/L. Having estimated these components one can calculate the compliance matrix by inverting the stiffness matrix, and subsequently the deflection $y(0)$ and the rotation $\omega(0)$ of the pile head for any load combination acting at the pile head, as well as head fixity conditions.

It is interesting to observe in Figure 6.110 that there exists a critical pile slenderness ratio L/D, beyond which pile stiffness becomes independent of the length of the pile, and the bottom part of the pile no longer contributes to its response to lateral load. Therefore one can argue that, if the top part of the soil profile of dimensionless thickness equal to the critical pile slenderness comprises uniform soil conditions, this method (but also Broms method) will provide reasonably accurate results, even when the pile is installed in layered soil. This is not limited to serviceability conditions, but can be extrapolated to the estimation of the collapse lateral load. However, the critical pile slenderness is not the same for all components of stiffness, and on top of that it varies with the pile-soil moduli ratio E_p/E_s.

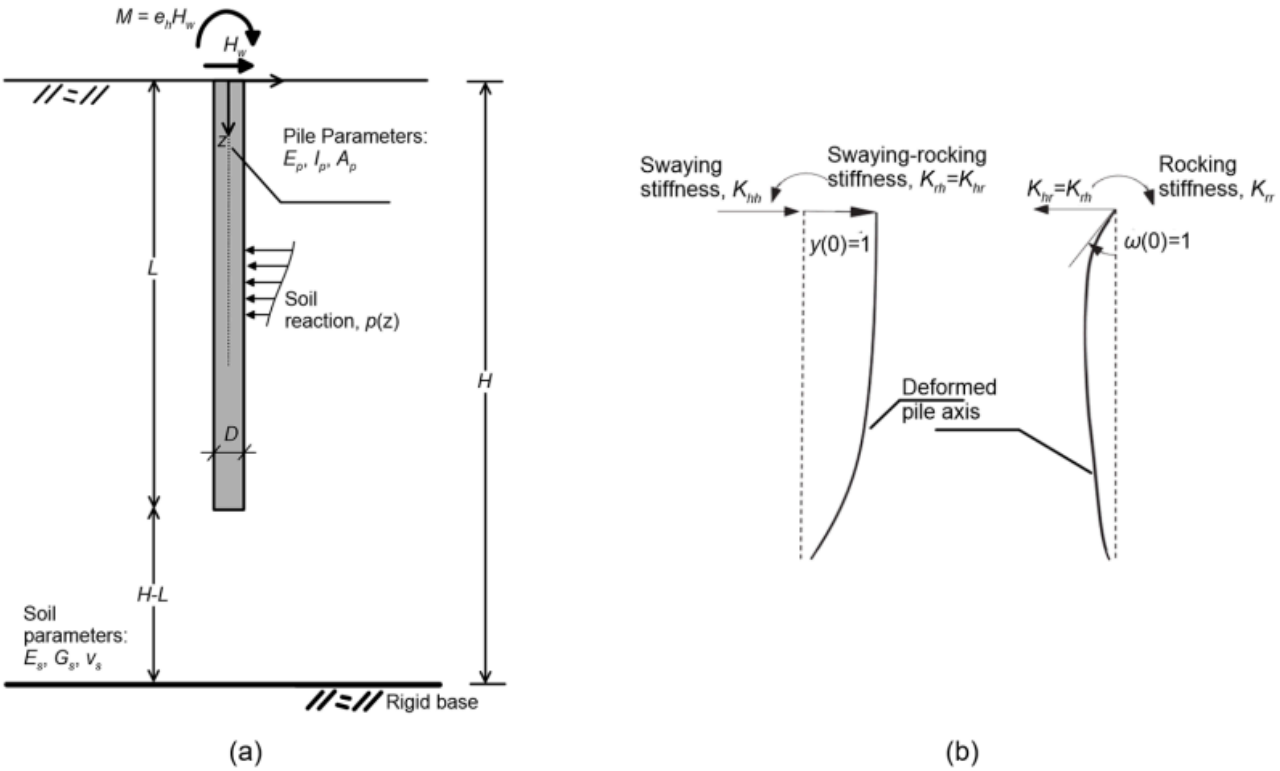

Figure 6.109. (a) Schematic of a floating pile embedded in a soil layer of finite thickness and subjected to lateral load and/or bending moment at its head; (b) Definition of the components of pile stiffness (Zheng *et al.* 2024).

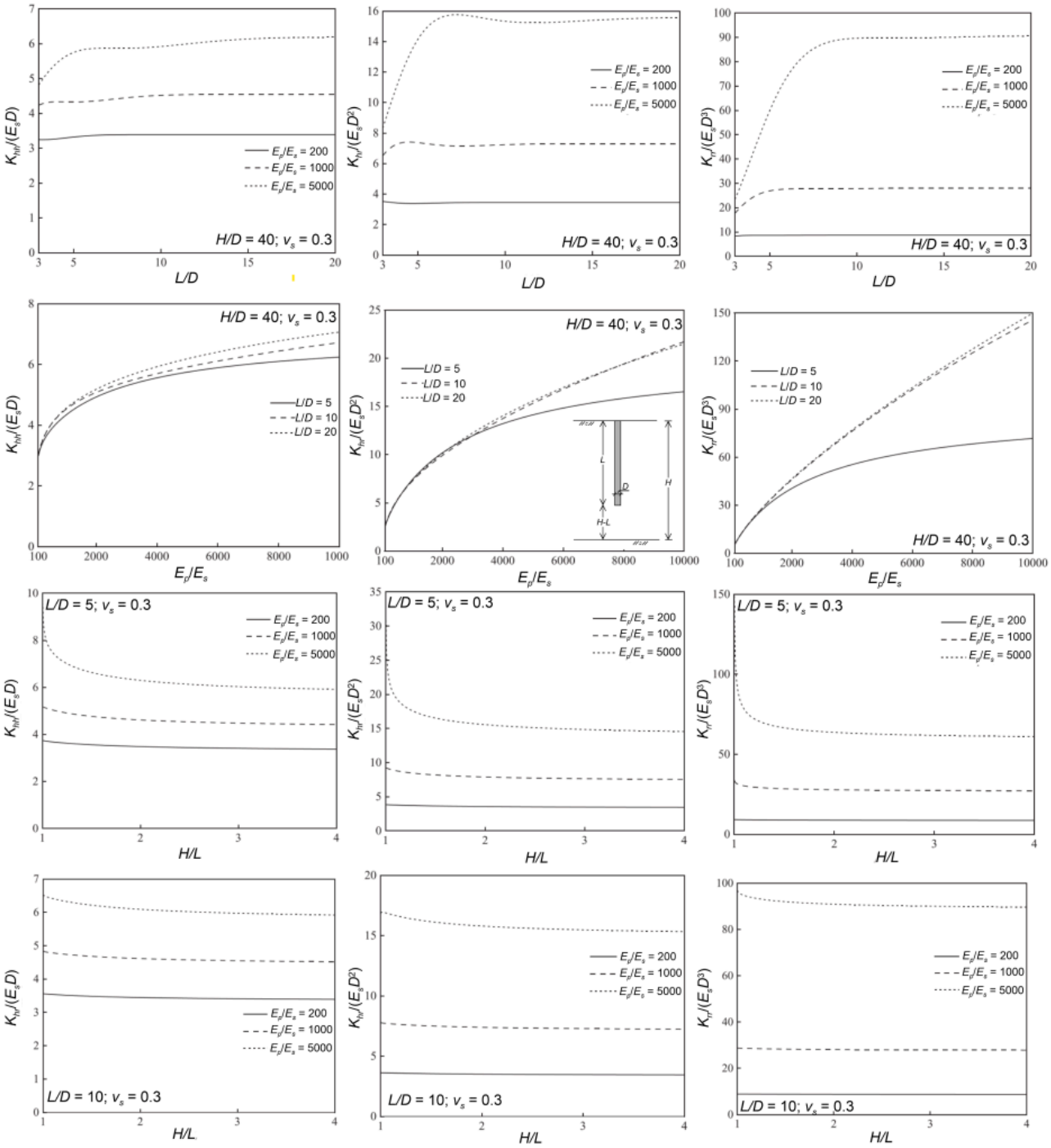

Figure 6.110. Variation of pile head stiffness components with pile-soil moduli ratio E_p/E_s, pile slenderness L/D and dimensionless thickness of the foundation soil layer H/L. Results for soil Poisson's ratio v_s = 0.3 (Results from Zheng *et al.* 2024).

EXAMPLE 6.14

Calculation of pile head deflection and rotation with the Zheng et al. (2024) method

A solid concrete pile (E_p = 20 GPa) of length L = 10 m and diameter D = 1 m is embedded in a deep H = 40 m soil layer. The Young's modulus of the soil is E_s = 20 MPa. 1) Calculate the deflection of the pile head $y(0)$ and the bending moment that will develop at the pile head M_w if the pile head is fixed against rotation ($\omega(0)$=0) and is subjected to lateral working load H_w = 200 kN. 2) Calculate the deflection of the pile head $y(0)$ and the rotation of the pile head $\omega(0)$ if the pile head is free to rotate and is subjected to lateral working load H_w = 200 kN.

Answer:

From Figure 6.110 we obtain for E_p/E_s = 1000, L/D = 10 and H/D = 40 the components of the stiffness matrix:

$$K_{hh} = 4.5E_sD = 90000\ \text{kN/m}$$

$$K_{hr} = 7.1E_sD^2 = 142000\ \text{kN}$$

$$K_{rr} = 28E_sD^3 = 560000\ \text{kNm}$$

We can now form the stiffness and compliance matrixes of the pile (Eq. 6.128):

$$\begin{bmatrix} H_w \\ M_w \end{bmatrix} = \begin{bmatrix} 90000\ \text{kN/m} & 142000\ \text{kN} \\ 142000\ \text{kN} & 560000\ \text{kNm} \end{bmatrix} \begin{bmatrix} y(0) \\ \omega(0) \end{bmatrix}$$

$$\begin{bmatrix} y(0) \\ \omega(0) \end{bmatrix} = [\mathbf{K}]^{-1} \begin{bmatrix} H_w \\ M_w \end{bmatrix} = \frac{1}{\det \mathbf{K}} \begin{bmatrix} K_{rr} & -K_{hr} \\ -K_{rh} & K_{hh} \end{bmatrix} \begin{bmatrix} H_w \\ M_w \end{bmatrix} = \frac{1}{K_{rr}K_{hh} - K_{hr}K_{rh}} \begin{bmatrix} K_{rr} & -K_{hr} \\ -K_{rh} & K_{hh} \end{bmatrix} \begin{bmatrix} H_w \\ M_w \end{bmatrix} =$$

$$= \frac{1}{30.236 \times 10^9\ \text{kN}^2} \begin{bmatrix} 560000\ \text{kNm} & -142000\ \text{kN} \\ -142000\ \text{kN} & 90000\ \text{kN/m} \end{bmatrix} \begin{bmatrix} H_w \\ M_w \end{bmatrix}$$

1. Pile head fixed against rotation ($\omega(0)$ = 0), and pile subjected to lateral working load H_w = 200 kN

Here we have two unknowns: The deflection of the pile head $y(0)$ and the bending moment that will develop on the pile head M_w. These are calculated as:

$$\begin{bmatrix} y(0) \\ 0 \end{bmatrix} = \begin{bmatrix} 18.521 \times 10^{-6}\dfrac{\text{m}}{\text{kN}} & -4.696 \times 10^{-6}\dfrac{1}{\text{kN}} \\ -4.696 \times 10^{-6}\dfrac{1}{\text{kN}} & 2.976 \times 10^{-6}\dfrac{1}{\text{kNm}} \end{bmatrix} \begin{bmatrix} 200 \\ M_w \end{bmatrix}$$

$$0 = -939.28 \times 10^{-6} + 2.976 \times 10^{-6} M_w \Rightarrow M_w = -315.5\ \text{kNm}$$

$$y(0) = 18.521 \times 10^{-6} \times 200 - 4.696 \times 10^{-6} \times (-315.5) = 5.18\ \text{mm}$$

2. Pile head free to rotate, and pile subjected to lateral working load H_w = 200 kN

Again we have two unknowns, the deflection $y(0)$ and the rotation $\omega(0)$ of the pile head. These are calculated as:

$$\begin{bmatrix} y(0) \\ \omega(0) \end{bmatrix} = \begin{bmatrix} 18.521 \times 10^{-6} \frac{\mathrm{m}}{\mathrm{kN}} & -4.696 \times 10^{-6} \frac{1}{\mathrm{kN}} \\ -4.696 \times 10^{-6} \frac{1}{\mathrm{kN}} & 2.976 \times 10^{-6} \frac{1}{\mathrm{kNm}} \end{bmatrix} \begin{bmatrix} 200 \\ 0 \end{bmatrix}$$

$$y(0) = 18.521 \times 10^{-6} \times 200 = 3.7\,\mathrm{mm}$$

$$\omega(0) = -4.696 \times 10^{-6} \times 200 = -9.39 \times 10^{-4}\mathrm{rad} = -0.0538\,\mathrm{deg}$$

6.27 NUMERICAL BEAM-ON-NONLINEAR WINKLER SPRING METHODS FOR THE ANALYSIS OF PILES SUBJECTED TO LATERAL LOADING

One important drawback of analytical methods, such as that of Broms, is the assumption of uniform soil conditions along the length of the pile. Since piles embedded in uniform soil are probably the exception rather than the rule, numerical methods are now being used extensively in practice for the analysis of piles subjected to lateral loading. Even relatively simple methods, such as the one described in the following, are not limited to uniform conditions (or to pile slenderness larger than the critical, as discussed earlier), and can account for multiple soil layers of varying thickness.

Since lateral loading of a pile is neither an axisymmetric nor a plane strain problem, two-dimensional finite element codes such as PLAXIS 2D cannot be used to model lateral loading of the soil-pile system. Instead, we use beam-on-nonlinear Winkler spring models (see Figure 6.91) where the pile is modelled as one-dimensional beam, and the soil surrounding the pile is replaced with non-linear springs, which provide the reaction on the pile p as function of its deflection y at any depth. External loads are applied on the head of the pile. While closed form solutions cannot be obtained for this problem if the $p–y$ relationship is non-linear, we can use the Finite Element Method to discretise the pile into a finite number of beam elements, and attach spring elements at the beam elements' nodes. Multilayered soil profiles can model in this way, by considering different $p–y$ relationships for different spring elements. Various commercial codes based on this concept are available in the market, and referring in detail to them is not within the scope of this chapter.

Pivotal to the successful analysis of piles with this method is the selection of appropriate $p–y$ relationships or curves, representative of the soil conditions, of the pile's geometry and of the type of loading, and the use of realistic input parameters for these expressions. A collection of widely-used mathematical expressions that provide $p–y$ relationships for different soil conditions is presented in the following sections, in the form of step-by-step workflows. Note that the presentation is limited to curves applicable to static, monotonic loading. For cyclic loads featuring a significant number of loading cycles, as the case of offshore platforms subjected to wave loads, the interested reader may refer to Reese and van Impe (2001).

6.27.1 *p-y* curves for piles embedded in soft clay, in the presence of free water

Step 1:

Estimate the undrained shear strength of the clay S_u, and the characteristic strain ε_{50}, which is the strain that develops in a clay sample during an undrained triaxial compression test when the deviatoric stress q on the sample becomes equal to $q = \sigma_1 – \sigma_3 = S_u$ i.e., is half the deviatoric stress at failure (Figure 6.111). If triaxial laboratory tests are not available e.g., when S_u is estimated from *in situ* tests, one can use the typical values listed in Table 6.17. Keep in mind that overconsolidated clays exhibit more brittle behaviour, and will fail at lower strain levels.

Table 6.17. Typical ε_{50} values for soft-to-hard clays (after Peck *et al.* 1974).

Clay consistency	Undrained shear strength	ε_{50}
Soft-to-firm	$S_u < 50$ kPa	0.020
Firm-to-stiff	$50 < S_u < 100$ kPa	0.010 to 0.007
Stiff-to-hard	$100 < S_u < 200$ kPa	0.007 to 0.005
Hard-to-very hard	$200 < S_u < 400$ kPa	0.004

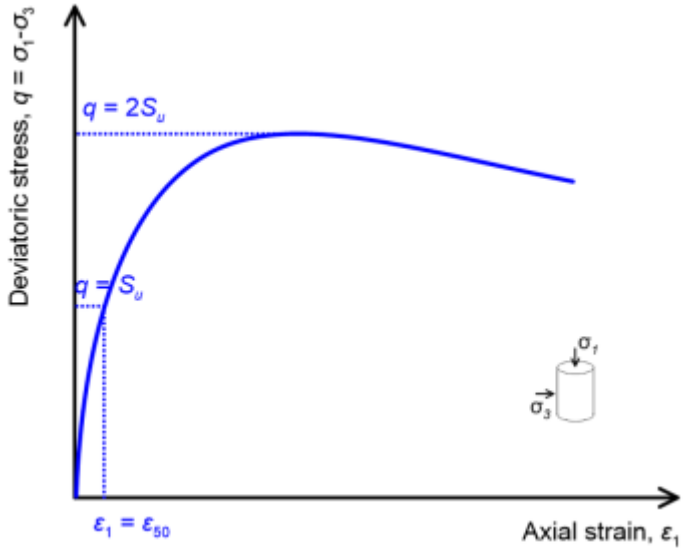

Figure 6.111. Definition of the characteristic strain ε_{50}.

Step 2:

Compute the ultimate soil reaction per unit length of the pile as the minimum of two values:

(6.129) $$p_f = \min \left\{ \begin{array}{c} \left(3 + \dfrac{\gamma'}{S_u} z + \dfrac{J}{D} z\right) S_u D \\ 9 S_u D \end{array} \right\}$$

where $\gamma' = \gamma - \gamma_w$ is the average submerged unit weight from the ground surface to the depth z where the p-y curve is estimated; $J = 0.5$ for soft clays or $J = 0.25$ for medium-to-firm clays (Matlock, 1970). The second term of Eq. 6.129 corresponds to the ultimate soil reaction developing on a smooth rigid pile in undrained perfectly-plastic soil, mentioned earlier in Chapter 6.24.

Step 3:

Compute the deflection of the pile y_{50} at one-half the ultimate soil reaction $p = 0.5 p_f$:

(6.130) $$y_{50} = 2.5 \varepsilon_{50} D$$

Step 4:

All the input parameters of the p-y curve have now been determined:

(6.131a) $p = 0.5 p_f \left(\frac{y}{y_{50}} \right)^{\frac{1}{3}}$ for $y < 8 y_{50}$

(6.131b) $p = p_f$ for $y \geq 8 y_{50}$

The shape of the *p*–*y* curve is depicted in Figure 6.112.

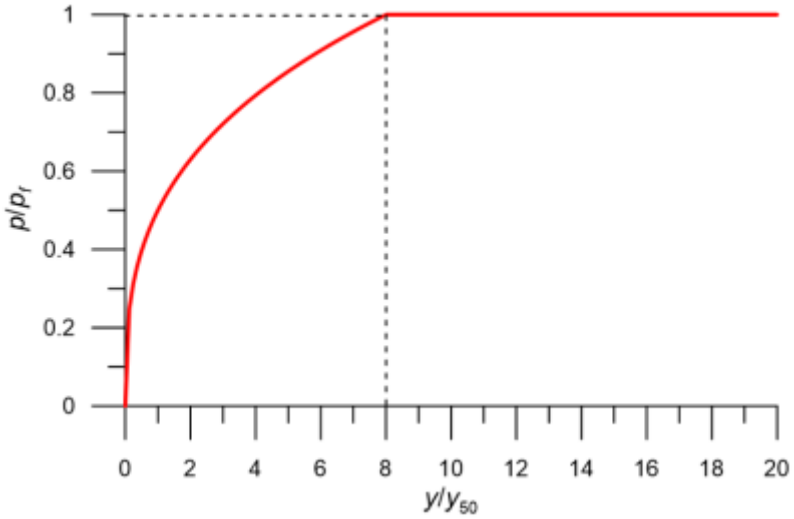

Figure 6.112. Shape of static *p*-*y* for a pile embedded in soft clay, in the presence of free water according to Matlock (1970).

For example, consider a 15-m long pile with diameter $D = 0.5$ m, driven in soft clay with undrained shear strength increasing with depth, z as $S_u = 20+z$ (kPa). The submerged unit weight of the clay is taken equal to $\gamma' = 6$ kN/m^3, and it is further assumed that $J = 0.5$ and $\varepsilon_{50} = 0.02$. Substituting in Eqs. 6.129 and 6.130 yields:

(6.132) $$p_f = \min \left\{ \begin{array}{c} \left(3 + \frac{6}{20+z} z + \frac{0.5}{0.5} z \right) (20+z)\, 0.5 \\ 9\,(20+z)\, 0.5 \end{array} \right\} \frac{\text{kN}}{\text{m}}$$

and

(6.133) $y_{50} = 2.5 \varepsilon_{50} D = 0.025$ m

Variation of the ultimate soil reaction per unit length of the pile with depth z is given in Eq. 6.132. Indicatively, for $z = 0$:

(6.134) $$p_f = \min \left\{ \begin{array}{c} 30 \\ 90 \end{array} \right\} \frac{\text{kN}}{\text{m}}$$

and the *p*-*y* curve is described by the function:

(6.135a) $p = 15 \left(\frac{y}{0.025} \right)^{\frac{1}{3}} \frac{\text{kN}}{\text{m}}$ for $y < 0.2$m

(6.135b) $p = 30 \frac{\text{kN}}{\text{m}}$ for $y \geq 8 y_{50}$

p-y curves for different depths along the length of the pile are illustrated in Figure 6.113. Notice that the ultimate soil reaction p_f increases with depth, but not the lateral pile movement necessary to mobilise it, as the latter depends only on the characteristic strain ε_{50} and on the pile's diameter.

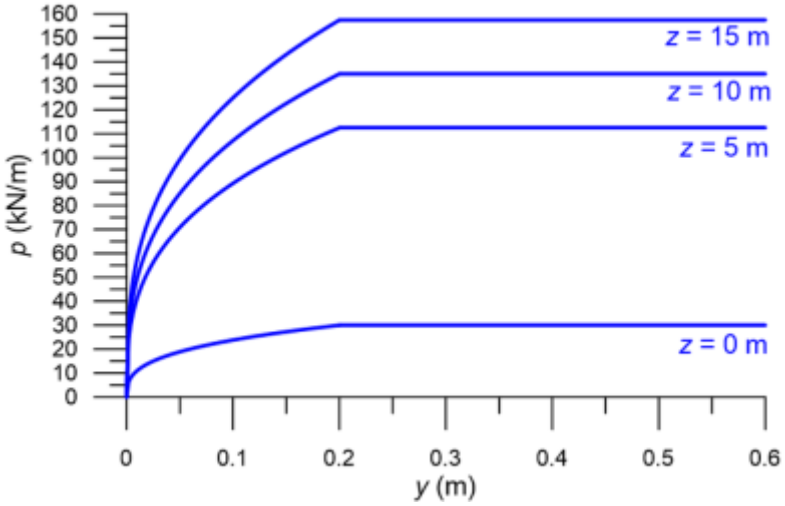

Figure 6.113. Indicative *p-y* curves along a 15-m pile embedded in soft clay in the presence of free water.

6.27.2 *p-y* curves for piles embedded in stiff clay, in the presence of free water

Step 1:

Estimate the undrained shear strength of the clay layer S_u at the depth z (measured from the soil surface) where the curve is determined, and the average undrained shear strength over the depth z, $S_{u,aver}$.

Step 2:

Compute the ultimate soil reaction per unit length of the pile as the minimum of two values:

$$\textbf{(6.136)}\ p_f = \min \left\{ \begin{array}{c} 2S_{u,aver}D + \gamma' Dz + 2.83 S_{u,aver} Dz \\ 11 S_u D \end{array} \right\}$$

where γ' is the average submerged unit weight from the ground surface to the depth z, defined above. The second term of Eq. 6.136 corresponds to the ultimate soil reaction developing on a rough rigid pile in undrained perfectly-plastic soil, as discussed earlier.

Step 3:

Estimate the factor A_s from the expressions presented in Figure 6.114, as function of z where the curve is determined. The provided expressions are for static, monotonic loads.

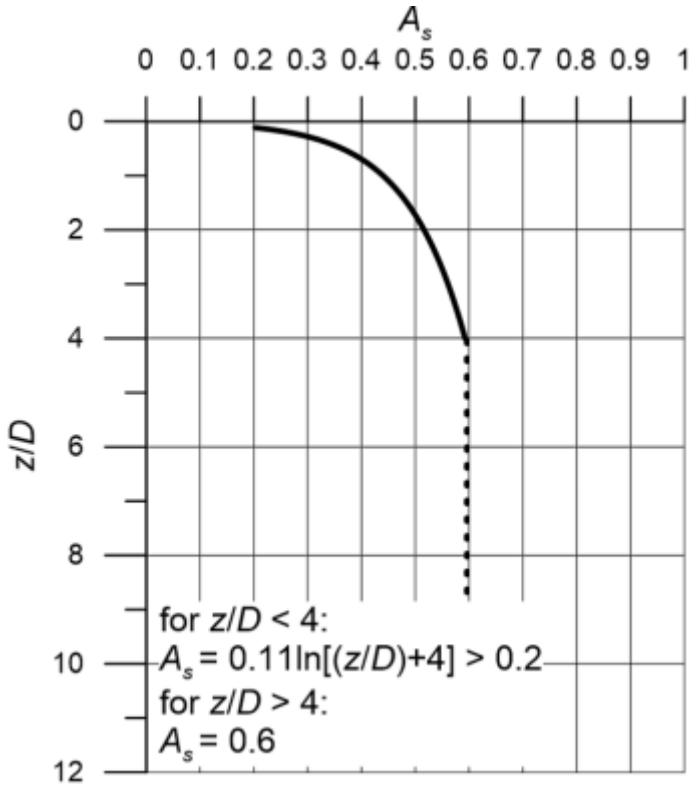

Figure 6.114. Variation of factor A_S with normalised depth *z/D*; Piles in clay.

Step 4:

Establish the initial straight-line part of the *p-y* curve, referred to as *linear (1)* in Figure 6.115:

(6.137) $p = k_s z y$

The inclination of its slope k_s is provided in the Table 6.18 below.

Table 6.18. Slope of the initial straight line part of the *p-y* curve for piles embedded in stiff, clay under the presence of free water (Reese and van Impe 2001).

Average undrained shear strength to depth *z* where the *p–y* curve is estimated	**k_s (static, kN/m^3)**
S_u = 50 to 100 kPa	135000
S_u = 100 to 200 kPa	270000
S_u = 300 to 400 kPa	540000

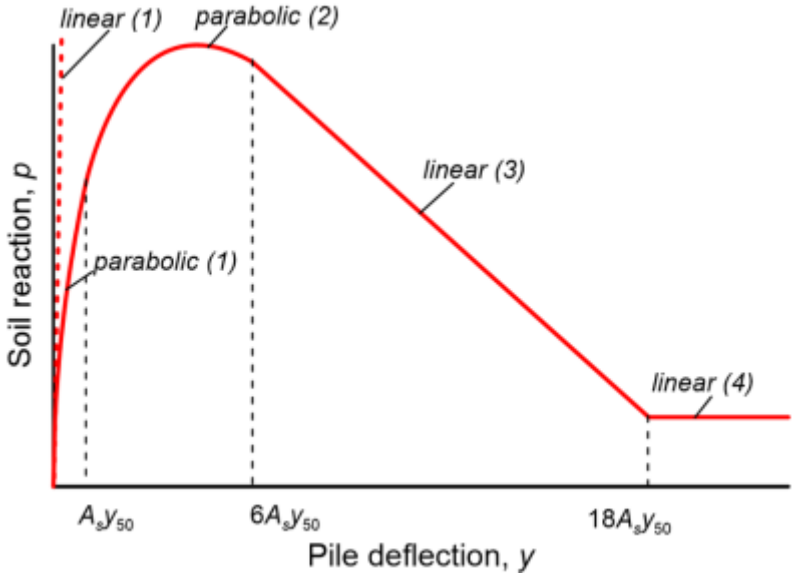

Figure 6.115. Segments of static *p-y* curve for a pile embedded in stiff clay, in the presence of free water. Monotonic static load case (after Reese et al. 1975).

Step 5:

Compute $y_{50}=\varepsilon_{50}D$. In the absence of undrained triaxial compression laboratory tests, one may use the typical values of ε_{50} provided in Table 6.17 above.

Step 6:

Establish the first parabolic part of the *p-y* curve, named *parabolic(1)* in Figure 6.115, using the following Eq. 6.138. It defines the part of the parabolic curve from the intersection with the initial straight line up to a pile lateral deflection equal to $A_s y_{50}$.

(6.138) $$p = 0.5 p_f \left(\frac{y}{y_{50}} \right)^{0.5} \text{ for } y < A_s y_{50}$$

Step 7:

Establish the second parabolic part of the *p-y* curve, named *parabolic(2)* in Figure 6.115, using Eq. 6.139. It defines the part of the *p-y* curve from $A_s y_{50}$ up to pile deflection $6A_s y_{50}$.

(6.139) $$p = 0.5 p_f \left(\frac{y}{y_{50}} \right)^{0.5} - 0.055 p_f \left(\frac{y - A_s y_{50}}{A_s y_{50}} \right)^{1.25} \text{ for } A_s y_{50} < y < 6A_s y_{50}$$

Step 8:

Establish the next linear part of the *p-y* curve, named *linear(3)* in Figure 6.115, according to Eq. 6.140. It defines the softening part of the *p-y* curve from $6A_s y_{50}$ up to pile deflection $18A_s y_{50}$.

(6.140) $$p = 0.5 p_f (6A_s)^{0.5} - 0.411 p_f - \frac{0.0625}{y_{50}} p_f \left(y - 6A_s y_{50} \right) \text{ for } 6A_s y_{50} < y < 18A_s y_{50}$$

Step 9:

Establish the final linear part of the *p-y* curve, named *linear(4)* in Figure 6.115, using Eq. 6.141. This segment corresponds to the residual soil reaction, at large relative soil-pile displacements.

(6.141) $$p = 0.5p_f(6A_s)^{0.5} - 0.411p_f - 0.75p_f A_s \text{ for } 18A_s y_{50} < y$$

In many practical cases we can ignore the initial linear part of the curve, as intersection of *linear(1)* with the *parabolic(1)* part takes place at very small pile deflection (of the order of 1 mm). This would be the case for a 15-m long pile with diameter D = 0.5 m, driven in stiff clay with assumed constant undrained shear strength S_u = 100 kPa and submerged unit weight γ' = 6 kN/m^3. The ultimate soil reaction per unit pile length can be estimated as:

(6.142) $$p_f = \min \left\{ \begin{array}{c} 100 + 6z + 283z \\ 550 \end{array} \right\} \frac{\text{kN}}{\text{m}}$$

whereas the factor A_s is calculated from the formulas depicted in Figure 6.114:

(6.143a) $$A_s = 0.11 \ln \left[\frac{z}{0.5} + 1 \right] > 0.2 \text{ for } z < 2\text{m}$$

(6.143b) $$A_s = 0.6 \text{ for } z > 2\text{m}$$

where z is the depth from the ground surface. From Table 6.17 for undrained shear strength of clay S_u = 100 kPa we obtain a characteristic strain $\varepsilon_{50} \approx 0.007$ therefore $y_{50} = \varepsilon_{50} D$ = 0.003 m.

The expressions providing the distinct parts of the *p-y* curve are presented in Table 6.19.

Table 6.19. Expressions defining the *p-y* curves for a 15-m long pile embedded in stiff clay in the presence of free water, for *z* > 2m.

Lateral pile deflection, y (m)	Soil reaction, p (kN/m)
$0 < y < 0.003A_s$	$0.5p_f \left(\frac{y}{0.003} \right)^{0.5}$
$0.003A_s < y < 0.018A_s$	$0.5p_f \left(\frac{y}{0.003} \right)^{0.5} - 0.055p_f \left(\frac{y - 0.003A_s}{0.003A_s} \right)^{1.25}$
$0.018A_s < y < 0.054A_s$	$0.5p_f(6A_s)^{0.5} - 0.411p_f - 20.83p_f\,(y - 0.018A_s)$
$y > 0.054A_s$	$p = 0.5p_f(6A_s)^{0.5} - 0.411p_f - 0.75p_f A_s$
For z > 2 m it is p_f = 550 kN/m and A_s = 0.6	

Notice from Eqs. 6.142 and 6.143 that in this particular case, both the factor A_s and the ultimate soil resistance do not change for the part of the pile embedded deeper than 2 m, thus the *p-y* response of the pile for z > 2 m will remain unaltered if the variation of the undrained soil strength with depth is not considered (Figure 6.116). Observe also in Figure 6.116 that the maximum soil reaction acting on the pile is not equal to p_f calculated from Eq. 6.136 (see also Eq. 6.139).

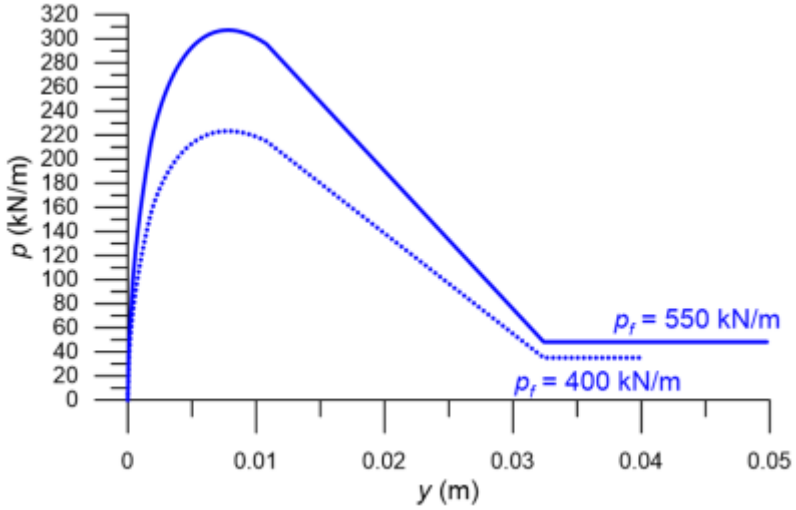

Figure 6.116. Indicative *p-y* curve for a 15-m pile embedded in stiff clay in the presence of free water, for $z > 2$m. The two curves correspond to different p_f values calculated from Eq. 6.136.

6.27.3 *p-y* curves for piles embedded in stiff clay, when no free water is present

Step 1:

Estimate the undrained shear strength of the clay S_u, and the characteristic strain ε_{50} from laboratory undrained triaxial compression tests. If such tests are not available, ε_{50} may be estimated from Table 6.17. Keep in mind that higher ε_{50} values will result in more conservative predictions of pile response to lateral loads.

Step 2:

Compute the ultimate soil resistance per unit length of the pile as the minimum of two values:

(6.144) $$p_f = \min \left\{ \begin{array}{c} \left(3 + \dfrac{\gamma}{S_u} z + \dfrac{J}{D} z\right) S_u D \\ 9 S_u D \end{array} \right\}$$

where the factor J takes values $J = 0.5$ for soft clays and $J = 0.25$ for medium-to-firm clays.

Step 3:

Compute the deflection y_{50} at one-half the ultimate soil reaction $p = 0.5p_f$:

(6.145) $$y_{50} = 2.5 \varepsilon_{50} D$$

Step 4:

All the input parameters of the *p-y* curve have now been determined:

(6.146a) $p = 0.5 p_f \left(\frac{y}{y_{50}} \right)^{0.25}$ for $y < 16 y_{50}$

(6.146b) $p = p_f$ for $y \geq 16 y_{50}$

The shape of the p-y curve is depicted in Figure 6.117.

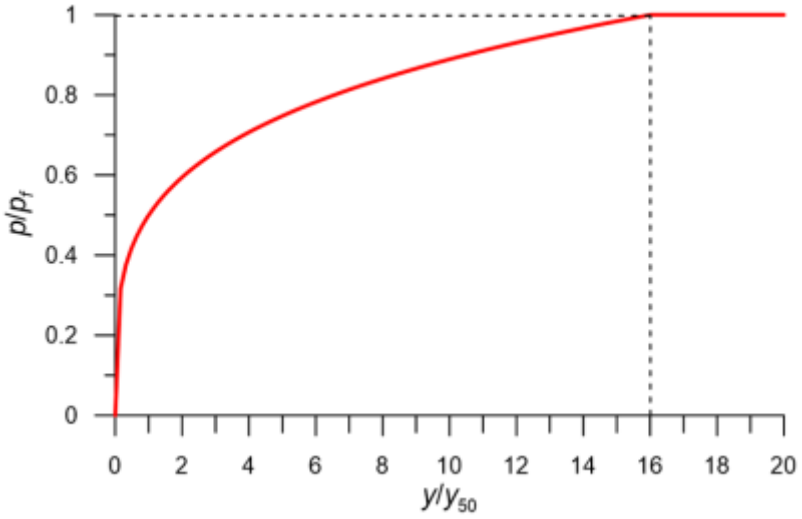

Figure 6.117. Shape of static *p-y* for a pile embedded in stiff clay, when no free water is present (after Reese *et al.* 1975).

For example, consider a 15-m long pile with diameter D = 0.5 m, driven in stiff clay with undrained shear strength S_u = 100 kPa and saturated unit weight γ_{sat} = 16 kN/m^3. Assuming J = 0.5 and ε_{50} = 0.007, Eq. 6.144 yields:

(6.147) $p_f = \min \left\{ \begin{array}{c} \left(3 + \frac{16}{100} z + \frac{0.5}{0.5} z \right) 100 \times 0.5 = 150 + 58 z \\ 9 \times 100 \times 0.5 = 450 \end{array} \right\} \frac{\text{kN}}{\text{m}}$

Further, substituting in Eq. 6.145:

(6.148) $y_{50} = 2.5 \varepsilon_{50} D = 0.0087 \text{ m}$

Notice from Eq. 6.147 that the ultimate soil resistance increases up to a depth z = 5.17 m, and remains constant for the part of the pile embedded in larger depths. For shallower depths, the variation of the ultimate soil resistance per unit length of the pile with depth z is given in Eq. 6.147. Indicatively, for z = 0:

(6.149) $p_f = \min \left\{ \begin{array}{c} 150 \\ 450 \end{array} \right\} \frac{\text{kN}}{\text{m}}$

and the *p-y* curve at z = 0 is described by the function:

(6.150a) $p = 75 \left(\frac{y}{0.0087} \right)^{0.25} \frac{\text{kN}}{\text{m}}$ for $y < 0.14 \text{ m}$

(6.150b) $p = 150 \frac{\text{kN}}{\text{m}}$ for $y \geq 0.14 \text{ m}$

p-y curves along the length of the pile are illustrated in Figure 6.118:

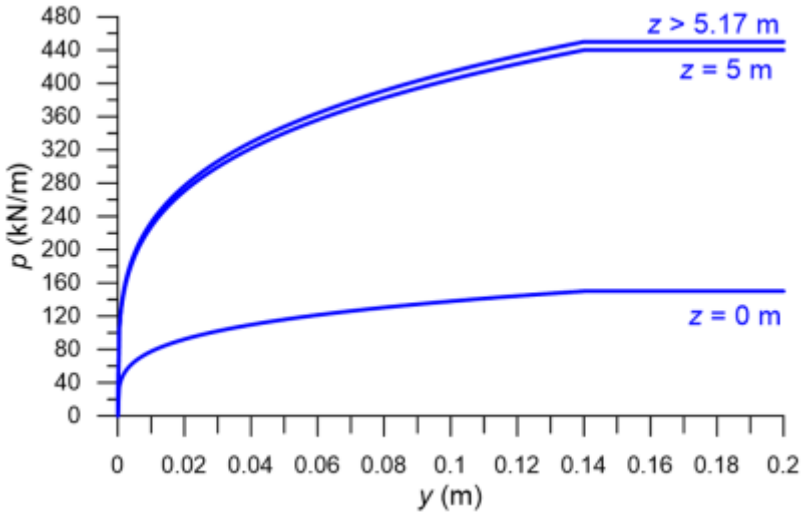

Figure 6.118. Indicative *p-y* curves along a 15-m pile embedded in stiff clay when no free water is present.

6.27.4 *p-y* curves for a pile in sand above and below the water table

Step 1:

Determine the friction angle, φ' of the sand, and its unit weight γ. Consider the submerged unit weight γ' for sands below the water table ($\gamma' = \gamma - \gamma_w$), and the bulk unit weight γ for sands above the water table.

Step 2:

Compute the ultimate soil reaction per unit length of the pile as the minimum of two values:

(6.151)

$$p_f = \min \left\{ \begin{array}{c} (\gamma z)\left[\dfrac{K_0 z \tan\varphi' \sin\beta}{\tan(\beta-\varphi')\cos\alpha} + \dfrac{\tan\beta}{\tan(\beta-\varphi')}(D + z\tan\beta\tan\alpha) + K_0 z \tan\beta(\tan\varphi'\sin\beta - \tan\alpha) - K_a D\right] \\ (D\gamma z)\left[K_a\left[(\tan^8\beta) - 1\right] + K_0 \tan\varphi' \tan^4\beta\right] \end{array} \right\}$$

Where $\alpha = \varphi'/2$; $\beta = 45^0 + \varphi'/2$; K_0 is the earth pressure coefficient at-rest recommended to be taken equal to $K_0 = 0.6$ for loose sand and $K_0 = 0.4$ for dense sand; K_A = active earth pressure coefficient $K_A = \tan^2(45^0 - \varphi'/2)$.

Step 3:

Use Figure 6.119a and the provided formulas to estimate the value of the factor A_s as function of depth measured from the soil surface z, and subsequently estimate the soil reaction developing when pile deflection reaches $y_1 = 3D/80$ as:

(6.152) $p_1 = A_s p_f$

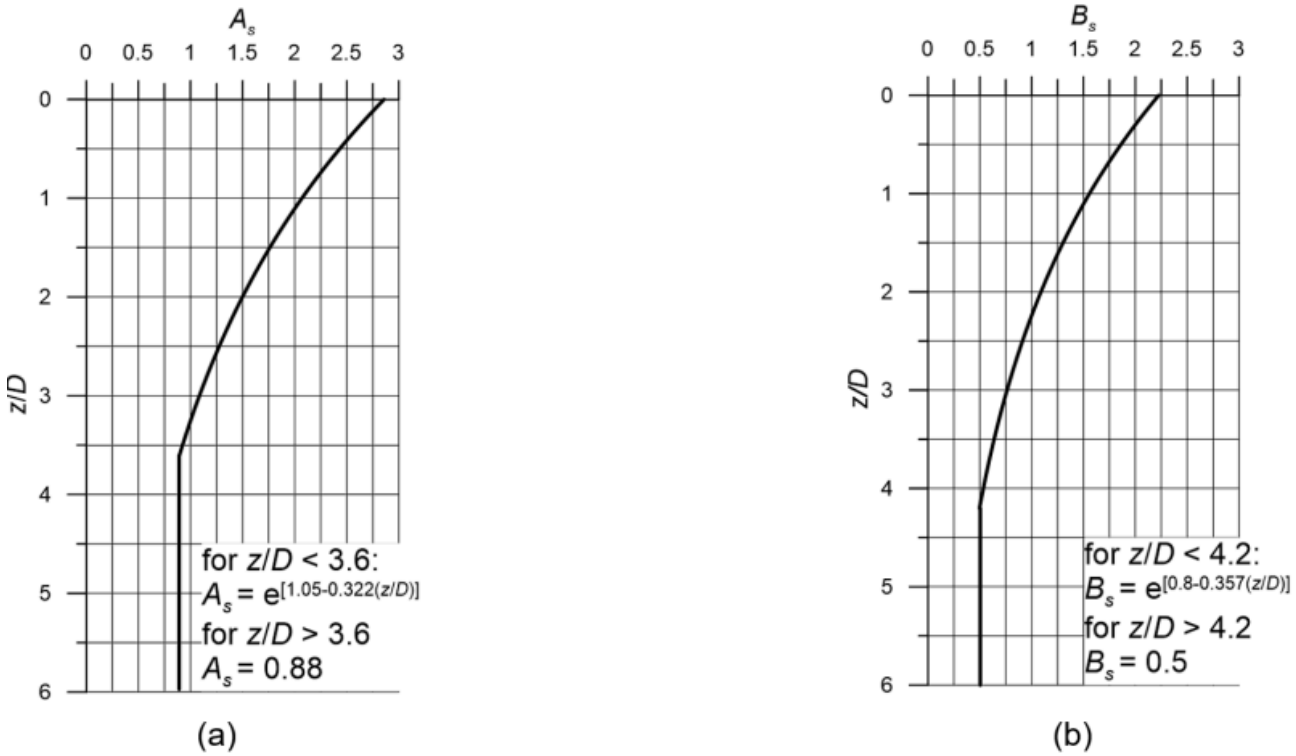

Figure 6.119. Variation of factors (a) A_S and (b) B_S with normalized depth z/D; Piles in sand.

Step 4:

Use Figure 6.119b and the provided formulas to estimate the value of factor B_s as function of depth measured from the soil surface z, and subsequently estimate the soil reaction developing when pile deflection reaches $y_2 = D/60$ as:

(6.153) $$p_2 = B_s p_f$$

Step 5:

Estimate the slope of the initial linear of the p-y curve, k_{py} from Table 6.20, depending on the relative density of the sand and groundwater table conditions.

Table 6.20. Slope of the initial linear part of the p-y curve for piles in sand above and below the water table (Reese and van Impe 2001).

Sand density	Sand below the water table	Sand above the water table
	k_{py} (static, kN/m^3)	k_{py} (static, kN/m^3)
Loose	5400	6800
Medium	16300	24400
Dense	34000	61000

Step 6:

Determine the factors m, n and C as:

(6.154) $$m = \frac{p_1 - p_2}{y_1 - y_2}$$

(6.155) $$n = \frac{p_2}{m y_2}$$

(6.156) $$C = \frac{p_2}{(y_2)^{\frac{1}{n}}}$$

Step 7:

The *p-y* consists of three linear and one parabolic segment (Figure 6.120), described by the expressions listed in Table 6.21.

Table 6.21. Expressions describing the segments of the *p-y* curve for piles in sand above and below the water table (see Figure 6.120).

Segment (Figure 6.120)	Pile deflection range, *y*	Lateral resistance, *p*
linear (1)	$0 < y < y_k = \left(\frac{C}{k_{py} z}\right)^{\left(\frac{n}{n-1}\right)}$	$p = k_{py} z y$
parabolic	$y_k < y < y_2 = \frac{D}{60}$	$p = C y^{\frac{1}{n}}$
linear (2)	$y_2 < y < y_1 = \frac{3D}{80}$	$p = p_2 + m\,(y - y_2)$
linear (3)	$y > y_1$	$p = p_1$

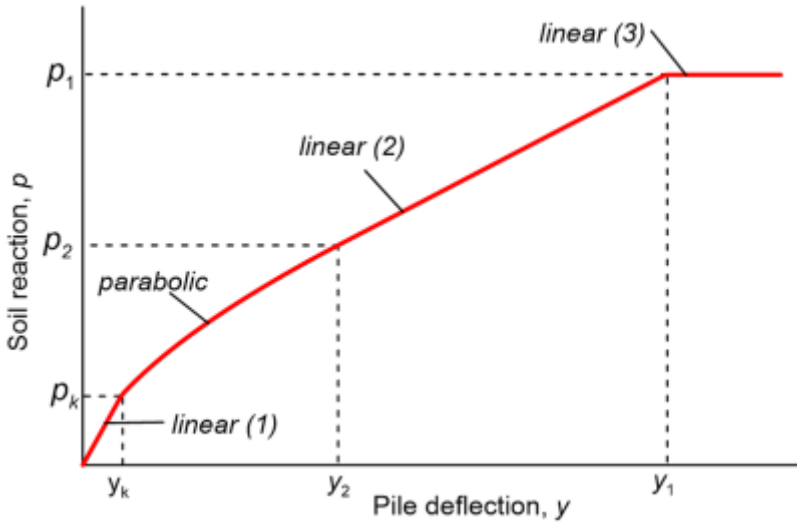

Figure 6.120. Segments of static *p-y* curve for a pile embedded in sand (after Reese *et al.*, 1974).

For example, consider a 15-m long pile with diameter D = 0.5 m, driven in medium-dense sand below the water table, with friction angle φ' = 35º and submerged unit weight γ' = 9.8 kN/m^3. First, the soil resistance is estimated from Eq. 6.151, and accordingly A_s and B_s are calculated from the expressions provided in Figure 6.119. Assuming k_{py} = 24000 kN/m^3 as an average value from Table 6.19 and K_0 = 0.4,

we can obtain all the necessary parameters to determine the segments of the *p-y* curves from Table 6.21, for different elevations z along the pile. Indicatively, for depths z = 5, 10 and 15 m, the parameters of the curves are presented in Table 6.22, and the curves are plotted in Figure 6.121.

Table 6.22. Parameters of the *p-y* curves, for a 15-m pile embedded in sand below the water table.

z (m)	$p_{f,1}$ (kN/m)	$p_{f,2}$ (kN/m)	A_s	B_s	p_2 (kN/m)	p_1 (kN/m)	y_k (m)	y_2 (m)	y_1 (m)
5	811.5	1317.9	0.88	0.50	405.7	714.1	0.000835	0.00833	0.01875
10	3078.5	2635.8	0.88	0.50	1317.9	2319.5	0.002876	0.00833	0.01875
15	6801.1	3953.8	0.88	0.50	1976.9	3479.3	0.002876	0.00833	0.01875

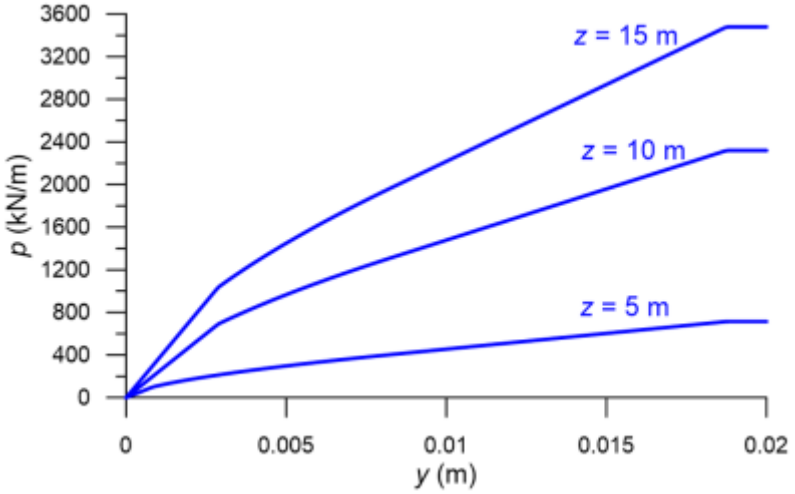

Figure 6.121. Indicative *p-y* curves along a 15-m pile embedded in dense sand below the water table.

A comparison of the indicative *p-y* curves presented in Figures 6.113, 6.116, 6.118 and 6.121 for clays and sands under variable groundwater table conditions is presented in Figure 6.122, for a typical depth below the ground surface z = 5 m. It is clear that the shape of the curves, and the ultimate reaction developing on the pile, strongly depend on the properties of the surrounding soil, and groundwater table conditions.

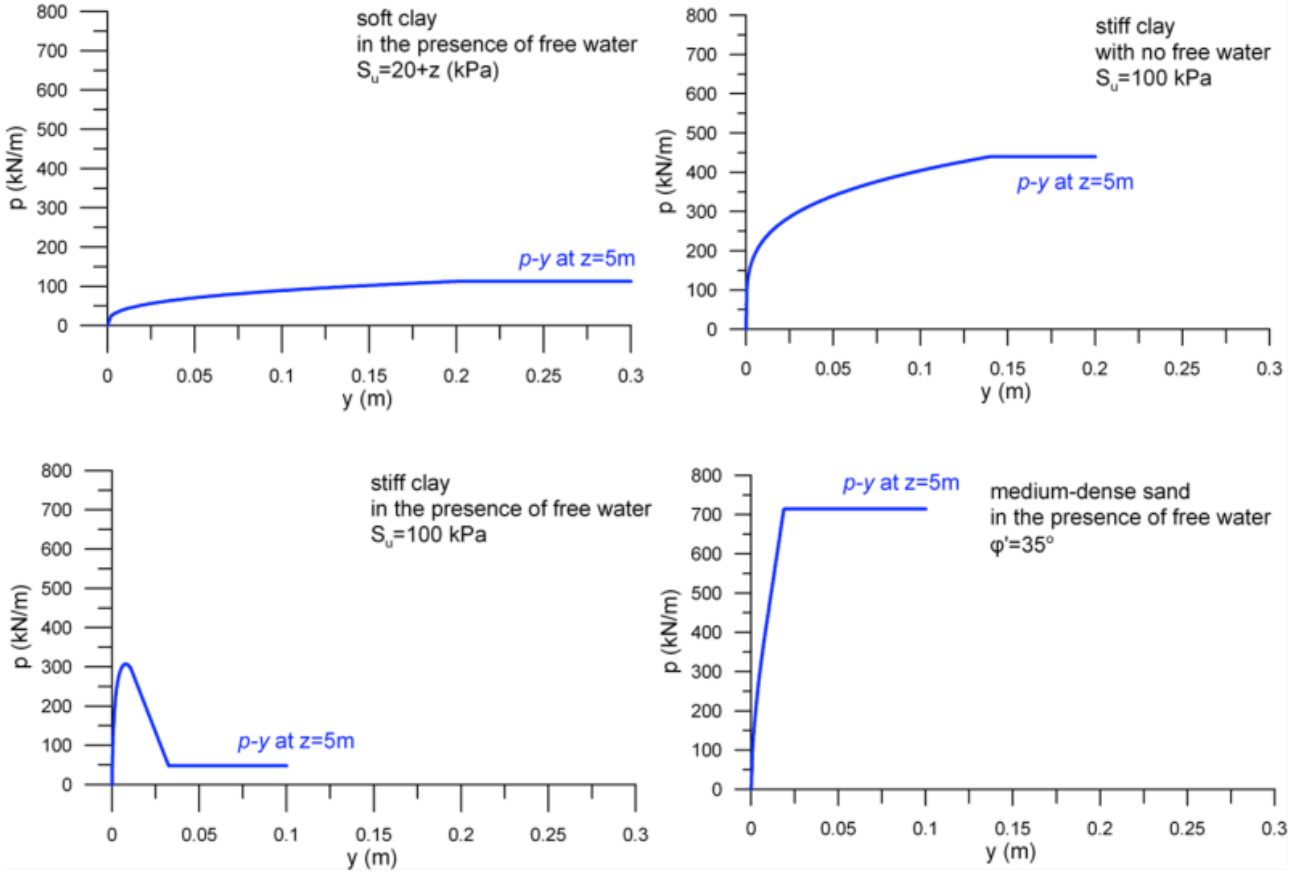

Figure 6.122. Comparison of indicative *p-y* curves for different soil and groundwater conditions.

EXAMPLE 6.15

Analysis of a concrete pile embedded in layered soil with the beam-on-nonlinear Winkler spring method for lateral loading

A single concrete free-head pile of diameter D = 0.6 m and length L = 10 m is embedded in a layered soil profile consisting of a stiff clay layer, underlain by dense sand. The soil layers are featuring the properties shown in the Figure below, while the water table is found below the pile toe. Determine: i) The variation of lateral pile deflection with depth, if a serviceability lateral load H_w = 100 kN is applied on the pile's head; ii) The variation of bending moment and shear forces along the pile, if a ultimate limit state lateral load H_f = 200 kN is applied on the pile's head; iii) Whether the pile has sufficient structural capacity to carry the developing internal forces due to the ultimate limit state lateral load, if the ultimate limit state axial force acting on the pile is Q_f = 500 kN.

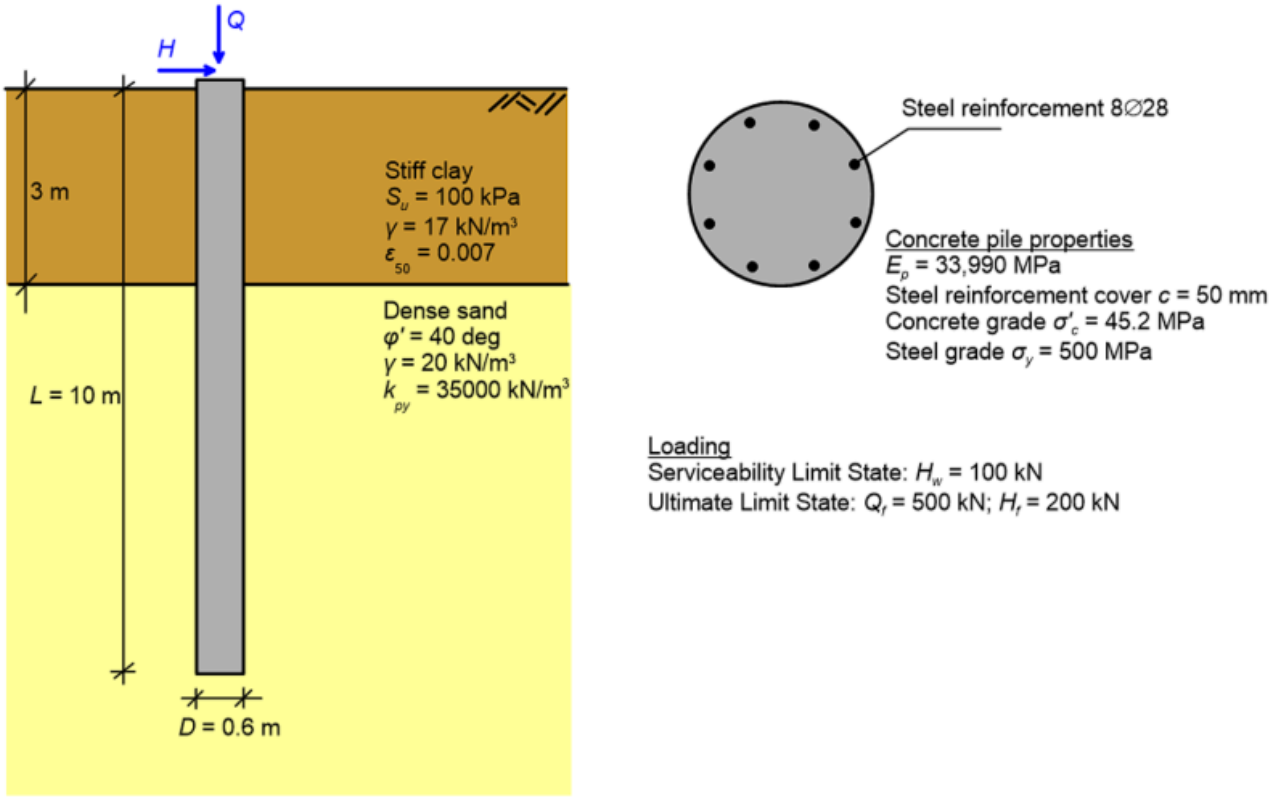

Example 6.15. Problem description and input parameters.

Answer:

To answer these questions, we must analyse the pile using the Finite Element Method, since the pile is embedded in layered soil (and the thickness of the surficial stiff clay layer 5D is less that the critical pile length, see Figure 6.110). We have sufficient information to determine the p–y curves along the length of the pile, following the steps described in Chapter 6.27 for piles in stiff clay without the presence of free groundwater (top 3 m of the pile) and for piles in sand (bottom 7 m of the pile). Thus we can set up a beam-on-nonlinear Winkler spring Finite Element model. The results presented in the following have been obtained with an in-house Finite Element code (Elphick 2014). Appropriate boundary conditions were set to account for the fact that the pile's head is free to rotate (hence the moment at the pile's head will be zero). Keep in mind that, according to the described earlier in Chapter 6.27, pile response to lateral loadings is

assumed independent on the axial compressive load applied on its head. However, the maximum bending moment that the concrete pile's section can carry depends on the compressive load, since the pile is made of reinforced concrete. Hence the ultimate limit state axial force acting on the pile Q_f is provided.

Figure 6.123 below presents the variation of lateral pile deflection with depth for lateral load H_w = 100 kN and the bending moment and shear force diagrams for lateral load H_f = 200 kN. Note that the code will return an error if the ultimate soil reaction is reached along the entire length of the pile i.e., if the pile fails with a *short pile failure* mode. As discussed earlier, designing a pile to fail with a "brittle" short pile failure mode is not recommended.

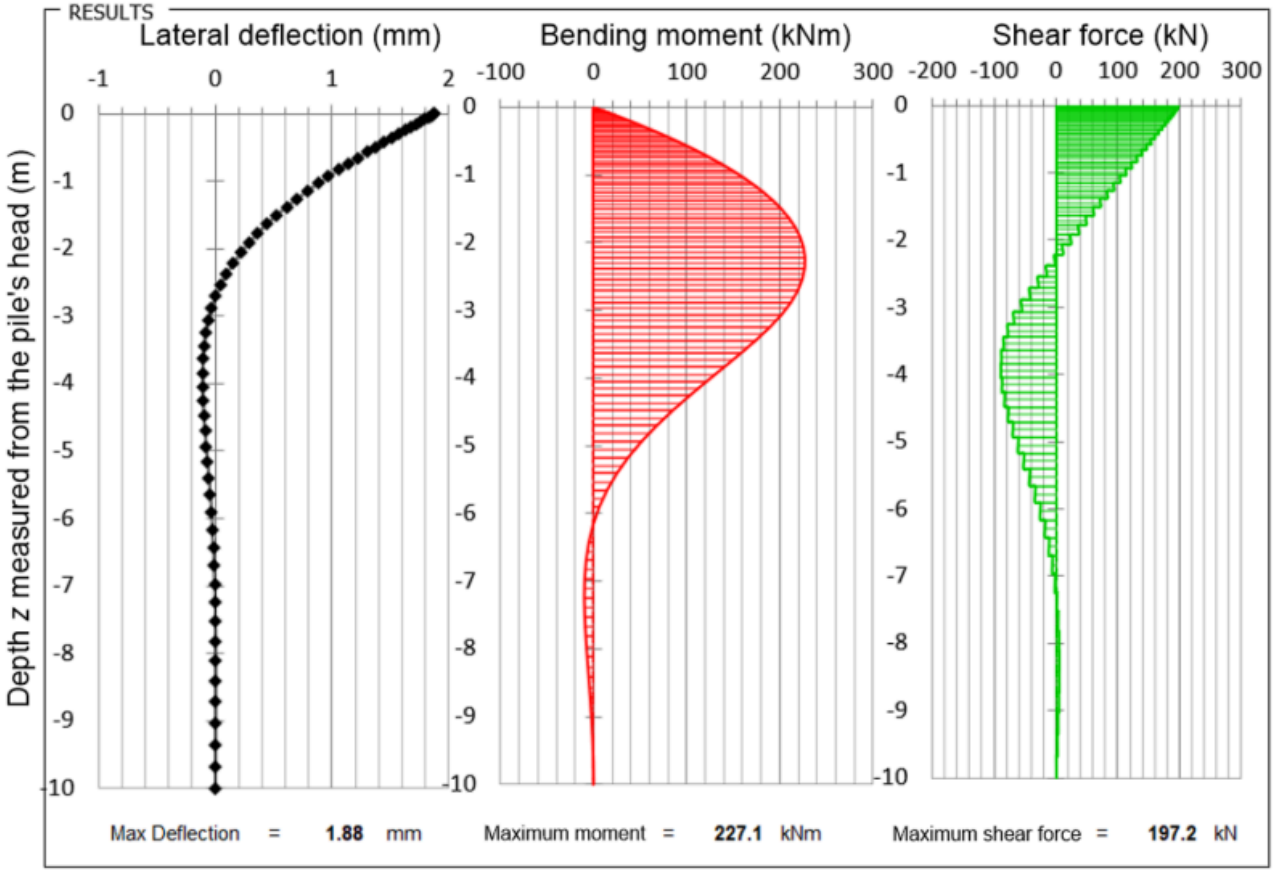

Figure 6.123. Variation of lateral pile deflection, bending moment and shear force along the length of the pile.

However, from the results presented above we cannot conclude whether the pile can safely transfer the ultimate limit state load to the subsoil, because we do not know whether its cross-section can carry the maximum moment (M_{max} = 227.1 kNm) without failure. For that we need to plot the strength interaction diagram of the pile's section, which depends on the properties of the pile (number and diameter of reinforcement bars, concrete and steel grade etc.). The strength interaction diagram is shown in Figure 6.124 where, for simplicity, we have assumed that the axial compressive load acting at the pile's head Q_f is constant along the pile's length. In reality the axial load will be reduced by the shaft friction resistance that will develop along a length of about z = 2.3 m i.e., the elevation where M_{max} develops on the pile. It is clear from Figure 6.124 that the $Q_f - M_{max}$ combination calculated during the Ultimate Limit State stage of the analysis falls within the safe region of the strength interaction diagram, therefore the pile can safely carry the applied lateral loading.

Finally, note that we have not applied any geotechnical reduction factors in this analysis. To do so, and thus comply with AS2159, we should divide the Ultimate Limit State lateral load and axial force with an appropriate value of φ_{gb} as well as use characteristic values of the soil parameters in the analysis. In addition, appropriate factors must be applied for the determination of the strength interaction diagram of the pile's section, according to the pertinent concrete design standard (AS3600).

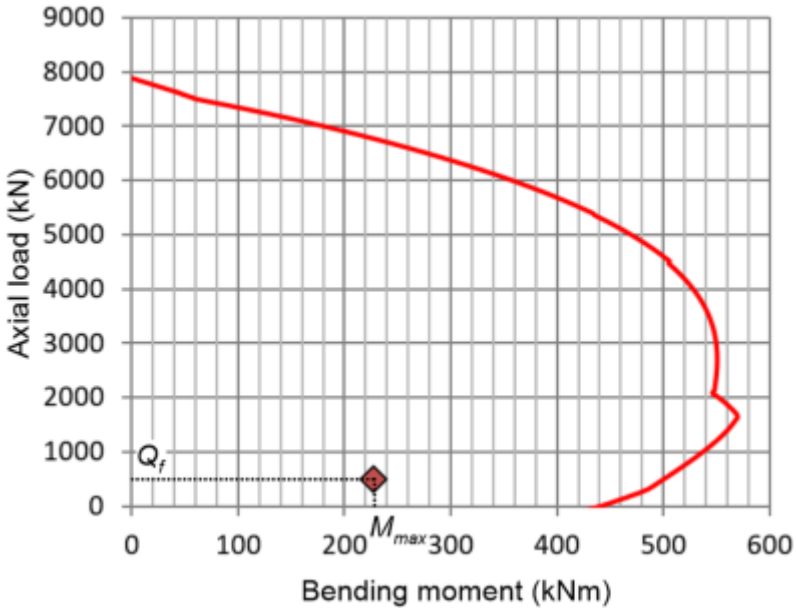

Figure 6.124. Strength interaction diagram.

6.28 PILE GROUP EFFECTS ON THE LATERAL LOAD RESPONSE OF PILES

As in the case of pile groups subjected to vertical loads (Chapter 6.20), the response of a group of piles to lateral loadings depends on pile-to-pile interaction effects. More specifically, the lateral deflection of the piles in a group whose head is connected with a rigid pile cap will be the same, when a lateral load is applied on the cap. If the piles are *in line* (Figures 6.125a and 6.125d) the lateral soil reaction that will develop on pile #2 for given pile cap deflection is less than the lateral reaction that will develop on a single pile under the same deflection, due to the existence of piles #1 and #3 e.g., pile #2 lies in the *"shadow zone"* of pile #1. Similarly, if the piles are *side-by-side* (Figures 6.125b and 6.125e) the soil reaction on pile #2 is influenced by the *"edge effect"*, again due to the existence of nearby piles #1 and #3. In the more general case of skewed piles (Figures 6.125c and 6.125f), these two effects are combined, rendering the assessment of the pile group response more complex.

Based on the work of Bogard and Matlock (1983), Brown *et al.* (1987), and Reese *et al.* (2006), *pile-to-pile* interaction effects under lateral loading can be quantified, by multiplying the *p-y* curve of a single pile (estimated according to Chapter 6.27) with a reduction factor β_g (Figure 6.126) that depends on the geometry of the group, the relative position of the pile in the pile group, and the direction of loading.

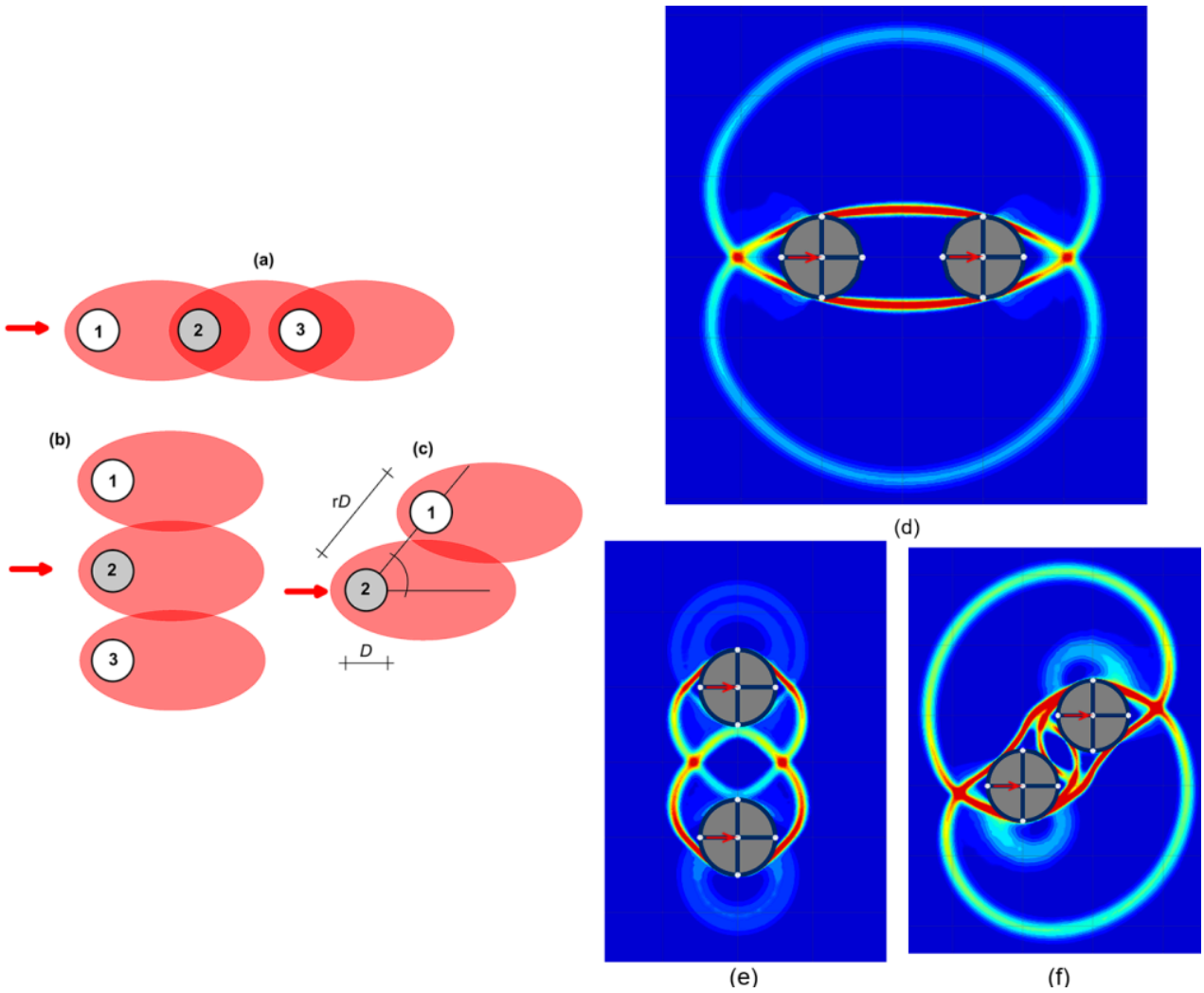

Figure 6.125. Influence of pile spacing on pile-soil-pile interaction: (a) Schematic of piles in line; (b) Schematic of piles side-by-side; (c) Schematic of the general case with piles at an angle with respect to the direction of the load; Plane-strain horizontal sections of rigid piles translating laterally in undrained soil: (d) piles in line; (e) piles side-by-side; (f) general case. The energy dissipation contours depict the shape of the composite failure surface mobilised when the ultimate soil reaction is reached.

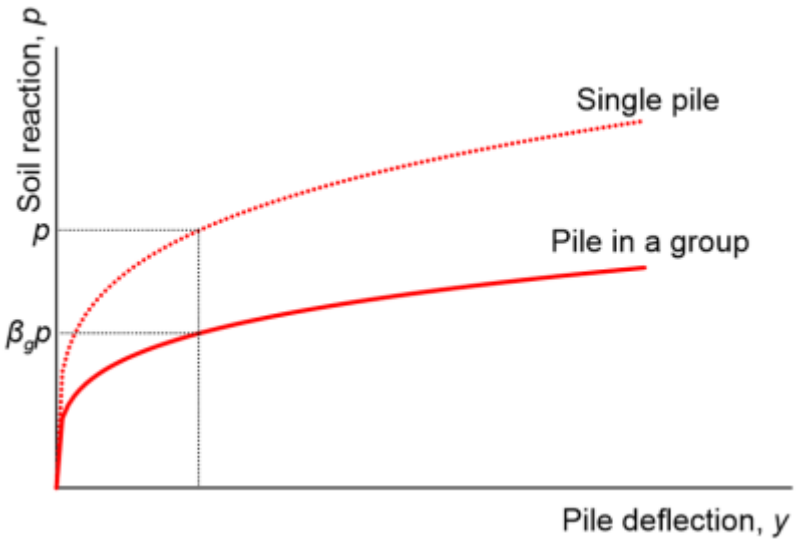

Figure 6.126. Employing the group factor β_g to modify *p-y* curves for pile group effects.

When the direction of the lateral load is perpendicular to the pile row (piles *side-by-side*), the reduction factor that accounts for interaction of any two side-by-side piles $\beta_{g,s}$ can be determined on the basis of Figure 6.127, as function of the piles' centre-to-centre spacing/pile diameter ratio, s :

(6.157) $\beta_{g,s} = 0.65s^{0.34}$ for $1 \leq s < 3.75$

(6.158) $\beta_{g,s} = 1$ for $3.75 \leq s$

All piles in the group must be considered when estimating the reduction factor, as discussed later. In the simple case of three piles spaced at sD depicted in Figure 6.127, the reduction factor that needs to be applied to the p–y curves of the middle reference pile will be equal to the product of the interaction factors of the reference pile (*ref*) with each one of the two side-by-side piles (S):

(6.159)
$\beta_g^{ref} = \beta_{g,s}^{ref \leftrightarrow S} \times \beta_{g,s}^{ref \leftrightarrow S}$ superscripts $^{\text{ref}\leftrightarrow\text{S}}$ etc.denote interaction between piles ref and S

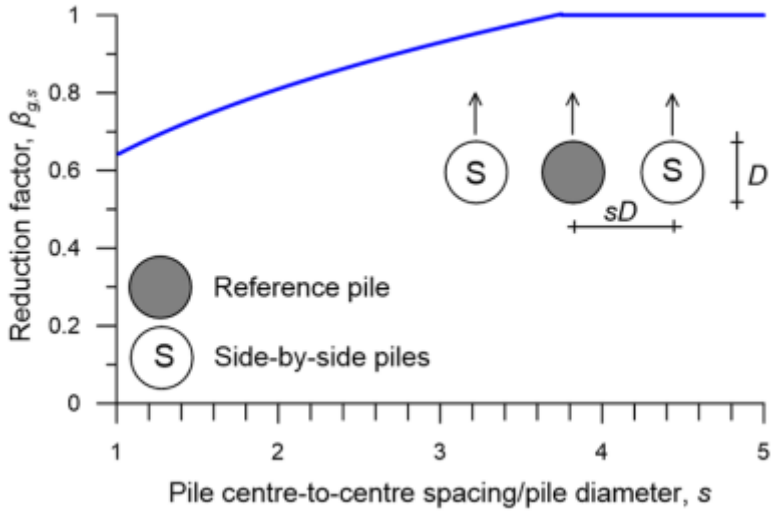

Figure 6.127. Reduction factor $\beta_{g,s}$ for piles in a row (side-by-side).

When the direction of the load is parallel to the pile row, the reduction factor for any given reference pile can be determined from Figure 6.128. For quantifying the interaction of the reference pile with the leading pile (L), Figure 6.128a is used to determine the factor $\beta_{g,l}$. Similarly, for quantifying the interaction of the reference pile with the trailing pile (T), factor $\beta_{g,t}$ is determined from Figure 6.128b. The relevant expressions are:

(6.160) $\beta_{g,l} = 0.7s^{0.26}$ for $1 \leq s < 4.00$

(6.161) $\beta_{g,l} = 1$ for $4.00 \leq s$

(6.162) $\beta_{g,t} = 0.48s^{0.38}$ for $1 \leq s < 7.00$

(6.163) $\beta_{g,t} = 1$ for $7.00 \leq s$

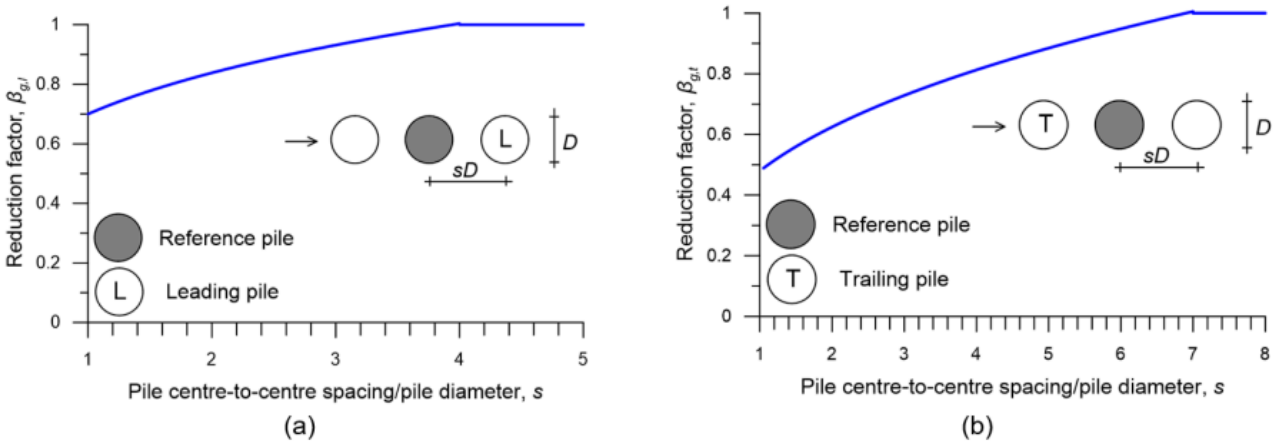

Figure 6.128. Reduction factor (a) $\beta_{g,l}$ for leading pile in a line (b) $\beta_{g,t}$ for trailing pile in a line (in-line).

All piles in the group must be taken into account when estimating the reduction factor for each pile. In this simple case of three piles shown in Figure 6.128, the reduction factor of the middle reference (*ref*) pile will be equal to the product of the factor that accounts for interaction of the reference pile with the leading pile (L), and of the factor that accounts for interaction of the reference pile with the trailing pile (T):

(6.164)
$$\beta_g^{ref} = \beta_{g,l}^{ref \leftrightarrow L} \times \beta_{g,t}^{ref \leftrightarrow T} \text{superscripts}^{\text{ref} \leftrightarrow \text{L}} \text{etc.denote interaction between piles ref and L}$$

In the general case of two skewed piles (Figure 6.129), the following procedure applies:

- Determine the factor $\beta_{g,a}$ from Figure 6.127 for side-by-side piles, while taking into account the distance between the pile centers, *rD*.
- Determine the factor $\beta_{g,b}$ from Figure 6.128 for in-line piles, depending which pile is considered (leading or trailing). Again, take as spacing the distance between the pile centers, *rD*.

Accordingly, the reduction factor for two skewed piles is estimated by means of geometric considerations as:

(6.165) $\beta_{g,sk} = \sqrt{\beta^2{}_{g,b}\cos^2\omega + \beta^2{}_{g,\alpha}\sin^2\omega}$

From the above it is clear that the value of the reduction factor depends not only on the arrangement (geometry and spacing) of the piles, but also on the direction of the load.

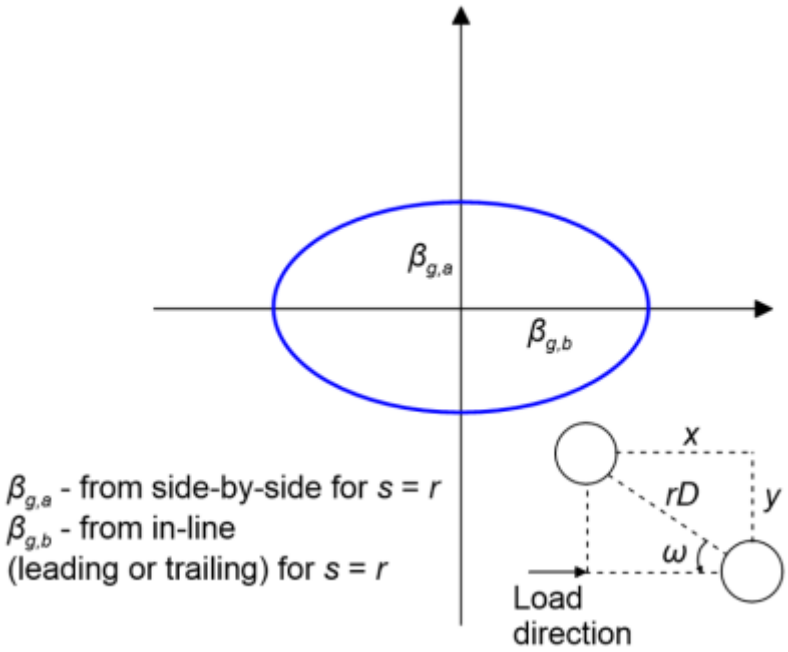

Figure 6.129. Estimating the reduction factor $\beta_{g,sk}$ of skewed piles. Angle ω is defined as the angle between the direction of the load and the line connecting the centers of the piles.

The above can be applied for determining the reduction factor of any individual pile in a multiple pile group. The group reduction factor of pile *j* in a group comprising *n* piles may be found by multiplying the reduction factors determined as above, while considering interaction with all the other piles in the group (Figure 6.130).

(6.166) $\beta_g^j = \beta_{g,sk}^{j\leftrightarrow 1} \times \beta_g^{j\leftrightarrow 2} \times \ldots \times \beta_{g,sk}^{j\leftrightarrow i} \times \ldots \times \beta_g^{j\leftrightarrow n}; i \neq j$ superscripts $^{j\leftrightarrow 1}$etc.denote interaction between piles j and 1

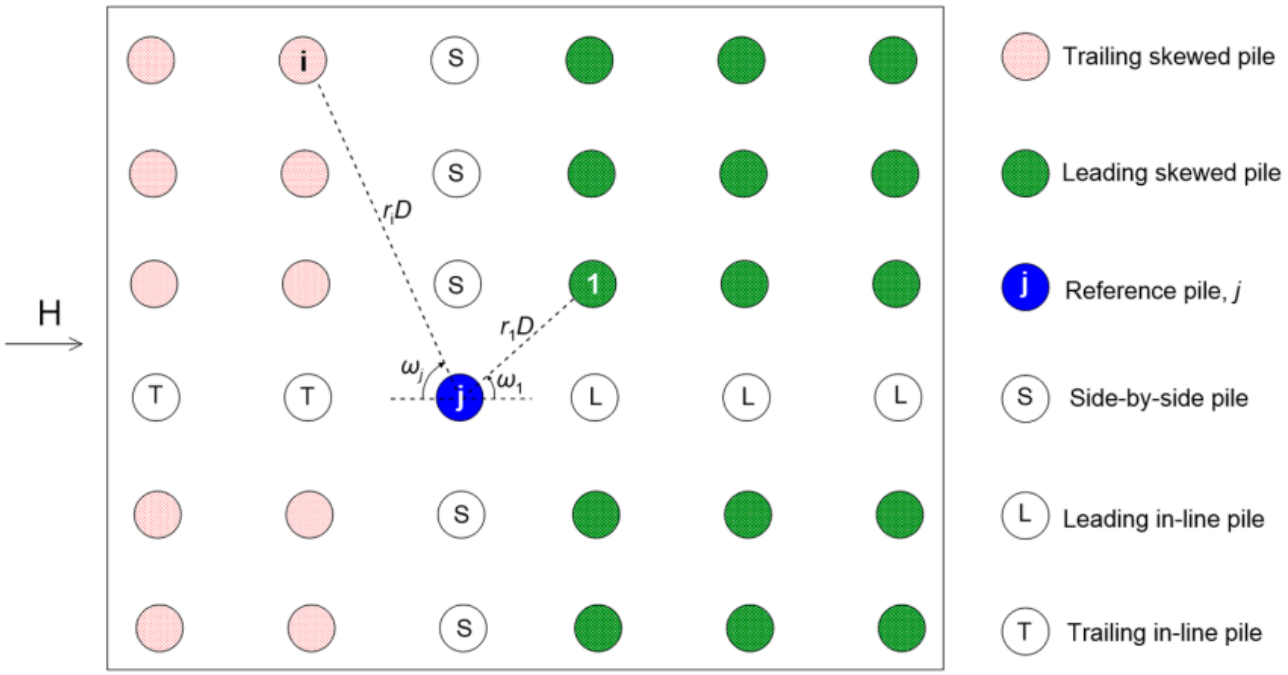

Figure 6.130. Estimating the reduction factor β_g^j of a random pile *j* in a multiple pile group.

This procedure, which must be followed for each individual pile of the group, is demonstrated in the following Example 6.16.

EXAMPLE 6.16

Estimation of the p-y curve reduction factor for a laterally loaded pile group

Determine the reduction factor $\beta_g{}^5$ for pile #5 shown in the figure below, when the lateral load acts along the weak axis of the group (X-X), and along the strong axis of the group (Y-Y). The diameter of all piles is equal to D.

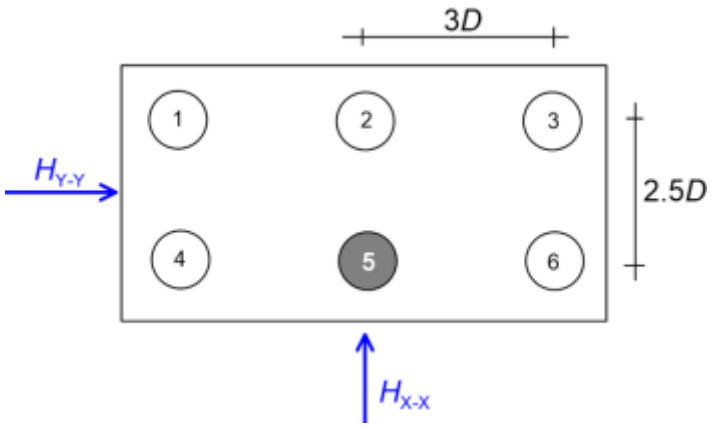

Example 6.16. Problem description and input parameters.

1. Load along the weak axis, $H_{X\text{-}X}$:

Interaction of pile #5 with all the remaining piles in the group must be considered, according to Eq. 6.166 and Figure 6.130, as:

$$\beta_g^5 = \begin{array}{l} \beta_{g,s}^{5\leftrightarrow 4}\,(\text{side by side}) \\ \times\beta_{g,s}^{5\leftrightarrow 6}(\text{side by side}) \\ \times\beta_{g,l}^{5\leftrightarrow 2}(\text{leading in line}) \\ \times\beta_{g,sk}^{5\leftrightarrow 1}(\text{leading skewed}) \\ \times\beta_{g,sk}^{5\leftrightarrow 3}(\text{leading skewed}) \end{array}$$

The individual interaction factors are determined from Figures 6.127–6.129 as:

$$\beta_{g,s}^{5\leftrightarrow 4} = \beta_{g,s}^{5\leftrightarrow 6} = 0.64 \times 3^{0.34} = 0.929$$

$$\beta_{g,l}^{5\leftrightarrow 2} = 0.70 \times 2.5^{0.26} = 0.888$$

$$\left(\begin{array}{l} \beta_{g,a}^{5\leftrightarrow 1} = 1.0 \\ \beta_{g,b}^{5\leftrightarrow 1} = 0.7\left(\sqrt{3^2+2.5^2}\right)^{0.26} = 0.997 \\ \omega = \tan^{-1}\left(\dfrac{3}{2.5}\right) = 50.2\ \text{deg} \end{array} \right) \rightarrow \beta_{g,sk}^{5\leftrightarrow 1} = \beta_{g,sk}^{5\leftrightarrow 3} = \sqrt{0.997^2\cos^2(50.2) + 1^2\sin^2(50.2)} = 0.998$$

The reduction factor for pile #5 is calculated from Eq. 6.166 as:

$$\beta_g^5 = \beta_{g,s}^{5\leftrightarrow 4} \times \beta_{g,s}^{5\leftrightarrow 6} \times \beta_{g,l}^{5\leftrightarrow 2} \times \beta_{g,sk}^{5\leftrightarrow 1} \times \beta_{g,sk}^{5\leftrightarrow 3} = 0.929 \times 0.929 \times 0.888 \times 0.998 \times 0.998 = 0.763$$

2. Load along the strong axis, $H_{\text{Y-Y}}$:

The procedure is similar, but notice that the relative position of the pile compared to its neighboring piles must be re-assessed according to Figure 6.130, as:

$$\beta_g^5 = \begin{array}{l} \beta_{g,s}^{5\leftrightarrow 4}\,(\text{trailining in line}) \\ \times\beta_{g,s}^{5\leftrightarrow 6}(\text{leading in line}) \\ \times\beta_{g,l}^{5\leftrightarrow 2}(\text{side by side}) \\ \times\beta_{g,sk}^{5\leftrightarrow 1}(\text{trailing skewed}) \\ \times\beta_{g,sk}^{5\leftrightarrow 3}(\text{leading skewed}) \end{array}$$

The individual interaction factors are determined from Figures 6.127–6.129 as:

$$\beta_{g,s}^{5\leftrightarrow 4} = 0.48 \times 3^{0.38} = 0.728$$

$$\beta_{g,s}^{5\leftrightarrow 6} = 0.70 \times 3^{0.26} = 0.931$$

$$\beta_{g,l}^{5\leftrightarrow 2} = 0.64 \times 2.5^{0.34} = 0.874$$

$$\left(\begin{array}{l} \beta_{g,a}^{5\leftrightarrow 1} = 1.0 \\ \beta_{g,b}^{5\leftrightarrow 1} = 0.48\left(\sqrt{3^2+2.5^2}\right)^{0.39} = 0.805 \\ \omega = \tan^{-1}\left(\dfrac{2.5}{3}\right) = 39.8\,\text{deg} \end{array} \right) \rightarrow \beta_{g,sk}^{5\leftrightarrow 1} = \sqrt{0.805^2\cos^2(39.8) + 1^2\sin^2(39.8)} = 0.890$$

$$\left(\begin{array}{l} \beta_{g,a}^{5\leftrightarrow 3} = 1.0 \\ \beta_{g,b}^{5\leftrightarrow 3} = 0.70\left(\sqrt{3^2+2.5^2}\right)^{0.26} = 0.997 \\ \omega = \tan^{-1}\left(\dfrac{2.5}{3}\right) = 39.8\,\text{deg} \end{array} \right) \rightarrow \beta_{g,sk}^{5\leftrightarrow 1} = \sqrt{0.997^2\cos^2(39.8) + 1^2\sin^2(39.8)} = 0.998$$

The reduction factor for pile #5 is calculated from Eq. 6.166 as:

$$\beta_g^5 = \beta_{g,s}^{5\leftrightarrow 4} \times \beta_{g,s}^{5\leftrightarrow 6} \times \beta_{g,l}^{5\leftrightarrow 2} \times \beta_{g,sk}^{5\leftrightarrow 1} \times \beta_{g,sk}^{5\leftrightarrow 3} = 0.728 \times 0.931 \times 0.874 \times 0.890 \times 0.998 = 0.526$$

6.29 REFERENCES

1. American Petroleum Institute (1984). API Recommended practice for planning, designing and constructing fixed offshore platforms. Report API RP-2A.
2. American Petroleum Institute (1986). API Recommended practice for planning, designing and constructing fixed offshore platforms. Report API RP-2A.
3. American Petroleum Institute (2000). API Recommended practice for planning, designing and constructing fixed offshore platforms. Report API RP-2A.
4. Australian Standard AS2159. Piling-Design and installation.
5. Australian Standard AS3600. Concrete structures
6. Australian/New Zealand Standard AS1170.0. Structural design actions. Part 0: General principles.
7. Australian/New Zealand Standard AS1170.1. Structural design actions. Part 1: Permanent, imposed and other actions.
8. Australian Standard AS5100.2. Bridge design-Design loads.
9. Baldi G, Belloti R, Ghionna V, Jamiolkowski M and Lo Presti DFC (1989) Modulus of sands from CPT's and DMT's. Proc. 12th Int Conf on Soil Mechanics and Foundations Engineering, Rio de Janeiro, 165-170.
10. Bogard D and Matlock HM (1983). Procedures for analysis of laterally loaded pile groups in clay. In: Proceedings, Geotechnical Practice in Offshore Engineering, American Society of Civil Engineers, pp 499-535.
11. Bowles JE (1997). Foundation analysis and design. 5th edition. McGraw-Hill.
12. Briaud JL and Miran J (1992). The cone penetrometer test. Rep. No. FHWA-SA-91-043, Federal Highway Administration, Washington DC.
13. Broms BB (1964a). Lateral resistance of piles in cohesive soils. Journal of the Soil Mechanics and Foundations Division, ASCE 90(SM2), pp 27-63.
14. Broms BB (1964b). Lateral resistance of piles in cohesionless soils. Journal of the Soil Mechanics and Foundations Division, ASCE 90(SM3), pp 123-156.
15. Broms BB (1965). Design of laterally loaded piles. Journal of the Soil Mechanics and Foundations Division, ASCE 91(SM3), pp 77-99.
16. Brown DA, Reese LC, and O'Neill MW (1987). Cyclic lateral loading of a large-scale pile group. Journal of Geotechnical Engineering Division, ASCE, Vol. 113, No. 11, pp 1326-1343.
17. Budhu M (2011). Soil mechanics and foundations. 3rd edition. John Wiley & Sons, Inc.
18. Bustamante M and Gianeselli L (1982). Pile capacity prediction by means of static penetrometer CPT. In: Proceedings, Second European Symposium on Penetration testing, Amsterdam, May, pp 493-500.
19. Coduto DP (1994) Foundation design: Principles and practice. Prentice-Hall USA.
20. Das BM (2007). Principles of foundation engineering. 6th edition. Thomson.
21. Davisson MT (1972). High capacity piles. In: Proceedings, Lecture Series Innovations in Foundation Construction, ASCE, Illinois section, Chicago.
22. Elphick A (2014) Latpile: a finite element code for the analysis of concrete piles subjected to lateral loads. The University of Newcastle, Australia
23. Federal Highway Administration FHWA (2006). Soils and Foundations. Reference Manual. Vols I & II, Publication No. FHWA NHI-06-088 and FHWA NHI-06-089, US Department of Transportation, December 2006.
24. Fellenius BH (1984). Negative skin friction and settlement of piles. Second International Seminar, Pile Foundations, Nayang Technological Institute, Singapore, November.
25. Fleming WGK, Weltman AJ, Randolph MF and Elson WK (1985). Piling Engineering. Halsted Press.
26. Goodman RE (1980). Introduction to rock mechanics. John Wiley & Sons, Inc.
27. Jaky J (1944). The coefficient of earth pressure at rest. J. Soc. Hungarian Architects Eng. Vol. 7, pp 355-358.
28. Janbu N (ed.) (1976). Static bearing capacity of friction piles. Proceedings, the 6th European Conference on Soil Mechanics and Foundation Engineering, Vol. 1.2, pp 479-488.
29. Jardine R, Chow F, Overy R and Standing J (2005) ICP design methods for driven piles in sands and clays. Thomas Telford

30. Kolk JH, Baaijens AE and Senders M (2005) Design criteria for pipe piles in silica sands. Proc. Int. Symp. on Frontiers in Offshore Geomechanics ISFOG, Taylor and Francis, 711-716
31. Lawton EC, Fragaszy RJ, Higgins JD, Kilian AP and Peters AJ (1986) Review of methods for estimating pile capacity. Transportation Research Record 1105, Transportation Research Board USA
32. Lehane BM, Schneider JA and Xu X (2005a) A review of design methods for offshore drive pile in siliceous sand. GEO 05358 The University of Western Australia
33. Lehane BM, Schneider JA and Xu X (2005b) The UWA-05 method for prediction of axial capacity of driven piles in sand. Proc of the International Symposium on Frontiers in Offshore Geotechnics, Peth, Australia IS-FOG 2005.
34. Matlock H (1970). Correlations for design of laterally loaded piles in soft clay. In: Proceedings, Offshore Technology Conference, Houston, Texas, paper No. 1204, pp 577-594
35. Michigan State Highway Commission (1965) A Performance investigation of pile driving hammers and piles. Final Report. Research Project 61 F-60, Lansing.
36. Monzon JC (2006) Review of CPT based design method for estimation axial capacity of driven piles in siliceous sand. Massachusetts Institute of Technology
37. O'Neill MW and Reese LC (1999). Drilled shafts: Construction procedures and design methods. FHWA-IF-99-025, Federal Highway Administration, Washington DC.
38. Peck RB, Hanson WE and Thornburn TH (1974) Foundation Engineering. 2nd edition. John Wiley & Sons, Inc.
39. Pells PJ, Rowe RK and Turner RM (1980) An experimental investigation into sideshear for socketed piles in sandstone. Proc, International Conference on Structural Foundations on Rock, Sydney, Vol I, pp 291-302.
40. Poulos HG (1968) Analysis of the settlement of pile groups. Géotechnique, 18, 449-471
41. Poulos HG (1989) Pile behaviour – theory and application. Géotechnique, 39(3), 365-415
42. Poulos HG and Davis EH (1991) Elastic solutions for soil and rock mechanics. Centre for Geotechnical Research, University of Sydney
43. Poulos HG and Mattes NS (1971) Displacements in a soil mass due to pile groups. Aust Geomech J G1 (1), 18-28
44. Randolph MF and Housbly GT The limiting pressure on a circular pile loaded laterally in cohesive soil. Géotechnique, Vol 34(4), pp 613-623.
45. Reese LC, Cox WR and Koch FD (1975). Field testing and analysis of laterally loaded piles in stiff clay. In: Proceedings, VII Annual Offshore Technology Conference, Houston, Texas, paper No. 2312, pp 672-690.
46. Reese LC, Isenhower WM and Wang ST (2006). Analysis and design of shallow and deep foundations. John Wiley & Sons, Inc.
47. Reese LC and van Impe WF (2001). Single piles and pile groups under lateral loading. Taylor & Francis Group.
48. Reissner H (1924). Zum Erddruckproblem. In: Proceedings, First International Congress of Applied Mechanics, Delft, pp 295-311.
49. Robertson PK and Kabal K (2022). Guide to Cone Penetration Testing. 7th Edition. Gregg Drilling & Testing Inc.
50. Rowe RK and Armitage HH (1987a) A design method for drilled piers in soft rock. Can Geotech J 24, 114-125.
51. Rowe RK and Armitage HH (1987b) Theoretical solutions for axial deformation of drilled shafts in rock. Can Geotech J 24, 114-125.
52. Rowe RK and Armitage HH (1984) The design of piles socketed into weak rock. Faculty of Engineering Science, The University of Western Ontario, London Ont, Research Report GEOT-11-84.
53. Schmertmann JH (1978). Guidelines for Cone Penetration test: Performance and Design. FHWA-TS-78-209, US Department of Transportation.
54. Schneider JA, Xu X and Lehane B (2008) Database assessment of CPT-based design methods for axial capacity of driven piles in siliceous sands. J Geotech Geoenv Engng 134(9)
55. Tomlinson MJ (1987). Pile design and construction practice. 3rd edition. Viewpoint Publications.
56. Vesic AS (1963) Bearing capacity of deep foundations in sand. Highway Research Record, p. 39
57. Zheng C, Chen M and Kouretzis G (2024) Closed-form solution for axially loaded end-bearing piles in two-layered soil. International Journal for Numerical and Analytical Methods in Geomechanics, 48(3), 837-852
58. Zheng C, Kouretzis G, Ding X (2023) Analytical solution for axial load transfer of floating piles. Computers and Geotechnics, 164, 105832.

59. Zheng C, Kouretzis G and Ding X (2024) Analysis of laterally loaded floating piles using a refined Tajimi model. International Journal for Numerical and Analytical Methods in Geomechanics, 48(11), 2727-2744

6.30 ADDITIONAL PROBLEMS

6.30.1

Determine the short-term design bearing capacity of the pile shown below, according to AS2159, assuming the basic geotechnical strength reduction factor to be $\varphi_{gb} = 0.5$.

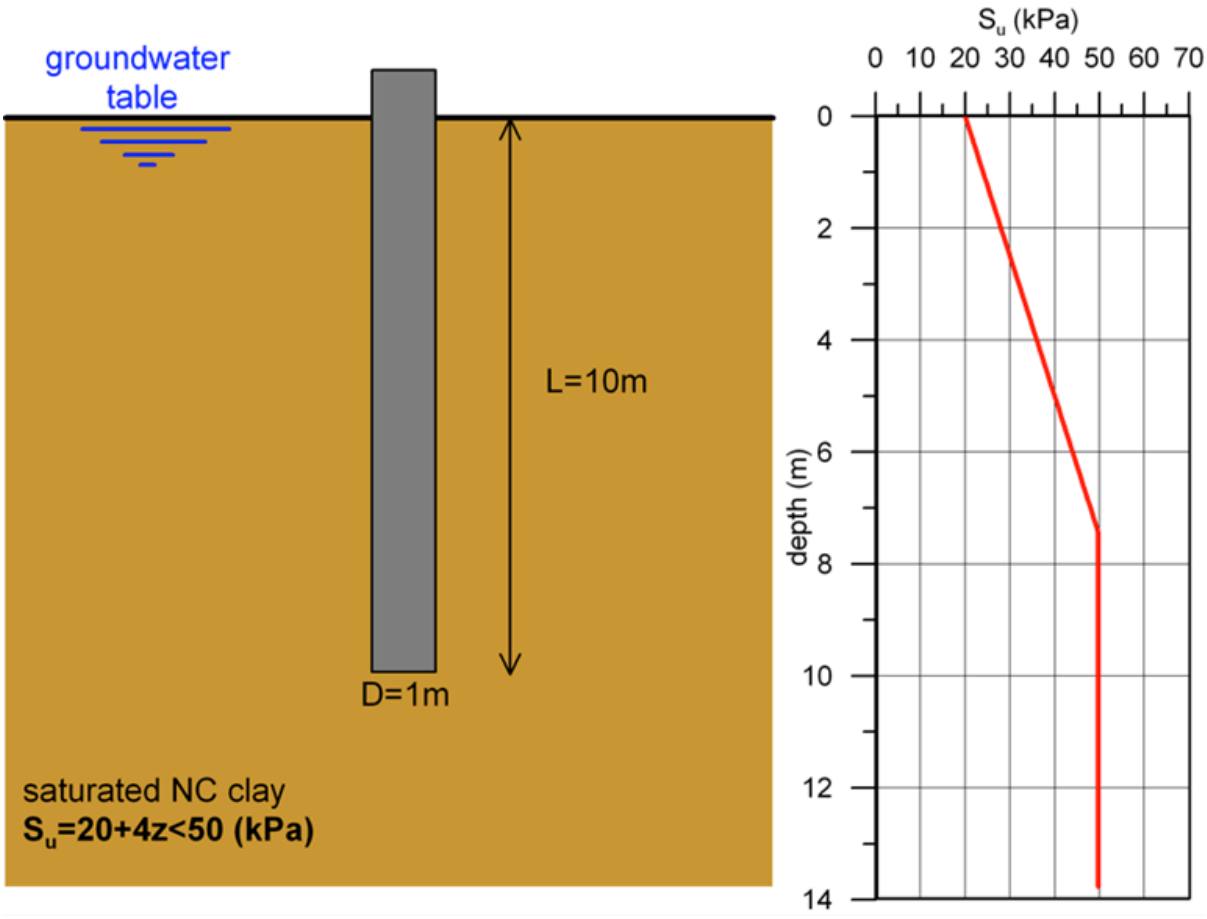

Example 6.30.1. Problem description and input parameters.

Answer:

$\varphi_{gb} Q_f = 731\ kN$

6.30.2

Determine the short-term design bearing capacity of the pile shown below, embedded in a multi-layered

clay formation. Assume that the surficial very soft organic clay layer does not contribute to the skin friction resistance of the pile. Follow AS2159 provisions, and consider the basic geotechnical strength reduction factor to be $\varphi_{gb} = 0.5$.

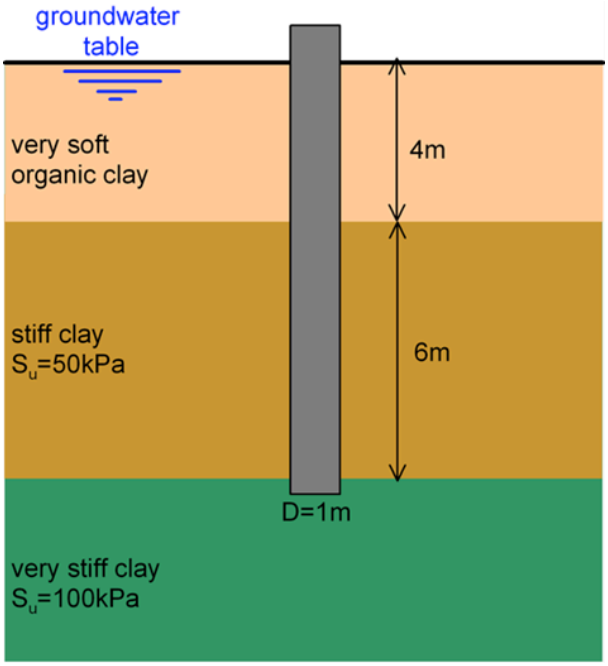

Example 6.30.2. Problem description and input parameters.

Answer:

$\varphi_{gb}Q_f = 542\ kN$

6.30.3

A shallow-water offshore structure is going to be founded on driven steel pipe piles. The geotechnical profile of the area consists of loose sand, underlain by a practically infinitely deep layer of stiff over-consolidated clay. According to the Structural Engineer, the design compressive load on each pile is 800 kN (including the weight of the pile), and the design tensile load is 500 kN.

Determine the necessary embedment depth of the piles L_b, assuming the basic geotechnical strength reduction factor to be $\varphi_{gb} = 0.5$. To account for disturbance of the sand during pile driving works, as well as possible scour, ignore the top 3 m of the sand layer when calculating the friction resistance of the pile.

Additional information:

- Interface friction angle for steel piles $\varphi_i = 0.5\varphi'$
- Reduction factor for uplift resistance of piles $\psi_t = 0.75$

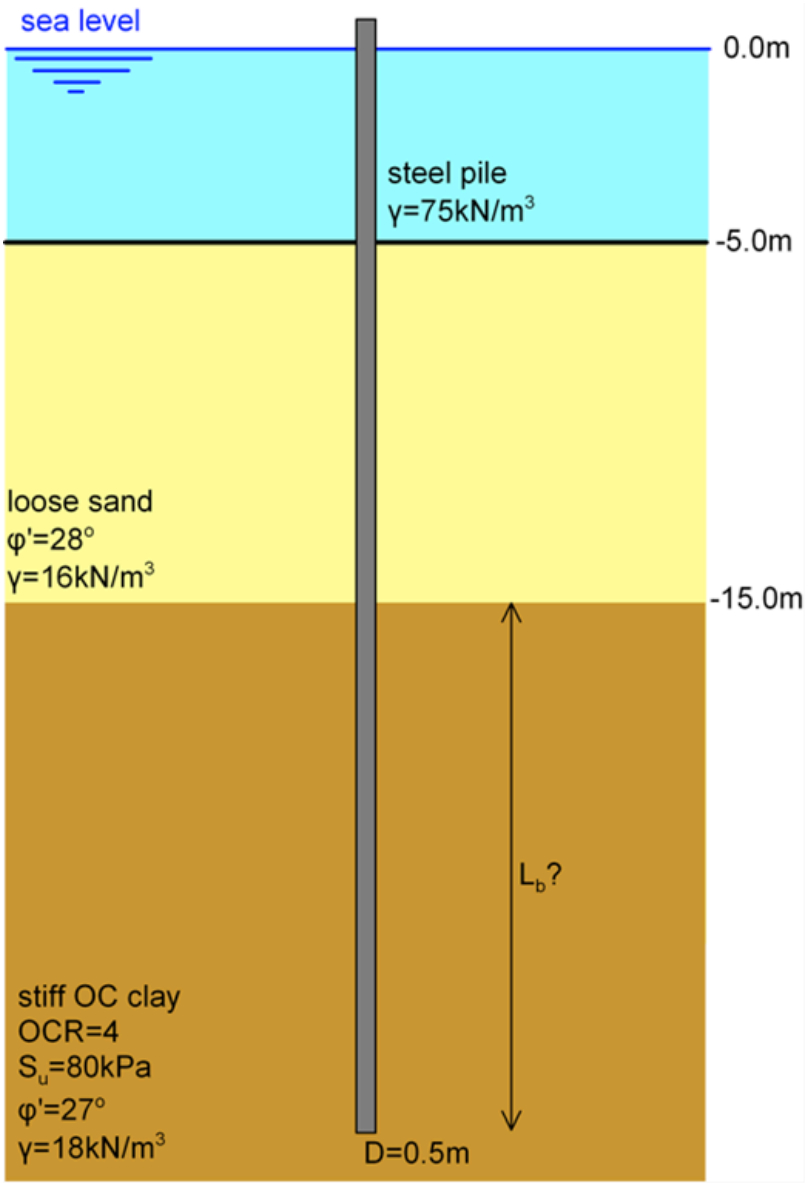

Example 6.30.3. Problem description and input parameters.

Answer:

$L_b = 18.5\ m$

6.30.4

A pre-stressed concrete pile with diameter D = 1 m and Young's modulus E_p = 30 GPa is driven into a uniform layer of soft-to-medium clay, with undrained Young's modulus E_u = 3 MPa.

a. Determine the necessary pile length so that the settlement under the working load Q_w = 1 MN is less than the allowable settlement ρ_D = 0.03 m.
b. An alternative nearby location is examined for the project, where a very stiff clay layer with E_u = 30 MPa is encountered at a depth of -10 m. If the pile is embedded in the stiff layer ($L \approx 10$ m), will the

settlement criterion be satisfied?
c. Assuming that the alternative location is selected, how many piles must be used to carry a working group load of $Q_{w,group}$ = 4 MN while still satisfying the settlement criterion?

Note: The settlement factor I_s involved in the estimation of the immediate settlement of friction piles can be obtained for this particular problem as $I_s = 0.618(L/D)^{-0.652}$.

Answer:

a. *19.2m*
b. *Yes*
c. *6 piles*

6.30.5

A cylindrical steel pipe pile of external diameter D_{ext} = 0.3 m, wall thickness t = 0.005 m and design yield strength σ_y = 450 MPa, is driven through a uniform layer of medium-dense sand with friction angle φ' = 33º and unit weight γ = 18 kN/m^3. The necessary pile length to carry the vertical load is L = 5 m. Assuming the pile is connected to a rigid cap *(fixed-head),* determine its collapse lateral load.

Note: Do not apply a geotechnical strength reduction factor on the collapse load.

Answer:

$H_f = 211.7\ kN$

6.30.6

A cylindrical pipe pile made of steel with yield strength σ_y = 450 MPa and featuring wall thickness t = 0.01 m is driven through a uniform clay layer with undrained shear strength S_u = 60 kPa. Assuming the pile is connected with a rigid cap *(fixed-head),* and "long pile" failure mode, determine the necessary external pile diameter so that its collapse lateral load is H_f = 300 kN.

Note: Do not apply a geotechnical strength reduction factor on the collapse load.

Answer:

$D_{ext} = 0.235\ m$

APPENDIX A: PHASE RELATIONSHIPS

Generally, soil is a three-phase material consisting of air, water and solids. Of course, fully saturated or dry soils are two-phase materials, but these are merely special cases. The relative volume or mass of each one of these phases will affect soil behaviour as continuum, and this has led to the definition of a series of quantities and relationships (*phase relationships*) that are correlated to the physical properties of soils. These quantities are defined in the following.

The water content w (often referred to as moisture content) is the ratio of the weight of the water phase W_w over the weight of the solids W_s. By definition, the water content can attain values from zero up to higher than one.

(A.1) $$w = \frac{W_w}{W_s}$$

It is reminded here that weight W is correlated to mass M as: $W = Mg$, where g is the gravity coefficient.

The degree of saturation S_r is the ratio of the volume of the water phase V_w over the total volume of voids V_v. By definition, the degree of saturation can attain values from zero (dry soil) up to one (fully saturated soil).

(A.2) $$S_r = \frac{V_w}{V_v}$$

The void ratio e is the ratio of the volume of voids V_v to the volume of solids V_s and can again attain values higher than one.

(A.3) $$e = \frac{V_v}{V_s}$$

The porosity n, defined as the volume of voids per unit volume of soil V is often used instead of the void ratio, although the two quantities as directly related as:

(A.4) $$n = \frac{V_v}{V} = \frac{V_v}{V_v + V_s} = \frac{e}{1+e}$$

or

(A.5) $$e = \frac{n}{1-n}$$

A third quantity used to quantify the relative volume of voids is the specific volume v, which is defined as the unit volume of soil V over the volume of solids V_s:

(A.6) $$v = \frac{V}{V_s} = \frac{V_v + V_s}{V_s} = 1 + e$$

The specific gravity of soil particles G_s is defined as the weight of the solids over the weight of a quantity water of the same volume:

(A.7) $$G_s = \frac{W_s}{V_s \gamma_w}$$

where $\gamma_w = M_w/V_w$ is the unit weight of water, $\gamma_w \approx 10$ kN/m^3. Specific gravity depends on soil mineralogy, for silica-based soils it is $G_s \approx 2.65$.

In the light of Eqs. A.7 and A.3 and considering that $M_w = V_w\gamma_w$ we can re-write Eq. A.2 that provides the degree of saturation as:

$$\textbf{(A.8)}\ S_r = \frac{V_w}{V_v} = \frac{W_w}{eV_s\gamma_w} = \frac{\frac{W_w}{W_s}}{e\frac{V_s}{W_s}\gamma_w} = \frac{w}{e\frac{1}{G_s}} = \frac{wG_s}{e}$$

So, for a fully saturated soil ($S_r = 1$) the water content and the void ratio are directly correlated as:

$$\textbf{(A.9)}\ e = wG_s$$

The unit weight, or more properly the *bulk* unit weight, γ of soil is its weight W per unit volume V. The terms unit weight and bulk unit weight are often used interchangeably, and are applicable to soils featuring any degree of saturation S_r.

$$\textbf{(A.10)}\ \gamma = \frac{W}{V}$$

We can further write:

$$\textbf{(A.11)}\ \gamma = \frac{W}{V} = \left(\frac{G_s + S_r e}{1+e}\right)\gamma_w = \frac{G_s\,(1+w)}{1+e}\gamma_w$$

Observe from Eq. A.11 that the unit weight of soil depends on its degree of saturation S_r. In the special case where the soil is saturated ($S_r = 1$) then Eq. A.11 becomes:

$$\textbf{(A.12)}\ \gamma_{sat} = \left(\frac{G_s + e}{1+e}\right)\gamma_w$$

where γ_{sat} is the saturated unit weight. On the other hand, in the special case where the soil is dry ($S_r = 0$) it is:

$$\textbf{(A.13)}\ \gamma_d = \left(\frac{G_s}{1+e}\right)\gamma_w$$

where γ_d is the dry unit weight. A correlation between the dry unit weight and the bulk unit weight can be found if we substitute Eq. A.11 into Eq. A.13 as:

$$\textbf{(A.14)}\ \gamma = (1+w)\,\gamma_d$$

The effective or buoyant unit weight of saturated soil submerged in water is defined as:

$$\textbf{(A.15)}\ \gamma' = \gamma_{sat} - \gamma_w = \left(\frac{G_s - 1}{1+e}\right)\gamma_w$$

Often, instead of the unit weight of soil, we use the mass density ρ equal to the ratio of the soil mass M per unit volume V:

$$\textbf{(A.16)}\ \rho = \frac{M}{V} = \frac{W}{Vg} = \frac{\gamma}{g}$$

where g again is the gravity coefficient. In a similar way we can define the saturated mass density ρ_{sat} :

(A.17) $$\rho_{sat} = \left(\frac{G_s + e}{1 + e}\right)\rho_w$$

where $\rho_w \approx 10\ \mathrm{Mg/m^3}$ is the mass density of water. Similarly, the dry mass density ρ_{dry} is:

(A.18) $$\rho_d = \left(\frac{G_s}{1 + e}\right)\rho_w$$

Note: Eq. A.11 is derived as:

$$\gamma = \frac{W}{V} = \frac{W_w + W_s}{V_v + V_s} = \frac{eS_r V_s \gamma_w + W_s}{eV_s + V_s} = \frac{eS_r V_s \gamma_w + G_s V_s \gamma_w}{V_s\,(1 + e)} = \frac{eS_r + G_s}{(1 + e)}\gamma_w$$

APPENDIX B: LIST OF MAIN SYMBOLS

Symbol	Meaning
$(RF)_\rho$	Settlement reduction factor for recessed piles
[K]	Pile stiffness matrix
[S]	Compliance matrix
A	Skempton's pore water coefficient
a_E	Factor to account for rate effects during cone penetration
A_G	Plan area of pile group
A_r	Area ratio of pipe piles
$A_{r,eff}$	Effective area ratio of pipe piles
a_u	Adhesion factor
B'	Effective footing width
B_q	Normalised pore pressure parameter from CPT tests
C_C	CPT correction factor for overburden stress
C_c	Compression index
C_N	SPT blow count correction factor for overburden stress
C_r	Recompression index
c_v	Coefficient of consolidation
C_α	Creep coefficient
D_{50}	Median grain size
D_e	Equivalent pier diameter
det	Determinant of a matrix
D_f	Embedment depth of shallow footings
D_r	Relative density of coarse-grained soils
e	Void ratio
e_h	Elevation of lateral load resultant
E'	Drained Young's modulus
e_b	Eccentricity along the footing width
E_b	Young's modulus of rockmass below the toe of socketed or end bearing piles
e_l	Eccentricity along the footing length
e_{max}	Maximum void ratio
e_{min}	Minimum void ratio
E_p	Young's modulus of pile material

E_r	Young's modulus of rockmass along the socket of socketed piles
E_s	Young's modulus of soil
E_t	Young's modulus of rockmass/soil along the recessed section of socketed piles
E_u	Undrained Young's modulus
F_R	Friction ratio from the interpretation of CPT tests
F_r	Normalised sleeve friction resistance from CPT tests
f_s	Sleeve friction resistance measured during CPT tests
f_{sf}	Skin friction resistance of piles subjected to compressive loads, carrying units of stress
$f_{sf,t}$	Skin friction resistance of piles subjected to tensile loads, carrying units of stress
g	Gravity coefficient
G	Shear modulus
G_0	Small-strain shear modulus
G_s	Specific gravity
h	Hydraulic head
H_f	Collapse load or ultimate geotechnical strength of a laterally loaded pile
H_w	Serviceability lateral load acting on a pile
i	Hydraulic gradient
I_B	Modified soil Behaviour Type index
I_b	Pile head stiffness factor for end bearing single piles
I_c	Soil Behaviour Type index
I_d	Design settlement influence factor for socketed piles
I_r	Rigidity index
I_s	Settlement factor for single friction piles
k	Soil permeability
K	Bulk modulus
K_0	Earth pressure coefficient at-rest
K_A	Active earth pressure coefficient
k_c	Bearing capacity factor used in the LCPC method to estimate the end bearing resistance of piles from CPT data
K_D	Horizontal stress index from DMT tests
K_f/K_c	Loading factor to account for the reduction in the normal stress acting at the soil-pile interface
K_h	Coefficient of subgrade reaction of laterally loaded piles

K_{hh}	Swaying component of pile head stiffness
K_{hr}, K_{rh}	Swaying-rocking component of pile head stiffness
K_p	Relative pile material stiffness
K_P	Passive earth pressure coefficient
K_{rr}	Rocking component of pile head stiffness
K_s	Punching shear resistance coefficient
K_{sr}	Punching shear coefficient
K_{Su}	Conversion factor for estimating the bearing capacity of shallow foundations on fine-grained soils from CPT data
K_φ	Conversion factor for estimating the bearing capacity of shallow foundations on coarse-grained soils from CPT data
L'	Effective footing length
L_e	Recess length of a socketed pile
L_p	Length of soil plug
M	Pile bending moment
M_{cs}	Inclination of the critical state line in the p'–q space
M_{max}	Maximum bending moment along the length of a pile
m_v	Coefficient of volume compressibility
M_w	Serviceability moment acting on pile head
M_y	Yield bending moment of pile section
n	Porosity
N	SPT number of blow counts
N^*_{cp}	Bearing capacity factor for drilled shafts in undrained soil (α-Method)
N' or N_1	Number of SPT blow counts corrected for overburden stress
N'_{60}	SPT number of blow counts for 60% hammer efficiency, corrected for overburden stress
N_{60}	SPT number of blow counts for 60% hammer efficiency
N_{70}	SPT number of blow counts for standard 70% hammer efficiency
N_c	Bearing capacity factor for footings on drained soil
N_{cp}	Bearing capacity factor for driven piles in undrained soil (α-Method)
N_{cu}	Bearing capacity factor for footings on undrained soil
n_g	Pile group efficiency
N_{kt}	Cone factor
N_q	Bearing capacity factor for footings on drained soil

N_{qp}	Bearing capacity factor for piles in drained soil (β-Method)
N_u	Alternative cone factor
N_γ	Bearing capacity factor for footings on drained soil
N_γ^*	Modified bearing capacity factor for footings on layered sand
N_φ	Bearing capacity factor for piles in rock
OCR	Overconsolidation ratio
p	Reaction from soil to lateral loading of a pile
p'	Mean effective stress
p_a	Atmospheric pressure
p_f	Ultimate soil reaction to lateral loading of pile
PI	Plasticity Index
q	Net bearing capacity, not accounting for the contribution of overburden soil, carrying units of stress
Q_b	End bearing resistance of piles, carrying units of force
q_b	End bearing stress at pile toe, at the ultimate limit state
q_{bf}	End-bearing resistance of piles, carrying units of stress
Q_{bw}	Serviceability load transferred to the pile toe
q_c	Cone resistance measured during CPT tests
Q_{ext}	External force applied on soil surface, carrying units of force
q_{ext}	External pressure applied on soil surface, carrying units of stress
q_f	Bearing capacity, or ultimate geotechnical strength in compression, carrying units of stress
Q_f	Collapse load, or ultimate geotechnical strength in compression, carrying units of force
$Q_{f,group}$	Collapse load or ultimate geotechnical strength of a group of piles subjected to axial compressive load, carrying units of force
$Q_{f,t}$	Collapse load, or ultimate geotechnical strength of piles in tension. carrying units of force
$Q_{f,test}$	Collapse load or ultimate geotechnical strength measured *in situ*
Q_{nf}	Negative skin friction resistance of piles, carrying units of force
q_s	Overburden pressure for shallow foundations, carrying units of stress
Q_{sf}	Skin friction resistance of piles subjected to compressive loads, carrying units of force
$Q_{sf,t}$	Skin friction resistance of piles subjected to tensile loads, carrying units of force
Q_{sfw}	Serviceability load transferred to the pile shaft, carrying units of force
q_t	Corrected cone resistance for pore pressure effects
Q_t	Dimensionless cone resistance

Q_{tn}	Normalised cone resistance
Q_{ult}	Design axial compressive load for piles socketed in rock, carrying units of force
Q_w	Serviceability load, carrying units of force
$Q_{w,group}$	Axial compressive load acting on the cap of a group of piles under serviceability conditions, carrying units of force
R_s	Factor for calculating settlement of a pile group connected with a rigid cap
R_{ug}	Ultimate geotechnical strength
s	Pile spacing
S^*	Design (factored) action load at the Ultimate Limit State
S_r	Degree of saturation
S_t	Soil sensitivity
S_u	Undrained shear strength of fine-grained soils
T_v	Time factor
U	Average degree of consolidation
u_0	Hydrostatic pore pressure
u_2	Pore water pressure measured during CPT tests
$u_{y,f}$	Pile head displacement required to mobilise the end-bearing resistance of the pile
V	Pile shear force
v'	Drained Poisson's ratio
v_p	Poisson's ratio of pile material
V_s	Volume of solids
V_S	Shear wave velocity
v_s	Soil Poisson's ratio
v_u	Undrained Poisson's ratio
V_v	Volume of voids
V_w	Volume of water
w	Water content or moisture content
W_p	Weight of pile
W_s	Weight of solids
W_w	Weight of water
y	Pile deflection
$y(0)$	Pile head deflection
α	Coefficient for calculating the skin friction resistance with LCPC CPT-based method

α'	Correction factor for calculating the skin friction resistance with Schmertmann's CPT-based method
α_i	Pile group interaction factor
β	Factor for calculating the skin friction resistance of piles with the β-Method
$\beta_{g,l}$	Reduction factor to account for pile group effects under lateral loading – leading in line pile
$\beta_{g,s}$	Reduction factor to account for pile group effects under lateral loading – side-by-side pile
$\beta_{g,sk}$	Reduction factor to account for pile group effects under lateral loading – skewed pile
$\beta_{g,t}$	Reduction factor to account for pile group effects under lateral loading – trailing in line pile
γ	Unit weight or bulk unit weight of soil
γ_{ij}	Shear strain
γ'	Effective or submerged unit weight of soil
γ_d	Dry unit weight of soil
γ_{sat}	Saturated unit weight of soil
γ_w	Unit weight of water
Δu	Excess pore pressure
ΔI_{vy}	Logarithm of clay sensitivity
$\Delta\sigma$	Total normal stress increments in soil, due to the application of external loadings
$\Delta\tau$	Shear stress increments in soil, due to the application of external loadings
ε	Normal strain
ε_{50}	Characteristic strain i.e., the strain corresponding to deviatoric stress equal to half the deviatoric stress at failure
ε_{vol}	Volumetric strain
κ	Alternative symbol for the recompression index (approximate)
λ	Alternative symbol for the compression index
λ_v	Correction factor for undrained shear strength measured from vane shear tests to account for rate effects
ν	Specific volume
ρ	Mass density or bulk mass density of soil
ρ_d	Dry mass density of soil
ρ_e	Immediate (elastic) settlement of shallow foundations and piles
ρ_{pc}	Primary consolidation settlement of shallow foundations and earthworks
ρ_s	Elastic pile shortening
ρ_{sat}	Saturated mass density of soil

ρ_{sc}	Secondary compression settlement or creep of shallow foundations and earthworks
ρ_w	Mass density of water
σ	Total normal stress
σ'	Effective stress
σ'_0	Effective geostatic stress
σ'_c	Preconsolidation stress
σ'_{hf}	Normal effective stress acting at the soil-pile interface when the collapse load of the pile is reached
σ_0	Total geostatic stress
σ_1	Major principal stress
σ_2	Intermediate principal stress
σ_3	Minor principal stress
σ_C	Confining stress
σ_c	Unconfined compressive strength of rockmass
σ_y	Design yield strength of pile material
τ_d	Characteristic side shear resistance at shaft-rock interface of socketed piles
φ'	Effective friction angle
φ_{cs}	Critical state friction angle
φ_g	Geotechnical strength reduction factor for shallow foundations, and for pile foundations when results of pile load tests are available
φ_{gb}	Basic geotechnical strength reduction factor for pile foundations
$\varphi_{gb}Q_f$	Design (factored) capacity of pile foundations
φ_gQ_f	Design (factored) capacity of shallow foundations
φ_i	Soil-pile interface friction angle
$\varphi_{i,cs}$	Constant volume interface friction angle
$\varphi_{i,f}$	Interface friction angle at failure
ψ	Dilation angle
ψ_t	Reduction factor for skin friction resistance due to Poisson effect
$\omega(0)$	Pile head rotation

VERSION HISTORY

This page provides a record of changes made to this textbook. Each set of edits is acknowledged with a 0.01 increase in the version number. The exported files for this toolkit reflect the most recent version.

If you find an error, please contact george.kouretzis@newcastle.edu.au.

Version	Date	Change	Details
1.01	July 2025	Published.	
1.02			